UNIVERSITY OF SOUTHAMPTON

The Accretion and Obscured Growth of Supermassive Black Holes

by

Peter G. Boorman

A thesis submitted in partial fulfillment for the degree of Doctor of Philosophy

in the

Faculty of Engineering and Physical Sciences

Department of Physics and Astronomy

June 2019

UNIVERSITY OF SOUTHAMPTON

Abstract

Faculty of Engineering and Physical Sciences
Department of Physics and Astronomy

Doctor of Philosophy

by Peter G. Boorman

It is widely accepted that black holes at the centres of galaxies grow to become 'super'massive through the process of accretion, though the exact mechanism by which black holes evolve across cosmic time is still poorly understood. Sensitive X-ray observations have enabled studies of the closest regions to growing supermassive black holes (aka Active Galactic Nuclei - AGN), and have revealed the majority are obscured by gas. Unfortunately though, the most obscured AGN are typically too enshrouded in thick gas to be detected in wide-field X-ray surveys. This has led to estimates of the fraction of heavily obscured AGN relative to the total population varying drastically between $\sim 20-70\%$, yet a determination of this fraction is essential to understand the evolution and demographics of all supermassive black holes.

The first study presented in this thesis creates a basis for robustly probing extreme obscuration of accreting supermassive black holes. This was done with sensitive high-energy X-ray observations from the NASA *NuSTAR* observatory, in combination with broadband optical and infrared multi-wavelength diagnostics.

The next step was to consider what coeval properties AGN obscuration has with the central supermassive black hole, and whether or not extreme obscuration can in some way be regulated by the central engine. This project was able to provide tentative evidence of an anti-correlation between intrinsic AGN luminosity and obscuration reprocessing, (the Compton-thick Iwasawa-Taniguchi effect) which potentially holds implications for future large surveys of AGN if the effect is not taken into account.

There exists a known bias against the most obscured AGN, even in our very most local volume. However, an understanding of the distribution of AGN obscuration is essential for constraining the cosmic origin of the Cosmic X-ray Background. For this reason, the final chapter presents the *NuSTAR* Local AGN $N_{\rm H}$ Distribution Survey (NuLANDS) – one of the largest legacy surveys of AGN currently underway with the X-ray space telescopes *NuSTAR*, *XMM*-Newton and *Neil Gehrels Swift Observatory* (>4 million seconds of total exposure), which is aimed at finding the elusive Compton-thick AGN population. Via multiwavelength techniques, NuLANDS is targeting AGN representatively of the underlying population, and has thus already led to the discovery and classification of multiple heavily obscured AGN previously hidden at X-ray wavelengths. The initial results from the survey indicate that $\geq 30\%$ of all AGN in the local Universe are heavily obscured, and that high-energy X-ray selection alone preferentially selects less-obscured AGN. As such, NuLANDS marks a major step in completing the local census of supermassive black hole growth, and will pave the way in quantifying the true distribution of obscured accretion in the local Universe.

"Thunderclouds' Enlightening, very very frightening."

Adapted from Freddie Mercury

Contents

List of Figures

List of Tables

Declaration of Authorship

I, Peter G. Boorman, declare that this thesis titled, 'The Accretion and Obscured Growth of Supermassive Black Holes' and the work presented in it are my own. I confirm that:

- This work was done wholly or mainly while in candidature for a research degree at this University.
- Where any part of this thesis has previously been submitted for a degree or any other qualification at this University or any other institution, this has been clearly stated.
- Where I have consulted the published work of others, this is always clearly attributed.
- Where I have quoted from the work of others, the source is always given. With the exception of such quotations, this thesis is entirely my own work.
- I have acknowledged all main sources of help.
- Where the thesis is based on work done by myself jointly with others, I have made clear exactly what was done by others and what I have contributed myself.

Signed: _____

Date: _____

Acknowledgements

First and foremost, I would like to thank my supervisor – Poshak Gandhi – for giving me this incredible opportunity 3.5 years ago, and for teaching me that nothing is incomprehensible if you give it enough time to comprehend. Thinking back, I must have knocked on his door an average of three to four times a day for the entirety of my Ph.D., and I am extremely grateful for the patience and thoroughness with which he always took time to answer my questions, worries and troubles. I am equally grateful to my second supervisor – Sebastian Hönig – for finding the time to explain the mundane as well as the complicated questions with an equal level of humility (and of course for the running tips!). These thanks extend to: Dr. Matt Middleton (aka my third supervisor), Dr. Diego Altamirano, Dr. Caitriona Jackman, Professor Christian Knigge, Dr. Francesco Shankar, Professor Tony Bird and Professor Mark Sullivan – your help and wisdom have enabled me to gain multiple skills that are priceless for my future. I would also like to thank Professor Fiona Harrison, Dr. Dan Stern, Dr. Claudio Ricci and Dr. Franz Bauer for hosting me at their institutions for extended periods throughout my studies (also to Claudio for answering my many many questions!).

I also thank countless current and previous members of the Southampton astronomy group for their support and countless advice, including (but not limited to): Dr. Mathew Smith (for always having the time to help no matter what), Dr. James Matthews, Dr. Chris Frohmaier, Dr. Rebecca French, Dr. Daniel Asmus, Dr. Johannes Buchner, Dr. Mislav Baloković, Dr. George Lansbury, Dr. Aru Beri (for X-ray analysis expertise paralleled with delicious recipe ideas), Dr. Mayukh Pahari, Dr. Aarran Shaw, Dr. Rob Firth, Dr. Sam Connolly, Dominic Ashton, Michael Johnson, Dr. Phil Wiseman, Dr. Adam Hill, Dr. Jamie Court, Dr. David Williamson, Dr. Jade Reidy, Dr. Andy Smith and Dr. Steve Browett. You have all truly helped more than you could possibly imagine.

I would like to thank my friends and family for your unwavering support throughout the process. Alex and Nikki – thank you for telling me how it is, and letting me realise the important things. To Charlotte – thank you for the countless adventures, 'crazy' runs, baking sessions, epic meal times, TV time and silly animal videos. You changed my life, and I will never forget any of it.

Finally, I thank my mother and father for their unconditional support throughout the entire Ph.D. process. To my father for believing in me, especially when I struggled to myself. To my mother – you do too much for me to list, but please know that I could not have done this without you.

This work was made possible by financial support from the Science and Technology Facility Council (STFC) and the Royal Astronomical Society (RAS).

Dedicated to my late Grandmother, Patricia Eula Potton, who was always there to remind me – "You've got a tongue in your head... So use it!"

–

"If ever there is tomorrow
when we're not together...
there is something you must always remember
You are braver than you believe, stronger than you seem and smarter than you think
But the most important thing is,
even if we're apart...
I'll always be with you."

– A.A.Milne

Chapter 1

Introduction

"You can't make an omelette without cracking some eggs."
– Mum

1.1 Thesis Aims and Open Questions

This thesis aims to answer some of the unsolved questions associated with obscured accretion. Such key open questions are:

1. What is the geometry and nature of the obscuring region?
2. What are the requirements for resolving degeneracies in this obscuration model parameter space?
3. What is the effect of intrinsic luminosity on the enshrouding obscuration surrounding Compton-thick AGN?
4. What do large AGN censuses tell us about the distribution of obscuration amongst the AGN population?

Addressing these questions now is timely due to the availability of new tools such as *NuSTAR* – the first instrument capable of true high-energy X-ray focusing above 10 keV. In the remainder of this chapter, I overview the key motivation for studying obscured AGN, as well as the tools I use in thesis to do so. Each chapter that follows the introduction addresses these open questions as follows. In Chapter 2, I address questions 1 & 2 by presenting a detailed spectral analysis of a robust Compton-thick AGN candidate, selected from previous works via multi-wavelength indicators and lower-sensitivity

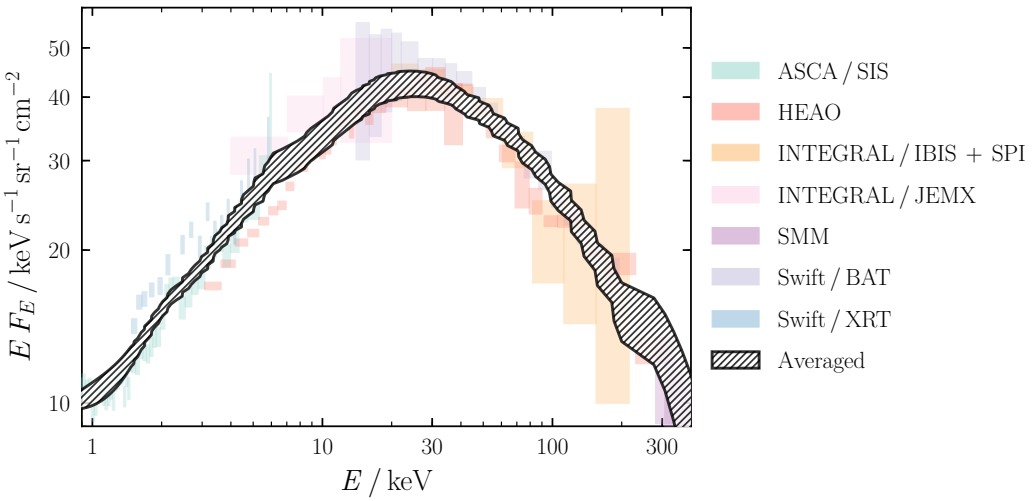

FIGURE 1.1: The broadband observed spectrum of the CXB radiation. Data provided by R. Gilli.

X-ray data below 10 keV. I test multiple obscurer geometries to establish the true intrinsic power of the source, as well as the nature of its obscurer from the X-ray regime. Chapter 3 then focusses on question 3, with a study of reprocessing vs. luminosity for a sample of heavily obscured AGN, over a wide redshift range. This work identified a tentative relation that is not compatible with the accepted schematic of heavily obscured AGN, potentially requiring an update to current X-ray models. Chapters 4 & 5 then address the final question with a large legacy survey of AGN, designed to be representative of the circumnuclear obscuration in AGN, critically incorporating extremely obscured sources. I then summarise my findings, and give an outlook for the future of obscured AGN studies in Chapter 6.

1.2 The Cosmic X-ray Background

The discovery of the diffuse isotropic Cosmic X-ray Background radiation (CXB; Giacconi *et al.* 1962) pre-dates that of the higher-intensity Cosmic Microwave Background (Penzias and Wilson 1965). However, the *origin* of the CXB was debated for decades after its discovery, and started the entire field of X-ray astronomy as a whole. The CXB spectrum encompasses approximately three orders of magnitude in energy – $E \sim 0.1$–300 keV, and exhibits a broad peak at ~ 30 keV – see Figure 1.1.

Two conflicting theories were proposed to explain the isotropic nature of the X-ray Background: a truly diffuse intergalactic hot gas, or the integrated (and unresolved) emission from a large number of isotropically distributed point sources. The former was proposed due to the similarity between the spectrum of the X-ray Background, and that of a hot plasma with temperature of $\sim 5 \times 10^8$ K – see Figure 1.2. Furthermore, early surveys

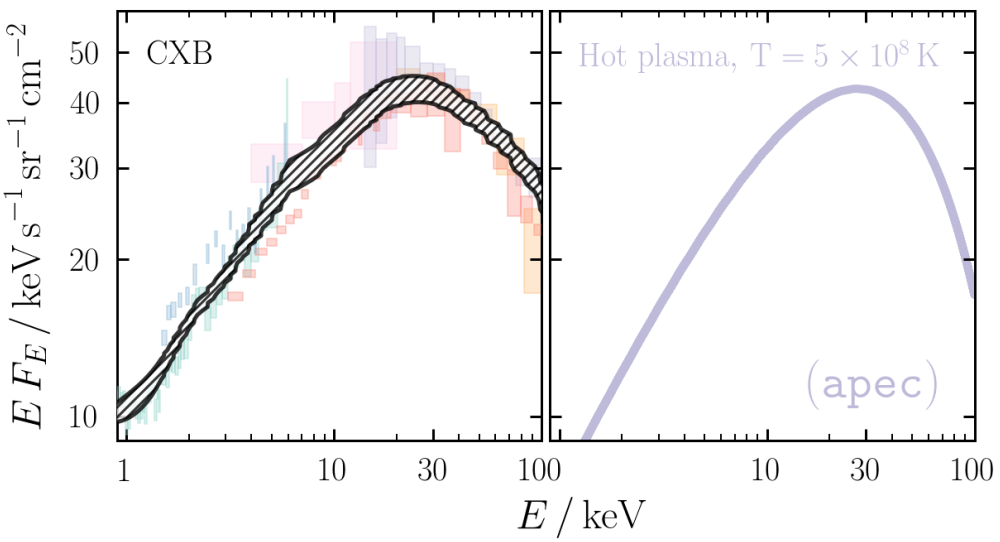

FIGURE 1.2: The CXB spectral shape compared to the spectrum of a hot collisionally ionised plasma.

proving the isotropy of the X-ray Background (e.g., with *Uhuru*; Giacconi *et al.* 1974 & *Ariel V*; McHardy *et al.* 1981) implied that the number of discrete sources had to be very large for the latter hypothesis to be true. However, the possibility of a hot diffuse plasma uniformly filling the Universe was ruled out by Mather *et al.* (1994) with the *COBE* satellite. The authors found very little distortion of the Cosmic Microwave Background that was required from scattering by hot electrons that would occupy such a hot plasma. This stringently confirmed that the CXB must have originated as the summed emission from faint discrete X-ray sources across cosmic time. Multiple surveys with X-ray satellites have now resolved varying fractions of the soft CXB spectrum, finding the vast majority of sources to be accreting supermassive black holes (e.g., Mushotzky *et al.* 2000; Lehmer *et al.* 2012; Harrison *et al.* 2015; Luo *et al.* 2017 – see Section 1.6.1 for more information).

1.3 Active Galactic Nuclei & Seyfert Galaxies

Ever since the first optical spectra of galaxies were taken, certain sources were seen to exhibit unusually strong emission and absorption lines from their cores (e.g., Fath 1909; Slipher 1917; Hubble 1926), though their numbers were relatively low. Due to this level of activity in their centers, such galaxies were named Active Galactic Nuclei (AGN). Seyfert (1943) was the first to study a sample of 7 AGN featuring high-excitation nuclear emission lines, revealing a diverse collection of spectra, in which some galaxies had very strong narrow permitted and forbidden lines (e.g., NGC 1068), whilst others were observed with very strong broad permitted emission lines (e.g., NGC 4051). Due to

his pioneering work, these galaxies were names Seyfert galaxies – a name that is still used today to describe active galaxies with typical bolometric luminosities $10^{42} \lesssim L_{\rm Bol} \,/\, {\rm erg\,s^{-1}} \lesssim 10^{45}$.

Although optical astronomy established the broad study of AGN, radio astronomy was responsible for a wide array of vital advancements since the 20th century. For example, dedicated radio surveys (e.g., Cambridge; Edge *et al.* (1959)) discovered a large number of bright point-like, 'quasi-stellar radio sources', or *quasars*. The coincidence of these sources with very bright high redshift 'quasi stellar objects' (QSOs) in the optical waveband (e.g., 3C 273; Schmidt 1963) led to the discovery that QSOs were extremely bright AGN, typically outshining the entire host galaxy completely with $L_{\rm Bol} \,/\, {\rm erg\,s^{-1}} \gtrsim 10^{45}$.

1.3.1 Seyfert Galaxies

Khachikian and Weedman (1974) were the first to sort AGN into two specific groups based on their optical spectral properties. Out of a total of 71 Seyfert galaxies, the authors reported that the observed differences in spectra could be broadly categorised into two types:

Type 2 Display forbidden atomic emission lines, as well as permitted Balmer lines, with the latter having width approximately $500 - 1000\,{\rm km\,s^{-1}}$. Non-active galaxies typically have Balmer widths of $\lesssim 200\,{\rm km\,s^{-1}}$.

Type 1 Display forbidden and permitted lines, just as Type 2 objects, but with the Balmer lines displaying widths of several $1000\,{\rm km\,s^{-1}}$.

Osterbrock (1981) then segregating AGN further into intermediate classes of Seyfert Types 1.2, 1.5, 1.8 & 1.9 based on the relative strength of broad and narrow lines. In addition to these intermediate Seyfert classes, there are also Narrow Line Seyfert 1 galaxies (Osterbrock and Pogge 1985), with the observed properties of Seyfert 1 galaxies, though with unusually narrow Balmer lines, as well as strong Fe II emission. There are a number of additional AGN classes outside of those for Seyfert galaxies, as shown in Figure 1.3. Seyfert galaxies often also display significant ultraviolet excesses commonly referred to as the 'big blue bump'. Such an excess has been attributed to the emission from hot stars (likely the case for Seyfert 2 galaxies), or from an accretion disc (as suggested for Seyfert 1 galaxies). However, the observed high luminosities across the full electromagnetic spectrum (i.e. infrared, optical, ultraviolet and X-ray) indicate that stars cannot be a major contributor to the emission observed in AGN.

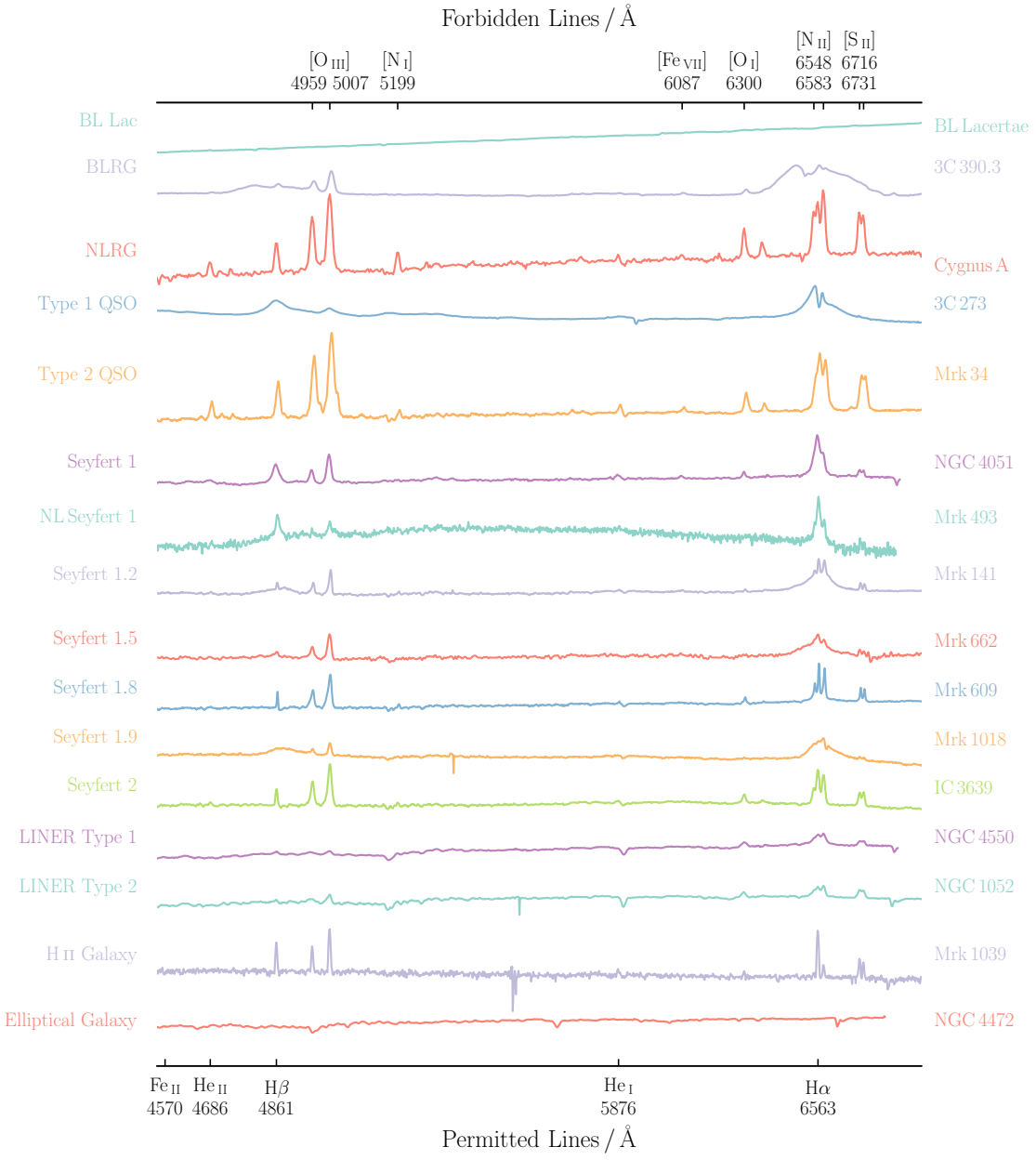

FIGURE 1.3: Compilation of different types of AGN optical spectra. From top to bottom: Featureless continuum of BL Lacertae, Broad Line Radio Galaxy, Narrow Line Radio Galaxy, Type 1 QSO, Type 2 QSO, Seyfert 1, Narrow Line Seyfert 1, Seyfert 1.2, Seyfert 1.5, Seyfert 1.8, Seyfert 1.9, Seyfert 2, Low Ionisation Nuclear Emission Region (LINER) Type 1, LINER Type 2, H II (star-forming) galaxy and elliptical galaxy.

Antonucci (1984) was one of the first pieces of evidence for Seyfert 1s and 2s sharing a common progenitor. The authors detected broad Balmer emission lines in the polarised optical spectrum of NGC 1068, which was direct evidence that Seyfert 2 galaxies hosted an emission region just like Seyfert 1s capable of producing broad emission lines (the Broad Line Region). However, in these systems the BLR was likely obscured along our line of sight by an obscuring structure, beginning the *unified model* of AGN.

1.3.2 The Power Source of an AGN

It is now widely accepted that supermassive black holes reside at the centers of almost all galaxies in the Universe (e.g., Fabian (2012); Event Horizon Telescope Collaboration *et al.* (2019), Figure 1.4). The process of accretion onto a supermassive black hole releases gravitational potential energy in the most efficient manner of any known physical process in the Universe. As matter falls into the potential well of the compact object, the simplest models involve the generation of an accretion disc that efficiently radiates the gravitational potential energy released.

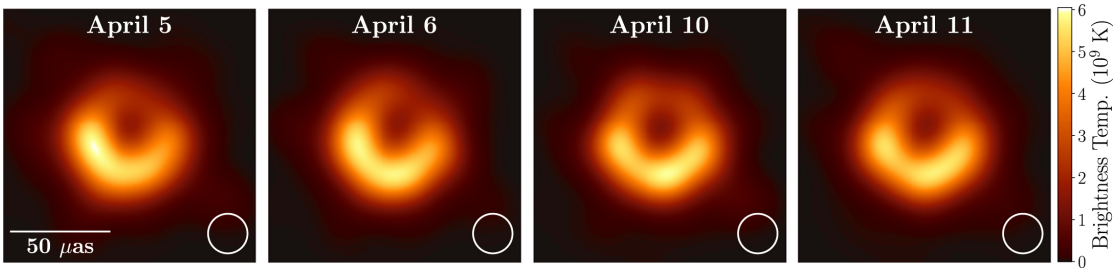

FIGURE 1.4: *Credit: Event Horizon Telescope Collaboration* et al. *(2019)* The first images produced of a black hole captured by the Event Horizon Telescope. The source is the active supermassive black hole in M 87. The material being accreted can be seen as well as the boundary to which light cannot escape the gravitational well of the black hole.

The gravitational energy released, ΔE from the accretion of a packet of mass, Δm onto a black hole of mass M and radius R is given by:

$$\Delta E = \frac{GM\Delta m}{R} \tag{1.1}$$

The total luminosity (energy emitted per unit time interval) produced is then given by:

$$L = \frac{GM\dot{M}}{R} = \eta \dot{M} c^2 \tag{1.2}$$

where $\dot{M}$ is the mass accretion rate, and η is the efficiency of the process. By re-arranging Equation 1.2, we see that $\eta \propto M/R$ – known as the *compactness* of the central object. The accretion rate required to power and AGN is then given by:

$$\dot{M} = \frac{L}{\eta c^2} \approx 1.8 \times 10^{-3} \left(\frac{L_{44}}{\eta}\right) M_\odot \, \mathrm{yr}^{-1} \tag{1.3}$$

This equation means that the amount of energy generated by converting gravitational potential energy into radiation via accretion relies on how large the efficiency η can become. The Schwarzschild radius is the event horizon for a static black hole[1], and can be used as a characteristic size scale for the compact object. Thus the energy released from the accretion of a packet of mass to within a few Schwarzschild radii of the accreting black hole gives an efficiency of $\eta \sim 0.1$ (Peterson 1997). The proton-proton chain associated with nuclear fusion[2] results in an energy conversion efficiency of just $\eta \sim 0.007$ – an order of magnitude less efficient than accretion onto a black hole. If we substitute $\eta = 0.1$ into Equation 1.3, for a bright quasar with luminosity $L_{\mathrm{QSO}} = 10^{46} \, \mathrm{erg \, s^{-1}}$, the accretion rate is $\dot{M} \sim 2 \, M_\odot \, \mathrm{yr}^{-1}$. The efficiency is theoretically predicted to increase with the spin of the black hole, since the last stable circular orbit is closer in for the rotating case.

If matter being accreted possesses some net angular momentum, any individual colliding particles will always conserve angular momentum as a whole, such that a steady-state accretion disc will form. For a packet of mass to fall onto the compact object requires a net loss of angular momentum. Thus if the entire accretion disc is to maintain a constant total angular momentum, some angular momentum must be transported outwards. A common method invoked to do this is the Rotational Instability (Balbus and Hawley 1991, MRI), in which a weak magnetic field is capable of inducing a strong shearing instability that can lead to a transport of angular momentum outwards, and allowing the accretion of material.

1.3.3 The Unified Model of AGN

The unified model of AGN aims to consolidate the diverse observed zoo of active galaxies as intrinsically an accreting supermassive black hole, with observed properties largely due to an orientation effect relative to anisotropic dusty obscurer, originally thought to be oriented as a smooth 'torus' (e.g., Antonucci 1993; Urry and Padovani 1995; Netzer 2015, see Fig 1.5). The model incorporates the aforementioned Seyfert galaxies and quasars, as well as radio galaxies and Low Ionisation Nuclear Emission Region sources (LINERs

[1] Given by $R_{\mathrm{S}} = \frac{2GM}{c^2}$.

[2] In which two protons are fused to produce a helium nucleus.

– Heckman 1980; Balmaverde and Capetti 2015), which are often likely the low-activity analogues of Seyfert galaxies.

The broad concept is that all AGN are supermassive black holes accreting matter from an accretion disc, spanning distances down to the last stable orbital radius of the black hole (e.g., Shakura and Sunyaev 1973). The emission peaks in the ultraviolet and optical wavelength ranges, providing a possible explanation for the big blue bump (e.g., Elvis *et al.* 1994). Close to the accretion disc, clouds of ionised gas orbit with large velocities, giving rise to the observed broad emission lines from the Broad Line Region. Further out on scales of $\sim$10–1000 pc, cooler clouds with slower orbital velocities give rise to the narrow emission lines from the Narrow Line Region (Capetti *et al.* 1996).

Polarisation observations of Type 1 and 2 AGN can be explained if the central engine is surrounded by an anisotropic torus of dust, additionally responsible for the collimation of the AGN radiation giving rise to the bi-conical shape of Narrow Line Regions, known as ionisation cones. Various techniques have been able to constrain the size of the toroidal structure to 0.1 – 10 pc in size (e.g., mid-infrared imaging – Packham *et al.* 2005, mid-infrared interferometry – Burtscher *et al.* 2013 and sub-mm – García-Burillo *et al.* 2016). However, these and many other observations suggest that the dust is more likely found in geometrically and optically thick clouds (e.g., Krolik and Begelman 1988; Stalevski *et al.* 2017; Hönig and Kishimoto 2017).

Extremely close to the vicinity of the black hole, a compact corona of hot electrons (with currently unknown geometry) Compton upscatter the ultraviolet accretion disc photons into the X-ray regime, giving rise to the intrinsic X-ray emission of AGN (e.g., Zoghbi *et al.* 2012). In addition to a dusty obscurer restricting the observation of the Broad Line Region, the central X-ray corona can be dramatically obscured by neutral absorption, often parameterised in terms of the equivalent line-of-sight column density ($N_{\rm H}$). Multiple works have found good agreement between optical spectral obscuration classification (arising from dust obscuring the Broad Line Region) and X-ray spectral classifications, (arising from gas obscuring the corona), with e.g., Koss *et al.* (2017) finding $\sim$94% of Type 2 Seyferts with $\log N_{\rm H}\ /\,{\rm cm}^{-2} > 21.9$ from X-ray spectroscopy.

All AGN are expected to emit some level of radio emission, though the fraction of observed radio emission spans $\sim$5 orders of magnitude in total. Various studies have found that just $\sim$10% of the population are capable of launching large-scale collimated jets that emit large amounts of synchrotron emission, and are dubbed radio-loud AGN[3] (e.g., Begelman *et al.* 1984; Panessa *et al.* 2016). In contrast, by far the dominant population are radio-quiet AGN, in which the $\sim$1000 times fainter radio emission can arise from a wide range of possible origins (see Panessa *et al.* (2019) for a recent review). Analogous

[3]Radio-loud AGN are traditionally defined as having $R = f(4400\,\text{Å})/f(6\,\text{cm}) > 10$.

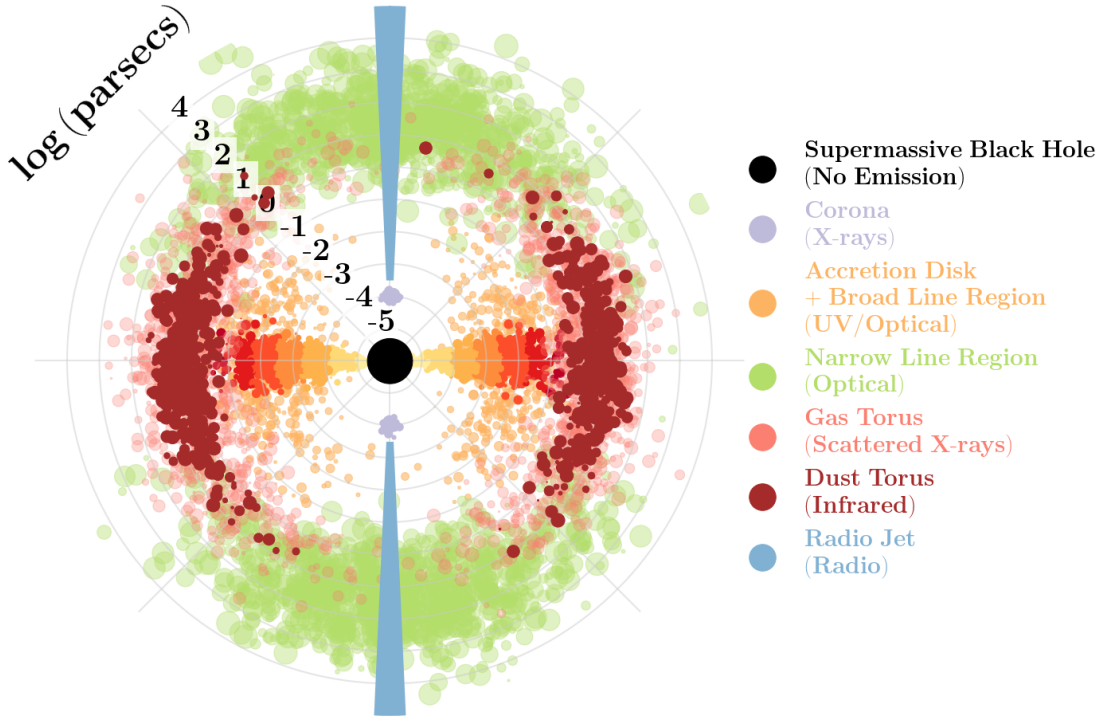

FIGURE 1.5: Schematic illustrating the unified model of AGN, essentially relying solely on the sight line of the observer relative to the central accretion disc.

to the unified model of radio-quiet AGN, Broad and Narrow Line Radio Galaxies are the equivalent of Seyfert 1 and 2 AGN. Furthermore, Optically Violent Variables (or BL Lacertae-like objects) are those in which the viewing angle is directly down the collimated jet. The simplified AGN schematic (adapted from Ramos Almeida and Ricci 2017) together with the broadband spectrum shown in the left and right panels of Figure 1.6, respectively, show the emission mechanisms described in this section.

1.3.4 Intrinsic (Unobscured) AGN X-ray Spectra

Compton-upscattered accretion disc photons from the corona forming the X-ray continuum emission of AGN typically takes the spectral form of a broadband powerlaw (Haardt and Maraschi 1991, 1993) with high-energy exponential cut-off around 300 keV[4] (Ballantyne 2014; Malizia *et al.* 2014; Fabian *et al.* 2015; Kamraj *et al.* 2018; Ricci *et al.* 2018). Furthermore, rapid variability of the continuum emission in unobscured AGN strongly indicates that the corona is very compact, of the order of 3–10 gravitational radii[5] (e.g., Fabian *et al.* 2009; Emmanoulopoulos *et al.* 2014).

[4]This corresponds to a coronal temperature of ~ 150 keV.

[5]The gravitational radius is defined as half the Schwarzschild radius – $R_{\rm G} = \frac{2{\rm G}M_{\rm BH}}{2c^2}$.

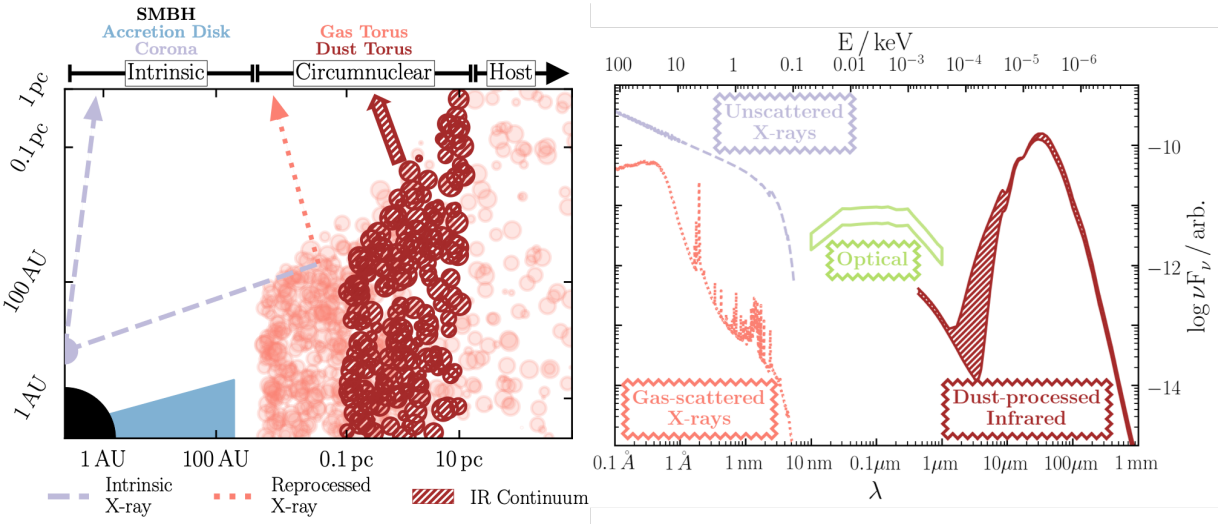

FIGURE 1.6: *Left:* Simplified schematic from Figure 1.5 (adapted from Ramos Almeida and Ricci (2017), showing the key emission regions. *Right:* Broadband X-ray spectrum corresponding to the emission shown on the left.

A portion of the X-ray flux emitted by the corona is reprocessed by the accretion disc, and re-emitted as secondary X-ray radiation (also referred to as reflected X-ray emission). The reflection spectrum from the accretion disc features two key components (Lightman and White 1988; Reynolds 1999):

1. A narrow[6] Fe Kα fluorescence emission line arising from neutral (and hence cold) iron, with a characteristic energy of 6.4 keV in the rest frame of the source. This emission line is typically the most prominent in the X-ray spectra of AGN, due to a combination of the fluorescence yield and relative cosmic abundances of the scattering medium.

2. An underlying (flat) Compton scattered continuum with a broad 'Compton hump' peaking at ~ 30 keV formed from the combination of photoelectric absorption at $E \lesssim 10$ keV and Compton downscattering from higher energies.

However, the accretion disc is likely not cold, such that the ionisation state of the reflecting material must be taken into account, known as the ionisation parameter, defined as $\xi = 4\,\pi\,F_x/n_e$ (García *et al.* 2013), where F_x is the net flux in the 1 – 1000 Ry (13.6 eV – 13.6 keV) energy region, and n_e is the electron number density in cm^{-2}. Figure 1.7 shows the effects of disc inclination (relative to the line of sight), powerlaw photon index, ionisation parameter and high-energy cut off on the emergent reflection spectrum with the XILLVER XSPEC table model (García *et al.* 2013). This model assumes X-ray

[6] I do not refer here to the relativistically broadened component of the iron line, generated by the extreme gravity of the central supermassive black hole.

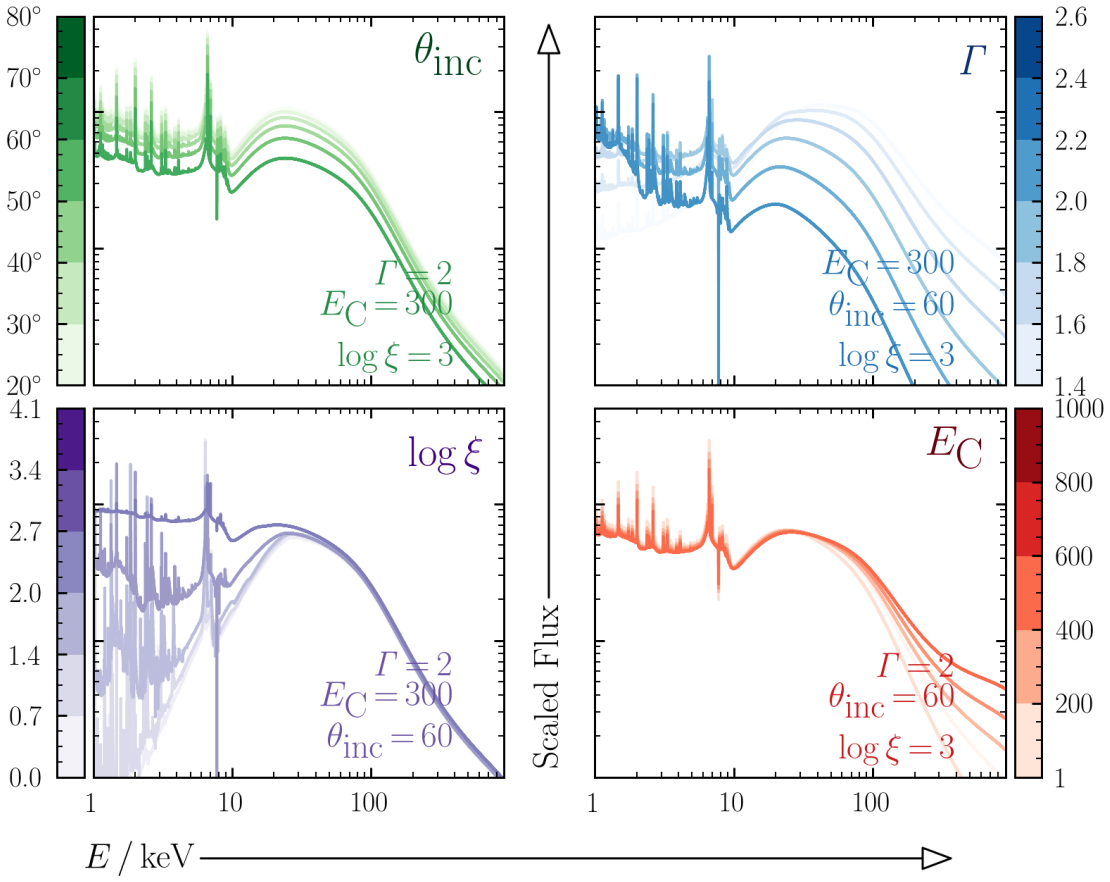

FIGURE 1.7: X-ray spectral simulations with the XILLVER XSPEC model, in which each panel shows the effect a given parameter has on the emergent spectrum. From upper left clockwise, the varying parameters are: slab inclination, intrinsic photon index, ionisation parameter and high-energy cut-off. The defaults of the other three parameters per simulation is shown in the lower right portion of each panel.

reprocessing from an infinitely wide slab of material[7], with the solid angle subtended by the reflecting material dependent on the reflection parameter, R.

1.3.5 Obscured AGN X-ray Spectra

Substantial evidence has now confirmed that the vast majority of AGN are obscured by gas with equivalent hydrogen column densities above the Galactic value (see Section 1.4 for more information on this statement). This gas obscuration acts to absorb and scatter the radiation via the photoelectric effect and Compton scattering, much as is found for non-relativistic accretion disc reflection (e.g., Matt *et al.* 2000). However, since the obscuration is assumed to lie far from the central engine for the vast majority of X-ray obscured AGN, the temperature of the obscuring material is often assumed to be lowly ionised or essentially neutral to zeroth order.

[7]This is very similar to the expected 'view' a compact corona situated above the accretion disc would see, due to the extreme size of the accretion disc relative to the corona.

In Figure 1.8, I show simulations with the `borus02` X-ray reprocessing model (Baloković *et al.* 2018). Since the X-ray obscuration is likely distributed in a vastly different structure than an infinitely thick and wide slab, this model assumes a point-source for the incident X-ray irradiation, that is reprocessed by a more physically realistic uniform-density 'torus' formed from a sphere with polar cutouts. In fact, for many physically-motivated X-ray reprocessing models, the geometrical configuration of the X-ray obscurer is often assumed to be axis-symmetric but anisotropic (Murphy and Yaqoob 2009; Ikeda *et al.* 2009; Brightman and Nandra 2011b), much has been invoked for dust distributions in infrared reprocessing models (e.g., Nenkova *et al.* 2008; Hönig and Kishimoto 2017). `borus02` produces the reprocessed emission, such that I also include an intrinsic cut-off powerlaw, as well as 'warm mirror' emission – i.e. the intrinsic powerlaw scattered through optically thin ionised gas in the polar regions – in the figure. As can be seen for the highest levels of $N_{\rm H}$, even the Compton hump starts to be diminished, since the Compton-scattered photons stand a relatively low chance of escape.

Using such models as `borus02` to model the strength and shape of the neutral Fe Kα fluorescence line together with the underlying Compton-scattered continuum (encompassing the flat $E < 10\,\mathrm{keV}$ continuum as well as the Compton hump at $\sim 30\,\mathrm{keV}$) can yield the line of sight obscuring column density to a source. Hence for robust and accurate estimates incorporating the full effects of photoelectric absorption, fluorescence and Compton scattering requires an observed X-ray spectrum with enough energy coverage to encompass all these features. However, many previous X-ray observations of AGN have typically been restricted to the $E \lesssim 10\,\mathrm{keV}$ energy region (e.g., *Suzaku*/XIS, *Chandra*, *XMM*-Newton), completely missing the Compton hump in AGN with redshift $z \lesssim 1$. Without the Compton hump, any attempt to fit AGN X-ray spectra in $E \lesssim 10\,\mathrm{keV}$ with the objective of constraining the line of sight $N_{\rm H}$ typically depends heavily on the Fe Kα fluorescence line alone, which can lead to ambiguous estimates, since the iron line can be effected by many factors in addition to the neutral X-ray obscurer.

1.4 AGN Selection of the Local AGN Population

There are a number of popular techniques in-place today to sample the local AGN population (i.e. where Malmquist biases ought to be minimal), each offering a unique insight that other wavelengths often cannot achieve. However, an optimal solution to understand the AGN population in a representative way of its obscuration requires methods that are not biased against a particular obscuration level. Thus optimum strategies for AGN selection by design incorporate several wavelength regimes together. Examples of optimal methodologies are included below.

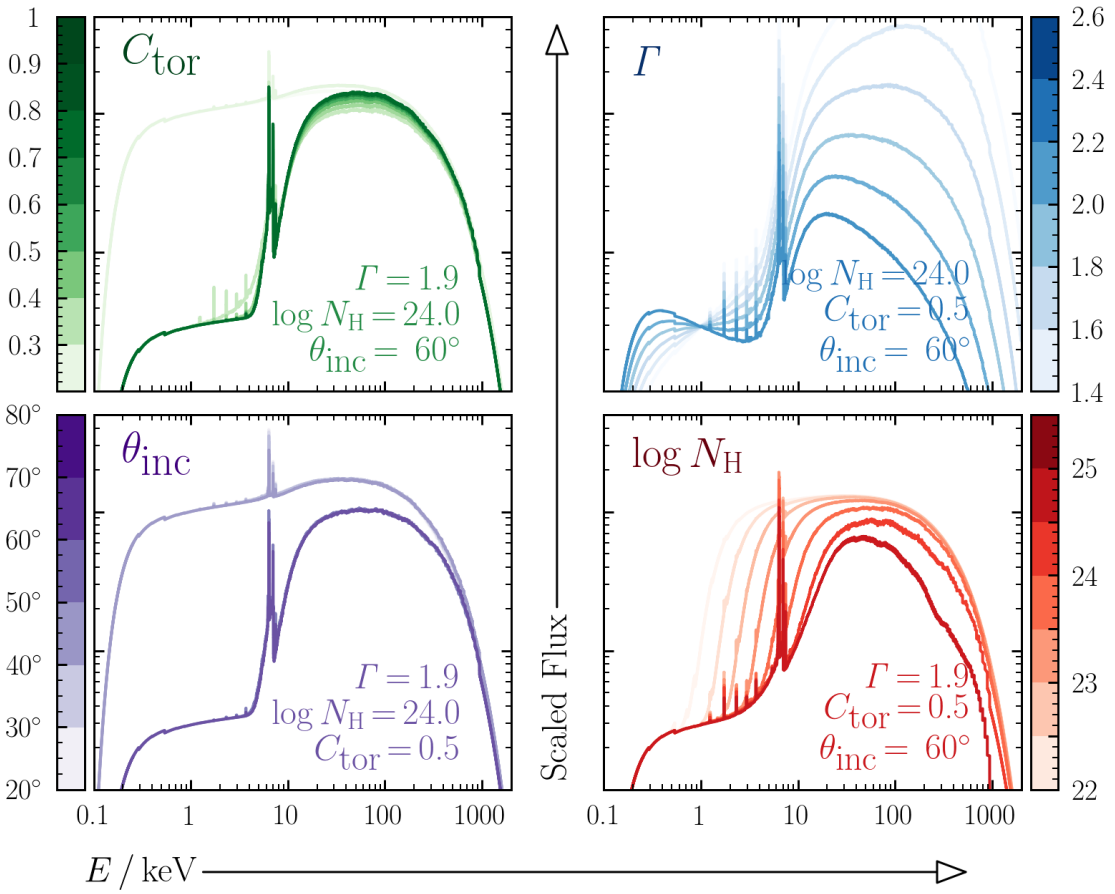

FIGURE 1.8: X-ray spectral simulations with the `borus02` XSPEC model, in which each panel shows the effect a given parameter has on the reprocessed spectrum. From upper left clockwise, the varying parameters are: torus covering fraction ($\equiv \cos\theta_{\rm oa}$), intrinsic photon index, viewing angle and line of sight hydrogen column density. The defaults of the other three parameters per simulation is shown in the lower right portion of each panel. Note for some inclination angles and covering fractions, the line of sight does not intercept the torus such that the emergent spectrum is only reprocessed by Galactic $N_{\rm H}$.

1.4.1 Flux-limited Hard X-ray Selection

Many studies have revealed that the vast majority of AGN are intrinsically obscured in X-rays with hydrogen column densities greater than the Galactic value ($N_{\rm H} \gtrsim 10^{22}\,{\rm cm}^{-2}$; Risaliti *et al.* 1999b; Burlon *et al.* 2011; Ricci *et al.* 2015; Koss *et al.* 2017). For $N_{\rm H} \lesssim 10^{24}\,{\rm cm}^{-2}$, the intrinsic power law typically dominates over any other spectral features in the X-ray band, since photons with $E > 10\,{\rm keV}$ can escape after one or more scatterings. As the column increases to $N_{\rm H} > 1.5 \times 10^{24}\,{\rm cm}^{-2}$, the obscuring material becomes optically thick in X-rays to Compton scattering, in the *Compton-thick* regime[8]. Here, the

[8]The definitive $N_{\rm H}$ column density threshold for the Compton-thick regime depends on additional factors such as elemental abundances (e.g., Section 2 of the MYTORUS manual, available at: `http://mytorus.com/mytorus-manual-v0p0.pdf`).

soft X-ray ($E \lesssim 10\,\mathrm{keV}$) spectrum is depleted and flattened due to the interplay of photoelectric absorption and Compton (down-) scattering (also see Figure 1.8, lower right panel). Depending on the orientation, geometry and column of the obscurer, the hard X-ray spectrum ($E \gtrsim 10\,\mathrm{keV}$) can either still be dominated by the direct intrinsic powerlaw component, absorbed along the line of sight (resulting in transmission-dominated Compton-thick AGN); or by a Compton-scattered reflection component, from intrinsic flux reprocessed by the obscurer into the line of sight (known as reflection-dominated Compton-thick AGN).

Absorption can occur over a broad range of host galaxy spatial scales, but the $\sim$parsec-scale obscuring torus of AGN unification schemes plays a key role in AGN classification (e.g., Antonucci 1993; Urry and Padovani 1995; Alexander and Hickox 2012; Brandt and Alexander 2015; Netzer 2015; Ramos Almeida and Ricci 2017). Hard X-ray observations are thus considered to be a very effective means to sample AGN populations, unbiased by *mild* obscuration with $\log N_{\mathrm{H}}\ /\,\mathrm{cm}^{-2} \lesssim 24$ (e.g., the *BeppoSAX* High-Energy Large Area Survey: Fiore *et al.* 1998, the *INTEGRAL* AGN sample: Malizia *et al.* 2009, the 70-month *Swift*/BAT Survey: Baumgartner *et al.* 2013). 'reflection-dominated' Compton-thick AGN however, are the most difficult population to detect in X-ray surveys (e.g., Matt *et al.* 2000; Comastri *et al.* 2015; Ricci *et al.* 2015). In fact, X-ray flux-limited surveys even in the very local Universe have been shown to be biased against Compton-thick AGN detection (e.g., Figure 3 of Ricci *et al.* 2015, Annuar et al., in prep.).

The incompleteness of hard X-ray flux-limited selection towards Compton-thick AGN is shown in Figure 1.9, in which the current understanding of the Milky Way's closest neighbouring extragalactic bodies are plotted within 5 Mpc in Supergalactic Coordinates in the upper panel. Within this small distance, just three AGN are known – Centaurus A, NGC 4945 and the Circinus Galaxy. All three AGN have $\log N_{\mathrm{H}}\ /\,\mathrm{cm}^{-2} > 23$, with NGC 4945 and Circinus being Compton-thick to $> 90\%$ confidence (e.g., Centaurus A; Markowitz *et al.* 2007, NGC 4945; Puccetti *et al.* 2014 and Circinus; Arévalo *et al.* 2014 – a volume-limited Compton-thick fraction (i.e. within 5 Mpc) of $68^{+20}_{-23}\%$[9]. However, if we now consider hard X-ray selection with the *Swift*/BAT AGN Spectroscopic Survey (using the hard X-ray detector onboard *Neil Gehrels Swift Observatory*), 838 AGN in total were detected after 70 months of contigual all-sky exposure down to a flux limit of $1.34 \times 10^{-11}\,\mathrm{erg\,s^{-1}\ cm^{-2}}$ in the 14 – 195 keV band within a few 100 Mpc (Baumgartner *et al.* 2013). By taking a conservative cut of 100 Mpc, I plot the equivalent plot as before, with the Milky Way at the center in the lower left panel. In the lower right panel, I present the Compton-thick fraction as a function of distance from the Milky Way. The

[9] Uncertainties on fractions are calculated with the beta function as a conservative estimate – see e.g., Ricci *et al.* 2017b for an application and Cameron 2011 for an explanation.

horizontal dashed blue line with 1-σ uncertainty represents the 'bias-corrected' Compton-thick fraction from Ricci *et al.* (2015), in which two assumptions of a torus model are imposed, with low and high torus covering. As can be seen, the Compton-thick fraction depletes dramatically with distance, illustrating the Compton-thick bias present in flux-limited hard X-ray selection.

As highlighted in Section 1.3.4, reflection from the accretion disc can mimic reflection from distant obscuration, such that comparatively strong reprocessed components from the intrinsic accretion disc can spuriously mimic heavily obscured AGN signatures (e.g., Gandhi *et al.* 2007; Treister *et al.* 2009; Vasudevan *et al.* 2016). Conversely, heavily obscured AGN signatures may be swamped by other spectral components resulting in erroneous low-column classifications in the case of low signal-to-noise or band-limited (i.e. non-*NuSTAR*) X-ray data (e.g., Gandhi *et al.* 2017). For these reasons, flux-limited hard X-ray selection is currently insufficient to probe the Compton-thick population in detail, and other methods are thus essential to do so.

1.4.2 Optical Narrow Line Region Emission

Originating in the Narrow Line Region, optical emission lines have been successfully used to select 'optimally' matched samples of obscured and unobscured sources (e.g., Risaliti *et al.* 1999a), by treating forbidden transitions such as the [OIII] λ 5007 Å emission line as 'bolometric' estimators of AGN power. The $\sim$kpc-scale extension of the Narrow Line Region means its emission should be insensitive to $\sim$pc-scale torus orientation angles, and thus more 'isotropic' than the small-scale X-ray emission associated with the compact corona and associated circumnuclear obscuration. This reasoning is the main argument for the existence of known correlations between intrinsic (unabsorbed) X-ray emission and observed (optical) [O III] emission (e.g., Panessa *et al.* 2006; Berney *et al.* 2015 – see Figure 1.10).

While certainly an effective means of identifying AGN that are heavily obscured in X-rays, using optical Narrow Line Region emission requires intensive spectroscopic surveys of large areas of the sky, which is often time-consuming and costly. In addition, more recent work has shown that geometric variations and time variability can cause significant inherent scatter in the [O III] power in particular, implying that it is not a strict and accurate estimator of the current bolometric AGN power (e.g., Berney *et al.* 2015; Ueda *et al.* 2015).

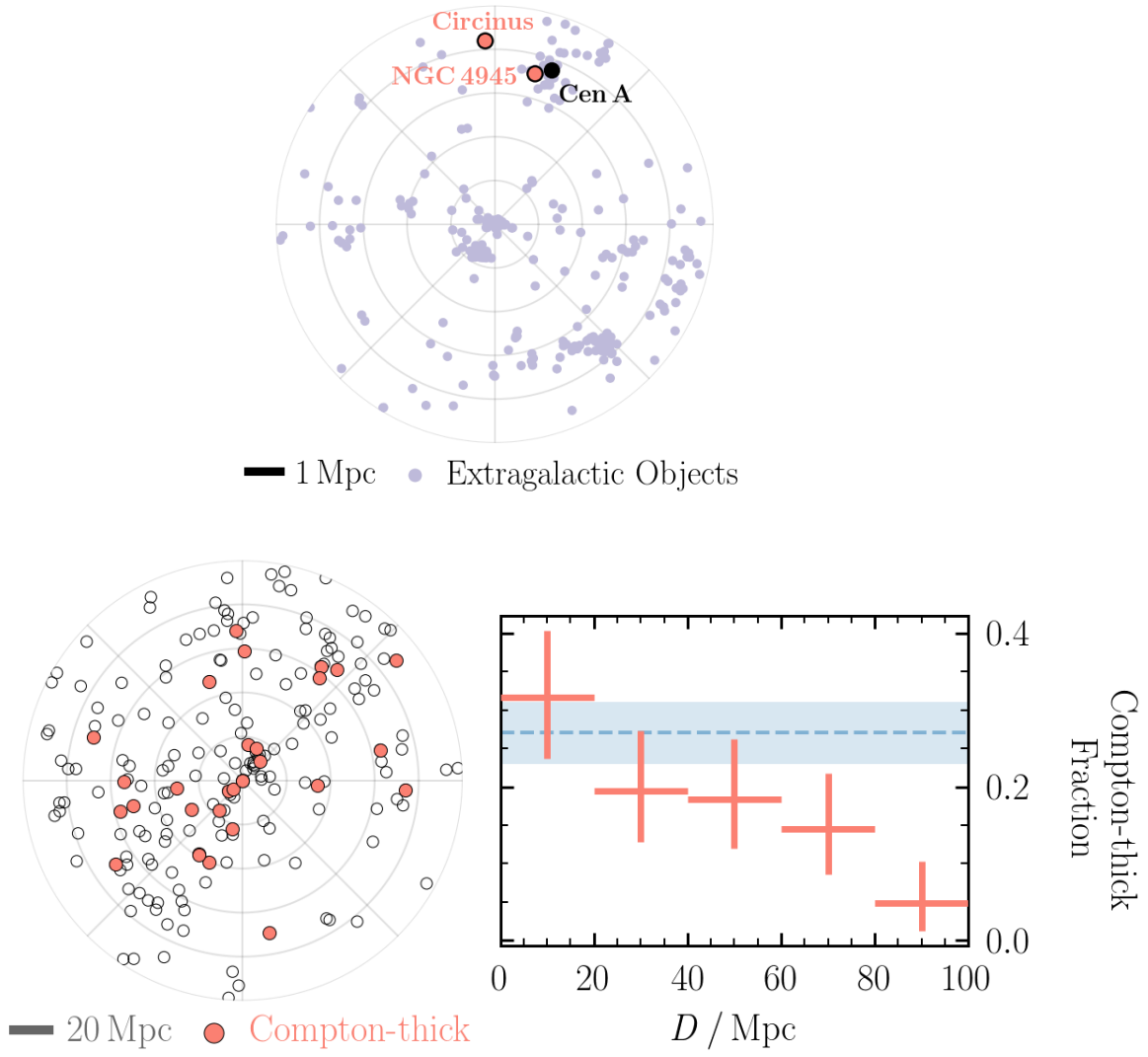

FIGURE 1.9: Illustration of our current understanding of the local AGN population. ***Upper panel:*** All extragalactic systems recorded in the NED-D database[10] within 5 Mpc from the Milky Way (located at the center of the plot). Concentric circles are 1 Mpc in distance, and all bodies are plotted in supergalactic coordinates – designed to align with a plane formed by several nearby galaxy clusters. Within 5 Mpc, just three AGN are known – all are obscured with $\log N_{\rm H}\ /\,{\rm cm}^{-2} > 23$, and two are Compton-thick.
Lower panels: Left: same as upper panel, but for the distribution of 70-month *Swift*/BAT all-sky survey AGN within 100 Mpc (concentric rings represent 20 Mpc in distance). Right: corresponding Compton-thick fraction of all *Swift*/BAT-detected AGN as a function of distance. The fraction is seen to deplete dramatically with distance below 'bias-corrected' value from Ricci *et al.* (2015) designed to correct for obscuration bias.

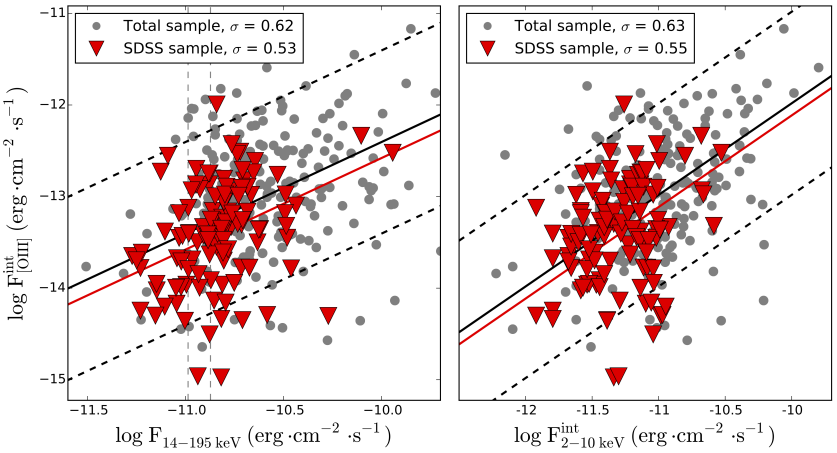

FIGURE 1.10: *Credit: Berney et al. (2015).* The correlations between observed [O III] luminosity and predicted intrinsic X-ray luminosities. The X-ray emission is believed to be originating from a compact corona is predicted to be effected by small-scale compact circumnuclear obscuration, whereas the Narrow Line Region in which the [O III] emission resides is not. The large inherent scatter is clearly visible for the relation.

1.4.3 Radio Low-frequency Surveys

Radio continuum luminosity holds potential to be an extremely effective method for isotropic AGN selection due to the associated minimal optical depth, especially with current instrumentation for the unbeamed extended jet component, which is best probed at low frequencies (e.g., Orr and Browne 1982; Giuricin *et al.* 1990; Singh *et al.* 2013), capable of selecting high-redshift radio-loud AGN representatively of their obscuration (e.g., Wilkes *et al.* 2013).

But the majority of AGN have so far been found to be radio-quiet (e.g., $\sim$7–10% of hard X-ray selected AGN; Panessa *et al.* 2016), so the source yield per unit volume with such surveys is typically small due to the current instrumental flux density limits in place. Future surveys with e.g., the LOw-Frequency ARray (LOFAR; van Haarlem *et al.* 2013) and Square Kilometre Array (SKA; Braun *et al.* 2015) will feature sensitivities capable of probing the radio-quiet population in detail, such that radio-quiet AGN selection directly in the radio will be possible (Jarvis 2007).

An alternative to unbiased blanket searches for radio-quiet AGN are dedicated pointed observations of local sources. The Legacy enhanced Multi-Element Radio Linked Interferometer Network (eMERLIN) Multi-band Imaging of Nearby Galaxies survey (LeMMINGs, PI: McHardy and Beswick; Beswick *et al.* 2014) offers to provide high spatial resolution and sensitivity observations of local sources. This legacy survey is following up a declination-limited portion of the optically selected Palomar nearby galaxy sample (Filippenko and Sargent 1985). The interim data release for LeMMINGS (Baldi *et al.* 2018) was able to probe a wide range of radio luminosities, critically including radio quiet

AGN, Low Luminosity AGN, and even star-forming galaxies shown to reveal previously hidden levels of central supermassive black hole activity.

1.4.4 Mid-infrared Line Emission

Complementary to optical lines, Narrow Line Region transitions can also be excited in the infrared by AGN activity. Commonly used lines include the [OIV] λ 14 and 26 μm emission lines, both of which have been adopted for isotropic AGN selection and tests of unification (e.g., Goulding and Alexander 2009; Dicken *et al.* 2014; Yang *et al.* 2015). Their high ionisation potentials and low optical depths imply that they are better than the optical Narrow Line Region lines at disentangling AGN activity from star-formation and probing through high levels of extinction, respectively. However, intensive infrared spectroscopic surveys are even more sparse than in the optical, and these lines are further subject to substantial scatter (e.g., Meléndez *et al.* 2008; Rigby *et al.* 2009; Diamond-Stanic *et al.* 2009; LaMassa *et al.* 2010).

Recently, additional focus has been on the [NeV] λ 14.32 and 24.32 μm (97.1 eV) high-excitation emission lines. These emission lines are theoretically unexpected to be generated by an ionising medium other than an accreting supermassive black hole, whereas the aforementioned [OIV] lines are postulated to be produced by powerful Wolf Rayet stars (e.g., Goulding and Alexander 2009). The currently-underway 15 Mpc sample (Annuar et al., in prep.) is using the $D < 15$ Mpc sample founded by Goulding and Alexander to be followed up in X-rays with *Chandra* and *NuSTAR*.

1.4.5 Mid-to-far infrared Continuum

Infrared AGN continuum emission partly arises from dust-reprocessing in the pc-scale toroidal obscurer, and is thus associated with much larger size scales than the $\sim 10^{-5}$–10^{-4} parsec-scale X-ray emitting corona. In addition, a significant infrared component could arise on even larger scales from 'polar' dust in the inner Narrow Line Region (Hönig *et al.* 2013; Asmus *et al.* 2016). A combination of low absorption optical depth in the infrared, together with the extended physical scales, results in the emission appearing largely isotropic (e.g., Buchanan *et al.* 2006; Levenson *et al.* 2009; Hönig *et al.* 2011). This has been shown to be the case for optically classified Type 1 and 2 AGN, including X-ray classified heavily obscured and Compton-thick AGN (e.g., Gandhi *et al.* 2009; Asmus *et al.* 2015 and Figure 1.11).

Longer (mid-to-far infrared) wavelengths appear to be more isotropic than the near-infrared (e.g., Hönig *et al.* 2011; Mateos *et al.* 2015). In fact, deviations from isotropy

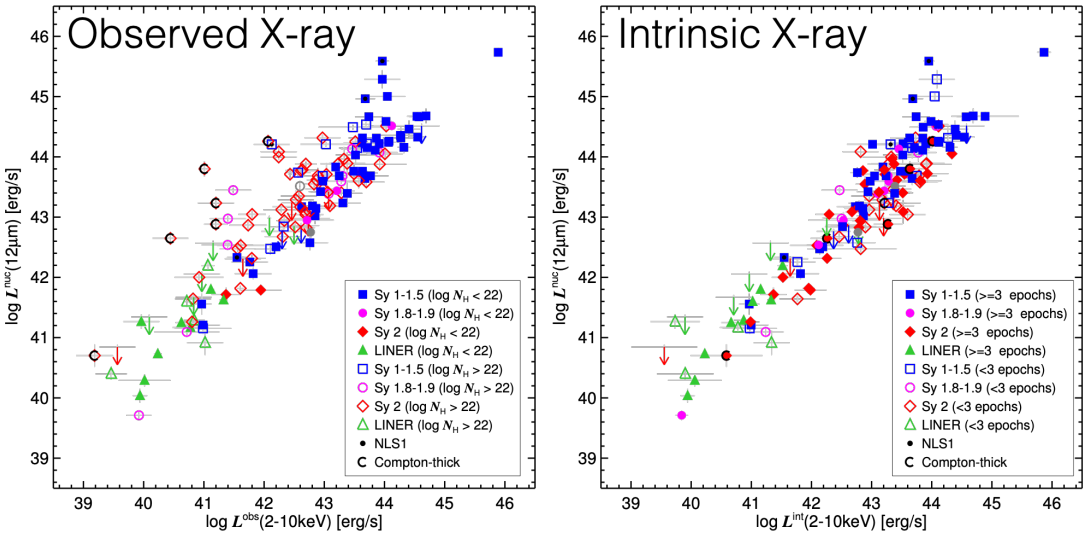

FIGURE 1.11: *Credit: Asmus et al. (2015).* The correlation between observed mid-infrared continuum luminosity and predicted intrinsic X-ray luminosities. *Left:* Observed 2 – 10 keV luminosity plotted against observed nuclear mid-infrared luminosity. Obscured AGN are seen to deviate from the correlation. *Right:* Predicted intrinsic 2 – 10 keV luminosity vs. nuclear mid-infrared luminosity. Remarkably, the correlation holds even for Compton-thick AGN, further indicating mid-infrared continuum selection to be unbiased by circumnuclear obscuration that effects the X-ray emission observed from AGN.

are mild in the mid-infrared, estimated to be a factor of $\lesssim 1.4$ at 12 μm, relative to the intrinsic 2 – 10 keV X-ray emission. The scatter of the correlation between the infrared and X-ray powers is also relatively small, at ≈ 0.35 dex (e.g., Asmus *et al.* 2015). The infrared-emitting region is clearly complex with emission from multiple nuclear scales, and there is much debate regarding its nature. Infrared continuum selection is not 100% reliable in terms of AGN selection, and contaminating host galaxy emission needs to be disentangled (e.g., Lacy *et al.* 2007; Stern *et al.* 2012; Mateos *et al.* 2012; Assef *et al.* 2018).

1.5 AGN Classifications

The difference between AGN selection and classification is critical to the outcomes and results of this thesis. There are three key techniques I have used, which are described in more detail below.

1.5.1 Optical Emission Line Diagnostics

In the optical waveband, emission-line ratios can efficiently separate characteristically higher-ionisation AGN from star-forming galaxies via so-called Baldwin *et al.* (1981,

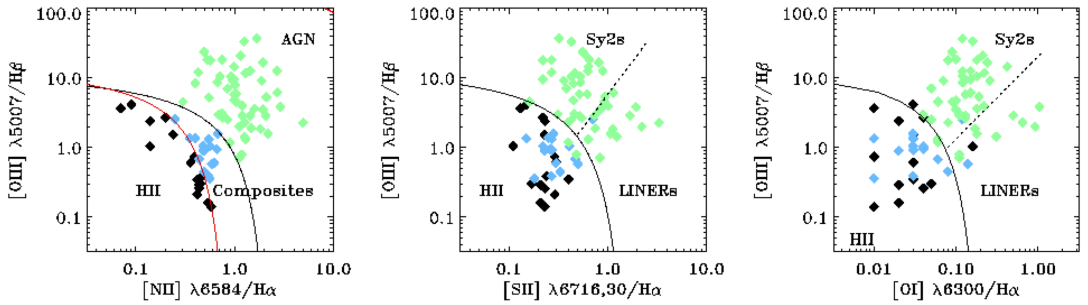

FIGURE 1.12: *Credit: Brightman and Nandra (2011b).* An example BPT diagnostic diagram used to classify the AGN in the 12 μm Galaxy Sample (Rush *et al.* 1993).

BPT) diagnostic diagrams with considerable success (e.g., Veilleux and Osterbrock 1987; Kewley *et al.* 2001; Kauffmann *et al.* 2003; Schawinski *et al.* 2007; LaMassa *et al.* 2019).

However, this process not only requires large and intensive spectroscopic surveys which have their own inherent selection biases, but also a considerable AGN contribution to the optical emission lines with respect to the host galaxy, missing optically-elusive AGN populations entirely (e.g., 'X-ray Bright Optically Normal Galaxies' - XBONGs, Moran *et al.* 2002). Additionally, BPT diagnostic diagrams do not efficiently select obscured AGN in which there is little Narrow Line Region emission, for example from deeply buried AGN.

1.5.2 Infrared Photometric Classifications (Infrared Colours)

In the mid-infrared ($\lambda \sim 10 - 30\mu$m), the optical depth is far lower and considerably more isotropic between different AGN optical classes (e.g., Gandhi *et al.* 2009; Asmus *et al.* 2015). However, host galaxy dust and star formation can mimic AGN signatures, such that care must be taken to disentangle AGN emission from contaminating sources (e.g., Lacy *et al.* 2007; Stern *et al.* 2012; Mateos *et al.* 2012; Assef *et al.* 2018).

Such techniques include infrared photometric colours. Due to the differing emission mechanisms in play, different astrophysical bodies present varying infrared photometric colours (see e.g., Figure 1.13). For AGN, these colour selections rely on the persistent and red emission of AGN, as compared to typically bluer stars and star-forming galaxies. For example, Figure 1.14 shows the infrared *WISE* and *IRAS* images for a local AGN with location signified by the cross hairs. As the wavelength of the *WISE* filter increases, the emission is persistently brighter, and in fact gets stronger. However, the bright point-like star that is very visible at shorter *WISE* wavelengths almost disappears at the longest wavelength filters. Infrared colours cuts have been developed for a variety of infrared instruments, and I show two such cuts in Figure 1.15, with the left and right panels

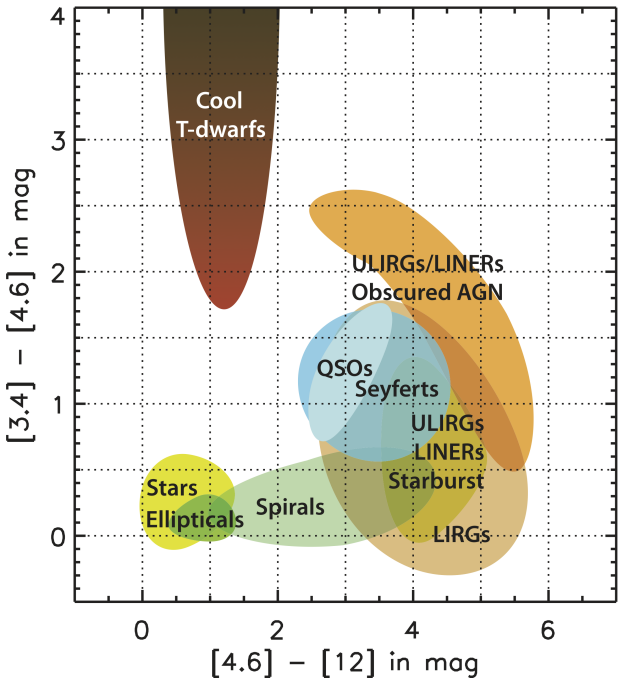

FIGURE 1.13: *Credit: Wright* et al. *(2010)* Infrared colour selection schematic, showing the characteristic regions of infrared colour space occupied by different classes of astrophysical object.

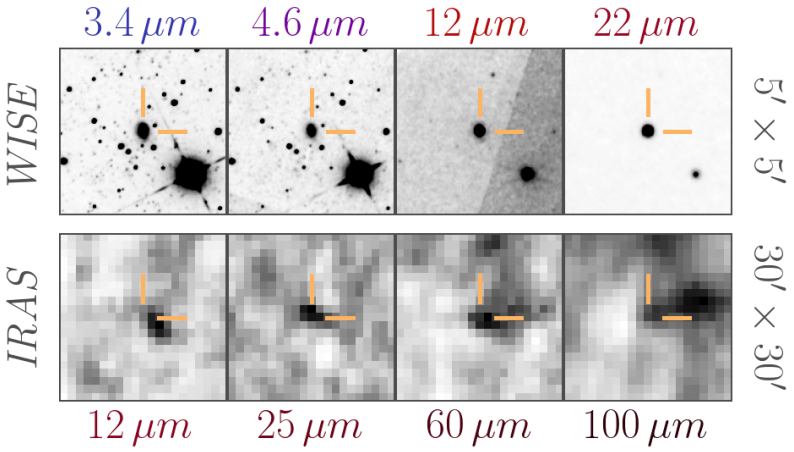

FIGURE 1.14: Example infrared images for a local AGN, in which up is North and left is East. The emission from the AGN becomes brighter with increasing wavelength, whereas the star point-like emission (located South-West) becomes much fainter.

corresponding to *Spitzer* and *WISE* colours, respectively from Lacy *et al.* (2007) and Stern *et al.* (2012).

1.5.3 Broadband X-ray Spectral Modelling

X-ray emission from mildy obscured ($\log N_{\rm H}$ / $\rm cm^{-2}$ $\lesssim$23), intrinsically powerful AGN is almost always identifiable from the soft ($E < 10\,\rm keV$) X-ray spectra, since sufficient

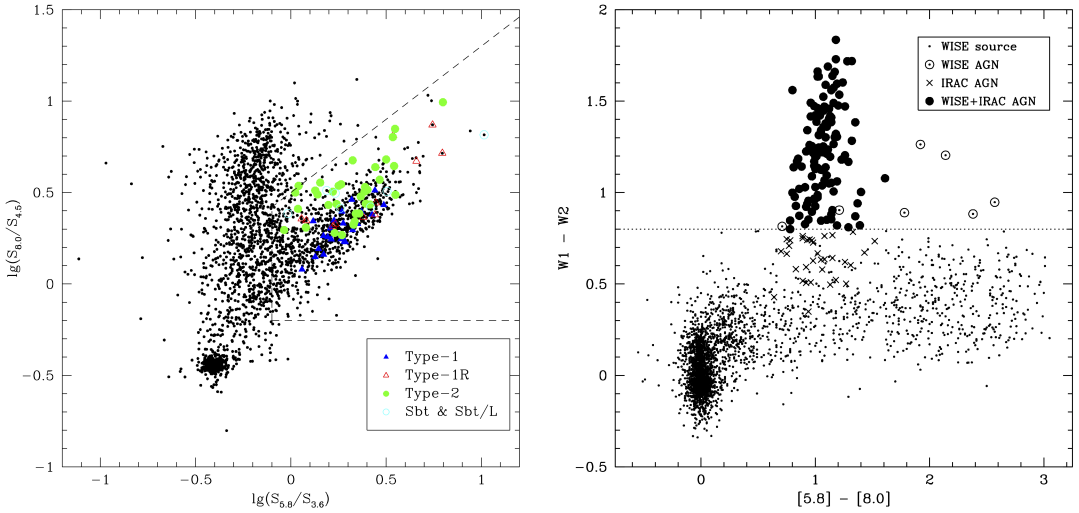

FIGURE 1.15: *Left*: *Credit: Lacy* et al. *(2007)*, *right*: *Credit: Stern* et al. *(2012)*. Left and right panels show example *Spitzer* and *WISE* colour-colour diagrams used to select AGN, respectively.

intrinsic emission is transmitted without being completely depleted by photoelectric absorption. Furthermore, contamination from off-nuclear X-ray sources is rare, though see e.g., Arévalo *et al.* (2014) for an example. However, to robustly classify obscured and heavily obscured AGN with a robust column density classification relies X-ray spectra beyond 10 keV, primarily so that modelling can encompass the effects of photoelectric absorption and Compton scattering simultaneously.

Despite a plethora of available X-ray data on a number of local sources in soft X-rays, hard X-ray data is somewhat rarer. Many X-ray missions to date have been capable of detecting photons above 10 keV, such as *BeppoSAX*, *Swift*/BAT, *Suzaku* and *INTEGRAL*. However, due to issues including high background levels, relatively small effective areas and very low angular resolution, few Compton-thick sources have been identified. The *Nuclear Spectroscopic Telescope ARray* (*NuSTAR*; Harrison *et al.* 2013) is the first mission in orbit capable of *true* X-ray imaging in the 3 – 79 keV energy range. The improvement with *NuSTAR* is evident with the large number of dedicated studies into not only well known Compton-thick AGN (Arévalo *et al.* 2014; Puccetti *et al.* 2014; Bauer *et al.* 2015; Marinucci *et al.* 2016), but also numerous new obscured and Compton-thick AGN candidates in the local Universe (Gandhi *et al.* 2014; Teng *et al.* 2014; Baloković *et al.* 2014; Ptak *et al.* 2015; Annuar *et al.* 2015; Koss *et al.* 2015; Puccetti *et al.* 2016; Masini *et al.* 2016; Koss *et al.* 2016a; Annuar *et al.* 2017; Kammoun *et al.* 2019), as well as carry out variability studies focusing on *changing-look* obscured AGN (Risaliti *et al.* 2013; Walton *et al.* 2014; Rivers *et al.* 2015; Marinucci *et al.* 2016; Ricci *et al.* 2016; Masini *et al.* 2017).

1.6 AGN Evolution

The masses of supermassive black holes found in the nuclei of galaxies are observed to correlate tightly with host galaxy bulge properties (e.g., Magorrian *et al.* 1998; Häring and Rix 2004; Kormendy and Ho 2013). This strongly implies that the supermassive black hole and galaxy bulge both co-evolve with one-another, and further suggests that the supermassive black hole plays a role in determining the final observed stellar mass of the bulge (e.g., Merloni and Heinz 2008; Fabian 2012). Therefore *AGN feedback* is the interaction between energy and radiation generated by accretion onto the central supermassive black hole, and the surrounding host galaxy gas.

Two possible modes for AGN feedback have been identified (Fabian 2012):

1. **Radiative Mode:** Operates in a typical galaxy bulge for a black hole accreting close to the Eddington limit.
2. **Kinetic Mode:** Operates mainly in large galaxies in which a radio jet is launched.

The radiative mode occurs via wind outflows (e.g., Merloni *et al.* 2010; Martín-Navarro and Mezcua 2018), and likely occurs when the galaxy has a large amount of cold gas with a heavily obscured central supermassive black hole (Fabian and Iwasawa 1999a). A major discovery in this field was that of *cosmic downsizing* – namely that the most luminous and massive AGN had the highest number densities at redshifts ~ 2, whereas lower luminosity sources peaked at considerably lower redshifts (first confirmed in the X-ray regime – Ueda *et al.* 2003). Such downsizing is unexpected from hierarchical growth models, in which the most massive objects form last, and suggests AGN feedback may be quenching their growth.

AGN quenching/feedback relies on a high number density of obscured AGN, and points to obscured growth being a vital evolutionary stage for the central supermassive black hole, *as well as* all host galaxies. Clearly the obscuration and accretion histories of all AGN across cosmic time are vital parameters to constrain, in order to understand how galaxies form, grow and die. In Section 1.6.1, I describe how the CXB radiation can be used to constrain such parameters and probe all AGN across cosmic time. I then highlight the key input parameter to all existing CXB synthesis models – the local Universe $N_{\rm H}$ distribution – before discussing optimum strategies to constrain it in Section 1.6.2.

The growth and hence accretion history of supermassive black holes undergoing AGN phases are vital to properly understand the evolution of galaxies. It is also possible that the obscured and Compton-thick fractions evolve with redshift though this remains

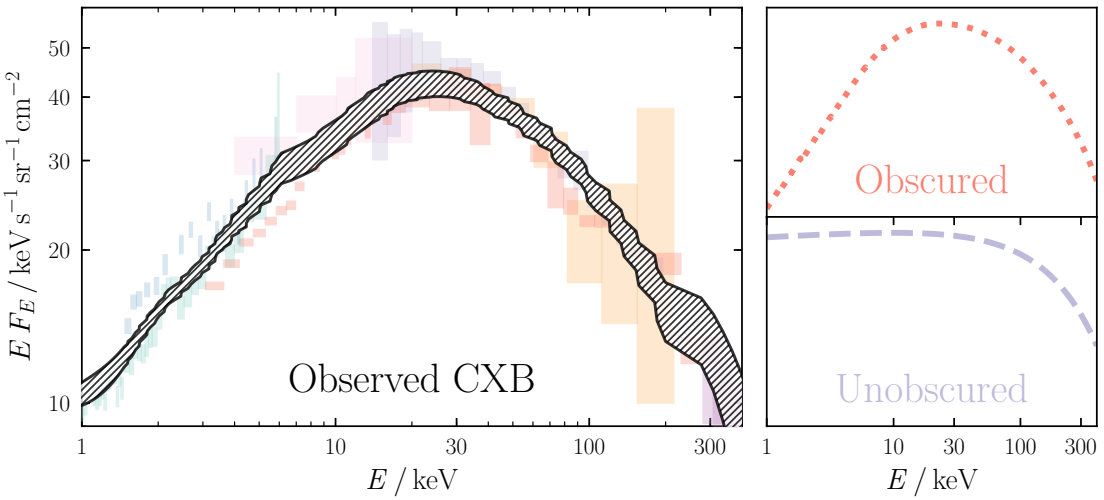

FIGURE 1.16: *Left:* Observed spectrum of the CXB. *Right:* upper and lower panels present simplified X-ray spectra of an obscured and unobscured AGN at redshift $z = 0$, respectively. The observed CXB spectrum clearly resembles that of the obscured AGN closely.

controversial (e.g., La Franca *et al.* 2005; Ueda *et al.* 2014; Buchner *et al.* 2015; Aird *et al.* 2015; Lanzuisi *et al.* 2018).

1.6.1 Synthesising the CXB

In Section 1.2, I highlighted the characteristic shape and properties of the observed Cosmic X-ray Background (CXB) – namely that the most plausible origin for the CXB is the integrated emission from point sources of X-rays across cosmic time, the majority of which are AGN. This means the CXB represents a major observational constraint on the evolution and growth of all AGN, their circumnuclear obscuration, and thus encompassing host galaxies. As a zeroth order prediction, one can draw similarities between the general observed shape of the CXB spectrum and that of a single obscured AGN in the local Universe vs. that of an unobscured one (see Figure 1.16). Clearly, the peak of the CXB ties in well with the concept of a Compton hump, perhaps suggesting the prevalent presence of obscured and Compton-thick AGN in the Universe.

Based on the assumption that the CXB is the result of summing every AGN spectrum across cosmic time, several works have aimed to model the evolution of AGN spectra with the CXB (in part) a vital boundary condition – broadly referred to as *CXB population synthesis models*. To-date there have been many population synthesis models of subtle methodological variations, designed to explain the observed spectral energy distribution of the CXB through the evolution of individual spectral templates of varying-obscuration AGN (Comastri *et al.* 1995; Gandhi and Fabian 2003; Gilli *et al.* 2007; Treister *et al.* 2009; Draper and Ballantyne 2010; Akylas *et al.* 2012; Ueda *et al.* 2014; Buchner *et al.*

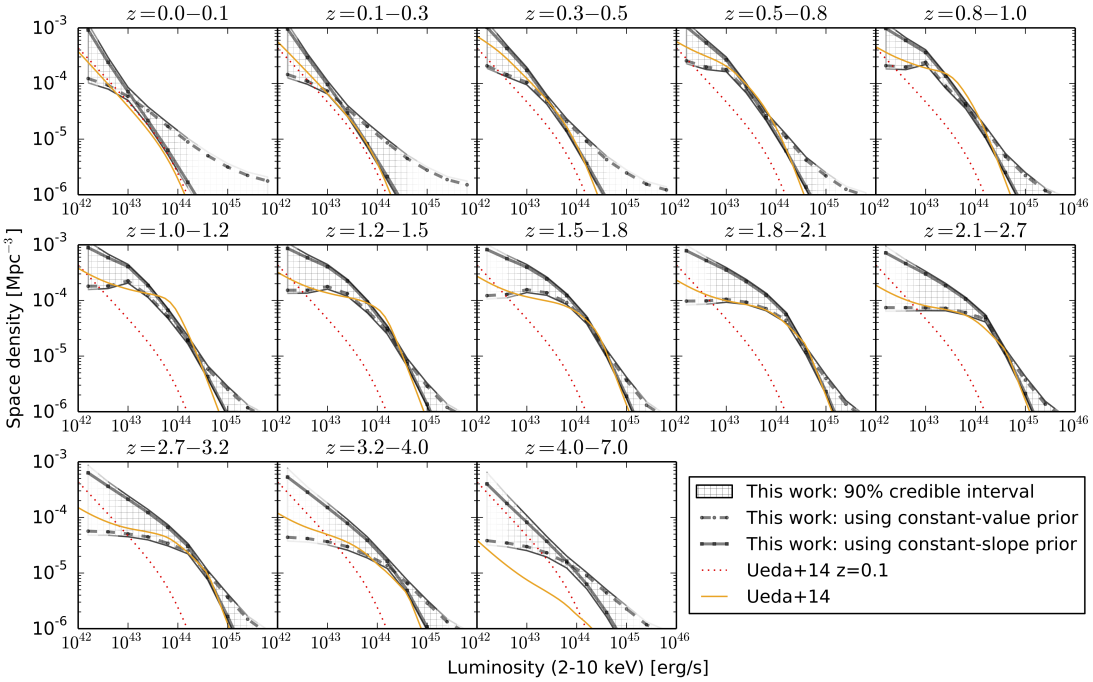

FIGURE 1.17: *Credit: Buchner* et al. *(2015).* Recent formulation of the X-ray Luminosity function derived with a non-parametric model.

2015; Aird *et al.* 2015; Tasnim Ananna *et al.* 2018). There is now a general three-pronged formalism adopted by many recent population synthesis models (e.g., Ueda *et al.* 2014; Buchner *et al.* 2015; Aird *et al.* 2015; Tasnim Ananna *et al.* 2018):

1. **AGN template spectrum:** This describes the spectral shape and relative normalisation of individual AGN, which depends on the $N_{\rm H}$ and intrinsic luminosity (the model used to generate Figure 1.8 is similar to many AGN template spectra used for population synthesis – i.e., a reprocessed component in combination with an intrinsic exponentially cut-off powerlaw and warm mirror).

2. **X-ray Luminosity Functions:** These describe the space density of AGN as a function of intrinsic luminosity and redshift (e.g., Maccacaro *et al.* 1991). Figure 1.17 presents a recent formulation of the AGN X-ray Luminosity Function in the 2 – 10 keV luminosity range by Buchner *et al.* (2015).

3. **Absorption Function:** First introduced by Ueda *et al.* (2003), this takes into account the fraction of AGN in each luminosity and redshift of the X-ray Luminosity Function that have a particular $N_{\rm H}$.

Figure 1.18 presents a recent CXB population synthesis model from Ananna *et al.* (2019), in which the authors used a neural network to find an X-ray Luminosity Function that satisfies the CXB spectrum and AGN/Compton-thick AGN number counts observed in

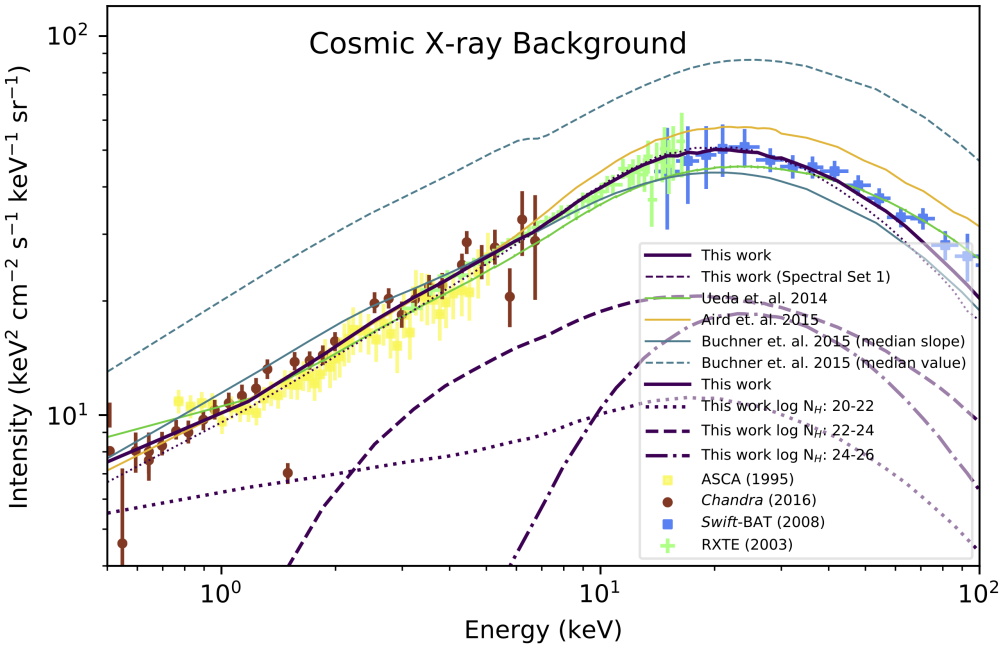

FIGURE 1.18: *Credit: Ananna et al. (2019).* Recent population synthesis model the CXB, requiring $56 \pm 7\%$ of all AGN are Compton-thick within $z \sim 1$.

multiple surveys. Interestingly, the statistically favourable model from Ananna *et al.* suggests that $56 \pm 7\%$ of all AGN are Compton-thick within $z \sim 1$.

1.6.2 The $N_{\rm H}$ Distribution

The absorption function of AGN – describing the evolution of AGN obscuration (the $N_{\rm H}$ distribution) with redshift and luminosity – is very difficult to directly (observationally) constrain with present instrumentation. This is because observed flux limits in any waveband decrease rapidly with not only distance (the 'Malmquist bias') but also with increasing obscuration (e.g., Guainazzi *et al.* 2005; Ricci *et al.* 2015, and Chapter 4). As a result, many works have found differing results as to the $N_{\rm H}$ distribution at early cosmic epochs, as well as its evolution.

1.6.2.1 The Local Universe

A popular strategy to acquire optimum constraints on the $N_{\rm H}$ distribution is to establish the $N_{\rm H}$ distribution in the local Universe, where Malmquist biases should be minimal, and evolve it to earlier cosmic epochs (e.g., Ueda *et al.* 2014). The most recent $N_{\rm H}$ distribution in the local Universe was provided by Ricci *et al.* (2017c), in which the $N_{\rm H}$ determination of a large sample of 70-month *Swift*/BAT-detected AGN were presented. By assuming a model for the orientation and geometry of the circumnuclear obscurer,

Ricci *et al.* corrected for biases against heavily obscured AGN to yield an *obscured* AGN fraction ($\log N_{\rm H}\ /\,{\rm cm}^{-2} > 22$) of $70 \pm 5\%$, and a Compton-thick fraction of $27 \pm 4\%$ (also in agreement with Akylas *et al.* 2016; Koss *et al.* 2016a). Due to the major depletion of *Swift*/BAT's sensitivity for $\log N_{\rm H}\ /\,{\rm cm}^{-2} \gtrsim 25$, this Compton-thick fraction is in fact a lower limit.

1.6.2.2 The Evolution of Obscuration

Since the tentative discovery of the evolution of the obscured AGN fraction with luminosity almost 30 years ago (Lawrence 1991), many works have now established similar relations at X-ray (e.g., Merloni *et al.* 2014), optical (e.g., Simpson 2005), infrared and radio wavelengths (e.g., Maiolino *et al.* 2007; Treister *et al.* 2008; Lusso *et al.* 2013; Mateos *et al.* 2017) with similar results. In particular, Merloni *et al.* (2014) consider AGN obscuration in both the optical and X-ray wavebands jointly, clearly showing a decrease of the obscured fraction with luminosity – more commonly known as the 'receding torus'. Recent studies have pointed to the Eddington ratio as the main driver of the receding torus, instead of just the intrinsic luminosity (e.g., Buchner *et al.* 2017; Ricci *et al.* 2017d; Ezhikode *et al.* 2017), in which the covering factor of dusty gas surrounding the central AGN is regulated by the radiation pressure from the AGN acting on obscuring dusty gas (e.g., Fabian *et al.* 2008). Such a connection between the circumnuclear obscuring covering factor and accretion power of the AGN indicates that the main source of obscuration is located within a few gravitational radii of the central supermassive black hole.

Despite the plethora of evidence for some form of receding torus, the evolution of the obscured fraction with redshift is less established (e.g., Dwelly and Page 2006). Although intrinsically difficult to constrain, there is broad agreement that the obscured fraction was at least as high in the distant Universe as today, with a possible increase with redshift (e.g., Ueda *et al.* 2014; Buchner *et al.* 2015).

1.6.2.3 Using Radiative Efficiency to Constrain Obscured Populations

The total radiation emitted by accretion onto supermassive black holes across cosmic time can be used to constrain the relic populations of supermassive black holes observed in the present Universe. This is known as Sołtan's Argument (first proposed by Sołtan 1982), and can be expressed with the following equation:

$$\rho_{\bullet}\, c^2 = U_{\rm T} \frac{1-\epsilon}{\epsilon} \tag{1.4}$$

Where $\rho_\bullet$ is the mass density of supermassive black holes in the present Universe accumulated from accretion, U_T is the total radiation density produced by supermassive black hole accretion, and ϵ the total radiative efficiency of the accretion processes.

By using the CXB, Fabian and Iwasawa (1999b) were able to predict the mass density of supermassive black holes by assuming an average radiative efficiency of $\epsilon \sim 0.1$. One major source of uncertainty with works using the Sołtan argument though is the fraction of obscured AGN. Recently, Comastri *et al.* (2015) showed that a hidden population of heavily Compton-thick AGN could be present without violating constraints from the X-ray and infrared backgrounds.

1.7 Observational Techniques

This thesis aims to create useful X-ray products – namely images and spectra. First I will overview the methods used to do this, before describing the process of modelling such data to deduce intrinsic parameters of the target sources.

1.7.1 X-ray Imaging

The first X-ray detectors were proportional counters, designed to produce an electrical signal from an incoming X-ray photon. The imaging capabilities of these instruments was advanced dramatically with the inclusion of coded aperture masks. These are sheets of X-ray-opaque material with a well-defined pattern cut out. This pattern then casts a shadow (the shadowgram) onto the surface of a detector when an X-ray source illuminates the surface. The location of emission on the sky can then be reproduced based around the condition of the pre-known coded aperture. Despite improving angular resolution, coded aperture masks still offer very limited imaging capabilities, though benefit from cheap manufacture costs, and large collecting areas.

X-ray photons in the range $0.5-150\,\mathrm{keV}$ are $\sim 200-60{,}000$ times more energetic than a typical ($\sim 5{,}100\,\text{Å}$) optical photon. As a result, normal incidence mirrors used to focus optical light will completely absorb X-ray photons. There are two main methods to overcome this:

1. **Grazing incidence:** The angle of incidence is $\propto \rho/E$, where ρ is the density of the reflecting surface, and E is the energy of the incident photon (Aschenbach 1985).

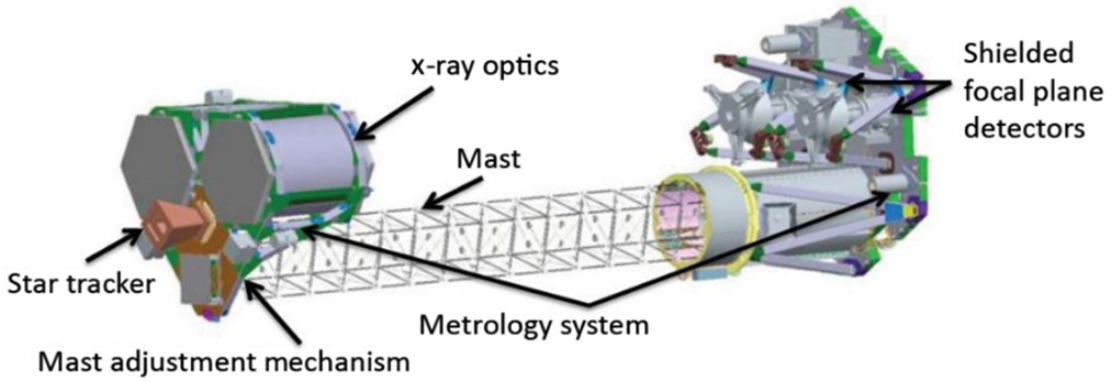

FIGURE 1.19: *Credit: Madsen et al. (2017).* A schematic of the *NuSTAR* observatory (not to scale).

2. **Smooth surfaces:** Due to the very low wavelength of X-ray photons, the surface of the reflector must be extremely smooth – e.g., the mirrors onboard *Chandra* are polished to an average surface roughness of a few angstroms.

However, it was not until 2013, that these requirements were accomplished for high-energy X-ray photons with energy $E > 10\,\mathrm{keV}$. The Nuclear Spectroscopic Telescope ARray (*NuSTAR* – Harrison *et al.* 2013) is the first X-ray astronomy observatory in space capable of focusing such photons. *NuSTAR* features a large focal length of 10.14 m, to attain almost parallel angles of incidence for the high-energy incoming X-ray photons. The science load consists of two multi-layer-coated Wolter-I conical approximation X-ray optics (Petre and Serlemitsos 1985) which focus onto two identical focal plane detectors. By combining almost parallel grazing angles of incidence with multi-layer coatings, a dramatic increase in energy upper limit of 78.4 keV was achieved[11]. The angular resolution of *NuSTAR* is 18″ Full Width at Half Maximum.

Since launching such a large payload into orbit would not be feasible, *NuSTAR* had to feature an extendable mast that unfolded and locked into place after reaching orbit. This mast is not sturdy enough to give rigidity between the focusing optics and science load (Focal Plane Modules), such that an additional metrology system and star tracker were mounted onto the science load to keep alignment to within an acceptable level of precision. A schematic of the *NuSTAR* observatory is included in Figure 1.19.

NuSTAR has enabled images to be created of some of the highest energy regions of the Universe, and has hence revolutionised our understanding of the hot and energetic

[11] This upper limit is caused by the Platinum K absorption edge.

Universe. Its successor – *HEX-P* is still at the mission concept phase, but offers the opportunity to extend *NuSTAR*'s focusing energy range, and to enhance spectral resolution for images of some of the most extreme astrophysical environments known. By combining the unique spectral coverage of *NuSTAR* with other soft X-ray instruments, the corresponding broadband X-ray spectra that result are powerful tools to probe the inner workings of AGN, via fitting models to the data.

1.7.2 X-ray Telescope Data

The end-user data from X-ray telescopes is a series of events, combined with secondary data on each event – the position on the detector that the event occurred, the clock time of the event, the energy channel of the event (known as the Pulse Height Analyser channel, PHA) and the grade of the event (used to filter spurious detection signals from e.g., flaring backgrounds or cosmic rays). Secondary derived values are generated including the projected position on the sky of the event arrival and the Pulse Invariant (PI) channel – i.e. the PHA corrected for detector variations.

The conversion of a PI channel into energy or wavelength format is accomplished with a Response Matrix File (RMF), providing probabilities of any given photon lying in certain bins. Thus, a given number of counts in a particular PI channel is a convolution of the observed source spectrum and the RMF. Unfortunately a direct reverse deconvolution of the RMF from the data (giving the observed source spectrum) is not possible, since this method is not stable to small changes in the observed data. An alternative approach is to convolve a model spectrum with an RMF and an Ancillary Response File (ARF) that accounts for secondary effects such as the effective area of the telescope as a function of energy. The result can then be statistically fit to the data – the process of which I discuss in the following section.

1.7.3 Statistical Modelling of AGN X-ray Spectra

When fitting a model to observed data, we are interested in deriving parameters of an underlying distribution given a sample of data, assumed to be taken from it – broadly named 'parameter estimation'.

1.7.3.1 Parameter Estimation with χ^2 Fitting

Intrinsic parameters of a system can be inferred by fitting a parameterised model to data. A common method is to use χ^2 (or Least Squares) fitting, to minimise the vertical

distance between the data and a model by varying parameters, and is weighted by the error on each data point. The statistic is given by:

$$\chi^2 = \sum_{i=1}^{N} \frac{(y_i - m_i)^2}{\sigma_i} \tag{1.5}$$

Where y, m and σ correspond to the observed data theoretically predicted model, and measured uncertainty, respectively.

1.7.3.2 Parameter Estimation with Maximum Likelihood

Maximum likelihood is the process used to determine model parameter values that maximise the likelihood that the model describes the observed data. The likelihood is the total probability of observing the data given the model (and by extension, the current parameters), which for Gaussian-distributed data is defined as:

$$L = \prod_{i=1}^{N} \frac{1}{\sigma_i \sqrt{2\pi}} exp\left[\frac{-\chi^2}{2}\right] \tag{1.6}$$

For observed X-ray spectra, this likelihood assumes that only the source in question is providing the data. However, there is almost always background that contributes to the observed data as well which needs to accounted for. In XSPEC, if a separate background file is included, the observed data becomes the background-subtracted data, and the uncertainties displayed become those of the data and background added in quadrature. The resultant likelihood is the same as in Equation 1.6, since subtracting twice the negative log likelihood results in another Gaussian formulation of likelihood, when twice the natural logarithm is considered.

The Poisson distribution is an approximation to the binomial distribution in which the mean is much less than the number being drawn. Poisson distributions are discrete and are essential for studying counting experiments in which a fixed number of events occur per unit time interval – e.g., a count rate from an astrophysical X-ray source. As the mean increases, the Poisson distribution becomes more symmetric and indistinguishable from the Gaussian distribution (see Figure 1.20 or Bevington 1969, Chapter 2.2).

For a scenario with S_i observed counts in T total exposure and M_i predicted count rates, the likelihood for the corresponding Poisson-distributed data is given by:

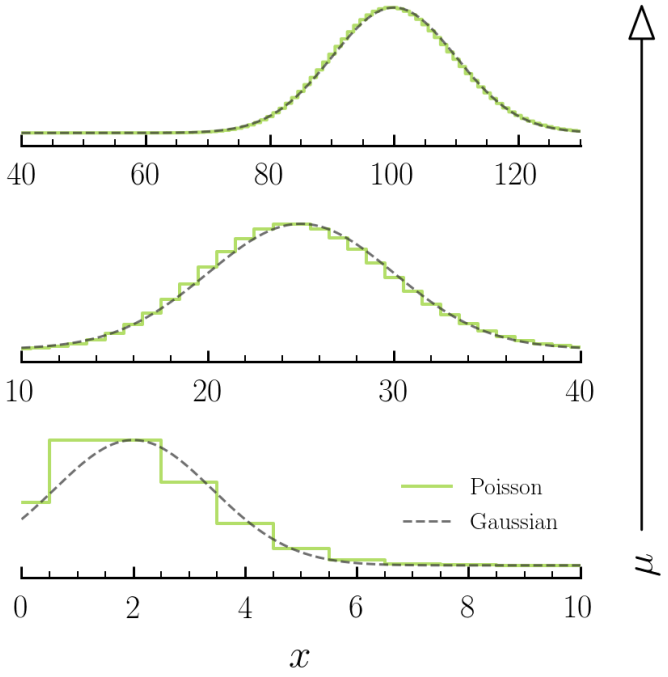

FIGURE 1.20: Three instances of the Poisson and Gaussian distributions for increasing values of the mean, μ. As the mean increases, the Poisson distribution is seen to resemble the Gaussian distribution in increased accuracy.

$$L = \prod_{i=1}^{N} (TM_i)^{S_i} \times \frac{e^{-TM_i}}{S_i!} \tag{1.7}$$

Where the expectation value (i.e. the mean) is given by the predicted count rate multiplied by the exposure time; TM_i. Cash (1979) derived the maximum likelihood statistic (named the C-statistic) for Poisson-distributed data, which characteristically asymptotes to the chi-squared distribution for large numbers of counts. Accounting for the background results in a more complex expression than with the case of Gaussian-distributed source and background counts, since the difference of two Poisson likelihoods is not described by another Poissonian. Furthermore, this strategy requires a physically-motivated model for the background, separate to the source counts. If a background with Poisson-distributed counts is present, but without a model to describe the background counts, the W-statistic (Wachter *et al.* 1979) can be used, provided each bin contains at least one count.[12]

[12]See https://heasarc.gsfc.nasa.gov/xanadu/xspec/manual/XSappendixStatistics.html for more information.

1.7.3.3 Goodness-of-fit: The Null Hypothesis

Parameter estimation is essential to infer intrinsic properties of a source, but crucially relies on our ability to measure the goodness-of-fit to the data. This is achieved by determining if a trend seen in the data is actually a trend, or a statistical fluctuation caused by the random sampling taken of the underlying distribution, known as sampling error. The null hypothesis is that there is no relationship in the data, and any relationship seen is purely an artefact of sampling error. By fitting a model to data (for example in XSPEC– Arnaud 1996), we can derive the null hypothesis probability – i.e. the probability that we can reject the null hypothesis, and that the trend seen in the data is real. Broadly speaking, a p-value of $\gtrsim 0.05$ is used to signify a statistically significant result.

1.7.3.4 Bayesian Statistics

Bayes' Theorem incorporates prior knowledge of some parameters in order to calculate the probability of the parameters themselves. Bayes' Theorem is analytically written in Equation 1.8, and ultimately seeks to find the posterior probability distribution of the model given the data. The posterior is directly related to the likelihood, as well as an input prior on the distributions of the model parameters. An additional normalising constant, known as the evidence, is also included but can be neglected since the probability must normalise to unity.

$$\underbrace{P(\boldsymbol{\Theta}|\mathbf{y})}_{\text{Posterior}} = \frac{\overbrace{P(\mathbf{y}|\boldsymbol{\Theta})}^{\text{Likelihood}} \times \overbrace{P(\boldsymbol{\Theta})}^{\text{Prior}}}{\underbrace{P(\mathbf{y})}_{\text{Evidence}}} \tag{1.8}$$

Where $\mathbf{y} = \{y_1, y_2, ..., y_n\}$ and $\boldsymbol{\Theta} = \{\theta_1, \theta_2, ..., \theta_n\}$ are the data points and model parameters, respectively.

1.7.3.5 Parameter Estimation with Monte Carlo Markov Chains (MCMC)

Monte Carlo Markov Chains sample from the posterior probability density function. A major benefit of MCMC is the ability to marginalise over 'nuisance parameters' – namely parameters that are only required to provide an accurate model to describe the data, though are not desired for the final result. By marginalising, we integrate over all possible values of the parameter and hence propagate any uncertainty in those parameters into the final result.

Since there can be many nuisance parameters for a given model, it can be very complex to solve such an integral, or even impossible. Therefore, by sampling parameters from the integrand distribution, one can numerically solve such an integral and derive the posterior distribution (Foreman-Mackey *et al.* 2013).

The first MCMC algorithm was the Metropolis-Hastings method, in which each step randomly chooses a new set of parameter values using a proposal distribution centered on the current position. Since each value in the proposal distribution covariance matrix is unknown, this method can be very time-consuming for large numbers of parameters.

An update to the Metropolis-Hastings algorithm was that defined by Goodman and Weare (2010), in which an ensemble of walkers are simultaneously evolved per step. The proposal distribution of one walker is based on the current location in parameter space of the remaining walkers, typically resulting in quicker convergence times for the model best-fit.

Both Metropolis-Hastings and Goodman-Weare algorithms are available for parameter estimation in XSPEC with the `chain` command, and a number of XSPEC fits presented in this thesis use the Goodman-Weare algorithm when specified.

Chapter 2

IC 3639 – A New Bona Fide Compton-thick AGN Unveiled by NuSTAR

"I find that if you just talk,
your mouth comes up with stuff."
– Karl Pilkington

2.1 Chapter Motivation and Aims

This chapter aims to uncover the nature of the obscurer in a candidate Compton-thick AGN using detailed spectral modelling and multiwavelength diagnostics. Such detailed studies of individual highly obscured AGN are the most effective way to understand the spectral components contributing to the missing fraction of the peak Cosmic X-ray Background flux. Specifically, I carry out the first robust broad-band X-ray spectral analysis of the nearby Seyfert 2 and candidate Compton-thick AGN IC 3639 (also called Tololo 1238-364). The study of this source was motivated by its exceptionally strong Fe Kα line detected with previous X-ray observations, as well as a surplus of observed mid-infrared flux as compared to the observed X-ray luminosity of the source. The source is hosted by a barred spiral galaxy (Hubble classification SBbc[1]) with redshift $z = 0.011$ corresponding luminosity distance $D = 53.6$ Mpc.

I use *NuSTAR* and archival X-ray data from the *Suzaku* and *Chandra* satellites to study this source. The *Suzaku* satellite operated in the energy range $\sim$0.1 – 600 keV and is thus

[1] http://leda.univ-lyon1.fr

capable of detecting hard X-rays. However, the hard X-ray energy range of *Suzaku* is covered by a non-imaging detector, leading to potential complications for faint sources, as outlined in Section 2.3.2.2. *Chandra* operates optimally in the energy range $\sim 0.1-8$ keV, with very high angular resolution. Consequently, the different capabilities of *NuSTAR*, *Suzaku* and *Chandra* complement each other so that a multi-instrument study provides a *broad-band* spectral energy range.

The chapter is structured accordingly: Section 2.2 explains the target selection, with Section 2.3 describing the details behind each X-ray observation of the source used as well as the spectral extraction processes. The corresponding X-ray spectral fitting and results are outlined in Sections 2.4 and 2.5, respectively. Finally, Section 2.6 outlines broadband spectral components determined from the fits, the intrinsic luminosity of the source and a multi-wavelength comparison with other Compton-thick sources. I conclude with a summary of the findings in Section 2.7.

2.2 The Target

The first published X-ray data of IC 3639 were reported by Risaliti *et al.* (1999a), where they suggest the source to be Compton-thick with column density $N_{\rm H} > 10^{25}\,{\rm cm}^{-2}$. This lower limit was determined from a soft X-ray spectrum provided by the *BeppoSAX* satellite (Boella *et al.* 1997), together with multi-wavelength diagnostic information (see Risaliti *et al.* 1999b and references therein for further details on the modelling used). Additionally, the EW of the Fe Kα fluorescence emission line was reported as $3.20^{+0.98}_{-1.74}$ keV. Such high EWs are extreme though not unheard of for obscured AGN (e.g., Levenson *et al.* 2002), and was a prime motivator for the *NuSTAR* observation. Optical images of the source, as well as surrounding source redshifts, infer IC 3639 to be part of a triple merger system (e.g.,Figure 2.1, upper left panel - IC 3639 is $\sim 1\farcm5$ away from its nearest galaxy neighbour to the North-East). However, Barnes and Webster (2001) use the HI detection in this interacting group to suggest that it is free of any significant ongoing galaxy interaction that may effect the AGN.

Miyazawa *et al.* (2009) analysed the source as part of a sample of 36 AGN observed by *Suzaku*, including the higher energy *Suzaku*/HXD PIN data. The source was found to have an obscuring column density of $7.47^{+4.81}_{-3.14} \times 10^{23}\,{\rm cm}^{-2}$ with photon index $1.76^{+0.52}_{-0.44}$, suggesting a line of sight column density below the Compton-thick limit. This *could* indicate variability between the 2007 *Suzaku* observation and the 1999 *BeppoSAX* observation reported by Risaliti *et al.*.

As outlined in Section 1.4, Compton-thick AGN are notoriously hard to detect due to their low count rate in the soft X-ray band. For this reason, key characteristics have proven very useful in indicating extreme obscuration. The first, most obvious indication is a prominent Fe Kα fluorescence line. Since the conventional Fe Kα line is a reprocessing feature, extreme EWs can occur if the fluorescing material is exposed to a greater X-ray flux than is directly observed. This would lead to the line appearing strong relative to the obscured continuum emission (Krolik and Kallman 1987).

Other Compton-thick diagnostics are provided through multi-wavelength analysis. For example, one of the most established is the comparison between the observed mid-infrared and X-ray luminosities of a given source, as a correlation has been shown to exist between observed mid-infrared and intrinsic (i.e. corrected) X-ray luminosities (Elvis *et al.* 1978; Krabbe *et al.* 2001; Horst *et al.* 2008; Gandhi *et al.* 2009; Levenson *et al.* 2009; Mateos *et al.* 2015; Stern 2015; Asmus *et al.* 2015). X-ray obscuration is expected to reduce the intrinsic X-ray luminosity of an AGN – typically of the order of two orders of magnitude or more – such that Compton-thick sources are dramatically offset from this relation. Indeed, IC 3639 shows an *observed* weak X-ray (2 – 10 keV) luminosity compared to the *predicted* value from this correlation. Another multi-wavelength technique compares emission lines originating in the Narrow Line Region (NLR) on larger scales than the X-ray emission, which arises close to the core of the AGN. Of the multitude of emission lines available for such analysis, one well studied correlation uses the optical [O III] emission-line flux at rest-frame $\lambda = 5007$Å. Panessa *et al.* (2006) and more recently Berney *et al.* (2015), among others, study a correlation between the observed [O III] emission-line luminosity and X-ray (2 – 10 keV) luminosity for a group of Seyfert galaxies, after correcting for obscuration. The correlation typically shows more scatter than with the mid-infrared, but IC 3639 again shows a weak X-ray flux compared to the observed [O III] luminosity. This strongly indicates heavy obscuration depleting the X-ray luminosity. For a comparison between the ratios of mid-infrared and [O III] emission flux to X-ray flux with the average value for (largely unobscured) Seyfert 1s, see LaMassa *et al.* (2010, Figure 2).

Dadina (2007) reports that the *BeppoSAX* observation of IC 3639 in both the 20 – 100 keV and 20 – 50 keV bands had negligible detection significance, and place an upper bound on the 20 – 100 keV flux of $F_{20-100\,\mathrm{keV}} \leqslant 9.12 \times 10^{-12}\,\mathrm{erg\,s^{-1}\,cm^{-2}}$. Additionally, IC 3639 lies below the *Swift*/BAT all-sky survey limit of $\sim 1.3 \times 10^{-11}\,\mathrm{erg\,s^{-1}\,cm^{-2}}$ in the 14 – 195 keV band (Baumgartner *et al.* 2013).

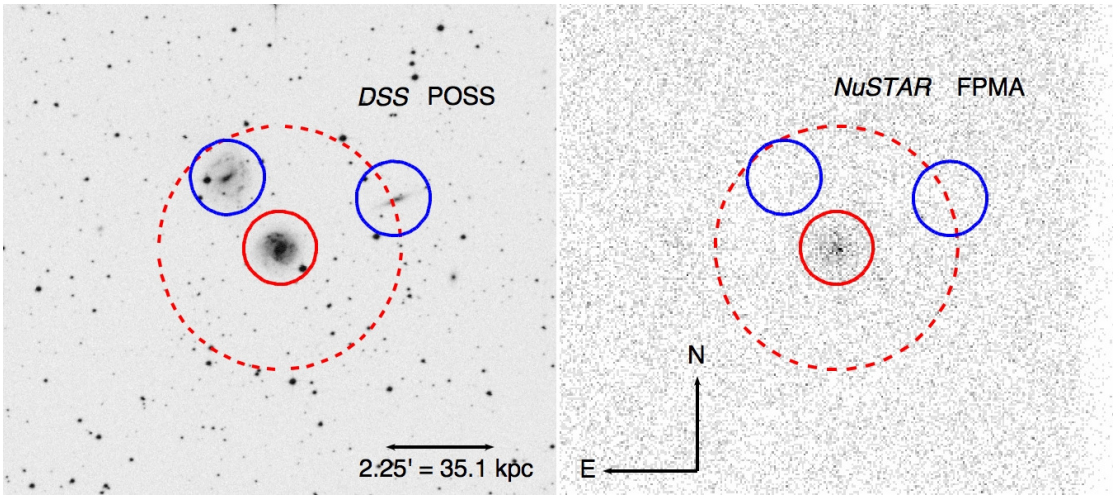

FIGURE 2.1: (Left) *Digitised Sky Survey* (*DSS*) optical image of the interacting triple galaxy group system, with IC 3639 shown in the center. The *NuSTAR* extraction regions for source and background are shown in red with solid and dashed lines respectively. The other two galaxies present in the triple system are highlighted with blue circles, each of radius 0′.76. (Right) *NuSTAR*/FPMA event file with source and background regions again shown in red solid and dashed lines respectively. The locations of the other two galaxies in the interacting triple system (visible in optical images) are shown by the blue circles. Clearly, *NuSTAR* does not significantly detect these other galaxies in the X-ray energy range.

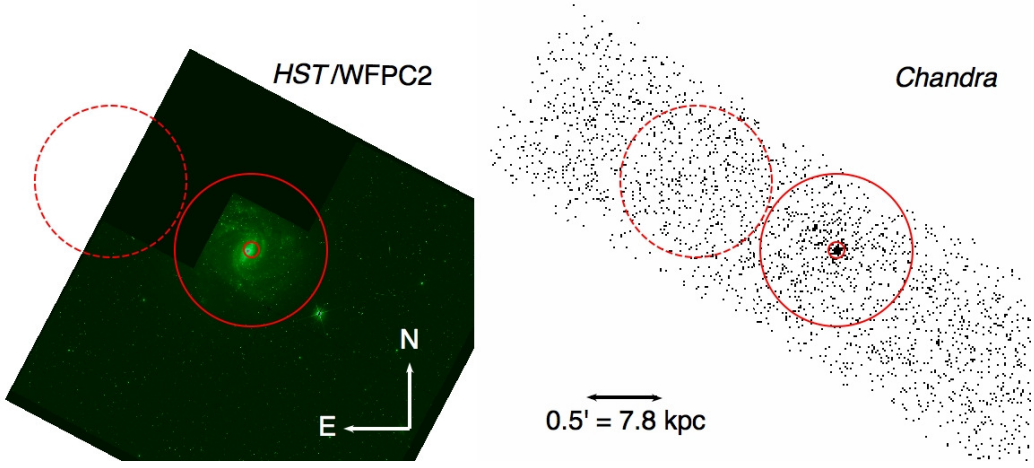

FIGURE 2.2: (Left) *Hubble Space Telescope* (*HST*) WFPC2 image of IC 3639, with superimposed regions defined from the *Chandra* image. The image confirms the barred spiral classification described in Section 2.1, orientated almost completely face-on to our line of sight. (Right) Full band *Chandra* image with 0′.5 radius extraction regions for background and annular count extraction region for off-nuclear emission superimposed. The annular extraction region has an inner radius of 0′.05.

2.3 Observations & Data Reduction

Archival observations for IC 3639 used in this paper were all extracted from the HEASARC archive[2]. Together, we use *Suzaku* (XIS & HXD), *Chandra* and recent *NuSTAR* data in this study. Table 2.1 shows the details of each of these observations.

Satellite	Obs. ID	Date / Y-M-D	Exp. / ks	PI
NuSTAR	60001164002	2015-01-09	58.7	P. Gandhi
Suzaku	702011010	2007-07-12	53.4	H. Awaki
Chandra	4844	2004-03-07	9.6	R. Pogge

Col. 1: Satellite name; Col. 2: Corresponding observation ID; Col. 3: Date of observation; Col. 4: Unfiltered exposure time for the observation; Col. 5: Principal Investigator (PI) of the observation.

TABLE 2.1: Details of observations used to analyse IC 3639.

2.3.1 *NuSTAR*

Data from both Focal Plane Modules (FPMA & FPMB) onboard the *NuSTAR* satellite were processed using the *NuSTAR* Data Analysis Software (NUSTARDAS) within the HEASOFT package. The corresponding CALDB files were used with the NUSTARDAS task NUPIPELINE to produce calibrated and cleaned event files. The spectra and response files were produced using the NUPRODUCTS task, after standard data screening procedures. The net count rate in the $3-79\,\mathrm{keV}$ band for FPMA & FPMB were $(9.413 \pm 0.549) \times 10^{-3}\,\mathrm{counts\,s^{-1}}$ and $(8.018 \pm 0.544) \times 10^{-3}\,\mathrm{counts\,s^{-1}}$, for net exposures of 58.7 ks and 58.6 ks, respectively (this corresponds to total count rates of $(1.686 \pm 0.054) \times 10^{-2}\,\mathrm{counts\,s^{-1}}$ and $(1.648 \pm 0.053) \times 10^{-2}\,\mathrm{counts\,s^{-1}}$ for FPMA & FPMB, respectively). Circular source regions of radius $0\farcm75$ were used to extract source counts from the corresponding event files. Background counts were extracted from annular regions of outer radius $2\farcm5$ and inner radius $0\farcm75$, centred on the source regions to avoid any cross-contamination between source and background counts. The background region was chosen to be as large as possible in the same module as the source.

The extracted spectra for FPMA and FPMB were then analysed using the XSPEC version 12.9.0 software package[3]. The energy range was constrained to the optimum energy range of *NuSTAR* and grouped so that each bin contained a signal to noise ratio of at least 4. The resulting spectra are shown in count rate units in Figure 2.3.

[2] Available from https://heasarc.gsfc.nasa.gov/cgi-bin/W3Browse/w3browse.pl.
[3] https://heasarc.gsfc.nasa.gov/xanadu/xspec/XspecManual.pdf

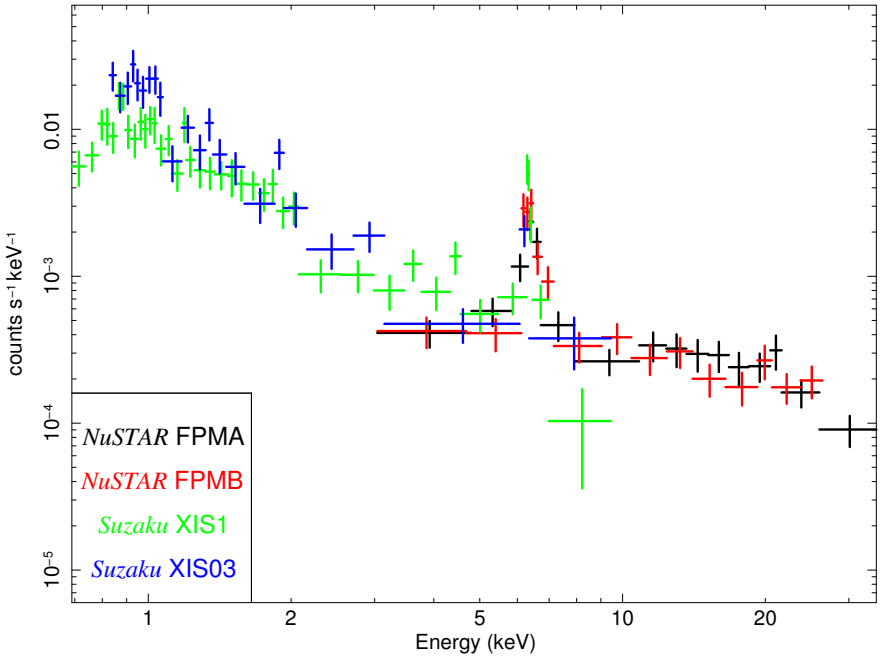

FIGURE 2.3: The *NuSTAR* FPMA and FPMB spectra plotted together with the *Suzaku*/XIS spectra in count rate units. All are binned with a signal to noise ratio of 4. The data has been normalised by the area scaling factor present in each response file - this was unity for each observation. XIS1 refers to the single back-illuminated detector on *Suzaku* used to collect the spectral counts, whereas XIS03 refers to the combined spectra from the two front-illuminated detectors, XIS0 and XIS1 - see Section 2.3.2.1 for further details.

Figure 2.1 shows the comparison of the *NuSTAR*/FPMA image with an optical *Digitised Sky Survey* (*DSS*) image. The blue regions highlight the counterparts of the merging triple, clearly visible in the optical. However, there is no detection of the separate galaxies in the *NuSTAR* image, with the primary emission originating from IC 3639.

2.3.2 *Suzaku*

When fully operational, *Suzaku* had four CCD X-ray imaging spectrometers (XISs) and a hard X-ray detector (HXD). Each XIS covered an energy range of 0.4 – 10 keV with typical resolution 120 eV[4]. During the lifetime of *Suzaku*, one of the four XIS detectors became non-operational, leaving two front illuminated detectors (XIS0 and XIS3), and one back illuminated detector (XIS1). The *Suzaku*/HXD was a non-imaging instrument designed for observations in the energy range 10 – 700 keV.

[4] Available from `isas.jaxa.jp/e/enterp/missions/suzaku/index.shtml`.

2.3.2.1 *Suzaku*/XIS

First, the XIMAGE software package[5] was used to create an image by summing over the three XIS cleaned event files. Next source counts were extracted from a circular region of radius 2′.6, with background counts extracted from an annular region of inner radius 2′.6 and outer radius 5′.0. The background annular region was again centred around the source region to avoid source and background count contamination. XSELECT was then used to extract a spectrum for each XIS detector cleaned event file using the source and background regions defined above. Lastly, the ADDASCASPEC command was used to combine the two front illuminated XIS spectra.

The final result was two spectra – one for the front illuminated cameras (XIS0 + XIS3, referred to as XIS03 herein) and one for the single back illuminated camera (XIS1). The net exposure times for XIS03 and XIS1 were 107.8 ks and 53.4 ks, respectively. The data were again grouped with a minimum signal to noise ratio of 4. Additionally the XIS spectra in the energy range 1.7 – 1.9 keV and 2.1 – 2.3 keV were ignored due to instrumental calibration uncertainties associated with the silicon and gold edges[6].

2.3.2.2 *Suzaku*/HXD

The corresponding spectrum for the *Suzaku*/HXD was generated with the FTOOLS command `hxdpinxbpi`. The data were then binned to allow a minimum of 500 counts per bin. The energy range 10 – 700 keV of *Suzaku*/HXD is achieved with Gadolinium Silicate (GSO) counters for >50 keV and PIN diodes for the range 15 – 50 keV. The GSO instrument is significantly less sensitive than *NuSTAR* and thus not used here. For the PIN instrument, a model has been designed to simulate the Non-X-ray Background (NXB). In the 15 – 40 keV range, current systematic uncertainties in the modelled NXB are estimated to be $\sim$3.2%. A *tuned* NXB file for the particle background is provided by the *Suzaku* team, whereas the Cosmic X-ray Background is evaluated separately and added to the tuned background resulting in a final *total* background. The modelled Cosmic X-ray Background is $\sim$5% of the total background for PIN. The FTOOL command `hxdpinxbpi` then uses the total background to produce a dead-time corrected PIN source and background (NXB + CXB) spectrum. The net source counts for IC 3639 are shown in red in Figure 2.4. The gross counts (source + background) are considerably higher than the net source counts and are shown in black on the same figure for comparison. The source flux was calculated in the energy range 10 – 40 keV for a simple power-law model. The corresponding fluxes for source + background ($F_{\mathrm{B,\,15\text{-}40\,keV}}$) and source alone

[5]For more information, see https://heasarc.gsfc.nasa.gov/xanadu/ximage/ximage.html.
[6]For further details, see http://heasarc.gsfc.nasa.gov/docs/suzaku/analysis/abc/node8.html.

($F_{\mathrm{S,\,15\text{-}40\,keV}}$), respectively, are:

$F_{\mathrm{B,\,15\text{-}40\,keV}} = 1.41 \pm 0.01 \times 10^{-10}\,\mathrm{erg\,s^{-1}\,cm^{-2}}$, and
$F_{\mathrm{S,\,15\text{-}40\,keV}} = 8.20\,^{+0.47}_{-8.20} \times 10^{-13}\,\mathrm{erg\,s^{-1}\,cm^{-2}}$.

The Cosmic X-ray Background is known to vary between different instruments on the order of $\sim$10% in the energy range considered here. For this reason, as a consistency check, we compared the background uncertainty from *Suzaku* (3 – 5%)[7] to the error in the total background found when the Cosmic X-ray Background flux component carried a 10% uncertainty. This altered the tuned background error to 2.9% – 4.8%. Thus, within acceptable precision, the total background appears to be unaltered by potential Cosmic X-ray Background cross-instrument fluctuations. If the source spectrum is less than $\sim$5 % of the tuned background, the detection is weak, and a source spectrum flux lower than $\sim$3% of the background would require careful assessment. The IC 3639 source counts are found to be $0.8\,^{+0.8}_{-0.9}$% of the tuned background counts in the 15 – 40 keV range. For this reason, we do not use the *Suzaku*/HXD data in our spectral analysis for IC 3639. This value contradicts Miyazawa *et al.* (2009) who report a 15 – 50 keV flux of $F_{15-50\,\mathrm{keV}} = 1.0 \times 10^{-11}\,\mathrm{erg\,s^{-1}\,cm^{-2}}$ – approximately two orders of magnitude higher than we find, as well as greater than the upper limit attained from the *BeppoSAX* satellite mentioned in Section 2.2.

We further find this result to be inconsistent with *NuSTAR*. Using a simple POWERLAW + GAUSSIAN model fitted to the *NuSTAR* data, we obtain $F^{\mathrm{FPMA}}_{15-50\,\mathrm{keV}} = 3.0\,^{+0.9}_{-0.5} \times 10^{-12}\,\mathrm{erg\,s^{-1}\,cm^{-2}}$ and $F^{\mathrm{FPMB}}_{15-50\,\mathrm{keV}} = 3.1\,^{+1.0}_{-0.4} \times 10^{-12}\,\mathrm{erg\,s^{-1}\,cm^{-2}}$. Extrapolating these fluxes to the 20 – 100 keV band gives $F_{20-100\,\mathrm{keV}} \sim 1.8 \times 10^{-12}\,\mathrm{erg\,s^{-1}\,cm^{-2}}$ for both FPMs, which is fully consistent with the upper limit found with the *BeppoSAX* satellite ($F^{BeppoSAX}_{20-100\,\mathrm{keV}} \leqslant 9.12 \times 10^{-12}\,\mathrm{erg\,s^{-1}\,cm^{-2}}$).

Figure 2.3 shows the *Suzaku*/XIS spectra over-plotted with the *NuSTAR* data. The spectral data for *Suzaku*/XIS and *NuSTAR* are consistent with each other in shape within the common energy range 3 – 10 keV. The composite spectrum formed spans approximately two dex in energy, from 0.7 – 34 keV, as a result of the minimum signal to noise ratio grouping procedures for each data set. In summary, it is highly probable that the source was not detected by *Suzaku*/HXD.

[7] For more information on the *Suzaku* background analysis, see http://heasarc.gsfc.nasa.gov/docs/suzaku/analysis/abc/node10.html.

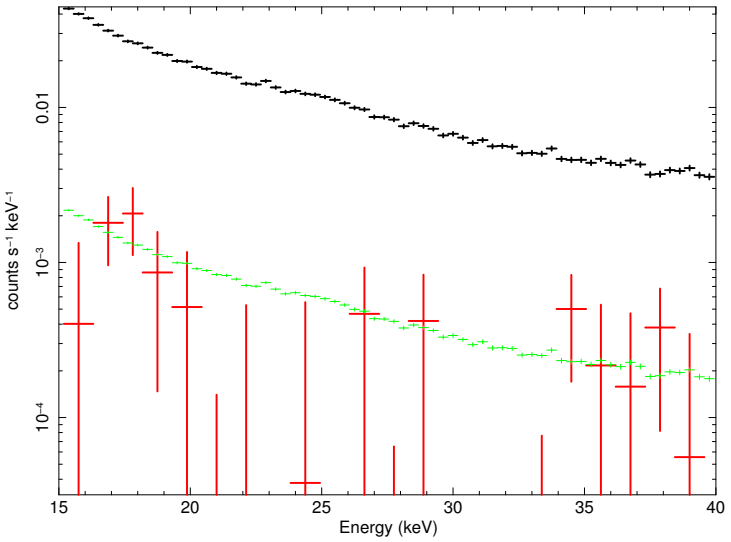

FIGURE 2.4: The *Suzaku*/HXD spectrum plotted in count rate units for gross counts (source + background), 5% gross counts (to compare the approximate threshold we use to classify a weak detection - see text for details) and net source counts shown in black, green and red, respectively. The *Suzaku*/HXD 15 – 40 keV spectral counts are shown not to be significantly detected by *Suzaku*, as discussed in Section 2.3.2.2.

2.3.3 *Chandra*

The *Chandra* level 2 event file was obtained from the HEASARC database. A fraction of the total collecting area of the detector was used in the *timed exposure mode* setting, where the CCD collects data for a set frame time. Selecting a frame time less than the default value (3.2 s for *Chandra*) reduces the probability of pile-up. This is where more than one photon in a particular bin from the same event is detected. An exposure time of 0.4 s per frame was used in the observation of IC 3639, which gives a reduced predicted pile-up fraction of $\sim 0.3\%$. This setting was chosen in the original *Chandra* observation proposal due to the previously unknown X-ray flux of the source, to minimise the potential and uncertain risk associated with pile-up.

Spectral extraction from the *Chandra* data was carried out with the CIAO 4.7 software package[8]. We primarily investigated the *Chandra* image of IC 3639 for potential contaminants located within the *Suzaku* and *NuSTAR* extraction regions. However, no particularly prominent contaminating sources were visible in the immediate vicinity of the AGN. A comparatively large circular source region of 2′.6 was used with the XIS image due to its larger point spread function (PSF) relative to *Chandra*. As a result, the XIS spectra will contain some flux from non-AGN related activity, unresolvable by that instrument. To account for this, the *Chandra* image was used to model as much of the unresolved non-AGN activity from the *Suzaku*/XIS image as possible. An annular *Chandra* source region with outer radius as close to that of the circular XIS source region

[8] http://cxc.harvard.edu/ciao/

as possible was created with inner region of radius 0.″05, excluding the central AGN. A simple power law was fitted to this spectrum, and was added to the model used with the *Suzaku*/XIS spectra. This power law is referred to as the Contamination Power Law (CPL) hereafter.

Ideally, the outer radius of the annular extraction radius used in the *Chandra* image would equal the radius of the circular source region used in the *Suzaku*/XIS image. However, as noted above, data were taken with a custom 1 / 8 sub-array on ACIS-S3. This meant that *Chandra* only observed part of the sky covered by the other instruments. As such, the image produced could not have a source region wider than $\sim 0.''5$, as opposed to the XIS source region of radius 2.′6. Accordingly, we used an annular region of outer radius 0.″5 for the *Chandra* image. The annular counts extraction region and circular background region of equal radius used with the *Chandra* image are shown in the right panel of Figure 2.2. The `specextract` command was used to create the spectral and response files for use in XSPEC. The *Chandra* spectrum was grouped with greater than or equal to 20 counts per bin prior to the CPL modelling. Furthermore, the flux of the CPL in the *Chandra* energy band (0.5 – 8 keV) was $F^{\rm CPL}_{0.5-8.0\,\rm keV} = 7.17 \times 10^{-14}\,\rm erg\,s^{-1}\,cm^{-2}$.

2.4 X-ray Spectral Fitting

The resulting spectral data sets for *Suzaku*/XIS and *NuSTAR* were used in the energy ranges 0.7 – 9.0 keV and 3.0 – 34.0 keV, respectively. Data above this threshold were excluded due to low signal to noise. Initially, the *Suzaku*/XIS and *NuSTAR* data were fitted independently of each other with a simple POWERLAW + GAUSSIAN model to give the following fluxes in the 2 – 10 keV energy band:

NuSTAR:
$F^{\rm FPMA}_{2-10\,\rm keV} = 1.81^{+0.16}_{-0.41} \times 10^{-13}\,\rm erg\,s^{-1}\,cm^{-2}$,
$F^{\rm FPMB}_{2-10\,\rm keV} = 1.86^{+0.17}_{-0.40} \times 10^{-13}\,\rm erg\,s^{-1}\,cm^{-2}$.

Suzaku/XIS:
$F^{\rm XIS03}_{2-10\,\rm keV} = 1.84 \pm 0.24 \times 10^{-13}\,\rm erg\,s^{-1}\,cm^{-2}$,
$F^{\rm XIS1}_{2-10\,\rm keV} = 2.12^{+0.34}_{-0.32} \times 10^{-13}\,\rm erg\,s^{-1}\,cm^{-2}$.

The overall match between these fluxes implies analysis can be carried out on the data sets together. A *Chandra* spectrum was extracted from a 3.″9 circular extraction region. However, there were only 35 counts present in the 2 – 10 keV band. By using the same

POWERLAW + GAUSSIAN model to determine the flux as with the other data sets, we get: $F_{2-10\,\mathrm{keV}}^{Chandra} = 9.51^{+7.83}_{-9.51} \times 10^{-14}\,\mathrm{erg\,s^{-1}\,cm^{-2}}$.
This flux is only mildly inconsistent with the other data sets, but also consistent with zero, due to the low signal to noise ratio of the data. Therefore the *Chandra* AGN data was not used for further spectral analysis, but the consistency found between this and the *Suzaku*/*NuSTAR* data sets suggests that we are classifying IC 3639 as a bona fide Compton-thick AGN robustly.

The power-law slope of the composite spectrum (*Suzaku* + *NuSTAR*) is hard, with photon index $\Gamma \sim 1.8$ and the EW of the Fe Kα line is very large (EW $\sim$ 2.4 keV). These are consistent characteristics of a heavily obscured AGN. Due to the high EWs found for the Fe Kα line with a power-law + Gaussian model, we proceeded to fit more physically motivated models as follows.

A general model structure was used with each spectrum, included in Equation 2.1. However, not all models used in this study required all the components listed in the template.

$$\begin{aligned}\textbf{TEMPLATE} = \mathrm{CONST} \times \mathrm{PHABS[GAL]} \times [\mathrm{APEC} + \mathrm{CPL} + \mathrm{SPL} + \\ (\mathrm{REFL} + \mathrm{OBSC} \times \mathrm{IPL} + \mathrm{F\_LINES})]\end{aligned} \tag{2.1}$$

Below, we give explicit details for each component in Equation 2.1:

- CONST: multiplying constant used to determine the cross-calibration between different instruments. The *NuSTAR*/FPMA constant was frozen to unity and the other three constants left free (Madsen *et al.* 2015 report cross-normalisation constants within 10% of FPMA).
- PHABS[GAL]: component used to account for photoelectric absorption through the Milky Way, based on H_{I} measurements along the line of sight (Dickey and Lockman 1990). This is represented as an obscuring column density in units of $\mathrm{cm^{-2}}$, and assumed constant between instruments (and so was frozen for each data set). The determined value was $5.86 \times 10^{20}\,\mathrm{cm^{-2}}$.
- APEC (Smith *et al.* 2001): model component used as a simple parameterisation of the softer energy X-ray emission associated with a thermally excited diffuse gas surrounding the AGN. Detailed studies of brighter local AGN indicate that photoionisation may provide a better description of the soft X-ray emission in AGN spectra (e.g.,Guainazzi *et al.* 2009; Bianchi *et al.* 2010), but such modelling would require much higher spectral resolution than currently available for IC 3639. The low-energy spectral shape for IC 3639 found with *Suzaku*/XIS is far softer than for the higher energy portion of the spectrum.

- CPL: component referring to the *Contamination Power Law*, used to account for the unresolved non-AGN emission contaminating the *Suzaku*/XIS spectral counts. See Section 2.3.3 for further details.

- SPL: component referring to the *Scattered Power Law*. This accounts for *intrinsic* AGN emission that has been scattered into our line of sight from regions closer to the AGN, such as the NLR. The power law photon index and normalisation were tied to the intrinsic AGN emission as a simplification. However, a constant multiplying the SPL component was left free to allow a variable fraction of observed flux arising from scattered emission.

- The final term in Equation 2.1 collectively consists of three parts:

  – REFL: reflected component, arising from the primary nuclear obscurer and has been modelled in varying ways. In this work, we use slab models (PEXRAV and PEXMON) as well as toroidal geometry models (TORUS and MYTORUS), described in Sections 2.4.1, 2.4.2 and 2.4.3 respectively.

  – OBSC × IPL: Most models include the direct transmitted component (*intrinsic power law* or IPL), after accounting for depletion due to absorption through the obscurer via the multiplying OBSC term.

  – F_LINES: component describing fluorescence emission lines believed to arise from photon interactions with the circumnuclear obscurer.

2.4.1 Slab models: PEXRAV and PEXMON

Slab models describe X-ray reflection off an infinitely thick and long flat slab, from a central illuminating source. PEXRAV (Magdziarz and Zdziarski 1995) comprises an exponentially cut-off power law illuminating spectrum reflected from neutral material. To acquire the reflection component alone, with no direct transmitted component, the reflection scaling factor parameter is set to a value $R < 0$.

Other parameters of interest include the power law photon index; cutoff energy; abundance of elements heavier than helium; iron abundance (relative to the previous abundance) and inclination angle of the slab (90° describes an edge-on configuration). The model gave far better reduced chi-squared values for a reflection-dominated configuration, and as such the reflection scaling factor was frozen to -1, corresponding to a 50% covering factor.

2.4.2 BNTORUS

Two tabular models are provided by Brightman and Nandra (2011a) to describe the obscurer self-consistently including the intrinsic emission and reflected line components. The spherical version describes a covering fraction of one in a geometry completely enclosing the source. The presence and morphology of NLRs in a multitude of sources favours a covering factor < 1, implying an anisotropic geometry for the shape of the obscurer in most Seyfert galaxies. For this reason, preliminary results were developed with this model, before analysis was carried out with toroidal models. For further discussion of the NLR of IC 3639, see Section 2.6.1.

The second BNTORUS model (model **T** hereafter) was used extensively in this study. This models a toroidal obscurer surrounding the source, with varying opening and inclination angles. Here, the opening angle describes the conical segment extending from both poles of the source (i.e. the half-opening angle). Because the obscurer is a spherical section in this model, the column density along different inclination angles does not vary, provided the line of sight intercepts the obscurer. The range of opening angles studied is restricted by the inclination angle since for inclination angles less than the opening angle, the source becomes unobscured. Thus to allow exploration of the full range of opening angles, we fixed the inclination angle to the upper limit allowed by the model: 87° (Brightman *et al.* 2015). The tables provided for BNTORUS are valid in the energy range $0.1 - 320\,\mathrm{keV}$, up to obscuring column densities of $10^{26}\,\mathrm{cm}^{-2}$. Equation 2.2 describes the form of model T used in XSPEC- all properties associated with the absorber are present in the TORUS term, and collectively used in the modelling process.

$$\begin{aligned} \text{MODEL } \mathbf{T} = \text{CONST} \times \text{PHABS} \times (\text{APEC} + \text{SPL} + \\ \text{CPL} + \text{TORUS}) \end{aligned} \tag{2.2}$$

Liu and Li (2015) report BNTORUS to over-predict the reflection component for edge-on geometries, resulting in uncertainties. However, varying the inclination angle did not drastically alter our fits and consistent results were acquired between both models T and M, described next.

2.4.3 MYTORUS

The MYTORUS model, developed by Murphy and Yaqoob (2009), describes a toroidal-shaped obscurer with a fixed half-opening angle of 60°, and free inclination angle. However, because the geometry here is a doughnut as opposed to a sphere, the line of sight column density will always be less than or equal to the equatorial column density (with equality representing an edge-on orientation with respect to the observer).

The full computational form of this model is shown in Equation 2.3, and encompasses the energy range 0.5 – 500 keV, for column densities up to $10^{25}\,\mathrm{cm}^{-2}$. Three separate tables are used to describe the different components encapsulating this model: the *transmitted absorption* or *zeroth order* continuum, altered by photoelectric absorption and Compton scattering; the *scattered component*, describing Compton scattering off the torus; and the *fluorescence emission* for neutral Fe Kα and Fe-Kβ together with their associated Compton shoulders. This study uses the *coupled* mode for this model, where model parameters are tied between different table components. For further details on the decoupled mode, which is often used for sources showing variability or non-toroidal geometries with high signal to noise data, refer to the publicly available MYTORUS examples,[9] or see Yaqoob (2012). The XSPEC notation of our model using MYTORUS is referred to as model M hereafter, and is as follows:

$$\begin{aligned} \text{MODEL } \mathbf{M} = \text{CONST} \times \text{PHABS} \times (\text{APEC} + \text{SPL} + \text{CPL} + \\ \text{POW} * \text{ETABLE}\{\texttt{trans. absorption}\} + \\ \text{ATABLE}\{\texttt{scattered}\} + \\ \text{ATABLE}\{\texttt{fluor\_lines}\}) \end{aligned} \tag{2.3}$$

2.5 Results from Spectral Fitting

In this section, we present the results of our X-ray spectral fitting of IC 3639 together with model-specific parameters shown in Table 2.2. Figures 2.5 and 2.6 show the spectra and best-fit models attained for models T and M, respectively. First we consider the EW of the Fe Kα line. As previously mentioned, an EW of the order of 1 keV has been taken to be indicative of strong reflection in prior works. Risaliti *et al.* (1999a) found the EW for IC 3639 to be $3.20^{+0.98}_{-1.74}$ keV. In order to determine an EW for the Fe Kα line here, we modelled a restricted energy range of $\sim 3-9$ keV with a simple POWERLAW + GAUSSIAN

[9] http://mytorus.com/mytorus-examples.html

model. Here the power law was used to represent the underlying continuum, and the Gaussian was used as a simple approximation to the Fe Kα fluorescence line. Additionally, all four data sets were multiplied by cross-calibration constants in the same way as described in the template model.

Due to low signal to noise, the continuum normalisation had a large uncertainty. As such, a robust error could not be directly determined on the EW using XSPEC. Alternatively, we carried out a four dimensional grid to step over all parameters of the model in XSPEC, excluding line energy, which was well defined and frozen at 6.36 keV in the observed frame. The EW was calculated for each grid value, and the corresponding confidence plot is shown in Figure 2.7. The horizontal black line represents the 90% confidence region for the chi-squared difference from the best-fit value, $\Delta\chi^2$. Here, the 90% confidence level refers to the chi-squared distribution for four free parameters with value $\Delta\chi^2 = 7.779$. Figure 2.8 shows the model used, fitted to the four data sets. This gave an EW of $2.94^{+2.79}_{-1.30}$ keV, consistent with Risaliti *et al.* (1999a). This is well above the approximate threshold of 1 keV often assumed to be associated with the presence of Compton-thick obscuration. However, Gohil and Ballantyne (2015) find the presence of dust in the obscuring medium can enhance the Fe Kα line detection even for Compton-thin gas. This is a further reason for the importance of consistent modelling to determine the column density more robustly. Additionally, the errors seem to favour a high EW, with the upper limit fully encapsulating the most extreme cases reported by Levenson *et al.* (2002).

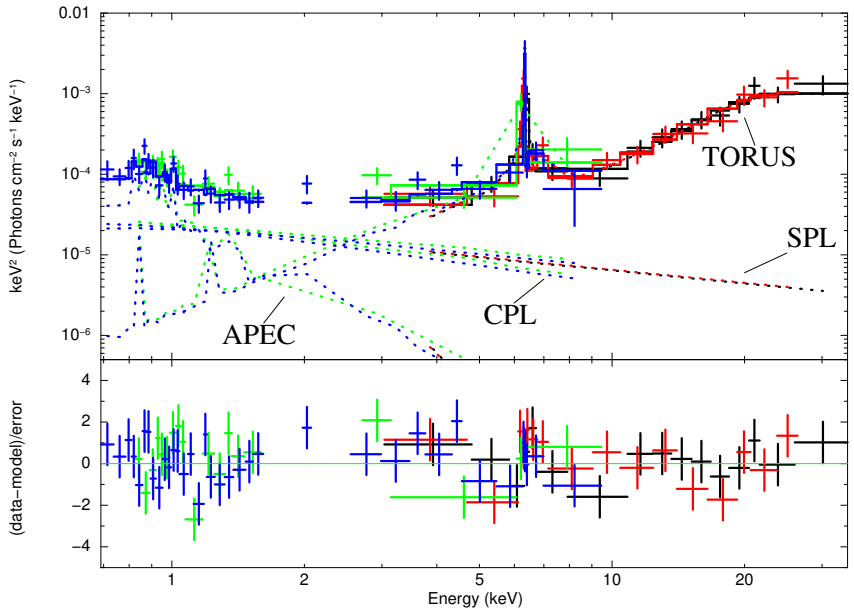

FIGURE 2.5: Best fit for spectral model T. Top panel represents the unfolded spectrum, with the bottom panel representing the residuals present. Both fits appear to show a slight residual still present around the iron line energy band of $\sim 6.4\,\mathrm{keV}$. Model components are labelled in accordance with the description in Section 2.4.2. Colour scheme is the same as in Figure 2.3.

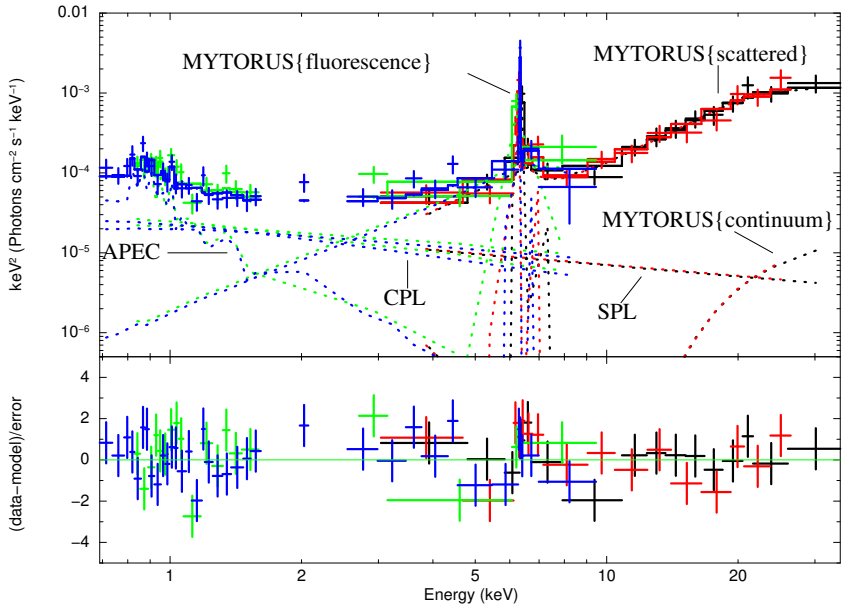

FIGURE 2.6: Best fit for spectral model M. Layout and colour scheme is the same as in Figure 2.5.Top panels in both represent the unfolded spectrum, with the bottom panel representing the residuals present. The fit again appears to show a slight residual present around the iron line energy band of $\sim 6.4\,\mathrm{keV}$. Model components are labelled in accordance with the description in Section 2.4.3. Although the components are labelled separately, all parameters between the tables for these components were tied together in the default *coupled mode* for the model - see the text for further details.

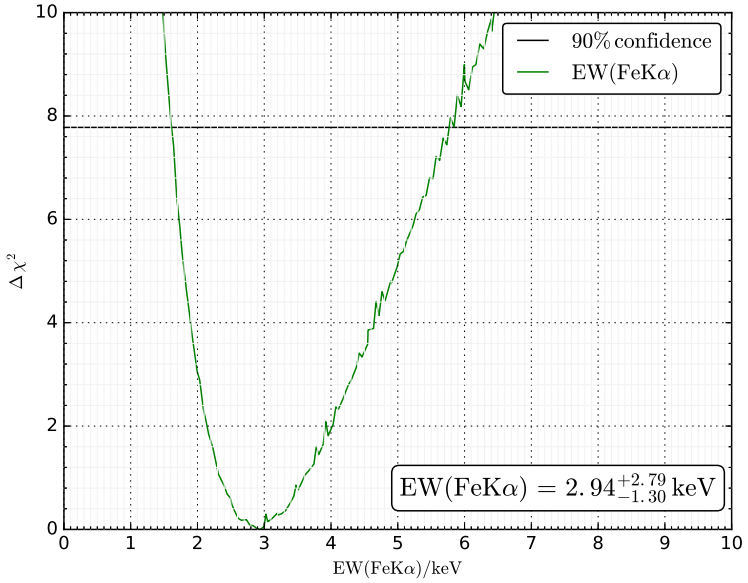

FIGURE 2.7: EW of the Fe Kα line as a function of $\Delta\chi^2$. The horizontal black line represents the 90% confidence level for the chi-squared distribution with four free parameters, of $\Delta\chi^2 = 7.779$. This was generated with a four dimensional grid over the best-fit parameters used in the model.

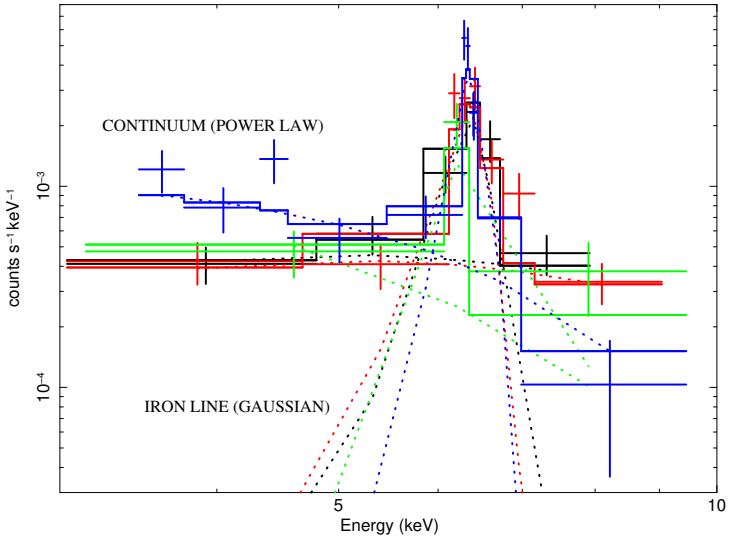

FIGURE 2.8: Fit generated with the simplified model for all four data sets, including cross-calibration constants. The colour scheme used is the same as in Figure 2.3. Dotted lines show individual additive model components used, labelled for clarity.

Both models T and M yield consistent cross-calibration constants between data sets (see Table 2.2), with the exception of cross-calibration between *NuSTAR*/FPMA and *Suzaku*/XIS 1. The cross-calibration constant between *NuSTAR* and *Suzaku* data significantly deviated from unity if the CPL component were removed. This strongly indicates that the extra CPL component is necessary. The varying cross-calibration between *Suzaku* and *NuSTAR* may be due to instrumental differences unaccounted for with the

CPL component, or perhaps a subtle signature of variability. To test these scenarios, the cross-calibration constants were fixed to those found by Madsen *et al.* (2015), who report accurate cross-calibration constants for *NuSTAR*/FPMA relative to a wide array of common X-ray instruments. This resulted in comparable reduced chi-squared values of 98 / 80 and 104 / 80 for models T and M respectively, together with marginally altered physical parameters from those presented in Table 2.2, arguing against significant variability present in the source.

The scattering fraction numerically represented by the constant multiplying the SPL component is comparable between models T and M. Even within the high upper limit found for either model, the total scattering fraction is $\lesssim 0.6\%$. Such values are not uncommon in previous Compton-thick studies (e.g., Gandhi *et al.* 2015b; Annuar *et al.* 2015), and suggest that a minor contribution of the total $< 10\,\mathrm{keV}$ flux arises from scattered emission, although proper modelling of higher signal to noise data describing the soft emission would be required to better constrain this.

Next we consider parameters relating to the absorber specifically. The equatorial column density for model T is the same as the column density along the line of sight, whereas the line of sight column density for model M is less than or equal to the equatorial column density. This is the reason for the two separate entries in Table 2.2 for model M. Model T indicates a strongly Compton-thick obscuring column density of $9.0 \times 10^{24}\,\mathrm{cm^{-2}}$ along the line of sight. For comparison, model M gives a similar line of sight column density at $9.8 \times 10^{24}\,\mathrm{cm^{-2}}$. Both models are unconstrained at the upper limit and also $> 3.0 \times 10^{24}\,\mathrm{cm^{-2}}$ for the lower limit, consistently within the Compton-thick regime (see Table 2.2).

Initially the inclination angle and opening angle were left free to vary in model T, but this led to the model diverging to the limits - i.e. the upper limit on inclination angle (describing an edge-on torus) and/or the lower limit on opening angle (describing a large covering fraction). The inclination angle for both models was tested by stepping over the parameter in XSPEC in the full allowable range, in addition to fixing the angle to intermediate values such as 60°. This did not result in a significant improvement in $\Delta\chi^2$, and in some cases worsened the fit. As discussed in Section 2.4.2, the inclination angle of model T was fixed to 87° to allow exploration of a full range of opening angles. In contrast, model M has a fixed half-opening angle (by default) and the inclination angle was left free. The inclination angle found for model M is lower than for model T, at $\sim 84°$, inconsistent with model T at the upper end. This could be affected by the model inconsistencies at edge-on inclinations for model T reported by Liu and Li (2015). This still suggests a near edge-on torus inclination however. In contrast, the opening angle for model T (29°) is lower than the fixed value in model M. A reduced opening angle implies

an increased covering factor surrounding the source and thus potentially a strengthened reprocessed component.

The intrinsic AGN spectrum can be studied via the continuum photon index. Both models consistently agree on a soft photon index of $\sim$2.5 - far softer than the average value of $\sim$1.9 found in large surveys (e.g., Mateos *et al.* 2005). However, our value is consistent with typical values within the uncertainties. To test this, the photon index was fixed to 1.9 in both models. The $\Delta\chi^2$ values increased to 97 / 78 and 101 / 78, yielding F-test statistics of 3.05 and 1.72 for models T and M, respectively. These values suggest that a photon index of 1.9 is marginally less likely, but not immediately ruled out in either case. Such high photon indices have been found before from these torus models used with Compton-thick sources (Baloković *et al.* 2014; Brightman *et al.* 2015) and could imply accretion at a large fraction of the Eddington rate (e.g., Brightman *et al.* 2016). The Eddington ratio is discussed further in Section 2.6.2. Additionally, the absorber is likely more complex in reality than a geometrically smooth torus as assumed in models T and M. This has been found in NGC 1068, by Bauer *et al.* (2015) for example, where a multi-component reflector is comprised of several layers of differing column densities. We include in the Appendix a contour plot between the intrinsic photon index and column density for models T and M as an example. The plots both show the unconstrained nature of $N_{\rm H}$ as well as the favoured soft photon index by either model.

Overall both models T and M give acceptable fit statistics – χ^2 / dof values of 94 / 77 and 99 / 77, respectively. Initial testing with model P yielded a lower reduced chi-squared of 85 / 76. Since the transmitted power law is not directly visible over any of the spectrum, constraining the reflection fraction (defined as the strength of the reflection component relative to a semi-infinite slab subtending 2π steradians on the sky fully reflecting the intrinsic power law) is highly uncertain. This was used as justification to fix the reflection scaling factor to -1. Other than the reflection-dominated nature of the source, there are few aspects to be learnt from the over simplified slab geometry of `pexmon`/`pexrav`. Furthermore, slab models effectively give a lower limit on the intrinsic power of the source, since the slab subtends 2π steradians on the sky, equivalent to a 50% unobscured covering factor, as opposed to the torus models, in which this solid angle is computed self-consistently with inclination. Model P did, however, appear to require a super-Solar iron abundance to explain the prominent iron line complex present in the spectra of IC 3639. The iron abundance (in units of the Solar abundance) and abundance of elements heavier than helium (in units of the iron abundance) were tied to each other and left free. This yielded an abundance of $2.0^{+0.7}_{-0.5}$. We tested this outcome by freezing the abundance and iron abundance to Solar values, as is default in models M and T. This resulted in a considerable increase in reduced chi-squared to 102 / 78. Fixing one of these individually of the other resulted in comparable best-fit reduced chi-squared

TABLE 2.2: Parameters determined from the X-ray spectral fitting of IC 3639.

Component	Parameter	Model T	Model M	Units
Fe Kα fluorescence emission-line	Equivalent width	.....$2.72^{+2.99}_{-0.93}$.....		keV
Cross-calibration constants	[FPMA↦FPMB]	$1.02^{+0.14}_{-0.15}$	$1.02^{+0.15}_{-0.14}$	-
	[FPMA↦XIS1]	$1.21^{+0.25}_{-0.21}$	$1.25^{+0.25}_{-0.23}$	-
	[FPMA↦XIS03]	$1.11^{+0.21}_{-0.16}$	$1.14^{+0.20}_{-0.19}$	-
Soft emission (APEC)	kT	$0.79^{+0.13}_{-0.09}$	$0.78^{+0.08}_{-0.10}$	keV
	$L^{\rm int}_{0.5-2\ {\rm keV}}{}^{\dagger}$	2.01	2.06	$\times 10^{40}$erg s^{-1}
Diffuse scattering fraction (SPL)	$f_{\rm scatt}$	$0.97^{+3.39}_{-0.63}$	$0.20^{+5.58}_{-0.15}$	$\times 10^{-3}$
Column densities	$N_{\rm H}$(eq)	$8.98^{+{\rm u}}_{-3.23}$	$10.0^{+{\rm u}}_{-4.1}$	$\times 10^{24}$cm^{-2}
	$N_{\rm H}$(los)		$9.76^{+{\rm u}}_{-6.15}$	
Orientation Angle	$\theta_{\rm inc}$	87.0$^{\rm f}$	$83.8^{+1.9}_{-17.2}$	deg
Half-opening Angle	$\theta_{\rm tor}$	$28.5^{+26.1}_{-{\rm u}}$	60.0$^{\rm f}$	
AGN continuum	$\Gamma_{\rm int}$	$2.54^{+0.27}_{-0.33}$	$2.46^{+u}_{-0.60}$	-
	$L^{\rm int}_{2-10\ {\rm keV}}{}^{\dagger}$	9.26	45.7	$\times 10^{42}$erg s^{-1}
	$L^{\rm int}_{0.5-30\ {\rm keV}}{}^{\dagger}$	2.99	14.0	$\times 10^{43}$erg s^{-1}
χ^2 / dof		94/77	99/77	-

$^{\rm f}$ - fixed values.
$\Gamma_{\rm int}$ - intrinsic AGN photon index, determined for the range 1.4 – 2.6.
†luminosities calculated with a distance to the source of 53.6 Mpc, from the best-fit values determined in XSPEC.
u - unconstrained.

values, but with the free parameter of the two significantly deviating from unity. In comparison, the fits shown in Figures 2.5 and 2.6, using the toroidal models T and M respectively, show a slight residual around the iron line region. This suggests both models are insufficiently describing the iron fluorescence in IC 3639. Besides strong reflection, high iron abundance is one possible cause of prominent iron fluorescence and may be partly responsible for the extreme Fe Kα line EW observed for IC 3639. Alternatively, Levenson *et al.* (2002) discuss how circumnuclear starbursts can also lead to strong iron emission. This is analysed further in Section 2.6.1, where the star formation rate is considered.

2.6 Discussion

2.6.1 Spectral Components

The line of sight obscuring column densities for models M and T are consistent with one another, both well within the Compton-thick regime and unconstrained at the upper

end. Our findings are also consistent with Risaliti *et al.* (1999a), arguing against source variability between the *NuSTAR* and *Suzaku* observations.

The column density determined here establishes IC 3639 as a Compton-thick AGN in a face-on host-galaxy. Such a configuration is uncommon but not unheard of (e.g., Annuar *et al.* 2015). However, Fischer *et al.* (2013) find no correlation between the orientations of the NLR and host-galaxy disc suggesting that the obscurer thought to be responsible for shaping the NLR in many galaxies may be independent of the host disk. Furthermore, Fischer *et al.* find IC 3639 to have ambiguous NLR kinematics – corresponding to a symmetrical ionised gas component on either side of the nucleus, but may not represent each half of a NLR bicone. A non-biconical outflow is consistent with heavy obscuration and could indicate a high covering factor, restricting NLR emission.

Levenson *et al.* (2002) find the highest Fe Kα EWs for sources with $N_{\rm H} \sim 6{\times}10^{24}\,{\rm cm}^{-2}$, in combination with large inclination angles. However from simulations, the authors found that the EW diminishes at even higher column densities since fluorescence photons cannot escape for such high optical depths, comparable with the $N_{\rm H}$ values determined here. It should be noted that their simulations are for a more simplistic geometry formulation with a square torus cross section (although Yaqoob *et al.* 2010 found Compton-thick lines of sight gave Fe Kα line strengths considerably less than the maximum possible for a given geometry). So this may indicate a secondary source of strong iron fluorescence for IC 3639, such as super-Solar iron abundance. As already stated, this was found in model P to help fit the residuals present in the iron-line energy region. Since models T and M assume Solar abundance, the final residuals present in Figures 2.5 and 2.6 around the iron line complex may be due to a super-Solar iron abundance present in IC 3639, or perhaps a high star formation rate, potentially leading to high supernovae type Ia rates in the host galaxy, which have been postulated to enhance iron abundance. Alternatively, Ricci *et al.* (2014) find that as the column density for Compton-thick AGN is increased, the EW of the iron fluorescence line is decreased. This indicates a suppression of the reflection component for *heavily* obscured systems, and suggests that the intrinsic iron line EW of IC 3639 could be even greater than we are observing here.

Regarding star formation rates, the intrinsic soft band (0.5 – 2 keV) luminosity found from the APEC component was $\sim 2.0 \times 10^{40}\,{\rm erg\,s^{-1}}$ for both models. Mineo *et al.* (2012) derive a conversion between soft X-ray luminosity and host-galaxy star formation rate. The authors determined the soft X-ray luminosity through the MEKAL XSPEC model, but for our purposes using the APEC-determined luminosity is sufficient/equivalent to establish an approximate estimate. By accounting for the dispersion in the Mineo *et al.* (2012) relation of 0.34 dex, we find the star formation rate, ${\rm SFR_{X\text{-}ray}} = 39^{+46}_{-21}\,{\rm M_\odot\,year^{-1}}$.

Using a total infrared luminosity calculated from the *IRAS* catalogued fluxes[10] of $L_{8-1000\,\mu\mathrm{m}} = 8.14 \times 10^{10}\,\mathrm{L}_{\odot}$, we find an infrared-derived star formation rate using the relation presented by Murphy *et al.* (2011) of $\mathrm{SFR}_{\mathrm{IR}} \sim 12\,\mathrm{M}_{\odot}\,\mathrm{year}^{-1}$.

Alternatively, Polycyclic Aromatic Hydrocarbon (PAH) features are believed to be prominent in the spectra of starburst galaxies, with a good correlation found between PAH strength and infrared luminosity. We make use of Equation (5) from Farrah *et al.* (2007), which uses an approximate scaling to account for the high rate of star formation observed in ultraluminous infrared galaxies. Using the 6.2 and 11.2 μm luminosities for IC 3639 from *Spitzer*/IRS data (Wu *et al.* 2009), with the equation of Farrah *et al.* gave a PAH-derived star formation rate of $\mathrm{SFR}_{\mathrm{IR[PAH]}} = 12 \pm 6\,\mathrm{M}_{\odot}\,\mathrm{yr}^{-1}$, fully consistent with the *IRAS*-derived value.

The X-ray star formation rate is higher than both infrared-derived (PAH and *IRAS*) star formation rates by a factor of $\sim 2-3$, but fully consistent within the uncertainties. All star formation rates determined here for IC 3639 are comparable with typical starburst galaxies from Brandl *et al.* (2006). We note that although Barnes and Webster (2001) find the interacting galaxy group hosting IC 3639 to be free of a strong merger, they still report the possibility of enhanced star formation via galaxy harassment. This being said, all factors presented here are consistent with the hypothesis of Levenson *et al.* 2002; namely that circumnuclear starbursts may lead to strong iron emission.

2.6.1.1 The Scattered & Contaminant Power Laws

The Scattered PowerLaw (SPL) and Contaminant PowerLaw (CPL) components found (shown in Figures 2.5 & 2.6 for models T and M, respectively) appear to agree in both slope and normalisation, warranting further investigation. We ran an MCMC chain of length 1,000,000 for models T& M, as well as for the original model used with the *Chandra* data to produce the CPL component. The result of the SPL and CPL normalisations and photon indices in this chain are shown in Figure 2.9. Clearly, the values found are broadly consistent with one another. Note that the SPL component is included in both the *NuSTAR* and *Suzaku*/XIS data, whereas the CPL component is only included in the *Suzaku*/XIS data. However, the *NuSTAR* data still has a PSF that is much larger than *Chandra*. For this reason, the SPL fit for $E \lesssim 8\,\mathrm{keV}$ to the *NuSTAR* data will encompass some of the emission accounted for in the CPL component. Thus, it is plausible that the SPL component that is tied between *Suzaku*/XIS and *NuSTAR* is actually dominated by the unresolved CPL emission present in the *NuSTAR* data.

[10] Available at: http://irsa.ipac.caltech.edu/applications/Gator/index.html.

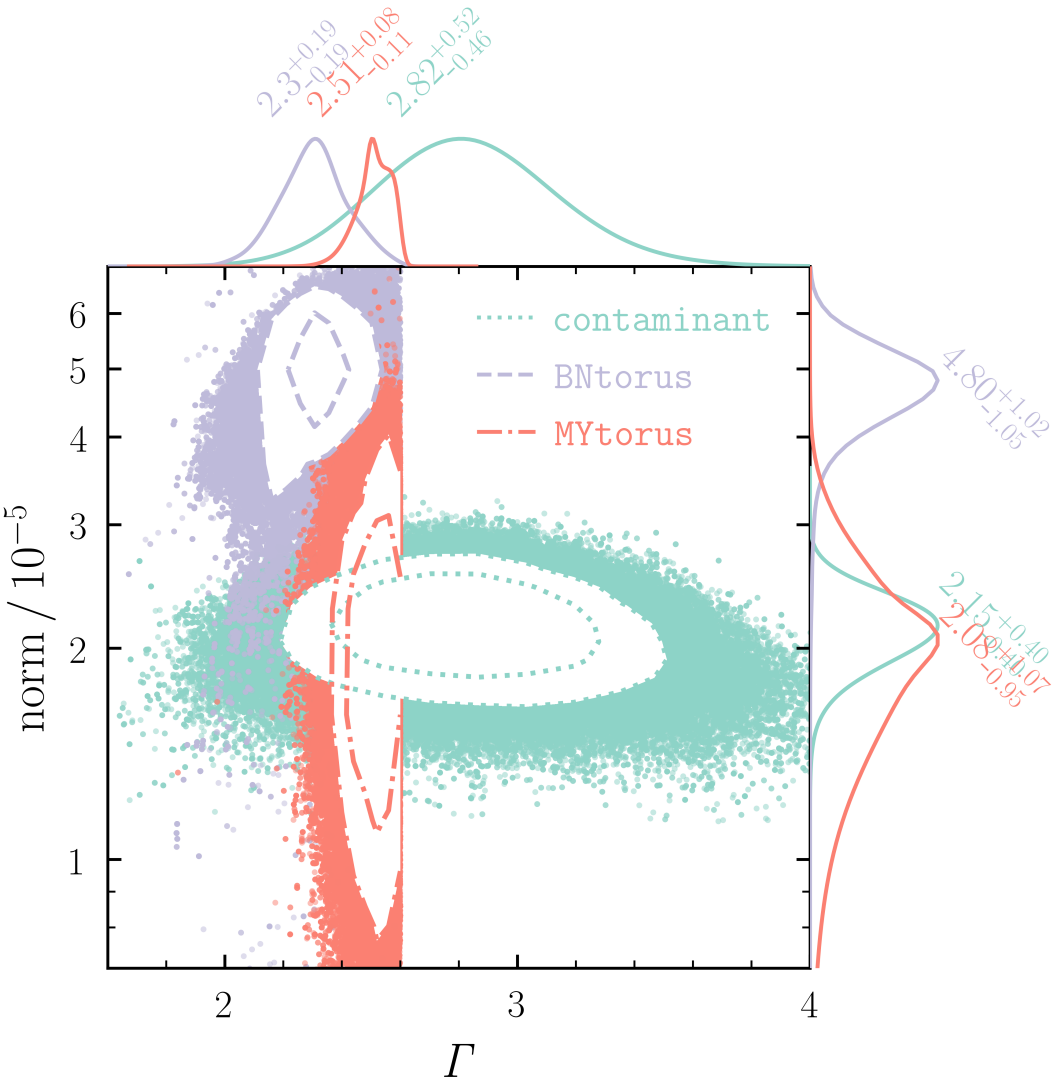

FIGURE 2.9: Confidence contours for the SPL and CPL components found in powerlaw photon index vs. normalisation parameter space. For the SPL component, the normalisation is the product of the intrinsic powerlaw normalisation and scattered fraction. All components are found to be broadly consistent, which we use as evidence for possible unresolved extended emission due to the *NuSTAR* PSF that is accounted for in the *Suzaku*/XIS data.

2.6.2 Intrinsic AGN Luminosity

The unobscured (*intrinsic*) luminosity of the source in the 2 – 10 keV band was calculated with the model-dependent photon index and normalisation of the IPL component. By stepping over the photon index and normalisation for either model in a two-dimensional grid, the intrinsic X-ray luminosity and corresponding $\Delta\chi^2$ value were determined. The envelope of all $\Delta\chi^2$ values for any given luminosity was then extracted, and is plotted in Figure 2.10 for models T and M, similar to the four-dimensional grid used in Figure 2.7 to determine the EW of the iron line. This gives a luminosity range of $\log L_{2-10\,\mathrm{keV}} \,/\, \mathrm{erg\,s^{-1}} = 42.3 - 44.0$, with intrinsic average X-ray luminosity $\log L_{2-10\,\mathrm{keV}} \,/\, \mathrm{erg\,s^{-1}} = 43.4^{+0.6}_{-1.1}$.

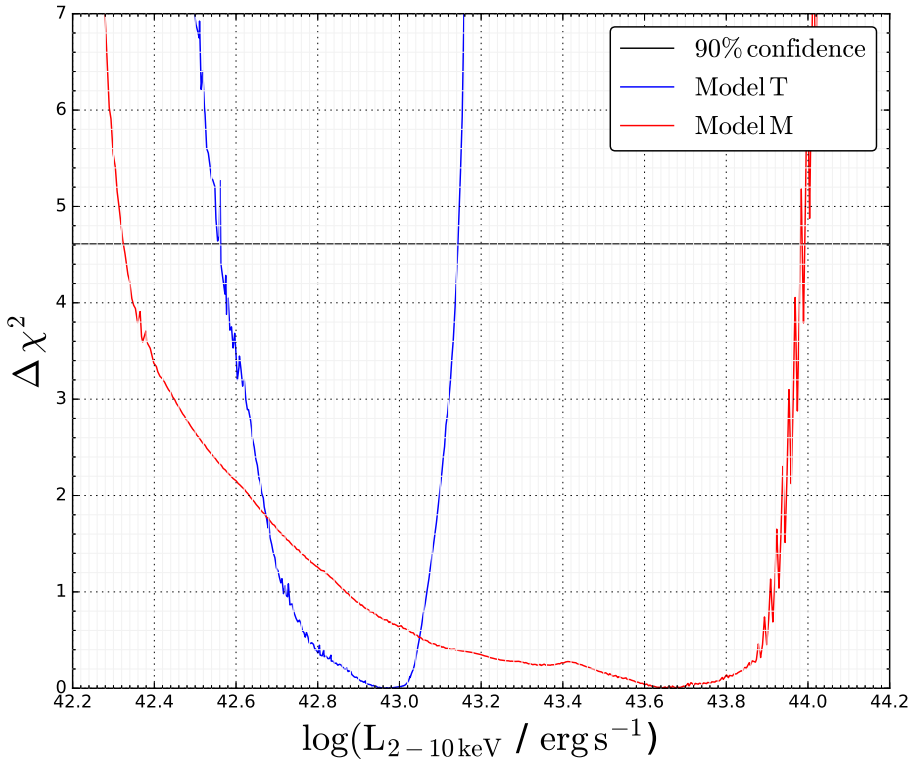

FIGURE 2.10: Intrinsic X-ray luminosity (2 – 10 keV) against $\Delta\chi^2$, corresponding to the difference between observed chi-squared value for a particular implementation of parameters and the best-fit chi-squared value corresponding to the best-fit parameter values presented in Table 2.2. The 90% confidence level is shown as a black line at $\Delta\chi^2 = 4.61$, in correspondence with the chi-squared distribution for two free parameters. Model M encompasses the full range of model T luminosities found.

As can be seen in Figure 2.10, luminosities for model M completely encompass luminosities for model T at 90% confidence. Additional tests appear to show that this wide range of allowable model M luminosities is due to an uncertain inclination angle. For example, we fixed the inclination angle to intermediate values in the range 70 – 84° for model M (approximate lower and upper limits found for the best fit). The envelope presented in Figure 2.10 fully encompassed the intermediate fixed inclination angle results. Furthermore, a three-dimensional parameter space analysis between inclination angle, photon index and normalisation showed an increase of intrinsic X-ray luminosity with inclination angle, but also an increase in best-fit chi-squared value.

Recent works have demonstrated a correlation between X-ray luminosity and accretion disc luminosity. For example, we use Equation (6) from Marchese *et al.* (2012) to approximate the accretion disc luminosity of IC 3639. In order to consistently use this relation which is calculated to the $1-\sigma$ confidence level, we have derived the 2 – 10 keV luminosity for IC 3639, based on Figure 2.10, but at the $1-\sigma$ confidence level for the chi-squared

distribution with two free parameters of $\Delta\chi^2 = 2.30$. This gives $\log L_{2-10\,\mathrm{keV}} \,/\, \mathrm{erg\,s^{-1}} = 43.4^{+0.6}_{-0.8}$ $(1\,\sigma)$, resulting in a disc luminosity:

$$\log L_{\mathrm{Disc}} \,/\, \mathrm{erg\,s^{-1}} = 44.5^{+0.7(+0.1)}_{-0.9(-0.2)}.$$

The upper and lower bounds in brackets represent the intrinsic scatter from the Marchese *et al.* relation, based on treating L_{Disc} or $L_{2-10\,\mathrm{keV}}$ as the independent variable. The other uncertainty represents the error associated with the observed $2-10\,\mathrm{keV}$ luminosity uncertainty.

To determine the black hole mass (M_{BH}), we used the stellar velocity dispersion from Marinucci *et al.* (2012) of $99 \pm 5\,\mathrm{km\,s^{-1}}$ with the $\mathrm{M}-\sigma$ relation from Gültekin *et al.* (2009) to give $\log M_{\mathrm{BH}} \,/\, \mathrm{M_\odot} = 6.8 \pm 0.2$, and thus $\log L_{\mathrm{Edd}}\,\mathrm{erg\,s^{-1}} = 44.9 \pm 0.2$. This corresponds to an Eddington ratio of:

$$\log \lambda_{\mathrm{Edd}} = -0.4^{+0.8}_{-1.1},$$

to the $1-\sigma$ confidence level. Here we have defined $\log \lambda_{\mathrm{Edd}} = \log\left(\dfrac{L_{\mathrm{Disc}}}{L_{\mathrm{Edd}}}\right)$. Using the accretion disc luminosity as opposed to the bolometric luminosity is acceptable since L_{Disc} should dominate the bolometric luminosity. The mean Eddington ratio corresponds to an Eddington rate of $\sim 40\%$. The uncertainty is rather large and dominated by the unknown obscurer geometry (cf. the broad model M contours in Figure 2.10), but these are robust uncertainties incorporating all systematics. Furthermore, as we discuss in the next section, the implied luminosity is high even at the lower uncertainty limit, and is consistent with other multi-wavelength diagnostics.

To compare with a bolometric luminosity determined Eddington ratio, we use the bolometric correction factor of $\sim 10-30$ from Vasudevan *et al.* (2010) for converting X-ray to bolometric luminosity. This gives a slightly shifted range of Eddington ratios of $\log \lambda_{\mathrm{Edd}} = -1.6 \rightarrow 0.6$, which corresponds to $\gtrsim 2.5\%$ of the Eddington rate (with the upper end being considerably super-Eddington).

2.6.3 Comparison with Other *Bona Fide* Compton-thick AGN

2.6.3.1 Ratio of Intrinsic to Observed Luminosity

The intrinsic parameters determined here with broad-band spectral fitting are consistent with multiple observations reported over the past ~ 20 years. This indicates a lack of extreme variability in the source, and allows us to stipulate IC 3639 as a *bona fide* Compton-thick AGN. To date, there exists just $\sim 20-30$ *bona fide* Compton-thick AGN, names of which are collated in Table 2.3. Here, a *bona fide* Compton-thick AGN shows Compton-thick column densities based on broadband X-ray spectral analysis (encompassing $E > 10$ keV), and lacks extreme variability in the X-ray band, indicative to unobscured sight-lines to the intrinsic accretion disc or variable absorption. The ID numbers presented in all bona fide Compton-thick source plots herein correspond to the values shown in Table 2.3.

IC 3639 appears to show a comparatively high ratio of intrinsic to observed luminosity relative to other bona fide Compton-thick AGN. Here I again specify the X-ray luminosity in the 2 – 10 keV band, and the intrinsic luminosity to be the absorption corrected luminosity. Given the observed 2 – 10 keV luminosity of $\log L_{\rm obs}\,{\rm erg\,s^{-1}} = 40.79^{+0.04}_{-0.11}$, IC 3639 has:

$$\log L_{\rm int} \,/\, L_{\rm obs} = 2.6^{+0.6}_{-1.1},$$

corresponding to a luminosity ratio of almost 300. In comparison with the other bona fide AGN listed in Table 2.3, there exists just one other source with such a comparatively high ratio – NGC 1068. The distribution of this ratio amongst the bona fide Compton-thick AGN is shown in Figure 2.11. Such a high value of the ratio complements the high column density predicted for the source based on multi-wavelength indicators, discussed next.

2.6.3.2 Multi-wavelength Indicators

The large correction from observed to intrinsic X-ray luminosity for IC 3639 should be checked with independent methods, and for this we use multi-wavelength comparisons with the mid-infrared and optical [O III] luminosities. Using the published value of the reddening-corrected [O III] flux for IC 3639 from LaMassa *et al.* (2010), the corresponding luminosity is $\log L_{\rm [OIII]} \,/\, {\rm erg\,s^{-1}} = 42.0$. Furthermore, the mid-infrared 12 μm luminosity for IC 3639 is $\log L_{12\,\mu{\rm m}} \,/\, {\rm erg\,s^{-1}} = 43.52 \pm 0.04$ (Asmus *et al.* 2014, 2015). The authors acquired this flux with high-angular resolution mid-infrared imaging performed

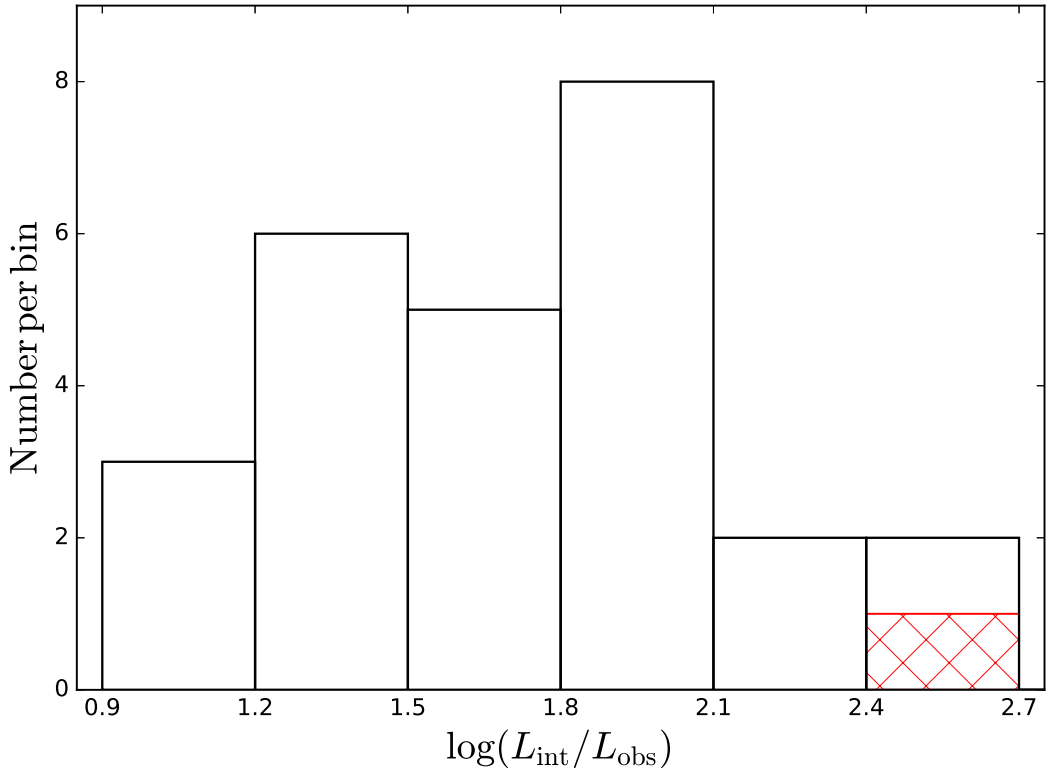

FIGURE 2.11: Distribution of ratios of intrinsic to observed 2 – 10 keV luminosity for the bona fide Compton-thick AGN listed in Table 2.3. IC 3639 shows a comparatively large ratio, at $2.6^{+0.6}_{-1.1}$, and is represented as a red hatched patch in the distribution. The other source in this bin is NGC 1068.

with ground-based 8-m class telescopes, which provides subarcsecond resolution $\lesssim 0\farcs4$, corresponding to a physical resolution of $\lesssim 100$ pc for IC 3639.

The [O III] emission-line vs. X-ray luminosity relation from Berney *et al.* (2015) is presented in Figure 2.12, upper panel, with the shaded region corresponding to the $1-\sigma$ confidence level from the original study. Over-plotted are all the bona fide Compton-thick AGN from Table 2.3. This plot illustrates the effect of correctly modelling the obscuration surrounding an AGN to provide more accurate estimations in the X-ray. Many of the sources have intrinsic X-ray luminosities in better agreement with the relation, IC 3639 being an example.

We also reproduce the relation between intrinsic X-ray and mid-infrared luminosity from Asmus *et al.* (2015) in Figure 2.12, lower panel. The shaded region shows the $1-\sigma$ confidence region acquired from Monte-Carlo simulations of the uncertainties in the original paper. The mid-infrared luminosities of bona fide Compton-thick AGN were either accumulated from Asmus *et al.* (2015) or from the *Wide-field Infrared Survey Explorer*

(*WISE*) all-sky survey[11], both calculated at 12 μm. Again, many bona fide Compton-thick AGN, including IC 3639, show improved agreement with the relation. The exception is NGC 4945, which has been scrutinised to explain its apparently under-luminous mid-infrared nature. For example, Puccetti *et al.* (2014) suggest most of the high-energy emission is transmitted rather than scattered, whereas Brightman *et al.* (2015) suggest the source to have a high covering factor. See Gandhi *et al.* (2015b) and Asmus *et al.* (2015) for further discussion of recent studies of NGC 4945.

The Berney *et al.* relation gives a predicted X-ray luminosity of $\log L_{2-10\,\mathrm{keV}}\ /\,\mathrm{erg\,s^{-1}} \sim 43.9 \pm 2.4$, whilst the Asmus *et al.* relation gives a predicted X-ray luminosity for IC 3639 of $\log L_{2-10\,\mathrm{keV}}\ /\,\mathrm{erg\,s^{-1}} = 43.17 \pm 0.37$. Thus both predicted intrinsic X-ray luminosities are fully consistent with the X-ray–derived 2 – 10 keV from broadband spectral modelling.

2.6.3.3 The Fe-Kα Fluorescence Line and the Future

A high EW is indicative of strong X-ray reprocessing in the regions surrounding the intrinsic X-ray source of an AGN. However, across the full spectrum of known bona fide Compton-thick AGN, there are a broad range of EWs, critically including values less than 1 keV. The lowest EW value determined to date for a bona fide Compton-thick AGN is reported by Gandhi *et al.* (2017) for NGC 7674, with an Fe Kα line EW of $0.38^{+0.10}_{-0.09}$ keV. Figure 2.13 compares the Fe Kα strength relative to a power law continuum for IC 3639 and NGC 7674. The data are from the combined *Suzaku*/XIS 03 detectors consistently for each source. IC 3639 shows a peak of the Fe Kα line consistent with ten times that of the continuum model, whereas NGC 7674 shows a peak of the Fe Kα line around two times the corresponding continuum power law model. This illustrates the broad range in EWs for Compton-thick AGN, and identifies the potential risk associated with quantifying obscuration based on a strong iron line.

A large EW could correlate with the large star formation rates found here. Levenson *et al.* (2002) suggest that the mechanical energy provided through periods of strong star formation could effectively inflate the torus, altering the covering factor and thus EW associated with the Fe Kα fluorescence line.

Future missions such as *Athena* (Nandra *et al.* 2013) hold the potential to resolve fluorescence complexes in much greater detail, in particular those arising from iron. Of particular relevance to Compton-thick AGN, resolved spectral imaging of the Compton shoulder to the Fe Kα line, located redward of the narrow core at 6.4 keV, and arising from Compton-scattering of fluorescence photons. Such high-resolution spectroscopy

[11] Available at http://irsa.ipac.caltech.edu/cgi-bin/Gator/nph-dd.

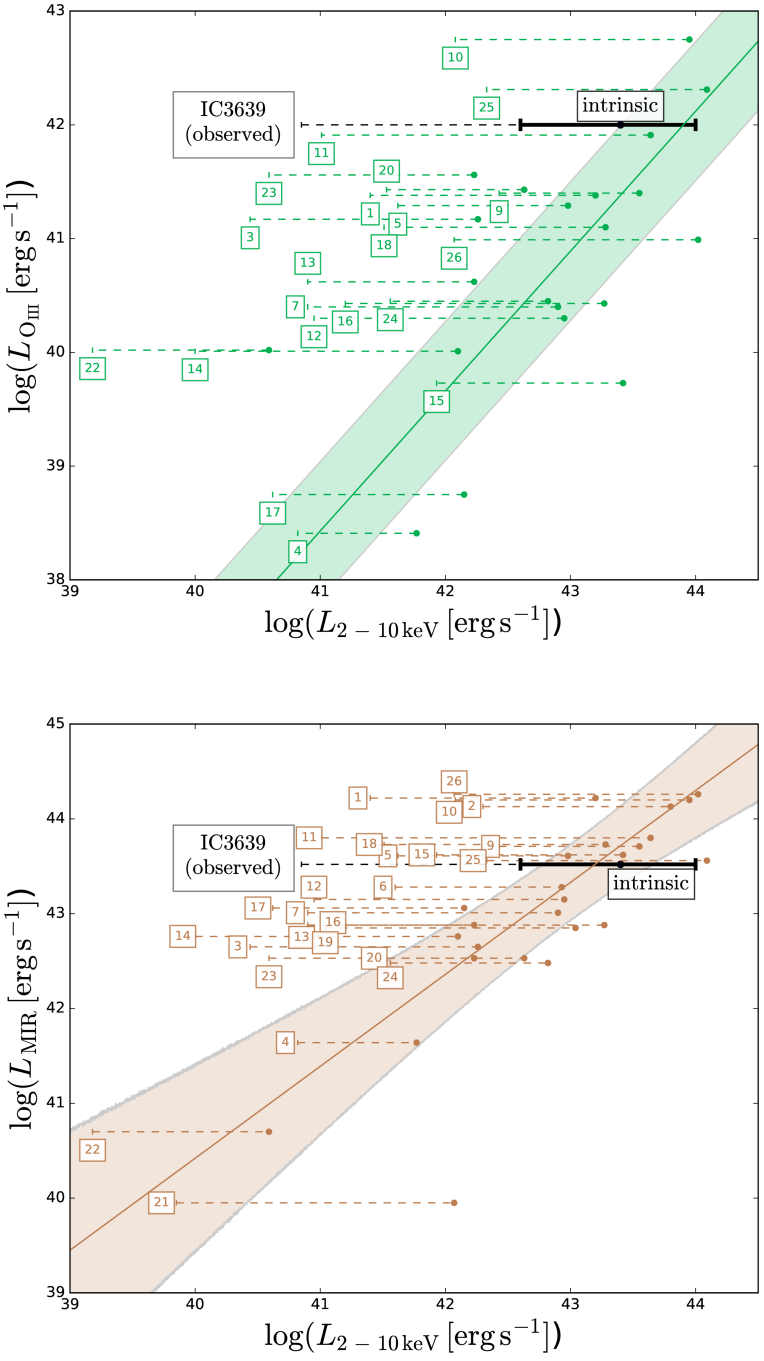

FIGURE 2.12: The bona fide Compton-thick AGN population (collected from the literature) compared to multi-wavelength isotropic indicators of AGN activity. Each plot features the observed–corrected X-ray luminosity vs. an isotropic indicator. Observed source X-ray luminosities before correcting for obscuration are represented as the left-most point of each horizontal correction dashed line, and intrinsic values as solid points. IC 3639 is shown in black, with uncertainty between models T and M for the X-ray emission represented as an error bar. Note the error bar represents the luminosity derived to the $1-\sigma$ level, $\log L_{2-10\,\mathrm{keV}}\ /\,\mathrm{erg\,s^{-1}} = 43.4^{+0.6}_{-0.8}$. All source IDs are given in Table 2.3. ***Upper*:** $L_{[\mathrm{OIII}]}-L_{2-10\,\mathrm{keV}}$ relation from Berney *et al.* (2015). The shaded region represents the $1-\sigma$ scatter from Berney *et al.* ***Lower*:** $L_{\mathrm{MIR}}-L_{2-10\,\mathrm{keV}}$ relation from Asmus *et al.* (2015). The shaded region represents the $1-\sigma$ scatter generated from Monte Carlo modelling of the relation uncertainties presented in the original paper.

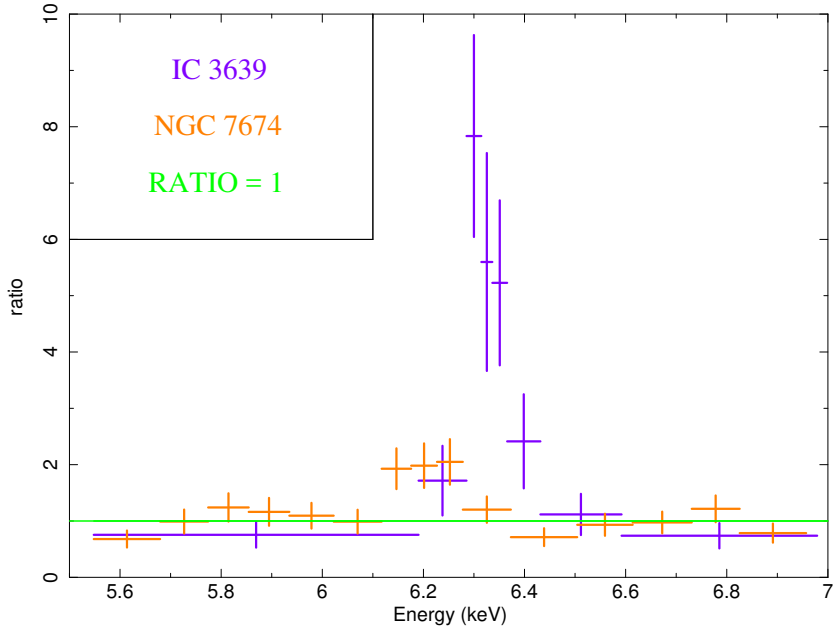

FIGURE 2.13: The ratio between a powerlaw model and observed X-ray data against energy. Purple and orange data sets show the comparative strength of the iron line relative to the continuum for IC 3639 and NGC 7674 respectively. The horizontal green line represents a ratio of unity.

TABLE 2.3: IDs corresponding to the known *bona fide* Compton-thick AGN, including IC 3639, in reference to Figures 2.11 and 2.12.

ID	Name	ID	Name	ID	Name
1	Arp 299B	11	NGC 1068	21	NGC 4945
2	CGC G420-15	12	NGC 1320	22	NGC 5194
3	Circinus Galaxy	13	NGC 2273	23	NGC 5643
4	ESO 005-G004	14	NGC 3079	24	NGC 5728
5	ESO 138-G001	15	NGC 3281	25	NGC 6240S
6	ESO 565-G019	16	NGC 3393	26	NGC 7674
7	IC 2560	17	NGC 4102		
8	IC 3639	18	NGC 424		
9	Mrk 3	19	NGC 4785		
10	Mrk 34	20	NGC 4939		

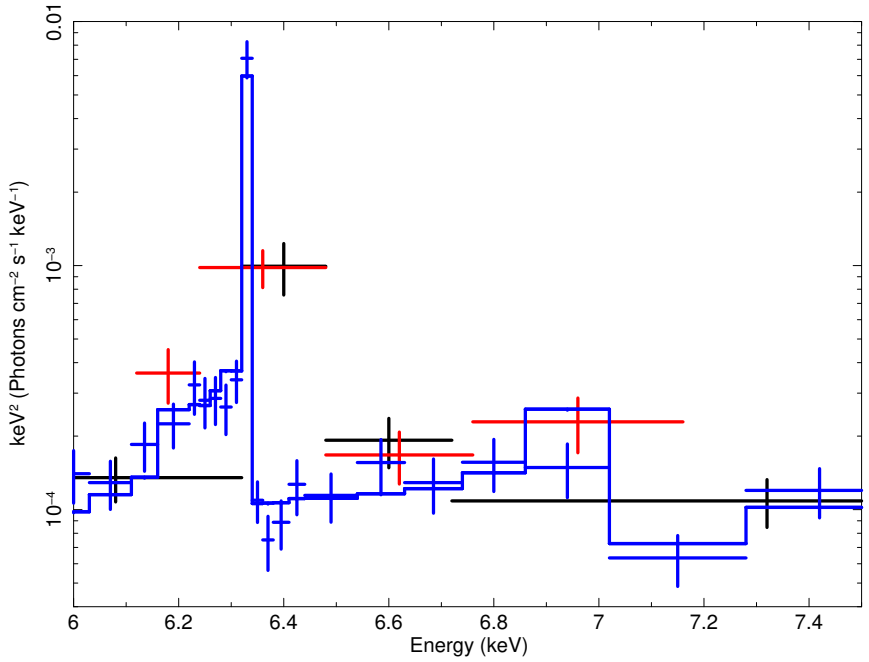

FIGURE 2.14: Simulated 100 ks *Athena* spectrum (shown in blue), together with the model used to generate the data. *NuSTAR*/FPMA & FPMB data points and model are superimposed in black & red respectively. The *Athena* data has additionally been re-binned for clarity. The Fe Kα line complex is clearly resolved with additional components visible, such as the Compton shoulder redward of the narrow core located at 6.4 keV.

could tell us a great deal about how buried Compton-thick AGN are in surrounding obscuration, and help constrain a geometry of the obscurer (e.g., Reynolds *et al.* 2014). Figure 2.14 illustrates simulated data for the proposed *Athena* X-ray Integral Field Unit (XIFU), which will have a spectral resolution of $\sim$2.5 eV at 6 keV. We used the response and background files provided by the *Athena* website[12] together with an exposure of 100 ks. Over-plotted are the equivalent *NuSTAR*/FPMA and FPMB data points from this work for the same region fitted with model T. A clear detection of the Compton shoulder and other fluorescence lines are visible with the *Athena* spectrum, which could be used to investigate super-Solar abundances of other elements than iron for IC 3639 in greater detail (the current simulation assumes Solar abundances).

2.6.3.4 Monte Carlo Markov Chain Analysis

As a final consideration for the source, I present here an updated MCMC analysis of the same X-ray data presented above. I use the XSPEC MCMC `chain` command, with the Goodman-Weare algorithm. As an approximate optimisation strategy, I use 400 walkers since the number of degrees of freedom (n) is 76 and ideally we require $\gtrsim 5\times n$

[12]Located here: `http://x-ifu-resources.irap.omp.eu/PUBLIC/BACKGROUND/5arcsec/`.

TABLE 2.4: MCMC results with `borus02` for IC 3639

Component	Value
kT / keV	$0.80^{+0.11}_{-0.14}$
$\Gamma^{\rm int}$	$2.33^{+0.25}_{-0.23}$
$\log N_{\rm H}$ / cm^{-2}	$24.80^{+0.60}_{-0.28}$
$C_{\rm T}$	$0.82^{+0.14}_{-0.31}$
$\theta_{\rm inc}$ / $^\circ$	40^{+26}_{-18}
$N_{\rm IPL}$ / photons keV^{-1} cm^2 s^{-1} at 1 keV	$\left(5.3^{+5.3}_{-3.6}\right) \times 10^{-3}$
$f_{\rm S}$ / %	$0.68^{+0.78}_{-0.38}$
$\log L_{2-10\,\rm keV}$ / erg s^{-1}	$42.46^{+0.21}_{-0.27}$
$\Delta\chi^2$ / n	96.88 / 76

(J. Buchner, private communication). The chain length was then fixed to 400,000, such that each walker experiences the equivalent of 1,000 steps. The chain burn-in length was arbitrarily set at 4,000, so that any minimal initial convergence artefacts required by the walkers was dropped. I use an updated X-ray model from that of BNTORUS– the `borus02` (Baloković *et al.* 2018)[13]. `borus02` was generated under the same physical geometry considerations as BNTORUS– namely a spherical obscurer with polar cutouts required to resemble a torus with variable covering. However, `borus02` rectifies the issues reported by Liu and Li (2015), by accounting for absorption of reflected photons from the back wall of the torus. This can have a dramatic effect for the $E < 10$ keV photons and substantially deplete the spectrum in this energy region, relative to that of BNTORUS (see e.g., Figure 3 of Baloković *et al.* 2018). The model parameters are the same as for the BNTORUS model above. Overall, we find a statistically acceptable fit to the data, with $\Delta\chi^2 / n = 96.88 / 76$ (null hypothesis probability = 0.0535), with consistent intrinsic luminosities for `borus02` as compared to both BNTORUS and MYTORUS. By calculating the number of chain steps with $N_{\rm H} > 1.5 \times 10^{24}$ cm^{-2}, we find that IC 3639 is Compton-thick to > 3.7 *sigma* confidence.

2.7 Summary

Recent *NuSTAR* observations were combined with archival *Suzaku* data of the nearby Type 2 Seyfert AGN, IC 3639. The key findings are enumerated below.

1 With the MYTORUS and BNTORUS models, I self-consistently fit the broadband spectral data available for IC 3639. Both fits (models M & T) predominantly show a very high level of obscuration, favouring column densities of order $N_{\rm H} \sim 10^{25}$ cm^{-2}.

[13] I used the v170709a tables for this fit, but all `borus02` model tables are available in XSPEC-compatible form at: `http://www.astro.caltech.edu/~mislavb/download/`.

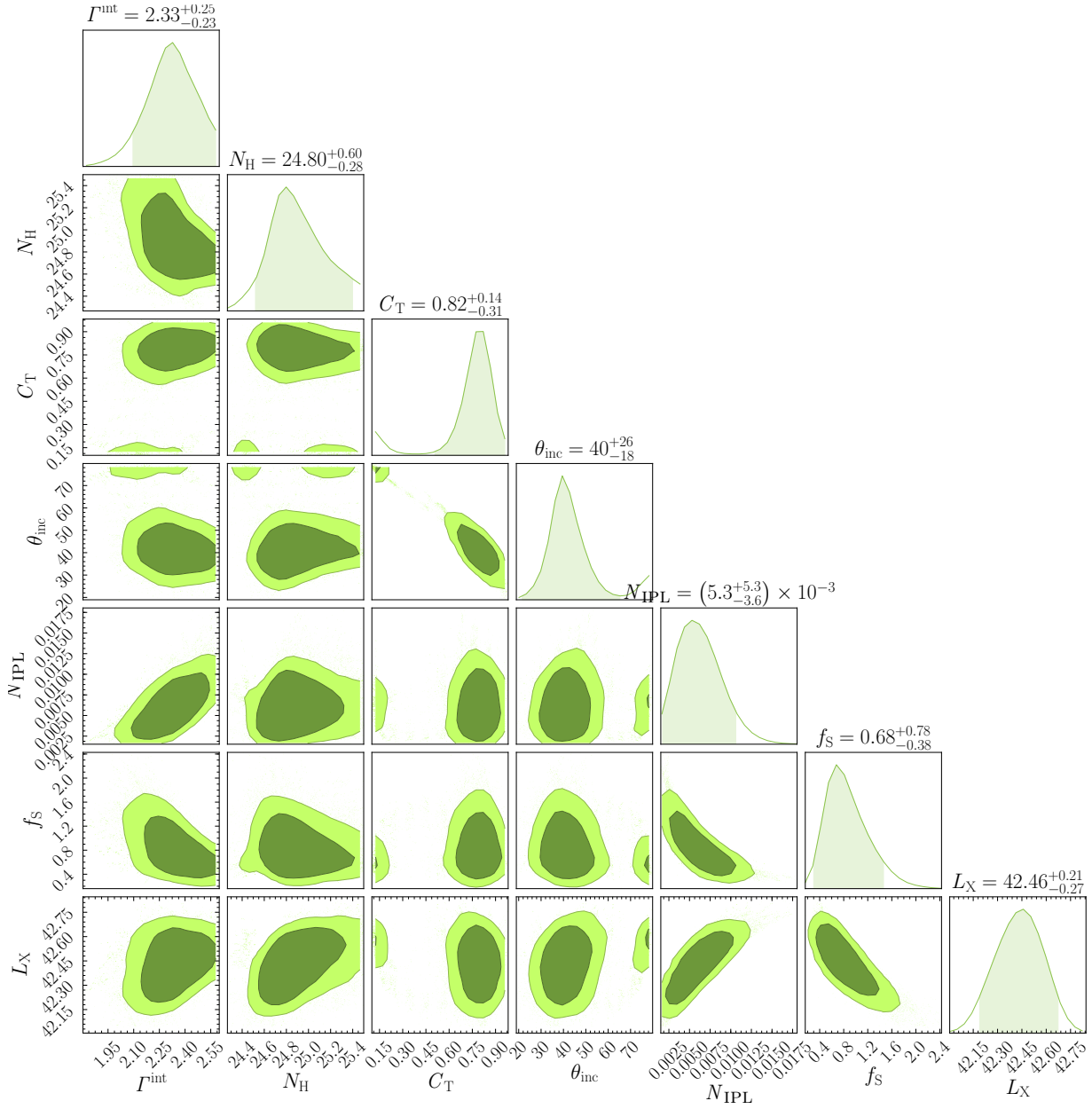

FIGURE 2.15: Corner plot presenting the best-fit parameters for IC 3639

This is consistent with previous results from the literature, suggesting a lack of variability over the past ~ 20 years between the *BeppoSAX* and *NuSTAR* observations. As a result, we classify IC 3639 as a *bona fide* Compton-thick AGN.

2 I find the *Suzaku*/HXD observation of the source to be a non-detection after accounting for the high background level and its reproducibility. This contradicts a previous study of the same *Suzaku*/HXD data set.

3 The combined results of the two torus models give an intrinsic X-ray luminosity (2 – 10 keV band) of $\log L_{2-10\,\mathrm{keV}} \,/\, \mathrm{erg\,s^{-1}} = 43.4^{+0.6}_{-1.1}$. This gave a source Eddington ratio of $\log \lambda_{\mathrm{Edd}} = -0.4^{+0.8}_{-1.1}$, at a $1-\sigma$ confidence level.

4 I find an extreme EW of the Fe Kα fluorescence line in IC 3639 of $2.94^{+2.79}_{-1.30}$ keV, consistent with Risaliti *et al.* (1999a), and one of the highest amongst bona fide Compton-thick AGN. The source also shows a high intrinsic to observed 2 – 10 keV luminosity ratio.

5 A multi-wavelength comparison between X-ray, mid-infrared continuum and [O III] emission line fluxes of IC 3639 with all known *bona fide* Compton-thick AGN give good agreement with known intrinsic correlations. This provides independent evidence that we are robustly measuring the absorption-corrected X-ray luminosity.

IC 3639 clearly represents an ideal candidate AGN for analysis with *NuSTAR*– i.e. a reflection-dominated spectrum with extreme narrow Fe Kα emission, all within the bandpass of *NuSTAR* (i.e. with a local redshift). However, this source was not detected after 70 months of contigual exposure with the hard X-ray detector *Swift*/BAT, that is frequently used to derive an unbiased view of the obscured AGN population. Furthermore, being able to select and make preliminary classifications based on narrow Fe Kα line profiles is potentially a powerful technique. However, Gandhi *et al.* (2017) present the analysis of NGC 7674 – another local bona-fide Compton-thick AGN classified by *NuSTAR* with one of the weakest Fe Kα emission features of any Compton-thick AGN known. To understand more about the ubiquitous Fe Kα line profile in Compton-thick AGN is thus of paramount importance not just for our unique sub-samples of well-studied local sources, but also for higher-redshift AGN, where accretion activity was higher. The next chapter tackles this issue with a comprehensive study of the Fe Kα line in a large sample of robustly classified Compton-thick AGN with bolometric luminosities $\log L_{\mathrm{bol}} \,/\, \mathrm{erg\,s^{-1}} \sim 41$–$47$, over a wide redshift range of $z \sim 0.0014 - 3.7$.

Chapter 3

An Iwasawa-Taniguchi Effect for Compton-thick Active Galactic Nuclei

"I have not failed.
I've just found 10,000 ways that won't work."
– Thomas Edison

Recent *NuSTAR* studies into specific Compton-thick AGN in the local Universe appear to show a trend of weaker Fe Kα line strength with increasing bolometric luminosity. This motivated the study presented in this chapter, aiming to investigate this trend in greater detail – specifically the presence of an Iwasawa-Taniguchi effect for Compton-thick AGN. Such an effect describes an anti-correlation between Fe Kα EW and bolometric luminosity, and is completely unexpected in Compton-thick AGN where the observed X-ray continuum and Fe Kα line are both the result of X-ray reprocessing, and thus should be coupled. I include an overview of this effect in Section 3.1, as well as a detailed motivation taken from specific candidate Compton-thick AGN – two of which only recently unveiled by *NuSTAR*.

3.1 Introduction

Modelling the strength and shape of the neutral Fe Kα fluorescence line together with the Compton hump can yield the line of sight obscuring column to a source. This requires an observed X-ray spectrum spanning the Compton hump at $\sim 30\,\mathrm{keV}$ and the soft X-ray emission $\lesssim 10\,\mathrm{keV}$, to provide constraints on the continuum and reflection components.

However, many previous X-ray observations of AGN have typically been restricted to the $E \lesssim 10\,\mathrm{keV}$ energy region (*Suzaku*/XIS, *Chandra*, *XMM*-Newton), completely missing the Compton hump for local sources. This typically means that any attempt to fit AGN X-ray spectra in this energy region with the objective of constraining the line of sight N_{H} depends heavily on the Fe Kα fluorescence line alone, and can be uncertain.

Despite being an indicator of high obscuring columns, the Equivalent Width (EW) of the narrow core of the neutral Fe Kα fluorescence line has been observed to anti-correlate with the underlying intrinsic X-ray continuum luminosity in samples of transmission-dominated AGN. This effect was first reported by Iwasawa and Taniguchi (1993) for a sample of 37 largely unobscured AGN, observed by the *Ginga* satellite. The best fit linear relation derived was of the form $\log \mathrm{EW}_{\mathrm{Fe\ K}\alpha} \propto -0.20 \pm 0.03 \log L_{2-10\,\mathrm{keV}}$. This is sometimes referred to as the 'X-ray Baldwin' effect due to the similarity with the study by Baldwin (1977) on the anti-correlation between the EW of the C IV 1549 Åultraviolet emission line and AGN continuum. However, here I refer to the X-ray Baldwin effect as the 'Iwasawa-Taniguchi' effect.

The Iwasawa-Taniguchi effect has been explored in further detail for different AGN classes. For example, Page *et al.* (2004) reported an Iwasawa-Taniguchi effect of $\log \mathrm{EW}_{\mathrm{Fe\ K}\alpha} \propto -0.17 \pm 0.08 \log L_{2-10\,\mathrm{keV}}$ for a sample of 53 Type 1 AGN observed by *XMM*-Newton, with the slope being consistent with that of Iwasawa and Taniguchi. However, Jiang *et al.* (2006) later reported a much shallower anti-correlation of $\log \mathrm{EW}_{\mathrm{Fe\ K}\alpha} \propto -0.10 \pm 0.05 \log L_{2-10\,\mathrm{keV}}$ for a sample of 75 radio-quiet AGN observed by *XMM*-Newton and *Chandra*. The authors attribute the reduction in slope of the anti-correlation to radio-loud contamination of previous AGN samples, proposing that radio-loud AGN could have an enhanced continuum contribution from a relativistic jet. The authors further postulated that short-term variability of the primary X-ray source could, in part, contribute to the anti-correlation. Despite the shallower gradient found, two measurements of the same gradient would be expected to differ by the separation between Iwasawa and Taniguchi and Jiang *et al.* $\sim 8\%$ of the time[1], and are thus not strongly inconsistent with each other. Bianchi *et al.* (2007) later studied the Iwasawa-Taniguchi effect for a sample of 157 radio-quiet unobscured Type 1 AGN, including Narrow Line Seyfert 1s (which share some spectral characteristics with obscured AGN). In contrast to Jiang *et al.* (2006), the authors found a somewhat steeper anti-correlation of $\log \mathrm{EW}_{\mathrm{Fe\ K}\alpha} \propto -0.17 \pm 0.03 \log L_{2-10\,\mathrm{keV}}$, fully consistent with the original Iwasawa-Taniguchi effect and Page *et al.* (2004). Bianchi *et al.* further suggest an additional strong anti-correlation between the Fe Kα fluorescence line EW and Eddington ratio. Indeed, Ricci *et al.* (2013b) tested the positive relation between the photon index and Eddington ratio found for AGN (Lu and Yu

[1]For more information on this calculation, see https://ned.ipac.caltech.edu/level5/Sept01/Orear/frames.html.

1999; Shemmer *et al.* 2006; Risaliti *et al.* 2009; Brightman *et al.* 2013; Trakhtenbrot *et al.* 2017), even into the Compton-thick regime (Brightman *et al.* 2016), finding that this could contribute to the Iwasawa-Taniguchi effect. This is because a lower Eddington ratio (and thus photon index, resulting in a flatter spectrum) would lead to more photons at the energy required to generate Fe Kα fluorescence, resulting in a larger Fe Kα EW.

Individual source variability has been shown to considerably affect the strength of the anti-correlation, with Shu *et al.* (2012) finding a reduction in the observed slope from $\log \mathrm{EW}_{\mathrm{Fe\ K}\alpha} \propto -0.22 \log L_{2-10\,\mathrm{keV}}$ to $\log \mathrm{EW}_{\mathrm{Fe\ K}\alpha} \propto -0.13 \log L_{2-10\,\mathrm{keV}}$, after accounting for the time-averaged Fe Kα strength in a sample of 32 AGN with $N_{\mathrm{H}} \lesssim 10^{23}\,\mathrm{cm}^{-2}$, observed multiple times by the *Chandra* High Energy Grating (HEG).

The conventional Iwasawa-Taniguchi effect describes the strength of the Fe Kα line relative to the intrinsic continuum (readily available for unobscured AGN), but a difficulty is introduced when trying to study the effect for obscured sources, which by definition start to lack a prominent transmitted intrinsic component in the Fe Kα flux, to measure the EW against. Ricci *et al.* (2014) report a significant detection of the Iwasawa-Taniguchi effect for two separate samples of Seyfert 1s and 2s, consistently of $\log L_{\mathrm{Fe\ K}\alpha}/L_{10-50\,\mathrm{keV}} \propto -0.11 \pm 0.01 \log L_{10-50\,\mathrm{keV}}$. Type 2 Seyferts are typically observed to be obscured in the optical and often X-rays also (e.g., Koss *et al.* 2017 finds this consistency $\sim$90% of the time with *Swift*/BAT). Thus the work of Ricci *et al.* was the first study into the effect for obscured sources, in which the higher $10-50\,\mathrm{keV}$ energy range was used to describe the intrinsic continuum and Fe Kα EW since photoelectric absorption is minimised for photons at harder energies. Interestingly, the authors postulate that the consistency of slopes between Seyfert 1s and 2s could indicate that the physical mechanism responsible for the Iwasawa-Taniguchi effect is unaffected by orientation under unification schemes. For a breakdown of the results into the Iwasawa-Taniguchi effect from the different works mentioned in this Chapter, see Table 1 of Ricci *et al.* (2013a).

Numerous physical scenarios have been considered to explain the observed Iwasawa-Taniguchi effect, with one of the most favoured being an intrinsic luminosity-dependent covering factor of neutral obscuring gas surrounding the AGN. This effect was first suggested in Lawrence and Elvis (1982) & Lawrence (1991) – dubbed the 'receding torus' – and has been observed in various large AGN samples. This idea is strengthened by the results from multiple studies reporting an increased number density of obscured AGN at lower X-ray luminosities (Ueda *et al.* 2011; Lusso *et al.* 2013; Merloni *et al.* 2014; Georgakakis *et al.* 2017). Simulations of torus reprocessing of X-ray emission have also shown that the Fe Kα line EW can be dramatically enhanced when the observer is exposed to

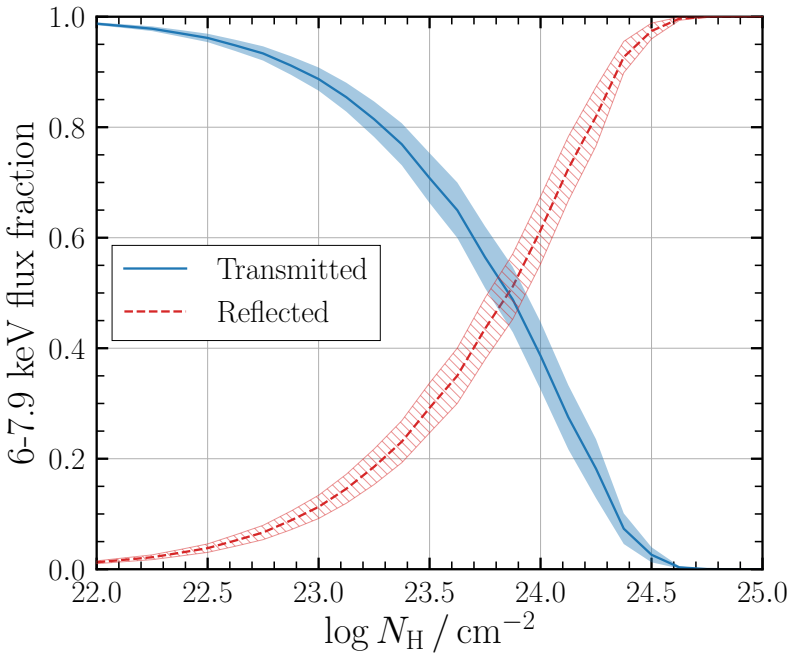

FIGURE 3.1: The contribution to the total observed flux in the Fe Kα region (approximated to $6 - 7.9\,$keV) from the direct transmitted component (blue) and Compton-scattered reflected component (red). This was simulated using the `borus02` X-ray reprocessor model (Baloković *et al.* 2018), for a spherically distributed obscurer with polar cutouts. For each column density, the average flux ratio for a series of covering factor/inclination angle combinations is plotted with the confidence region showing the range between the minimum and maximum found around the average.

less intrinsic flux than the reprocessor (Krolik *et al.* 1994), which is physically attained with higher covering factors of the central AGN.

A receding torus model provides a possible explanation for the Iwasawa-Taniguchi effect in which the observed spectrum contains a dominant unscattered transmitted component, as is the case for transmission-dominated (but obscured) AGN. The prominence of the direct transmitted component would scale with intrinsic luminosity, resulting in the narrow Fe Kα line (arising from the reflection component) being diminished by the brightened intrinsic power law. To illustrate the contribution to the observed flux from the transmitted component vs. the reflected component from an anisotropic X-ray reprocessor, Figure 3.1 shows the relative contribution to the total line flux (approximated here to $6 - 7.9\,$keV) from the transmitted component (blue) and reflected component (red). This was simulated with the `borus02_v170709a` (`borus02`[2]) model (Baloković *et al.* 2018), in which the obscurer is spherically distributed with polar cutouts. For each column density, we plot the average flux ratio for a series of covering factor/inclination angle combinations, and sources are predicted to become reflection-dominated in the Fe Kα line for $\log N_{\rm H}$ cm^{-2} $\gtrsim 23.6$.

[2] Available at `http://www.astro.caltech.edu/~mislavb/download/index.html`.

Recent dedicated studies into specific X-ray-obscured AGN appear to show a trend of decreased neutral Fe Kα line EW with increasing luminosity. Here we highlight three Compton-thick case studies for comparison:

1. Local low luminosity Compton-thick Seyferts typically show prominent iron transition lines. One of the strongest observed Fe Kα line EWs found to date was for IC 3639 (Boorman *et al.* 2016); a reflection-dominated Compton-thick AGN with infrared bolometric luminosity in the $8-1000\,\mu$m wavelength range, $\log L_{8-1000\,\mu\mathrm{m}} / L_{\odot} \sim 10.9$ and $\mathrm{EW}_{\mathrm{Fe\ K}\alpha} \sim 3\,\mathrm{keV}$, relative to the observed underlying reflection continuum.

2. On the other hand, NGC 7674 (Gandhi *et al.* 2017) is a heavily Compton-thick Seyfert 2, with a higher infrared bolometric luminosity of $\log L_{8-1000\,\mu\mathrm{m}} / L_{\odot} \sim 11.6$. Yet the source has an observed EW of the neutral line of $\mathrm{EW}_{\mathrm{Fe\ K}\alpha} \sim 0.4\,\mathrm{keV}$: the lowest constrained EW of the Fe Kα line detected for any bona-fide Compton-thick AGN to date.

3. At the highest luminosities, LESS J033229.4-275619 (Gilli *et al.* 2011, 2014) is the most distant ($z \sim 4.75$) Compton-thick AGN classified to date, with infrared bolometric luminosity $\log L_{8-1000\,\mu\mathrm{m}} / L_{\odot} \sim 12.8$. Interestingly, the neutral Fe Kα fluorescence line is not detected in the observed X-ray spectrum attained with 4 Ms of *Chandra* Deep Field South exposure, yet with a prominent ionised Hydrogen-like Fe Kα feature at $\sim 6.9\,\mathrm{keV}$ to $\sim 2\,\sigma$ confidence. The rest-frame EW of this feature was found to be $2.8^{+1.7}_{-1.4}\,\mathrm{keV}$.

We note that there is increasing observational evidence for prominent ionised Fe Kα lines in Luminous InfraRed Galaxies (LIRGs: $\log L_{8-1000\,\mu\mathrm{m}} / L_{\odot} > 11$) (Iwasawa *et al.* 2009). Although the contribution to the infrared flux from star formation will increase with bolometric flux, the AGN contribution also increases. This means a higher infrared flux should indicate a more intrinsically luminous AGN. These three case studies are illustrated in Figure 3.2, in which we plot the data/model `ratio` for each source after fitting a powerlaw to the observed spectrum. Although NGC 7674 appears to show a large component to the observed flux around $6-6.5\,\mathrm{keV}$, the narrow core of the neutral Fe Kα line is considerably weaker. The panels have been binned for clarity.

This chapter presents the first study into an Iwasawa-Taniguchi effect for Compton-thick AGN, with Fe Kα EWs (measured relative to the observed X-ray continuum) vs. rest-frame mid-infrared $12\,\mu$m luminosity ($L_{12\,\mu\mathrm{m}}$; taken as a proxy for the intrinsic AGN bolometric luminosity). The cosmology adopted for computing luminosity distances is $H_0 = 67.3\,\mathrm{km\,s^{-1}\,Mpc^{-1}}$, $\Omega_{\Lambda} = 0.685$ and $\Omega_{\mathrm{m}} = 0.315$ (Planck Collaboration 2014)[3] The

[3]Redshift-dependent distances are used for consistency across the full sample. Only a handful of the closest AGN have redshift-independent distances which scatter around our adopted luminosity distances.

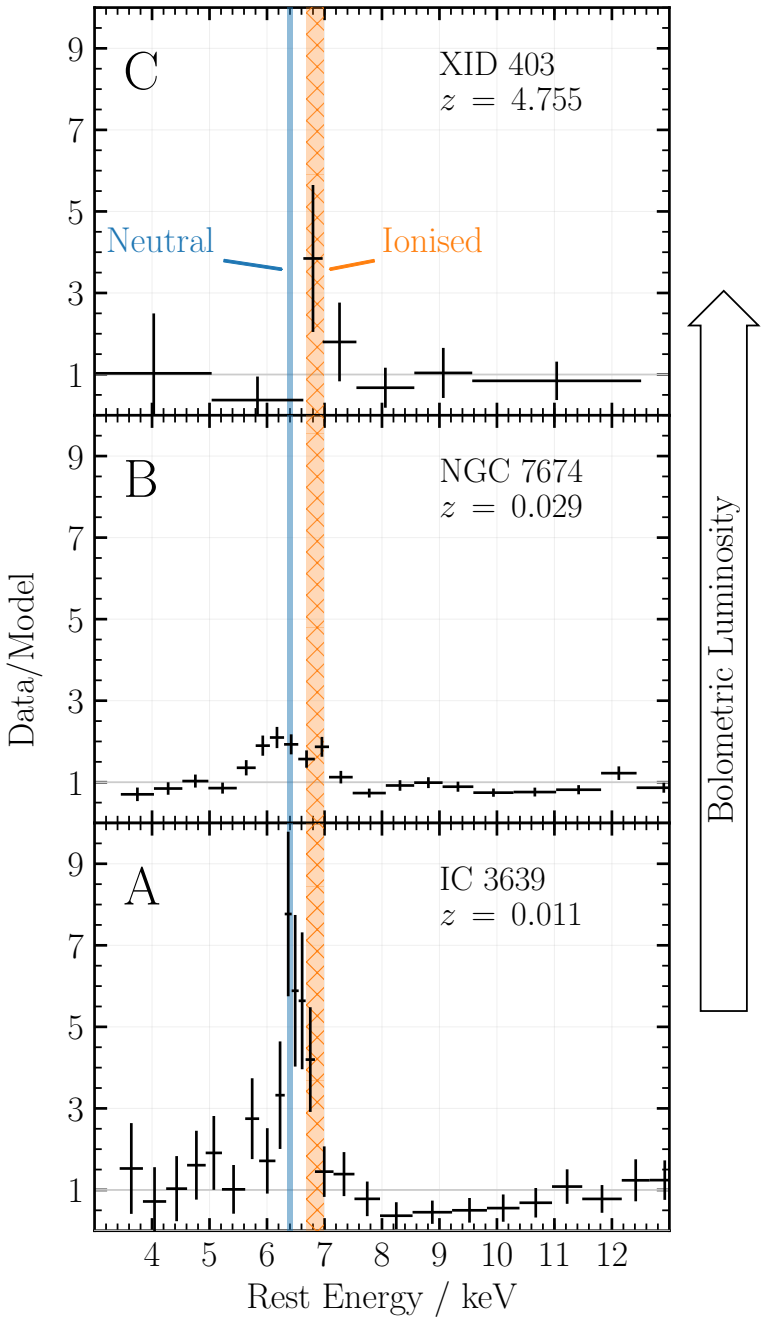

FIGURE 3.2: Three Compton-thick case studies motivating the study of a Compton-thick Iwasawa-Taniguchi effect. Panel A: IC 3639 (Boorman *et al.* 2016): a local Compton-thick AGN at $z = 0.011$ with bolometric infrared luminosity $\log L_{8-1000\,\mu\mathrm{m}} / L_{\odot} \sim 10.9$, and one of the strongest neutral Fe Kα lines reported in the literature. Panel B: NGC 7674 (Gandhi *et al.* 2017): a local Compton-thick AGN, and Luminous InfraRed Galaxy with bolometric infrared luminosity, $\log L_{8-1000\,\mu\mathrm{m}} / L_{\odot} \sim 11.6$. Contrastingly, this source has the lowest neutral Fe Kα EW reported for any local Compton-thick AGN. Furthermore, the spectrum clearly shows a contribution to the residuals in the ionised energy region. Panel C: LESS J033229.4-275619 (Gilli *et al.* 2014): the highest redshift Compton-thick AGN currently known, with $\log L_{8-1000\,\mu\mathrm{m}} / L_{\odot} \sim 12.8$. The spectrum plotted is from a 7 Ms observation of *Chandra* Deep Field South. The neutral emission is not detected, yet a considerable flux contribution can be seen in the higher-energy ionised emission line region > 6.4 keV. Each source was fitted with a redshifted powerlaw in XSPEC, and the resulting data/-model `ratio` is shown. For all panels, the narrow core of the neutral Fe Kα line is shown with the orange region at $E = 6.35 - 6.45$ keV, and the ionised line region is shown in blue hatch at $E = 6.69 - 6.98$ keV (to encompass both the 6.7 and 6.97 keV ionised lines).

chapter is organised as follows: Section 3.2 describes the source selection and sample used in the statistical analysis. Section 3.3 then describes the method for clarifying candidate Compton-thick AGN, as well as for determining the $L_{12\,\mu\mathrm{m}}$ and Fe Kα EW values. I then discuss the straight-line fitting procedure, and Section 3.4 comprises the main results, followed by the discussion and implications of the effect if confirmed on future larger Compton-thick AGN samples, in Section 3.5. A summary of the findings are given in Section 3.6.

3.2 The Sample

The primary goal whilst collating Compton-thick candidates from the literature was to cover a broad redshift (and hence luminosity) range. This enables us to encompass the extremes of such an effect (i.e. for the minimum and maximum luminosities), as well as consider possible biasing factors induced by high-redshift. Furthermore, X-ray spectra encompassing the observed frame neutral Fe Kα fluorescence line, at $6.4/(1+z)$ keV in the rest-frame, were required. In order to robustly quantify the EW required a detection of the underlying observed continuum, neighbouring the line centroid. The high and low redshift subsamples included in this work are detailed below.

3.2.1 High Redshift

For higher redshift (typically fainter) sources, *Chandra* observations were ideal due to low background and optimal sensitivities in the $0.5-8$ keV energy range. At high redshift, the k-corrected Compton hump also shifts to the observed *Chandra* energy range. A considerable contribution to our sample thus includes the Brightman *et al.* (2014) compilation of Compton-thick AGN candidates collated from archival deep *Chandra* surveys. The original work includes ~ 100 Compton-thick candidates. We refined this sample, by applying the following criteria:

1. > 50 total X-ray counts detected in the *Chandra* energy band.
2. A spectroscopic redshift.
3. A line of sight column density of $N_{\mathrm{H}} \geq 1.5 \times 10^{24}\,\mathrm{cm}^{-2}$ at 90% confidence, determined by Brightman *et al.* (2014).
4. Infrared detection by the *Wide-field Infrared Survey Explorer* (*WISE*[4]) or *Spitzer Space Telescope* (*Spitzer*) to enable a reliable $L_{12\,\mu\mathrm{m}}$ estimate.

[4] A 'reliable' *WISE* detection corresponds to a detection with signal to noise > 5. See http://wise2.ipac.caltech.edu/docs/release/allsky/expsup/sec5_3.html for further details.

Of the resulting candidates, a further two were excluded due to a disagreement with our Compton-thick classification (COSMOS 0661 & COSMOS 1517 - see Section 3.3), leaving a total of 27 sources from Brightman *et al.* (2014). An additional five high redshift sources come from further Compton-thick studies by Feruglio *et al.* (2011); Corral *et al.* (2016, BzK 4892), Georgantopoulos *et al.* (2013, XMMID 324), Lanzuisi *et al.* (2015, XMMID 2608, XMMID 60152) and Hlavacek-Larrondo *et al.* (2017, IRAS F15307+3252). In total, 32 sources make up our high redshift subsample of Compton-thick AGN candidates.

3.2.2 Low Redshift

A major contribution to our low redshift subsample comes from Ricci *et al.* (2015). The sample consists of 55 Compton-thick AGN candidates selected from the *Neil Gehrels Swift*/Burst Alert Telescope (BAT) 70-month catalogue, all within the local Universe (average $z = 0.055$). Of these 55, we rejected 19 sources without publicly available *NuSTAR* observations. *NuSTAR* (Harrison *et al.* 2013) is the first true hard X-ray imaging instrument in the $3 - 79$ keV energy range, encompassing the full underlying reflection continuum for low redshift AGN, and thus ideal for studying Compton-thick candidates. By combining with soft X-ray observations, many works have constrained the $N_{\rm H}$ values for numerous obscured, Compton-thick and changing-look AGN to date (e.g. Arévalo *et al.* 2014, Circinus Galaxy; Baloković *et al.* 2014, NGC 424, NGC 1320, IC 2560; Gandhi *et al.* 2014, Mrk 34; Teng *et al.* 2014, Mrk 231; Annuar *et al.* 2015, NGC 5643; Bauer *et al.* 2015, NGC 1068; Ptak *et al.* 2015, Arp 299; Boorman *et al.* 2016, IC 3639; Megamaser sample; Masini *et al.* 2017, Mrk 1210; Ricci *et al.* 2016, IC 751; Ricci *et al.* 2017a, WISE J1036 +0449; Annuar *et al.* 2017, NGC 1448; Gandhi *et al.* 2017, NGC 7674), hence our preference for *NuSTAR* availability.

An additional three sources from the Ricci *et al.* (2015) sample were excluded due to a disagreement with our mid-infrared diagnostic Compton-thick classification (2MASX J09235371-3141305; MCG -02-12-017; NGC 6232, Section 3.3).

The last contribution to our low redshift subsample comes from the Gandhi *et al.* (2014) compilation of bona-fide Compton-thick AGN, updated to include IC 3639 (Boorman *et al.* 2016), NGC 1448 (Annuar *et al.* 2017) and NGC 7674 (Gandhi *et al.* 2017), whilst excluding changing-look candidates: Mrk 3 (Ricci *et al.* 2015, find a sub-Compton-thick column density to 90% confidence), NGC 4102, NGC 4939[5], NGC 4785 (Gandhi *et al.* 2015b; Marchesi *et al.* 2017) and NGC 7582 (Rivers *et al.* 2015). In total, 40 sources make up our low redshift subsample of Compton-thick candidates. Full details of the 72 (low + high redshift) Compton-thick candidates are included in Table 3.1.

[5]Our own analysis of the archival *XMM*-Newton EPIC/PN spectrum as compared to the more recent *NuSTAR* FPMA & FPMB spectra strongly indicate a changing-look AGN for these sources.

3.3 Method

3.3.1 Infrared Luminosities

In selecting a suitable proxy for the bolometric luminosity of each source, we adhered to the following criteria: (1) the bolometric luminosity could not be derived from the spectral energy region responsible for the neutral Fe Kα line nor from the continuum surrounding the line that would be used to derive an EW, and (2) the proxy should be prominent and well detected for Compton-thick AGN.

We used the infrared contribution to the broadband spectra of our AGN sample, which is considered to have sizeable contributions in this wavelength range due to reprocessing of the primary intrinsic AGN emission. Since typical AGN contributions to composite galaxy spectra dominate at $\sim 6 - 20\,\mu$m (Mullaney *et al.* 2011), we used the rest-frame $12\,\mu$m luminosity of each source.

To determine the rest-frame $12\,\mu$m luminosity, we used the infrared spectral templates of Mullaney *et al.* (2011) to interpolate the rest-frame $12\,\mu$m flux from *observed-frame* flux measurements as close to $12\,\mu$m as possible. For high-quality infrared observations, we use the *WISE* and *Spitzer* Multiband Imaging Photometer (MIPS). *WISE* had four imaging channels onboard ($W1$, $W2$, $W3$ & $W4$) corresponding to $\lambda = 3.35\,\mu$m, $4.60\,\mu$m, $11.56\,\mu$m, $22.09\,\mu$m, respectively (Wright *et al.* 2010). Alternatively, *Spitzer*/MIPS was capable of imaging in spectral bands centered on $\lambda = 24\,\mu$m, $70\,\mu$m, $160\,\mu$m. For $z \lesssim 0.84$ a robust interpolation could be made from $W3$ and $W4$ observations. However, for higher redshift sources in which the k-correction shifts the rest-frame $12\,\mu$m luminosity to wavelengths beyond $W4$ (or for poorly constrained/faint observations from *WISE*), we use *Spitzer*/MIPS.

For archival *WISE* observations, we use the AllWISE Source Catalog[6] to get profile-fitted magnitudes and the NASA Extragalactic Database (NED)[7] to search for archival *Spitzer*/MIPS observations.

To test how representative the Mullaney *et al.* (2011) template was for predicting the $12\,\mu$m luminosity for the AGN in our sample with $L_{2-10\,\mathrm{keV}} < 10^{42}\,\mathrm{erg\,s^{-1}}$ or $L_{2-10\,\mathrm{keV}} > 10^{44}\,\mathrm{erg\,s^{-1}}$, we compared the interpolated luminosities with those predicted from the Type 2 AGN template from Polletta *et al.* (2007), which were derived over a wider range of luminosities. On average, the offset between the interpolated luminosities from the two templates was only ~ 0.06 dex.

[6] Available from http://irsa.ipac.caltech.edu/cgi-bin/Gator/nph-dd.
[7] http://ned.ipac.caltech.edu.

3.3.2 Compton-thick Confirmation of Sample

Strong correlations between mid-infrared and intrinsic X-ray emission have been found with ground-based high angular resolution observations of AGN, at $\sim 12\,\mu$m (Horst *et al.* 2008; Levenson *et al.* 2009; Gandhi *et al.* 2009; Asmus *et al.* 2015). Similar correlations have been found as a function of larger aperture $6\,\mu$m luminosity, with akin results (Lutz *et al.* 2004; Lanzuisi *et al.* 2009; Mateos *et al.* 2015; Stern 2015; Chen *et al.* 2017). The $12\,\mu$m luminosity correlation has been used with considerable success for identifying candidate Compton-thick AGN. Correcting X-ray absorption in Compton-thick sources acts to increase the observed X-ray luminosity to values consistent with the relation. See Chapter 1 for the effects of absorption correction on X-ray luminosities relative to their observed mid-infrared luminosities for the Gandhi *et al.* (2014) compilation of bona fide Compton-thick AGN. Here we use the study of the X-ray vs. $12\,\mu$m correlation reported in Asmus *et al.* (2015) to classify our sample as candidate Compton-thick.

The rest-frame observed (i.e. absorbed) $2-10\,$keV luminosity was computed from a fit to the available X-ray spectra within XSPEC (for objects without a reported observed X-ray flux), and plotted against the rest-frame $12\,\mu$m luminosity, interpolated from the Mullaney *et al.* (2011) AGN spectral template. These observed fluxes are plotted in Figure 3.3 (grey points), with a 30% and 15% uncertainty on the X-ray and $12\,\mu$m luminosities, respectively. The original correlation found by Asmus *et al.* (2015) is shown with a solid (green) line for clarity, together with the 1-σ scatter. On average, the sample displays a mean ratio of observed X-ray to mid-infrared flux of -2.0 ± 0.7 dex, and this is shown over plotted with a dashed (grey) line and shading. An average deviation of greater than two orders of magnitude from the relation is indicative of Compton-thick levels of obscuration found in previous works. However, from this relation, 2MASX J09235371-3141305, MCG -02-12-017, NGC 6232, COSMOS 0661 and COSMOS 1517 displayed mid-infrared fluxes that agreed with the observed X-ray flux within the uncertainties found by Asmus *et al.* (2015). This could suggest that the observed X-ray flux has a major contribution from the transmitted component, i.e. is only partially obscured and thus were excluded from our Compton-thick sample.

3.3.2.1 Star Formation Contamination of $L_{12\,\mu\mathrm{m}}$

To test for infrared star formation contamination, we first used the $12\,\mu$m observations from Asmus *et al.* (2014). This work minimised star-formation contamination in measuring mid-infrared fluxes of local sources by using high-angular resolution ($\lesssim 0.4\,$arcsec) imaging with ground-based 8 m class telescopes. Such contamination would not be excluded from *WISE*-based measurements, that were used in our sample for these sources,

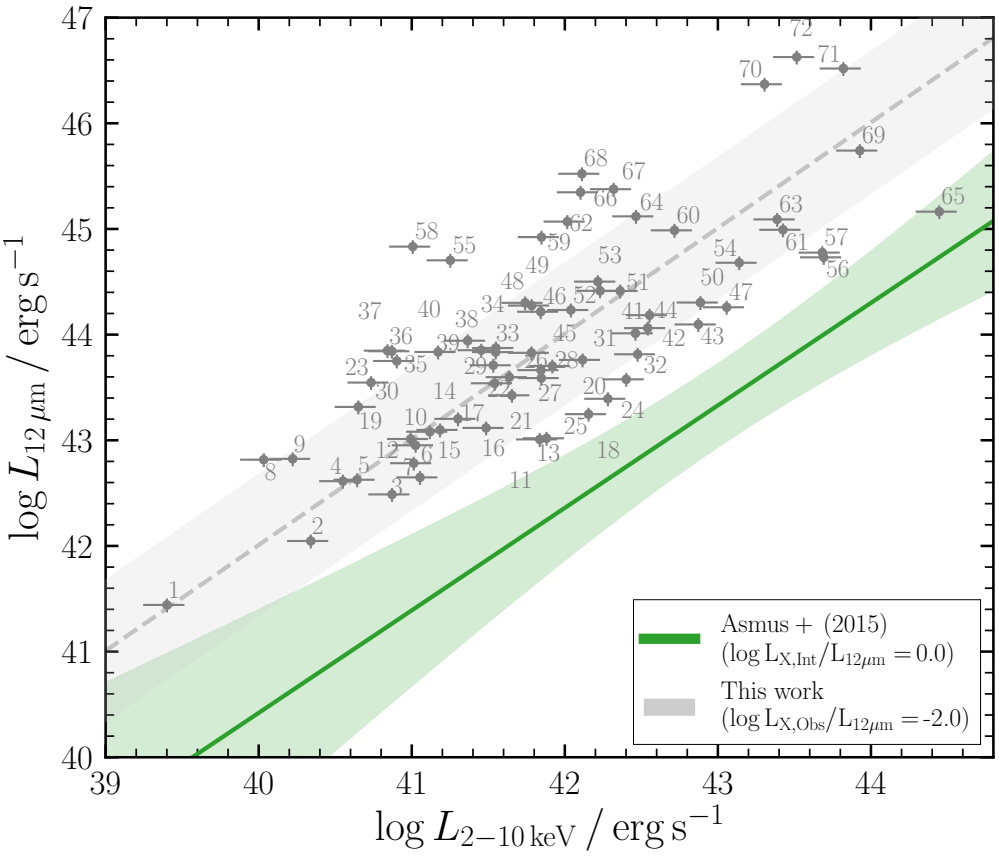

FIGURE 3.3: Predicted rest-frame 12 μm source luminosity (interpolated from the Mullaney *et al.* (2011) infrared AGN spectral template) vs. the rest-frame observed $2-10$ keV luminosity of our sample of Compton-thick AGN. The solid (green) line is the best fit correlation from Asmus *et al.* (2015), together with the 1-σ scatter in light green shading. All sources were assigned a 30% and 15% uncertainty to the X-ray and 12 μm luminosities, respectively. The sample shows diminished X-ray emission relative to 12 μm emission by a factor of greater than 2 orders of magnitude on average, indicative of Compton-thick obscuration. The average observed correlation is shown with a grey dotted line and shaded standard deviation. Labels refer to the ID column in Table 3.1.

due to the larger angular resolution of 6.1, 6.4, 6.5 and 12.0 arcsec for $W1$, $W2$, $W3$ and $W4$, respectively. Out of our sample of 72, 16 sources have measured fluxes in Asmus *et al.* (2014). Figure 3.4 shows the original sample plotted in Figure 3.3 in grey and the orange points show these 16 sources with 12 μm luminosities and 1-σ uncertainty quoted in Asmus *et al.*. The dotted orange line shows the average X-ray to mid-infrared flux ratio for these 16 sources, which is clearly consistent with the ratio for the full sample. To fully account for this in the remainder of our sample without high angular resolution measurements, we conservatively use the average change in flux between *WISE* and Asmus *et al.* of 0.29 dex, added in quadrature to the original 15% uncertainty assigned

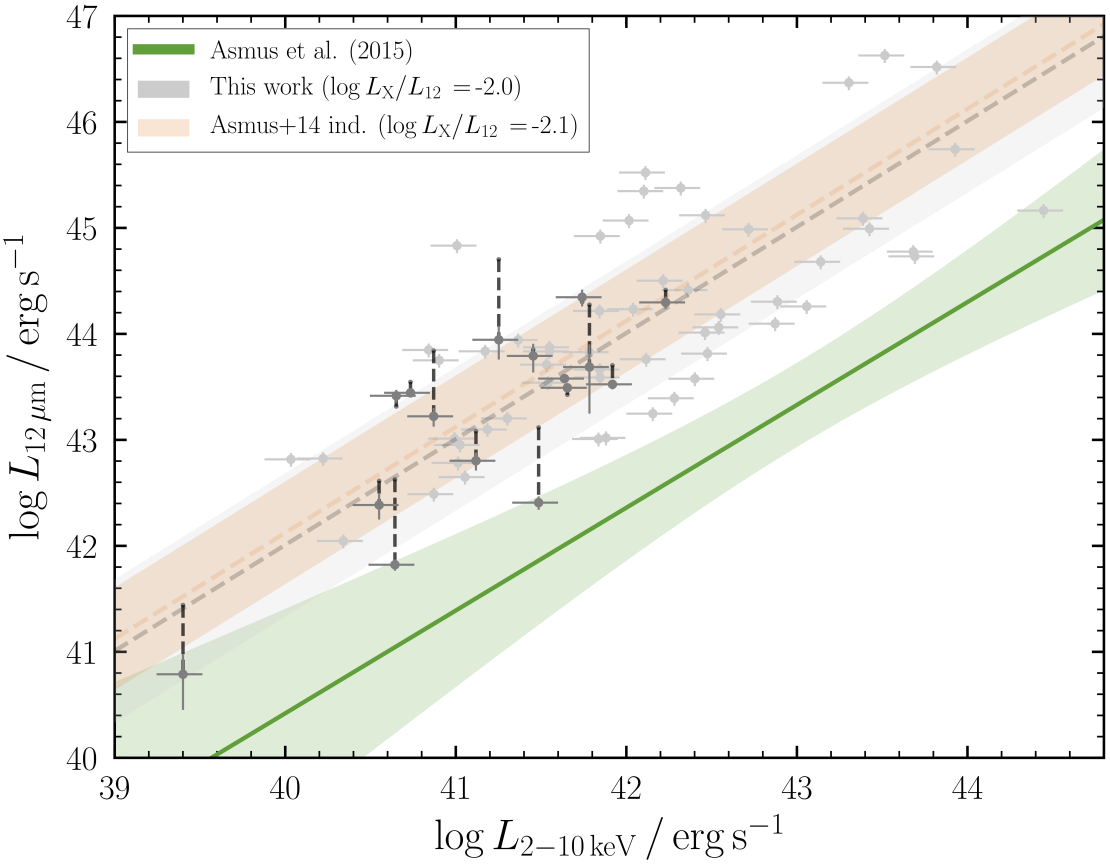

FIGURE 3.4: The possible effects of star formation on our sample. In light grey, we show the original interpolated 12 μm source luminosities we inferred for each source, together with the 1-σ scatter, as in Figure 3.3. Of the full sample, 16 had literature 12 μm fluxes reported by Asmus *et al.* (2014) using high-angular resolution mid-infrared imaging performed with ground-based 8 m class telescopes. This provides subarcsecond resolution ($\lesssim$0.″4), and as such is able to minimise star formation contamination surrounding the AGN as possible, that is not excluded with *WISE*-based fluxes. The orange dotted line shows the average observed luminosities for the 16 sources alone. Clearly there is some deviation, but the average observed luminosity ratio between X-ray and mid-infrared is still consistent with the original grey one within uncertainties. The three sources with corrected mid-infrared luminosities consistent with the Asmus *et al.* (2015) relation are ID1: NGC 5194, ID5: ESO 005–G004 and ID14: NGC 5728.

to the template interpolated flux as the lower error bar for all sources lacking a mid-infrared observation from Asmus *et al.* (2014), giving 0.30 dex. For the 16 sources with measured fluxes from Asmus *et al.*, we use the quoted rest-frame 12 μm luminosities and uncertainties therein.

3.3.3 Rest-frame Fe Kα Line EWs

Due to the well-documented complexity associated with NGC 1068 (Bauer *et al.* 2015), NGC 4945 (Puccetti *et al.* 2014) and the Circinus Galaxy (Arévalo *et al.* 2014), our simplified phenomenological model could not provide a reasonable description of the

data for these sources. For this reason, we use the EWs quoted in Ricci *et al.* (2015), converted to the rest-frame for the corresponding sources. Additionally, we did not have access to spectra for 4 high-redshift sources. The source of the EWs we use for our analysis are included in Table 3.1, column (12). In total, we computed the rest-frame neutral Fe Kα fluorescence line EW for 65/72 sources, as follows:

1. Any counts with $E < 3/4\,\mathrm{keV}$ in the source rest-frame were ignored for *Chandra*/*NuSTAR*, respectively, in order to remove as much soft X-ray contamination from non-primary AGN sources as possible. Such sources include intrinsic AGN emission scattered into the line of sight, a relativistic jet, X-ray binaries present in the host or photoionised gas. Furthermore, all counts above 7 keV in the observed frame were excluded to account for the instrument-based sensitivities of *Chandra*. The corresponding upper limit for *NuSTAR* was $\sim$14–15 keV in the observed frame, optimising the measurement of the continuum over the most sensitive *NuSTAR* energy range.

2. In the low counts regime, we used Cash-statistics (C-stat; Cash 1979) during fitting. Spectra were either grouped to allow a minimum number of counts, or a minimum signal to noise ratio per bin, while retaining enough spectral resolution for the Fe Kα line. We generally favoured fitting with C-stat unless sources had enough counts or high enough signal to noise to warrant the use of χ^2 statistics on a correspondingly signal to noise-binned spectrum. We experimented with different binning strategies within the sources fitted with C-stat, and found consistent outcomes.

3. Next we fitted each spectrum with a simplified phenomenological model consisting of photoelectric absorption acting on a composite power law plus a narrow Gaussian of Full Width at Half Maximum, FWHM$\approx$ 2 eV (σ = 1 eV), modelling the observed continuum plus the narrow core of the Fe Kα fluorescence line. This model was used only to constrain the shape of the observed spectrum, and the EW of the Fe Kα line. If a given source had an observed excess of emission in the softer energy band ($E \lesssim 4\,\mathrm{keV}$) an `apec` component was additionally included in the model to account for this. In XSPEC, this baseline model takes the form:

$$\begin{aligned} \mathrm{MODEL} = \mathrm{GAL\_PHABS} \times (\mathrm{APEC} + \\ \mathrm{ZPHABS} \times (\mathrm{ZPOWERLAW}[\Gamma = 1.4] + \\ \mathrm{ZGAUSS}[\mathrm{E_L} = 6.4\,\mathrm{keV}])) \end{aligned} \tag{3.1}$$

GAL_PHABS refers to an additional minor contribution to the absorption from the Milky Way Galaxy. Items in square brackets refer to fixed parameters. Although many studies suggest the intrinsic power law of AGN have average photon indices of ~ 1.9, we required our model to provide a reasonable fit to the *observed* spectrum. Thus we fit the spectra with a flatter (lower) photon index of 1.4, as this is closer to the value found for the flat ($< 10\,\mathrm{keV}$) reflection spectra typically observed for Compton-thick AGN.

4. We then computed two-dimensional confidence contours over the ZPOWERLAW and ZGAUSSIAN model component normalisations (whilst leaving N_{H} and, if required to describe the soft region of the observed spectrum, the `apec` normalisation, free).

5. These contours were translated to confidence on the Fe Kα EW, and plotted as a function of the statistical test difference from the best fit acquired (either $\Delta\chi^2$ or ΔC-stat depending on the source). This enabled us to determine the minimum, and hence presumed best fit rest-frame EW, together with the 1-σ uncertainty. Irrespective of using χ^2 or C-stat, we use a delta statistic of $+2.30$ to represent the 1-σ (68%) confidence level for two interesting parameters[8].

6. For sources in which the normalisation of the Fe Kα line could not be constrained in the fit, we use the limit derived by XSPEC on this parameter to calculate an upper bound on the EW. For any sources that yielded an unphysical EW $> 5\,\mathrm{keV}$, we set the limit to this value. This is applicable to 3 sources: CDFS 443, CDFS 454 & COSMOS 2180, with EW $\lesssim 12\,\mathrm{keV}$, EW $\lesssim 48\,\mathrm{keV}$ and EW $\lesssim 11\,\mathrm{keV}$, respectively. See the Appendix for the grouped spectrum used for each source.

3.3.4 Fitting Procedure

Our final sample consists of 72 sources, including 18 upper limits on Fe Kα EW. All sources without quoted luminosities in Asmus *et al.* (2014) were assigned the same lower uncertainty of 0.3 dex on 12 μm luminosity specified in Section 3.3.2. We then fitted a linear regression to the EW vs. rest-frame 12 μm luminosity. To account for all the uncertainties present in our sample whilst determining a fit, our fitting procedure was as follows:

1. The dataset was bootstrapped by randomly sampling data points from the original whilst allowing repeats. The new dataset was the same size as the parent sample.

2. Each point in the bootstrapped dataset was randomly resampled depending on the uncertainty of each point, as follows:

[8] https://heasarc.gsfc.nasa.gov/xanadu/xspec/manual/XSappendixStatistics.html

(a) *Non-detections/upper limits:* new points were randomly drawn from a uniform distribution in the interval [log 100 eV, log `limit`],

(b) *Detections:* A new value was generated from a Gaussian distribution with standard deviation given by the 1-σ error being considered for that point.

To avoid strongly unphysical values from biasing the simulations, we truncated the randomised EWs to between 100 eV and 5 keV.

3. A linear least-squares regression was carried out on the Monte Carlo simulated dataset using the `scipy.linregress` Python package. The Spearman's Rank Correlation Coefficient (ρ) was then found using the `scipy.spearmanr` package for each fit.

4. Steps (i) – (iii) were repeated in order to obtain a distribution of gradients, y-intercepts and ρ values for the original dataset.

3.4 Results

Table 3.1 includes details of each source used in our final sample, and the Appendix contains the best fit spectrum and EW contour for each source used, as well as the sources ruled out in our analysis. After carrying out 20,000 iterations, we obtain a best fit linear regression to the data of:

$$\log(\mathrm{EW}_{\mathrm{Fe\,K}\alpha}/\mathrm{keV}) = -(0.08 \pm 0.04)\log(\mathrm{L}_{12\,\mu\mathrm{m}}/10^{44}\,\mathrm{erg\,s^{-1}}) + 2.87 \pm 0.05 \quad (3.2)$$

Figure 3.5 shows all rest-frame 12 μm luminosities vs. rest-frame neutral Fe Kα fluorescence line EWs. Blue arrows represent upper limits. As a comparison to previous studies into the Iwasawa-Taniguchi effect, we further include the gradients of previous works: Iwasawa and Taniguchi (1993), Page *et al.* (2004), Bianchi *et al.* (2007) and Ricci *et al.* (2014), normalised to the same y-intercept at 10^{44} erg s^{-1}. We make this renormalisation since the EWs we report for our sample are measured relative to the observed spectrum, which for Compton-thick obscuration is drastically different to the observed spectrum for unobscured AGN, not to mention our proxy for the bolometric luminosity is different to that previously used by other studies.

To test the significance of the fit, we computed the Spearman's Rank Correlation Coefficient (ρ) of the correlation for the sample, excluding upper limits. Upper limits were

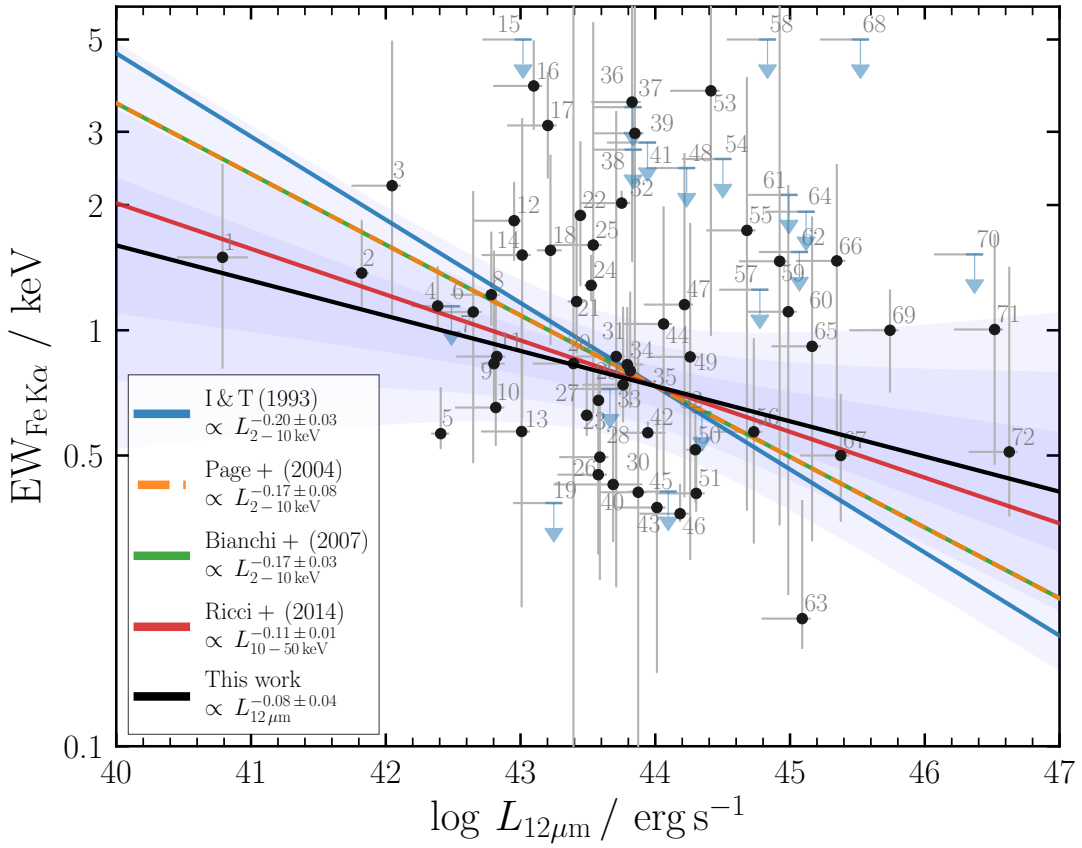

FIGURE 3.5: Plot of $L_{12\,\mu\mathrm{m}}$ vs. (rest-frame) neutral Fe Kα fluorescence line EWs. Blue arrows represent upper limits. As a comparison to previous studies into the Iwasawa-Taniguchi effect, we further include the gradients of previous works Iwasawa and Taniguchi (1993, I & T (1993)), Page *et al.* (2004, Page+ (2004)), Bianchi *et al.* (2007, Bianchi+ (2007)) and Ricci *et al.* (2014, Ricci+ (2014)). These correlations have all been renormalised to match our best fit y-intercept at $10^{44}\,\mathrm{erg\,s^{-1}}$ for comparison, since we are using the 12 μm luminosity, which is different from the intrinsic luminosity proxies used by other Iwasawa-Taniguchi effect studies. The blue shaded region represents the standard deviation from the mean of our best fit, with lighter shading corresponding to incrementally lower integers of standard deviation.

excluded since ρ tests the strength of a monotonic relationship between variables, which can be dramatically effected by the large range of values/orders of variables attainable with the inclusion of limits in our Monte Carlo-based fitting method. This left 54 sources, and gave a value of $\rho = -0.28 \pm 0.12$. Figure 3.6 shows the corresponding distribution in ρ found, indicating a negative correlation to 98.7% confidence.

Our best fit gradient is fully consistent with Ricci *et al.* (2014) within 1-σ errors, who attempted to take into account time-averaging of the spectra for determining EWs – see Section 3.5 for further discussion on this result. The gradient found here is also flatter than the Bianchi *et al.* (2007) best fit gradient, but consistent within 90% confidence. We include the distributions of our best linear fit gradients and y-intercepts in the left and

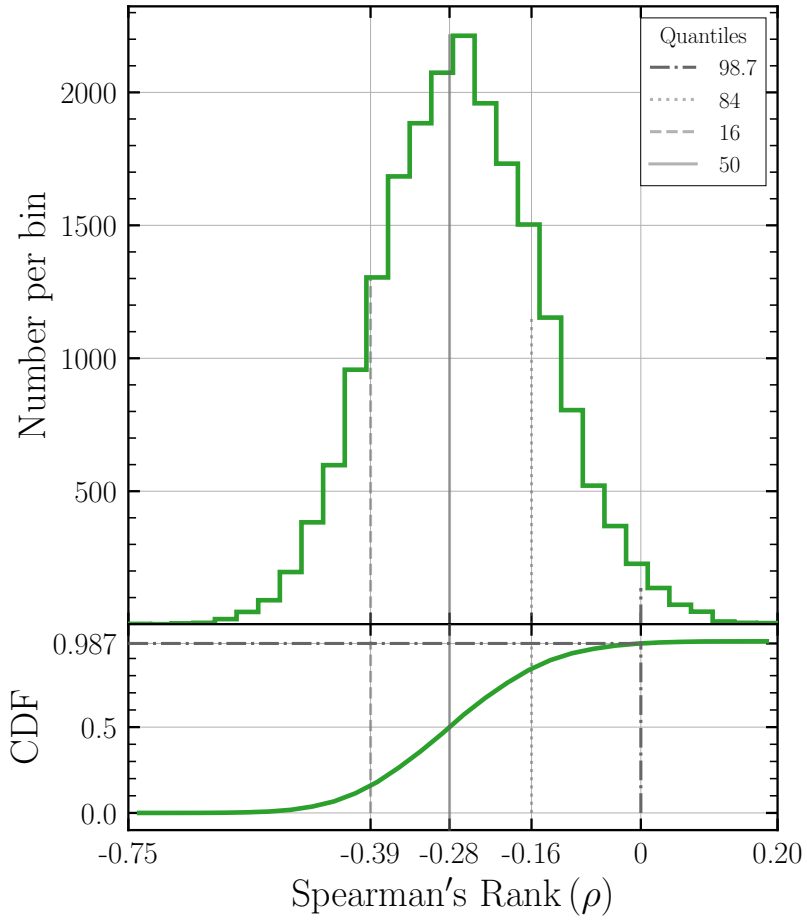

FIGURE 3.6: Distribution of Spearman's Rank Correlation Coefficients (ρ) generated from 20,000 iterations of steps (1) - (3) of our fitting procedure, outlined in Section 3.3.4, for a dataset excluding all upper limits (54 in total). The 16th, 50th and 84th quantiles are shown with dashed, solid and dotted lines, respectively. The dotted (purple) line additionally shows the correlation to be negative to 98.7% confidence.

right panels of Figure 3.7, respectively for the 20,000 iteration Monte Carlo simulations (including upper limits).

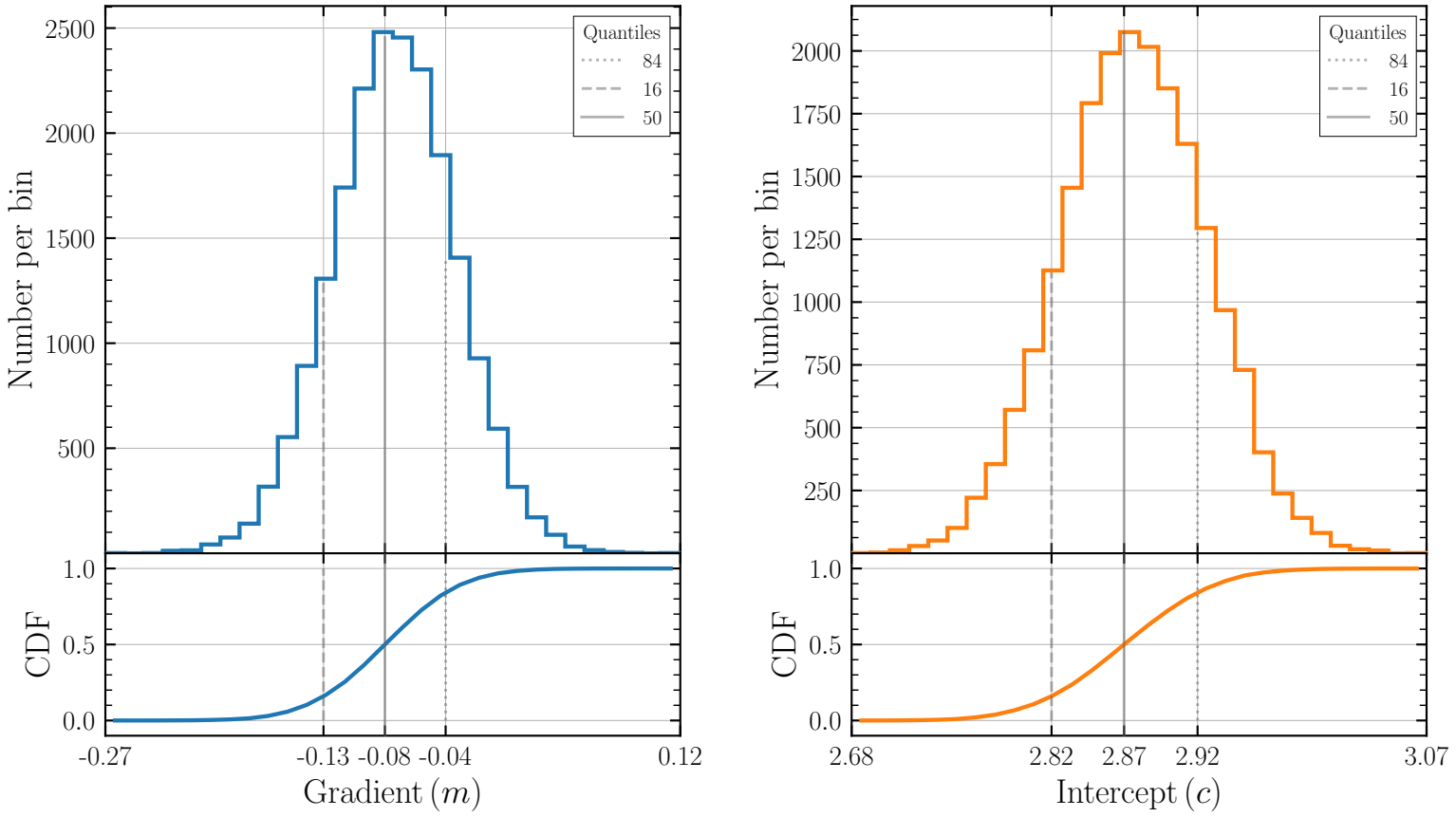

FIGURE 3.7: Distributions of linear regression (*Left*) gradients and (*Right*) y-intercepts generated from 20,000 iterations of steps (1) - (3) of our fitting procedure (Section 3.3.4). The 16th, 50th and 84th quantiles are shown with dashed, solid and dotted lines in both panels, respectively.

TABLE 3.1: Complete list of all sources used in determining the anti-correlation plotted in Figure 3.5, ordered by rest-frame 12 μm luminosity. Information on specific columns is as follows: (1) ID specific to each source, corresponding to the index featured on plots throughout the paper. (2) source name. (3) spectroscopic redshift. (4) right ascension in degrees. (5) declination in degrees; (6) Source reference. (7) Logarithm of the observed rest-frame $2-10$ keV luminosity, measured in erg s^{-1}; (8) Logarithm of the rest-frame 12 μm luminosity predicted from the Mullaney *et al.* (2011) infrared spectral template; (9) Rest-frame neutral Fe Kα fluorescence line EW measured in keV; (10) and (11) upper and lower limits on the rest-frame neutral Fe Kα fluorescence line EW measured in keV (values of 0 and -1 respectively denote an upper limit to EW). (12) reference used for EW value. References: Feruglio *et al.* (2011, Fer11); Goulding *et al.* (2012, Gou12); Georgantopoulos *et al.* (2013, Geo13); Brightman *et al.* (2014, Br14); Gandhi *et al.* (2014, Gan14); Baloković *et al.* (2014, Bal14); Lanzuisi *et al.* (2015, Lan15); Ricci *et al.* (2015, Ric15); Ptak *et al.* (2015, Pta15); Masini *et al.* (2016, Mas16), Corral *et al.* (2016, Cor16); Gandhi *et al.* (2017, Gan17); Hlavacek-Larrondo *et al.* (2017, H-L17); Annuar *et al.* (2017, Ann17); Boo18: This work.

ID	Identifier	z	RA	DEC	source ref.	$\log L^{\rm obs}_{2-10\,\rm keV}$	$\log L_{12\,\mu\rm m}$	EW	+EW	−EW	EW ref.
(1)	(2)	(3)	(4)	(5)	(6)	(7)	(8)	(9)	(10)	(11)	(12)
1	NGC 5194	0.002	202.4696	47.1953	Gou12	39.4	40.8	1.50	1.01	0.69	Boo18
2	ESO 005-G004	0.006	91.4233	-86.6319	Ric15	40.6	41.8	1.37	0.47	0.23	Boo18
3	NGC 1448	0.004	56.1329	-44.6447	Ann17	40.3	42.0	2.23	2.73	1.13	Boo18
4	NGC 5643	0.004	218.1696	-44.1744	Ric15	40.6	42.4	1.14	0.28	0.13	Boo18
5	NGC 5728	0.009	220.5996	-17.2531	Ric15	41.5	42.4	0.56	0.16	0.05	Boo18
6	CDFS 345	0.123	53.1028	-27.9120	Bri14	40.9	42.5	1.14	0	-1	Boo18
7	NGC 4180	0.007	183.2627	7.0388	Ric15	41.1	42.6	1.11	1.05	0.63	Boo18
8	ESO 137-G034	0.009	248.8088	-58.0800	Ric15	41.0	42.8	1.22	0.51	0.19	Boo18
9	NGC 3393	0.012	162.0975	-25.1619	Ric15	41.1	42.8	0.83	0.72	0.16	Boo18
10	NGC 3079	0.004	150.4908	55.6797	Ric15	40.0	42.8	0.65	0.61	0.12	Boo18
11	NGC 4945	0.002	196.3646	-49.4683	Ric15	40.2	42.8	0.86	0.03	0.03	Ric15
12	NGC 2273	0.006	102.5358	60.8458	Mas16	41.0	43.0	1.83	0.44	0.36	Boo18
13	NGC 6921	0.014	307.1202	25.7234	Ric15	41.8	43.0	0.57	0.52	0.35	Boo18
14	2MFGC02280	0.015	42.6775	54.7049	Ric15	41.0	43.0	1.52	1.71	0.90	Boo18

Table 3.1 : *cont.*

ID	Identifier	z	RA	DEC	source ref.	$\log L_{2-10\,\mathrm{keV}}^{\mathrm{obs}}$	$\log L_{12\,\mu\mathrm{m}}$	EW	+EW	−EW	EW ref.
(1)	(2)	(3)	(4)	(5)	(6)	(7)	(8)	(9)	(10)	(11)	(12)
15	CDFS 443	0.895	53.1335	-27.7478	Bri14	41.9	43.0	5.00	0	-1	Boo18
16	IC 2560	0.010	154.0779	-33.5639	Bal14	41.2	43.1	3.87	1.10	0.83	Boo18
17	NGC 1320	0.009	51.2029	-3.0422	Bal14	41.3	43.2	3.11	1.06	0.78	Boo18
18	NGC 7130	0.016	327.0812	-34.9511	Ric15	40.9	43.2	1.56	1.08	0.63	Boo18
19	ESO 464-G016	0.036	315.5991	-28.1748	Ric15	42.2	43.2	0.38	0	-1	Boo18
20	CDFS 296	0.518	53.2734	-27.8709	Bri14	42.3	43.4	0.83	5.74	0.74	Boo18
21	NGC 7479	0.008	346.2358	12.3228	Ric15	40.7	43.4	1.17	0.68	0.29	Boo18
22	IC 3639	0.011	190.2200	-36.7558	Boo16	40.7	43.4	1.89	0.95	0.61	Boo18
23	NGC 1194	0.014	45.9546	-1.1036	Ric15	41.7	43.5	0.62	0.17	0.07	Boo18
24	NGC 3281	0.011	157.9671	-34.8536	Gou12	41.9	43.5	1.28	0.23	0.10	Boo18
25	CDFS 114	0.310	53.0356	-27.7800	Bri14	41.5	43.5	1.60	3.89	0.97	Boo18
26	MCG +08-03-018	0.020	20.6434	50.0550	Ric15	42.4	43.6	0.45	0.19	0.16	Boo18
27	ESO 138-G001	0.009	252.8338	-59.2347	Ric15	41.6	43.6	0.68	0.11	0.04	Boo18
28	MCG +06-16-028	0.016	108.5162	35.2793	Ric15	41.8	43.6	0.50	0.29	0.24	Boo18
29	CGCG 164-019	0.030	221.4033	27.0347	Ric15	41.8	43.7	0.72	0	-1	Boo18
30	Arp 299B	0.010	172.1292	58.5614	Pta15	41.8	43.7	0.43	0.15	0.12	Boo18
31	CDFS 273	0.229	53.0825	-27.6897	Bri14	41.5	43.7	0.86	2.49	0.62	Boo18
32	Circinus Galaxy	0.001	213.2912	-65.3392	Ric15	40.9	43.8	2.02	0.14	0.01	Ric15
33	ESO 201-IG004	0.036	57.5954	-50.3025	Ric15	42.1	43.8	0.74	0.40	0.14	Boo18
34	NGC 424	0.012	17.8650	-38.0833	Ric15	41.5	43.8	0.83	0.31	0.13	Boo18

Table 3.1 : *cont.*

ID	Identifier	z	RA	DEC	source ref.	$\log L_{2-10\,\mathrm{keV}}^{\mathrm{obs}}$	$\log L_{12\,\mu\mathrm{m}}$	EW	+EW	−EW	EW ref.
(1)	(2)	(3)	(4)	(5)	(6)	(7)	(8)	(9)	(10)	(11)	(12)
35	NGC 7212NED02	0.027	331.7583	10.2335	Ric15	42.5	43.8	0.80	0.44	0.15	Boo18
36	CDFS 065	0.664	53.0673	-27.8282	Bri14	41.8	43.8	3.54	5.66	2.07	Boo18
37	CDFS 421	0.738	53.0770	-27.7656	Bri14	41.5	43.8	3.44	0	-1	Boo18
38	CDFS 347	0.280	53.1458	-27.9035	Bri14	41.2	43.8	2.72	0	-1	Boo18
39	CDFS 384	0.150	53.1750	-27.6639	Bri14	40.8	43.8	2.98	7.92	2.20	Boo18
40	ESO 406-G004	0.029	340.6390	-37.1853	Ric15	41.5	43.9	0.41	0.45	0.33	Boo18
41	CDFS 063	0.670	53.0751	-27.8315	Bri14	41.4	43.9	2.83	0	-1	Boo18
42	NGC 1068	0.004	40.6696	-0.0133	Ric15	41.3	43.9	0.57	0.04	0.01	Ric15
43	NGC 1229	0.036	47.0451	-22.9601	Ric15	42.5	44.0	0.37	0.24	0.22	Boo18
44	CDFS 400	1.090	53.1049	-27.9138	Bri14	42.5	44.1	1.04	0.94	0.59	Boo18
45	IGR J14175-4641	0.077	214.2652	-46.6948	Ric15	42.9	44.1	0.41	0	-1	Boo18
46	CGCG 420-015	0.029	73.3571	4.0617	Ric15	42.6	44.2	0.36	0.06	0.02	Boo18
47	CDFS 158	0.738	53.0941	-27.7406	Bri14	41.8	44.2	1.15	1.51	0.75	Boo18
48	AEGIS 567	0.536	214.8070	52.8973	Bri14	42.0	44.2	2.45	0	-1	Boo18
49	Mrk 34	0.050	158.5358	60.0311	Gan14	43.1	44.3	0.86	0.94	0.58	Boo18
50	NGC 7674	0.029	351.9862	8.7792	Gan17	42.2	44.3	0.52	0.17	0.13	Boo18
51	NGC 6240	0.024	253.2454	2.4008	Ric15	42.9	44.3	0.41	0.15	0.04	Boo18
52	MCG +10-14-025	0.039	143.9654	61.3529	Ric15	41.7	44.3	0.64	0	-1	Boo18
53	CDFS 459	1.609	53.1228	-27.7228	Bri14	42.4	44.4	3.76	31.54	2.79	Boo18
54	AEGIS 602	0.769	214.8420	52.9219	Bri14	42.2	44.5	2.58	0	-1	Boo18

Table 3.1 : *cont.*

ID	Identifier	z	RA	DEC	source ref.	$\log L_{2-10\,\mathrm{keV}}^{\mathrm{obs}}$	$\log L_{12\,\mu\mathrm{m}}$	EW	+EW	−EW	EW ref.
(1)	(2)	(3)	(4)	(5)	(6)	(7)	(8)	(9)	(10)	(11)	(12)
55	CDFS 264	2.026	53.0588	-27.7084	Bri14	43.1	44.7	1.74	2.31	1.37	Boo18
56	XMMID 60152	0.579	150.3122	1.7302	Lan15	43.7	44.7	0.57	0.38	0.26	Lan15
57	CDFS 039	3.660	53.0785	-27.8598	Bri14	43.7	44.8	1.25	0	-1	Boo18
58	CDFS 454	0.650	53.0446	-27.8019	Bri14	41.0	44.8	5.00	0	-1	Boo18
59	CDFS 448	0.680	53.0808	-27.6811	Bri14	41.8	44.9	1.47	4.86	1.12	Boo18
60	CDFS 401	1.370	52.9604	-27.8699	Bri14	42.7	45.0	1.11	1.12	0.88	Boo18
61	COSMOS 0581	1.778	150.2910	2.0895	Bri14	43.4	45.0	2.12	0	-1	Boo18
62	COSMOS 0987	0.353	149.7929	2.1256	Bri14	42.0	45.1	1.54	0	-1	Boo18
63	2MASX J03561995-6251391	0.108	59.0831	-62.8609	Ric15	43.4	45.1	0.20	0.19	0.03	Boo18
64	CDFS 460	2.145	53.0976	-27.7155	Bri14	42.5	45.1	1.93	0	-1	Boo18
65	COSMOS 0363	2.704	150.0459	2.2013	Bri14	44.4	45.2	0.91	0.96	0.60	Boo18
66	COSMOS 0482	0.120	150.4250	2.0663	Bri14	42.1	45.3	1.47	1.04	0.91	Boo18
67	XMMID 2608	0.125	150.4249	2.0660	Lan15	42.3	45.4	0.50	0.20	0.15	Lan15
68	COSMOS 2180	0.350	149.9758	2.4615	Bri14	42.1	45.5	5.00	0	-1	Boo18
69	BzK 4892	2.578	53.1488	-27.8211	Fer11	43.9	45.7	1.00	0.25	0.29	Coral16
70	CDFS 382	0.667	52.9624	-27.6879	Bri14	43.3	46.4	1.52	0	-1	Boo18
71	IRAS F15307+3252	0.930	233.1838	32.7131	H-L17	43.8	46.5	1.00	0.70	0.53	Boo18
72	XMMID 324	1.222	53.2051	-27.6806	Geo13	43.5	46.6	0.51	0.91	0.15	Geo13

3.5 Discussion

Our results indicate the presence of an Iwasawa-Taniguchi effect for Compton-thick AGN. This is surprising, since the majority of our sample is presumed to have a noticeable flux contribution from the reflected component in the $\sim 6-7.9\,\mathrm{keV}$ energy region (e.g., Figure 3.1 - we will address this further in Section 3.5.2.1), and the Fe Kα EW is not expected to vary relative to the underlying Compton-scattered reflection continuum. Here we discuss the significance of our result, as well as possible physical interpretations if confirmed on larger samples.

3.5.1 Significance of Result

Initially, we tested whether an anti-correlation best described the data. We fitted our data to a horizontal line, i.e. with a fixed gradient of zero, representing a best-fit with one parameter – the y-intercept. This gave a best-fit y-intercept of 2.88 ± 0.05 (consistent with our previous result).

We next calculated the chi-squared for this line with the original data, and for our best-fit line with the original data (including limits), yielding the following results:

- For a gradient of zero, $\chi^2 = 1049.00/71$ d.o.f.
- For a free gradient fit, $\chi^2 = 961.19/70$ d.o.f.

This corresponds to a $\Delta\chi^2$ of 87.81 for the inclusion of one extra parameter. However, even with the additional parameter both reduced χ^2 values are significantly >1, and does not allow us to draw any strong conclusions from the reduced χ^2 test alone. We additionally note caution with this method as we are including limits in our χ^2 calculation by estimating an errorbar associated with the point half way between the limit and the minimum EW allowed in our MC fitting of 100 eV. This is an estimation, and so may not be fully representative of the data.

Assuming that our uncertainties fully encapsulate uncertainties due to measurement error, we deduce that there must be an additional, unknown source of scatter due to unknown astrophysics. To account for this we include an additional, constant, 'intrinsic dispersion' to our measurement uncertainties in quadrature. The required value of $\sigma_{\mathrm{int}} = 0.17$ suggests that this term is subdominant, though non-negligible, as compared to the measurement uncertainty, which has $< \sigma > = 0.35$ dex. We note that a few particularly bright local AGN dominate the two χ^2 values reported above. For example, the Circinus Galaxy contributes over half of the χ^2 values due to its very small EW

Reference (1)	Metric (2)	Value (3)	No. of sources (4)	Obscuration class (5)
This work	Prob.	98.7%	54	Compton-thick
Ricci *et al.* 2014	Prob.	99%	47	Seyfert 2
Bianchi *et al.* 2007	Prob.	99.6%	157	Unobscured
Jiang *et al.* 2006	ρ	-0.47	101	Unobscured
Page *et al.* 2004	Prob.	$>99.98\%$	53	Unobscured
Iwasawa and Taniguchi 1993	Corr. coeff.	>0.8	37	Unobscured

TABLE 3.2: Summary of the anti-correlation probability significances found for the studies into the Iwasawa-Taniguchi effect included in Figure 3.5. The table lists the (1) study reference, (2) the correlation metric used to quantify the significance of the resulting anti-correlation: 'Prob.' - probability of an anti-correlation; 'ρ' - Spearman's Rank correlation coefficient; 'Corr. coeff.' - correlation coefficient, (3) the value of the correlation metric found by the work, (4) the number of objects in each sample, and (5) the obscuration classes of the sources included in the corresponding work.

measurement uncertainties (see Table 3.1). This is consistent with the presence of additional unknown physics accounting for the scatter. None of the previous studies on the Iwasawa-Taniguchi effect have incorporated this intrinsic scatter, so it warrants closer investigation in the future.

As a comparison of our main statistical significance test – the Spearman's Rank – to previous works, Table 3.2 includes the anti-correlation significance metric quoted for the studies into the Iwasawa-Taniguchi effect that we include in Figure 3.5, as well as the obscuration type of the sources included in these samples.

3.5.1.1 AGN Dominance

In addition to estimating the effect of star formation contamination using high angular resolution observations (see Section 3.3.2.1), we sought to test the AGN dominance of our interpolated infrared luminosities. We use the colour criteria of Stern *et al.* (2012), Mateos *et al.* (2012) and Lacy *et al.* (2007) for observed flux densities (used to renormalise the Mullaney *et al.* 2011 AGN template and interpolate a rest-frame 12 μm flux) from *WISE* and *Spitzer*, respectively. However, Stern *et al.* (2012) do note that the efficiency of such mid-infrared colour selections of AGN increases strongly with X-ray luminosity. As such, lower luminosity sources, e.g. with $L_{2-10\,\mathrm{keV}} \lesssim 10^{43}\,\mathrm{erg\,s^{-1}}$, in our sample may not display AGN-like mid-infrared colours, and thus may lie outside the corresponding thresholds. Alternatively, the sources lying outside the selection criteria may not be intrinsically weak - for example, Gandhi *et al.* (2015b) notes that bluer $W1-W2$

colours could arise from strong host star formation contamination or anisotropic/weak reprocessed torus emission. As such, sources satisfying any one of these three colour thresholds are most likely to not display star formation contamination, and be AGN-dominated in the mid-infrared. The flux densities are plotted in Figure 3.8. In total, 38/72 sources satisfy either Stern *et al.* (2012) and Mateos *et al.* (2012) combined (for *WISE*-based observations) or Lacy *et al.* (2007, for *Spitzer*-based observations). This potentially indicates some form of star formation contamination (or another form of contaminant) present in the sources that do not satisfy these criteria. However, running a fit to only the 38 predicted AGN-dominated sources in our sample results in a gradient of $\mathrm{m} = -0.04 \pm 0.06$ between EW and $L_{12\,\mu\mathrm{m}}$, fully consistent with the main fit presented in Section 3.4, albeit with larger uncertainty.

As a further test of contamination in our sample, we carried out a fit only to sources displaying a deficit in observed X-ray to 12 μm luminosity of greater than two orders of magnitude (see Figure 3.3). This again returned a consistent result with our main fit of $\mathrm{m} = -0.08 \pm 0.05$ for 36 sources. These tests suggest that any star formation contamination does not dominate the trend that we observe.

3.5.1.2 Binning

Lastly, we carried out a fit to the sample binned by 12 μm luminosity. A maximum binning of 9 sources optimised total number of bins together with sources per bin. We approximated all upper limits as the average between the limit and $\log 100\,\mathrm{eV}$, then assigned a 1-σ error to the new point that encompassed $\log 100\,\mathrm{eV}$ to the limit. The corresponding binned EW error for each bin was then given by:

$$\sigma_{\mathrm{EW}} = \frac{\sqrt{\sum \delta \mathrm{EW}^2}}{N} \tag{3.3}$$

Here N refers to the number of sources in each bin. The best fit gradient we get to the binned data is $\log \mathrm{EW}_{\mathrm{Fe\,K}\alpha} \propto -0.06^{+0.05}_{-0.08} \log L_{12\,\mu\mathrm{m}}$, and is plotted in Figure 3.9 with a red solid line and one standard deviation shading. The best fit to the original sample is shown with a dashed black line, which is fully consistent with the binned gradient. The binned data has been renormalised to have the same y-intercept as the original result for easier visual comparison of gradients. The background grey points show the original data.

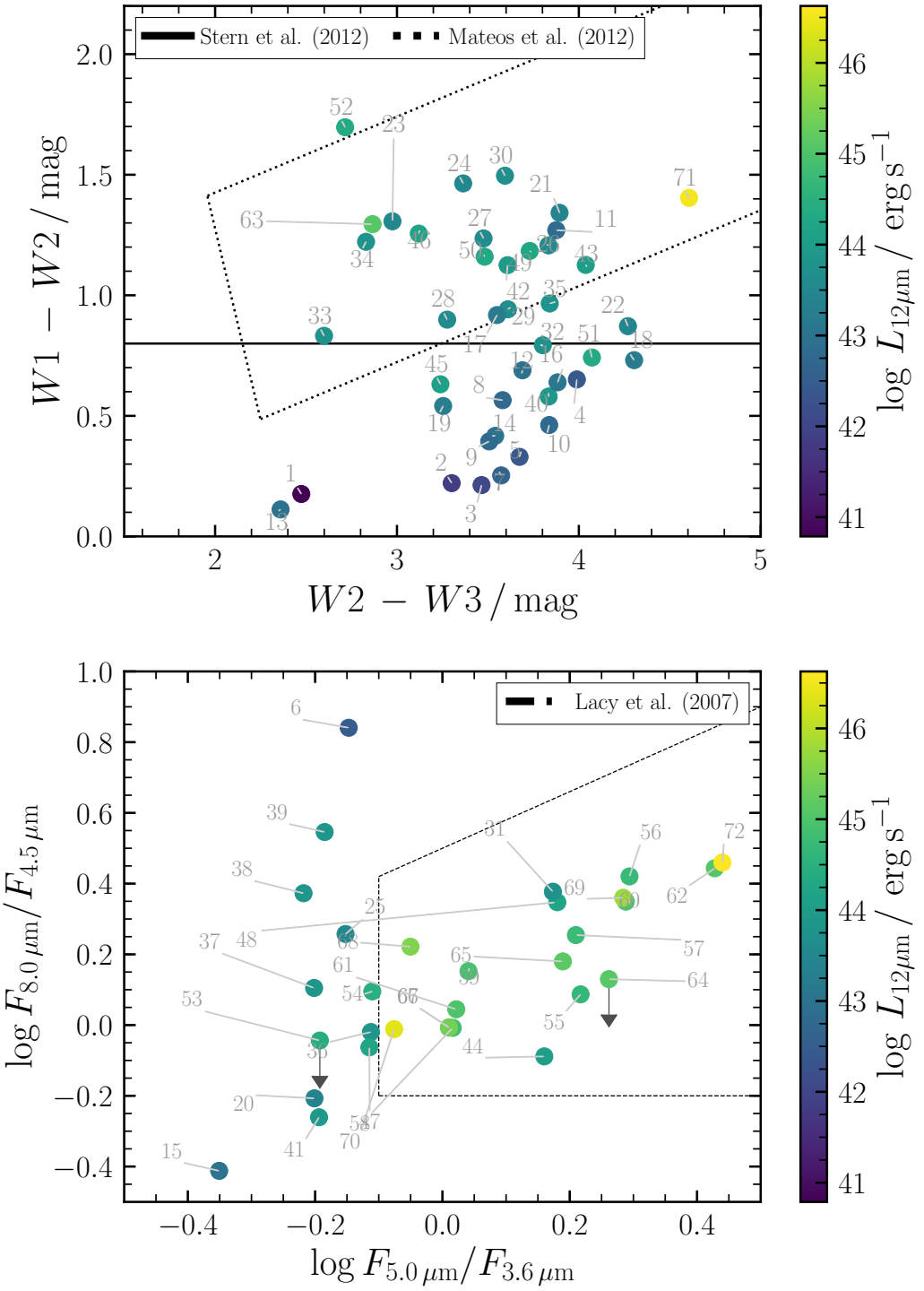

FIGURE 3.8: Colour selection criteria for *WISE* (top panel) and *Spitzer* (bottom panel) flux densities. The *WISE* thresholds are from Stern *et al.* (2012) and Mateos *et al.* (2012), and the *Spitzer* colour wedge is from Lacy *et al.* (2007). In total, 38/72 sources lie outside these criteria, but after testing the possible effects of star formation on these sources, we still require a significant anti-correlation to fit the data - see Section 3.3.2.1 for details.

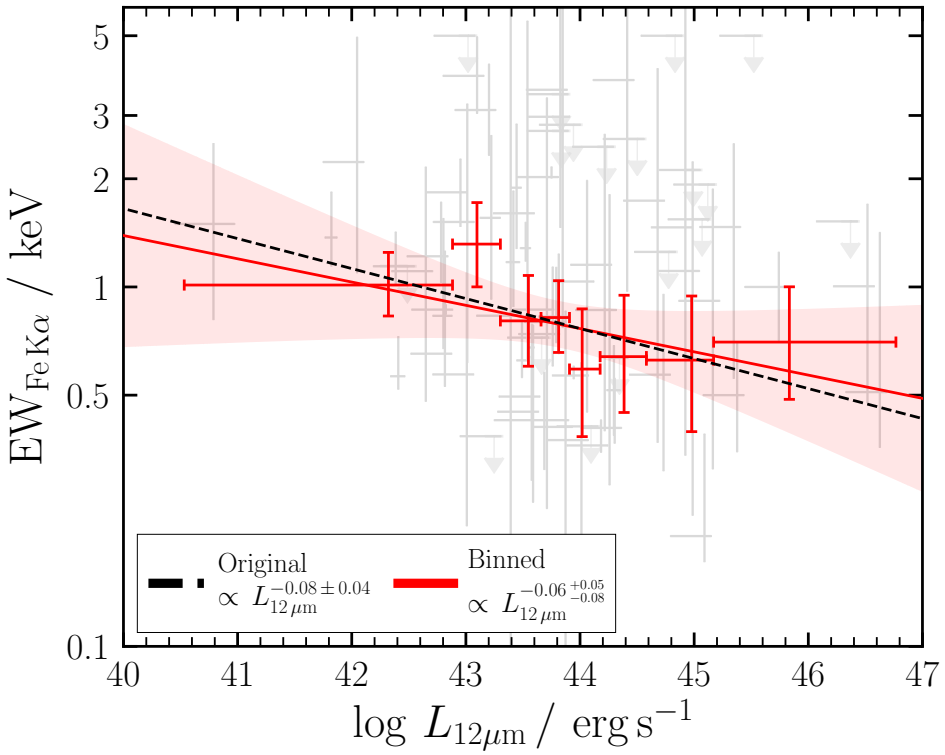

FIGURE 3.9: The best fit to the binned sample, with a maximum of 9 sources per bin (see the text for details of the binning method used). The red shaded region shows the standard deviation from the mean of our fit, which is fully consistent with the original best fit found for the unbinned data, shown with a black dotted line. This has been renormalised to the same y-intercept as the binned fit to allow an easier comparison between gradients. Background grey points show the source data that was binned.

3.5.2 Physical Interpretation

3.5.2.1 Covering Factor Dependence

The EW of the Fe Kα line measured solely relative to the reprocessed continuum is very rarely < 1 keV (e.g., see Figure 8 of Murphy and Yaqoob 2009). One way to achieve an observed EW significantly less than 1 keV is via leaked intrinsic AGN emission contributing some flux to the observed spectrum in the Fe Kα region. Two possible scenarios for this would be in transmission-dominated Compton-thick AGN, or a 'clumpy' torus. Typical X-ray spectral model predictions (see Figure 3.1) for AGN show that for column densities, $N_{\mathrm{H}} \gtrsim 1.5 \times 10^{24}\,\mathrm{cm}^{-2}$, the observed reflected flux is $\gtrsim 10$ times more than the transmitted flux. Below this column density, an AGN could have a reasonable contribution in flux from the transmitted component, and hence a variable continuum with intrinsic luminosity. One way to obtain less reflected flux with increasing column would be a decreased covering factor, the luminosity dependence of which has

been dubbed the 'receding torus'. This has been suggested to explain the Iwasawa-Taniguchi effect for unobscured and mildly obscured sources in the past (e.g. Page *et al.* 2004; Ricci *et al.* 2013a, see Section 3.1 of this chapter). However, Lawrence and Elvis (2010) discusses that the apparent decrease of obscured AGN fraction with bolometric luminosity is much less significant in infrared and radio samples than with X-ray samples, suggesting that the receding torus model may not exist in nature.

In Figure 3.10, we show a colour map of simulated EWs predicted from the `borus02` model for an edge on (inclination angle 84°) viewing angle, with varying column densities and covering factors. All spectra were simulated using `fakeit` from within XSPEC with the *NuSTAR* simulation files provided by the *NuSTAR* team[9]. The resulting spectrum was re-fit in the 6 – 7 keV energy region by a POWERLAW + GAUSSIAN model. The simulated spectrum was then modelled with the same model as specified in Section 3.3, and the EW derived using the `eqwidth` command in XSPEC. We also overplot the limiting contour at which all EWs are > 1 keV, which we take as a proxy for reflection-dominance. Interestingly, for lower covering factors (higher opening angles), the column density can be high ($\log N_{\rm H}$ / cm^{-2} > 24.3 in some cases), and still feature a spectrum with presumably leaked transmitted emission. Since our original $N_{\rm H}$ selection was $\log N_{\rm H}$ / cm^{-2} > 24.18 ($N_{\rm H} > 1.5 \times 10^{24}$ cm^{-2}) to 90% confidence from literature values, this plot cannot rule out that the higher luminosity sources (with assumed lower covering factors) would feature some sort of leaked transmitted flux contributing to the continuum around 6.4 keV and decreasing observed neutral Fe Kα EW. Furthermore, if the luminosity-dependent covering factor explanation is correct, then we are currently lacking such reflection-dominated Compton-thick AGN at high luminosities since the Fe Kα EW is predicted to always be greater than 1 keV for $N_{\rm H} \gtrsim 1.5 \times 10^{24}$ cm^{-2}.

As an additional test, we selected sources with literature best fit *lower* 90% uncertainty on the column density to be $N_{\rm H} \gtrsim 1.5 \times 10^{24}$ cm^{-2}. This returned 14 sources, with only two sources at higher redshift (COSMOS 0363; $z = 2.704$ and BzK 4892; $z = 2.578$). Although the corresponding best fit to this sample returns a gradient of $\mathrm{m} = -0.10^{+0.07}_{-0.08}$, which is entirely consistent with the result for the full sample, we lack enough robust reflection-dominated sources at higher redshifts to draw precise conclusions for a transmitted component altering the narrow Fe Kα line.

An alternative way to detect a considerable contribution from the transmitted component in Compton-thick AGN would be via changing-look AGN obscuration-based variability. In this scenario, the Compton-thick obscurer is clumpy, enabling clouds of differing column to traverse the line of sight, potentially resulting in leaked intrinsic emission. Such extreme eclipsing events from unobscured to Compton-thick levels of obscuration have

[9] Available from `https://www.nustar.caltech.edu/page/response_files`.

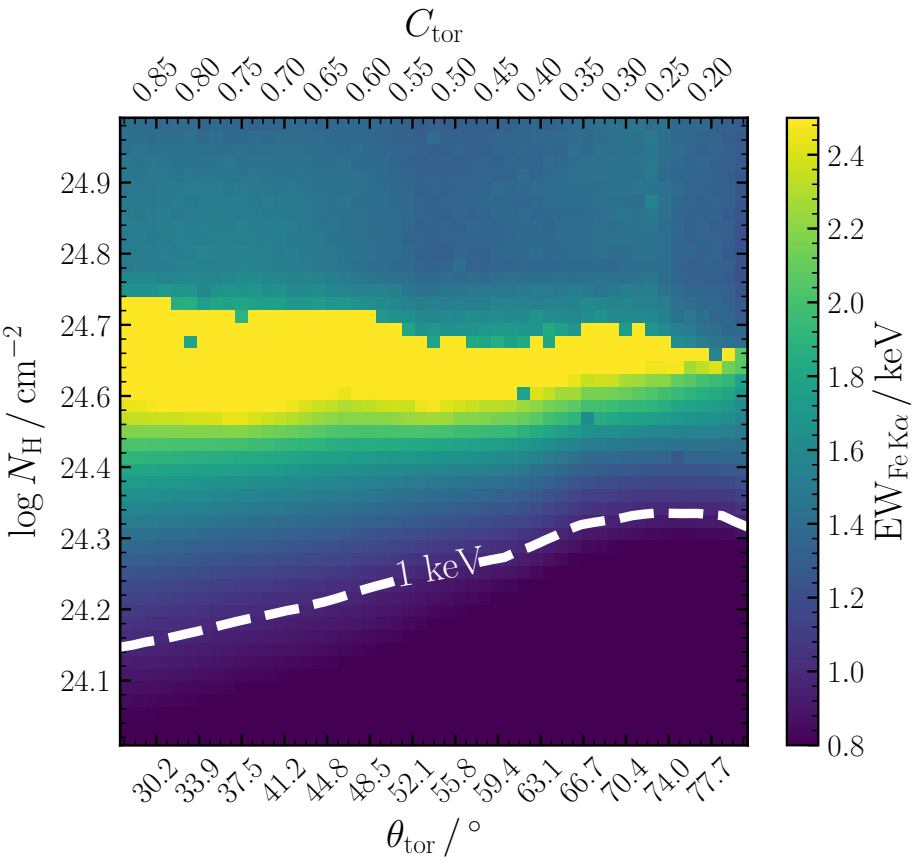

FIGURE 3.10: A colour map of simulated neutral Fe Kα EW for a series of line of sight column densities ($N_{\rm H}$) and torus covering factors ($C_{\rm tor} = \cos\theta_{\rm tor}$) in the `borus02` (Baloković *et al.* 2018) model. For these simulations, the line of sight column density and equatorial column density were tied together. The simulated spectra were then fit in the 6 – 7 keV energy region with a POWERLAW + GAUSSIAN model to derive a predicted EW. The contour shows the boundary at which all EW are predicted to be > 1 keV. All EWs predicted to be < 0.8 keV or > 2.5 keV were capped (shown with the same minimum and maximum colour, respectively). Due to our selection of sources with $\log N_{\rm H}$ / cm^{-2} > 24.18 to 90% confidence from literature values, we cannot rule out sources having at least a partial EW dependence with covering factor, as seen by this region of the colour map.

been observed previously (e.g., Risaliti *et al.* 2007), but are rare. As such, this is unlikely to be responsible for the diminished Fe Kα lines observed in all higher luminosity sources of the sample where we see the greatest decrease in EW, but may play a non-negligible role.

3.5.2.2 Ionisation

Finally, we consider the effects of ionisation on Compton-thick AGN X-ray spectra. As mentioned in Section 3.1, many obscured candidate AGN not only show diminished neutral Fe Kα line EWs, but also increased ionised Fe Kα EWs with intrinsic luminosity

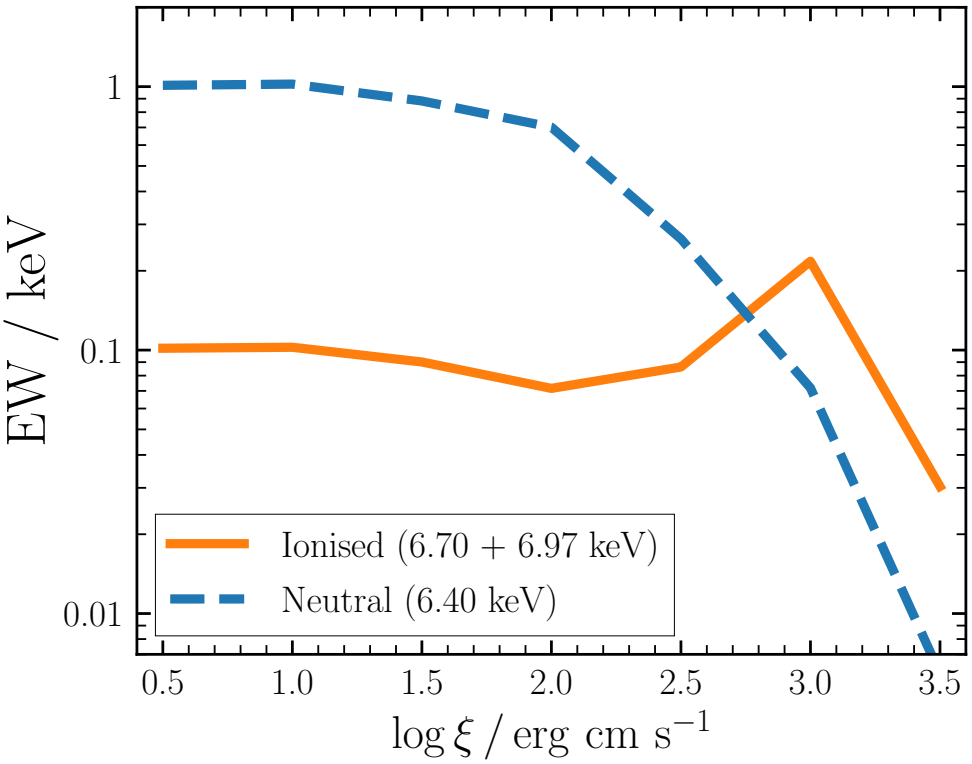

FIGURE 3.11: XILLVER-simulated EWs of the ionised Fe Kα lines at 6.70 and 6.97 keV (solid orange line) together with neutral Fe Kα line EW (dotted blue line) as a function of ionisation parameter. The EWs were calculated by integrating the flux in the continuum between 5.9 – 7.2 keV, subtracted from the flux in the lines (integrated $\pm$ 0.05 keV of each predicted line centroid), and then divided by the interpolated continuum at the line centroid. The spectra were simulated assuming an inclination angle of 18.2° (the most face-on angle allowed by the model to simulate maximal reflection).

(e.g., Iwasawa *et al.* 2009). Indeed, a correlation between spectral slope (a proxy for the accretion efficiency of AGN) with the Fe Kα line energy was found by Dewangan (2002). From Figure 3.5, one would expect this effect to be most prevalent for intrinsically bright (i.e. high $L_{\rm bol}$ and/or high Eddington ratio) systems, which may be more *intrinsically* UV-luminous relative to X-rays.

To robustly test this would require an ionised toroidal X-ray reprocessing model, which is currently unavailable. For this reason, we use the XILLVER (García *et al.* 2013) disc reflection model, which calculates a spectrum from the accretion disc surrounding AGN including reflection and also ionised emission lines. Figure 3.11 illustrates the approximate EWs of the ionised 6.70 and 6.97 keV iron emission lines and neutral Fe Kα line as a function of ionisation parameter. This is defined as $\xi = 4\pi F_x/n_e$ (García *et al.* 2013), where F_x is the net flux in the 1 – 1000 Ry (13.6 eV – 13.6 keV) energy region, and n_e is the electron number density in cm^{-2}. From Figure 3.11, one can infer that the dominance of ionised lines increases with respect to the neutral ones for high values of ξ. Thus, ionisation could be a potential explanation for our results.

To place some kind of constraint on the physical nature of potential ionising obscurers, we made simple phenomenological arguments as follows. By re-arranging the ionisation parameter equation above, we get $\xi = L_x/(n_e \times R^2)$. If we approximate from Figure 3.11 that to achieve a notable ionised EW requires $\log \xi \sim 3$, and substitute an approximate torus inner radius of $R \sim 1\,\mathrm{pc} \sim 3 \times 10^{18}\,\mathrm{cm}$, we acquire $n_e \sim 10^4\,\mathrm{cm}^{-3}$. Thus one would require very low densities to reach such an ionisation level, which seems unlikely for the torus or even an accretion disk. An alternative region with enough compactness is the Broad Line Region – a potential source of obscuration in the higher-luminosity sources in which we find ionised emission lines of appreciable strength.

3.5.2.3 The Warm Mirror

Another possibility for a depleted neutral Fe Kα line in a Compton-thick AGN would be dilution of the reflection spectrum by scattered primary emission from the AGN that is reprocessed by a diffuse ionised 'mirror' in a line of sight direction of lower column density. Such a component would scale with intrinsic luminosity and thus contribute to the Iwasawa-Taniguchi effect. For example, a considerable scattered fraction of intrinsic emission was found to explain the observed X-ray spectrum of the local Compton-thick AGN NGC 7674 by Gandhi *et al.* (2017). The authors find a fraction of $\sim 2-10\%$ to 90% confidence could explain the low observed EW of the neutral Fe Kα line from this Compton-thick source. More recently, Matt and Iwasawa (2019) sought to explain the Iwasawa-Taniguchi relation we find with such an ionised mirror. The authors find this is possible if the warm mirror has column density $N_{\mathrm{H}} = 7.5 \times 10^{22}\,\mathrm{cm}^{-2}$. However, given the likely wide variety of AGN obscurer geometries, the presence of a warm mirror in all may be unfeasible.

3.5.2.4 Dual AGN

A second tentative explanation for an obscured Iwasawa-Taniguchi effect comes from dual AGN candidate systems, in which a spatially unresolved, less-obscured AGN is present in combination with a heavily obscured source. Supermassive black hole evolution simulations (from, e.g. Hopkins *et al.* 2008) predict luminous quasars to originate from gas-rich mergers. Immediately post-merger, these sources are predicted to be deeply embedded in the large dust and gas reservoirs that are rapidly being accreted, which absorb optical to X-ray emission and reprocess this at infrared wavelengths. Depending on the spatial separation of the merging supermassive black holes, the extracted X-ray spectrum could actually be the combined contribution from two components of differing obscuration levels. Examples exist in previous literature – for example, Koss *et al.* (2016b) used *NuSTAR*

to spatially resolve the emission from the dual AGN in NGC 6921. The authors found the two AGN components to be Compton-thick, but were able to separately study each independently in the >10 keV waveband attainable with *NuSTAR*. If one component of a dual AGN were less obscured, but contributed a considerable proportion of the total flux contribution, this could result in a diminished Fe Kα complex in some post-merger candidates such as HyperLuminous ($L_{8-1000\,\mu\mathrm{m}} > 10^{13}\,\mathrm{L}_{\odot}$) InfraRed Galaxies (e.g., Farrah *et al.* 2016, Dust Obscured Galaxies (Dey *et al.* 2008, DOGs) and Hot DOGs (Wu *et al.* 2012). For example, recent works have postulated the presence of dual AGN in NGC 7674 (Kharb *et al.* 2017) and Mrk 273 (Iwasawa *et al.* 2017). Furthermore, Vito *et al.* (2018) recently studied the X-ray emission from 20 Hot DOGs, and found typical predicted X-ray line of sight column densities of $N_{\mathrm{H}} \sim 1-1.5\times10^{24}\,\mathrm{cm}^{-2}$. This is illustrated in Figure 3.12, in which the composite spectrum is plotted with a black solid line, formed by combining the spectrum from a reflection-dominated AGN ($\log N_{\mathrm{H}}\ /\,\mathrm{cm}^{-2} = 24.5$; red dashed line) and an unobscured AGN ($\log N_{\mathrm{H}}\ /\,\mathrm{cm}^{-2} = 22$; blue dot-dashed line). Higher angular resolution X-ray instruments or increased sensitivity gravitational wave detectors (e.g., with *LISA*) would be required to separate the two components and stringently test this hypothesis. We further note that both a strong scattered component as well as dual AGN would struggle to explain the observed prominence of ionised iron emission lines often observed in the X-ray spectra of infrared-luminous systems (e.g., Teng *et al.* 2014; Gilli *et al.* 2014; Farrah *et al.* 2016).

3.5.2.5 X-ray Scattering by Dust Grains

A final possibility arises from the effects of dust grains on X-ray photons. Typical X-ray reprocessing spectral models consist of ray-tracing through a dust-free gas, but do not consider the possible effects that dust grains have on the observed X-ray spectrum in detail. In fact, Draine (2003) has shown that $\sim$90% of the incident power at energy $E = 6.4$ keV on dust grains scatter with angle, $\theta_{\mathrm{s}} < 0.05°$, relative to the incident photon direction. Gohil and Ballantyne (2015) further found that such a large anisotropic emission associated with dust grains, as opposed to the isotropic emission of hot gas typically invoked in X-ray reprocessing torus models could enhance the Fe Kα line EW relative to the underlying reflection continuum by up to factors of $\sim$8 for Compton-thick gas. More luminous AGN would be expected to have a larger dust sublimation radius, and thus have an altered Fe Kα EW relative to the less luminous sources, presumably with smaller dust sublimation radii. Such a scenario effectively decouples the Fe Kα line from the underlying reflection continuum, and there is already tentative evidence suggesting that these two components may arise from physically separate regions within the torus dust sublimation zone (Gandhi *et al.* 2015a). However, a full radiative transfer

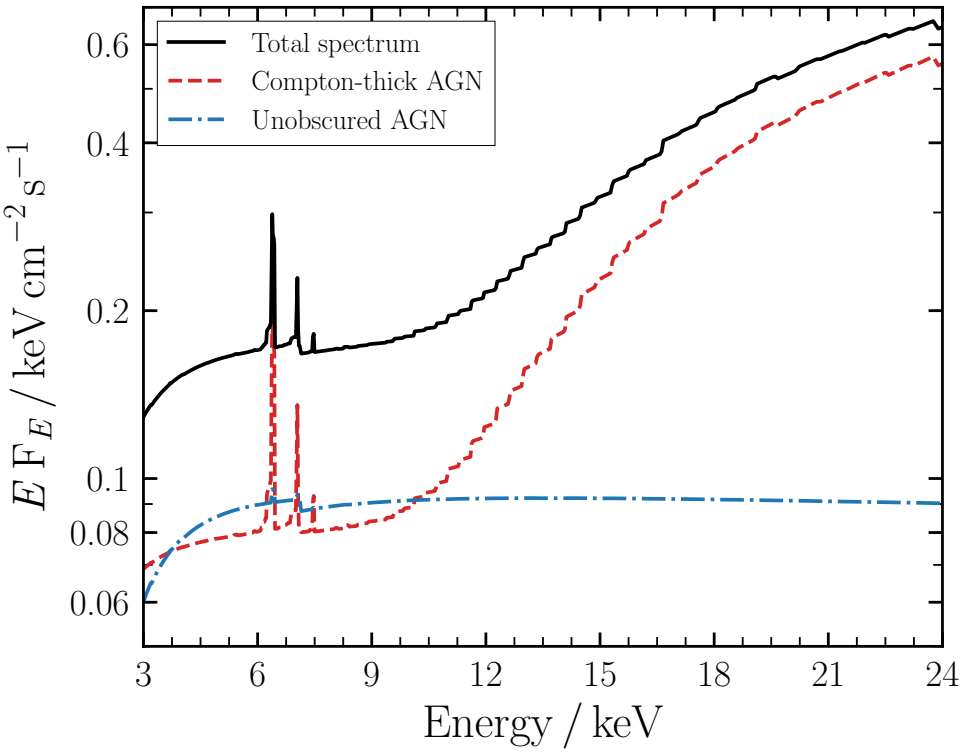

FIGURE 3.12: Dual-AGN schematic to explain the lower observed Fe Kα EWs observed in luminous and ultraluminous infrared galaxies ($L_{8-1000\,\mu\mathrm{m}} > 10^{11}\,\mathrm{L}_\odot$ and $L_{8-1000\,\mu\mathrm{m}} > 10^{12}\,\mathrm{L}_\odot$, respectively). If an AGN were observed post-merger, the two supermassive black holes could exist temporarily separately, but spatially unresolved, leading to an observed (solid black line) composite spectra from two AGN. The individual unobscured (dot-dash, blue) and obscured (dashed, red) predicted AGN spectra are also plotted. Depending on the relative contributions in observed flux from either component, the total spectrum could have characteristics of a mildly obscured AGN, despite containing a heavily obscured source. Both the AGN spectra were simulated using the `borus02` model.

simulation for the effect of dust on observed X-ray spectra from obscured AGN is outside the scope of this work, and will be the topic of future X-ray model being developed (Boorman *et al.*, in prep.).

3.5.3 Implications

3.5.3.1 Redshift Evolution of Compton-thick AGN

As stated earlier, multiple works predict the obscured fraction of AGN to decrease with increasing luminosity and/or Eddington fraction (e.g., Ueda *et al.* 2011; Merloni *et al.* 2014; Georgakakis *et al.* 2017). In addition, since the number of luminous AGN is predicted to increase with redshift, this would imply a redshift evolution of obscuration amongst AGN. However, the anti-correlation we report could lead to a correction to

X-ray inferred column densities, that were derived based on fitting an observed Fe Kα. From Figure 3.5, this correction factor would be largest for the most luminous sources. Depending on the relative contributions at different luminosities, this could then alter the obscured fraction dependence with luminosity. Some evidence has indicated a weak or no evolution of the obscured AGN fraction. For example, Vito *et al.* (2014) studied a sample of 141 X-ray selected AGN at $3 < z \leq 5$ and found no evidence for an anti-correlation between obscured fraction and luminosity, despite suggesting that this may be due to the non-detection of the lower luminosity obscured sources at higher redshift. In contrast, Mateos *et al.* (2017) only found a weak luminosity dependence of the Type 2 AGN fraction for covering factors derived from infrared clumpy torus modelling for $z \leq 1$, and Buchner *et al.* (2015) further derived the Compton-thick fraction evolution with redshift and accretion luminosity for a sample of $\sim$2000 AGN from *Chandra*, finding no evolution.

To test if our result is biased by redshift, we further separated our sample into two redshift bins, below and above the median redshift of 0.038. Figure 3.13 shows the redshift distribution of our sample with the median redshift shown with an orange vertical line. Carrying out a fit to either redshift bin independently yielded consistent gradients of $\mathrm{m} = -0.19^{+0.06}_{-0.07}$ and $\mathrm{m} = -0.04 \pm 0.08$, for the low and high redshift bins respectively, albeit with large scatter.

3.5.3.2 The Growth Rate of AGN

Current X-ray reprocessing torus models do not account for the possible effects of dust grains, and/or reflector ionisation on the observed reflection spectrum. To zeroth order, such a model could interpret a less prominent neutral Fe Kα line as evidence for a lower obscuring column than the true value for intrinsically bright, heavily obscured objects if our results are confirmed using larger sample studies. In the most extreme case, a Compton-thick system could be predicted to be only mildly obscured. From Figure 3.3, this would mean underpredicting the intrinsic X-ray luminosity, and hence the growth rate of such systems, potentially by factors of around two orders of magnitude.

3.5.4 The Future

One of the major sources of uncertainty in the relation we report here is on the EW of the Fe Kα line. However, many future X-ray missions can improve on this uncertainty, such as the *X-Ray Imaging and Spectroscopy Mission* (*XRISM*[10]), or *Athena*

[10] https://heasarc.gsfc.nasa.gov/docs/xarm/

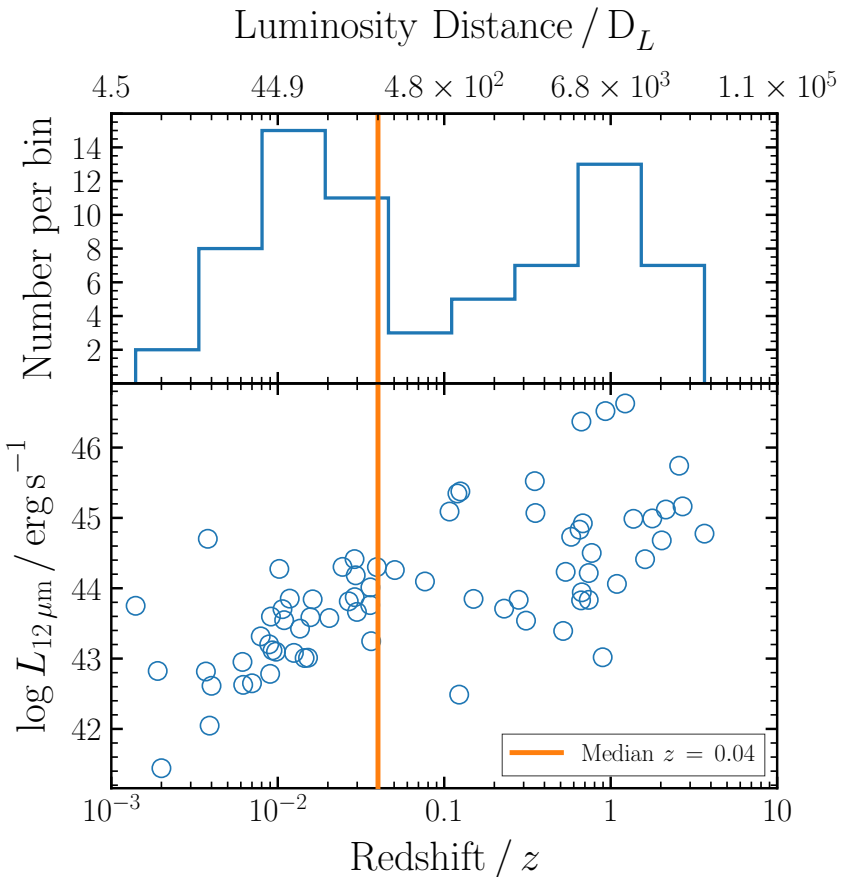

FIGURE 3.13: Redshift distribution of our sample, according to the rest-frame 12 μm luminosity. The median redshift was chosen to split the sample into two redshift bins, in order to provide comparable numbers of sources in either bin.

(Nandra *et al.* 2013). *XRISM* will enable high spectral resolution studies of the Fe Kα line (e.g., Hitomi Collaboration *et al.* 2017) and be able to test the ionisation scenario directly. Additionally, *Athena* will probe high redshift Compton-thick AGN sensitively. Figure 3.14 shows the possibilities with the *Athena* Wide Field Imager (WFI), with a 20 ks simulated spectrum shown in purple together with the original 4 Ms *Chandra* Deep Field South observed spectrum for CDFS 384 from our sample, shown in black. Clearly the signal to noise is dramatically enhanced at the Fe Kα (rest-frame 6.4 keV) line as well as the neighbouring continuum, enabling a huge improvement on the calculated EW contour in the lower panel of the figure. The simulated spectrum was calculated from the original best fit model to the observed *Chandra* spectrum. What this figure clearly shows, however, is that the confidence range on the EW of such obscured objects will be powerfully improved with the advent of such high-sensitivity instruments in the future.

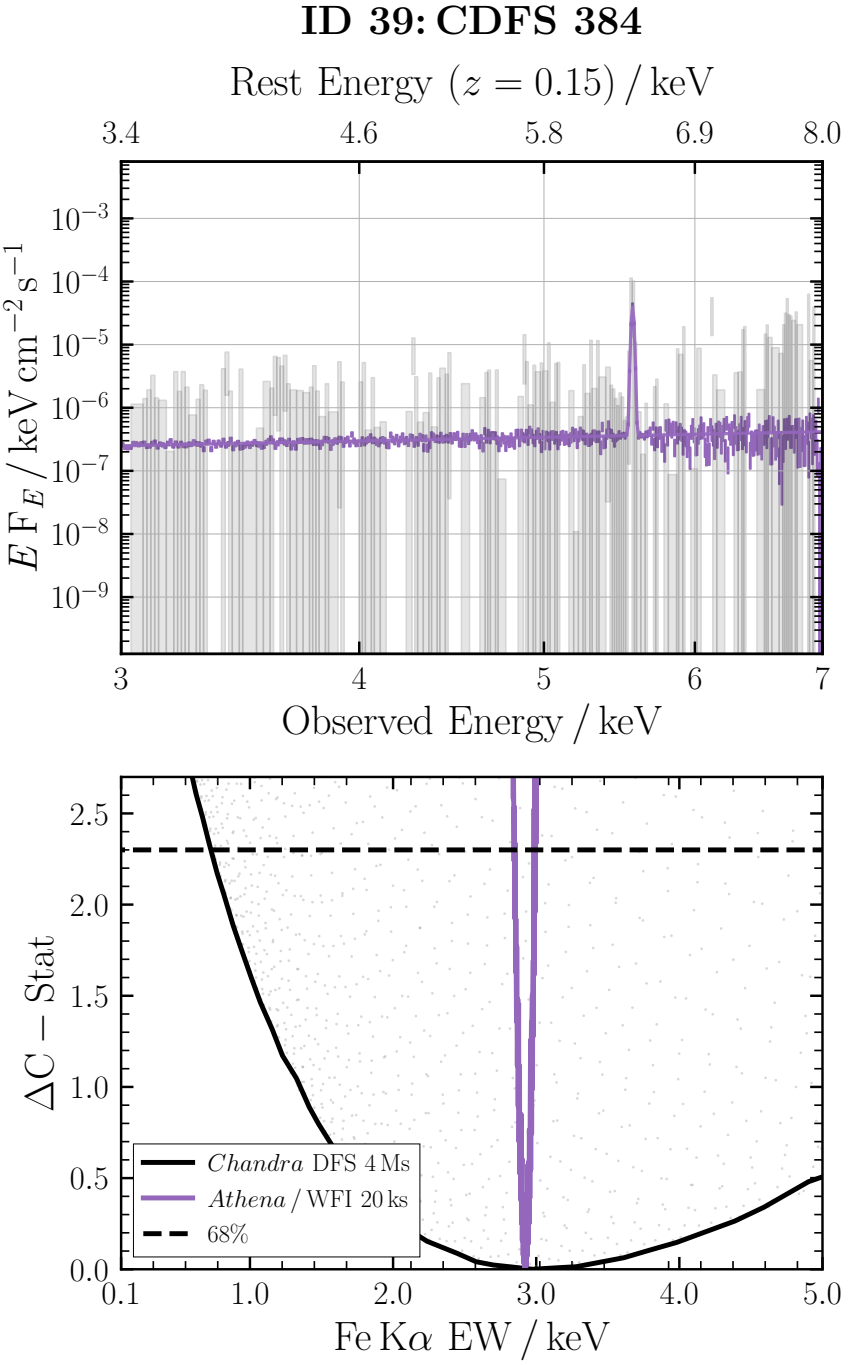

FIGURE 3.14: Top panel: Observed *Chandra* Deep Field South (CDFS) 4 Ms spectrum for CDFS 384 together with simulated *Athena*/WFI spectrum for a 20 ks observation, shown in black and purple, respectively. Lower panel: Reported EW contour for CDFS 384 used in the paper, together with the improved contour attained with the simulated *Athena*/WFI spectrum shown above. A dramatic improvement to the signal to noise of the observed spectrum is clearly attainable with *Athena*, not to mention the improved EW confidence region. Such observations of Compton-thick AGN are to be carried out as part of the *Athena* mission, with the aim to study obscured accretion and galaxy formation with the WFI instrument.

3.6 Summary

This chapter presents the first study into the Iwasawa-Taniguchi effect for Compton-thick AGN. The key findings are enumerated below:

1. A sample of 72 Compton-thick candidate AGN was selected from the literature, covering a redshift range of $z \sim 0.0014 - 3.7$. The candidates were confirmed via an offset between predicted intrinsic and observed X-ray luminosity, given the rest-frame 12 μm luminosity interpolated from the Mullaney *et al.* (2011) AGN infrared spectral template.

2. We find an anti-correlation between the rest-frame equivalent width of the narrow core of the neutral Fe Kα fluorescence emission line and the mid-infrared 12 μm continuum luminosity, which we use as a proxy for the bolometric AGN luminosity. From the Spearman's Rank, we find the anti-correlation to be significant to 98.7% confidence. However as the $\Delta\chi^2$ fit to a linear relationship between $\log \mathrm{EW}_{\mathrm{Fe\,K}\alpha}$ and $\log L_{12\,\mu\mathrm{m}}$ is considerably larger than 1, we cannot draw any strong conclusions regarding the exact parametric form of any such relationship. One possible reason for the large observed scatter is from some other parameter(s) which have yet to be identified (see Section 3.5).

3. We discuss five possible interpretations of such an anti-correlation:

   (a) A luminosity-dependent covering factor (Section 3.5.2.1). We deduce that if this is the sole reason, then our sample are not reflection-dominated Compton-thick AGN. Since the Compton-thick Iwasawa-Taniguchi effect we find is most prominent for the sources with Fe Kα EW < 1 keV, this interpretation would effectively mean we are currently lacking any reflection-dominated high-redshift Compton-thick AGN.

   (b) Luminosity-dependent ionisation state of the circumnuclear reprocessing material (Section 3.5.2.2). Based on simple arguments, for sources displaying higher-ionisation emission lines in their X-ray spectra, we find that the Broad Line Region may be the source of the obscuration.

   (c) Dilution of the Fe Kα line flux by 'warm mirror' emission (Section 3.5.2.3). Although a probable explanation for some sources, the likely complex range of AGN obscurer geometries may render this scenario unlikely as an explanation for *all* Compton-thick AGN.

   (d) Effects of unresolved dual AGN of differing column densities resulting in a diluted observed Fe Kα line (Section 3.5.2.4). We conclude that this tentative

interpretation requires next-generation instrumentation to stringently test, such as the upcoming *LISA* gravitation wave detector.

(e) The tentative possibility of the anisotropic scattering of X-ray photons by dust grains leading to the decoupling of the Fe Kα line from the underlying Compton-scattered continuum (Section 3.5.2.5). Such effects are not included in current X-ray reprocessing models, though previous studies indicate they are important for the Fe Kα line energy band.

4. If the Compton-thick Iwasawa-Taniguchi effect is confirmed on larger samples, we discuss possible implications as follows:

   (a) The repercussions of incorrectly classifying Compton-thick AGN as less obscured (Section 3.5.3.1): One key result of our study is that an AGN can be Compton-thick with an observed Fe Kα line EW < 1 keV. Current X-ray torus models do not easily reproduce such a pattern. As a result, this could lead to more luminous AGN primarily being classified with obscurations An increased number density of Compton-thick AGN at higher redshifts due to predicted higher intrinsic luminosities .

   (b) Current X-ray reprocessing models do not account for this effect, and as such may incorrectly interpret a weak Fe Kα line as a signature of lower obscuration reprocessing, leading to an under-estimation of the true intrinsic luminosity and hence growth rate of X-ray-obscured AGN.

   (c) If a luminosity-dependent covering factor can explain the Iwasawa-Taniguchi effect, it would imply that we are still lacking a population of truly reflection-dominated, luminous Compton-thick AGN, since for $N_{\rm H} \gtrsim 1.5 \times 10^{24}\,{\rm cm}^{-2}$, the EW of the Fe K$\alpha$ line is predicted to always be > 1 keV, contrary to what we find (see Figure 3.10).

This work further illustrates that the Fe Kα line alone cannot be directly used to accurately determine the line of sight column density to a source, and future dedicated studies of Compton-thick AGN over broad redshift ranges are required to confirm this effect. Matt and Iwasawa (2019) have proposed an altered AGN schematic to explain my results, in which the obscuring structure's polar cutouts are instead filled with ionising gas. When the obscurer sublimates due to increased ionising radiation from the source, for example due to increased Eddington ratios or luminosity, the ionising gas content and covering factor increases. This ionising gas contributes to the 'Warm Mirror' emission discussed in Section 3.5.2.3, and would potentially be stronger for brighter sources as we find here.

With the advancements of future breakthrough missions such as *Athena* and *Lynx*, the prospects for the higher-redshift Compton-thick AGN population are outstanding. However, for the nearer future, dedicated local studies are the only way to scrutinise the Fe Kα line in Compton-thick AGN. However, the majority of Compton-thick AGN selected in the local Universe to date are not reflection-dominated, just to the reliance on hard X-ray *Swift*/BAT selection. In the following chapter, I present the *NuSTAR* Local AGN $N_{\rm H}$ Distribution Survey (NuLANDS) – a substantial *NuSTAR* Extragalactic Legacy Survey of AGN in the local Universe, designed to first identify how many Compton-thick AGN there are, and is fully representative of X-ray-obscuring $N_{\rm H}$ well into the Compton-thick regime.

Chapter 4

The *NuSTAR* Local AGN $N_{\rm H}$ Distribution Survey: Prospects for Mitigating Obscuration Bias in Local AGN Selection

"All my life I've had one dream – to achieve my many goals."

– Homer Simpson

In this chapter, we aim to derive a sample of AGN that is selected representatively of their circumnuclear obscuration. Our motivation lies in the ability of such a sample to probe the true column density distribution in the local Universe – a vital boundary constraint for AGN evolutionary models. Specifically, we wish to derive a survey strategy capable of sampling AGN in a way that is more representative than X-ray flux-limited selection, especially in the extreme $N_{\rm H}$ regime. As described in Section 1.4, complementary methodologies exist to do this, and in Section 4.1, I outline the optimum strategy we employ.

4.1 Introduction

The evolution of and accretion onto SuperMassive Black Holes (SMBHs, $\log M_{\rm BH} / M_{\odot} \sim 6-9.5$; Ramos Almeida and Ricci 2017) hosted in the nuclei of galaxies can be constrained

from the broadband Cosmic X-ray Background (CXB; Giacconi *et al.* 1962). This is because the integrated X-ray emission from accreting SMBHs, or Active Galactic Nuclei (AGN), across cosmic time, is predicted to dominate the CXB across the observed energy range, $E \sim 1 - 300\,\mathrm{keV}$ (e.g., Setti and Woltjer 1989; Comastri *et al.* 1995; Mushotzky *et al.* 2000; Gandhi and Fabian 2003; Gilli *et al.* 2007; Treister *et al.* 2009; Brandt and Alexander 2015; Ananna *et al.* 2019; also see Section 1.6.1). In particular, AGN in the Seyfert luminosity range ($L_{2-10\,\mathrm{keV}} \sim 10^{42-44}\,\mathrm{erg\,s^{-1}}$) completely dominate the CXB emissivity to beyond $z = 1$, and are likely to contribute between $\approx$30–50% of the emissivity between $z = 1$–5 (Ueda *et al.* 2014; Buchner *et al.* 2015). These sources are thus crucial to understand, but are best probed in detail only in the local Universe.

Synthesis of the CXB spectrum with different AGN populations requires knowledge of the distribution of sources in terms of obscuring neutral hydrogen column density (N_H). Typically the observed Compton-thick fraction in X-ray surveys is $\lesssim 15\%$ before (e.g., Masini *et al.* 2018) and $\sim 10 - 30\%$ after applying 'bias corrections' (e.g., Burlon *et al.* 2011; Ricci *et al.* 2015). But higher fractions are often discussed in the literature, even in the local Universe where Malmquist biases ought to be minimal (e.g., Ananna *et al.* 2019, Annuar et al., in prep.). The local N_H distribution is the $z = 0$ boundary condition imposed in CXB evolutionary models (e.g., Ueda *et al.* 2014), so accurate determination of the number of obscured and Compton-thick AGN locally is crucial. Thus independent selection strategies are clearly required that are not biased against detection of highly obscured AGN in the same way as X-ray flux-limited surveys.

As described in Section 1.4, such complementary methodologies include optical narrow line emission, radio low-frequency surveys, mid-infrared line emission, and mid-to-far infrared continuum. These techniques are effective because the unified scheme of AGN ascribes observed differences between AGN classes primarily to the orientation of the parsec-scale anisotropic obscurer (the 'torus') relative to the line-of-sight, whereas all the above methods probe emission from much larger scales. While each of these techniques provides a means of isotropic AGN torus selection to first order, each has associated advantages and disadvantages. But to quantify the effectiveness of any one strategy relative to another requires a comparison of sample properties according to multiple bolometric indicators, and thus requires the construction of samples with several of the listed indicators available.

The purpose of this chapter is to devise a survey strategy capable of sampling AGN in a way that is more representative of the AGN population than X-ray flux-limited selection, especially in the extreme N_H regime. As a first step, we adopt infrared continuum selection herein, because (i) of the availability of legacy all-sky infrared imaging surveys, which (ii) allow collation of substantial AGN sample sizes with (iii) follow-up

optical source classification already available. This method is useful for comparing sample properties in the parameter space of infrared continuum, optical emission line, and hard X-ray bolometric indicators. Finally, (iv) we require high quality broadband X-ray spectral characterisation for $N_{\rm H}$ measurement.

Our survey is the '***Nu****STAR* **L**ocal **A**GN $\boldsymbol{N}_{\rm H}$ **D**istribution **S**urvey' (**NuLANDS**). The sample derivation follows in Section 4.2, with Section 4.2.5 highlighting its representative nature. I then present the *Swift*/BAT-dominated NuLANDS $N_{\rm H}$ distribution as well as prospects for the final sample in Section 4.3, before summarising the findings in Section 4.4.

4.2 The NuLANDS Sample

4.2.1 Sample Selection

The isotropy of mid-to-far infrared torus continuum emission lies at the heart of the NuLANDS selection strategy. Specifically, we used the studies of de Grijp *et al.* (1987, dG87 hereafter) and Keel *et al.* (1994, K94 hereafter), who selected objects from the *InfraRed Astronomy Satellite* (*IRAS* – Neugebauer *et al.* 1984) all-sky Point Source Catalog version 1 (Beichman *et al.* 1988). Importantly, K94 showed that there is no significant difference between optical Type 1 and 2 AGN in their sample, when comparing the Narrow Line Region and infrared fluxes as bolometric indicators. This congruence is what motivated us to use their sample as a starting point. The criteria applied by dG87 to select their sample was as follows:

1. ***IRAS* 60 $\boldsymbol{\mu}$m flux density, $\boldsymbol{F_{60\,\mu\rm m} > 0.5\,Jy}$.** This flux density cut approximately corresponds to the nominal depth of *IRAS* for point sources away from confused regions of the sky.
2. **Detections at 25 and 60 $\boldsymbol{\mu}$m.** These were required for source classification, discussed below.
3. **Source coordinates restricted to Galactic latitude $\boldsymbol{|b| > 10°}$ and outside the Magellanic Clouds** to minimise confusion by avoiding dense stellar fields.

We matched the resultant sources to the AllWISE Source Catalog to enable accurate coordinates and source identifications. Of all sources, only one was not matched – IRAS 0346+253[1].

[1]Matched to IRAS 03462+2521 on SIMBAD.

While capable of isotropically selecting AGN, the above criteria will also pick up sources from a variety of classes, including Galactic objects and star-forming galaxies, so the sample must be pruned in order to isolate the AGN.

4.2.2 Sample Classification

Source classification was carried out by dG87 and subsequently refined by de Grijp *et al.* (1992, dG92 hereafter) as follows.

4. **Application of a warm colour cut such that the *IRAS* 25 to 60 μm spectral index[2] $\alpha_{25,60}$ lies in the range -1.5 $< \alpha_{25,60} <$ 0.** This colour cut favours selection of AGN because star-formation-dominated galaxies are typically characterised by cooler dust temperatures of the interstellar medium peaking at $\gtrsim 50\,\mu$m (e.g., dG85, Dale *et al.* 2001). In addition, the lower bound on this colour cut was imposed to restrict selection of particularly blue objects, such as typical stars with blackbody spectra that peak in the ultraviolet – optical wavebands[3]. Application of this colour cut was the final step in the selection and classification applied by dG87, resulting in a catalogue of 563 sources. Figure 4.1 illustrates the effectiveness of this selection – the Mullaney *et al.* (2011) template spectral energy distributions for active and non-active galaxies are compared with the selection criteria overplotted. Clearly, the dG87 selection preferentially selects AGN, as compared to the non-active galaxy spectrum that peaks at cooler temperatures. But this cut is not fully reliable for AGN isolation, i.e. it can still include contaminants such as stars and star-forming galaxies that lie in the warm tail of the distribution of dust temperatures. The infrared luminosity itself need not be dominated by the AGN alone.

5. **Optical emission line diagnostic classification:** To confirm the nature of the warm *IRAS* sample, dG92 carried out optical spectroscopic observations of 563 warm *IRAS* AGN candidates from the catalogue of dG87. Classification of the extragalactic sources was then based upon emission line velocity width and flux ratio measurements using commonly adopted criteria (Heckman 1980; Baldwin *et al.* 1981; Veilleux and Osterbrock 1987). Sources which had broader (by 500 km s^{-1}) permitted than forbidden emission lines were classified as Type 1 AGN. All remaining sources were classified with emission line flux ratios including [O III]/Hβ

[2] $F_\nu \propto \nu^{-\alpha}$, where F_ν is the flux density, ν is the frequency and α is the spectral index.

[3] For future work into this sample, the lower bound on blue spectra is not necessary since we require optical spectroscopy of each source ultimately. For this reason, in Chapter 6, I discuss an ongoing effort to re-derive the warm *IRAS* sample without applying a lower bound to the colour cut.

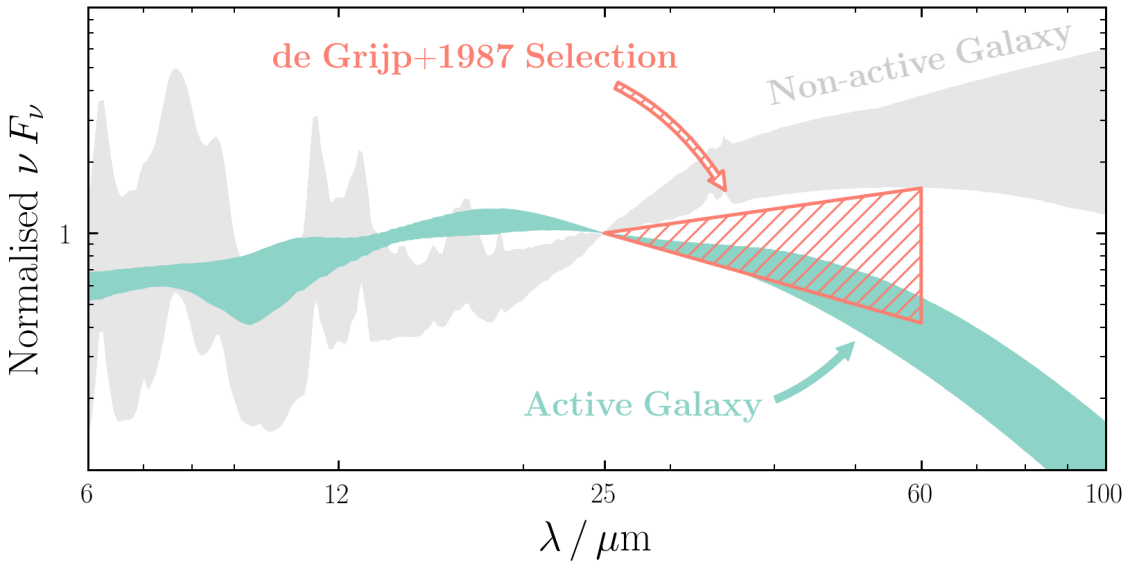

FIGURE 4.1: Plot of the effectiveness of the warm colour cut from dG87 to select warm active galaxies over cooler non-actiive galaxies with far-infrared spectra that peak at cooler termperatures. The AGN and non-AGN spectral energy distribution templates used are from Mullaney *et al.* (2011).

and [N II]/Hα.[4] Emission line fluxes were corrected for the underlying stellar continuum, and dereddened for host galaxy dust based upon the measurement of the Balmer decrement.

The resultant dG92 sample was classified as follows:

i) 128 Galactic foreground objects;

ii) 124 H II galaxies;

iii) 80 Type 1 AGN;

iv) 140 Type 2 AGN;

v) 75 objects randomly unobserved, and thus not classified;[5]

vi) 16 others, including Low Ionisation Nuclear Emission Region sources (LINERs), uncertain classifications, and one BL Lacertae (BL Lac) object.

At this point, the sample consists of **220** securely classified Type 1 and 2 AGN in dG92. Their median redshift is $z = 0.039$, corresponding to a luminosity distance of ~ 180 Mpc.

[4] 7% of the sources classified as Type 2 AGN have no reported line ratios in dG92. We confirmed all of these to have corroborating classifications in other literature publications.

[5] These sources, as well as a subset of the optically classified sources with line flux limits and H II galaxies presented in dG92 are the targets of an ongoing optical followup campaign primarily at the Palomar Observatory.

4.2.3 Sample Culling for Unification Tests and X-ray Follow-up

In addition to the above criteria of dG92, we finally applied two additional criteria in order to establish a well-characterised sample that (i) is suitable for X-ray follow-up within reasonable exposure times, and (ii) also allows comparison between multiwavelength bolometric luminosity indicators in order to assess the isotropic nature of the sample. These criteria are:

6. **Hβ and [O III] Limits:** Of the 220 AGN in dG92, 77 had either upper limits or no stated line fluxes for Hβ or [O III] or both. For sources where Hβ is undetected, dereddening corrections and hence intrinsic emission line fluxes will only remain as lower limits. We require such intrinsic emission line fluxes in order to compare the effectiveness of the optical [O III] and hard X-ray luminosities as bolometric AGN power indicators. These sources were thus excluded in order to form a well-characterised sample with reddening-corrected emission line fluxes, leaving 143 objects. The impact of their exclusion will be discussed in the following sections.

7. **Volume Cut:** Finally, by applying a redshift cut of $z < 0.044$ ($D \lesssim 200\,\mathrm{Mpc}$), we arrive at a core sample of **84** NuLANDS AGN. This volume restriction was applied in order to have a tractable sample in terms of legacy follow-up with *NuSTAR* while allowing a significant constraint on the Compton-thick fraction.

An all-sky map showing the NuLANDS sample of 84 AGN is plotted in Figure 4.2, and the redshift distribution vs. 60 μm luminosities (νL_ν at 60 μm) is shown in Figure 4.3. Of this sample, 30 sources lack hard X-ray constraints from *NuSTAR* and were undetected in the 70-month *Swift*/BAT catalog (black-outline points in Figures 4.2 & 4.3). These are the targets of an ongoing $\sim 1\,\mathrm{Ms}$ *NuSTAR* legacy observing component of NuLANDS, with an average exposure time per source of $\approx 30\,\mathrm{ks}$. Together with archival and scheduled soft X-ray observations from *Suzaku*, *Swift*/XRT, *XMM*-Newton and *Chandra*, *NuSTAR* will provide the first constraints on N_H for these sources via broadband X-ray spectroscopy.

As a sidenote, we discuss why we rely on an *IRAS*-selected sample, as opposed to using more modern missions such as *WISE*. The primary reason is that *IRAS* better matches expected X-ray spectral sensitivity attainable with *NuSTAR*. To test this, we ran X-ray simulations: we estimated the $2-10\,\mathrm{keV}$ intrinsic flux of a source at the median of the NuLANDS infrared flux distribution, with the conversion based upon the infrared–X-ray correlation of Asmus *et al.* (2015). Assuming a $\Gamma = 1.9$ powerlaw model, we simulated the observed *NuSTAR* spectrum for an AGN obscured by $\log N_\mathrm{H} \ / \mathrm{cm}^{-2} = 25$ in XSPEC. Our simulation predicted ~ 250 counts in the $3-78\,\mathrm{keV}$ band, corresponding to a flux $F_{3-78\,\mathrm{keV}} \sim 3 \times 10^{-12}\,\mathrm{erg\,s^{-1}\ cm^{-2}}$, including 213 counts above 10 keV. This amount of

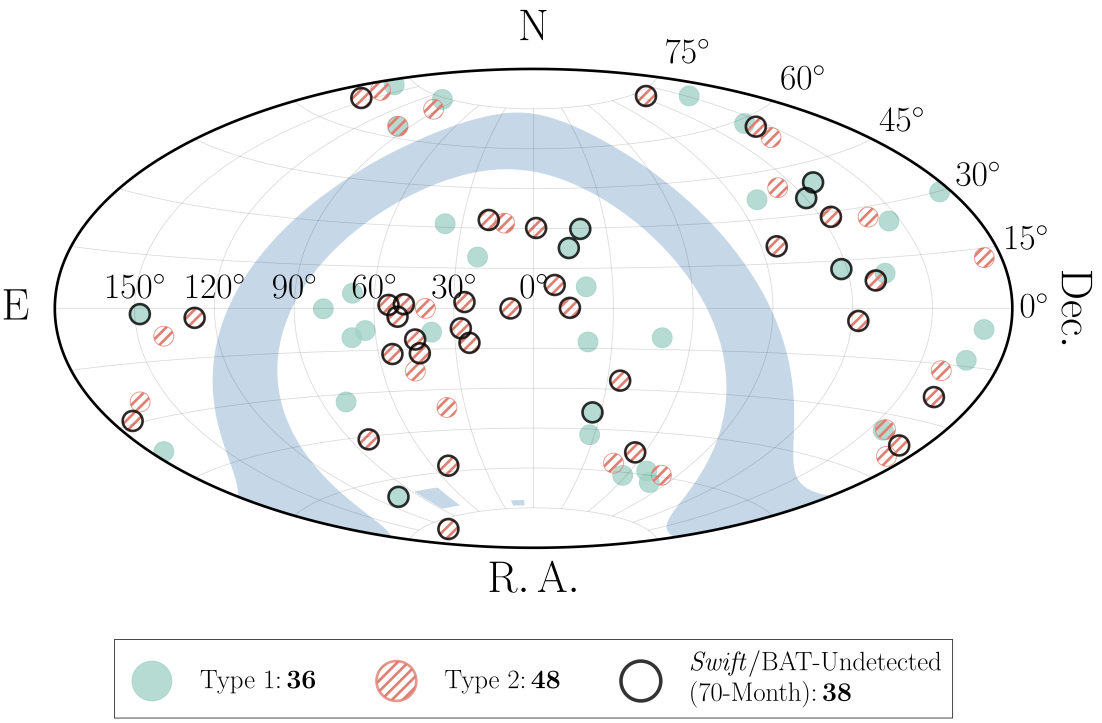

FIGURE 4.2: Skymap of the NuLANDS sample in celestial coordinates plotted with the Aitoff projection. Filled green and hatched orange points show Type 1 and 2 AGN classifications from dG92, respectively. Black outlined points are those not detected in the 70-month *Swift*/BAT catalog. The shaded blue regions indicate ±10° of the Galactic plane and Magellanic Clouds, excluded in deriving the Warm *IRAS* Sample (see Item 3. in the sample derivation in Section 4.2). Thus, NuLANDS encompasses ∼72.5% of the sky, or 32,384 deg^2.

counts should be adequate for broadband spectral modelling. Using deeper surveys such as *WISE* would equate to correspondingly less counts with *NuSTAR*, and $N_{\rm H}$ constraints would be much weaker. Hence probing to deeper limits would not be fruitful with current X-ray implementation.

We also examined the *WISE* colours in order to quantify the fraction of sources that are AGN-dominated in the infrared. $\sim 60-80\%$ ($1-\sigma$ Poisson uncertainty from Gehrels 1986) of sources satisfied the Stern *et al.* (2012) and Mateos *et al.* (2012) infrared colour cut criteria implying AGN dominance. At the median redshift of our sample – 0.0247 – the 6 arcsec-diameter angular resolution of *WISE* $W3$ (12 μm) equates to a physical scale of ~ 3.3 kpc.

Optically weak AGN that are excluded with BPT diagnostic diagrams (i.e. those classified as H II or LINERs are expected to be missed representatively of Type 1 and 2 AGN. To check that this did not bias the final NuLANDS sample, we assumed the very conservative approach that all 149 sources with $z < 0.044$, not classified as Seyferts in the optical, were actually Seyferts. This accounts for any possible confusion associated

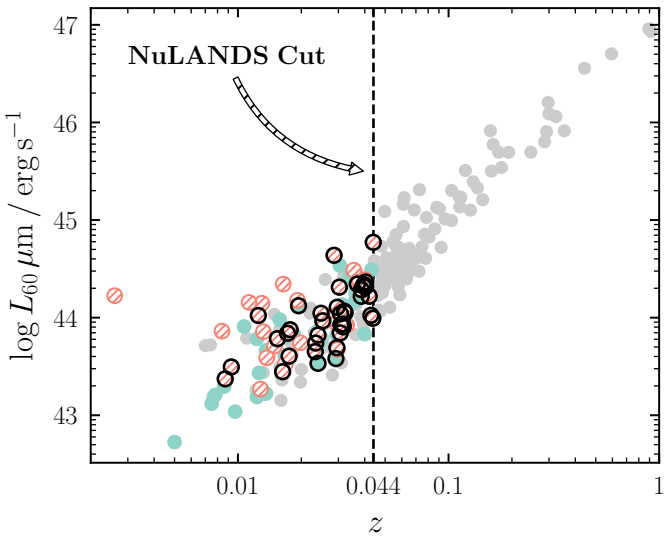

FIGURE 4.3: Redshift distribution of the NuLANDS sample according to the 60 μm luminosity – the original bolometric indicator used by dG87. Colour scheme is the same as in Figure 4.2, but with all 220 warm *IRAS* AGN shown in grey.

with optical-classified quiescent galaxies actually harbouring concealed AGN. Of these, 40 sources had a Seyfert classification, whereas 109 did not. For the 109 remaining sources, we simulated their Seyfert types many times, assuming the luminosity dependence on obscured AGN fraction given in Ricci *et al.* (2017c) (and including the fraction for Compton-thick sources from Ricci *et al.* 2015). The result is plotted in Figure 4.4 – I found consistent obscured AGN fractions between the possible optically missed sources and the 84 NuLANDS sources, indicating no significant bias arising in NuLANDS from optical spectral classifications.

4.2.4 AGN Dominance

Here we include the multiwavelength confirmation of AGN activity in the NuLANDS sample. As the sample was primarily selected in the infrared, despite the selection being based around 'Seyfert-like' colours, there may be some unknown source of contamination arising from star formation in the sample. As such, it is useful to check that all 84 sources show a considerable AGN component to the observed SED as a precautionary check of the nature of the nucleus of these systems. In the left panel of Figure 4.5, we show the *WISE* colour plot of $W2-W3$ vs. $W1-W2$, with the AGN selection criteria of Stern *et al.* (2012) and Mateos *et al.* (2012) with a solid and dotted line, respectively. The sources occupying the region of colour space agreeing with these thresholds can be inferred as an indicator of AGN activity, but there has been many reports on the efficiency of infrared AGN selection as a function of intrinsic AGN luminosity. For this reason, the sources lying outside these criteria may be sub-quasar luminosity AGN, as

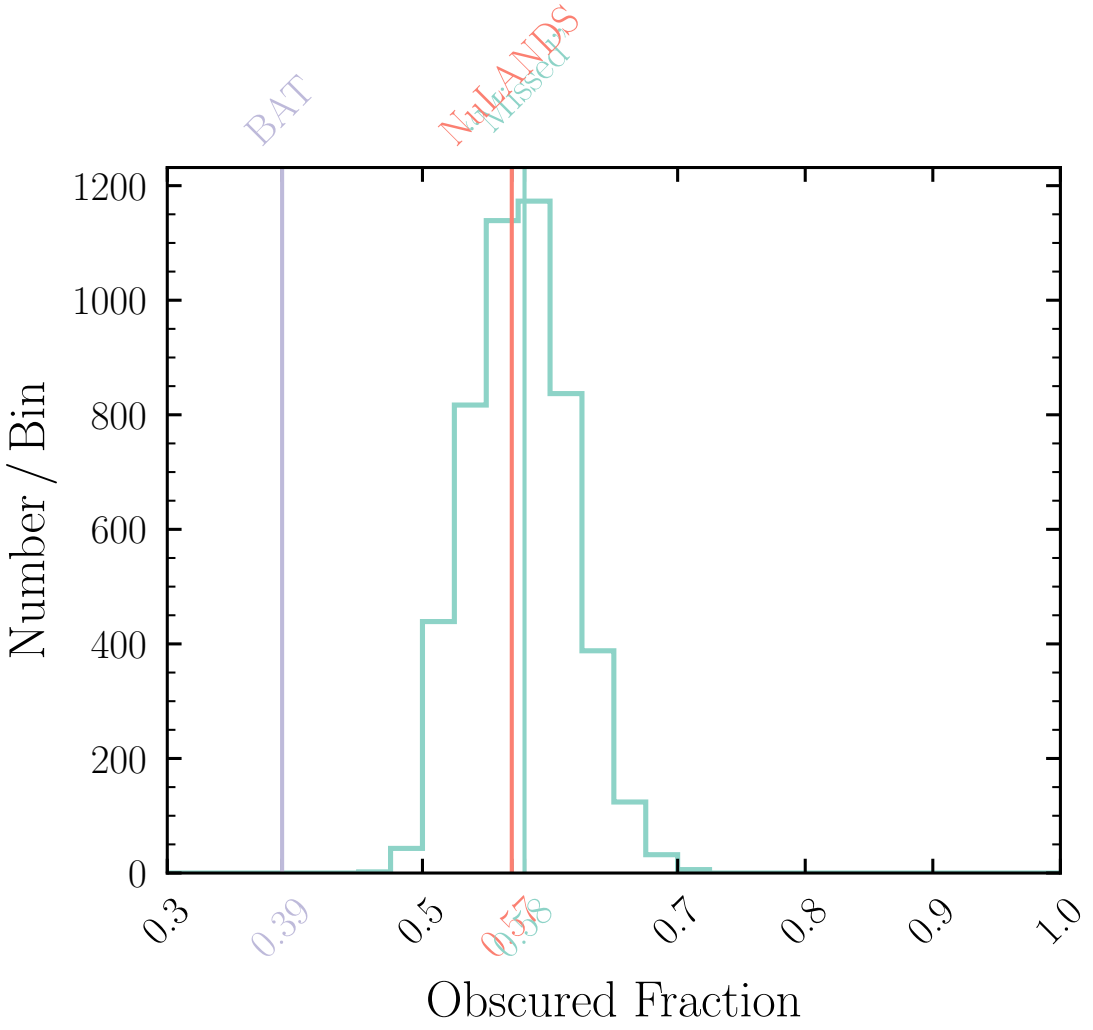

FIGURE 4.4: Distribution of simulated obscured fractions for the 70-month *Swift*/BAT-detected portion of NuLANDS, the full NuLANDS sample and the sources excluded from NuLANDS based on the optical selection criteria. The simulated obscured fractions (see the text for details on this process) for NuLANDS and the missed sources are consistent, indicating that no significant bias is imposed by the optical selection.

is expected in the local Universe. In addition, a total of 72/83 are AGN-dominated by the 90% reliability selection cut of Assef *et al.* (2018), and 54/83 satisfy the Stern *et al.* (2012) and Mateos *et al.* (2012) colour criteria. Of the NuLANDS *NuSTAR* targets, just 4/30 do not meet the Assef *et al.* (2018) 90% reliability cut, *all of which* are bona-fide AGN from Véron-Cetty and Véron (2010): KUG 0312 +013 (Seyfert 2), UGC 9826 (Seyfert 1.5), Mrk 315 (Seyfert 1.5) and CGCG 498 -038 (Seyfert 2).

The BPT diagram in the right panel of Figure 4.5 shows the largely AGN-dominated nature of the sample, with only one source lying in the 'composite' region. We use this plot as a strong constraint on all NuLANDS sources that there is an AGN present in each source. Using this prior assumption will be vital for characterising extremely faint X-ray observations of particular NuLANDS sources.

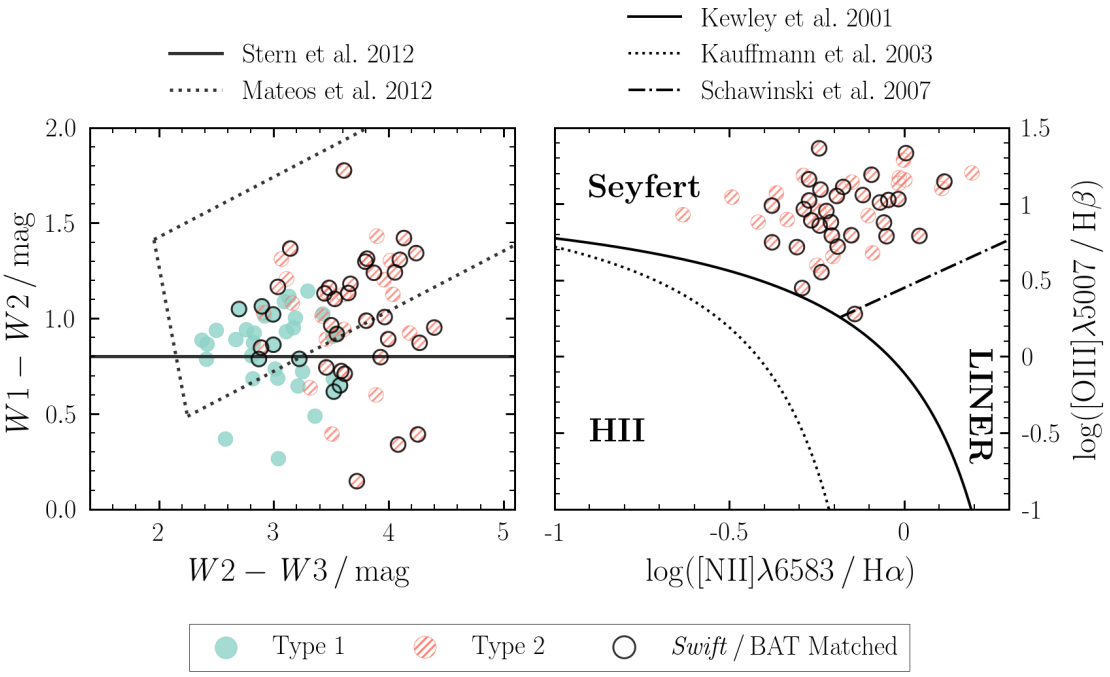

FIGURE 4.5: Observed optical and mid-infrared AGN classification diagnostics. (*Left*) The *WISE* mid-infrared colours of every NuLANDS source. A total of 72/83 are AGN-dominated by the 90% reliability selection cut of Assef *et al.* (2018), and 54/83 satisfy the established and widely-used Stern *et al.* (2012) and Mateos *et al.* (2012) colour criteria, although we note that the sources not classifying these cuts may have a competing contribution from host galaxy starlight. Of the *NuSTAR* targets, just 4/30 do not meet the Assef *et al.* (2018) 90% reliability cut, *all of which* are bon-fide AGN from Véron-Cetty and Véron (2010). (*Right*) BPT diagnostic for all Type 2 AGN in NuLANDS. Type 1 AGN were originally classified by dG92 based on broader permitted than forbidden line widths, instead of line ratio diagnostics. Thus these sources are excluded from the plot.

4.2.5 Sample Biases and Representativeness

Figure 4.7 compares the effectiveness of NuLANDS for sampling the parameter space of isotropic luminosity indicators, through their corresponding flux ratios. The upper two panels feature the 60 μm flux as the denominator. Left panels then show the two distributions of optical ([O III] λ5007) to far-infrared flux ratios, segregated by AGN optical type. As was found for the full 220 AGN by K94, Type 1s are indistinguishable from Type 2s here, with a KS statistic p-value of 0.631, when comparing NLR to 60 μm infrared continuum fluxes. The right-hand panel then shows the corresponding ratios for the hard X-ray 14 – 195 keV to far-infrared fluxes. The hard X-ray fluxes are from the most recent *Swift*/BAT all-sky catalogue compiled from 105 months of contigual exposure of the sky (Oh *et al.* 2018). Non-detections correspond to the 90% sky sensitivity upper limit of the survey ($F_{14-195\,\mathrm{keV}} < 8.40 \times 10^{-12}\,\mathrm{erg\,s^{-1}\ cm^{-2}}$). The observed Type 1/2

distributions are considerably different, with Type 2 AGN skewed towards considerably lower *Swift*/BAT fluxes, and a KS p-value between each of 8.58×10^{-5} for comparison with the 60 μm infrared flux. Incorporating limits properly using the Kaplan-Meier test for left-censored data (Kaplan and Meier 1958) enhances the discrepancy further (lower section of the right-hand panels). We also carried out the same flux ratio distribution tests by segregation on X-ray-derived $\log N_{\rm H}$ / cm^{-2} values above or below 22 (instead of the optical type segregation) to designate X-ray obscured and unobscured AGN, respectively. The results were entirely consistent for the optical to infrared and hard X-ray to infrared flux ratio distributions.

These tests imply that the NuLANDS sample is matched between the AGN classes in terms of optical [O III] λ5007 narrow line with the infrared 60 μm bolometric luminosity indicators, but *not* in terms of observed *Swift*/BAT flux. Under the orientation-based unification scheme of AGN tori, such a hard X-ray deficit is expected if the *Swift*/BAT fluxes are diminished as a result of heavy line-of-sight obscuration in heavily obscured and Compton-thick nuclear tori which does not effect NLR optical classification. NuLANDS is able to detect these candidate heavily obscured AGN missed by hard X-ray flux limited selection. X-ray properties of the sources already observed and future prospects for the sample are discussed in later sections. There are several important issues to consider if one is to place these results in proper context, which are discussed below.

1. **Incompleteness:** NuLANDS is not designed to provide a *complete* flux or volume limited sampling of AGN. Firstly, the optical spectroscopic follow-up is itself incomplete, with $\sim$13% of sources optically unobserved by dG92. The choice of which source to observe or ignore was random, so we do not expect any preferential bias in this regard. Instead, our aim has been to collate a sample that is as representative of AGN circumnuclear obscuration as possible, in the sense of minimising the impact of selection and classification effects that preferentially favour or disfavour sources at any given X-ray $N_{\rm H}$.

2. **Missing Infrared-faint AGN:** There is a class of 'hot-dust-poor' AGN with observed mid-infrared emission lower than expected from their near-infrared fluxes, implying low torus covering factors (Hao *et al.* 2010). Such sources could be missed from our initial infrared flux-limited selection, where 0.5 Jy corresponds to a luminosity $L_{60\,\mu{\rm m}} \approx 10^{44}\,{\rm erg\,s^{-1}}$ at the high redshift end. However, Hao *et al.* find that this class comprises just $\sim$6% of the AGN population at $z < 2$. In the local universe, the prevalence of these AGN remains unclear, with only one AGN – NGC 4945 – known to show significant infrared deficit relative to the canonical infrared–X-ray luminosity relation (Asmus *et al.* 2015). Another potential source, though with a milder deficit, is NGC 4785 (Gandhi *et al.* 2015b). Interestingly,

both sources are Compton-thick AGN. These small numbers suggest a minimal bias, even if present.

3. **Host Galaxy Biases:** There are three potential host galaxy biases of most relevance here:

   3(i) **Source Selection from 60 μm Emission:** The dG92 sample is selected at 60 μm. Although the subsequent warm colour cut favours AGN and optical spectroscopy is then used to isolate sources that host AGN, this does not necessarily imply that the 60 μm emission must be AGN-*dominated*. We are treating the 60 μm emission as a 'bolometric' indicator, but this emission is implicitly a bolometric source of flux (AGN + host galaxy). Using this flux is valid for our purposes because we do not expect the flux-limited infrared selection to favour or disfavour sources at any particular $N_{\rm H}$. Nevertheless, it is possible to carry out stronger tests by choosing shorter wavelengths as the primary bolometric luminosity indicators, since torus emission typically peaks below $\sim$60 μm (e.g., Polletta *et al.* 2007; Assef *et al.* 2010; Mullaney *et al.* 2011). To test the effect of using shorter wavelengths, we ran the same tests with the 25 μm flux as the normalising flux for both [O III] and *Swift*/BAT, which yielded completely consistent results to the initial 60 μm tests. These results are shown in the lower two panels of Figure 4.7.

   3(ii) **Infrared Classification:** The warm *IRAS* colour cut will favour infrared-bright AGN that can dominate above host galaxy emission, especially at 25 μm. Conversely, AGN that are infrared-weak relative to stellar emission will end up being classified as having 'cool' infrared colours and will drop out from the sample. Under the torus-based unification scheme, this bias should act uniformly both Type 1 and 2 classes and be independent of $N_{\rm H}$. However, there is evidence (albeit controversial) suggesting that obscured AGN preferentially occur in star-forming galaxies (e.g., Villarroel *et al.* 2017, though see Zou *et al.* 2019 for contradictory findings on star formation rate). If so, this bias would imply a higher intrinsic prevalence of X-ray obscured AGN in 'infrared–cool' systems, which NuLANDS would preferentially miss.

   3(iii) **Optical Classification:** In a similar fashion, optical AGN classification requires the presence of AGN permitted and/or forbidden lines that can stand out above the host galaxy continuum. Host emission flux can swamp such NLR lines, rendering them 'elusive' to detect (e.g., Moran *et al.* 2002). Both Type 1 and 2 AGN could be affected in this manner, depending upon spectroscopic signal to noise and the fraction of host galaxy vs. AGN flux captured

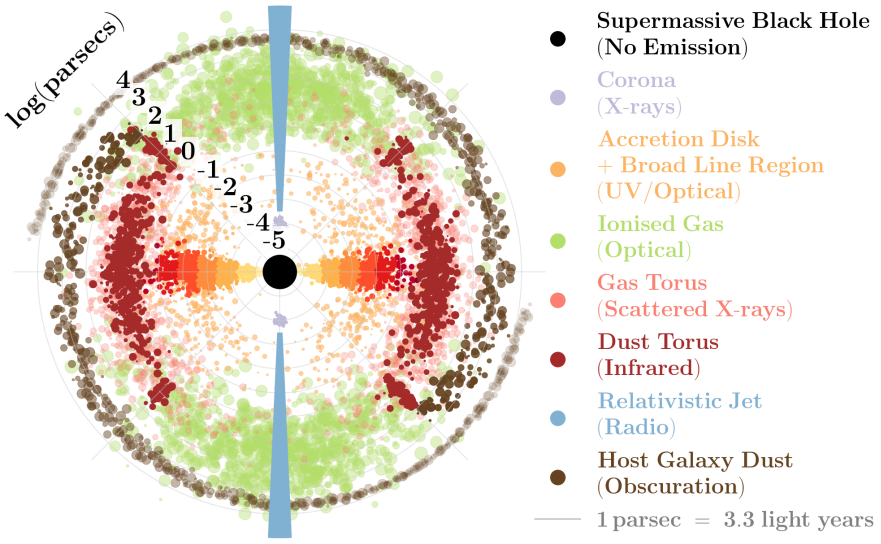

FIGURE 4.6: Graphical interpretation of the unified model depicted in Figure 1.5, but now depicting host galaxy dust that can act to obscure the Narrow Line Region, and hence bias against classifying AGN with optical spectroscopy in which the Narrow Line Region lines are required.

through the spectroscopic aperture. However, recent work suggests that dilution cannot solely explain AGN mis-classification satisfactorily (Agostino and Salim 2018).

Lastly, large-scale host galaxy dust would preferentially adversely influence the detection of narrow lines (see Figure 4.6 for a visual depiction of this), with sources ultimately being classified as inactive, weakly active (e.g., LINER) or as H II galaxies. If host dust reddening is strong enough to render Hβ undetectable, the Balmer decrement, and hence the intrinsic line fluxes, would be underestimated, and we have excluded such sources from NuLANDS. Including them is likely to skew the [O III]–to–60 μm flux ratio of Type 2s to lower values than Type 1s, and the classes would no longer be well matched.

The classification biases discussed above all act towards preferentially missing Type 2 (and possibly also Compton-thick) AGN, suggesting an even higher intrinsic obscured fraction. Such a bias would indicate that NuLANDS is tracing the nuclear (torus–based) obscuration of local AGN well, corresponding to the circumnuclear structure giving rise to the Type 1/2 dichotomy in the unified model, but is not representative in terms of host galaxy obscured sources.

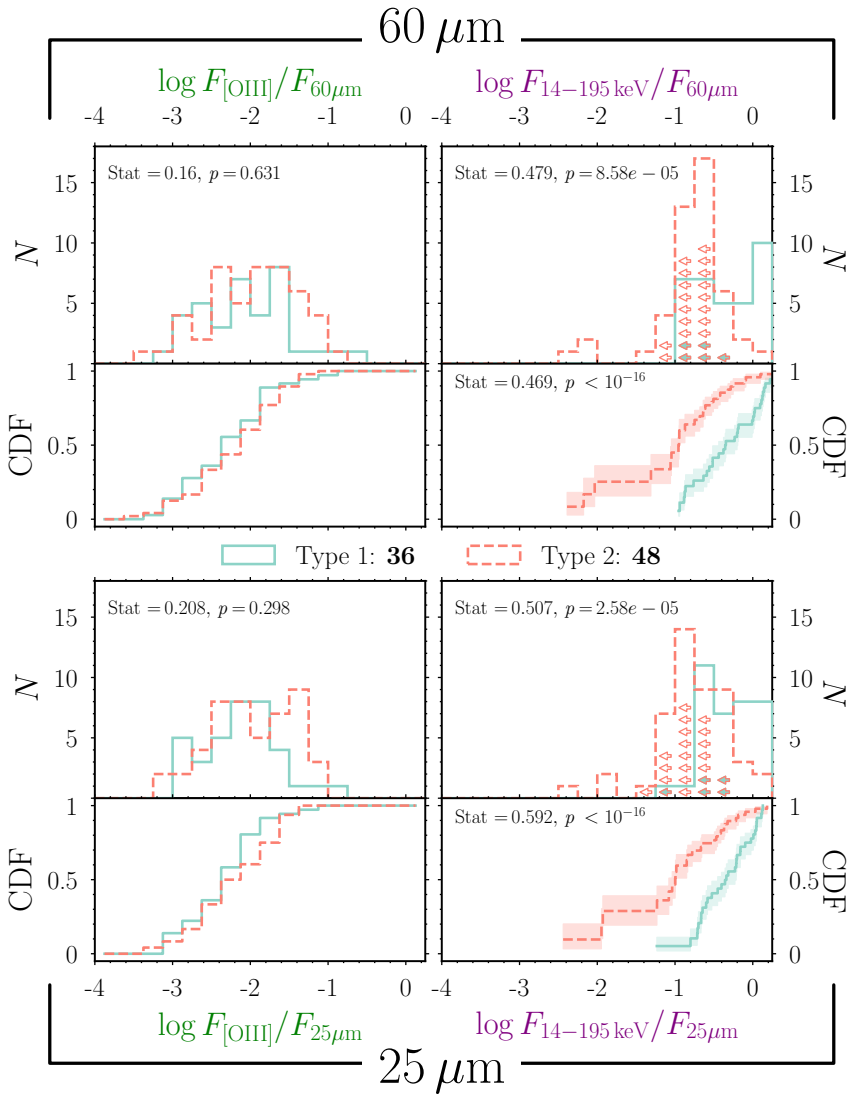

FIGURE 4.7: All four panels show the comparative flux ratio distributions for Type 1 and 2 AGN in NuLANDS (Type 1 and 2 AGN are shown with solid orange and dashed green lines in all panels, respectively). The upper section of each panel shows the distribution, whereas the lower section shows the cumulative distribution. Where relevant, the KS Statistic and p-value are shown in the top left corner.
Left, *Upper*: Distributions of optical [O III] λ5007 to far-infrared 60 μm flux ratios. The KS p-value between Type 1 and 2 is 0.631 indicating that both distributions could have been sampled from the same underlying distribution, in agreement with the unified paradigm.
Left, *Lower*: Distributions of optical [O III] λ5007 to far-infrared 25 μm flux ratios. The KS p-value between Type 1 and 2 AGN is very similar to the flux ratio for 60 μm.
Right, *Upper*: The distributions of 14 – 195 keV hard X-ray *Swift*/BAT 105-month to 60 μm flux ratios. For sources not detected in the 105-month catalogue, we assign an upper limit given by Oh *et al.* (2018) of 8.40×10^{-12} erg s^{-1} cm^{-2}. The KS p-value is $8.5{\times}10^{-5}$. The cumulative distributions derived with the Kaplan-Meier survival method, incorporating upper limits gave a vanishingly small KSp-value. Such a small p-value shows that the observed hard X-ray flux does not trace the far-infrared flux in the same way that the [O III] emission does. This mismatch could be due to a bias in hard X-ray selection - see the text for details.
Right, *Lower*: The equivalent distributions for 14 – 195 keV hard X-ray *Swift*/BAT 105-month to 25 μm flux ratios. Similar conclusions to the upper right panel are found.

4.3 *Swift*/BAT-dominated $N_{\rm H}$ Distribution

Here we present the $N_{\rm H}$ distribution for NuLANDS using only the 46/84 sources detected in the *Swift*/BAT 70-month catalog. We primarily used the comprehensive spectral analyses presented in Ricci *et al.* (2017c, Table C3), selecting $N_{\rm H}$ values of the neutral component of the absorber. However, we investigated sources with a recent archival neutral $N_{\rm H}$ value other than Ricci *et al.*, which differed by more than an order of magnitude. Only in one case, we used an alternative $N_{\rm H}$ value for NGC 262 from Baloković *et al.* (prep), who find $\log N_{\rm H}\ /\,{\rm cm}^{-2} = 22.97 \pm 0.01$ with hard X-ray data from *NuSTAR*, as opposed to Ricci *et al.* who find $\log N_{\rm H}\ /\,{\rm cm}^{-2} = 23.12^{+0.03}_{-0.02}$ with hard X-ray data from *Swift*/BAT[6].

The corresponding $N_{\rm H}$ distribution is presented in Figure 4.8 with errors from Poisson sampling statistics in Gehrels (1986). The dotted grey histogram indicates the observed $N_{\rm H}$ distribution from the 70-month *Swift*/BAT catalog, and bias-corrected distribution shown with a dashed blue histogram with corresponding uncertainty, all from Ricci *et al.* (2017c). There is an apparent abundance of NuLANDS sources with $\log N_{\rm H} = 20-21$, due to a preference of these among the *Swift*/BAT-detected sources. Whereas for the full 84-NuLANDS sample, $\sim 45\%$ will be *Swift*/BAT-undetected– a considerable increase, that is predicted to populate the $\log N_{\rm H}\ /\,{\rm cm}^{-2} \gtrsim 22$ bins in the $N_{\rm H}$ distribution. Furthermore, NuLANDS has been structured to test the circumnuclear obscurer giving rise to the Type 1/2 dichotomy of AGN, and excludes likely host-contaminated sources which would populate the $21 \lesssim \log N_{\rm H} \lesssim 23$ bins of the distribution – see Section 4.2.5 for discussion on this bias.

To compare the *Swift*/BAT-detected NuLANDS result to expectations from the full NuLANDS survey of 84 AGN, we ran Monte Carlo simulations. Of the 46 sources, the number of Type 1:Type 2 sources is 28:18, whereas the full NuLANDS sample has a ratio of $36{:}48 \equiv 1{:}1.33$. We drew random ensembles of 13 Type 1 AGN from the present sample of 28, to ensure a Type 1: 2 ratio of 1:1.33, as is expected at the end of the survey for all 84 sources. This simulation ensured we used the entire current sample of 24 Type 2 AGN in the 46 *Swift*/BAT-detected sources. We then calculated the flux ratios of the hard X-ray $14-195\,{\rm keV}$ to $60\,\mu{\rm m}$ fluxes for separated Type 1 and Type 2 subsamples. Finally, we calculated the KS statistic p-value between the Type 1 and 2 sources' hard X-ray to $60\,\mu{\rm m}$ flux ratios on each iteration. The randomisation was repeated many times in order to yield a distribution of KS statistic p-values, which we normalised by the median p-value to give Δp – plotted in Figure 4.9. The left panel shows the CDFs of

[6]Neutral $N_{\rm H}$ were preferentially selected over warm absorber $N_{\rm H}$ found for a subset of the sources, since the spectral curvature associated with warm absorption is typically minimal in contrast with neutral $N_{\rm H}$, despite depending on the ionisation state and covering of the obscurer.

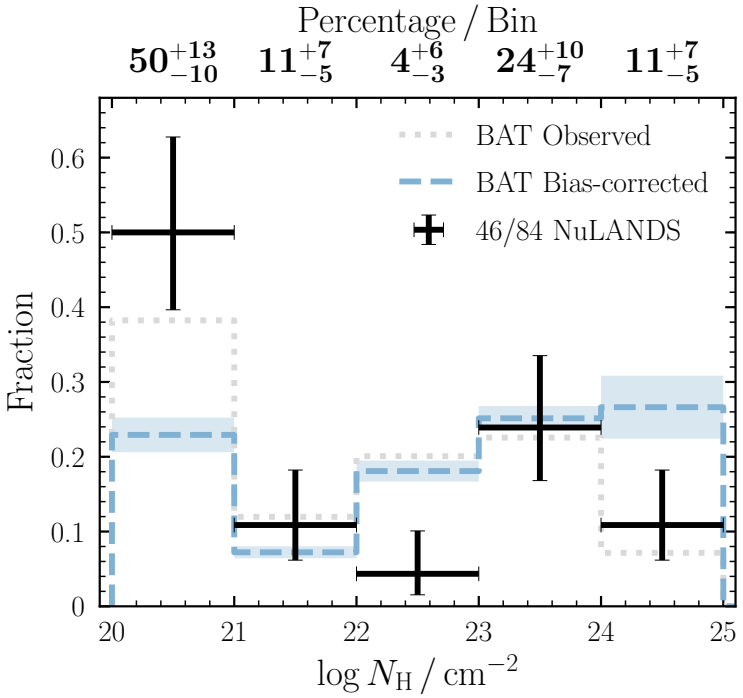

FIGURE 4.8: Current NuLANDS $N_{\rm H}$ distribution (solid error bars) for 46/84 *Swift*/BAT-detected sources in the NuLANDS survey. Dotted grey and dashed blue histograms are the observed and intrinsic $N_{\rm H}$ distributions, respectively, for the 70-month catalog from Ricci *et al.* (2017c).

the flux ratio for Type 1 and 2 AGN. The shaded region denotes the range of simulated Type 1 flux ratios, whilst the red dashed line shows the Type 2 flux ratios for the current sample, which were fixed in our simulation.

The vertical grey dashed line in Figure 4.9 denotes the Δp-value for the ratio of hard X-ray to 60 μm flux, conservatively including limits as detections – see the upper right panel of Figure 4.7, Section 4.2.5. We find the vast majority of simulated runs have a Δp-value higher than this conservative estimate, indicating that with the final Type 1:2 ratio of the NuLANDS sample, the sources will be much more representative of AGN obscured by a unified circumnuclear obscurer. This result also indicates the $N_{\rm H}$ distribution in Figure 4.8 is a conservative estimate on obscured AGN with $\log N_{\rm H}$ / cm^{-2} $\gtrsim$ 22, especially Compton-thick AGN with $\log N_{\rm H}$ / cm^{-2} $\gtrsim$ 24 in NuLANDS.

We are also able to make predictions for the column densities of the remaining 30 sources in NuLANDS[7], by comparing their expected intrinsic (i.e. unobscured) hard X-ray fluxes with the observed *Swift*/BAT limits. The intrinsic 14 – 195 keV flux of each of the 30 was predicted from the mid-infrared *WISE* $W3$ ($\sim$ 12 μm) colour with the relation from Asmus *et al.* (2015), assuming an X-ray powerlaw spectrum with $\Gamma = 1.9$. We then measured the signal-to-noise ratios in the 105-month *Swift*/BAT maps, extracted from

[7]The final 8 sources have been targeted as part of dedicated *NuSTAR* observations, but were also not detected in the 70-month *Swift*/BAT catalog.

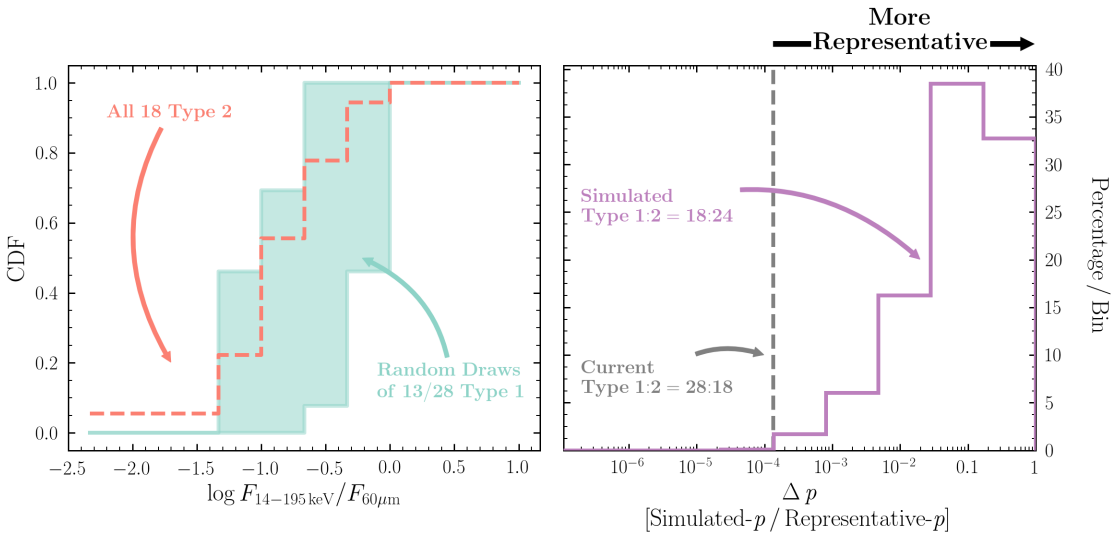

FIGURE 4.9: ***Left*** The cumulative distributions of hard X-ray 14 – 195 keV to 60 μm flux ratios for the Type 1 and 2 AGN. The range in cumulative distributions of Type 1 AGN for each ensemble is shaded in blue, whereas the single Type 2 cumulative distribution is shown with a dashed red line. ***Right*** Simulation of the prospects of the full NuLANDS sample, by drawing ensembles from the current data in order to attain a Type 1:Type 2 fraction equal to 18:24 as expected at the end of the survey. The distribution of KSp-values – normalised by the median to give Δp – between the hard X-ray-to-60 μm flux ratios of each AGN Type for each ensemble (purple histogram). The vertical grey dashed line shows the conservative KS p-value derived for the full NuLANDS sample, shown in Figure 4.7, upper right.

each source position, which we take as a proxy of the observed 14 – 195 keV *Swift*/BAT flux. Figure 4.10 shows this observed signal to noise ratio plotted against the predicted intrinsic 14 – 195 keV flux. There is a significant population of sources with predicted intrinsic flux *above* the 105-month detection threshold from Oh *et al.* (2018), yet with observed 105-month integrated *Swift*/BAT signal-to-noise *below* 3 – an arbitrary threshold of minimal significance. Interpreting this mismatch between predicted unobscured emission and observed emission to arise from obscuration further indicates a high number of obscured sources to come. A large proportion of these sources (23/30) are optically classified by dG92 as Type 2 AGN, consistent with the unification paradigm, and may indicate a Compton-thick fraction for the full NuLANDS sample exceeding the current value reported in Figure 4.8. Although a prediction, we note that observational constraints have already been used to imply that the Compton-thick fraction is larger than predicted from hard X-ray-selected samples (e.g., Comastri *et al.* 2015).

4.4 Summary

This chapter introduces the NuLANDS Extragalactic Legacy Survey. The key conclusions are:

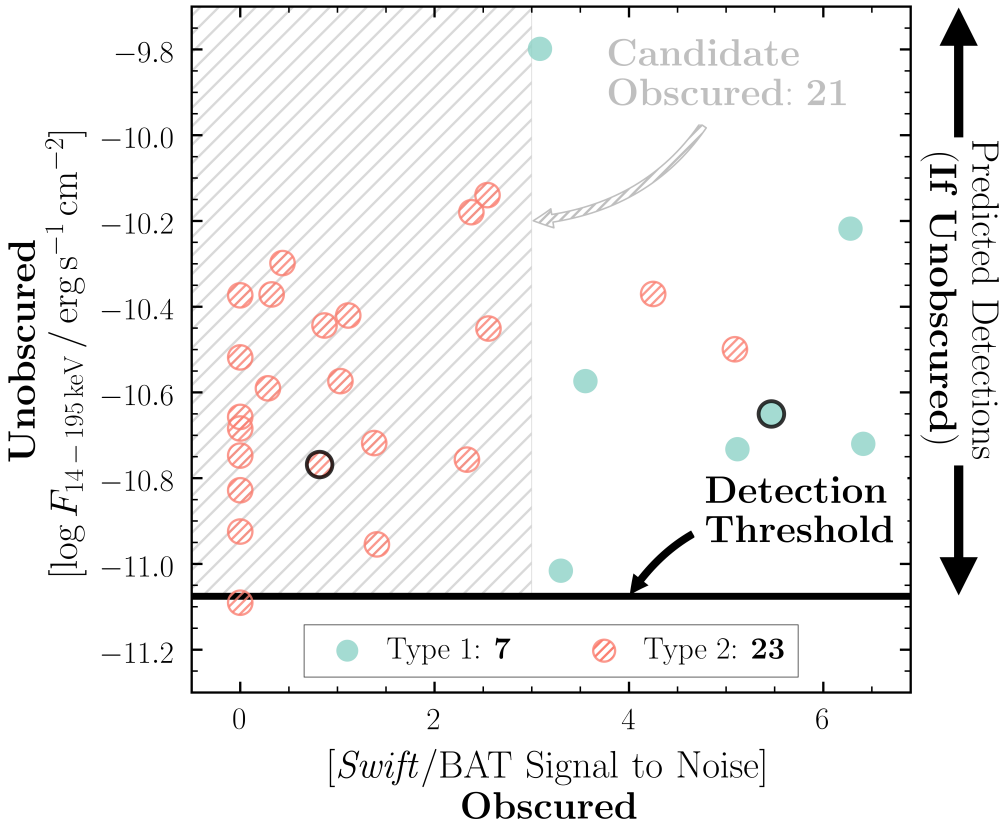

FIGURE 4.10: Predictions for the upcoming 30 NuLANDS *NuSTAR* targets, all of which were undetected in the 70-month *Swift*/BAT catalog. The corresponding observed *Swift*/BAT signal to noise ratio extracted from the source location in the *Swift*/BAT maps is plotted against the predicted unobscured, *intrinsic* X-ray flux 14–195 keV range. We identify a hashed 'candidate obscured' wedge for sources with intrinsic infrared-predicted 14–195 keV flux above the 90% 105-month *Swift*/BAT nominal flux threshold, yet with observed *Swift*/BAT signal to noise > 3 - see the text for details.

1. NuLANDS is constructed to be a *representative* selection of AGN circumnuclear obscuration that gives rise to the Type 1/2 dichotomy for AGN. Critically, NuLANDS is unbiased by X-ray obscuring columns up to and including the Compton-thick regime, typically missed in X-ray-selected samples. NuLANDS is not meant to be a complete sample in the typical flux-limited survey sense, but is predicted to encompass unobscured, obscured and Compton-thick AGN populations in a fully representative way (Section 4.2.5). The survey is all-sky selected, and in terms of luminosity is expected to sample $\langle L_{2-10\,\mathrm{keV}} \rangle \sim 10^{41-44}\,\mathrm{erg\,s^{-1}}$- local counterparts of sources that dominate the CXB emissivity at $z \sim 1$ (e.g., Figure 12 of Ueda *et al.* 2014).

2. We find the observed Compton-thick fraction for a broadly hard X-ray-selected subsample of NuLANDS to be 11%, with a considerable portion of sources (50%) having unobscured $\log N_{\mathrm{H}}\ \mathrm{cm}^{-2} = 20-21$. We infer this 'skew' in observed N_{H} to be a hard X-ray-selection bias against heavily obscured sources (Section 4.3).

3. Of the remaining 30 sources to be observed in the full NuLANDS sample, we show that a large number are predicted to have heavily suppressed observed X-ray emission relative to the mid-infrared-derived intrinsic X-ray flux (Figure 4.10). Inferring depleted X-ray flux as arising from obscuration, this result indicates the remaining obscured AGN fraction (with $\log N_{\rm H}\ /\,{\rm cm}^{-2}\ > 22$) to be higher than the currently observed value.

NuLANDS is thus predicted to mark a major step in identifying the true importance of obscured accretion in the evolution of AGN, and will the pave the way in determining bias corrections in single-wavelength sampling of the AGN population.

Chapter 5

The NuLANDS $N_{\rm H}$ Distribution

"Remember to look up at the stars and not down at your feet. Try to make sense of what you see and wonder about what makes the universe exist. Be curious. And however difficult life may seem, there is always something you can do and succeed at. It matters that you don't just give up."

– Stephen Hawking

5.1 Introduction

The primary aim for NuLANDS is to generate an $N_{\rm H}$ distribution in the local Universe, representative of the underlying population of nuclear-obscured AGN. In Chapter 4, I showed that the *Swift*/BAT sample of AGN is biased against heavily obscured AGN, likely due to the flux limit of the survey combined with the relative faintness of Compton-thick AGN given this flux limit. Furthermore, via comparison of isotropic flux indicator ratios, the NuLANDS sample appears to be unaffected by such a bias. This chapter presents the X-ray spectral analysis of all sources observed in NuLANDS by *NuSTAR*, as of May 2019, as well as the current $N_{\rm H}$ distribution found after incorporating these new AGN – a majority of which have never been targeted in X-rays previously.

The chapter is structured as follows: I start by presenting the data sources and extraction techniques used to generate as broadband and high-quality X-ray spectra as possible for each source, as well as the resulting X-ray spectra in Section 5.2. I then present the strategy for deriving reliable and robust $N_{\rm H}$ estimates for each source in NuLANDS in Section 5.3. Next, I present all spectral results acquired to-date used to constrain the hydrogen column density along the line of sight to each source in Section 5.4.2. Finally, in Section 5.5, I present three realisations of possible $N_{\rm H}$ distributions, each dependent on different input model assumptions.

5.2 Data & Source Properties

The ultimate goal for analysing each source is to have soft and hard X-ray coverage for each, in order to establish robust $N_{\rm H}$ estimates for the line of sight obscuration. Of the 27 sources analysed, 24 have hard X-ray constraints from *NuSTAR* observations, and 20 have high-quality soft X-ray spectra. Of the 3 sources not observed by *NuSTAR*, all were sufficiently bright to yield good-quality soft spectra from *XMM*-Newton, for which a preliminary $N_{\rm H}$ estimation is presented here[1]. The following sub sections present the sample analysed here, as well as describes the spectral extraction process for each X-ray observatory that we use data from. All spectra were binned to contain at least 1 count per bin, and the resulting spectra fitted using the C-stat statistic[2].

5.2.1 Source Properties

Here I present the source properties (including host properties), as well as the infrared source fluxes for each of the 84 NuLANDS AGN, segregated by optical classification type from dG87.

[1] These sources will be observed by *NuSTAR* as part of the NuLANDS survey in the near future.

[2] Due to the unmodelled background, XSPEC automatically uses the W-stat statistic instead – see Section 1.7.3 for more details.

TABLE 5.1: Source properties of all Seyfert 1 AGN in the NuLANDS sample.

dG92 ID	NED	SIMBAD	R. A.	DEC.	MORPH	INC	TYPE	z	D_L	$N_{H,G}$	HERE
(1)	(2)	(3)	(4)	(5)	(6)	(7)	(8)	(9)	(10)	(11)	(12)
27	Mrk 0359	Mrk 359	21.885	19.179	S0	45.47	S1n	0.0167	75.3	4.26	–
47	NGC 0931	NGC 931	37.060	31.312	Sbc	81.28	S1.0	0.0158	71.2	6.64	–
54	NGC 0985	NGC 985	38.658	-8.788	I	45.21	S1.5	0.0431	198.2	3.17	–
114	2MASS J04145265–0755396	2E 955	63.719	-7.928	–	–	S1.5	0.0379	173.6	5.28	–
132	3C 120	Mrk 1506	68.296	5.354	S0	65.05	S1.5	0.0327	149.3	10.60	–
139	Mrk 0618	Mrk 618	69.093	-10.376	SBb	43.53	S1.0	0.0344	157.2	4.61	–
171	ARK 120	Mrk 1095	79.048	-0.150	E	51.78	S1.0	0.0312	142.3	9.77	–
174	ESO 362 – G018	ESO 362 –18	79.899	-32.658	S0-a	70.93	S1.5	0.0126	56.7	1.75	–
203	UGC 03478	UGC 3478	98.197	63.674	SABb	76.77	S1n	0.0123	55.3	6.86	–
209	IC 0450	IC 450	103.051	74.427	S0-a	63.19	S1.5	0.0184	83.1	6.89	–
213	FAIRALL 0265	FRL 265	104.124	-65.560	Sa	51.58	–	0.0295	134.3	6.23	–
260	Mrk 1239	Mrk 1239	148.080	-1.612	E	–	S1n	0.0194	87.7	3.69	–
278	NGC 3516	NGC 3516	166.705	72.573	S0	36.93	–	0.0086	38.6	3.45	–
286	NGC 3783	NGC 3783	174.757	-37.739	SBa	26.65	S1.5	0.0107	48.1	9.91	–
292	NGC 4253	NGC 4253	184.610	29.813	SBa	47.19	S1n	0.0123	55.3	1.78	–
301	NGC 4593	NGC 4593	189.914	-5.344	Sb	34.03	S1.0	0.0078	35.0	1.89	–
309	NGC 4748	NGC 4748	193.052	-13.415	S?	51.48	S1n	0.0136	61.2	3.52	–
324	ESO 383 – G035	ESO 383 –35	203.974	-34.296	Sab	58.78	–	0.0075	33.6	3.92	–
332	UGC 08823	Mrk 279	208.264	69.308	S0	58.76	S1.0	0.0294	133.9	1.52	–
344	NGC 5548	NGC 5548	214.498	25.137	S0-a	41.42	S1.5	0.0169	76.2	1.55	–
350	UGC 09412	Mrk 817	219.092	58.794	S0-a	24.59	S1.5	0.0305	139.0	1.15	–
359	Mrk 0841	Mrk 841	226.005	10.438	E	–	S1.5	0.0362	165.7	2.22	–
369	UGC 09826	UGC 9826	230.387	39.201	SBc	51.95	S1.5	0.0292	132.9	1.58	✓

Continued on next page

TABLE 5.1: Source properties of all Seyfert 1 AGN in the NuLANDS sample.

dG92 ID	NED	SIMBAD	R. A.	DEC.	MORPH	INC	TYPE	z	D_L	$N_{\rm H,G}$	HERE
(1)	(2)	(3)	(4)	(5)	(6)	(7)	(8)	(9)	(10)	(11)	(12)
390	UGC 10120	Mrk 493	239.790	35.030	Sb	55.68	S1n	0.0316	144.1	2.11	✓
398	IC 1198	IC 1198	242.152	12.331	SBab	63.45	S1.5	0.0323	147.4	3.71	✓
442	2MASX J17232321+3630097	2MASX J17232321+3630097	260.847	36.503	E	90	S1	0.04	183.5	3.89	–
473	ESO 140 – G043	ESO 140 –43	281.225	-62.365	SBbc	72.61	S1.5	0.0136	61.2	7.01	–
484	ESO 141 – G055	ESO 141 –55	290.309	-58.670	Sb	52.4	S1.2	0.036	164.7	4.83	–
497	NGC 6860	NGC 6860	302.195	-61.100	SBb	57.99	S1.5	0.0097	43.5	3.15	–
509	Mrk 0509	Mrk 509	311.041	-10.724	–	36.44	S1.5	0.034	155.3	4.25	–
530	NGC 7213	NGC 7213	332.318	-47.167	Sa	39.09	S3b	0.005	22.4	1.06	–
531	ESO 344 – G016	ESO 344 –16	333.675	-38.806	Sb	43.66	S1.5	0.0394	180.7	1.23	✓
537	Mrk 0915	Mrk 915	339.194	-12.545	Scd	67	S1.8	0.0242	109.8	5.34	–
538	UGC 12138	UGC 12138	340.071	8.054	SBa	19.9	S1.8	0.0246	111.6	6.39	–
540	UGC 12163	UGC 12163	340.664	29.725	Sb	47.04	S3	0.024	108.9	5.34	–
547	Mrk 0315	Mrk 315	346.011	22.624	E	61.86	S1.5	0.0385	176.5	6.01	–

TABLE 5.2: Source properties of all Seyfert 2 AGN in the NuLANDS sample.

dG92 ID	NED	SIMBAD	R. A.	DEC.	MORPH	INC	TYPE	z	D_L	$N_{H,G}$	HERE
(1)	(2)	(3)	(4)	(5)	(6)	(7)	(8)	(9)	(10)	(11)	(12)
9	FGC 0061	2MFGC 403	8.681	-0.041	Sb	83.9	S2	0.042	193.0	2.34	–
16	NGC 0262	NGC 262	12.196	31.957	S0-a	68	S1h	0.0149	67.1	5.79	–
26	NGC 0449	NGC 449	19.030	33.089	SBa	60.8	S2	0.0154	69.4	5.32	✓
30	KUG 0135 –131	2MASX J01380539 –1252105	24.522	-12.870	S0-a	54.3	S2	0.0404	185.4	1.55	✓
33	Mrk 0573	Mrk 573	25.991	2.350	S0-a	26.74	S1h	0.0172	77.6	2.52	✓
37	2MASX J01500266 –0725482	ICRF J015002.6 –072548	27.511	-7.430	–	42.58	S1h	0.0177	79.9	2.03	–
52	IC 1816	IC 1816	37.962	-36.672	SBab	15.23	S2	0.0168	75.8	2.58	–
57	NGC 1068	M 77	40.670	-0.013	Sb	34.7	S1h	0.0026	11.6	2.92	–
64	2MASX J02560264 –1629159	2MASS J02560264 –1629155	44.011	-16.488	–	33.49	S1.9	0.0315	143.7	3.52	✓
67	MCG –02 –08 –039	MCG –02 –08 –039	45.128	-11.416	Sa	55.85	–	0.0296	134.8	5.12	✓
72	NGC 1229	NGC 1229	47.045	-22.960	SBbc	56.44	S2	0.0355	162.4	1.72	–
78	KUG 0312+013	2MASX J03150536+0130304	48.772	1.508	–	57.24	S2	0.0233	105.6	6.69	–
84	2MASX J03241196 –5750116	6dFGS gJ032412.0 –575012	51.050	-57.837	–	80.83	S2	0.0437	201.1	2.68	✓
83	NGC 1320	NGC 1320	51.203	-3.042	Sa	80.53	S2	0.0087	39.0	3.77	–
96	2MASX J03381036+0114178	2MASX J03381036+0114178	54.543	1.238	–	63.94	–	0.0396	181.7	7.18	✓
98	IRAS 03362 –1641	LEDA 13422	54.640	-16.538	Sab	82.58	–	0.0369	168.9	7.06	✓
179	ESO 253 – G003	ESO 253 –3	81.325	-46.006	Sa	65	S2	0.0439	202.0	3.54	–
196	UGC 03426	Mrk 3	93.901	71.037	S0	35.67	S1h	0.013	58.5	9.67	–
201	VII Zw 073	2MASX J06302561+6340411	97.606	63.678	–	–	S2	0.0402	184.5	6.89	–
244	ESO 018 – G009	ESO 18 –9	126.033	-77.783	Sc	34.27	–	0.0175	79.0	7.36	✓
245	CGCG 004 –040	2MASX J08301445 –0252494	127.560	-2.881	Sab	48.3	S2	0.0404	185.4	3.12	–
253	MCG –01 –24 –012	MCG –01 –24 –012	140.193	-8.056	SABc	66.6	S2	0.0198	89.5	3.02	–
263	KUG 1021+675	2MASX J10251299+6717493	156.304	67.297	Sc	0	S2	0.0386	176.9	1.88	✓

Continued on next page

TABLE 5.2: Source properties of all Seyfert 2 AGN in the NuLANDS sample.

dG92 ID	NED	SIMBAD	R. A.	DEC.	MORPH	INC	TYPE	z	D_L	$N_{H,G}$	HERE
(1)	(2)	(3)	(4)	(5)	(6)	(7)	(8)	(9)	(10)	(11)	(12)
270	CGCG 333–049	MCG+12–10–067	161.036	70.405	Sb	66.92	S2	0.0328	149.7	2.46	–
272	NGC 3393	NGC 3393	162.098	-25.162	SBa	30.94	S2	0.0137	61.7	6.18	–
282	ESO 439 – G009	ESO 439–9	171.848	-29.258	SBab	80.49	S2	0.0234	106.1	5.44	–
293	NGC 4388	NGC 4388	186.445	12.662	SBb	90	S1h	0.0084	37.7	2.58	–
299	NGC 4507	NGC 4507	188.903	-39.909	Sab	32.45	S1h	0.0132	59.4	7.04	–
302	IC 3639	IC 3639	190.220	-36.756	SBbc	21.76	S1h	0.0125	56.2	5.86	–
313	NGC 4968	NGC 4968	196.775	-23.677	S0	90	–	0.0093	41.7	8.36	✓
317	MCG –03–34–064	MCG –03–34–064	200.602	-16.728	S0	57.15	S1h	0.0164	74.0	4.99	–
322	ESO 383 – G018	ESO 383–18	203.359	-34.015	Sb	90	S1.8	0.0128	57.6	4.04	–
347	SBS 1426+573	2MASX J14281793+5710187	217.075	57.172	Sc	36.98	S2	0.0428	196.8	1.23	✓
352	Mrk 0477	Mrk 477	220.159	53.504	S0	51.34	S2	0.0378	173.2	1.05	–
354	CGCG 164–019	2MASX J14453684+2702060	221.404	27.035	S0-a	–	S1.9	0.0294	133.9	2.50	–
367	CGCG 077–080	2MASX J15205324+0823491	230.222	8.397	S0-a	65.45	S2	0.0306	139.5	2.46	✓
377	UGC 09944	UGC 9944	233.949	73.451	Sbc	79.6	S2	0.0248	112.5	2.86	✓
379	CGCG 166–047	2MASX J15435731+2831269	235.989	28.524	SBbc	–	S2	0.032	146.0	2.32	✓
383	2MASX J15504152–0353175	IRAS 15480–0344	237.673	-3.888	E	53.22	S1h	0.0303	138.1	9.10	–
409	WISE J163032.66+392303.2	2MASX J16303265+3923031	247.636	39.384	S0-a	79.95	S2	0.0297	135.3	0.94	–
447	CGCG 112–010	MCG+03–45–003	263.891	20.796	Sbc	34.79	S	0.024	108.9	7.26	–
471	FAIRALL 0049	FRL 49	279.243	-59.402	E-S0	–	S1h	0.0192	86.8	6.48	–
501	IC 4995	IC 4995	304.996	-52.622	S0	56.59	S2	0.0163	73.5	4.08	–
512	IC 5063	IC 5063	313.010	-57.069	S0-a	51.01	S1h	0.0113	50.8	6.10	–
524	2MASX J21391374–2646315	2MASX J21391374–2646315	324.807	-26.775	Sc	24.41	S1.9	0.0308	140.4	2.35	✓
549	UGC 12348	UGC 12348	346.328	0.190	SBa	90	S2	0.0253	114.9	3.92	–

Continued on next page

TABLE 5.2: Source properties of all Seyfert 2 AGN in the NuLANDS sample.

dG92 ID	NED	SIMBAD	R. A.	DEC.	MORPH	INC	TYPE	z	D_L	$N_{\rm H,G}$	HERE
(1)	(2)	(3)	(4)	(5)	(6)	(7)	(8)	(9)	(10)	(11)	(12)
555	NGC 7674	NGC 7674	351.986	8.779	SBbc	26.68	S1h	0.0286	130.2	4.27	–
559	CGCG 498–038	2MASX J23554421+3012439	358.934	30.212	S0	41.42	S2	0.0307	139.9	4.59	✓

Notes. Columns are as follows: (1) specific ID from dG92; (2) identifier from NED; (3) identifier from SIMBAD; (4) & (5) Right Ascension and Declination in degrees; (6) & (7) host galaxy morphology and line of sight inclination from Hyperleda; (8) AGN type from Véron-Cetty and Véron (2010); (9) & (10) spectroscopic redshift from dG92 and luminosity distance using the assumed cosmology; (11) Galactic $N_{\rm H}$ from Kalberla *et al.* (2005) that was included in all spectral fits; (12) checklist as to whether or not the source is analysed in this chapter.

TABLE 5.3: Source fluxes of all Seyfert 1 AGN in the NuLANDS sample.

dG92	$S12$	$S25$	$S60$	$S100$	$\alpha_{25,60}^{\nu 2.1}$	$W1$	$W2$	$W3$	$W4$
(1)	(2)	(3)	(4)	(5)	(6)	(7)	(8)	(9)	(10)
27	< 0.25	0.48 ± 0.07	1.26 ± 0.14	1.83 ± 0.27	-1.11 ± 0.2	26.3 ± 0.539	28.4 ± 0.501	104.0 ± 1.45	243.0 ± 32.7
47	0.66 ± 0.05	1.31 ± 0.11	2.76 ± 0.25	4.92 ± 0.49	-0.85 ± 0.14	83.4 ± 1.71	129.0 ± 2.41	425.0 ± 5.92	870.0 ± 114.0
54	< 0.27	0.55 ± 0.06	1.44 ± 0.13	2.0 ± 0.16	-1.11 ± 0.16	38.7 ± 0.829	51.6 ± 0.959	176.0 ± 2.45	441.0 ± 58.5
114	< 0.26	0.54 ± 0.05	0.66 ± 0.06	< 1.0	-0.24 ± 0.15	44.0 ± 0.902	66.8 ± 1.24	212.0 ± 2.75	432.0 ± 58.3
132	0.33 ± 0.05	0.71 ± 0.06	1.32 ± 0.09	2.64 ± 0.19	-0.71 ± 0.13	59.9 ± 1.28	84.5 ± 1.57	230.0 ± 2.98	529.0 ± 69.7
139	0.33 ± 0.02	0.79 ± 0.06	2.75 ± 0.19	4.08 ± 0.29	-1.42 ± 0.11	47.2 ± 1.01	75.2 ± 1.47	288.0 ± 4.01	620.0 ± 82.3
171	< 0.4	0.47 ± 0.05	0.66 ± 0.07	1.3 ± 0.14	-0.37 ± 0.16	110.0 ± 2.35	138.0 ± 2.43	225.0 ± 2.93	338.0 ± 6.6
174	< 0.25	0.59 ± 0.05	1.48 ± 0.12	2.02 ± 0.14	-1.06 ± 0.13	34.9 ± 0.747	36.4 ± 0.677	171.0 ± 2.22	428.0 ± 57.3
203	< 0.25	0.35 ± 0.05	1.46 ± 0.12	3.21 ± 0.29	-1.63 ± 0.17	37.9 ± 0.811	39.5 ± 0.734	97.4 ± 1.36	236.0 ± 30.8
209	< 0.31	0.68 ± 0.06	1.12 ± 0.1	0.82 ± 0.11	-0.57 ± 0.15	134.0 ± 2.87	154.0 ± 2.85	262.0 ± 3.64	562.0 ± 76.9
213	< 0.25	0.19 ± 0.02	0.78 ± 0.05	1.13 ± 0.11	-1.6 ± 0.17	24.7 ± 0.505	28.3 ± 0.499	73.4 ± 1.02	157.0 ± 20.7
260	0.7 ± 0.06	1.2 ± 0.11	1.41 ± 0.13	1.06 ± 0.24	-0.18 ± 0.15	183.0 ± 3.91	266.0 ± 4.95	589.0 ± 7.65	995.0 ± 13.8
278	0.45 ± 0.04	0.92 ± 0.06	1.74 ± 0.12	2.17 ± 0.13	-0.73 ± 0.11	1.53 ± 0.0372	1.09 ± 0.0325	3.3 ± 0.181	35.8 ± 6.04
286	0.77 ± 0.06	2.44 ± 0.17	3.37 ± 0.37	5.12 ± 0.56	-0.37 ± 0.15	138.0 ± 2.82	193.0 ± 3.4	668.0 ± 9.29	1810.0 ± 228.0
292	0.41 ± 0.05	1.38 ± 0.15	4.06 ± 0.49	4.25 ± 0.47	-1.24 ± 0.19	52.8 ± 1.13	67.6 ± 1.26	316.0 ± 4.1	1060.0 ± 139.0
301	0.34 ± 0.07	0.92 ± 0.22	2.81 ± 0.34	6.0 ± 0.72	-1.27 ± 0.31	83.5 ± 1.79	91.3 ± 1.7	270.0 ± 3.5	576.0 ± 75.9
309	< 0.25	0.5 ± 0.09	1.19 ± 0.13	2.32 ± 0.23	-0.98 ± 0.23	24.1 ± 0.493	21.0 ± 0.37	85.0 ± 1.1	255.0 ± 34.7
324	0.4 ± 0.03	0.81 ± 0.07	1.12 ± 0.09	< 1.0	-0.38 ± 0.14	103.0 ± 2.21	134.0 ± 2.62	334.0 ± 4.96	670.0 ± 87.6
332	< 0.25	0.26 ± 0.03	1.08 ± 0.17	2.28 ± 0.18	-1.64 ± 0.22	22.8 ± 0.488	29.7 ± 0.551	142.0 ± 1.98	338.0 ± 43.8
344	0.36 ± 0.04	0.76 ± 0.08	1.04 ± 0.09	1.73 ± 0.19	-0.36 ± 0.15	66.4 ± 1.42	77.4 ± 1.44	189.0 ± 2.45	467.0 ± 60.1
350	0.36 ± 0.02	1.22 ± 0.07	2.24 ± 0.16	2.28 ± 0.14	-0.7 ± 0.11	64.9 ± 1.33	84.8 ± 1.58	274.0 ± 3.81	843.0 ± 109.0
359	< 0.39	0.45 ± 0.05	0.49 ± 0.05	< 1.0	-0.1 ± 0.18	26.1 ± 0.558	37.2 ± 0.656	161.0 ± 2.08	399.0 ± 52.6
369	< 0.25	0.16 ± 0.02	0.5 ± 0.04	0.87 ± 0.12	-1.26 ± 0.2	7.56 ± 0.162	7.62 ± 0.142	37.9 ± 0.563	101.0 ± 13.6

Continued on next page

TABLE 5.3: Source fluxes of all Seyfert 1 AGN in the NuLANDS sample.

dG92	$S12$	$S25$	$S60$	$S100$	$\alpha_{25,60}^{v2.1}$	$W1$	$W2$	$W3$	$W4$
(1)	(2)	(3)	(4)	(5)	(6)	(7)	(8)	(9)	(10)
390	< 0.25	0.27 ± 0.05	0.64 ± 0.04	1.34 ± 0.23	-0.97 ± 0.21	19.9 ± 0.425	24.4 ± 0.453	71.0 ± 0.988	146.0 ± 19.7
398	< 0.25	0.36 ± 0.05	0.82 ± 0.11	1.02 ± 0.11	-0.94 ± 0.22	20.7 ± 0.444	23.8 ± 0.419	85.3 ± 1.35	220.0 ± 29.6
442	< 0.27	0.09 ± 0.01	0.34 ± 0.04	< 1.14	-1.52 ± 0.2	25.9 ± 0.555	34.3 ± 0.638	80.2 ± 1.12	139.0 ± 19.4
473	0.38 ± 0.03	0.86 ± 0.24	2.0 ± 0.16	2.62 ± 0.52	-0.96 ± 0.33	114.0 ± 2.44	141.0 ± 2.63	350.0 ± 4.54	791.0 ± 101.0
484	0.25 ± 0.02	0.35 ± 0.03	0.62 ± 0.04	< 4.76	-0.64 ± 0.13	77.9 ± 1.59	96.2 ± 1.7	164.0 ± 2.44	303.0 ± 6.21
497	0.24 ± 0.02	0.35 ± 0.04	1.05 ± 0.08	2.58 ± 0.18	-1.24 ± 0.16	103.0 ± 2.21	136.0 ± 2.53	250.0 ± 3.71	410.0 ± 8.0
509	0.34 ± 0.03	0.74 ± 0.06	1.42 ± 0.11	1.43 ± 0.2	-0.74 ± 0.13	98.4 ± 2.11	124.0 ± 2.31	268.0 ± 3.22	575.0 ± 76.9
530	0.63 ± 0.08	0.74 ± 0.07	2.56 ± 0.26	8.63 ± 0.95	-1.42 ± 0.15	155.0 ± 3.17	121.0 ± 2.13	239.0 ± 3.55	455.0 ± 59.5
531	< 0.4	0.45 ± 0.14	0.77 ± 0.14	< 1.08	-0.6 ± 0.41	56.3 ± 1.15	83.2 ± 1.55	221.0 ± 2.87	394.0 ± 51.0
537	< 0.52	0.32 ± 0.05	0.45 ± 0.08	< 1.08	-0.39 ± 0.28	20.9 ± 0.448	21.0 ± 0.391	74.4 ± 1.17	210.0 ± 28.5
538	< 0.41	0.41 ± 0.05	0.86 ± 0.08	1.43 ± 0.11	-0.83 ± 0.17	27.3 ± 0.585	28.6 ± 0.505	86.1 ± 1.2	230.0 ± 30.1
540	< 0.25	0.57 ± 0.06	1.0 ± 0.11	1.04 ± 0.11	-0.65 ± 0.17	37.2 ± 0.762	52.9 ± 0.984	154.0 ± 1.85	391.0 ± 50.7
547	< 0.39	0.37 ± 0.06	1.5 ± 0.17	< 2.83	-1.59 ± 0.22	21.6 ± 0.442	21.2 ± 0.373	100.0 ± 1.39	199.0 ± 27.0

TABLE 5.4: Source fluxes of all Seyfert 2 AGN in the NuLANDS sample.

dG92	$S12$	$S25$	$S60$	$S100$	$\alpha_{25,60}^{v2.1}$	$W1$	$W2$	$W3$	$W4$
(1)	(2)	(3)	(4)	(5)	(6)	(7)	(8)	(9)	(10)
9	< 0.64	0.31 ± 0.05	1.01 ± 0.1	1.43 ± 0.66	-1.33 ± 0.23	5.32 ± 0.114	15.1 ± 0.282	77.8 ± 1.01	215.0 ± 29.4
16	0.31 ± 0.1	0.77 ± 0.08	1.44 ± 0.14	1.83 ± 0.16	-0.71 ± 0.16	54.0 ± 1.21	91.1 ± 1.69	295.0 ± 4.1	638.0 ± 83.4
26	< 1.79	0.8 ± 0.13	2.3 ± 0.3	2.85 ± 0.34	-1.21 ± 0.24	11.1 ± 0.228	20.6 ± 0.364	165.0 ± 2.15	700.0 ± 90.0
30	< 0.46	0.47 ± 0.05	0.97 ± 0.1	1.23 ± 0.12	-0.83 ± 0.17	10.1 ± 0.264	18.5 ± 0.414	113.0 ± 2.2	305.0 ± 44.7
33	< 0.29	0.8 ± 0.09	1.27 ± 0.15	1.26 ± 0.16	-0.53 ± 0.19	30.3 ± 0.648	47.7 ± 0.887	253.0 ± 3.53	633.0 ± 82.1
37	0.28 ± 0.03	0.83 ± 0.1	1.1 ± 0.12	< 1.05	-0.33 ± 0.19	9.43 ± 0.202	18.0 ± 0.335	165.0 ± 2.14	527.0 ± 66.2
52	< 0.25	0.42 ± 0.03	1.42 ± 0.1	2.4 ± 0.14	-1.38 ± 0.11	17.9 ± 0.382	17.2 ± 0.32	114.0 ± 1.59	331.0 ± 44.3
57	38.3 ± 1.92	86.83 ± 3.47	185.8 ± 14.86	240.5 ± 19.24	-0.87 ± 0.1	6670.0 ± 1330.0	10400.0 ± 3370.0	53400.0 ± 23200.0	90400.0 ± 83.3
64	< 0.25	0.29 ± 0.04	0.72 ± 0.06	1.44 ± 0.79	-1.05 ± 0.17	11.7 ± 0.251	15.8 ± 0.294	73.4 ± 1.09	217.0 ± 29.3
67	< 0.29	0.49 ± 0.05	0.56 ± 0.04	0.77 ± 0.1	-0.15 ± 0.15	9.47 ± 0.194	12.6 ± 0.235	134.0 ± 1.74	329.0 ± 43.7
72	0.22 ± 0.02	0.8 ± 0.07	1.55 ± 0.12	1.95 ± 0.25	-0.75 ± 0.14	9.37 ± 0.201	14.7 ± 0.286	111.0 ± 1.55	487.0 ± 63.6
78	< 0.25	0.28 ± 0.04	0.85 ± 0.07	1.99 ± 0.18	-1.26 ± 0.18	8.99 ± 0.193	5.71 ± 0.112	32.5 ± 0.574	122.0 ± 17.6
84	< 0.25	0.29 ± 0.03	0.76 ± 0.05	< 1.25	-1.09 ± 0.16	6.51 ± 0.133	12.7 ± 0.236	42.4 ± 0.63	107.0 ± 14.5
83	0.33 ± 0.03	1.08 ± 0.09	2.36 ± 0.24	2.88 ± 0.26	-0.9 ± 0.15	48.8 ± 0.954	63.1 ± 1.17	306.0 ± 3.69	826.0 ± 107.0
96	< 0.25	0.46 ± 0.04	0.67 ± 0.06	< 1.0	-0.42 ± 0.15	3.97 ± 0.13	8.16 ± 0.175	67.8 ± 1.01	306.0 ± 42.0
98	< 0.39	0.54 ± 0.05	1.05 ± 0.09	< 3.55	-0.75 ± 0.15	28.8 ± 0.617	46.8 ± 0.738	141.0 ± 1.44	408.0 ± 51.7
179	0.24 ± 0.05	1.01 ± 0.06	2.8 ± 0.2	2.97 ± 0.33	-1.17 ± 0.11	28.7 ± 0.588	47.3 ± 0.879	256.0 ± 3.56	762.0 ± 98.0
196	0.7 ± 0.04	2.84 ± 0.17	3.91 ± 0.31	3.49 ± 0.31	-0.37 ± 0.11	61.9 ± 1.32	76.4 ± 1.42	nan $\pm$ nan	nan $\pm$ nan
201	< 0.25	0.5 ± 0.04	1.76 ± 0.12	2.46 ± 0.17	-1.43 ± 0.12	7.19 ± 0.195	9.34 ± 0.209	81.1 ± 1.2	331.0 ± 44.6
244	< 0.28	0.45 ± 0.06	1.32 ± 0.13	4.65 ± 0.74	-1.22 ± 0.2	12.4 ± 0.265	21.5 ± 0.4	140.0 ± 1.82	329.0 ± 42.7
245	< 0.25	0.42 ± 0.05	1.52 ± 0.14	1.82 ± 0.15	-1.48 ± 0.17	7.15 ± 0.153	12.4 ± 0.243	96.1 ± 1.34	310.0 ± 41.8
253	< 0.25	0.48 ± 0.13	0.62 ± 0.07	1.11 ± 0.12	-0.3 ± 0.35	12.8 ± 0.274	20.2 ± 0.375	91.1 ± 1.27	299.0 ± 40.1
263	< 0.35	0.43 ± 0.03	0.77 ± 0.05	< 1.49	-0.67 ± 0.11	16.2 ± 0.346	24.8 ± 0.437	118.0 ± 1.64	314.0 ± 41.1

Continued on next page

TABLE 5.4: Source fluxes of all Seyfert 2 AGN in the NuLANDS sample.

dG92	$S12$	$S25$	$S60$	$S100$	$\alpha_{25,60}^{v2.1}$	$W1$	$W2$	$W3$	$W4$
(1)	(2)	(3)	(4)	(5)	(6)	(7)	(8)	(9)	(10)
270	< 0.25	0.26 ± 0.03	0.95 ± 0.09	2.82 ± 0.17	-1.47 ± 0.16	14.2 ± 0.304	17.9 ± 0.333	79.9 ± 1.11	177.0 ± 23.6
272	< 0.25	0.71 ± 0.08	2.38 ± 0.29	3.94 ± 0.47	-1.38 ± 0.19	31.2 ± 0.639	24.9 ± 0.463	116.0 ± 1.61	562.0 ± 73.5
282	< 0.25	0.29 ± 0.04	0.66 ± 0.07	< 1.21	-0.92 ± 0.21	13.3 ± 0.284	10.1 ± 0.187	79.7 ± 1.11	215.0 ± 29.3
293	1.0 ± 0.08	3.55 ± 0.25	10.9 ± 1.2	17.79 ± 2.49	-1.28 ± 0.15	74.7 ± 1.53	105.0 ± 1.86	454.0 ± 6.31	1860.0 ± 238.0
299	0.46 ± 0.04	1.41 ± 0.14	4.58 ± 0.55	5.6 ± 0.67	-1.35 ± 0.18	108.0 ± 2.2	162.0 ± 3.0	548.0 ± 7.11	1320.0 ± 167.0
302	0.65 ± 0.06	2.3 ± 0.21	7.2 ± 0.86	11.14 ± 1.45	-1.3 ± 0.17	38.2 ± 0.781	47.3 ± 0.834	445.0 ± 5.77	1840.0 ± 231.0
313	0.37 ± 0.05	1.25 ± 0.24	2.34 ± 0.28	3.34 ± 0.37	-0.72 ± 0.26	31.2 ± 0.638	39.3 ± 0.73	288.0 ± 3.73	818.0 ± 109.0
317	0.89 ± 0.1	2.79 ± 0.28	5.71 ± 0.74	5.81 ± 0.76	-0.82 ± 0.19	54.6 ± 1.17	113.0 ± 2.11	757.0 ± 9.82	2060.0 ± 263.0
322	< 0.25	0.39 ± 0.05	0.65 ± 0.06	< 1.0	-0.59 ± 0.17	45.5 ± 0.931	84.4 ± 1.65	262.0 ± 3.65	489.0 ± 8.18
347	< 0.25	0.17 ± 0.02	0.52 ± 0.05	0.75 ± 0.08	-1.27 ± 0.19	9.26 ± 0.198	10.2 ± 0.189	45.4 ± 0.632	122.0 ± 16.3
352	< 0.25	0.54 ± 0.04	1.34 ± 0.08	1.85 ± 0.13	-1.05 ± 0.11	9.46 ± 0.194	15.9 ± 0.296	112.0 ± 1.56	425.0 ± 55.1
354	< 0.25	0.34 ± 0.04	0.78 ± 0.06	1.24 ± 0.17	-0.96 ± 0.16	10.9 ± 0.223	14.4 ± 0.268	73.8 ± 1.03	206.0 ± 27.8
367	< 0.28	0.25 ± 0.04	0.89 ± 0.1	1.61 ± 0.11	-1.45 ± 0.22	15.5 ± 0.332	16.8 ± 0.328	84.2 ± 1.09	181.0 ± 23.8
377	< 0.29	0.61 ± 0.04	1.31 ± 0.08	2.01 ± 0.1	-0.88 ± 0.11	16.5 ± 0.339	30.8 ± 0.572	190.0 ± 2.47	455.0 ± 60.0
379	< 0.25	0.38 ± 0.03	1.24 ± 0.07	1.47 ± 0.1	-1.36 ± 0.11	5.74 ± 0.123	8.06 ± 0.157	57.3 ± 0.797	251.0 ± 33.3
383	< 0.28	0.74 ± 0.07	1.18 ± 0.09	< 4.27	-0.52 ± 0.14	18.9 ± 0.387	26.0 ± 0.46	160.0 ± 2.22	530.0 ± 71.5
409	< 0.41	0.18 ± 0.03	0.69 ± 0.05	< 1.0	-1.51 ± 0.18	8.32 ± 0.17	8.3 ± 0.154	32.5 ± 0.512	159.0 ± 21.6
447	< 0.25	0.39 ± 0.04	0.7 ± 0.08	1.57 ± 0.19	-0.66 ± 0.18	11.5 ± 0.247	18.2 ± 0.355	79.7 ± 1.03	266.0 ± 34.5
471	0.59 ± 0.04	1.37 ± 0.11	3.21 ± 0.29	4.25 ± 0.43	-0.97 ± 0.14	129.0 ± 2.64	185.0 ± 3.27	498.0 ± 6.93	1110.0 ± 143.0
501	< 0.25	0.36 ± 0.03	0.9 ± 0.06	1.28 ± 0.45	-1.04 ± 0.13	19.1 ± 0.374	20.4 ± 0.38	105.0 ± 1.47	282.0 ± 37.7
512	1.16 ± 0.08	3.84 ± 0.27	5.98 ± 0.72	4.43 ± 0.4	-0.51 ± 0.16	64.1 ± 1.31	118.0 ± 2.2	880.0 ± 13.1	2730.0 ± 334.0
524	< 0.25	0.3 ± 0.05	1.22 ± 0.11	1.74 ± 0.17	-1.6 ± 0.2	8.25 ± 0.177	9.55 ± 0.177	65.7 ± 1.04	223.0 ± 30.6
549	< 0.25	0.49 ± 0.18	1.06 ± 0.11	1.62 ± 0.16	-0.88 ± 0.44	29.8 ± 0.637	36.0 ± 0.704	95.1 ± 1.32	245.0 ± 32.8

Continued on next page

TABLE 5.4: Source fluxes of all Seyfert 2 AGN in the NuLANDS sample.

dG92	$S12$	$S25$	$S60$	$S100$	$\alpha_{25,60}^{v2.1}$	$W1$	$W2$	$W3$	$W4$
(1)	(2)	(3)	(4)	(5)	(6)	(7)	(8)	(9)	(10)
555	0.72 ± 0.1	1.92 ± 0.21	5.57 ± 0.67	8.48 ± 1.1	-1.22 ± 0.19	60.5 ± 1.18	97.8 ± 1.73	445.0 ± 5.36	1310.0 ± 175.0
559	< 0.45	0.39 ± 0.05	0.7 ± 0.08	< 1.0	-0.68 ± 0.2	9.12 ± 0.195	7.26 ± 0.135	67.4 ± 0.938	267.0 ± 36.0

Notes. Columns are as follows: (1) specific ID from dG92; (2) – (5) *IRAS* flux densities in the 12 μm, 25 μm, 60 μm and 100 μm wavebands in Jy; (6) spectral index defined between 25 μm and 60 μm with the updated photometry from the *IRAS* Point Source Catalog v2.1; (7) – (10) *WISE* flux densities for the 3.4 μm, 4.6 μm, 12 μm and 22 μm filter in Jy.

5.2.2 X-ray Data

5.2.2.1 *Swift*/XRT

The *Swift*/XRT data for IC 1198 were acquired from the online *Swift*/XRT Products tool.[3] Images in different energy regions, as well as spectra were generated using the online tool following standard procedures.[4]

5.2.2.2 *XMM*-Newton

The *XMM*-Newton data were analysed using the Scientific Analysis System (SAS v.16.0.0). Observation Data Files were processed using the SAS commands EPPROC and EMPROC to generate calibrated and concatenated events files. Intervals of background flaring activity were filtered on visual inspection of the light curves in energy regions recommended in the SAS threads[5], and corresponding images for the PN, MOS1 and MOS2 detectors were generated using the command EVSELECT.

5.2.2.3 *Chandra*

The *Chandra* data were analysed using CIAO v4.11. Observation data were downloaded and reprocessed using the CHANDRA_REPRO command to apply the latest calibrations for CIAO and the CALDB. The level 2 events images were then opened in DS9 for each source to create circular source and annular background regions. The source regions were chosen to be 5 pixels in radius, and the background annuli were created to be as large as possible whilst still lying on the chip. Source, background and response spectral files were then generated with the SPECEXTRACT command in CIAO.

5.2.2.4 *NuSTAR*

The *NuSTAR* data for both Focal Plane Modules (FPMA and FPMB) were processed using the *NuSTAR* Data Analysis Software (NUSTARDAS v1.6.0) package within HEASOFT v6.19. The task NUPIPELINE was used with the corresponding CALDB v20170503 files to generate cleaned events files. Spectra and response files for both FPMs were generated using the NUPRODUCTS task for circular source regions and off-source circular background regions as large as possible on the same detector as the source. We adopted

[3] Available from: http://www.swift.ac.uk/user_objects/index.php.
[4] See: http://www.swift.ac.uk/user_objects/docs.php.
[5] For more information, see https://www.cosmos.esa.int/web/xmm-newton/sas-thread-epic-filterbackground.

the same source coordinates as reported in the AllWISE Source Catalog[6] as the primary source location for extracting counts.

5.2.2.5 All Source X-ray Data

Table 5.5 presents the X-ray data for each source analysed here, and the extracted spectra for each of the 27 sources is presented in Figure 5.1.

[6] http://irsa.ipac.caltech.edu/Missions/wise.html.

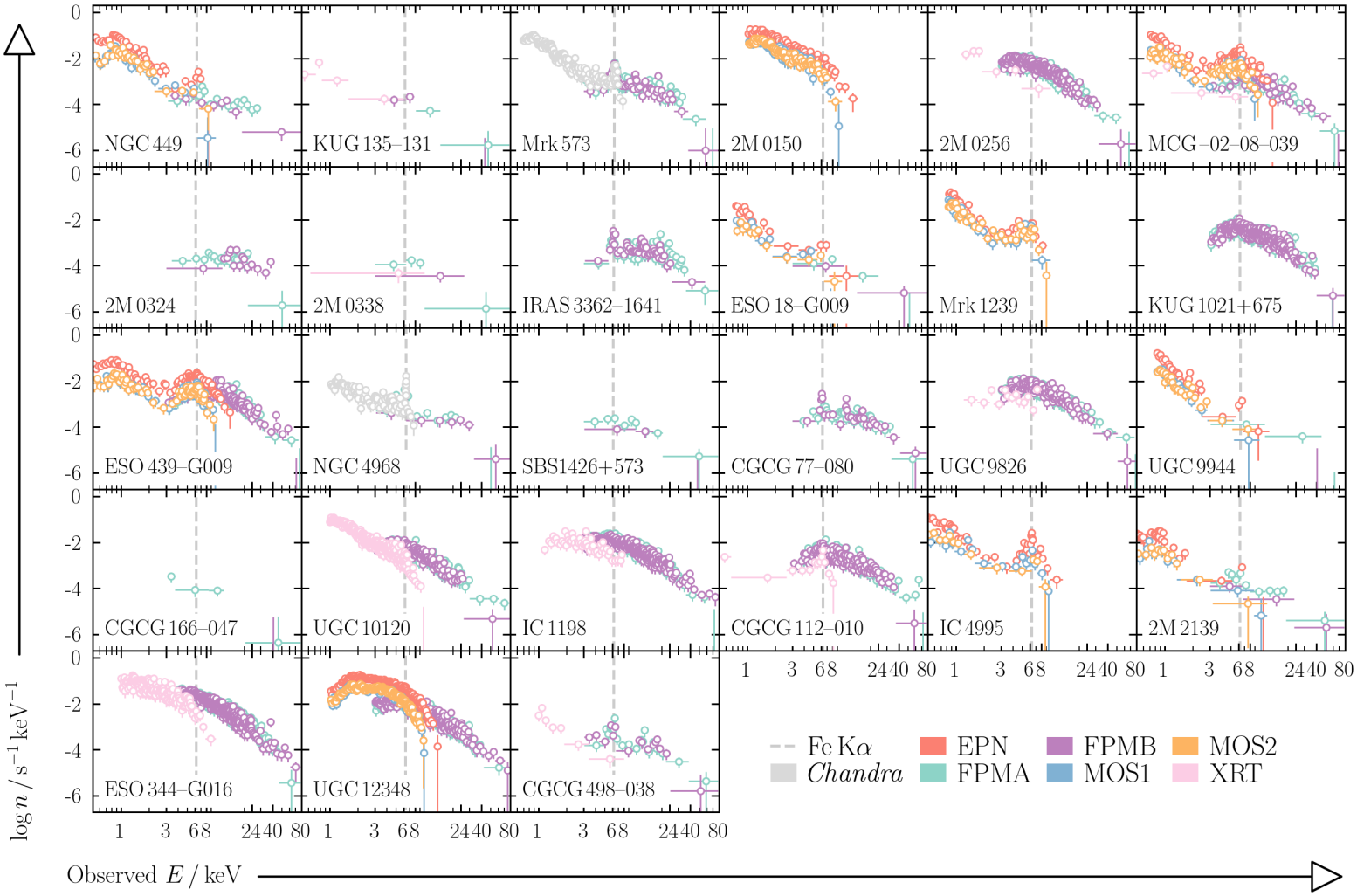

FIGURE 5.1: Observed 0.5 – 78 keV X-ray spectra in count rate units of each source observed as part of the NuLANDS Legacy Survey. We additionally include 3 sources with archival *NuSTAR* observations, but no published spectral analysis, as well as 3 sources with high-quality *XMM*-Newton data already available, but no *NuSTAR*.

TABLE 5.5: Details of all X-ray data used in the analysis of this chapter.

	NuSTAR Observations							Soft X-ray Observations						
dG92 ID	Inst.	Obs. ID	Date	C_S / ks^{-1}	t	N_S	S/N	Inst.	Obs. ID	Date	C_S / ks^{-1}	t	N_S	S/N
(1)	(2)	(3)	(4)	(5)	(6)	(7)	(8)	(9)	(10)	(11)	(12)	(13)	(14)	(15)
26	FPMA	60360002002	2017-12-08	2.78 ± 0.34	31.4	87	8.31	EPN	0200430301	2004-01-09	62.12 ± 2.74	8.6	535	23.14
	FPMB	–	–	1.89 ± 0.31	31.1	59	7.74	EMOS1	–	–	16.67 ± 1.23	11.4	191	13.84
	–	–	–	–	–	–	–	EMOS2	–	–	17.71 ± 1.28	11.5	204	14.29
30	FPMA	60361018002	2019-02-11	0.59 ± 0.23	43.6	26	2.71	XRT	00081998001	2019-02-11	3.04 ± 0.73	6.5	20	4.51
	FPMB	–	–	0.75 ± 0.38	43.3	32	5.74	–	–	–	–	–	–	–
33	FPMA	60360004002	2018-01-06	12.74 ± 0.75	28.6	364	17.28	ACIS	13124	2010-09-17	54.72 ± 1.02	52.4	2866	53.54
	FPMB	–	–	11.96 ± 0.77	28.4	339	18.44	–	–	–	–	–	–	–
37	–	–	–	–	–	–	–	EPN	0200431101	2004-01-21	220.68 ± 5.06	9	1977	43.72
	–	–	–	–	–	–	–	EMOS1	–	–	72.98 ± 2.55	11.5	843	29.04
	–	–	–	–	–	–	–	EMOS2	–	–	80.26 ± 2.67	11.6	928	30.46
64	FPMA	60362027002	2019-02-21	51.88 ± 1.17	39.8	2062	44.37	XRT	00083047001	2014-01-01	25.08 ± 4.79	1.1	28	5.33
	FPMB	–	–	49.47 ± 1.17	39.5	1955	44.22	–	–	–	–	–	–	–
67	FPMA	60360010002	2018-03-11	13.47 ± 0.8	26.2	353	17.12	EPN	0301150201	2006-01-23	97.1 ± 3.54	18.5	1801	42.44
	FPMB	–	–	13.07 ± 0.83	26.1	342	18.51	EMOS1	–	–	23.97 ± 1.33	22.8	547	23.4
	–	–	–	–	–	–	–	EMOS2	–	–	26.77 ± 1.35	22.9	612	24.75
	–	–	–	–	–	–	–	XRT	–	–	3.42 ± 0.82	5.5	19	4.41
84	FPMA	60361022002	2019-03-19	3.76 ± 0.41	39.4	148	9.5	–	–	–	–	–	–	–
	FPMB	–	–	2.58 ± 0.43	39.2	101	10.08	–	–	–	–	–	–	–
96	FPMA	60362026002	2018-12-27	1.09 ± 0.35	36.6	40	3.35	XRT	00037223001	2008-03-26	0.45 ± 0.29	8.6	4	2.25
	FPMB	–	–	0.66 ± 0.4	36.3	24	5	–	–	–	–	–	–	–

Continued on next page

TABLE 5.5: Details of all X-ray data used in the analysis of this chapter.

	NuSTAR Observations							Soft X-ray Observations						
dG92 ID	Inst.	Obs. ID	Date	C_S / ks^{-1}	t	N_S	S/N	Inst.	Obs. ID	Date	C_S / ks^{-1}	t	N_S	S/N
(1)	(2)	(3)	(4)	(5)	(6)	(7)	(8)	(9)	(10)	(11)	(12)	(13)	(14)	(15)
98	FPMA	60362030002	2019-02-12	9.9 ± 0.64	41.5	411	16.05	–	–	–	–	–	–	–
	FPMB	–	–	8.5 ± 0.66	41.3	351	18.76	–	–	–	–	–	–	–
244	FPMA	60362029002	2017-10-29	1.29 ± 0.4	27.5	35	3.39	EPN	0805150401	2017-10-29	16.53 ± 1.68	7.4	122	11.07
	FPMB	–	–	1.02 ± 0.46	27.4	28	5.37	EMOS1	–	–	4.57 ± 0.58	17.2	79	8.9
	–	–	–	–	–	–	–	EMOS2	–	–	3.8 ± 0.52	17.6	67	8.24
260	–	–	–	–	–	–	–	EPN	0065790101	2001-11-12	64.43 ± 4.03	4.3	280	16.04
	–	–	–	–	–	–	–	EMOS1	–	–	25.7 ± 1.77	9.3	238	15.45
	–	–	–	–	–	–	–	EMOS2	–	–	28.56 ± 1.85	9.3	265	16.31
263	FPMA	60361016002	2018-07-30	38.71 ± 0.89	52	2014	43.48	–	–	–	–	–	–	–
	FPMB	–	–	35.75 ± 0.88	51.7	1850	43.01	–	–	–	–	–	–	–
282	FPMA	60101012002	2015-12-20	47.37 ± 1.59	20.1	954	29.92	EPN	0762920301	2015-06-07	113.61 ± 3.64	28.8	3277	57.25
	FPMB	–	–	44.1 ± 1.55	20.4	898	29.97	EMOS1	–	–	24.37 ± 1.25	34.1	831	28.84
	–	–	–	–	–	–	–	EMOS2	–	–	25.24 ± 1.14	34.1	861	29.34
313	FPMA	90361004002	2017-08-19	8.91 ± 1.17	9.2	82	7.76	ACIS	17126	2015-03-09	11.26 ± 0.48	49.4	557	23.6
	FPMB	–	–	5.32 ± 1.07	9.2	49	7.05	–	–	–	–	–	–	–
347	FPMA	60361021002	2018-09-24	2.04 ± 0.35	40.5	83	6.05	–	–	–	–	–	–	–
	FPMB	–	–	1.03 ± 0.38	40.3	42	6.5	–	–	–	–	–	–	–
367	FPMA	60362028002	2019-03-01	5.59 ± 0.47	40.8	228	12.17	–	–	–	–	–	–	–
	FPMB	–	–	5.1 ± 0.51	40.4	206	14.38	–	–	–	–	–	–	–
369	FPMA	60360008002	2017-10-11	46.12 ± 1.72	18	832	27.24	XRT	00081988002	2017-10-11	9.27 ± 1.16	6.9	64	8.03
	FPMB	–	–	44.12 ± 1.74	17.9	789	28.11	–	–	–	–	–	–	–

Continued on next page

TABLE 5.5: Details of all X-ray data used in the analysis of this chapter.

	NuSTAR Observations							Soft X-ray Observations						
dG92 ID	Inst.	Obs. ID	Date	C_S / ks^{-1}	t	N_S	S/N	Inst.	Obs. ID	Date	C_S / ks^{-1}	t	N_S	S/N
(1)	(2)	(3)	(4)	(5)	(6)	(7)	(8)	(9)	(10)	(11)	(12)	(13)	(14)	(15)
377	FPMA	60361023002	2017-06-09	1.61 ± 0.66	22.2	36	2.77	EPN	0307002401	2005-06-23	44.2 ± 2.11	10.9	480	21.92
	FPMB	–	–	0.0 ± 0.0	21.9	0	0	EMOS1	–	–	11.69 ± 0.92	15.3	179	13.38
	–	–	–	–	–	–	–	EMOS2	–	–	11.8 ± 0.92	15.2	179	13.4
379	FPMA	60362024002	2018-12-09	1.09 ± 0.31	39.5	43	3.7	–	–	–	–	–	–	–
	FPMB	–	–	0.0 ± 0.0	39.3	0	0	–	–	–	–	–	–	–
390	FPMA	60361013002	2018-03-22	48.81 ± 1.45	24.9	1213	33.74	XRT	00035080001	2005-11-05	86.21 ± 1.17	63.7	5495	74.13
	FPMB	–	–	45.09 ± 1.43	24.8	1116	33.41	–	–	–	–	–	–	–
398	FPMA	60361014002	2017-05-07	117.79 ± 2.25	27	3177	53.11	XRT	00081994001	2017-05-07	38.67 ± 2.42	6.6	256	16.01
	FPMB	–	–	108.15 ± 2.21	26.9	2907	53.92	–	–	–	–	–	–	–
447	FPMA	60061278002	2015-01-29	35.24 ± 1.37	20.6	727	25.95	XRT	00039847001	2009-11-23	6.17 ± 0.81	9.8	60	7.8
	FPMB	–	–	31.43 ± 1.33	20.6	646	25.43	–	–	–	–	–	–	–
501	–	–	–	–	–	–	–	EPN	0200430601	2004-09-25	64.87 ± 3.48	6	390	18.73
	–	–	–	–	–	–	–	EMOS1	–	–	17.39 ± 1.83	6	104	10.2
	–	–	–	–	–	–	–	EMOS2	–	–	16.59 ± 2.12	4.9	81	9.01
524	FPMA	60362025002	2017-05-09	2.16 ± 0.34	42.7	92	6.63	EPN	0805150801	2017-05-09	13.01 ± 1.28	10.7	139	11.79
	FPMB	–	–	1.04 ± 0.36	42.5	44	6.65	EMOS1	–	–	3.44 ± 0.51	17.3	59	7.74
	–	–	–	–	–	–	–	EMOS2	–	–	3.47 ± 0.51	17.6	61	7.86
531	FPMA	60361017002	2017-06-29	203.26 ± 2.92	24.9	5056	69.72	XRT	00081997001	2017-06-29	154.81 ± 5.24	5.6	874	29.57
	FPMB	–	–	192.5 ± 2.86	24.8	4776	69.12	–	–	–	–	–	–	–
549	FPMA	60001147002	2014-12-09	99.6 ± 2.13	23.5	2340	46.91	EPN	0743010501	2014-12-09	567.93 ± 5.01	28.7	16272	127.56
	FPMB	–	–	104.67 ± 2.21	23.4	2449	49.49	EMOS1	–	–	179.68 ± 2.44	33.8	6077	77.96

Continued on next page

TABLE 5.5: Details of all X-ray data used in the analysis of this chapter.

	NuSTAR Observations							Soft X-ray Observations						
dG92 ID	Inst.	Obs. ID	Date	C_S / ks^{-1}	t	N_S	S/N	Inst.	Obs. ID	Date	C_S / ks^{-1}	t	N_S	S/N
(1)	(2)	(3)	(4)	(5)	(6)	(7)	(8)	(9)	(10)	(11)	(12)	(13)	(14)	(15)
	–	–	–	–	–	–	–	EMOS2	–	–	196.7 ± 2.52	34	6683	81.75
559	FPMA	60361012002	2018-01-10	3.66 ± 0.41	39.1	143	9.19	XRT	00049753001	2013-07-20	1.98 ± 0.35	17.3	34	5.88
	FPMB	–	–	3.46 ± 0.46	39	135	11.66	–	–	–	–	–	–	–

Notes. Columns are as follows: (1) specific ID from dG92; (2) – (4) *NuSTAR* Focal Plane Module used, *NuSTAR* observation ID and date of observation; (5) background-subtracted count rate in the *NuSTAR* instrument; (6) exposure time with *NuSTAR* in ks; (7) background-subtracted counts; (8) signal to noise with *NuSTAR*; (9) – (11) soft X-ray facility used, corresponding observation ID and date of observation; (12) background-subtracted count rate with the soft instrument; (13) exposure time in ks; (14) background-subtracted counts; (15) signal to noise with the soft instrument.

5.3 Method and Results for $N_{\rm H}$ Determination Strategy

The $N_{\rm H}$ determination strategy adopted in this chapter involves three specific stages – details of which are enumerated below.

1. **Stage 1 – Observed Spectral Shape & Fe Kα Strength:** Each observed *NuSTAR* spectrum was fit with a phenomenological model of similar form to Chapter 3, in order to derive an estimate of the *observed* spectral shape, as well as constrain the EW of the narrow Fe Kα line. With this information, we can hope to determine any observed characteristics of these AGN, and any potential reasons for having been undetected by *Swift*/BAT.

2. **Stage 2: Broadband X-ray Spectral Modelling for Intrinsic $N_{\rm H}$ and Luminosity:** Each source was then fit with a physically-motivated spectral model in order to derive intrinsic properties – namely the line-of-sight column density ($N_{\rm H}$) and intrinsic X-ray luminosity. A total of three model realisations were used in order to derive a conservative prediction for the $N_{\rm H}$.

3. **Stage 3: Multi-wavelength Diagnostics:** Each derived intrinsic X-ray luminosity (and hence corresponding $N_{\rm H}$ value) were checked by comparing known multi-wavelength luminosity correlations with the corresponding predicted intrinsic X-ray luminosity provided by our spectral fits.

5.4 Results

Here I present the detailed method and results of each of the aforementioned strategy steps. First, Section 5.4.1 presents the results from deriving observed spectral photon indices and narrow Fe Kα EWs, and then Section 5.4.2 presents the spectral analysis and multi-wavelength indicators to derive robust $N_{\rm H}$ estimates for each source. All X-ray spectral fits were carried out in XSPEC (v12.10.0c). Where applicable, the Monte Carlo Markov Chain command `chain` was used to derive uncertainties, as well as separate to a chain with the XSPEC ERROR command. The `chain` length was fixed to 200,000 with 2,000 walkers and burn-in length of 2,000 using the Goodman-Weare algorithm (Goodman and Weare 2010).

5.4.1 Observed Spectral Shape & Fe Kα Strength

Intrinsically, AGN X-ray emission is well-described by a broadband powerlaw with photon index Γ and exponential cut-off $E_{\rm C}$[7]. We therefore begin by fitting each *NuSTAR* spectrum with a simplified phenomenological model, consisting of an absorbed `powerlaw` plus narrow `Gaussian` ($\sigma = 1\,$eV) fixed to a rest-frame fluorescence line energy core of $E_{\rm L} = 6.4\,$keV. This model was used only to constrain the shape of the observed spectrum, and the observed equivalent width (EW) of the narrow Fe Kα line. Due to the apparent ubiquity of strong Fe Kα lines in heavily obscured AGN (e.g., Risaliti *et al.* 1999b; Ricci *et al.* 2017b, though we find conflicting results in Chapter 3), we use an observed strong Fe Kα line and flat spectrum as indicative of heavily nuclear obscuration. In XSPEC notation, the model takes the form:

$$\begin{aligned} \text{OBS} = \overbrace{\text{CONSTANT}}^{\text{Cross-calibration}} \times \overbrace{\text{PHABS}}^{\text{Gal. absorption}} \times (\overbrace{\text{ZPOWERLW}}^{\text{Observed continuum}} \\ + \underbrace{\text{ZGAUSS}\,[E_{\rm L} = 6.4\,\text{keV},\, \sigma = 1\,\text{eV}]}_{\text{Narrow Fe K}\alpha\text{ emission}} + \underbrace{\text{CONTAMINANT}}_{\text{2M 2139 only}}). \end{aligned} \tag{5.1}$$

I applied this model to the *NuSTAR* data for each source in the 3 – 78 keV band[8], and derived an EW of the narrow Fe Kα line from the `chain` fits of the spectral parameters. An example spectral fit and EW vs. photon index (Γ) for the first source in the analysis, NGC 449, is shown in Figure 5.2, and the table of results for this fitting procedure is presented in Table 5.6. All individual source fits and corresponding MCMC confidence contours are shown in the Appendix, Section C.1.

[7] Powerlaw flux emission with exponential cut-off is mathematically defined as $F(E) \propto E^{\,2-\Gamma} \times e^{E/E_{\rm C}}$, where E is the photon energy, Γ the photon index with well-defined distribution peaking at $\sim 1.7 - 1.9$ (Piconcelli *et al.* 2005; Ricci *et al.* 2017c) and $E_{\rm cut}$ is the e-folding cut-off at $\sim 300\,$keV (Ballantyne 2014; Malizia *et al.* 2014).

[8] For the 3 sources where *NuSTAR* data was not available, we used the *XMM*-Newton data instead.

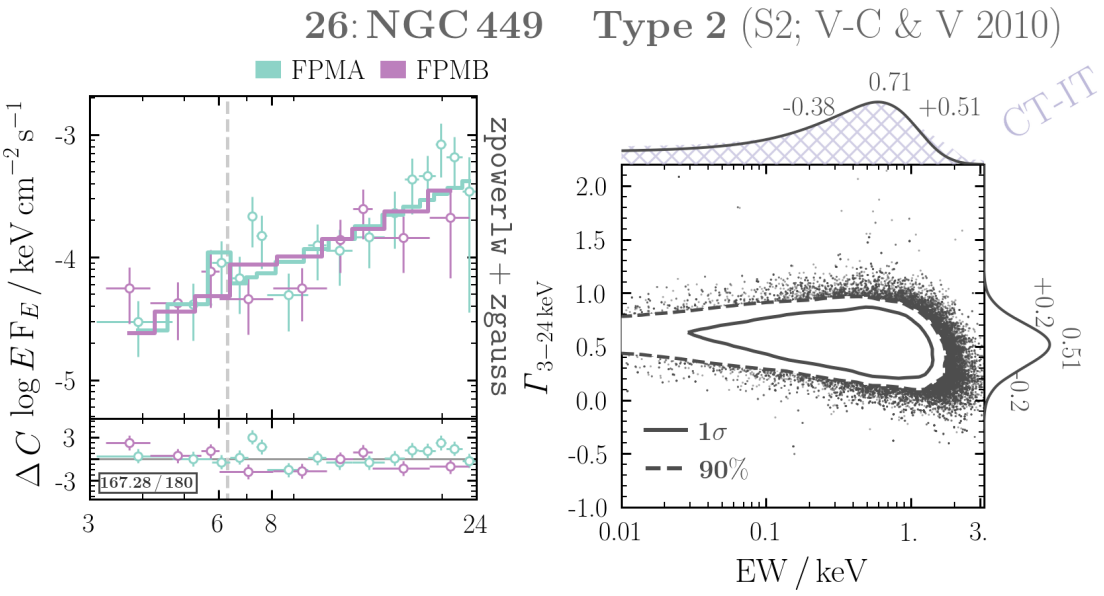

FIGURE 5.2: *Left:* Observed 3 – 24 keV X-ray spectrum fit with Equation 5.1 in unfolded units. For the 3 sources in which *NuSTAR* data was not available, I fit the observed *XMM*-Newton spectra instead. *Right:* Narrow Fe Kα EW vs. observed photon index confidence contour resulting from the MCMC chain. An individual figure for every source is available in the Appendix, Section C.1.

TABLE 5.6: XSPEC `chain` results for the Observed Model.

dG92 ID	$EW_{Fe\,K\alpha}$	$EW_{Fe\,K\alpha}$ [e90 E90]	$EW_{Fe\,K\alpha}$>1keV	Γ	Γ [e90 E90]	$L_{Fe\,K\alpha}$	$L_{Fe\,K\alpha}$ [e90 E90]	$\Delta C/n$
(1)	(2)	(3)	(4)	(5)	(6)	(7)	(8)	(9)
26	0.71	[0.15 1.65]	0.27	0.51	[0.17 0.84]	39.77	[39.12 40.10]	167.28/180
30	1.47	[0.18 70.82]	0.66	1.41	[0.64 4.18]	40.35	[39.51 40.73]	286.81/314
33	1.82	[1.32 2.43]	1.00	0.53	[0.36 0.69]	40.73	[40.61 40.83]	463.83/547
37	0.16	[0.03 0.34]	0.00	2.20	[1.98 2.44]	39.99	[39.33 40.30]	163.33/158
64	0.08	[0.02 0.15]	0.00	2.02	[1.96 2.08]	40.75	[40.05 41.04]	779.73/794
67	1.17	[0.78 1.62]	0.75	0.70	[0.54 0.85]	41.10	[40.94 41.22]	477.07/526
84	1.32	[0.35 2.86]	0.68	-0.57	[-0.88 -0.27]	40.60	[40.07 40.89]	360.25/387
96	2.03	[0.50 5.65]	0.83	1.11	[0.47 1.86]	40.57	[40.03 40.86]	228.46/264
98	2.15	[1.37 3.19]	1.00	-0.56	[-0.76 -0.37]	41.02	[40.85 41.15]	495.79/560
244	3.59	[1.06 8812.12]	0.96	1.68	[0.70 6.76]	40.02	[39.64 40.27]	210.19/200
260	0.84	[0.40 1.47]	0.31	0.33	[-0.15 0.81]	40.95	[40.66 41.16]	83.12/87
263	0.44	[0.33 0.56]	0.00	1.14	[1.08 1.20]	41.48	[41.36 41.57]	1014.71/906
282	0.33	[0.17 0.51]	0.00	0.59	[0.51 0.68]	40.88	[40.60 41.06]	728.52/776
313	2.72	[1.34 4.95]	0.99	0.47	[0.04 0.88]	40.08	[39.83 40.26]	190.35/178
347	0.50	[0.05 1.48]	0.16	0.80	[0.37 1.25]	40.28	[39.35 40.70]	317.22/312
367	1.06	[0.45 1.87]	0.56	-0.04	[-0.27 0.19]	40.57	[40.23 40.78]	409.42/507
369	0.21	[0.08 0.36]	0.00	1.38	[1.29 1.48]	40.91	[40.49 41.14]	613.89/710
377	3.46	[0.90 8123.56]	0.94	0.43	[-0.35 5.53]	40.27	[39.82 40.53]	290.25/288

Continued on next page

TABLE 5.6: XSPEC `chain` results for the Observed Model.

dG92 ID	$EW_{Fe\,K\alpha}$	$EW_{Fe\,K\alpha}$ [e90 E90]	$EW_{Fe\,K\alpha}$>1keV	Γ	Γ [e90 E90]	$L_{Fe\,K\alpha}$	$L_{Fe\,K\alpha}$ [e90 E90]	$\Delta C/n$
(1)	(2)	(3)	(4)	(5)	(6)	(7)	(8)	(9)
379	1.24	[0.16 4.49]	0.60	1.34	[0.61 2.30]	40.08	[39.24 40.46]	226.77/233
390	0.17	[0.07 0.28]	0.00	1.90	[1.82 1.98]	41.06	[40.69 41.27]	608.83/710
398	0.14	[0.07 0.21]	0.00	1.57	[1.52 1.61]	41.22	[40.93 41.40]	881.32/940
447	0.39	[0.21 0.60]	0.00	0.75	[0.65 0.85]	40.88	[40.62 41.06]	587.68/701
501	1.80	[1.20 2.59]	0.99	-0.28	[-0.69 0.12]	40.70	[40.55 40.82]	97.68/93
524	1.88	[0.77 3.71]	0.89	0.80	[0.28 1.32]	40.44	[40.10 40.65]	271.62/323
531	0.07	[0.03 0.12]	0.00	1.96	[1.92 2.00]	41.51	[41.07 41.74]	934.89/942
549	0.12	[0.05 0.20]	0.00	1.80	[1.74 1.85]	41.03	[40.66 41.23]	809.49/848
559	2.25	[1.28 3.74]	0.99	0.27	[-0.06 0.59]	40.73	[40.54 40.89]	334.63/388

Notes. Columns are as follows: (1) specific ID from dG92; (2) EW of the narrow Fe Kα line from the *NuSTAR* spectra; (3) 90% confidence region determined from the `chain` for the Fe Kα EW; (4) fraction of `chain` iterations that resulted in an EW greater than 1 keV[a]; (5) observed photon index of the fit spectrum – note that values less than 1.4 are indicative of obscuration, in which photoelectric absorption and Compton-scattering have flattened the observed spectrum; (6) 90% confidence region on the observed photon index from the MCMC `chain`; (7) luminosity in the narrow Fe Kα line; (8) 90% error region on the Fe Kα line luminosity and (9) the change in C-stat divided by the number of degrees of freedom of the best-fit.

[a]This threshold is often used in the literature to indirectly infer a large line of sight obscurer to a source.

5.4.2 Robust $N_{\rm H}$ Derivation

As the basis of the representative nature of NuLANDS relies upon some form of AGN unification, we initially consider an X-ray model for all sources derived from emission through a toroidal structure. Equation 5.2 shows the XSPEC notation for the TORUS model considered, incorporating `borus02`[9] (Baloković *et al.* 2018). This tabular model is produced from Monte Carlo radiative transfer simulations of reprocessed X-ray emission through a spherical distribution of gas with polar cutouts, resembling a simplified torus geometry. According to Baloković *et al.*, the currently available `borus02` XSPEC tables are appropriate for fitting medium-quality broadband X-ray spectra with the energy resolution of modern CCD detectors (FWHM $\gtrsim$ 130 eV), making them ideal for analysis of the NuLANDS *NuSTAR* spectra.

$$\begin{aligned}\texttt{Torus} = \overbrace{\texttt{constant}}^{\text{Cross-calibration}} \times \overbrace{\texttt{phabs}}^{\text{Gal. absorption}} \times (\overbrace{\texttt{apec}}^{\text{Soft emission}} \\ + \underbrace{\texttt{borus02}}_{\text{Reprocessed}} + \underbrace{\texttt{zphabs} \times \texttt{cabs} \times \texttt{zpowerlw}}_{\text{Direct transmitted emission}} \\ + \underbrace{\texttt{constant} \times \texttt{zpowerlw}}_{\text{Warm mirror}} + \underbrace{\texttt{contaminant}}_{\text{2M 2139 only}}).\end{aligned} \tag{5.2}$$

The model parameters included in `borus02` are: (1) intrinsic photon index; (2) high-energy e-folding cutoff; (3) line-of-sight obscuring column density; (4) covering factor of the torus, defined as the cosine of the half-opening angle of the conical polar cutouts; (5) cosine of the inclination angle, measured from the polar axis; (6) redshift to the source and (7) normalisation of the intrinsic powerlaw emission. The reprocessed `borus02` component was then added to a direct absorbed cutoff powerlaw emission component (`cutoffpl` in XSPEC), accounting for the intrinsic coronal emission of the AGN.

Cross-calibration constants were included between all datasets, and were frozen to the values derived by Madsen *et al.* (2015) who determined accurate cross-calibration constants for *NuSTAR* FPMA with other widely used X-ray instruments, only if visual inspection of the spectra showed the soft and hard spectra to agree with one another. We found evidence for variability in one source – MCG–02–08–039, and hence the cross-calibration constants were left free to vary all fits for this source.

We further include Galactic absorption and an `apec` component to account for the soft X-ray emission. This component is used to model the soft X-ray emission from a diffuse

[9] All `borus02` model tables are available in XSPEC-compatible form at: `http://www.astro.caltech.edu/~mislavb/download/`. We use the v170709a tables for our spectral fits.

collisionally-ionised gas of electrons, and is primarily used to provide a satisfactory fit to the softest energy region $E < 3\,\mathrm{keV}$. A warm mirror representing electron scattering of the intrinsic AGN emission by a diffuse ionised gas through lower $N_{\rm H}$ material on scales larger than the torus was also included. The photon index and normalisation of the 'warm mirror' `zpowerlw` were tied to the intrinsic powerlaw parameters, and the scattered fraction was restricted to $< 10\%$.

In total, 8 sources were found to have $\log N_{\rm H}$ values below the minimum allowed by the `borus02` model of $\log N_{\rm H} \ / \mathrm{cm}^{-2} = 22$. These sources were thus fit separately with the phenomenological model `pexmon`, which combines PEXRAV (Magdziarz and Zdziarski 1995), designed to analytically reproduce the primary and reprocessed emission from an infinitely thick and long slab subtending 2π steradians on the sky, with self-consistent Gaussian components added by Nandra *et al.* (2007) to encompass fluorescent emission lines. This intrinsic emission was then obscured by the same column density as that along the line of sight through the use of the `phabs` and `cabs` models to account for absorption from the photoelectric effect and Compton-scattering, respectively.

Marchesi *et al.* (2018) recently found that inclusion of high-quality *NuSTAR* data to an AGN spectral fit resulted in intrinsic photon indices closer to a canonical value of $\Gamma \sim 1.7 - 1.8$. Additionally, multiple studies of heavily obscured AGN have found very soft photon indices (e.g., Baloković *et al.* 2014; Annuar *et al.* 2017). To test how extreme Γ values could effect our fits, we performed spectral fits for two X-ray spectral model instances on every source: one with the intrinsic Γ free to vary, and one in which Γ was fixed to a canonical 1.9 value.

Tables 5.7 & 5.8 summarise the X-ray spectral fit results with our TORUS model for the **T**hawed **G**amma (**TG**) and **F**rozen **G**amma (**FG**) models, respectively by using the `chain` command in XSPEC.

TABLE 5.7: XSPEC `chain` results for the TG Model.

dG92 ID	$\log N_H$	$\log N_H$ [e68 E68]	$\log N_H$ [e90 E90]	$\log L_{2-10\,keV}$	$\log L_{2-10\,keV}$ [e68 E68]	$\log L_{2-10\,keV}$ [e90 E90]	$\Delta C/n$
(1)	(2)	(3)	(4)	(5)	(6)	(7)	(8)
26	24.10	[24.05 24.16]	[24.01 24.19]	42.17	[42.09 42.26]	[42.03 42.31]	375.12/380
30	22.27	[22.06 22.86]	[22.01 23.36]	41.55	[41.45 41.67]	[41.36 41.77]	264.02/670
33	24.15	[24.10 24.19]	[24.07 24.22]	42.72	[42.65 42.79]	[42.61 42.83]	1052.78/1042
37	21.62	[21.56 21.67]	[21.51 21.71]	41.81	[41.80 41.82]	[41.79 41.83]	355.96/371
64	22.27	[22.18 22.35]	[22.12 22.41]	42.89	[42.88 42.91]	[42.87 42.92]	806.9/1136
67	23.49	[23.46 23.52]	[23.44 23.54]	42.39	[42.36 42.43]	[42.33 42.45]	1040.64/1305
84	24.47	[24.39 24.58]	[24.31 24.69]	43.50	[43.29 43.63]	[43.16 43.73]	361.21/384
96	23.86	[23.71 24.00]	[23.58 24.21]	42.25	[42.02 42.44]	[41.86 42.61]	238.4/650
98	24.35	[24.29 24.42]	[24.23 24.48]	43.26	[43.16 43.35]	[43.08 43.41]	909.98/945
244	23.18	[23.05 23.32]	[22.91 23.41]	40.91	[40.81 41.02]	[40.73 41.09]	373.09/356
260	23.56	[23.50 23.63]	[23.46 23.67]	42.60	[42.52 42.67]	[42.47 42.73]	208.51/242
263	23.14	[23.10 23.26]	[23.07 23.35]	42.94	[42.92 42.96]	[42.89 42.98]	977.41/903
282	23.69	[23.67 23.71]	[23.66 23.73]	42.94	[42.89 42.97]	[42.86 42.99]	1347.23/1344
313	25.25	[25.18 25.35]	[25.11 25.42]	44.24	[44.15 44.34]	[44.07 44.41]	434.85/431
347	23.66	[23.33 24.14]	[23.08 24.82]	41.79	[41.62 41.92]	[41.46 42.03]	316.79/311
367	24.24	[24.14 24.35]	[24.07 24.49]	42.62	[42.47 42.74]	[42.39 42.82]	403.34/504
369	22.61	[22.53 22.70]	[22.48 22.76]	42.61	[42.59 42.64]	[42.57 42.66]	675.89/769
377	23.84	[23.76 23.93]	[23.69 24.00]	41.91	[41.77 42.06]	[41.66 42.17]	525.56/472

Continued on next page

TABLE 5.7: XSPEC `chain` results for the TG Model.

dG92 ID (1)	$\log N_H$ (2)	$\log N_H$ [e68 E68] (3)	$\log N_H$ [e90 E90] (4)	$\log L_{2-10\,keV}$ (5)	$\log L_{2-10\,keV}$ [e68 E68] (6)	$\log L_{2-10\,keV}$ [e90 E90] (7)	$\Delta C/n$ (8)
379	22.95	[22.38 23.50]	[22.13 23.84]	41.18	[41.04 41.36]	[40.94 41.54]	228.67/233
390	20.36	[20.13 20.62]	[20.04 20.78]	42.80	[42.80 42.81]	[42.79 42.82]	1169.87/1304
398	22.20	[22.15 22.24]	[22.12 22.27]	43.06	[43.05 43.07]	[43.04 43.08]	1689.19/1798
447	23.31	[23.26 23.35]	[23.23 23.38]	42.55	[42.52 42.58]	[42.50 42.60]	655.21/761
501	23.82	[23.77 23.86]	[23.74 23.90]	42.48	[42.39 42.57]	[42.33 42.63]	254.02/214
524	24.57	[24.40 24.78]	[24.29 24.97]	42.72	[42.55 42.88]	[42.44 42.98]	510.84/764
531	22.00	[21.97 22.02]	[21.95 22.04]	43.63	[43.62 43.64]	[43.62 43.64]	1733.17/1818
549	22.43	[22.42 22.43]	[22.41 22.44]	42.98	[42.97 42.98]	[42.97 42.98]	1833.32/1750
559	24.79	[24.55 24.99]	[24.45 25.18]	43.41	[43.21 43.57]	[43.11 43.70]	352.87/414

Notes. Columns are as follows: (1) specific ID from dG92; (2) median $\log N_H$ value from the MCMC chain in cm^{-2}; (3) – (4) 68% & 90% confidence regions determined from the `chain` for $\log N_H$; (5) median intrinsic $\log L_{2-10\,keV}$ value from the MCMC chain in $erg\,s^{-1}$; (6) – (7) 68% & 90% confidence regions determined from the `chain` for $\log L_{2-10\,keV}$ and (8) the change in C-stat divided by the number of degrees of freedom of the best-fit.

TABLE 5.8: XSPEC `chain` results for the FG Model.

dG92 ID	$\log N_H$	$\log N_H$ [e68 E68]	$\log N_H$ [e90 E90]	$\log L_{2-10\,keV}$	$\log L_{2-10\,keV}$ [e68 E68]	$\log L_{2-10\,keV}$ [e90 E90]	$\Delta C/n$
(1)	(2)	(3)	(4)	(5)	(6)	(7)	(8)
26	24.11	[24.05 24.18]	[24.00 24.22]	41.91	[41.81 42.01]	[41.74 42.07]	387.81/381
30	22.28	[22.07 22.88]	[22.02 23.39]	41.52	[41.42 41.63]	[41.32 41.71]	264.36/671
33	23.99	[23.94 24.04]	[23.91 24.07]	42.25	[42.20 42.31]	[42.17 42.34]	1090.95/1043
37	21.45	[21.40 21.49]	[21.37 21.52]	41.83	[41.82 41.84]	[41.81 41.85]	363.46/372
64	21.67	[21.43 21.83]	[21.19 21.92]	42.80	[42.79 42.81]	[42.78 42.81]	877.12/1137
67	23.53	[23.51 23.56]	[23.49 23.58]	42.49	[42.46 42.52]	[42.45 42.54]	1054.88/1306
84	24.48	[24.39 24.60]	[24.30 24.71]	43.51	[43.26 43.71]	[43.10 43.84]	361.72/385
96	23.70	[23.48 23.88]	[23.28 24.01]	41.81	[41.60 42.00]	[41.43 42.11]	243.07/651
98	24.37	[24.30 24.44]	[24.23 24.51]	43.32	[43.20 43.43]	[43.10 43.50]	909.72/946
244	23.21	[23.06 23.35]	[22.89 23.44]	40.95	[40.84 41.06]	[40.74 41.13]	372.39/357
260	23.58	[23.51 23.64]	[23.47 23.68]	42.64	[42.55 42.73]	[42.50 42.78]	208.48/243
263	23.52	[23.44 23.58]	[23.39 23.63]	43.08	[43.06 43.12]	[43.04 43.14]	983.26/904
282	23.76	[23.74 23.78]	[23.72 23.79]	43.09	[43.06 43.12]	[43.04 43.14]	1358.67/1345
313	25.31	[25.14 25.45]	[24.90 25.50]	43.58	[43.47 43.66]	[43.38 43.72]	443.43/432
347	23.84	[23.57 24.10]	[23.39 24.27]	42.12	[41.93 42.32]	[41.80 42.46]	317.58/312
367	24.24	[24.14 24.37]	[24.08 24.49]	42.65	[42.57 42.75]	[42.51 42.83]	403.23/505
369	22.91	[22.85 22.96]	[22.82 23.00]	42.74	[42.72 42.76]	[42.71 42.77]	698.75/770
377	23.73	[23.62 23.84]	[23.52 23.91]	41.63	[41.49 41.77]	[41.39 41.87]	526.54/473

Continued on next page

TABLE 5.8: XSPEC `chain` results for the FG Model.

dG92 ID (1)	$\log N_H$ (2)	$\log N_H$ [e68 E68] (3)	$\log N_H$ [e90 E90] (4)	$\log L_{2-10\,keV}$ (5)	$\log L_{2-10\,keV}$ [e68 E68] (6)	$\log L_{2-10\,keV}$ [e90 E90] (7)	$\Delta C/n$ (8)
379	23.10	[22.44 23.61]	[22.15 23.83]	41.27	[41.10 41.50]	[41.00 41.67]	229.63/234
390	20.07	[20.02 20.21]	[20.00 20.45]	42.85	[42.84 42.85]	[42.84 42.86]	1407.27/1305
398	22.43	[22.40 22.46]	[22.38 22.47]	43.14	[43.13 43.14]	[43.12 43.15]	1792.42/1799
447	23.50	[23.46 23.53]	[23.44 23.55]	42.77	[42.75 42.80]	[42.73 42.81]	683.05/762
501	23.79	[23.74 23.84]	[23.70 23.88]	42.31	[42.22 42.40]	[42.16 42.46]	260.21/215
524	24.91	[24.54 25.26]	[24.32 25.42]	42.49	[42.25 42.65]	[42.10 42.75]	521.16/765
531	21.79	[21.75 21.82]	[21.73 21.84]	43.58	[43.58 43.58]	[43.57 43.59]	1841.07/1819
549	22.47	[22.46 22.47]	[22.46 22.47]	42.99	[42.98 42.99]	[42.98 42.99]	1869.62/1751
559	24.99	[24.72 25.22]	[24.61 25.38]	43.44	[43.19 43.65]	[43.06 43.76]	353.5/415

Notes. Columns are the same as in Table 5.7.

5.4.2.1 Multi-wavelength Diagnostics

The intrinsic luminosity derived from each broadband spectral fit is calculated from the best-fit intrinsic Γ and normalisation. To check the reliability of our X-ray–derived intrinsic $2-10\,\mathrm{keV}$ luminosities, we compare these to the optical [O III] and mid-infrared $12\,\mu\mathrm{m}$ (from *WISE* $W3$) luminosities, in the same manner as in Sections 2.5 and 3.3 of this thesis. We do note caution with this technique, as there are several potential caveats – e.g., host contamination in the *WISE* $W3$ fluxes used to calculate the $12\,\mu\mathrm{m}$ luminosities, large X-ray model degeneracies between parameters leading to large uncertainties (see e.g., Section 2.5). However, this observed infrared vs. depleted X-ray flux method has been a very effective strategy for a number of previous X-ray surveys for identifying obscured AGN candidates, that have later been confirmed with broadband X-ray spectroscopy (e.g., Gandhi *et al.* 2014; Annuar *et al.* 2017; Lansbury *et al.* 2017).

By carrying out these comparisons, we found that the majority of obscured AGN fit with `borus02` had derived intrinsic luminosities below that expected from both the $12\,\mu\mathrm{m}$ and [O III] luminosities. In fact, a number of sources were found to be intrinsically X-ray-underluminous by more than an order of magnitude relative to the $12\,\mu\mathrm{m}$ or [O III] luminosities. This deficit in predicted intrinsic X-ray luminosity is shown in Figure 5.3, with the observed and predicted intrinsic X-ray luminosity plotted against the more isotropic [O III] and infrared luminosities.

To test this result, we carried out an additional spectral fit for all sources fit with the Torus model. This spectral fit had a fixed $\Gamma = 1.9$, as well as a normalisation that was fixed to the value required to give an intrinsic X-ray luminosity equal to that predicted from the $12\,\mu\mathrm{m}$ luminosity (via the Asmus *et al.* 2015 relation). Of course, such an assumption is not without caveats, but with the addition of this model our $N_{\rm H}$ values derived will encompass a wider possible range that we deem more conservative to include in the final $N_{\rm H}$ distribution. This model is referred to as **F**ixed **G**amma & **N**ormalisation (**FGN**) hereafter. The X-ray spectral results derived with the `chain` command in Xspec for the TGN model are summarised in Table 5.9.

TABLE 5.9: XSPEC `chain` results for the FGN Model.

dG92 ID (1)	$\log N_H$ (2)	$\log N_H$ [e68 E68] (3)	$\log N_H$ [e90 E90] (4)	$\log L_{2-10\,keV}$ (5)	$\log L_{2-10\,keV}$ [e68 E68] (6)	$\log L_{2-10\,keV}$ [e90 E90] (7)	$\Delta C/n$ (8)
26	24.92	[24.79 25.05]	[24.69 25.16]	43.07	[43.07 43.07]	[43.07 43.07]	382.94/380
30	25.19	[24.97 25.39]	[24.81 25.47]	43.77	[43.77 43.77]	[43.77 43.77]	280.85/671
33	24.86	[24.79 24.94]	[24.72 25.00]	43.36	[43.36 43.36]	[43.36 43.36]	1106.71/1044
67	24.15	[24.11 24.17]	[24.10 24.18]	43.56	[43.56 43.56]	[43.56 43.56]	1884.74/1307
84	24.42	[24.36 24.52]	[24.33 24.62]	43.41	[43.41 43.41]	[43.41 43.41]	363.33/386
96	25.11	[24.97 25.33]	[24.91 25.44]	43.53	[43.53 43.53]	[43.53 43.53]	256.9/652
98	24.46	[24.44 24.49]	[24.42 24.54]	43.79	[43.79 43.79]	[43.79 43.79]	909.81/947
244	24.79	[24.72 24.89]	[24.69 25.05]	43.11	[43.11 43.11]	[43.11 43.11]	368.51/357
260	24.18	[24.16 24.19]	[24.15 24.21]	43.84	[43.84 43.84]	[43.84 43.84]	295.9/244
263	24.66	[24.52 24.99]	[24.47 25.28]	43.75	[43.75 43.75]	[43.75 43.75]	1045.11/905
282	23.77	[23.77 23.78]	[23.76 23.79]	43.12	[43.12 43.12]	[43.12 43.12]	1356.29/1346
313	25.22	[25.03 25.39]	[24.86 25.46]	42.86	[42.86 42.86]	[42.86 42.86]	440.96/433
347	24.81	[24.73 24.94]	[24.69 25.16]	43.42	[43.42 43.42]	[43.42 43.42]	326.63/313
367	24.81	[24.61 25.05]	[24.51 25.24]	43.39	[43.39 43.39]	[43.39 43.39]	409.67/506
369	23.47	[23.42 23.53]	[23.39 23.56]	42.99	[42.99 42.99]	[42.99 42.99]	776.55/770
377	24.78	[24.73 24.87]	[24.70 25.00]	43.56	[43.56 43.56]	[43.56 43.56]	481.61/473
379	24.95	[24.73 25.31]	[24.67 25.44]	43.26	[43.26 43.26]	[43.26 43.26]	231.11/233
447	23.83	[23.82 23.85]	[23.81 23.86]	43.14	[43.14 43.14]	[43.14 43.14]	787.98/762

Continued on next page

TABLE 5.9: XSPEC `chain` results for the FGN Model.

dG92 ID	$\log N_H$	$\log N_H$ [e68 E68]	$\log N_H$ [e90 E90]	$\log L_{2-10\,keV}$	$\log L_{2-10\,keV}$ [e68 E68]	$\log L_{2-10\,keV}$ [e90 E90]	$\Delta C/n$
(1)	(2)	(3)	(4)	(5)	(6)	(7)	(8)
501	24.08	[24.06 24.09]	[24.05 24.11]	42.92	[42.92 42.92]	[42.92 42.92]	288.78/216
524	25.20	[24.92 25.43]	[24.34 25.49]	43.28	[43.28 43.28]	[43.28 43.28]	521.39/766
559	24.74	[24.65 24.86]	[24.60 25.01]	43.29	[43.29 43.29]	[43.29 43.29]	353.57/416

Notes. Columns are the same as in Tables 5.7 and 5.8. Note the intrinsic luminosities were not generated with the chain since they were fixed to the predicted value from the infrared prior to fitting.

Figure 5.4 illustrates the comprehensive analysis carried out for each source in determining an $N_{\rm H}$ estimate, with each panel's content described as follows. All source analysis summary plots can be found in the Appendix, Section C.2.

- *1st Row Left Panel:* Optical colour image centered on the target with dimension $1' \times 1'$.
- *1st Row Right Panel:* Infrared images from *WISE* (upper row) and *IRAS* (lower row).
- *2nd Row Left Panel:* Soft X-ray image of the source (if available), with the number of counts denoted by the lower colour bar.
- *2nd Row Right Panel:* Hard X-ray image from *NuSTAR*/FPMA (if available) with the number of counts denoted by the lower colour bar.
- *3rd Row Left Panel:* X-ray spectrum in unfolded flux units, followed by the ΔC of each of the fits considered. The model used (i.e. `pexmon` or `borus02`-based) is annotated on the side of the spectrum.
- *3rd Row Right Panel:* Confidence contour derived from the MCMC `chain` on intrinsic luminosity vs. line of sight $N_{\rm H}$. The blue and purple contours illustrate the constraints from the TG and FG models, respectively. The green contour on the top of the plot illustrates the constraint on $N_{\rm H}$ derived when the intrinsic luminosity was fixed to that of the infrared luminosity in the FGN model. Additionally, the $12\,\mu$m and [O III] luminosity prediction for the intrinsic X-ray luminosity is shown as orange and green hatched distributions on the side of the contour plot. Finally, the horizontal dashed line shows the X-ray luminosity threshold corresponding to the nominal flux cut from the 70-month survey at the redshift of the source.
- *4th Row Left Panel:* Infrared colour criteria for determining AGN dominance. The R90 cut refers to the 90% reliability criteria specified in Assef *et al.* (2018) for selecting AGN.
- *4th Row Right Panel:* BPT diagnostic diagram used with the optical flux ratios provided in dG92. The solid, dashed and dot-dashed lines are from Kewley *et al.* (2001), Kauffmann *et al.* (2003) and Schawinski *et al.* (2007), respectively.

5.4.2.2 Implementation of New EWs to the Compton-thick Iwasawa-Taniguchi Effect

We selected 15 Compton-thick candidates in which the FGN model-derived column densities gave a lower 90% confidence interval $N_{\rm H} > 1.5 \times 10^{24}\,{\rm cm}^{-2}$. Although it is likely

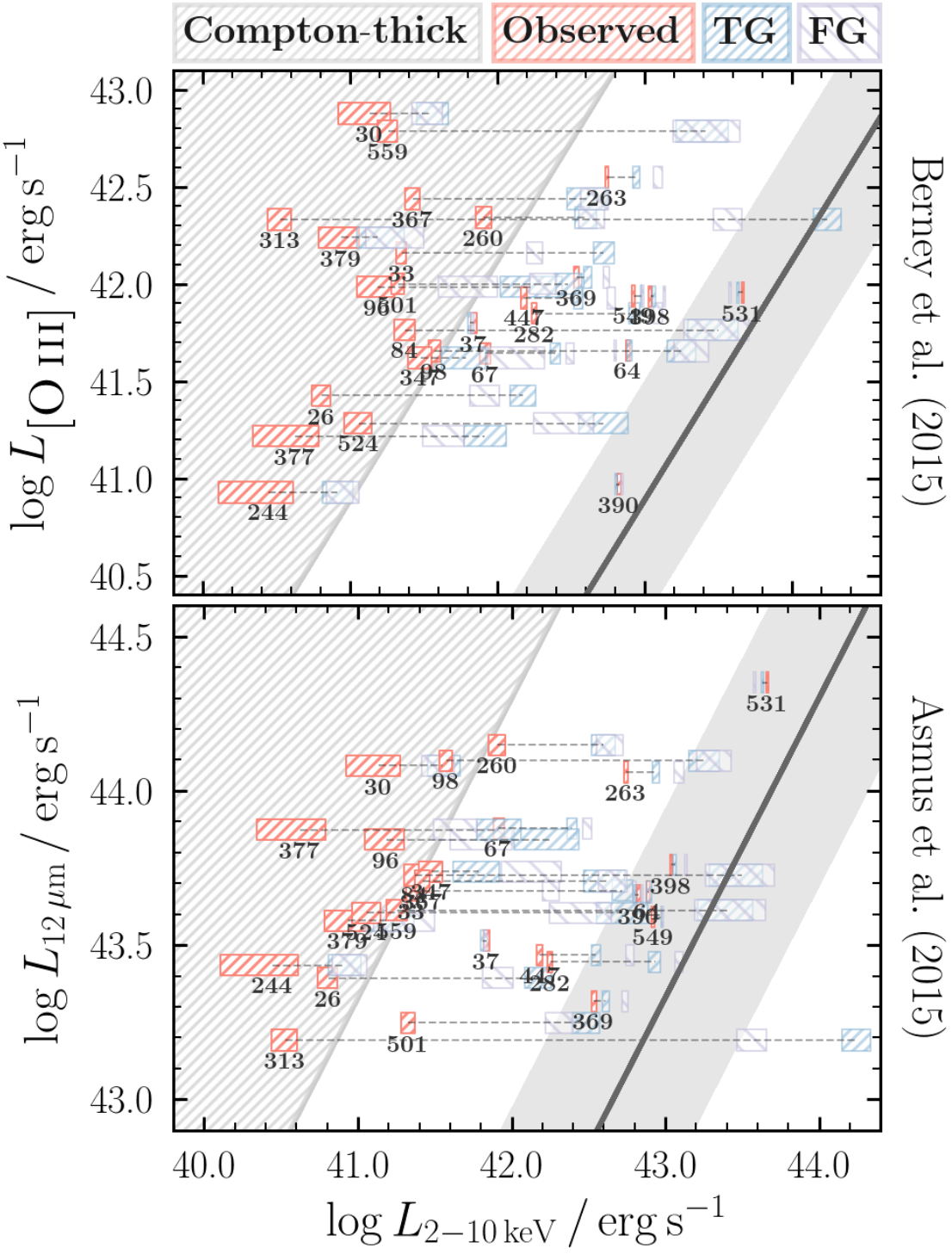

FIGURE 5.3: Multi-wavelength diagnostics to check the X-ray spectral modelling results for the TG and FG models. In both panels, red, blue and purple hatching represents the uncertainty in X-ray luminosity for the observed, TG predicted intrinsic and FG predicted intrinsic luminosities, respectively. All uncertainties are the 68% confidence region from the corresponding `chain` (note observed luminosities were derived from the powerlaw normalisation in the observed spectral fit). The approximate region associated with Compton-thick AGN – i.e. a 2 dex decrement in observed X-ray luminosity, relative to either diagnostic is additionally hatched for clarity. Horizontal dashed lines represent the obscuration correction to the predicted intrinsic X-ray luminosity. Both intrinsic relations are plotted with 1 σ uncertainty shading. *Upper:* Comparison between the dereddened [O III] optical line luminosity from dG92, and the intrinsic relation of Berney *et al.* (2015). *Lower:* Comparison with nuclear mid-infrared emission from Asmus *et al.* (2015).

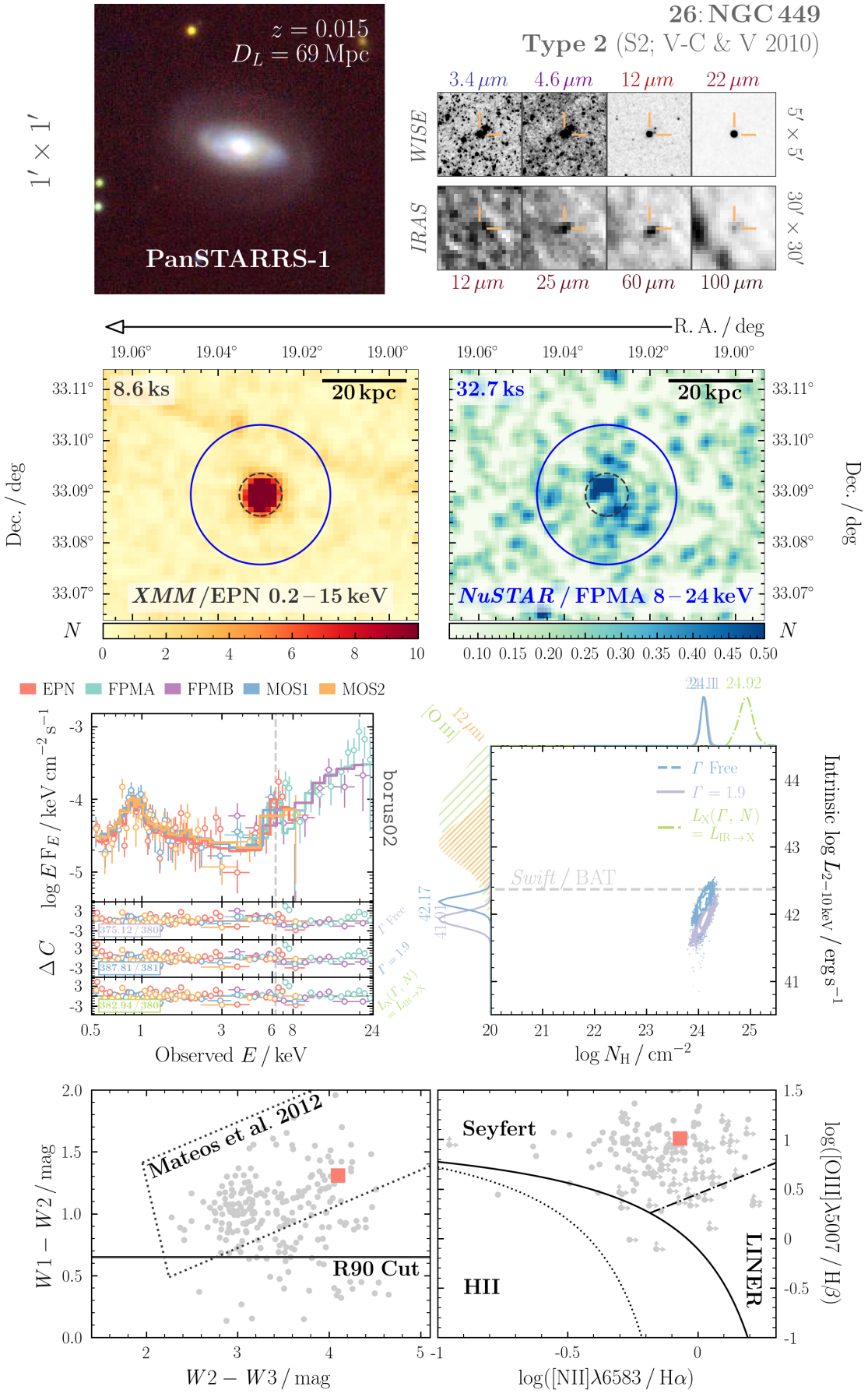

FIGURE 5.4: Example $N_{\rm H}$ Determination Graphic for NGC 449.

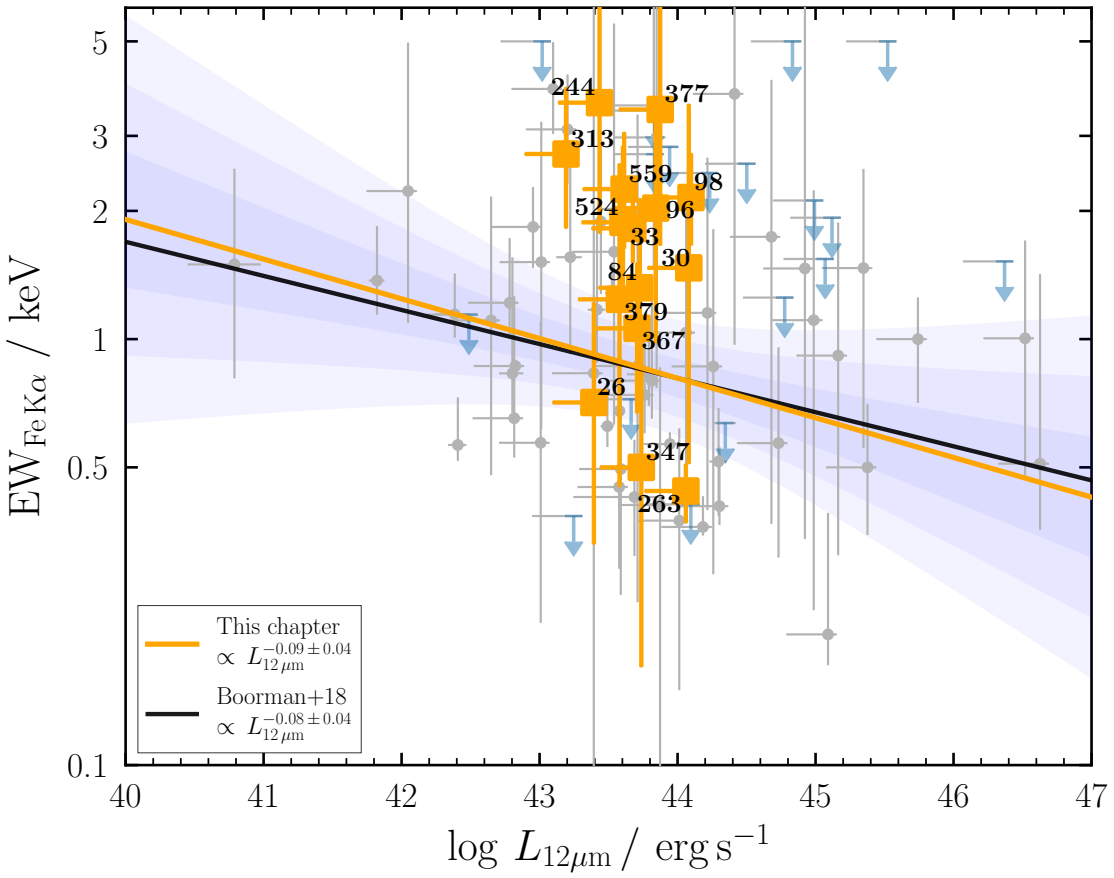

FIGURE 5.5: Figure illustrating the effect of implementing the new NuLANDS Compton-thick AGN into the Compton-thick Iwasawa-Taniguchi effect presented in Chapter 3. Compton-thick candidates were selected from the FGN model. Though this model clearly overestimates $N_{\rm H}$, a conservative lower limit on $N_{\rm H}$ of $1.5 \times 10^{24}\,{\rm cm}^{-2}$ was considered to select the most robust Compton-thick candidates from the model.

that the FGN model may be artificially increasing $N_{\rm H}$, the conservative cut was chosen to select only the most robust Compton-thick candidates from the model. By implementing these additional 15 sources into the same fitting procedure as outlined in Section 3.3, together with the sources already included in the Compton-thick Iwasawa-Taniguchi effect plot, the best-fit found was $\log(\rm EW_{Fe\,K\alpha}) = -0.09^{+0.04}_{-0.04}\log(\rm L_{12\mu m}/10^{44}) + 2.91^{+0.05}_{-0.05}$. This result has a fully consistent gradient with the work presented in Chapter 3, and the resulting Spearman's Rank found indicated that a negative correlation in the data was required to the 98.5% significance level. The resulting fit with the additional sources shown in orange is presented in Figure 5.5.

5.5 Discussion: The Current $N_{\rm H}$ Distribution

Here I present the first $N_{\rm H}$ distribution for NuLANDS using the data currently in-hand, comprising 78 sources as follows: 46 sources detected in the *Swift*/BAT 70-month

catalogue; 8 *Swift*/BAT-undetected sources targeted separately with *NuSTAR* – 5 of which with published $N_{\rm H}$ values & 3 for which we present the $N_{\rm H}$ analysis for the first time; and 24 newly observed sources from Section 5.2.2.5. Of the 5 archived *Swift*/BAT-undetected sources observed by *NuSTAR* – 3 are bona-fide Compton-thick (NGC 1320: Balokovi ́c *et al.* 2014; IC 3639: Boorman *et al.* 2016; NGC 7674: Gandhi *et al.* 2017).

For the 46 *Swift*/BAT-matched sources, we primarily used the comprehensive spectral analyses presented in Ricci *et al.* (2017c, Table C3), selecting $N_{\rm H}$ values of the neutral component of the absorber. However, we investigated sources with a recent archival neutral $N_{\rm H}$ value other than Ricci *et al.*, which differed by more than an order of magnitude. Only in one case, we used an alternative $N_{\rm H}$ value for NGC 262 from Balokovi ́c *et al.* (prep), who find $\log N_{\rm H}\ /\,{\rm cm}^{-2} = 22.97 \pm 0.01$ with hard X-ray data from *NuSTAR*, as opposed to Ricci *et al.* who find $\log N_{\rm H}\ /\,{\rm cm}^{-2} = 23.12^{+0.03}_{-0.02}$ with hard X-ray data from *Swift*/BAT.

To generate an $N_{\rm H}$ distribution that encompasses uncertainties on $N_{\rm H}$ values found from spectral fits, we employed Monte Carlo simulations. For each value of $\log N_{\rm H}$, we simulated a new value based on the uncertainties as follows:

- Upper limits were simulated by generating a uniform random number from the limiting $\log N_{\rm H}$ value to 19. We chose 19 since a number of sources were had $\log N_{\rm H} < 20$ from Ricci *et al.* (2017c). Since our upper limit simulations here result in $\log N_{\rm H}$ values below 20 for these sources, we extend our $N_{\rm H}$ distribution, so that the lowest bin is from $\log N_{\rm H}\ /\,{\rm cm}^{-2} = 19-21$
- Lower limits were simulated by generated a uniform random number from the limiting value to 26. We chose this limiting value since no current physically-motivated X-ray-reprocessing models allow $\log N_{\rm H}$ estimation above 26, since such obscured material results in a negligible amount of escaping flux. In fact, for values of $\log N_{\rm H} > 26$, it is highly likely that current instrumentation would be insufficient to detect any X-ray flux at all. Furthermore, most CXB population synthesis models encompass $\log N_{\rm H}\ /\,{\rm cm}^{-2} \leq 26$. As with the lower limits, we extend the highest $\log N_{\rm H}$ bin in the $N_{\rm H}$ distributions to encompass $\log N_{\rm H}\ /\,{\rm cm}^{-2} = 24-26$, as our Compton-thick bin.
- Constrained $\log N_{\rm H}$ values were simulated with a Gaussian, assuming the standard deviation to be given by the corresponding uncertainty.

These simulations were carried out for each of the `chain`–derived $\log N_{\rm H}$ values, separately, and the corresponding $N_{\rm H}$ distributions for the TG, FG and FGN models are shown in Figures 5.6, 5.7 & 5.8, respectively. Note that the $N_{\rm H}$ distributions for each

contain 78/84 observed sources. Uncertainties on fractions were derived using Beta function approximations, as have been used previously in the literature (e.g., Ricci *et al.* 2017c).

Furthermore, NuLANDS has been structured to test the circumnuclear obscurer giving rise to the Type 1/2 dichotomy of AGN, and excludes likely host-contaminated sources which would populate the $21 \lesssim \log N_{\rm H}\ /{\rm cm}^{-2} \lesssim 23$ bins of the distribution – see Section 4.2.5 for discussion on this.

As can be seen, for the TG & FG models, the Compton-thick fraction is in agreement with the Compton-thick fraction predicted from model-dependent bias corrections in the *Swift*/BAT survey from Ricci *et al.* (2015). Agreement between 'bias-corrected' hard X-ray and NuLANDS already implies that NuLANDS is resolving the true population of Compton-thick AGN that hard X-ray selection is typically not sensitive to. Thus NuLANDS and by extension – infrared continuum selection – represents a powerful tool for selecting and probing the most obscured accretion events in the local Universe.

Interestingly for the FGN model, the Compton-thick fraction is seen to exceed that of the bias-corrected hard X-ray value. A higher Compton-thick fraction than with the TG and FG models is unsurprising, since the latter models were found to almost consistently under-predict the intrinsic X-ray luminosities of sources, relative to the infrared and optical. Thus purely by forcing the intrinsic X-ray to be brighter, the model is expected to tend towards more obscured realisations to explain the observed flux level. Nevertheless, I note that established works into the mid-infrared X-ray correlation, multiple authors note the remarkable outcome that after accounting for obscuration, even Compton-thick AGN were found to agree with the relation (e.g., Gandhi *et al.* 2009; Asmus *et al.* 2015). Thus, assuming the intrinsic luminosity as I have done here may point to a possible higher Compton-thick fraction than is found with current modelling. Possible physical reasons for favouring the FGN model could include an enhanced warm mirror scattered component or possible dual AGN unresolved by *NuSTAR* (see Section 3.5.2.4). In addition, our value of the FGN Compton-thick fraction is fully consistent with that predicted from Ananna *et al.* (2019) ($50 \pm 9\%$ within $z = 0.1$).

Due to the results from the FGN model, we note here a possible issue in X-ray reprocessing models that was predicted in Chapter 3, namely – for smaller EWs of the narrow Fe Kα line, models could potentially predict lower obscuration than the true value. From the EW confidence ranges in Table 5.6, only 5 sources show an EW > 1 keV to $> 2\sigma$ significance (based on column 4 of the table), yet multi-wavelength diagnostics strongly indicate the AGN to be more intrinsically powerful than predicted from the TG and FG models. In Figure 5.9, the $\log N_{\rm H}$ per source per model is plotted against the EW of the narrow Fe Kα line found with the observed model. I have overplotted two red

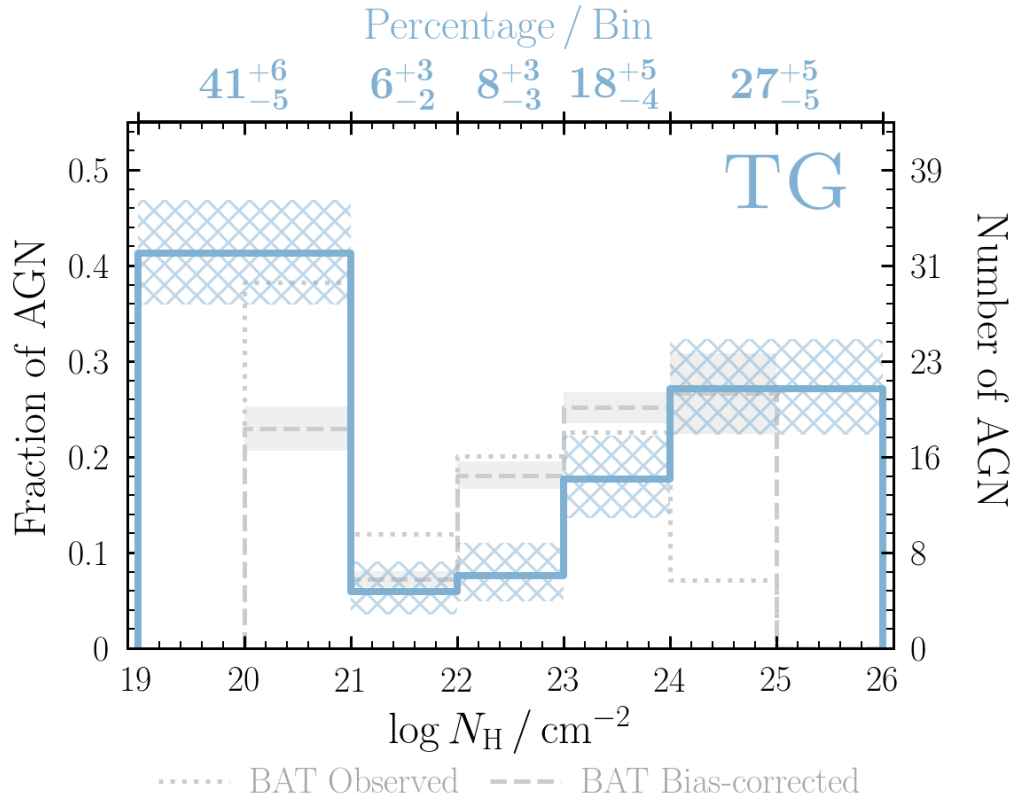

FIGURE 5.6: Current NuLANDS $N_{\rm H}$ distribution for the TG (Thawed-Gamma) model, with XSPEC `chain` constraints shown with hatched shading. Dotted grey and dashed histograms are the observed and intrinsic $N_{\rm H}$ distributions, respectively, for the 70-month catalogue from Ricci *et al.* (2017c).

shaded regions to illustrate sections of parameter space that are unexpected with current modelling, namely: (1) EW >1 keV & $N_{\rm H}$ $<1.5\times10^{24}$ cm^{-2} and (2) EW <1 keV & $N_{\rm H}$ $>1.5\times10^{24}$ cm^{-2}. In particular, (2) broadly appears to only be satisfied for the FGN model, in which the intrinsic luminosity is forced, resulting in a higher obscuration required to explain the observed low luminosity. An existence of Compton-thick AGN with weaker Fe Kα lines may indicate that current models struggle to explain faint observed luminosities with high obscuration without a large Fe Kα EW.

5.6 Summary

This chapter presents the spectral analysis of 27 NuLANDS AGN, as well as the 93% complete $N_{\rm H}$ distribution for the NuLANDS Extragalactic Legacy Survey. The key conclusions are:

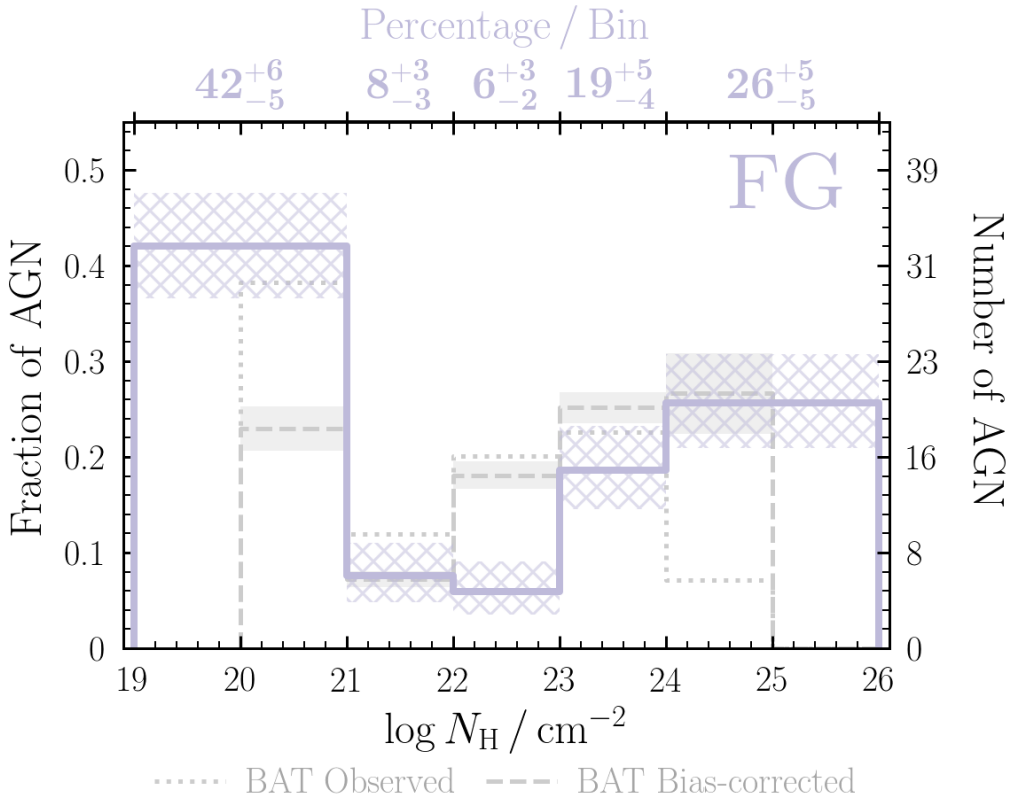

FIGURE 5.7: Current NuLANDS $N_{\rm H}$ distribution for the FG (Fixed-Gamma) model, with XSPEC `chain` constraints shown with hatched shading. Dotted grey and dashed blue histograms are the observed and intrinsic $N_{\rm H}$ distributions, respectively, for the 70-month catalogue from Ricci *et al.* (2017c).

1. By analysing the hard X-ray–undetected sources with physically motivated torus-reprocessing models of obscuration, we find broad agreement between the bias-corrected X-ray and NuLANDS $N_{\rm H}$ distributions in the $\log N_{\rm H}\ /\,{\rm cm}^{-2} > 23$ regime. We additionally find possible evidence for an even higher Compton-thick fraction by testing the assumption that the predicted intrinsic luminosity from the infrared luminosity is correct.

2. We find a surplus of unobscured sources with $\log N_{\rm H}\ /\,{\rm cm}^{-2} < 21$, as well as a deficit of $\log N_{\rm H}\ /\,{\rm cm}^{-2} = 22-23$, relative to the bias-corrected *Swift*/BAT $N_{\rm H}$ distribution. If this apparent deficit of mildy obscured AGN is a real effect, we find two possible explanations for this: (1) the remaining sources to be observed will occupy this bin and reduce the unobscured fraction in doing so, or (2) the sources excluded from NuLANDS with faint Hβ line fluxes occupy this bin, and are obscured by large-scale host galaxy dust, disentangled from the central nuclear obscuration giving rise to the Type 1/Type 2 dichotomy of AGN.

3. For one specific model realisation in which we assume the infrared-predicted intrinsic X-ray luminosity from Asmus *et al.* (2015) is correct (the FGN model), we find

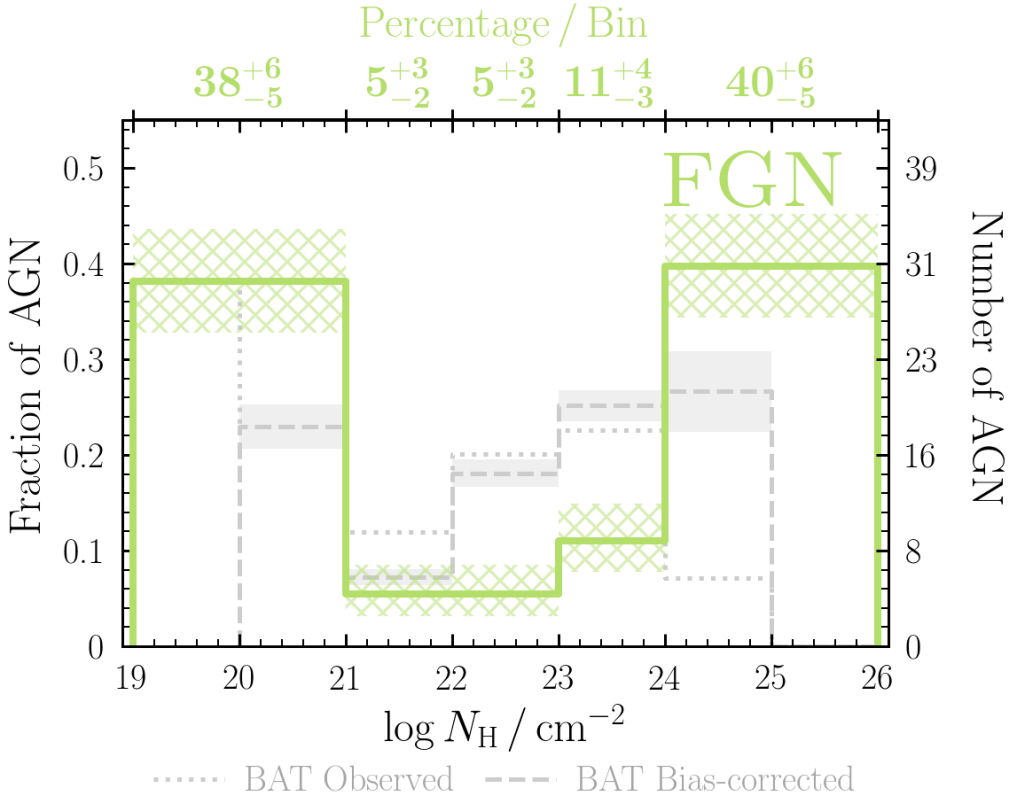

FIGURE 5.8: Current NuLANDS $N_{\rm H}$ distribution for the FGN (Fixed-Gamma & Normalisation) model, with XSPEC `chain` constraints shown with hatched shading. Dotted grey and dashed blue histograms are the observed and intrinsic $N_{\rm H}$ distributions, respectively, for the 70-month catalogue from Ricci *et al.* (2017c).

a significantly higher Compton-thick fraction, that is consistent with the high fraction found in the recent CXB population synthesis model by Ananna *et al.* (2019). This model realisation is likely an over-simplification, but does approximately trace the level of obscuration required to reproduce the established mid-infrared vs. X-ray correlation. We note that this correlation has been found by multiple works to hold for a diverse range of AGN types, critically including Compton-thick sources (e.g., Gandhi *et al.* 2009; Asmus *et al.* 2015).

4. Of the 9 remaining sources to be observed by *NuSTAR*, 6 are Seyfert 2s and 3 are Seyfert 1s. Due to their strength and prevalence as AGN in optical and infrared wavelengths, combined with faint or non-existent X-ray constraints, we anticipate the obscured AGN fraction in the NuLANDS $N_{\rm H}$ distribution will increase by the end of the survey.

The Compton-thick fraction in NuLANDS is at least consistent with current bias-corrections, with the potential to exceed it with the remaining sources to be observed, and considering possible modelling anomalies. If the true Compton-thick fraction in the local Universe

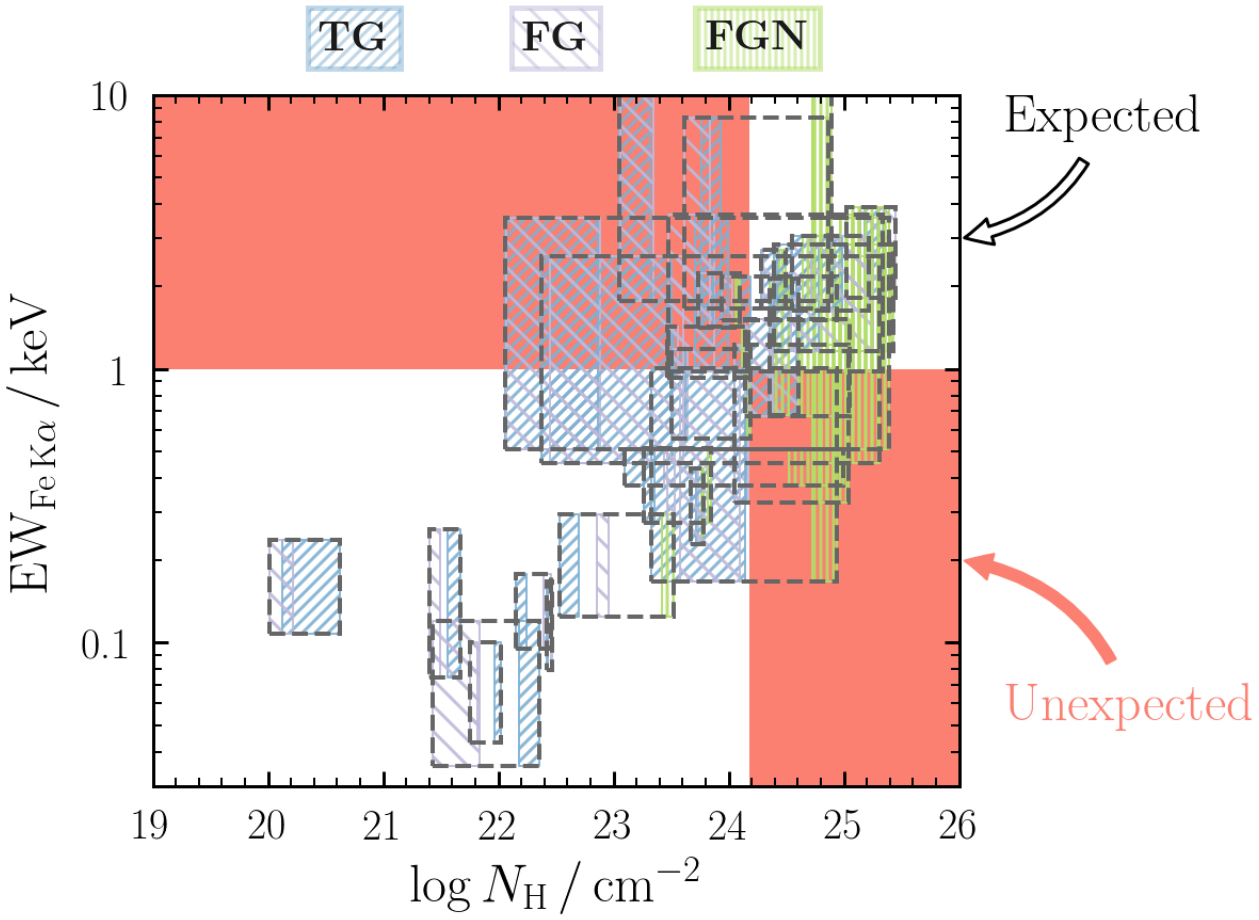

FIGURE 5.9: A plot of $\log N_{\rm H}$ derived from each of the TG, FG and FGN models vs. narrow Fe Kα EW derived from the observed model. Shown in red shading are two regions unexpected in typical modelling, namely: (1) EW > 1 keV & $N_{\rm H}$ $< 1.5 \times 10^{24}$ cm^{-2} and (2) EW < 1 keV & $N_{\rm H}$ $> 1.5 \times 10^{24}$ cm^{-2}.

exceeds the currently predicted hard X-ray bias-corrected value, this will have implications for synthesis models of the CXB spectrum that require the local $N_{\rm H}$ distribution as a critical local boundary condition that is evolved to high redshift (e.g., Ueda *et al.* 2014; Ananna *et al.* 2019).

Chapter 6

Summary, Conclusions & Outlook

"Good, better, best.
Never let it rest...
Until your good is better and your better is best."
– St. Jerome

The focus of this thesis was to probe the obscured accretion of supermassive black holes, with the ultimate aim of helping to understand its importance in driving global black hole growth. Having addressed some of the current questions highlighted in the introductory chapters, I will provide some concluding remarks. First, I summarise my findings in Section 6.1, before commenting on how future work will be capable of unveiling the true underlying distribution of AGN across cosmic time in Section 6.2. I present final remarks in Section 6.3

6.1 Key Findings

In order to establish a census of obscured accretion in the local Universe, the first step I partook was to develop a robust formalism for characterising obscured AGN, by using multiple wavebands and diagnostics. The high-sensitivity hard X-ray imaging capabilities of *NuSTAR* to target and analyse Compton-thick candidates was pivotal in robustly classifying Compton-thick AGN. For example, in Chapter 2, I used the broadband X-ray spectrum from *NuSTAR*, *Suzaku* and *Chandra* to classify a single obscured candidate as Compton-thick to high significance. I then combined an optical large scale ionised gas tracer ([O III] line emission) with mid-infrared continuum emission to show that the X-ray–inferred parameters agreed with the global energy output of the system.

In Chapter 3, I then studied obscured accretion in a large number of Compton-thick AGN candidates to relatively deep redshifts ($z < 3.7$). The sample study gave me the skills necessary to analyse low signal to noise data, and to extract useful information from such datasets. The key results of Chapter 3 – namely a new anti-correlation for Compton-thick AGN have already been debated in the literature, with Matt and Iwasawa (2019) proposing a new AGN schematic to explain the observed effect. If confirmed on larger samples with the next generation of X-ray observatories, this 'Compton-thick Iwasawa-Taniguchi effect' will require a vital revision to the traditional image of unification that is often found to be valid in X-rays.

An additional key finding from Chapter 3 was the observed spread in Fe Kα equivalent widths among the Compton-thick AGN population, with a sizeable number extending down below 1 keV. This finding is in stark contrast to the widely popular criterion that Compton-thick AGN have strong Fe Kα equivalent widths *above* 1 keV. Current X-ray models may thus conclude that a small Fe Kα EW indicates less obscuration, which is not always the case. Thus, a large amount of heavily obscured accretion may exist which are currently unknown and unaccounted for correctly in cosmological models. To sample the obscured AGN population irrespective of Fe Kα lines constraints, in Chapters 4 and 5, I presented NuLANDS– the *NuSTAR* Local AGN $N_{\rm H}$ Distribution Survey. NuLANDS is designed explicitly to identify obscured AGN irrespective of X-ray obscuration bias, and derive a representative $N_{\rm H}$ distribution for the local Universe.

Despite the *NuSTAR* component of NuLANDS being planned for completion after the date of submission, the current constraints that I have acquired for the $N_{\rm H}$ distribution show that the Compton-thick fraction is at least as high as model-dependent bias corrections have previously suggested, with the potential for an even higher obscured fraction than was previously considered. With the final observations likely to take place over the coming months, I will stringently determine the column density distribution for an infrared-derived sample of AGN. Such an $N_{\rm H}$ distribution will be pivotal to determine the proportions of obscured accretion in the Universe as a function of redshift – a vital first-step in understanding how supermassive black holes form and grow, but is only a small piece of the puzzle. In Figure 6.1, I show the current Compton-thick fraction in NuLANDS as a function of distance, as compared to the equivalent data from *Swift*/BAT. As can be seen, a dramatic turn-off is visible for *Swift*/BAT due to the obscuration bias of flux-limited hard X-ray selection. However, the NuLANDS data shows the distance dependence to be consistent with uniform for twice the distance of *Swift*/BAT– a remarkable achievement for the survey, illustrating the power of isotropic infrared selection.

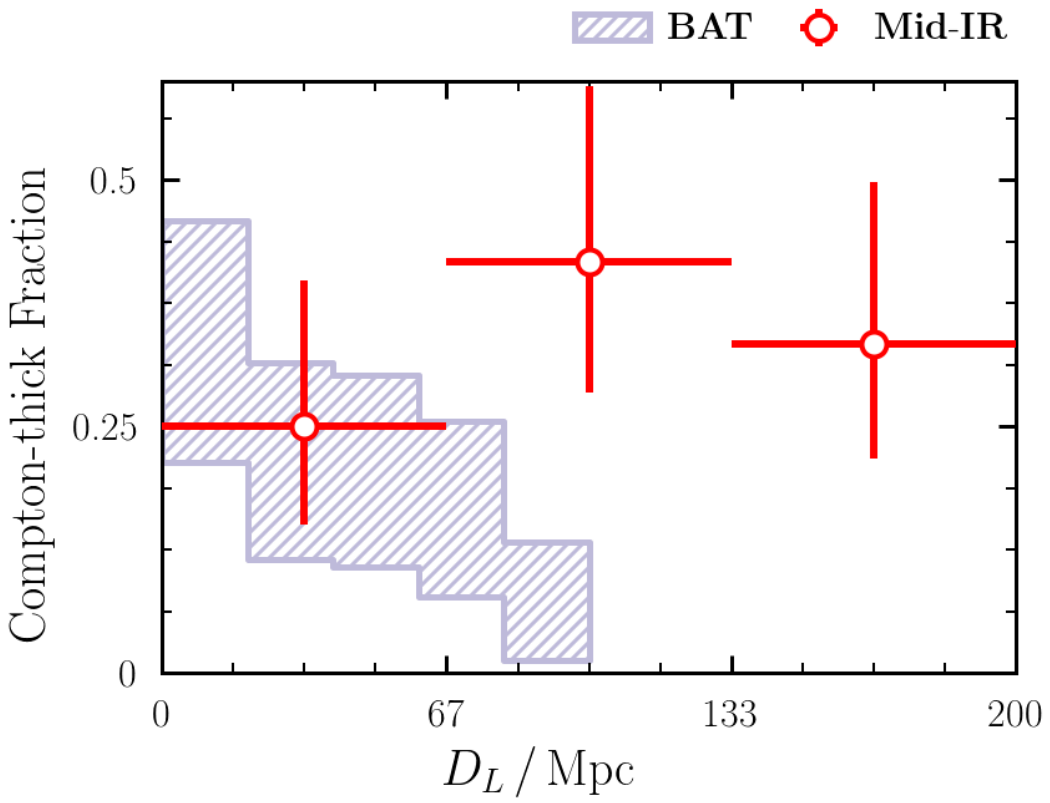

FIGURE 6.1: The Compton-thick fraction found in NuLANDS with current observations as a function of distance, as compared to the equivalent plot for the 70-month *Swift*/BAT survey. The NuLANDS Compton-thick fraction is consistent with being uniform out to $\sim$200 Mpc, whereas *Swift*/BAT is seen to diminish dramatically by 100 Mpc.

6.2 Future Avenues of Research

In this section, I highlight some immediate goals of my research that I wish to pursue in the near future.

6.2.1 Alternate $N_{\rm H}$ Distributions and Deriving an Obscuration Geometry

Once the $N_{\rm H}$ distribution has been derived for the current full NuLANDS sample, there are a number of wider projects I would like to engage with. Firstly, due to the early exclusion of optical line flux limits, the current NuLANDS sample is predicted to miss AGN with large-scale host galaxy dust that is predicted to obscure the central engine with enough obscuration to effect the AGN optical line emission (but not necessarily the X-ray emission). I thus plan to propose a secondary *NuSTAR* Extragalactic Legacy Survey, targeting the sources with optical line flux limits that were excluded previously.

Such a sample will give a more complete picture of the column density distribution in the local Universe, by removing potential optical bias from the infrared-derived sample.

With the final derived $N_{\rm H}$ distribution, considerable constraints on the geometry of AGN obscurers can be made by deriving a geometry. With a grid of luminosity, redshift and $N_{\rm H}$ values, one could calculate the detection probability of an AGN with these different parameters, in part by assuming a spectral model. By varying spectral models, the result could be used to favour or disfavour particular geometrical models of the X-ray obscurer surrounding AGN.

6.2.2 The Capabilities with Future High-Resolution X-ray Spectroscopy

Microcalorimeter technology onboard the future *X-ray Imaging and Spectroscopy Mission* (*XRISM*) (Guainazzi and Tashiro 2018) and *Athena* (Nandra *et al.* 2013) X-ray observatories – capable of spectral resolution R ($= E/\Delta E$) exceeding 1000 – will revolutionise studies of the Fe Kα line in AGN. Through observations of large samples, these instruments will be able to constrain to minute accuracy the location and dynamics of the Fe Kα emitting source that has only been capable to date with the brightest sources with the *Chandra* High Energy Transmission Grating (e.g., Shu *et al.* 2011; Gandhi *et al.* 2015a). Such studies have not been capable with Compton-thick AGN in the source quantities required to draw conclusions on the population. However, I aim to use the next-generation in high-resolution X-ray spectroscopy instruments for Compton-thick AGN, such as the newly discovered sources from NuLANDS (see Chapter 5).

Two possible targets for *XRISM* are simulated with 300 ks exposures in Figure 6.2. The left panel shows a simulation of NGC 4968 – a relatively faint Compton-thick AGN with considerable iron line emission (LaMassa *et al.* 2017). *XRISM* fully resolves the 'Compton Shoulder' redward of the 6.4 keV line core – capable of constraining the geometry of AGN obscurers (e.g., Odaka *et al.* 2016). The simulated model includes an absorption feature at 8 keV, showing the potential for studying outflows in such highly obscured sources also (e.g., Parker *et al.* 2017). The right panel shows a simulation of NGC 7674 – a median X-ray flux Compton-thick AGN with one of the weakest Fe Kα lines found for the local bona fide Compton-thick AGN (Gandhi *et al.* 2017). Despite being weak, *XRISM* will be able to fully resolve the Fe Kα line doublet into its two separate components – an impossible feat with all instruments to date. Such detailed line profiles will constrain broadening effects and line fluxes – critical for probing the geometry, dynamics and composition of Fe Kα-emitting region. *Athena* will improve upon the capabilities of *XRISM* with a Wide Field Imager (WFI) and X-ray Integral Field Unit (X-IFU) with X-ray spectral resolutions of ≤ 150 eV at 6 keV and 2.5 eV between 0.2 – 12 keV, respectively.

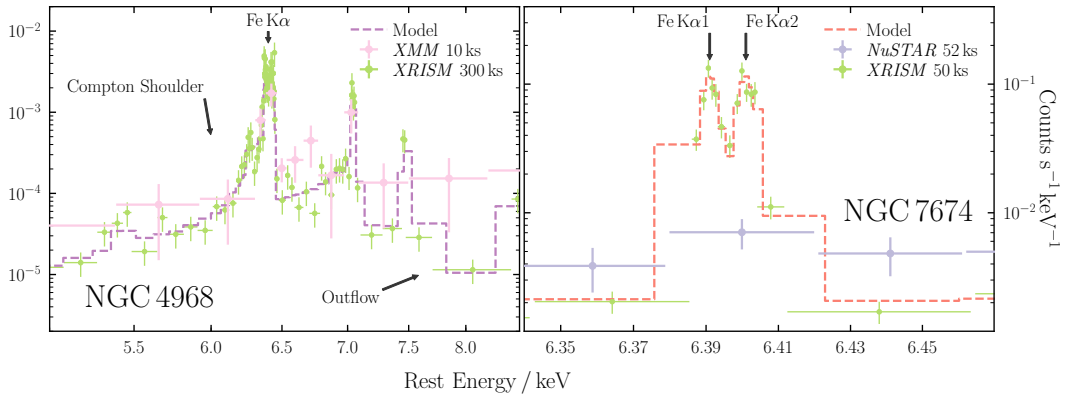

FIGURE 6.2: *XRISM* simulations (300 ks) of the Compton-thick AGN NGC 4968 & NGC 7674 in left and right panels, respectively. *Left:* The *XRISM* spectrum resolves an outflow included in the model at 8 keV, as well as the Compton Shoulder < 6.4 keV – ï£¡ï£¡ both holding significant clues to the intrinsic gas dynamics associated with the emission region of the Fe Kα line. *Right:* The Fe Kα line doublet is fully resolved into its two narrow components – essential for inferring the geometry and dynamics of the Fe Kα line-emitting source.

The capabilities attainable with these instruments are shown in possible simulations of local and distant Compton-thick AGN in Sections 2.6.3.3 and 3.5.4, respectively.

To use these immense advancements in X-ray spectral resolution, I have begun the implementation of my own Monte Carlo Radiative Transfer code over the last few months of my Ph.D. that currently reproduces the spectrum of an AGN surrounded by a uniform-density spherical torus with polar cutouts (identical to the current `borus02` geometry). Examples of my current simulations are shown in Figures 6.3 and 6.4. To implement capabilities attainable with future high-resolution spectroscopy instruments, I plan to implement routines to derive gas dynamics, metallicites and kinematics via fully-resolved narrow fluorescent emission lines.

In addition, I plan to update my code to simulate X-ray reprocessing through distributions of spherical gas clouds. This is a similar method to the widely-used *infrared* `CAT3D-Wind` model (Hönig and Kishimoto 2017), in which ultraviolet–sub-mm spectra are produced from photon interactions with spherical dust clouds. I intend to merge `CAT3D-Wind` with my X-ray model to simulate X-ray–sub-mm spectra and constrain the dust-to-gas ratio in AGN.

6.2.3 Ongoing & Future Large Surveys of AGN

Currently, I am part of an ongoing survey with the Palomar Hale 200 inch telescope to follow-up all warm *IRAS* AGN from the original dG87 sample that were optically unclassified, optically elusive (i.e. with line flux upper limits) or with non-AGN spectroscopic

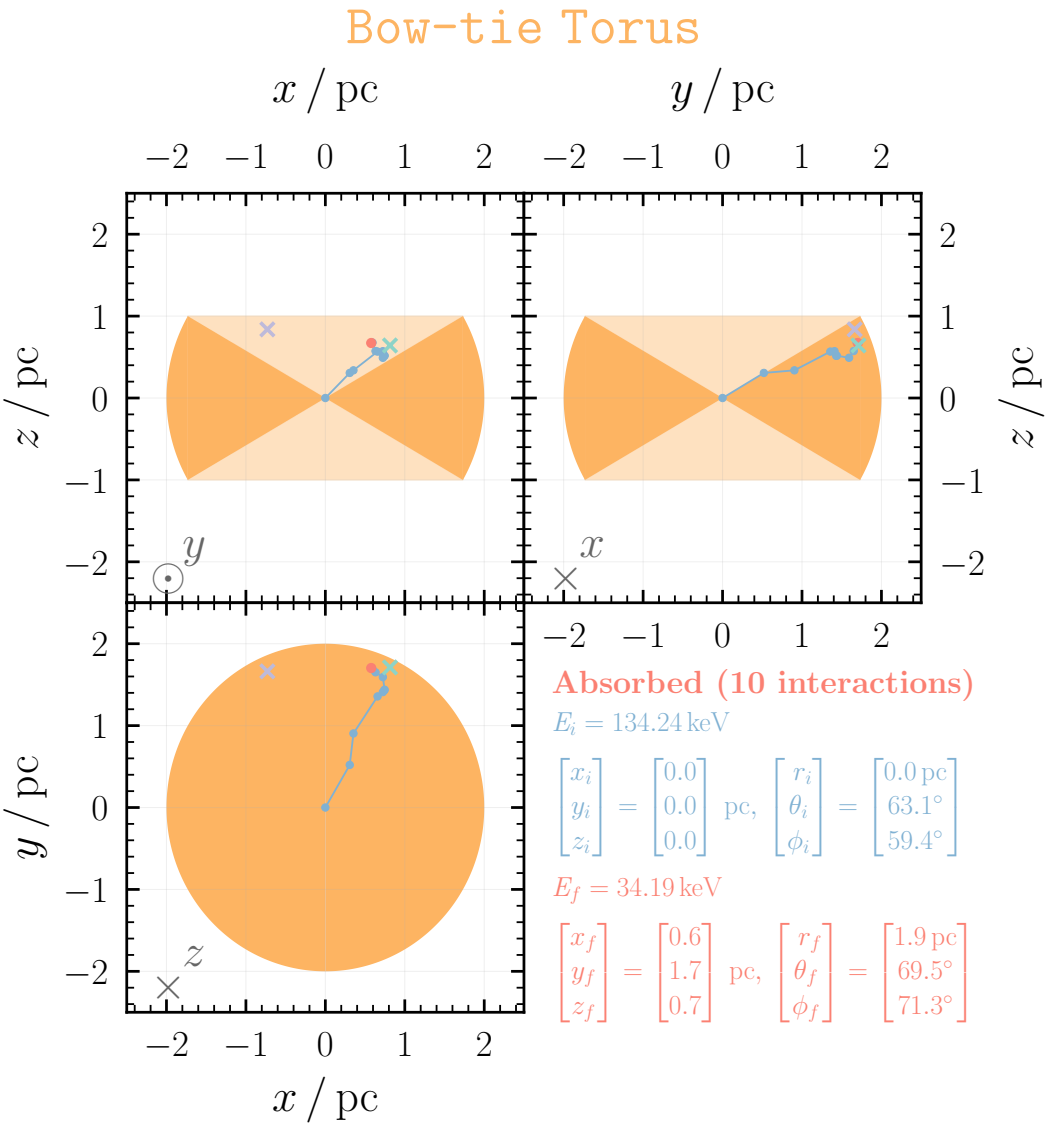

FIGURE 6.3: Schematic for the current geometrical setup of my Monte Carlo Radiative Transfer simulations through spherical torii with polar cutouts. This particular photon run was absorbed by the torus after 10 scatterings. The crosses mark analytically solved intersection locations, which are used to compute the relative N_{H} a photon sees after each scattering.

classifications. To-date, 16 new AGN have been identified that were previously unclassified, or incorrectly classified due to lower previous sensitivities. With updated AGN classifications in the optical regime, we will be able to stringently confirm the presence of a powerful AGN that may have been missed previously.

In the near future, I am involved with two ongoing efforts to provide multi-wavelength follow-up of infrared-derived AGN samples. The first effort is a large ESO programme proposed with the VLT/X-SHOOTER optical spectrograph of a large sample of local infrared-derived AGN. The targets are selected to have *WISE* colours satisfying the 90% reliability threshold for AGN selection outlined in Assef *et al.* (2018), yet with no known

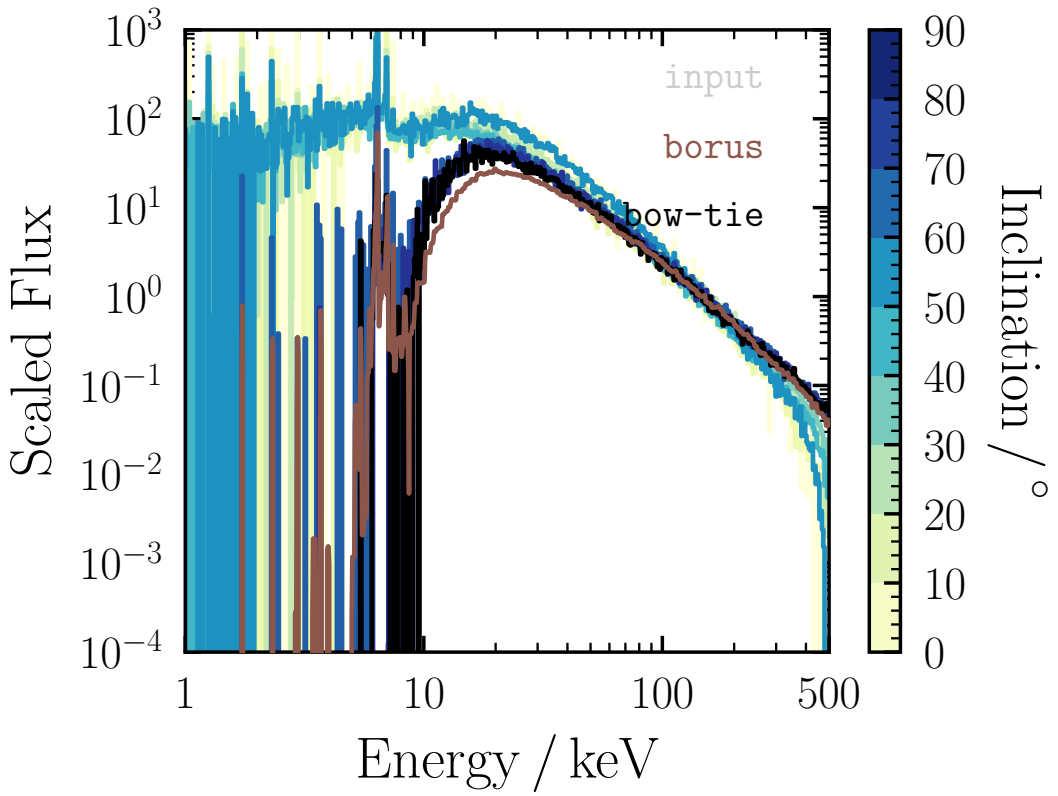

FIGURE 6.4: The resulting spectra for particular torus parameters. The observed inclination dependence is in close agreement with the analogous `borus02` model that simulates an identical geometry.

counterpart in the 70-month *Swift*/BAT survey. Good-quality optical spectra with X-SHOOTER will be able to stringently confirm, or provide upper limits to the presence of powerful AGN in each source that are potentially heavily obscured at X-ray wavelengths, due to its improved sensitivities on any existing optical spectroscopic constraints.

The second sample is a large programme with VLT/VISIR to follow-up an alternative warm *IRAS* sample (derivation akin to the NuLANDS sample but for the updated *IRAS* Point Source Catalog v2.1) with high-angular resolution infrared photometry and spectroscopy. Just as the seminal work by Gandhi *et al.* (2009) and Asmus *et al.* (2015) showed, such high angular resolution of local AGN candidates is capable of tracing the true intrinsic luminosity of the AGN output in the mid-infrared, largely unaffected by host-galaxy contamination.

The *extended ROentgen Survey with an Imaging Telescope Array* (*eROSITA*; Merloni *et al.* 2012) will carry out an extensive all-sky *true* imaging survey in the 0.5 – 2 keV 20 times more sensitive than *ROSAT* as well as in the 2 – 10 keV band for the first time. This survey is expected to yield a sample of $\sim$3 million AGN, and I am a team member for the Local AGN Search with *eROSITA* (LASeR; Asmus et al., in prep.). LASeR is using the observed deficit vs. surplus of X-ray vs. infrared flux (respectively) known to

indicate obscured AGN (see e.g., Figure 4.10). LASeR will essentially derive the first complete census of AGN activity within a strict volume and intrinsic luminosity cut. The primary goal of LASeR will be to provide the first complete selection of intrinsically powerful AGN, unbiased by obscuration effects present in individual wavebands. By gaining a full picture of the AGN population within the very local cosmological volume, we will gain powerful insights for cosmological simulations that critically require the local population as a boundary condition (e.g., population synthesis of the CXB; Ueda *et al.* 2014; Ananna *et al.* 2019).

In the distant future with radio flux detection thresholds reaching the micro and nano Jy regime in the coming years, the underlying AGN population is representatively attainable in the distant Universe for the first time (Padovani *et al.* 2017). In particular, galaxy and AGN studies with the Square Kilometer Array (e.g., Jarvis 2007, Pacific Conference Series-380-251) will provide obscuration-unbiased samples of AGN out to considerably more distant redshifts than have been attainable previously. For example, the ASKAP Evolutionary Map of the Universe survey; Norris *et al.* 2011, Astron. Soc. of Australia-28-215; is predicted to detect $\sim$70 million galaxies – half of which will likely host AGN.

Current and ongoing large surveys of AGN will probe the true underlying AGN population. This thesis lays the foundations for future large surveys to build upon, as we head towards the first unbiased view of supermassive black hole activity across cosmic time.

6.3 Closing Remarks

Obscuration is a ubiquitous feature in AGN, yet still after more than half a century since the dawn of X-ray astronomy, the generation of an understanding of obscured accretion across cosmic time is far from complete. I have demonstrated that through techniques incorporating high-sensitivity hard X-ray spectroscopy, multi-wavelength diagnostics and physically-motivated models, one can derive the underlying properties of obscured accretion.

Appendix A

IC 3639 – A New Bona Fide Compton-thick AGN Unveiled by *NuSTAR*

Here we include the contour plots between photon index and column density for both toroidal models T and M. The column density plotted for model T (Figure A.1, upper panel) corresponds to the line of sight column density, whereas the column used in the model M contour plot (Figure A.1, bottom panel) corresponds to the equatorial column density. To 99% confidence (blue contour line), the corresponding line of sight obscuring column density for both models is $\gtrsim 4 \times 10^{24}\,\mathrm{cm}^{-2}$ – well into the Compton-thick regime, and is unconstrained at the upper end allowed by either model. Although the model T contour plot illustrates a wider range in parameter space than the model M contour, the values found are clearly consistent between the two graphs.

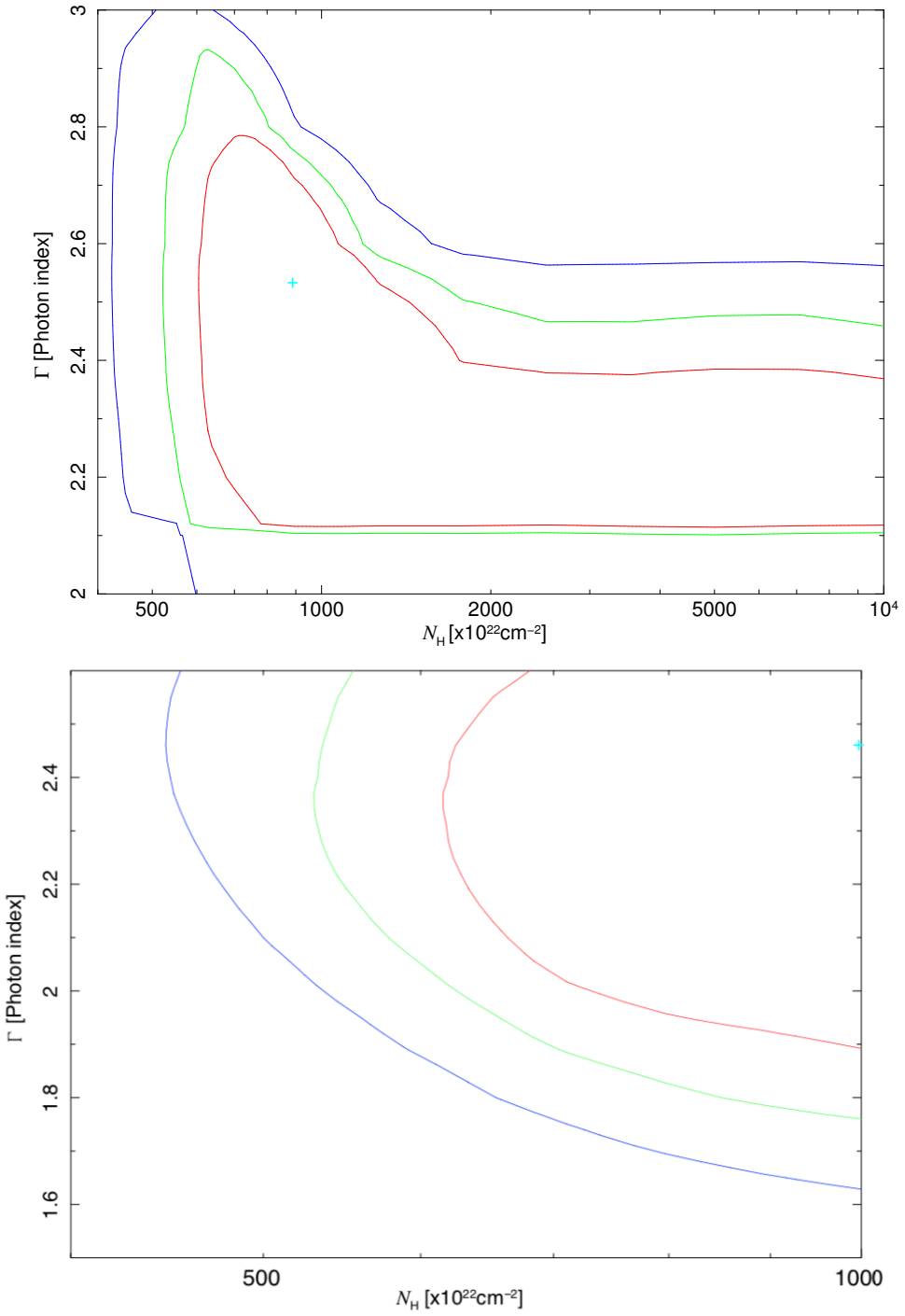

FIGURE A.1: Contour plots for the BNTORUS model (model T – upper panel), and MYTORUS model (model M – bottom panel), between power law photon index and obscuring column density. The model T contour shows the line of sight obscuring column density, whereas model M shows the equatorial column density. The line of sight column is Compton-thick to 99% confidence for both models. In addition, the plots illustrate the unconstrained nature of the obscuring column, even beyond the model maximum of $N_{\rm H} = 1.0 \times 10^{26}\,{\rm cm}^{-2}$ for model T. The red, green and blue contours represent the $1-\sigma$, 90% and 99% confidence levels, respectively. The cyan cross represents the best-fit values found with XSPEC.

Appendix B

An Iwasawa-Taniguchi Effect for Compton-thick Active Galactic Nuclei

All spectra presented here are plotted with energies in the source observed frame on the lower axis, with the source rest-frame energy shown on the upper axis. Sources with an additional `apec` component included in the spectral fit are shown with a corresponding label in their legend.

The grouping used is annotated on each plot and has one of two possibilities:

1. Binning by a minimum number of counts per bin.
2. Binning to have a minimum signal to noise ratio in each bin.

All sources were fitted with a simplified phenomenological model consisting of photoelectric absorption acting on a composite powerlaw (Γ, the photon index of the powerlaw was assigned to 1.4 for all cases) plus a narrow Gaussian of FWHM $\approx 2\,\mathrm{eV}$ ($\sigma = 1\,\mathrm{eV}$), modelling the observed continuum and narrow core of the Fe Kα fluorescence line, respectively. See Section 3.3 for further details on the spectral model adopted. The corresponding confidence contours shown (where applicable) in the top right panel illustrate a delta statistic of +2.30 to represent the 1-σ (68%) confidence level for two interesting parameters[1].

All spectra shown feature the spectral fit to the data and the DEL (defined as the (data − model)/error) for the fit in the top and bottom panels, respectively.

[1] https://heasarc.gsfc.nasa.gov/xanadu/xspec/manual/XSappendixStatistics.html

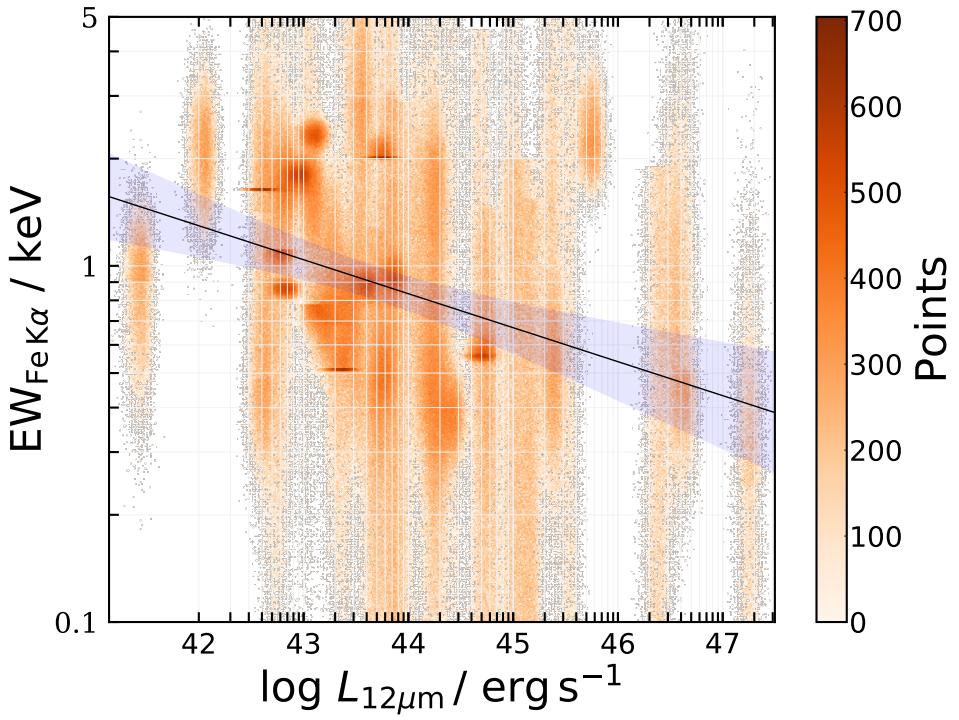

FIGURE B.1: Heatmap showing the simulated data points for a fitting procedure issued with 100,000 iterations, in which the data was reproduced this many times in order to account for the asymmetric errorbars and limits.

B.1 Testing our Monte Carlo Bootstrapping Fitting Code

In Figure B.1, I present the heatmap of all 100,000 simulated data points for one realisation of a fit to the EW data. As can be seen, marginal edge effects due to the presence of small numbers of extreme EW values are present – this is due to sources with lower limits on EW being restricted to $EW \leq 5\,keV$ and $EW \geq 0.01\,keV$. Since the vast majority of simulated data points are shown in the main body of the plotting region, this is evidence that the simulated data points were acceptable realisations of the data.

B.2 Sources Excluded

NuSTAR data was not publicly available for 19/55 low redshift sources from the *Neil Gehrels Swift Observatory*/BAT sample of Ricci *et al.* (2015), and so were excluded from this work. See Section 3.2.2 for more information. This excluded ESO 565-G019, which is in the Gandhi *et al.* (2014) bona-fide Compton-thick AGN sample, and has been studied individually in Gandhi *et al.* (2013) with *Suzaku* data.

In addition, our own analysis of the archival archival *XMM*-Newton EPIC/PN spectrum as compared to the more recent *NuSTAR* FPMA & FPMB spectra strongly indicated a changing-look AGN scenario for NGC 4102 and NGC 4939. These sources were thus excluded since changing-look AGN could adhere to variable obscuration effects.

Finally, 5 sources had observed rest-frame 2 – 10 keV fluxes in agreement with the interpolated rest-frame 12 μm, predicted from the relation presented in Asmus *et al.* (2015). These 5 sources were ruled out from our sample, and their spectra are shown in Figure B.2.

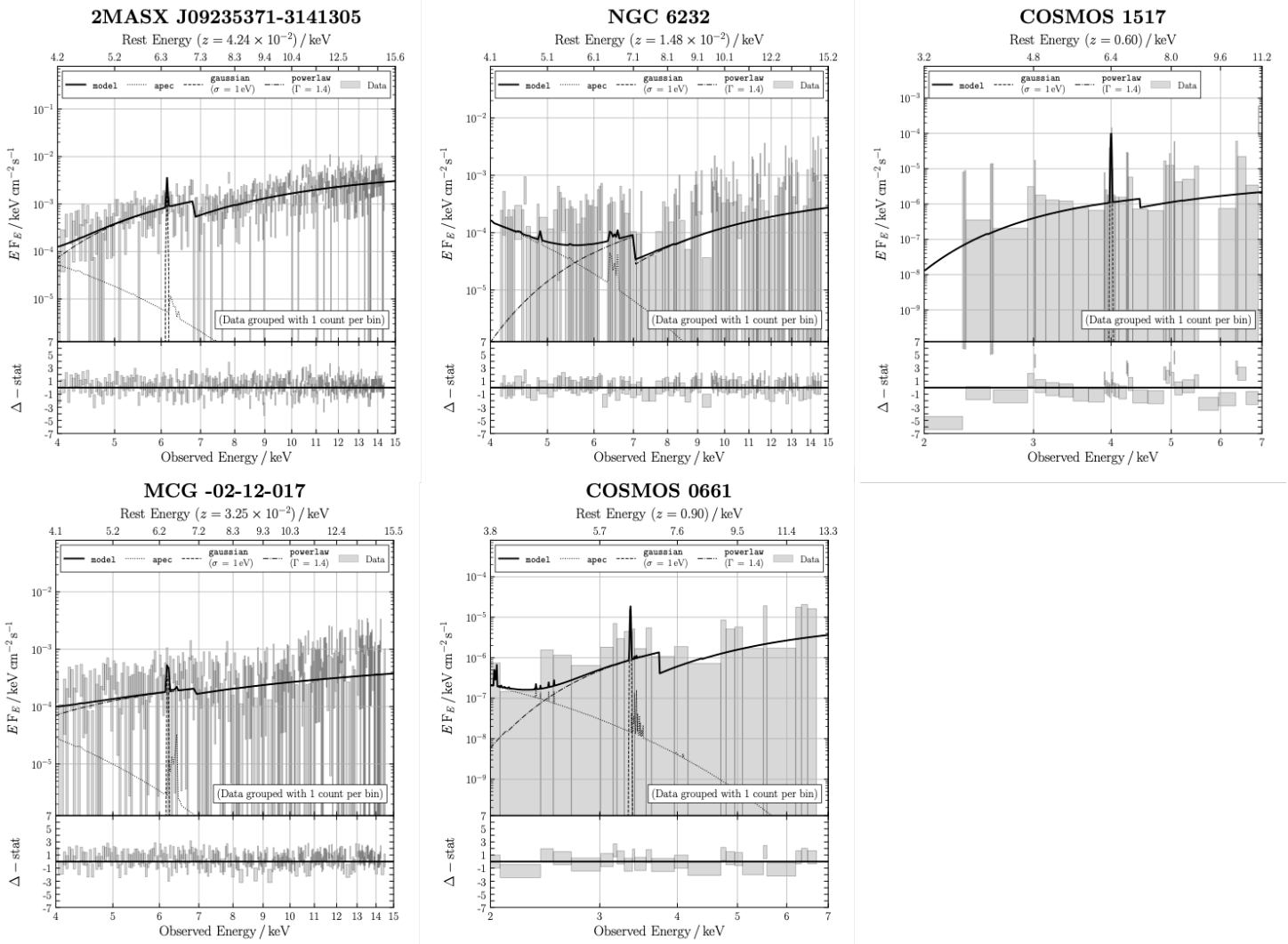

FIGURE B.2: Spectra of the 5 sources ruled out in our analysis due to an agreement with the Asmus *et al.* (2015) correlation between observed X-ray and mid-infrared luminosity, which can infer less than Compton-thick obscuration. For details of the spectrum, see the description at the start of the Appendix. The top and bottom panels show the spectral fit to the data and the DEL (defined as the (data − model)/error) for the fit, respectively.

B.3 Sources Included

Here we include individual spectra and EW contours for the sources we derive EWs for ourselves. The sources are ordered in ascending $12\,\mu$m luminosity, as in Table 1 of the paper. We used the limit derived from best-fit parameters for 3 sources that the contour method did not provide a reasonable constraint for. These sources are: COSMOS 0581, COSMOS 0987 and CDFS 460. Furthermore, due to an unphysical EW determined for CDFS 443, CDFS 454 and COSMOS 2180, we fixed the EW for these sources to be $< 5\,$keV.

The upper right panel for each source figure indicates the contour plot for the EW, with the grid best-fit values shown as faint grey points. Statistical details of the spectral fit are tabulated in the bottom right panel of each source figure. All uncertainties shown from the intersection of the horizontal black line with the solid line contour correspond to the 68% confidence level for two interesting parameters.

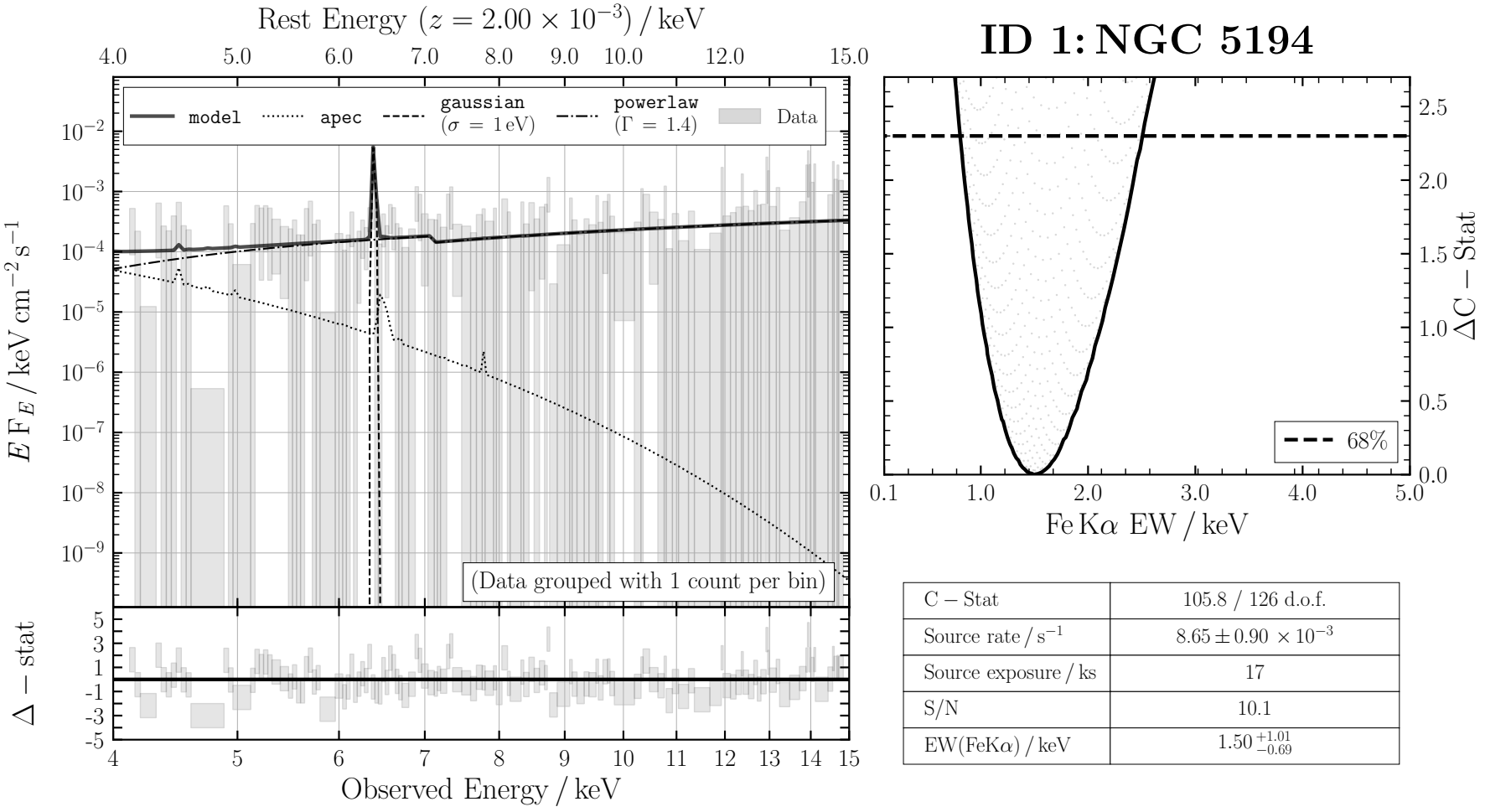

C − Stat	105.8 / 126 d.o.f.
Source rate / s^{-1}	$8.65 \pm 0.90 \times 10^{-3}$
Source exposure / ks	17
S/N	10.1
EW(FeKα) / keV	$1.50^{+1.01}_{-0.69}$

FIGURE B.3: ID 1: NGC 5194

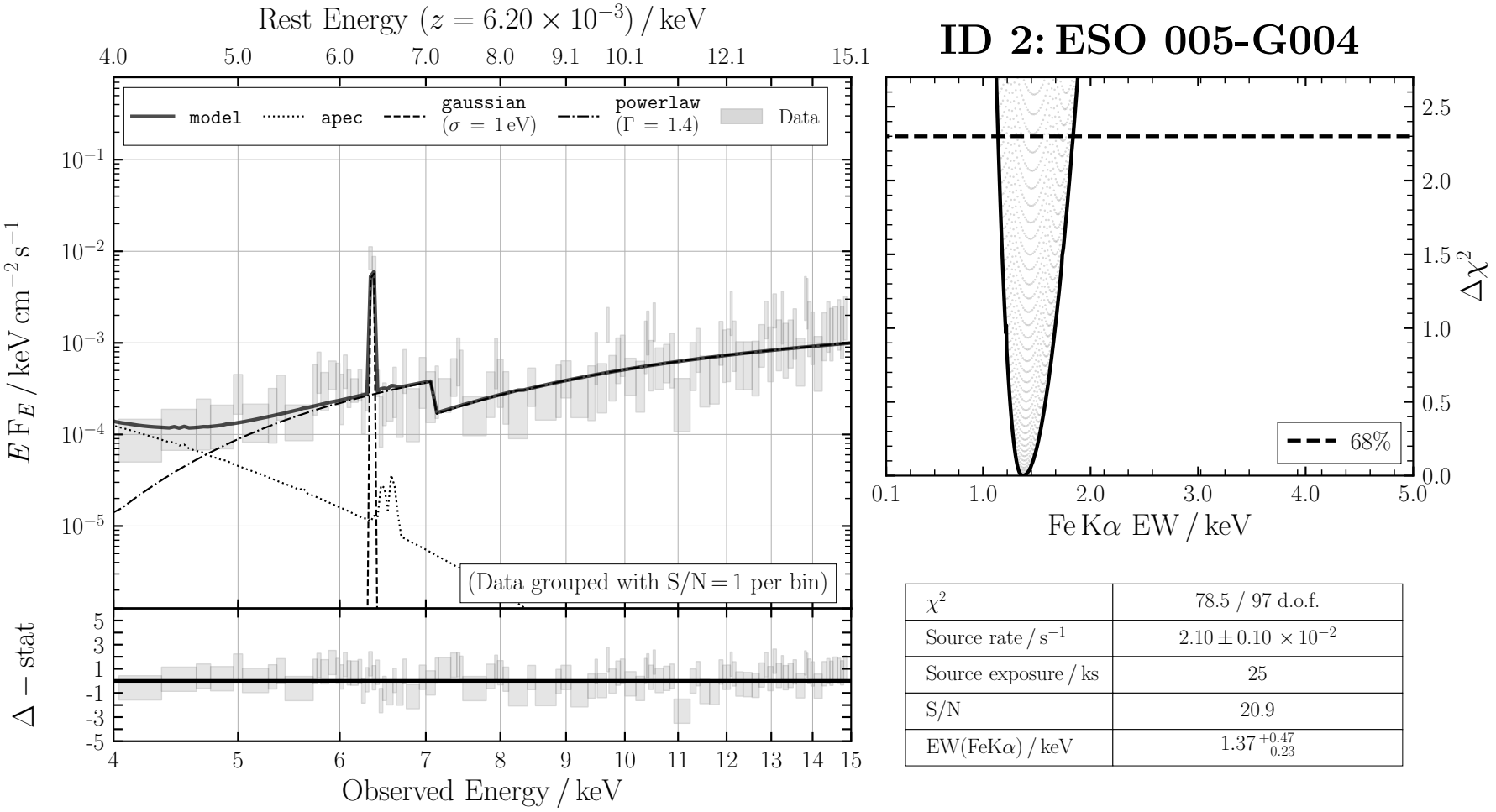

χ^2	78.5 / 97 d.o.f.
Source rate / s^{-1}	$2.10 \pm 0.10 \times 10^{-2}$
Source exposure / ks	25
S/N	20.9
EW(FeKα) / keV	$1.37^{+0.47}_{-0.23}$

FIGURE B.4: ID 2: ESO 005-G004

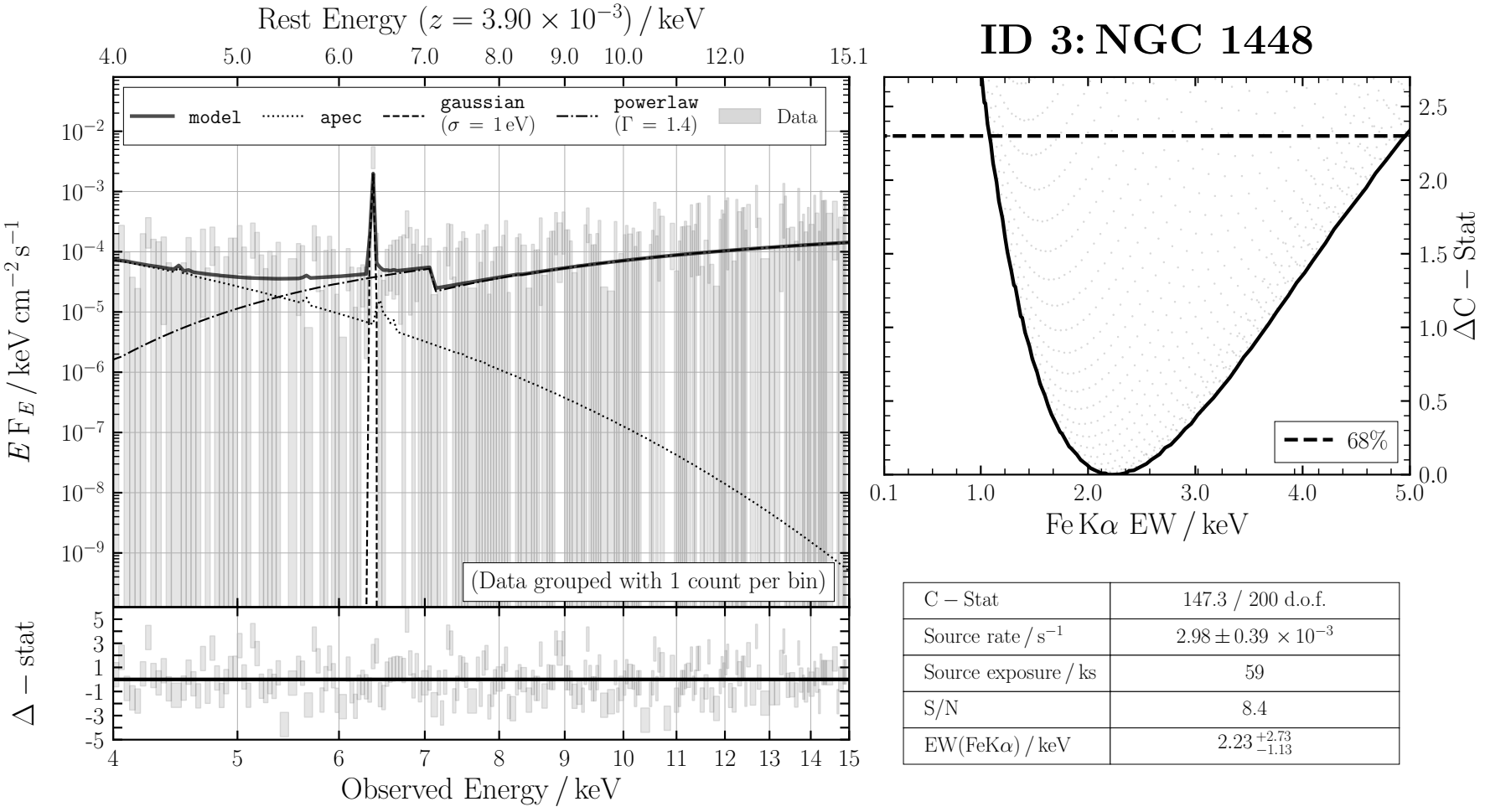

C − Stat	147.3 / 200 d.o.f.
Source rate / s^{-1}	$2.98 \pm 0.39 \times 10^{-3}$
Source exposure / ks	59
S/N	8.4
EW(FeKα) / keV	$2.23^{+2.73}_{-1.13}$

FIGURE B.5: ID 3: NGC 1448

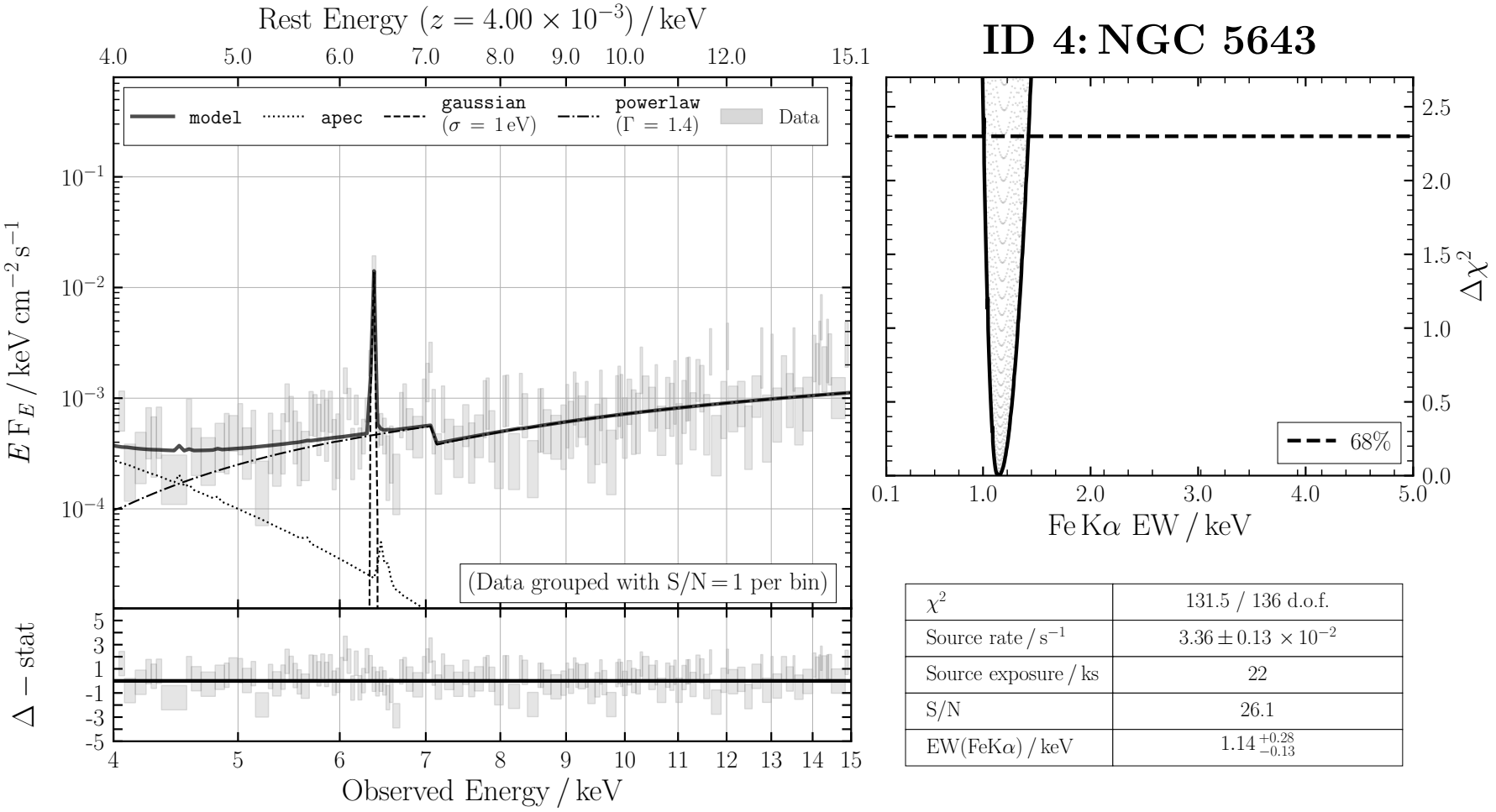

χ^2	131.5 / 136 d.o.f.
Source rate / s^{-1}	$3.36 \pm 0.13 \times 10^{-2}$
Source exposure / ks	22
S/N	26.1
EW(FeKα) / keV	$1.14^{+0.28}_{-0.13}$

Figure B.6: ID 4: NGC 5643

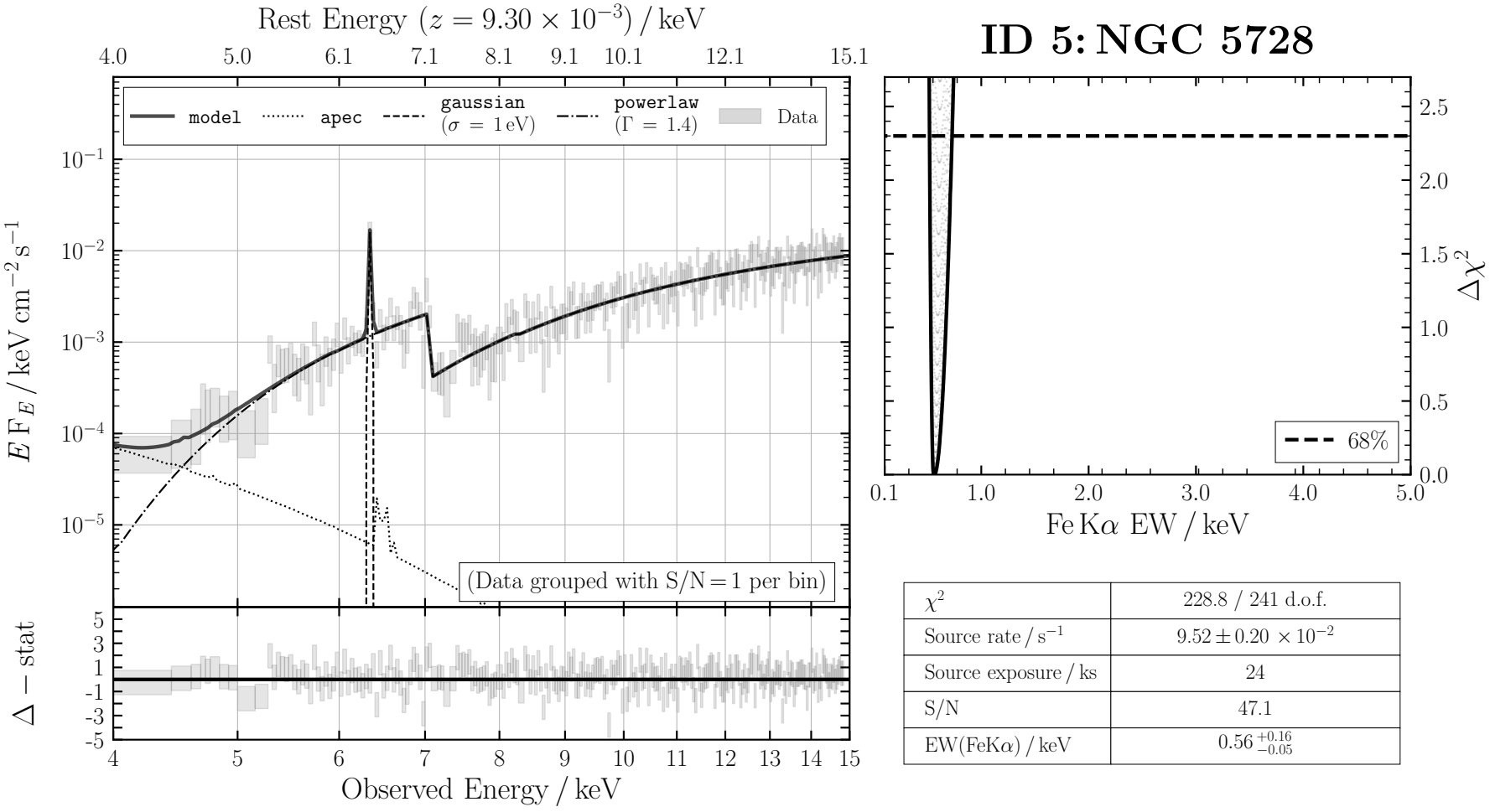

χ^2	228.8 / 241 d.o.f.
Source rate / s^{-1}	$9.52 \pm 0.20 \times 10^{-2}$
Source exposure / ks	24
S/N	47.1
EW(FeKα) / keV	$0.56^{+0.16}_{-0.05}$

FIGURE B.7: ID 5: NGC 5728

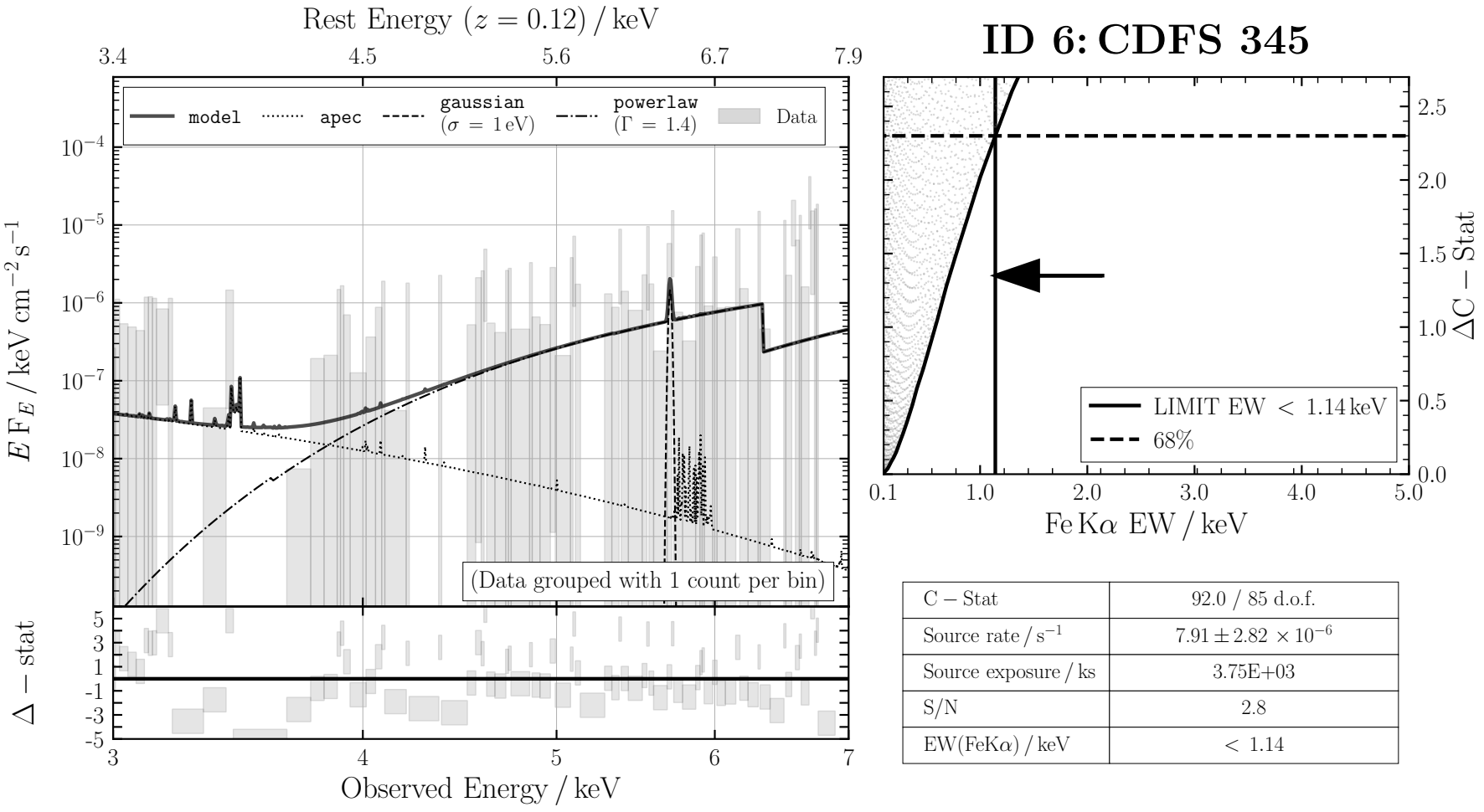

C − Stat	92.0 / 85 d.o.f.
Source rate / s^{-1}	$7.91 \pm 2.82 \times 10^{-6}$
Source exposure / ks	3.75E+03
S/N	2.8
EW(FeKα) / keV	< 1.14

FIGURE B.8: ID 6: CDFS 345

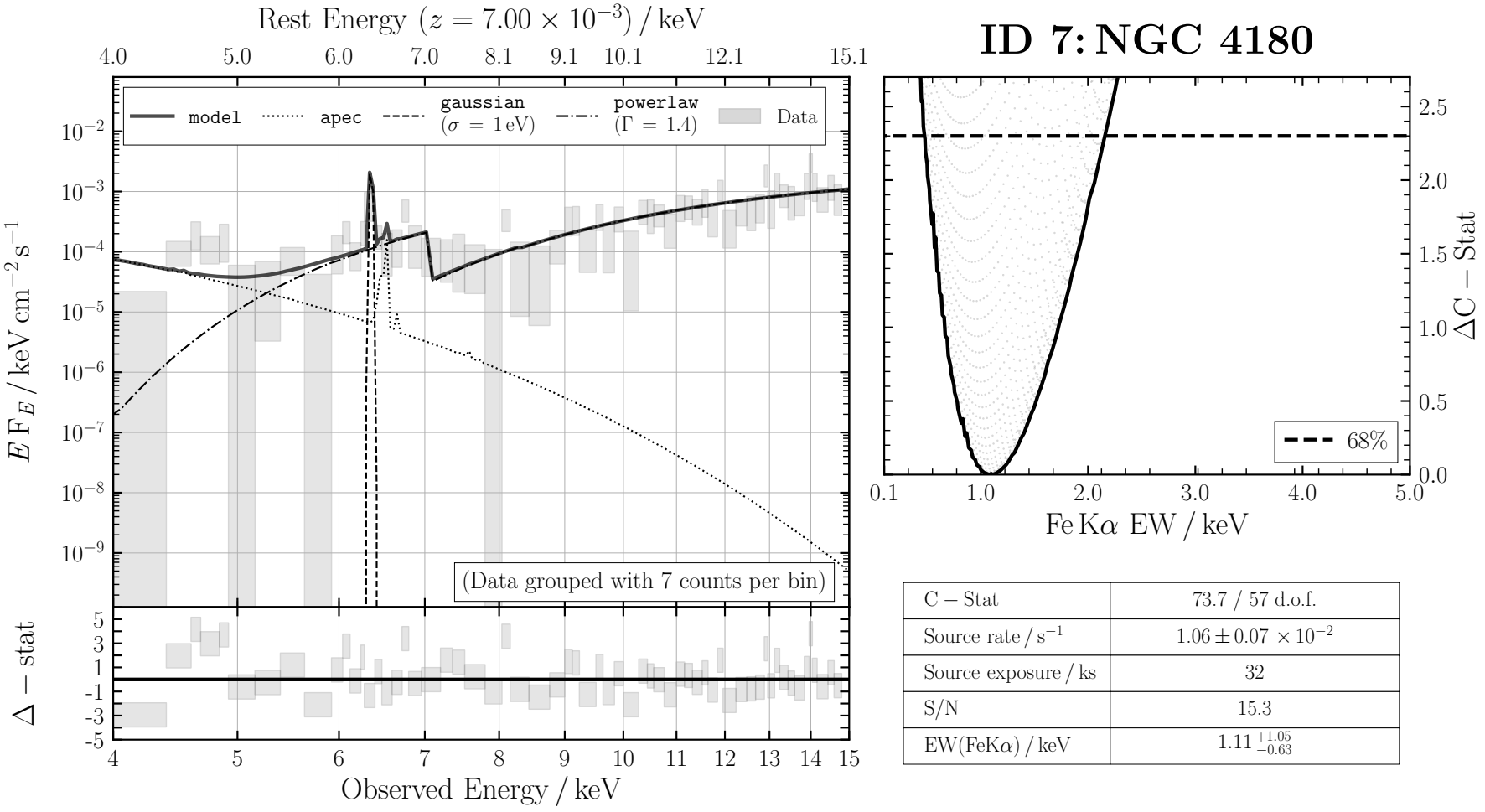

C − Stat	73.7 / 57 d.o.f.
Source rate / s^{-1}	$1.06 \pm 0.07 \times 10^{-2}$
Source exposure / ks	32
S/N	15.3
EW(FeKα) / keV	$1.11^{+1.05}_{-0.63}$

FIGURE B.9: ID 7: NGC 4180

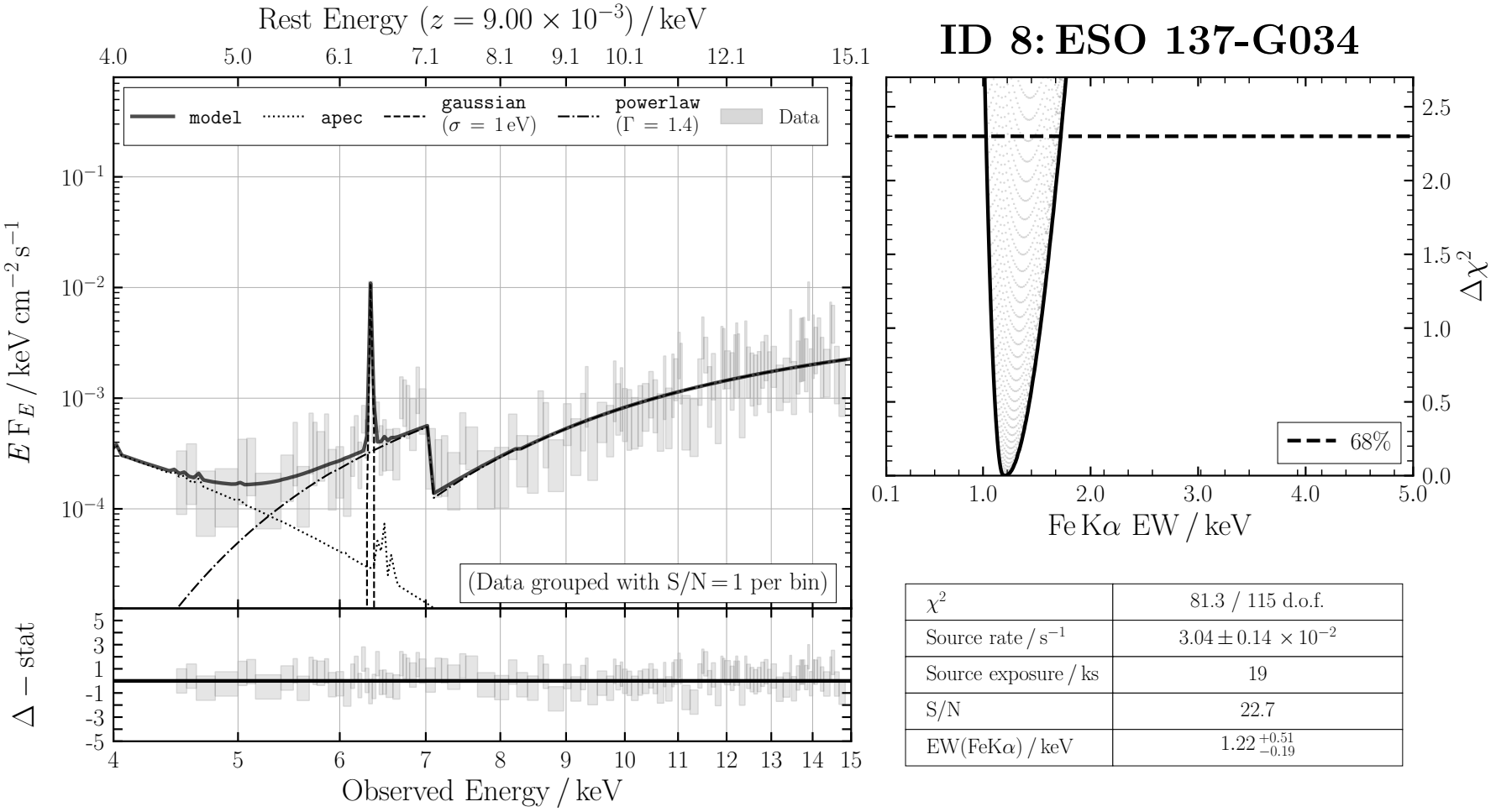

χ^2	81.3 / 115 d.o.f.
Source rate / s^{-1}	$3.04 \pm 0.14 \times 10^{-2}$
Source exposure / ks	19
S/N	22.7
EW(FeKα) / keV	$1.22^{+0.51}_{-0.19}$

FIGURE B.10: ID 8: ESO 137-G034

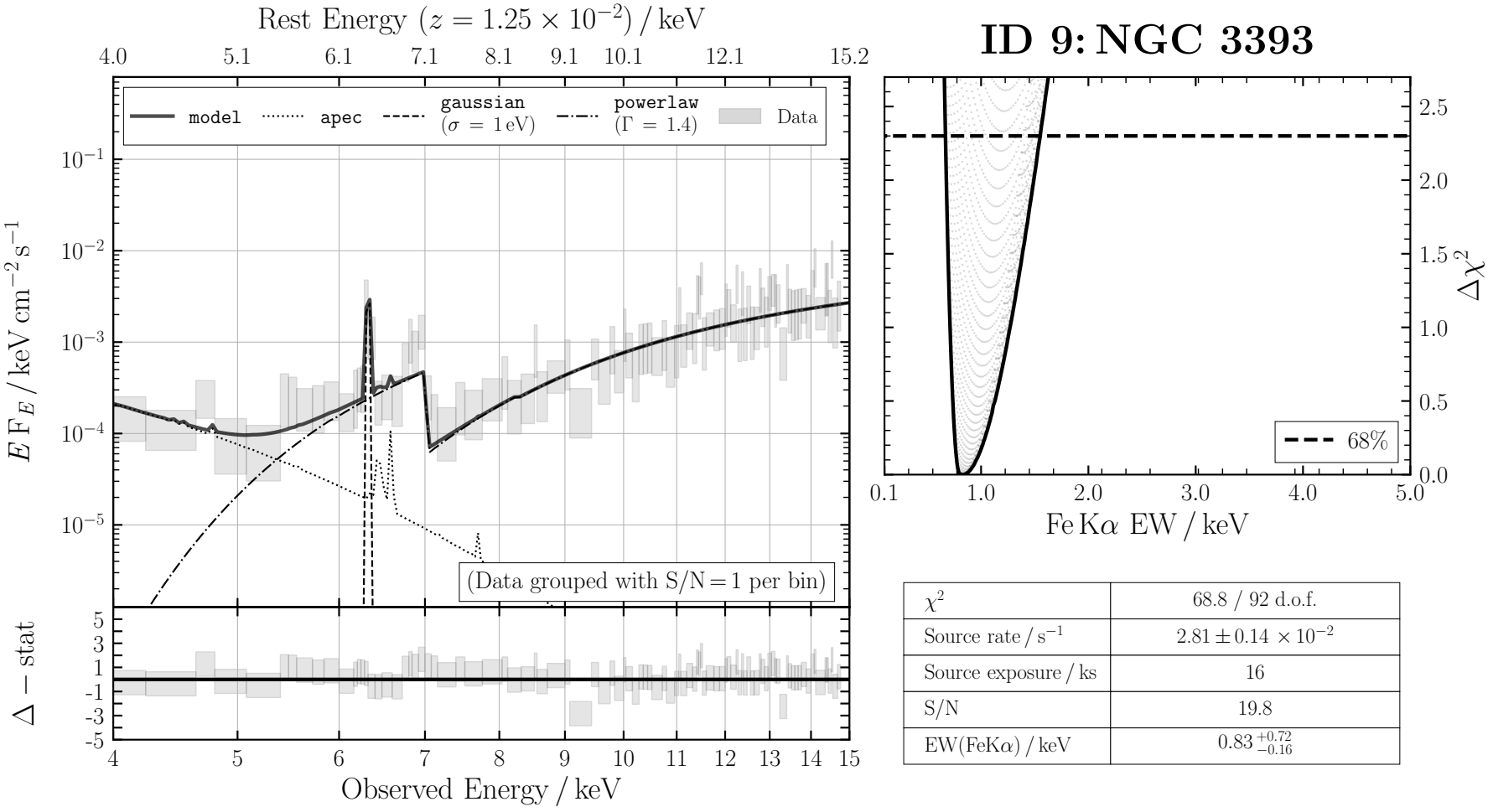

χ^2	68.8 / 92 d.o.f.
Source rate / s^{-1}	$2.81 \pm 0.14 \times 10^{-2}$
Source exposure / ks	16
S/N	19.8
EW(FeKα) / keV	$0.83^{+0.72}_{-0.16}$

FIGURE B.11: ID 9: NGC 3393

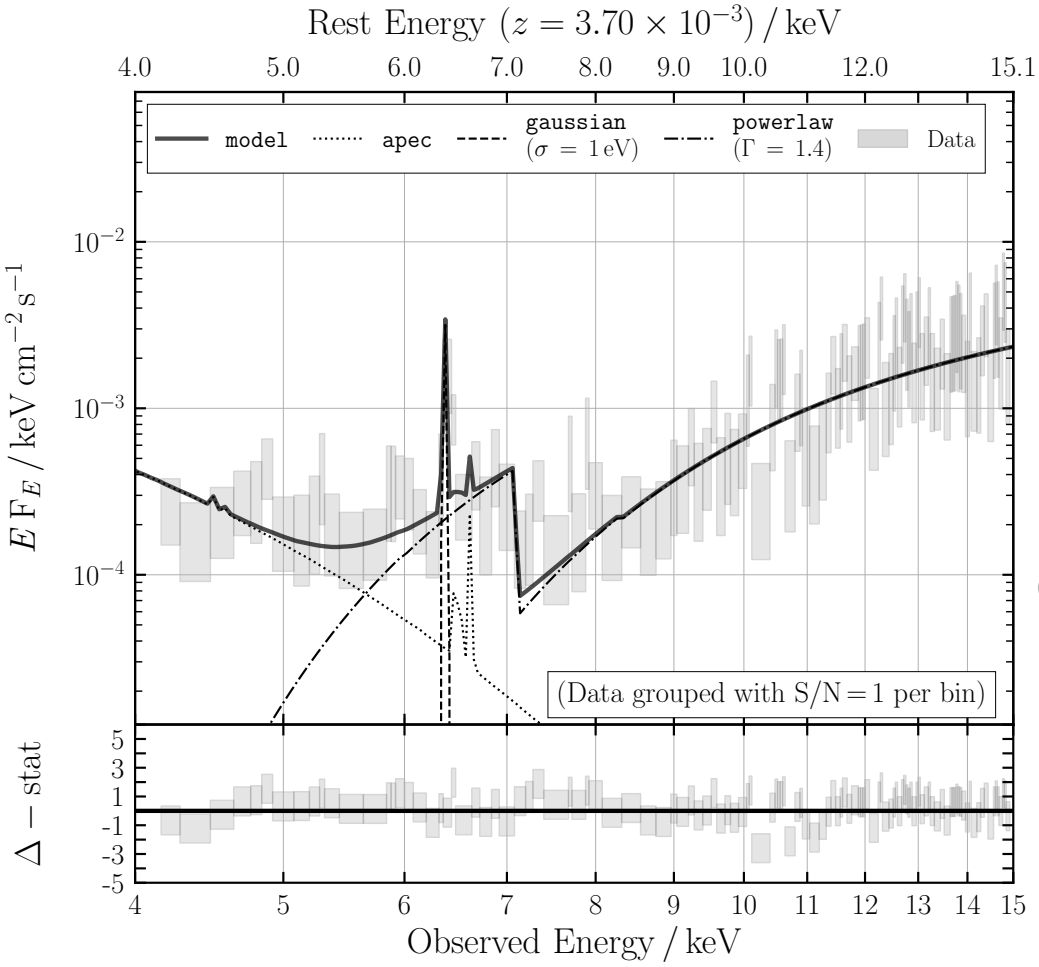

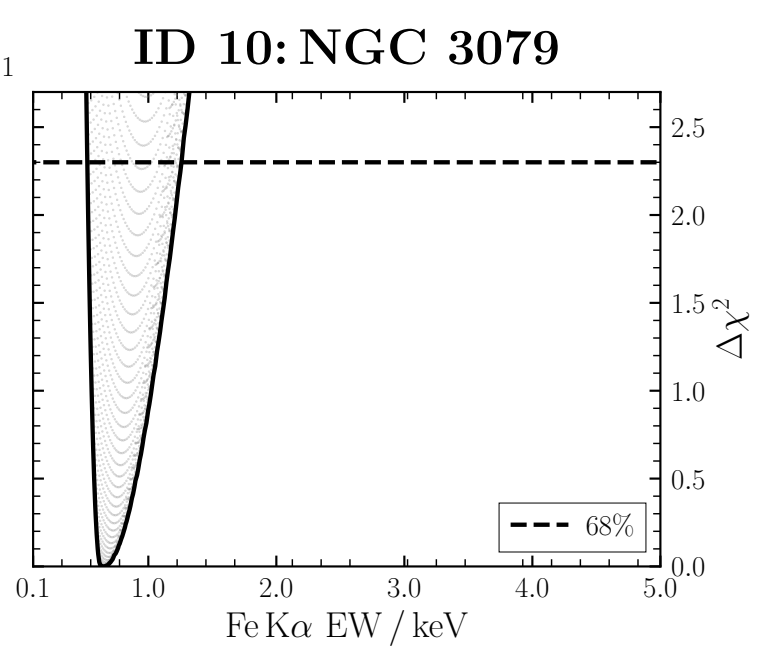

χ^2	93.0 / 114 d.o.f.
Source rate / s^{-1}	$2.55 \pm 0.12 \times 10^{-2}$
Source exposure / ks	22
S/N	22.1
EW(FeKα) / keV	$0.65\,^{+0.61}_{-0.12}$

FIGURE B.12: ID 10: NGC 3079

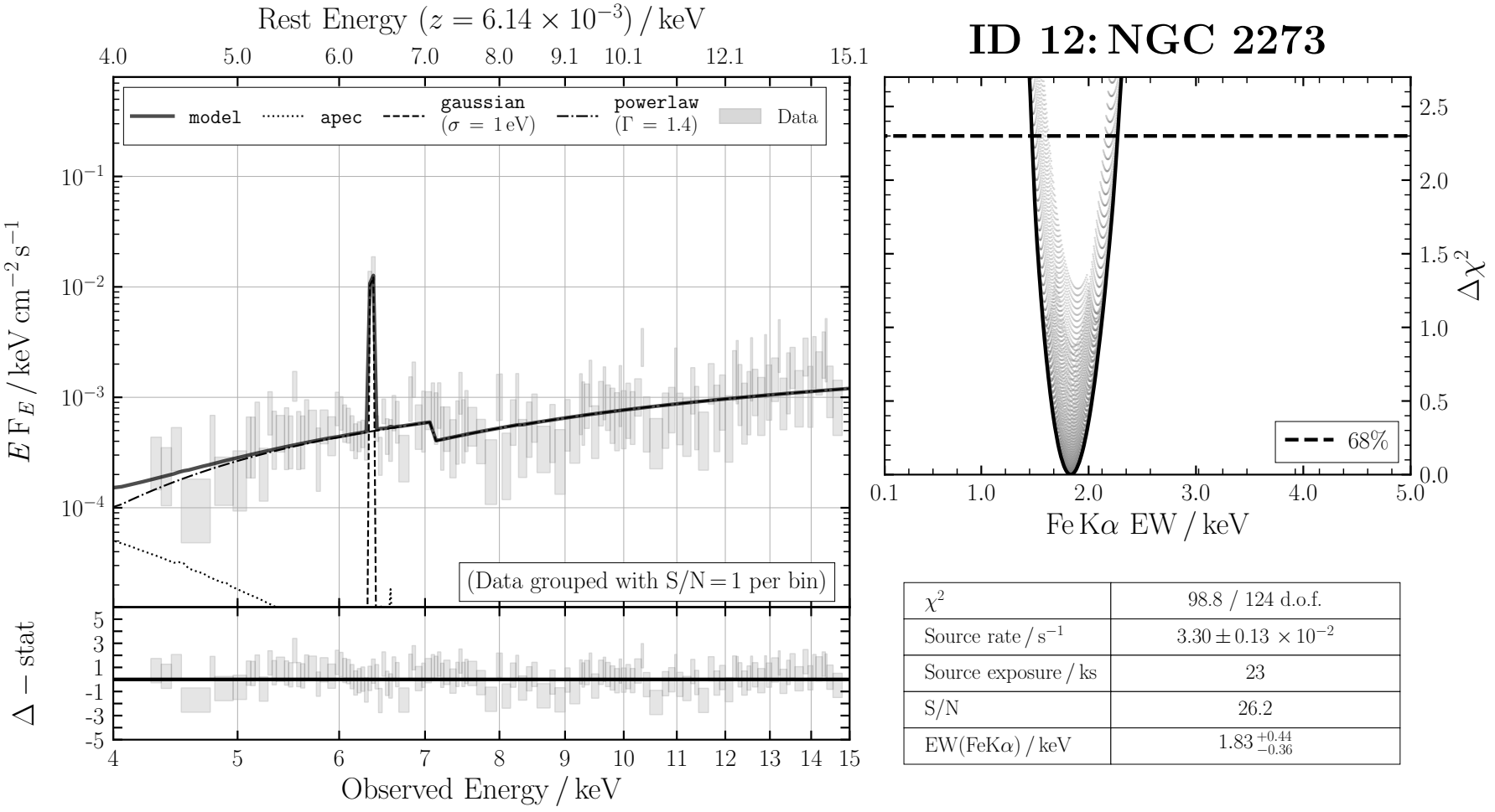

χ^2	98.8 / 124 d.o.f.
Source rate / s^{-1}	$3.30 \pm 0.13 \times 10^{-2}$
Source exposure / ks	23
S/N	26.2
EW(FeKα) / keV	$1.83^{+0.44}_{-0.36}$

FIGURE B.13: ID 12: NGC 2273

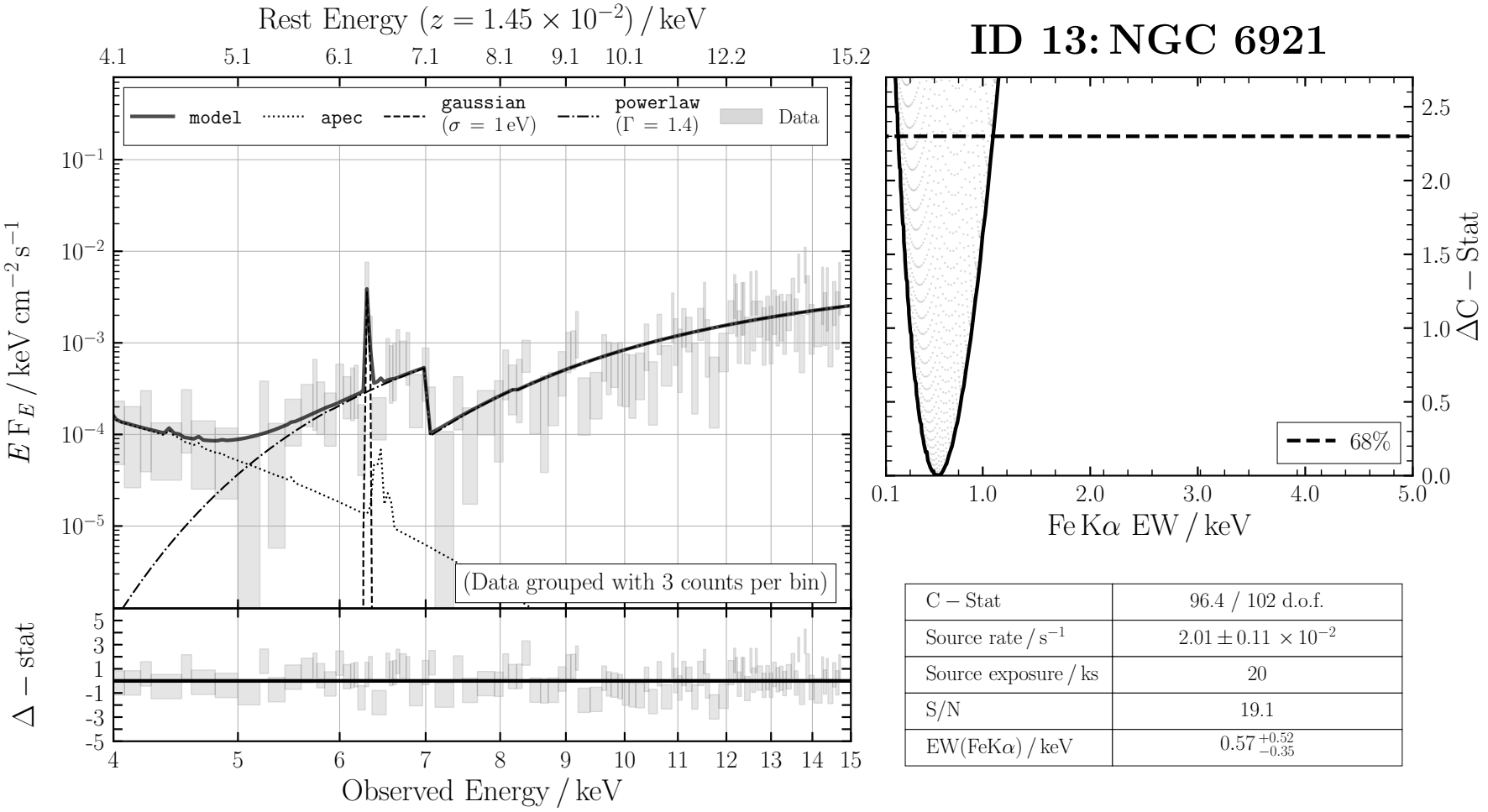

C − Stat	96.4 / 102 d.o.f.
Source rate / s^{-1}	$2.01 \pm 0.11 \times 10^{-2}$
Source exposure / ks	20
S/N	19.1
EW(FeKα) / keV	$0.57^{+0.52}_{-0.35}$

FIGURE B.14: ID 13: NGC 6921

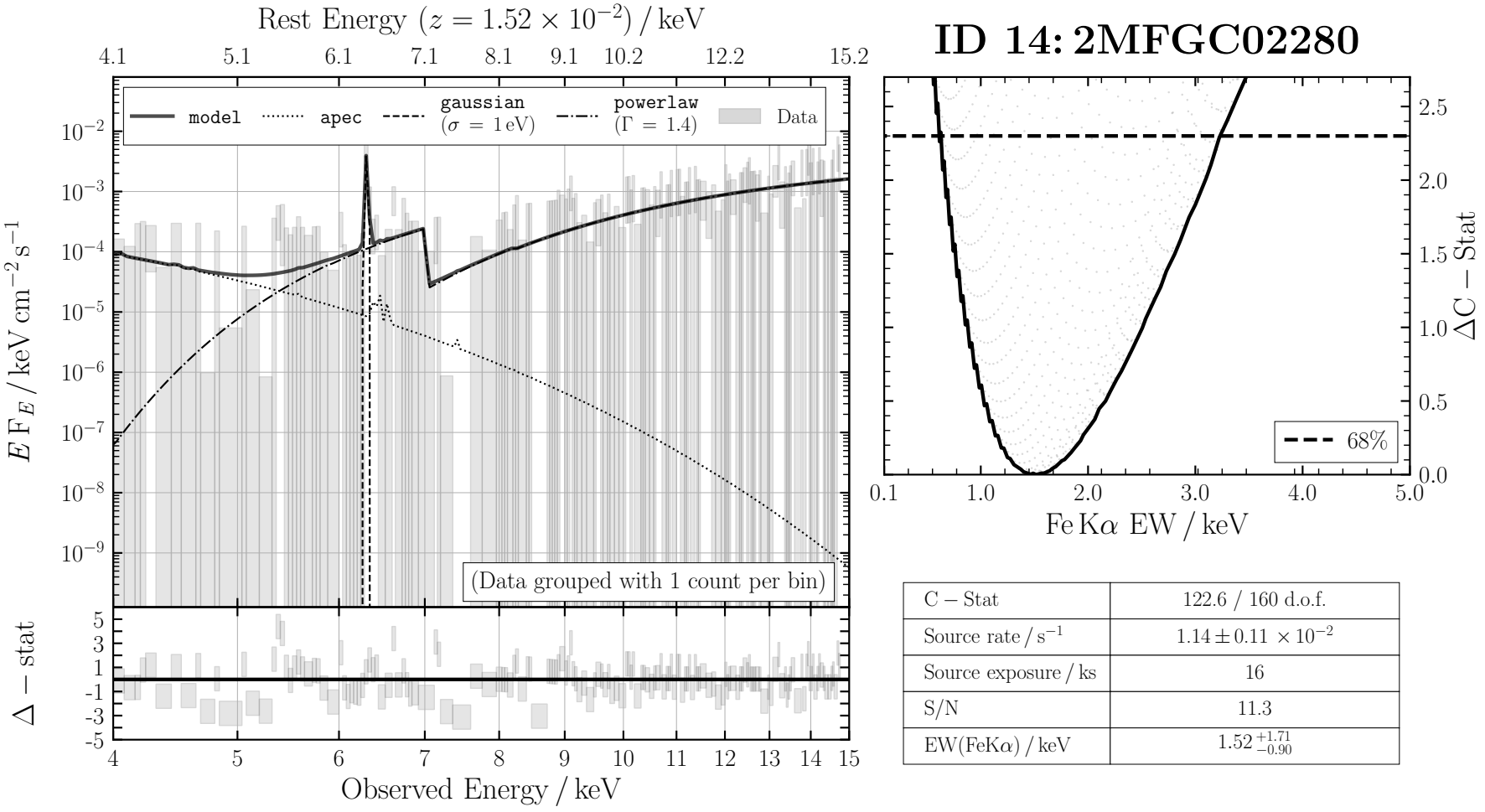

C − Stat	122.6 / 160 d.o.f.
Source rate / s^{-1}	$1.14 \pm 0.11 \times 10^{-2}$
Source exposure / ks	16
S/N	11.3
EW(FeKα) / keV	$1.52^{+1.71}_{-0.90}$

FIGURE B.15: ID 14: 2MFGC02280

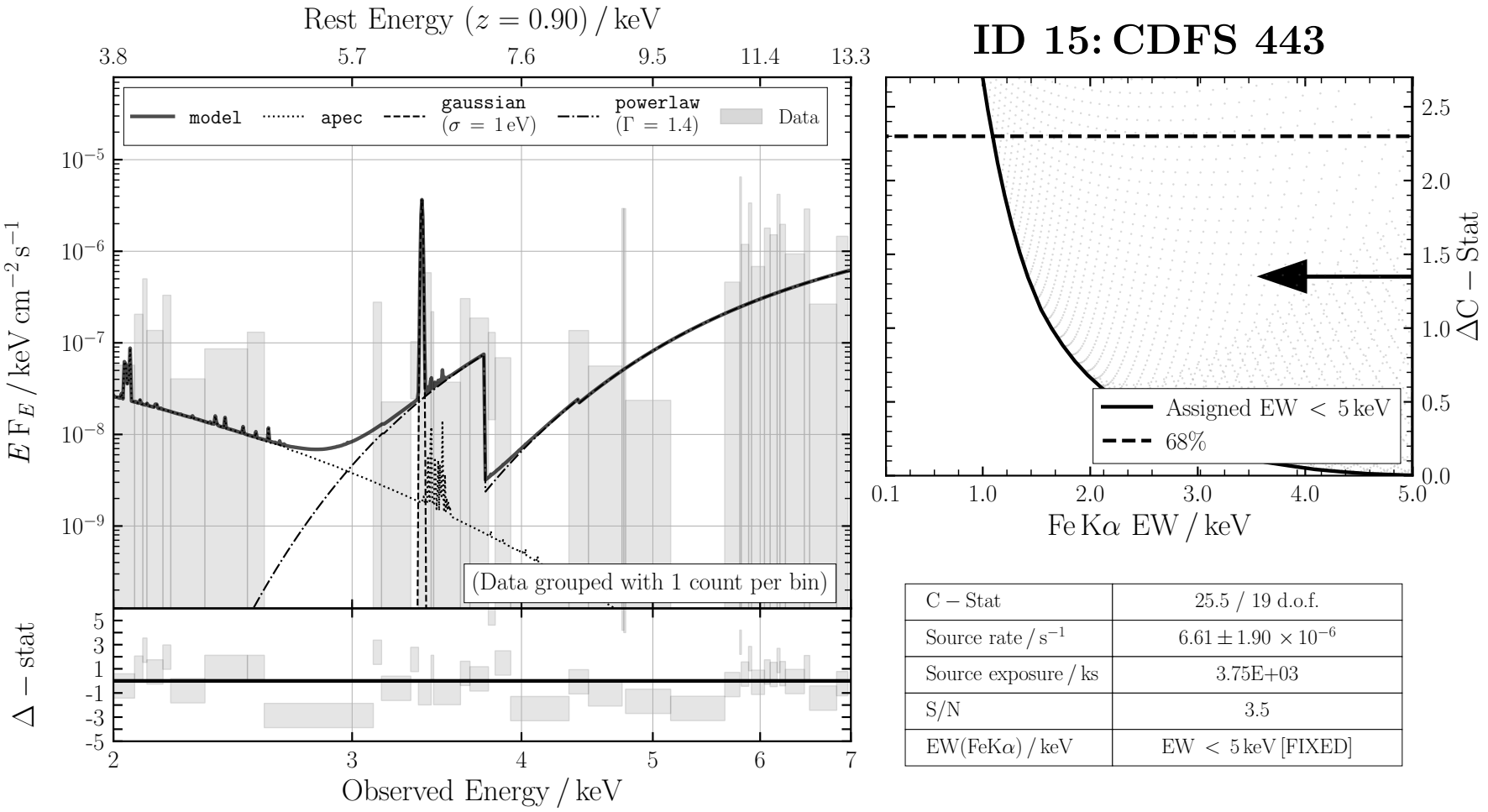

C − Stat	25.5 / 19 d.o.f.
Source rate / s^{-1}	$6.61 \pm 1.90 \times 10^{-6}$
Source exposure / ks	3.75E+03
S/N	3.5
EW(FeKα) / keV	EW < 5 keV [FIXED]

FIGURE B.16: ID 15: CDFS 443

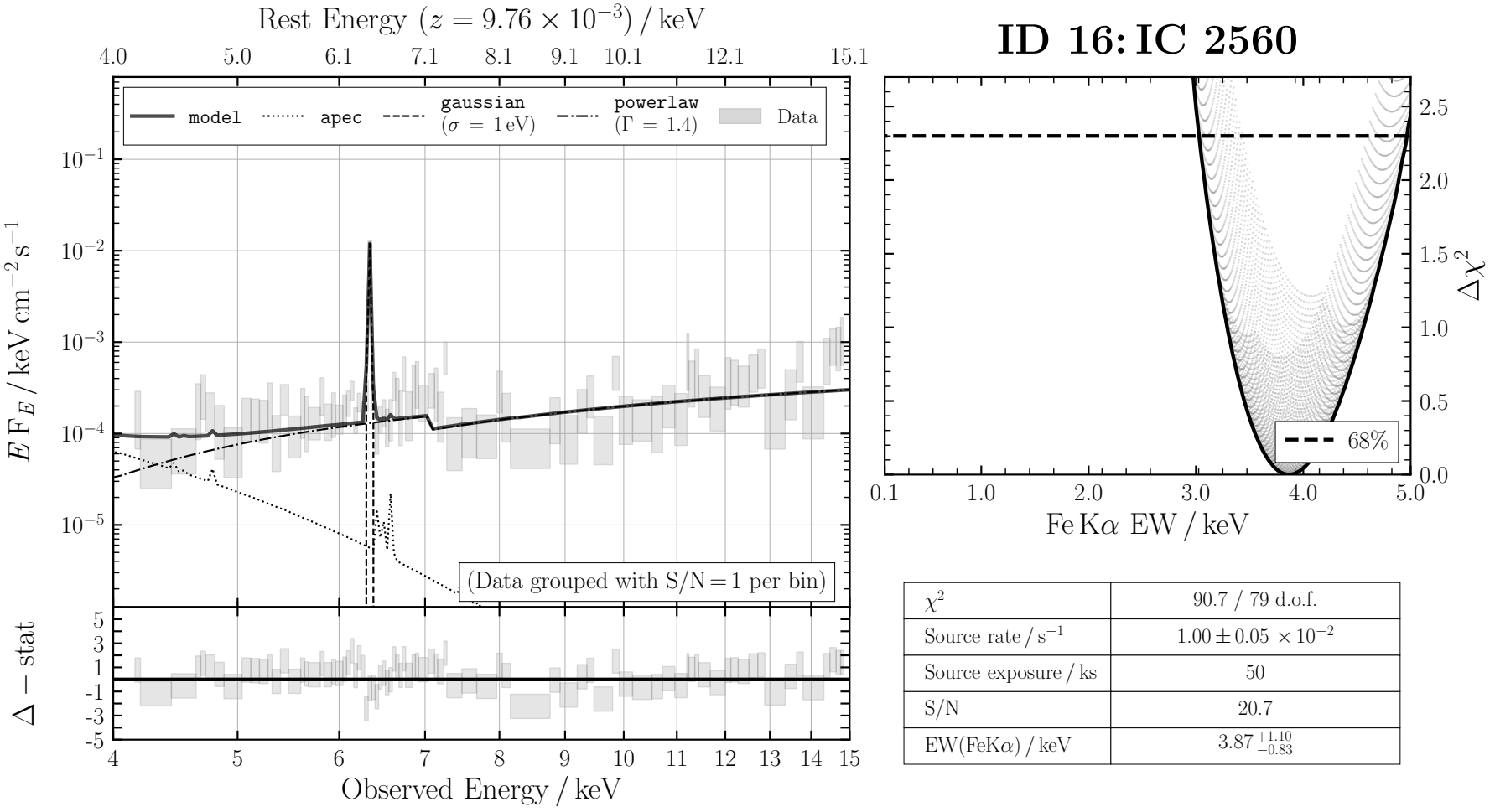

χ^2	90.7 / 79 d.o.f.
Source rate / s^{-1}	$1.00 \pm 0.05 \times 10^{-2}$
Source exposure / ks	50
S/N	20.7
EW(FeKα) / keV	$3.87^{+1.10}_{-0.83}$

FIGURE B.17: ID 16: IC 2560

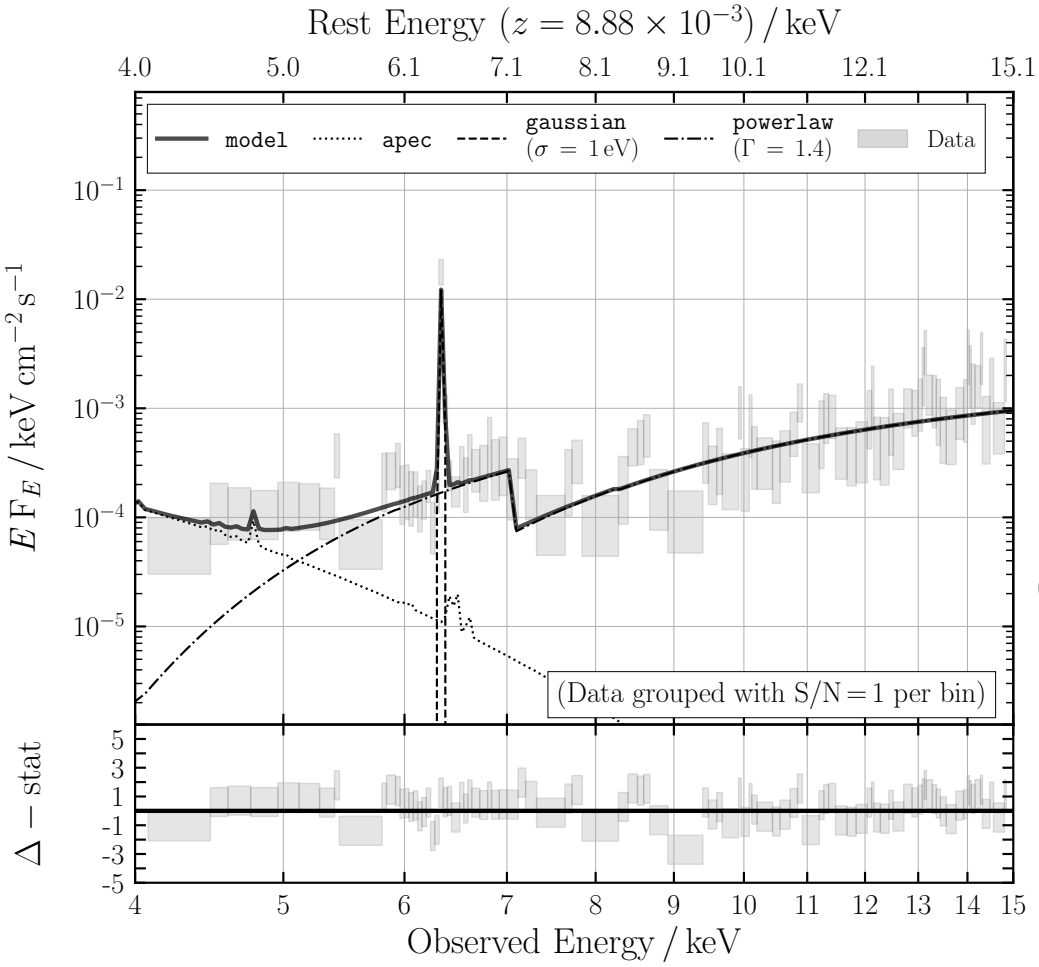

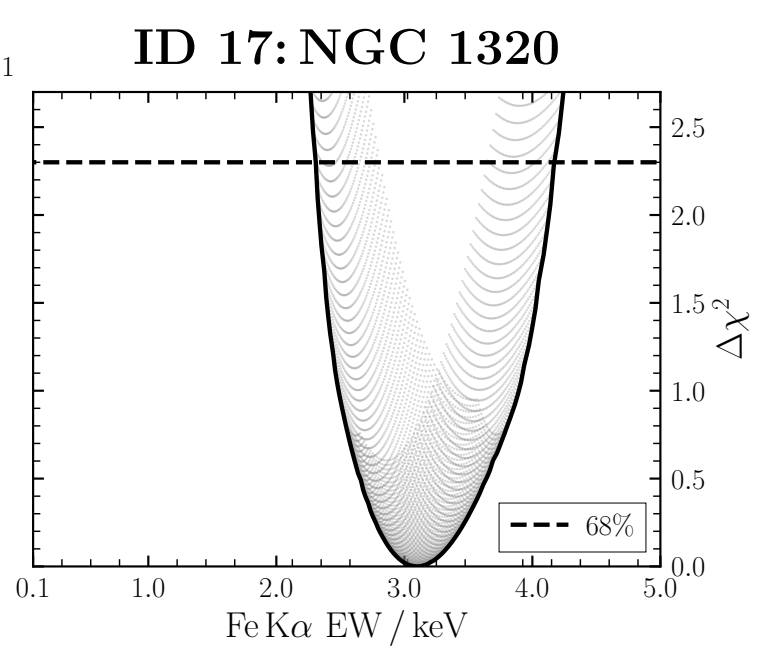

χ^2	85.2 / 89 d.o.f.
Source rate / s^{-1}	$1.80 \pm 0.09 \times 10^{-2}$
Source exposure / ks	28
S/N	20.7
EW(FeKα) / keV	$3.11\,^{+1.06}_{-0.78}$

FIGURE B.18: ID 17: NGC 1320

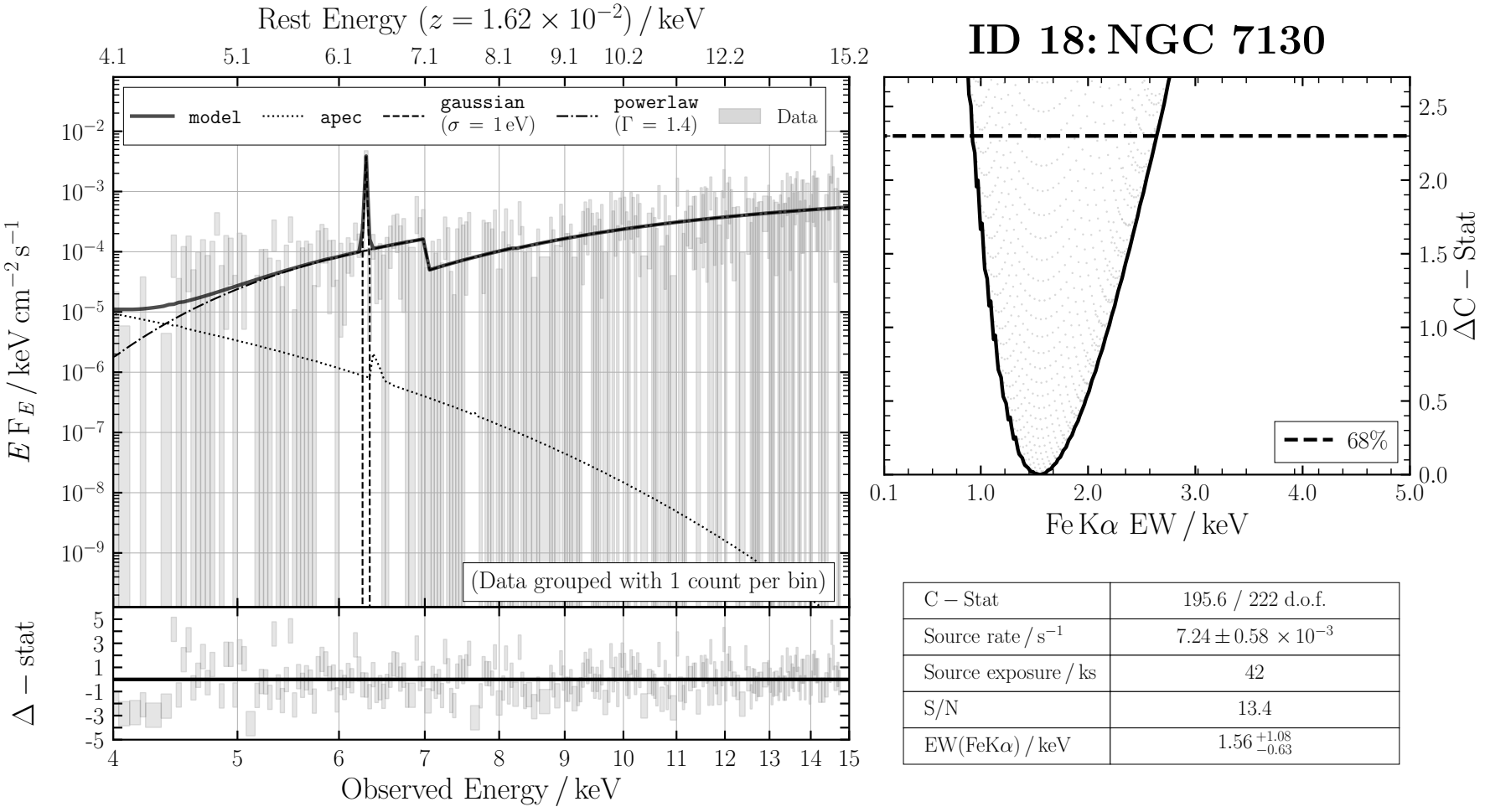

C − Stat	195.6 / 222 d.o.f.
Source rate / s^{-1}	$7.24 \pm 0.58 \times 10^{-3}$
Source exposure / ks	42
S/N	13.4
EW(FeKα) / keV	$1.56^{+1.08}_{-0.63}$

FIGURE B.19: ID 18: NGC 7130

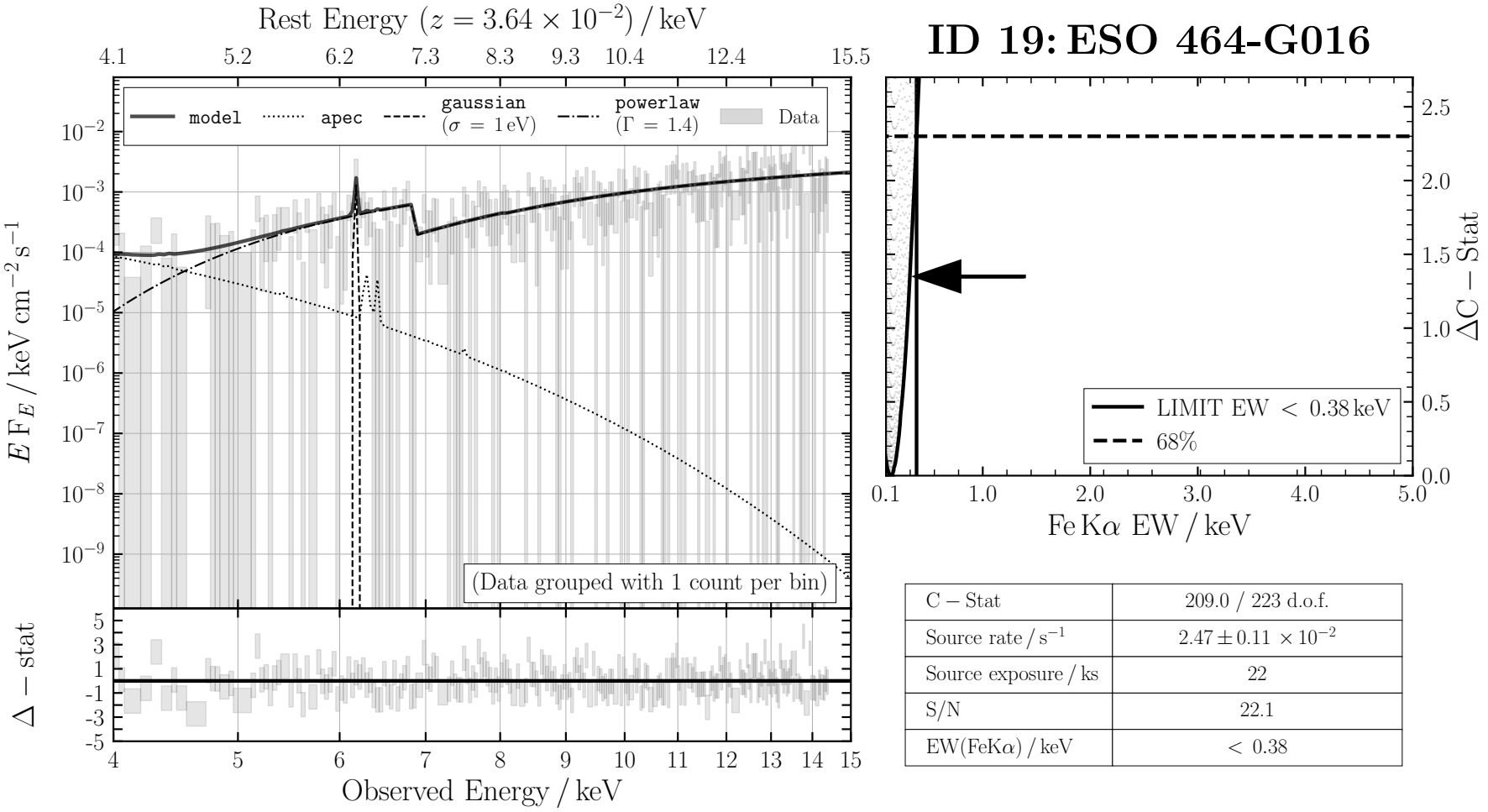

C − Stat	209.0 / 223 d.o.f.
Source rate / s^{-1}	$2.47 \pm 0.11 \times 10^{-2}$
Source exposure / ks	22
S/N	22.1
EW(FeKα) / keV	< 0.38

FIGURE B.20: ID 19: ESO 464-G016

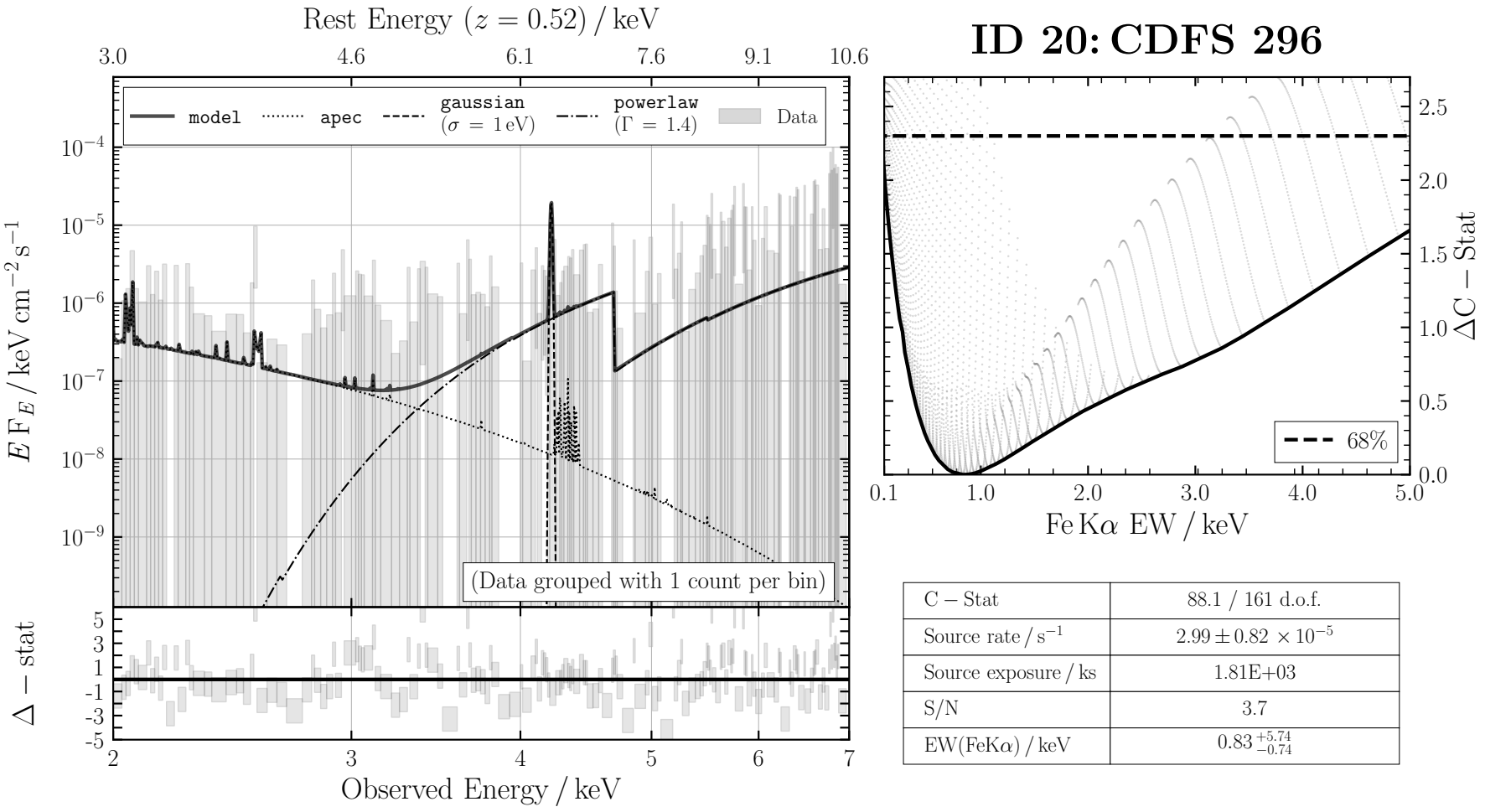

C − Stat	88.1 / 161 d.o.f.
Source rate / s^{-1}	$2.99 \pm 0.82 \times 10^{-5}$
Source exposure / ks	1.81E+03
S/N	3.7
EW(FeKα) / keV	$0.83\,^{+5.74}_{-0.74}$

FIGURE B.21: ID 20: CDFS 296

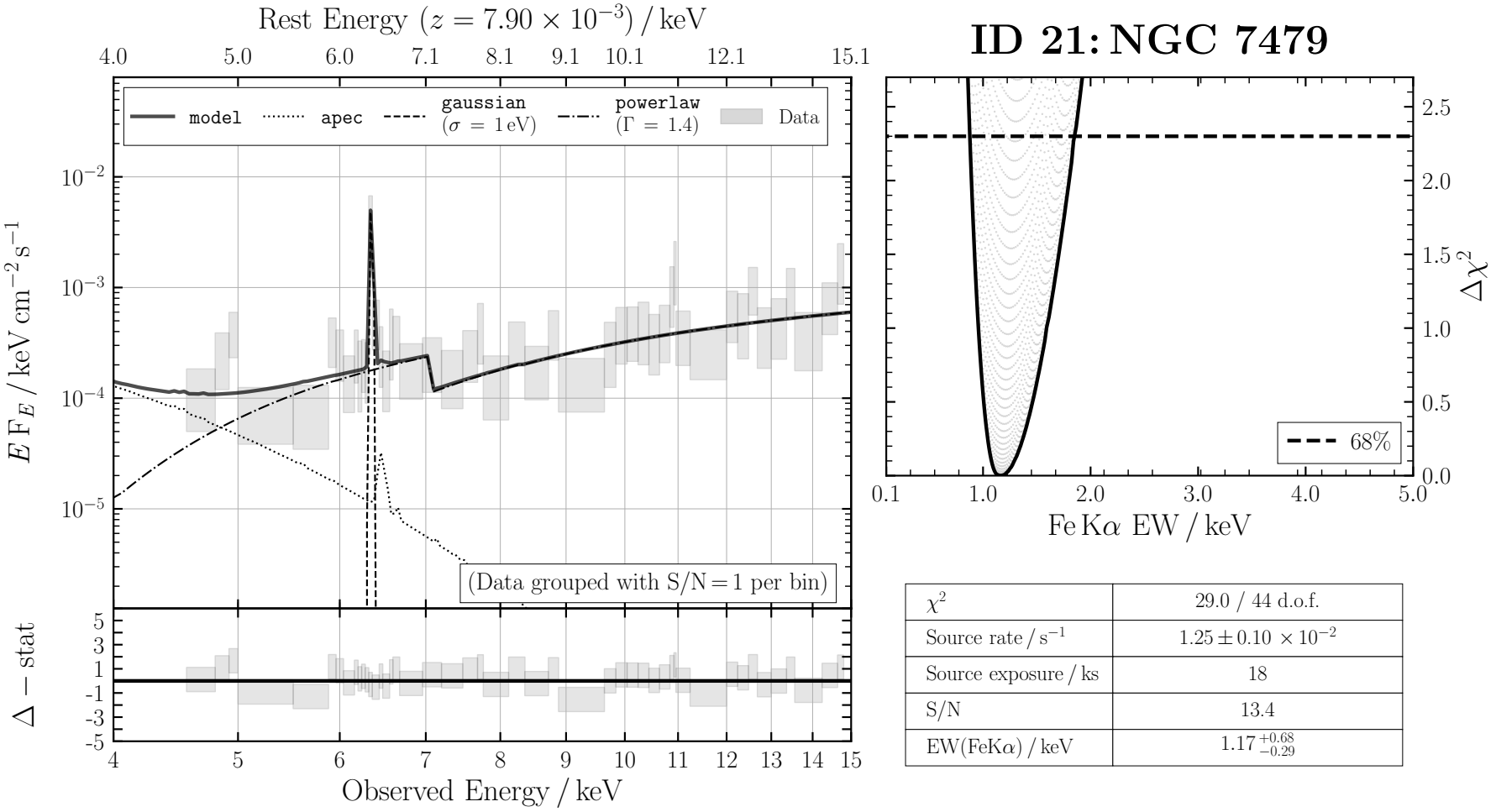

χ^2	29.0 / 44 d.o.f.
Source rate / s^{-1}	$1.25 \pm 0.10 \times 10^{-2}$
Source exposure / ks	18
S/N	13.4
EW(FeKα) / keV	$1.17^{+0.68}_{-0.29}$

FIGURE B.22: ID 21: NGC 7479

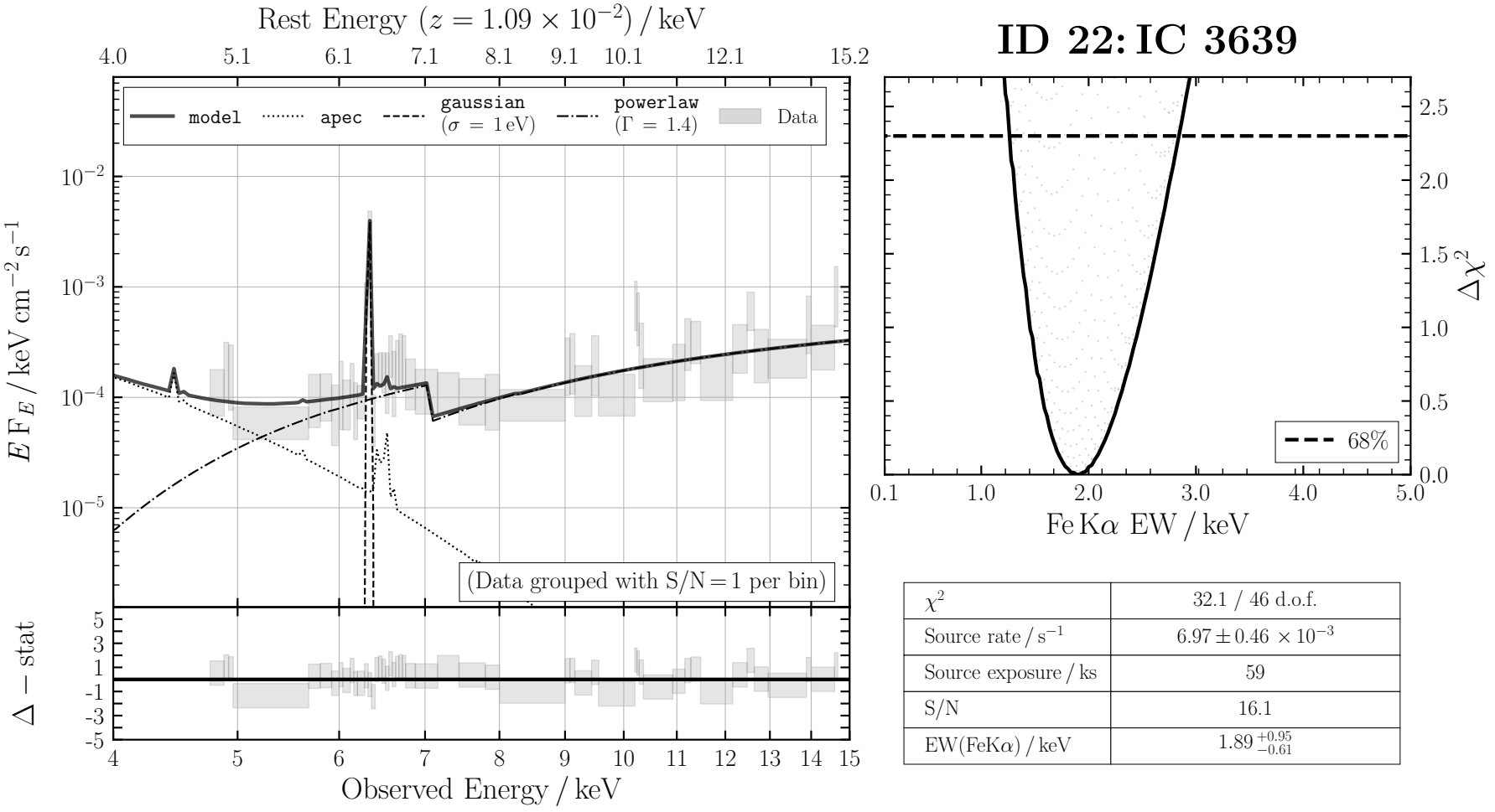

χ^2	32.1 / 46 d.o.f.
Source rate / s^{-1}	$6.97 \pm 0.46 \times 10^{-3}$
Source exposure / ks	59
S/N	16.1
EW(FeKα) / keV	$1.89^{+0.95}_{-0.61}$

FIGURE B.23: ID 22: IC 3639

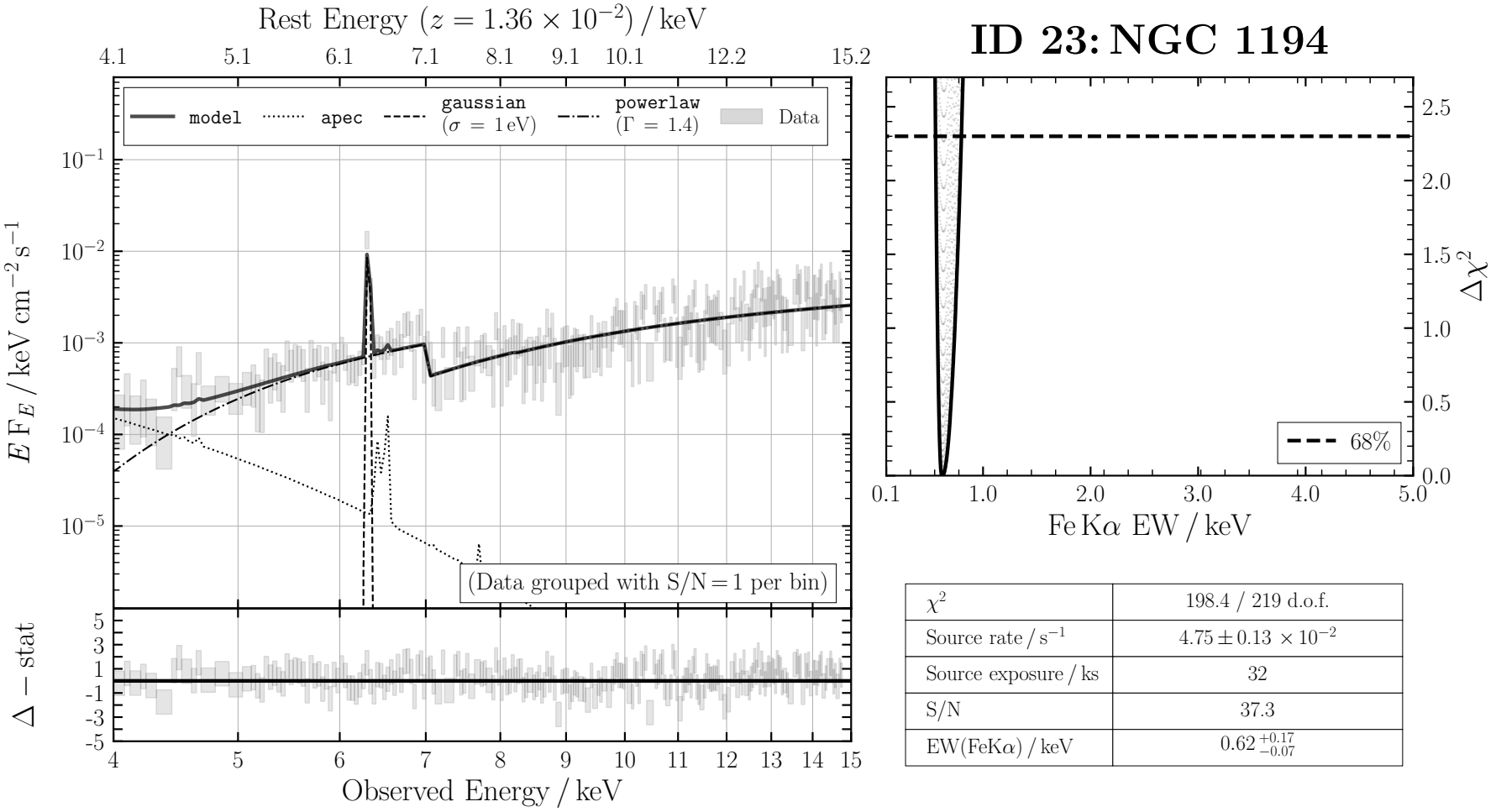

χ^2	198.4 / 219 d.o.f.
Source rate / s^{-1}	$4.75 \pm 0.13 \times 10^{-2}$
Source exposure / ks	32
S/N	37.3
EW(FeKα) / keV	$0.62^{+0.17}_{-0.07}$

FIGURE B.24: ID 23: NGC 1194

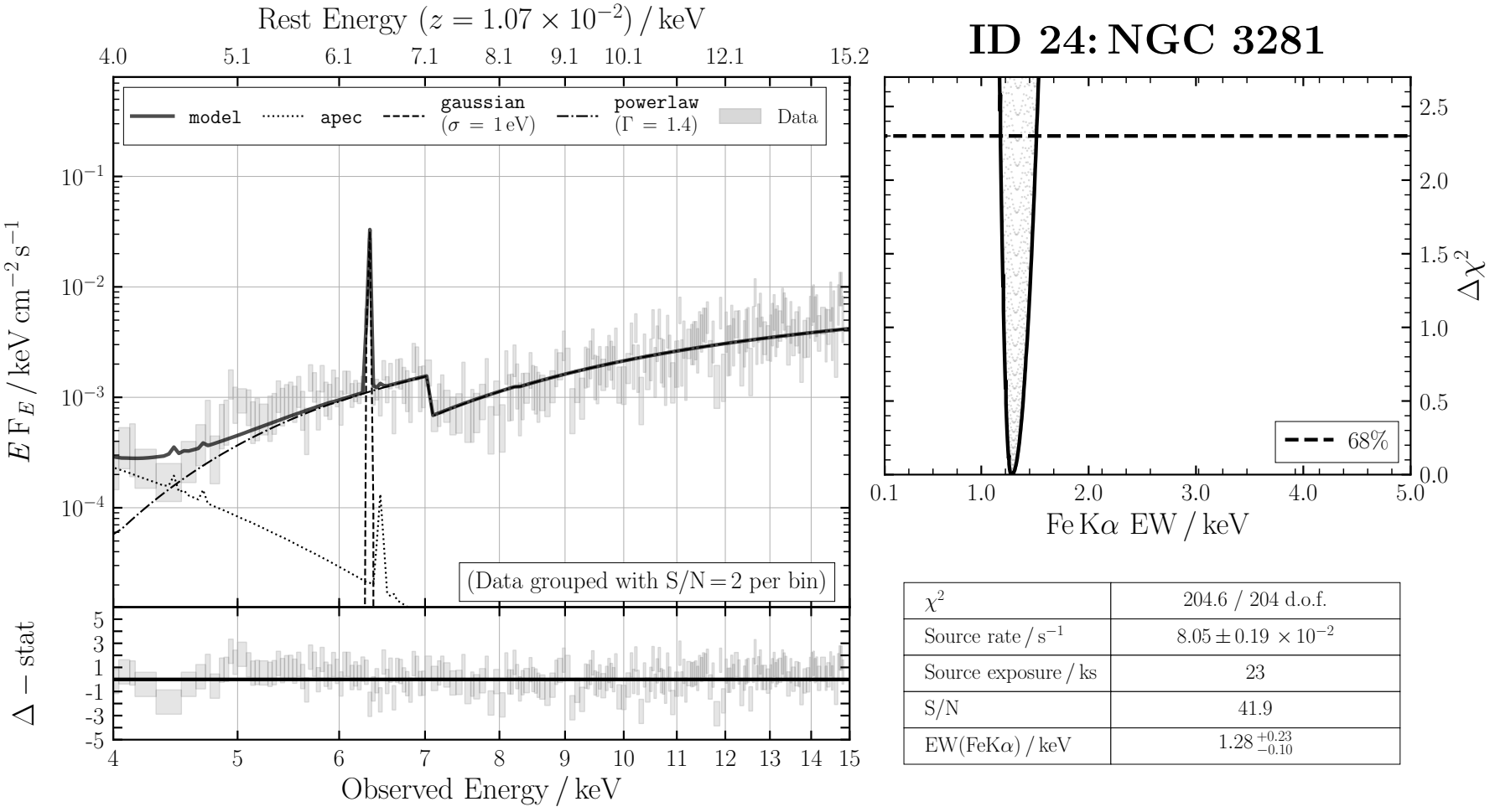

χ^2	204.6 / 204 d.o.f.
Source rate / s^{-1}	$8.05 \pm 0.19 \times 10^{-2}$
Source exposure / ks	23
S/N	41.9
EW(FeKα) / keV	$1.28^{+0.23}_{-0.10}$

FIGURE B.25: ID 24: NGC 3281

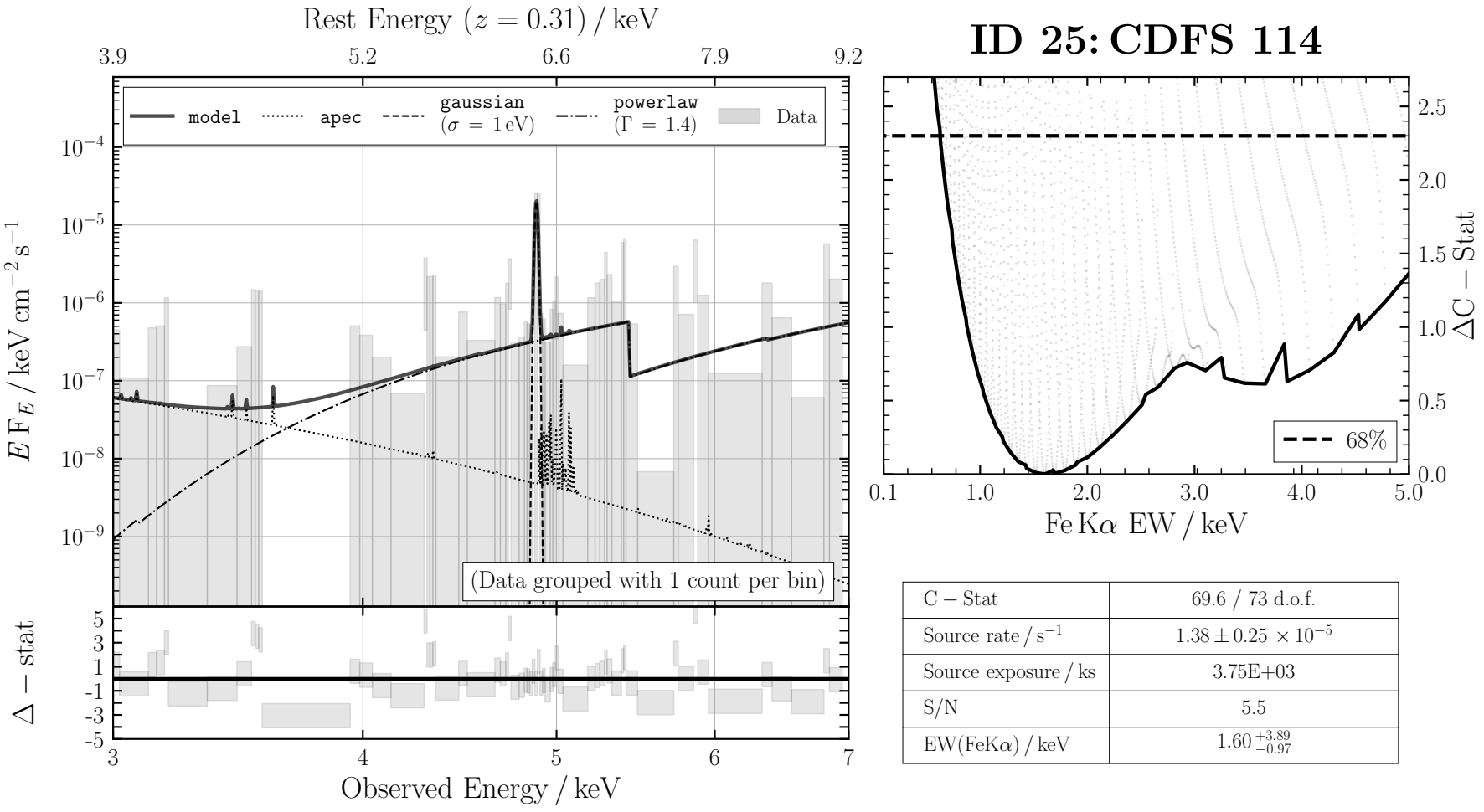

C − Stat	69.6 / 73 d.o.f.
Source rate / s^{-1}	$1.38 \pm 0.25 \times 10^{-5}$
Source exposure / ks	3.75E+03
S/N	5.5
EW(FeKα) / keV	$1.60\,^{+3.89}_{-0.97}$

FIGURE B.26: ID 25: CDFS 114

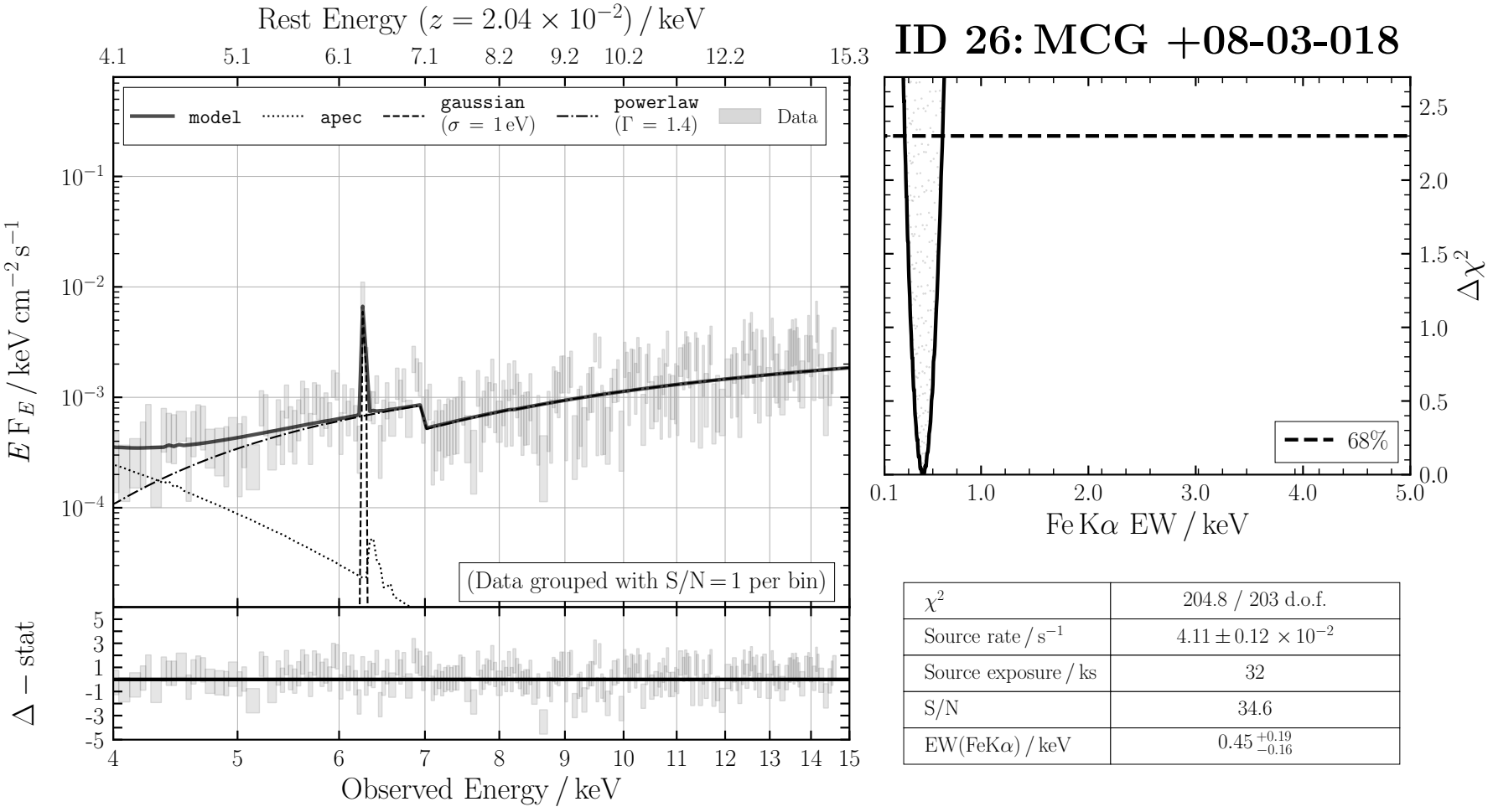

χ^2	204.8 / 203 d.o.f.
Source rate / s^{-1}	$4.11 \pm 0.12 \times 10^{-2}$
Source exposure / ks	32
S/N	34.6
EW(FeKα) / keV	$0.45^{+0.19}_{-0.16}$

FIGURE B.27: ID 26: MCG +08-03-018

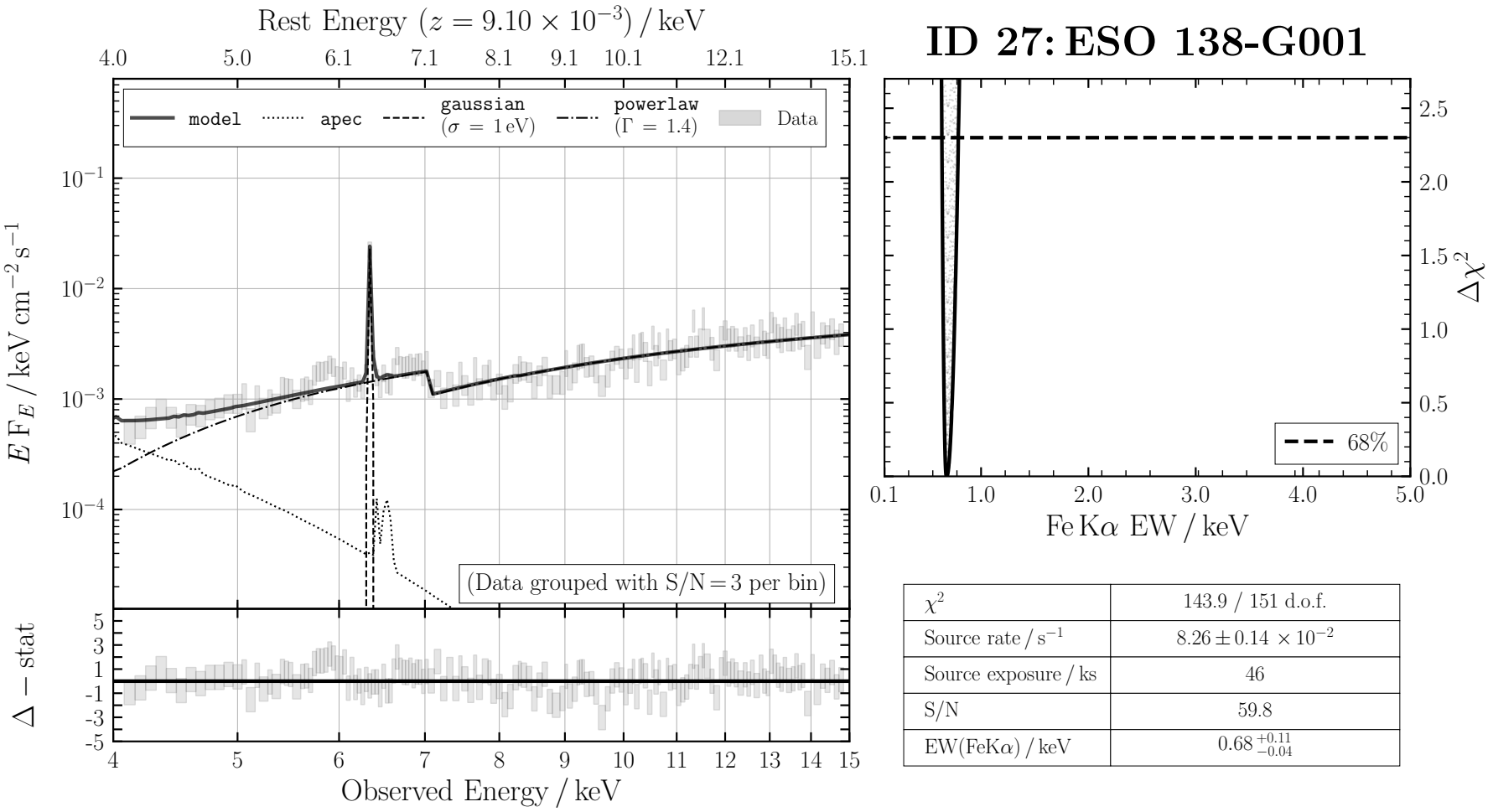

χ^2	143.9 / 151 d.o.f.
Source rate / s^{-1}	$8.26 \pm 0.14 \times 10^{-2}$
Source exposure / ks	46
S/N	59.8
EW(FeKα) / keV	$0.68^{+0.11}_{-0.04}$

FIGURE B.28: ID 27: ESO 138-G001

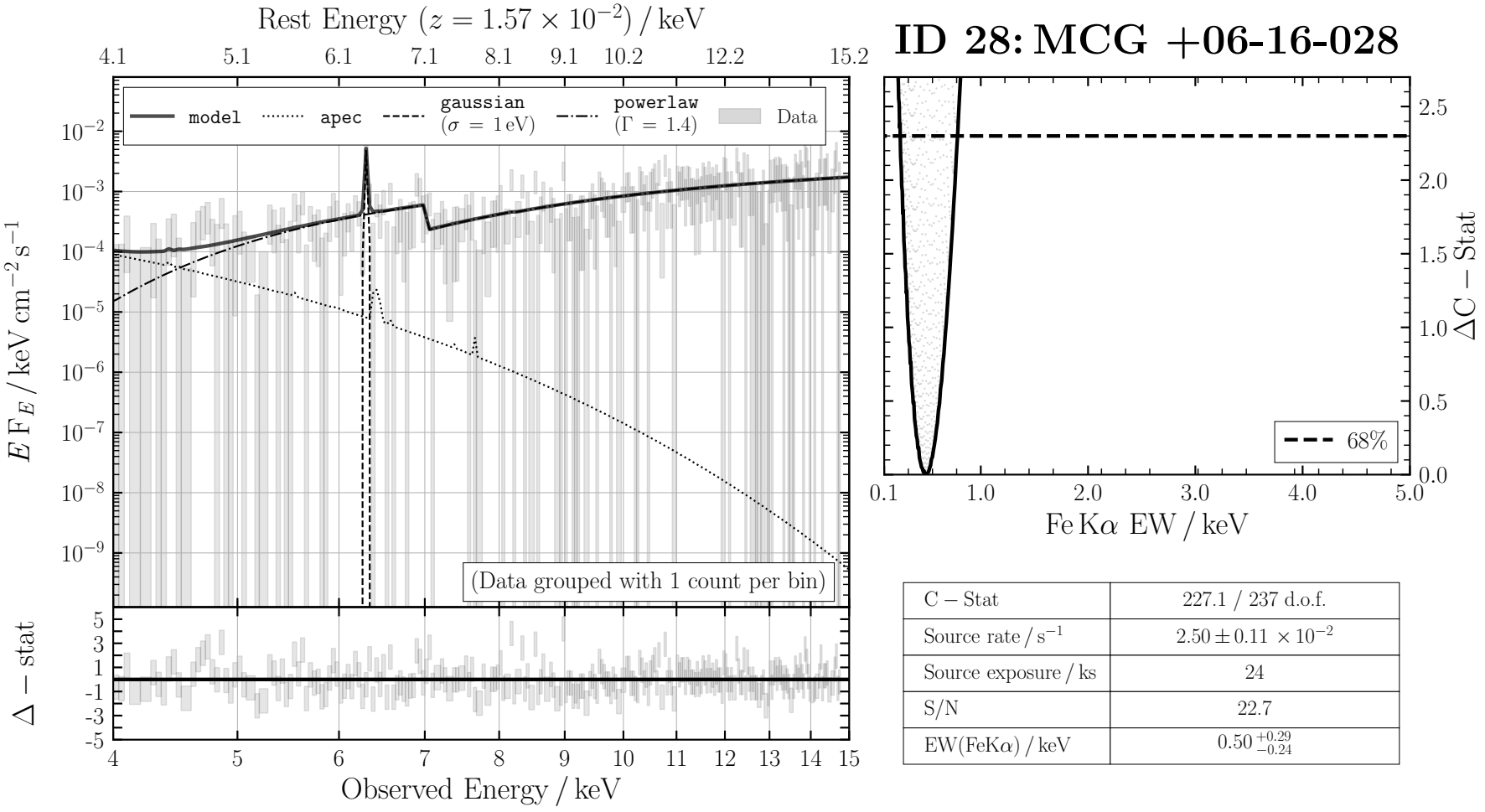

C − Stat	227.1 / 237 d.o.f.
Source rate / s^{-1}	$2.50 \pm 0.11 \times 10^{-2}$
Source exposure / ks	24
S/N	22.7
EW(FeKα) / keV	$0.50^{+0.29}_{-0.24}$

FIGURE B.29: ID 28: MCG +06-16-028

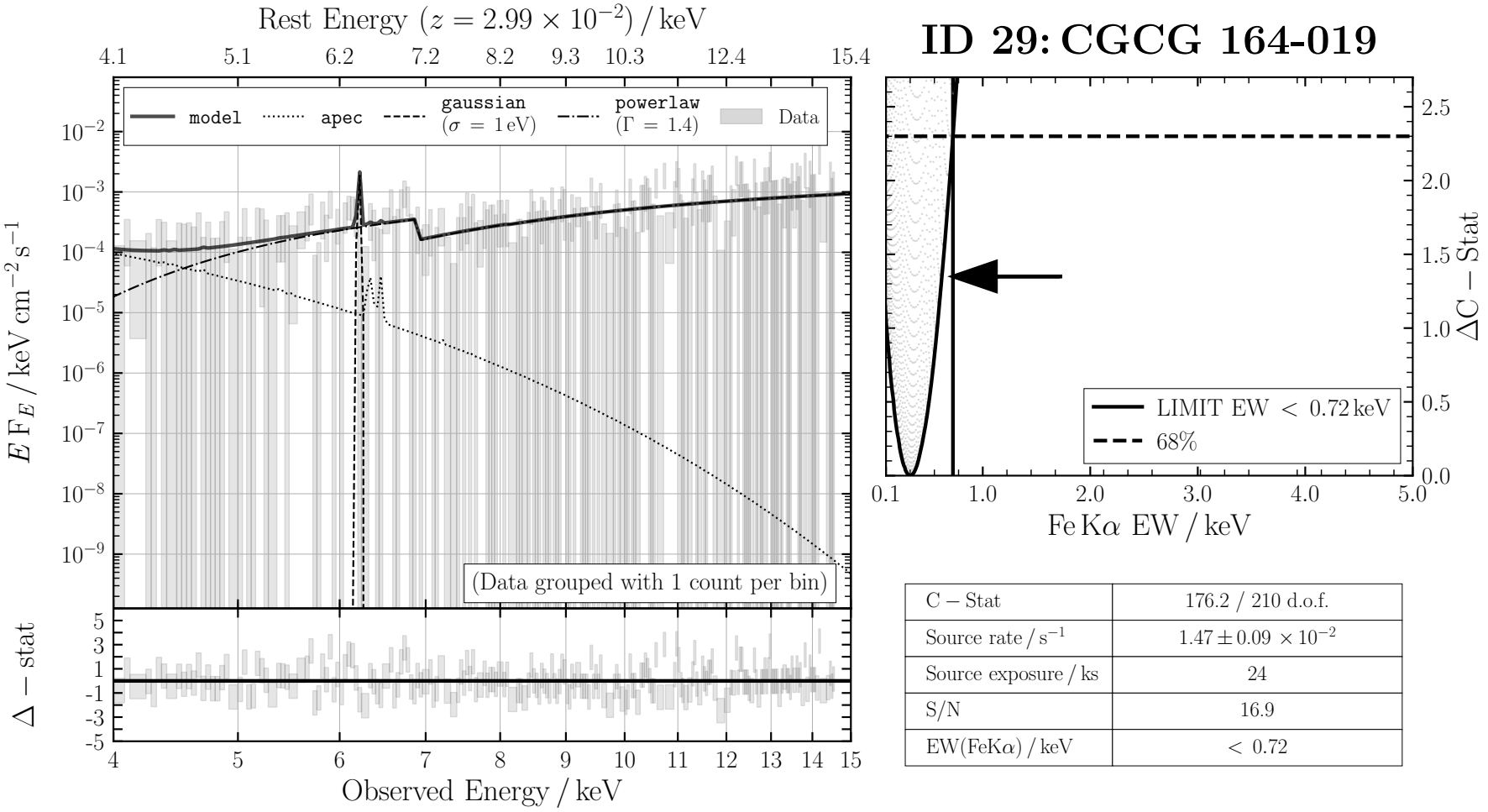

C − Stat	176.2 / 210 d.o.f.
Source rate / s^{-1}	$1.47 \pm 0.09 \times 10^{-2}$
Source exposure / ks	24
S/N	16.9
EW(FeKα) / keV	< 0.72

FIGURE B.30: ID 29: CGCG 164-019

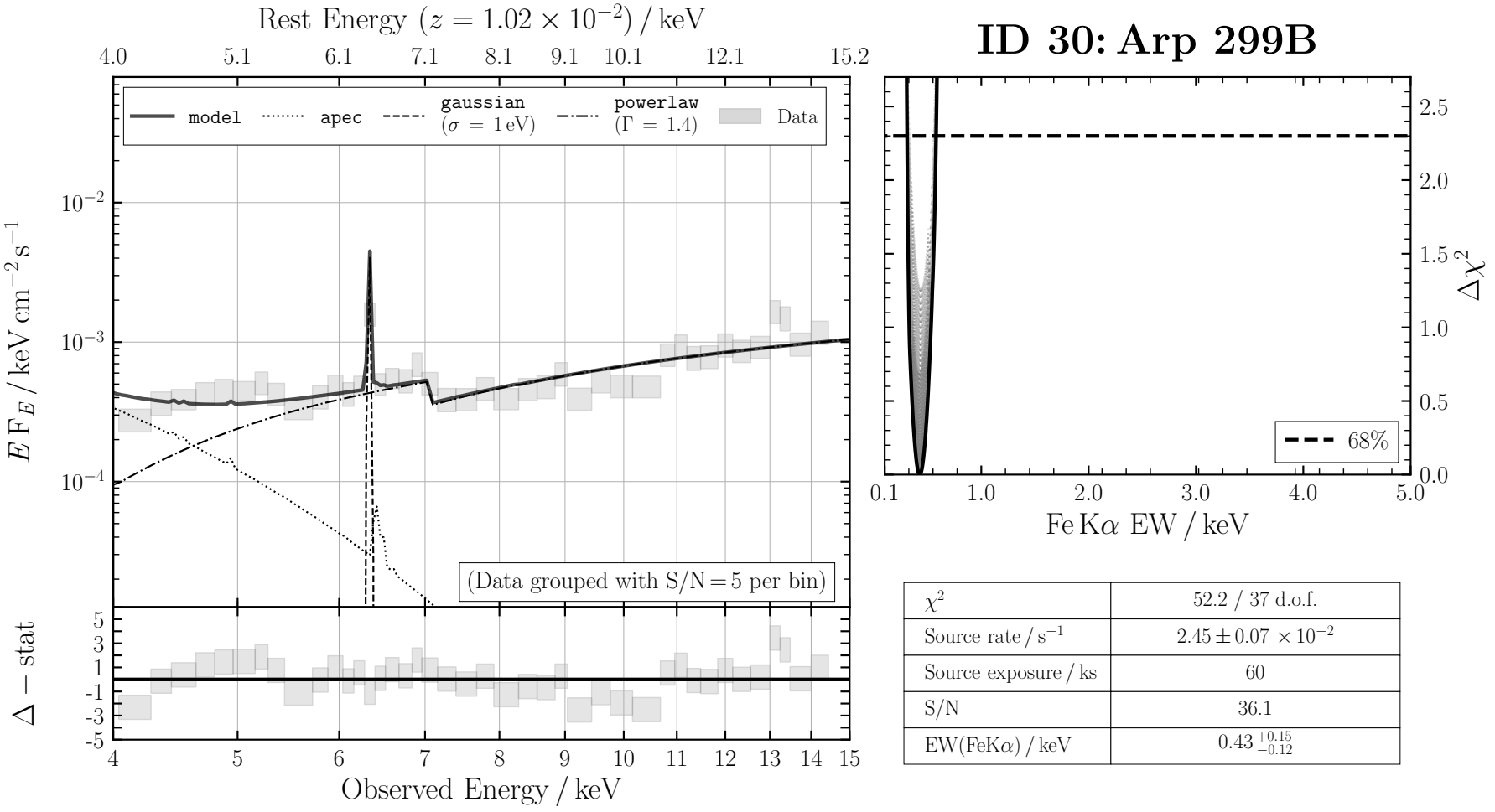

χ^2	52.2 / 37 d.o.f.
Source rate / s^{-1}	$2.45 \pm 0.07 \times 10^{-2}$
Source exposure / ks	60
S/N	36.1
EW(FeKα) / keV	$0.43^{+0.15}_{-0.12}$

FIGURE B.31: ID 30: Arp 299B

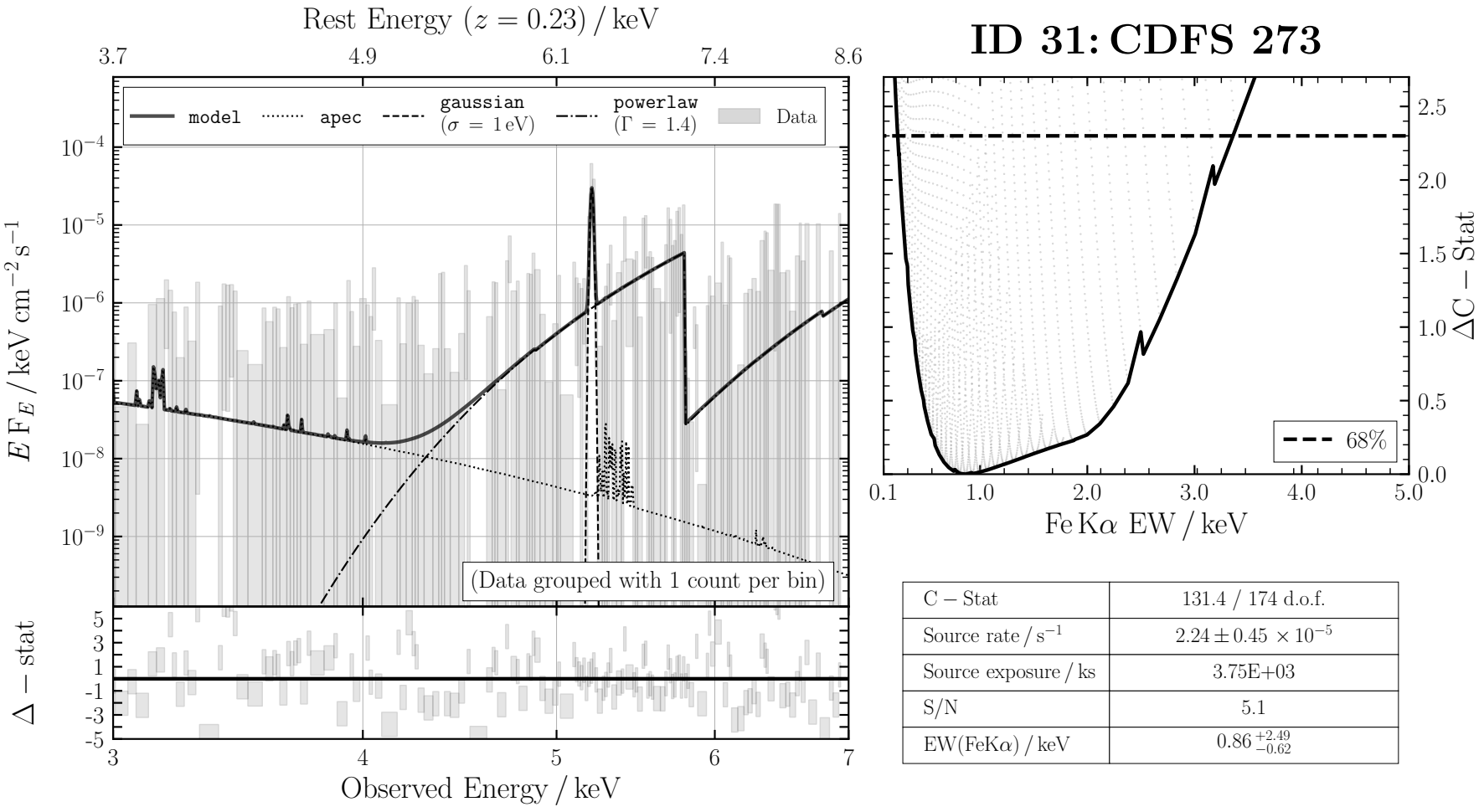

C − Stat	131.4 / 174 d.o.f.
Source rate / s^{-1}	$2.24 \pm 0.45 \times 10^{-5}$
Source exposure / ks	3.75E+03
S/N	5.1
EW(FeKα) / keV	$0.86\,^{+2.49}_{-0.62}$

FIGURE B.32: ID 31: CDFS 273

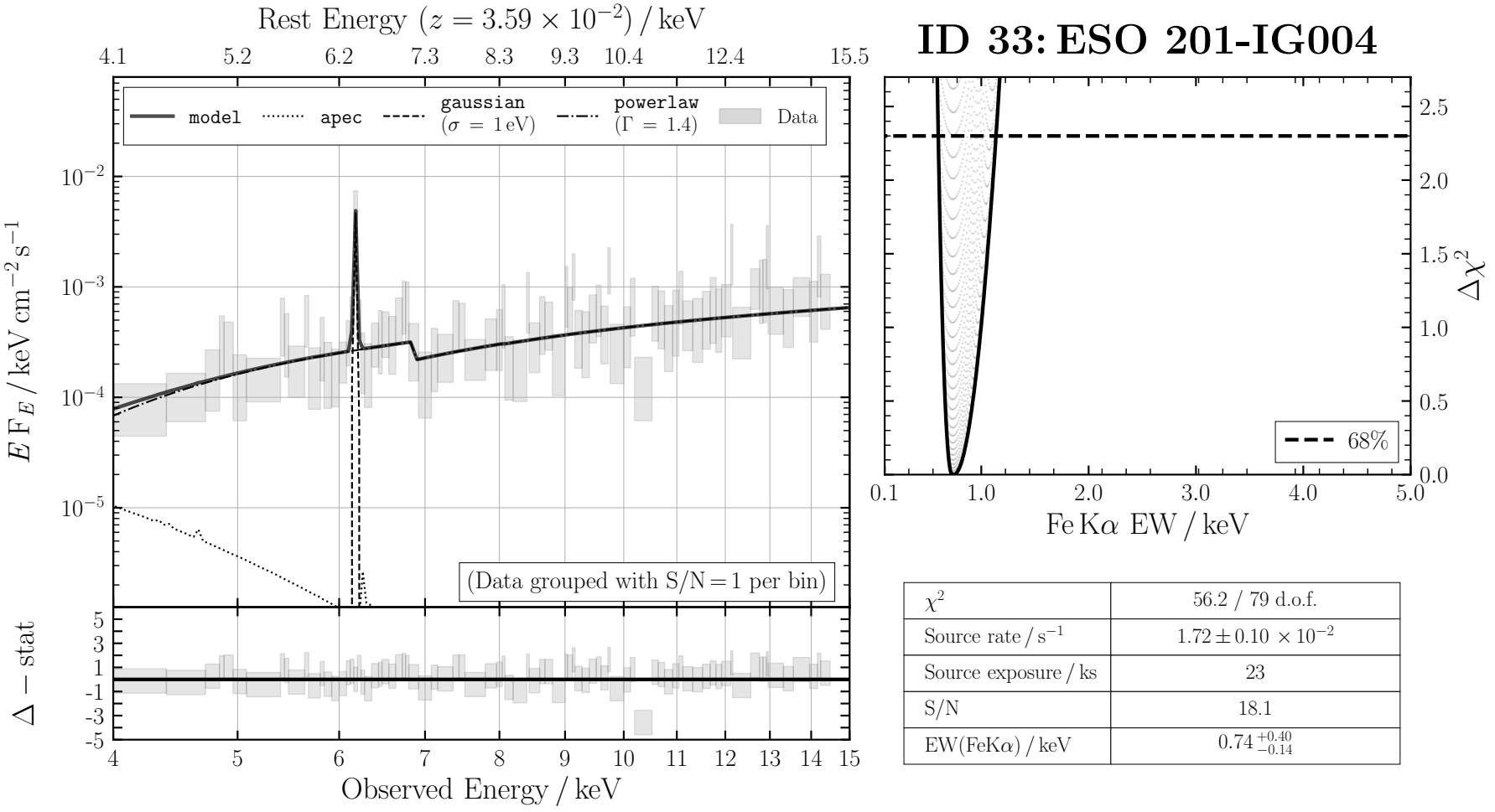

χ^2	56.2 / 79 d.o.f.
Source rate / s^{-1}	$1.72 \pm 0.10 \times 10^{-2}$
Source exposure / ks	23
S/N	18.1
EW(FeKα) / keV	$0.74^{+0.40}_{-0.14}$

FIGURE B.33: ID 33: ESO 201-IG004

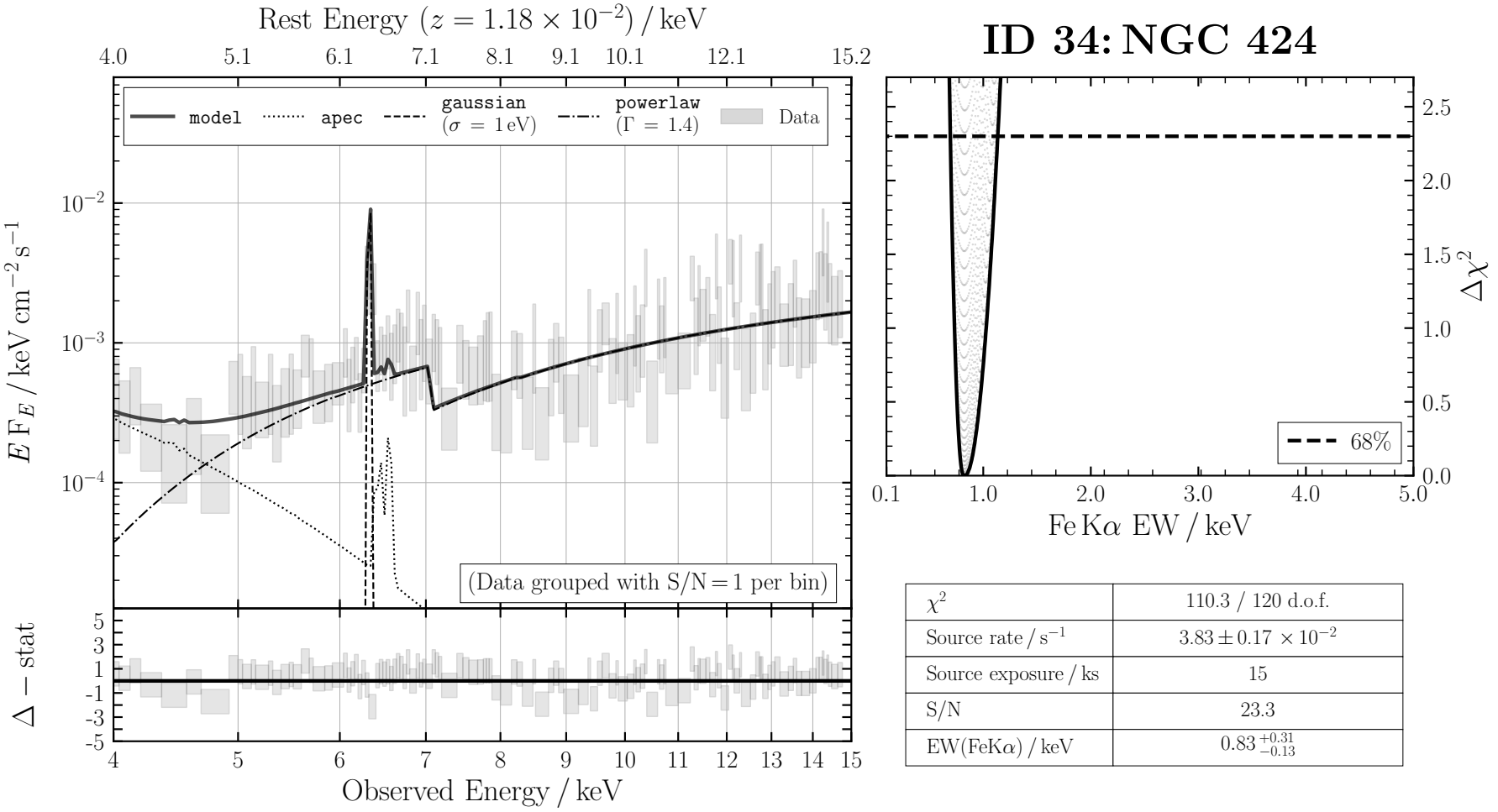

χ^2	110.3 / 120 d.o.f.
Source rate / s^{-1}	$3.83 \pm 0.17 \times 10^{-2}$
Source exposure / ks	15
S/N	23.3
EW(FeKα) / keV	$0.83^{+0.31}_{-0.13}$

FIGURE B.34: ID 34: NGC 424

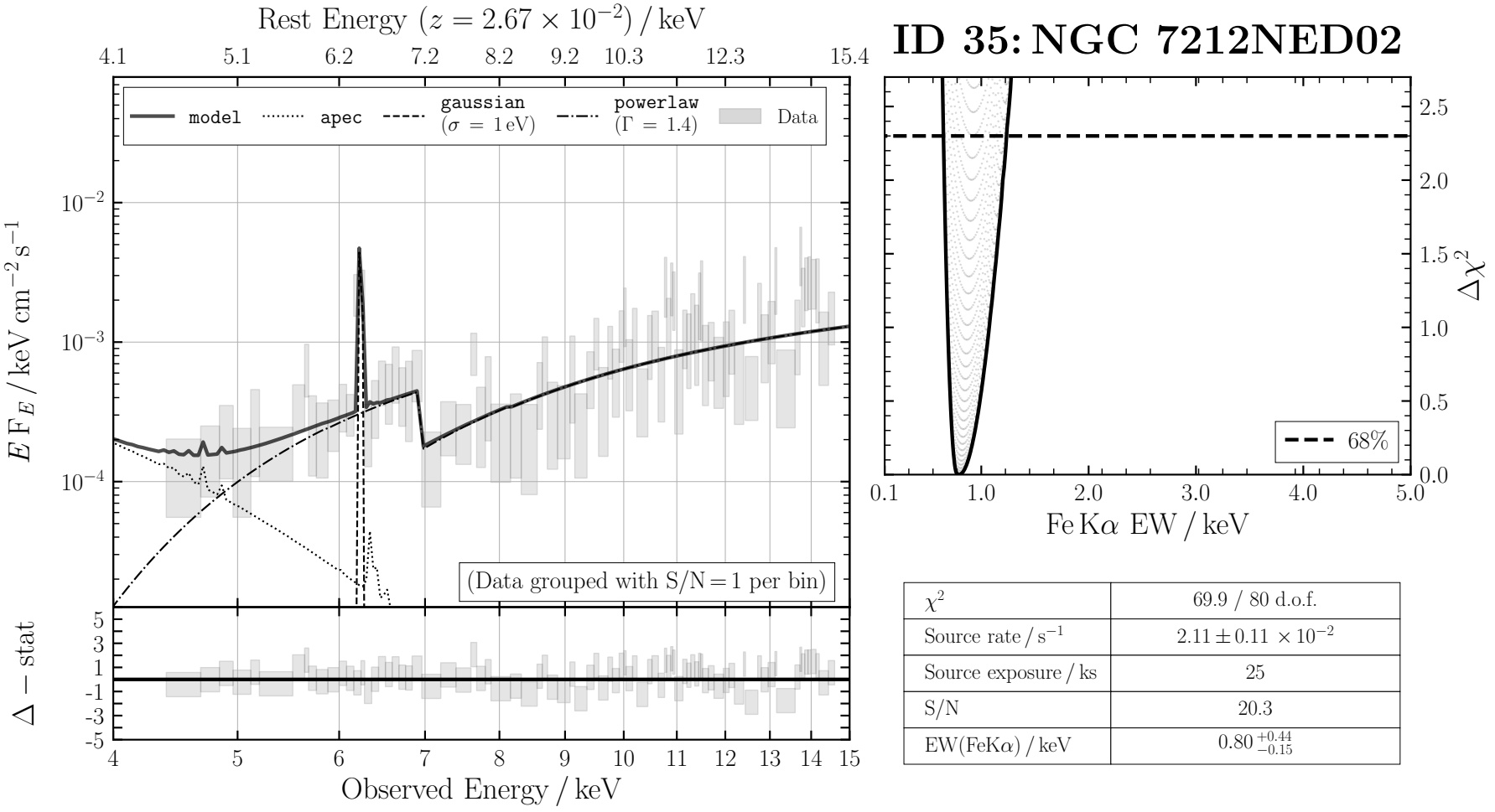

χ^2	69.9 / 80 d.o.f.
Source rate / s^{-1}	$2.11 \pm 0.11 \times 10^{-2}$
Source exposure / ks	25
S/N	20.3
EW(FeKα) / keV	$0.80\,^{+0.44}_{-0.15}$

FIGURE B.35: ID 35: NGC 7212 NED02

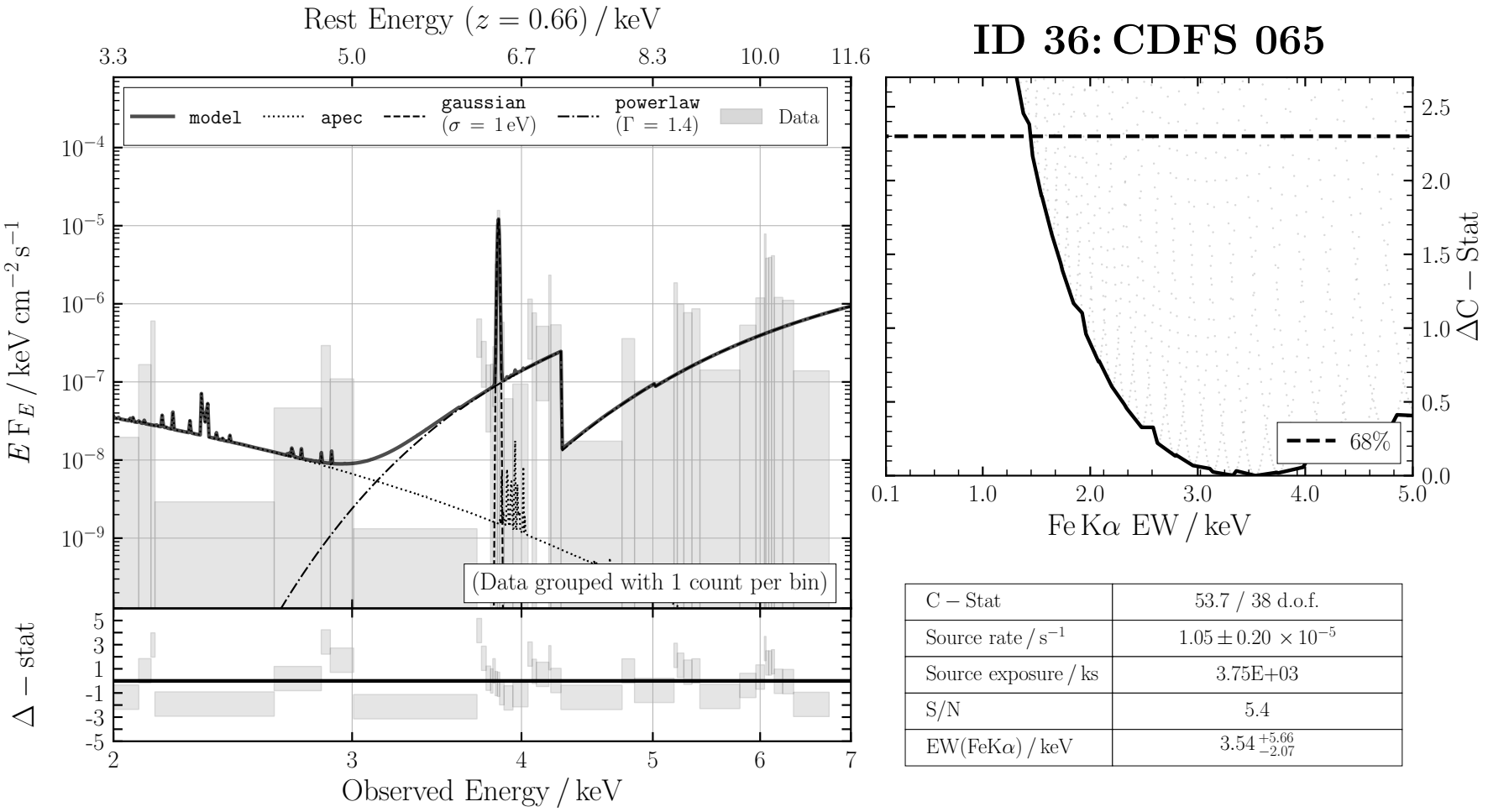

C − Stat	53.7 / 38 d.o.f.
Source rate / s^{-1}	$1.05 \pm 0.20 \times 10^{-5}$
Source exposure / ks	3.75E+03
S/N	5.4
EW(FeKα) / keV	$3.54\,^{+5.66}_{-2.07}$

FIGURE B.36: ID 36: CDFS 065

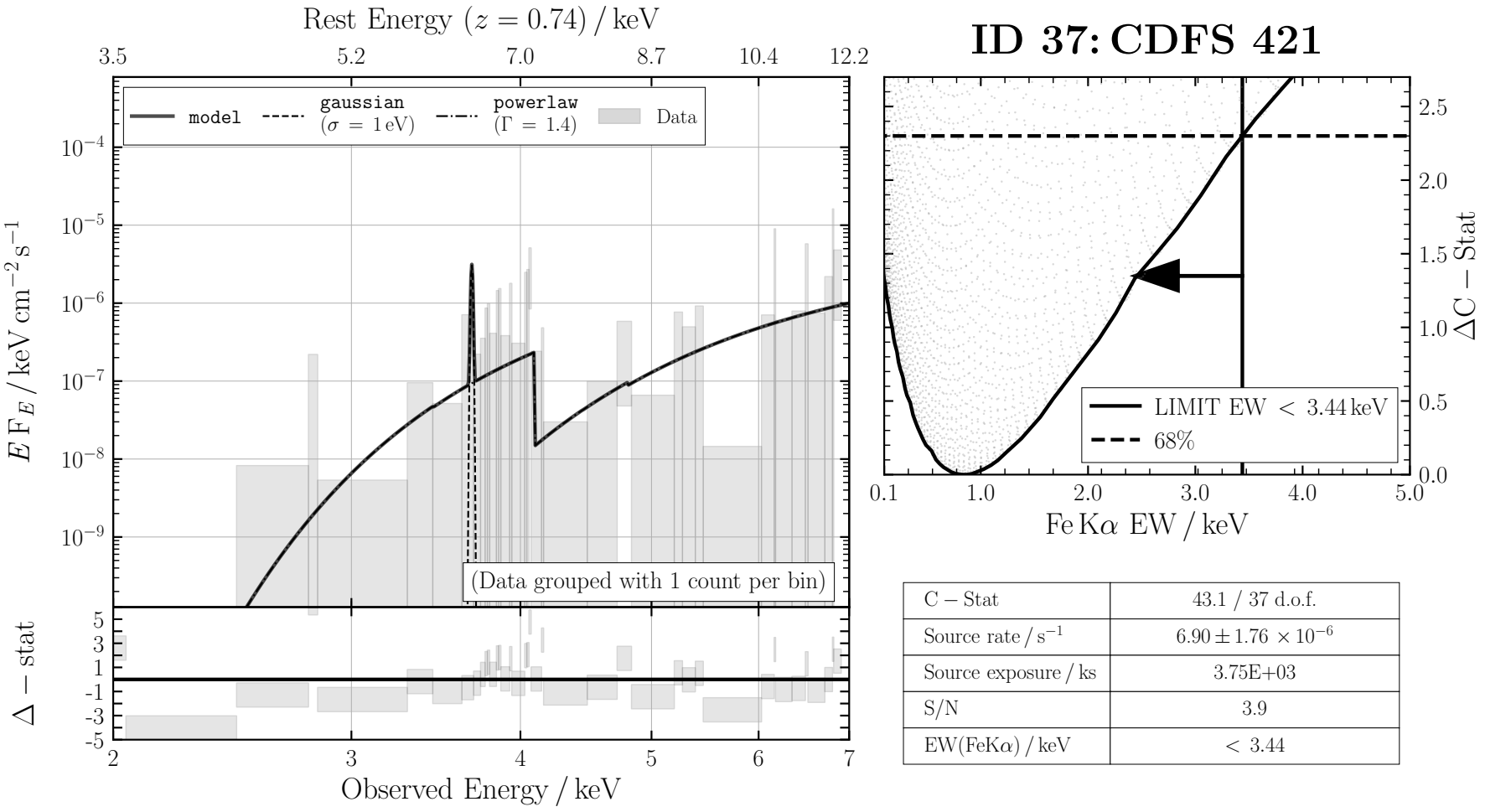

C − Stat	43.1 / 37 d.o.f.
Source rate / s^{-1}	$6.90 \pm 1.76 \times 10^{-6}$
Source exposure / ks	3.75E+03
S/N	3.9
EW(FeKα) / keV	< 3.44

FIGURE B.37: ID 37: CDFS 421

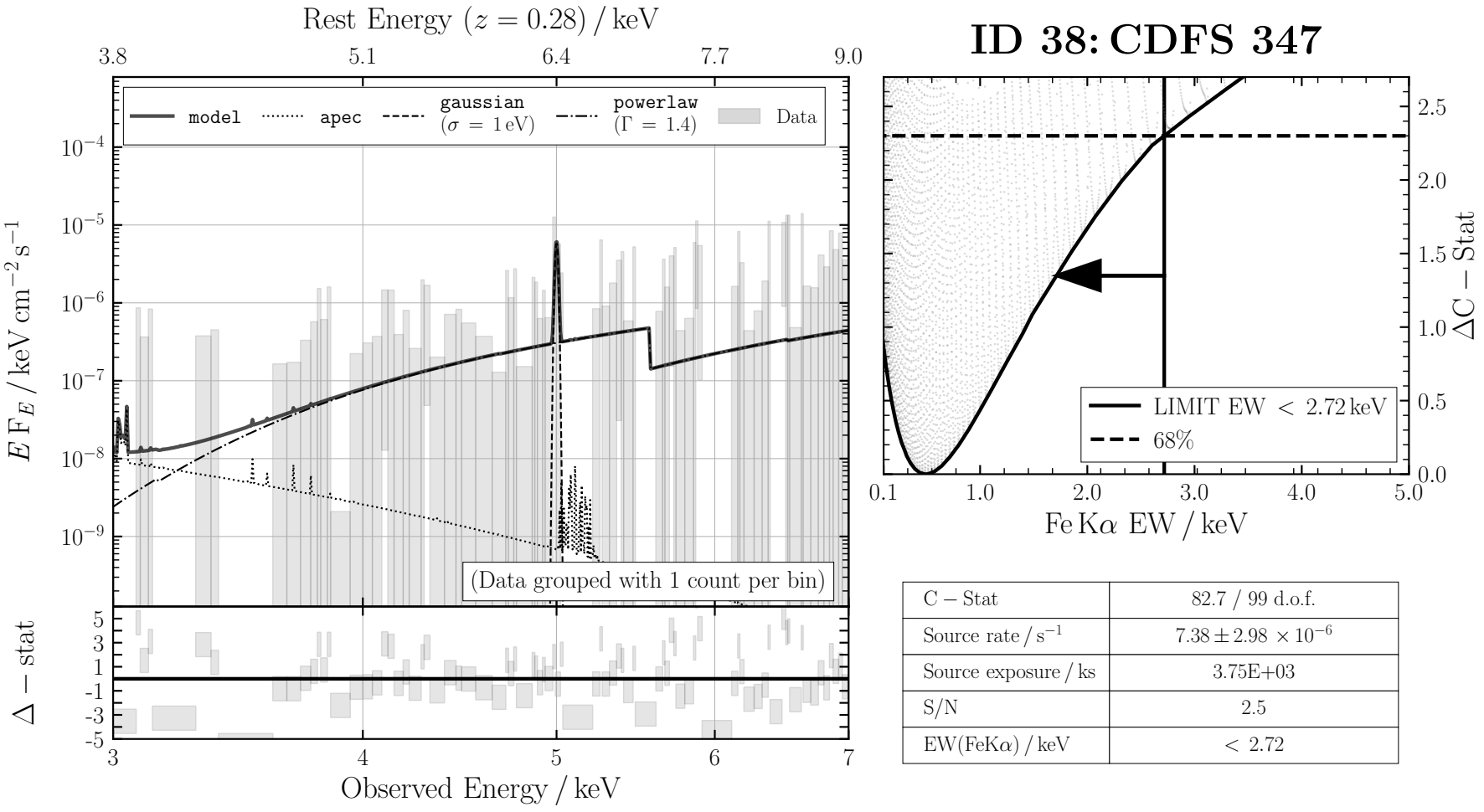

C − Stat	82.7 / 99 d.o.f.
Source rate / s^{-1}	$7.38 \pm 2.98 \times 10^{-6}$
Source exposure / ks	3.75E+03
S/N	2.5
EW(FeKα) / keV	< 2.72

FIGURE B.38: ID 38: CDFS 347

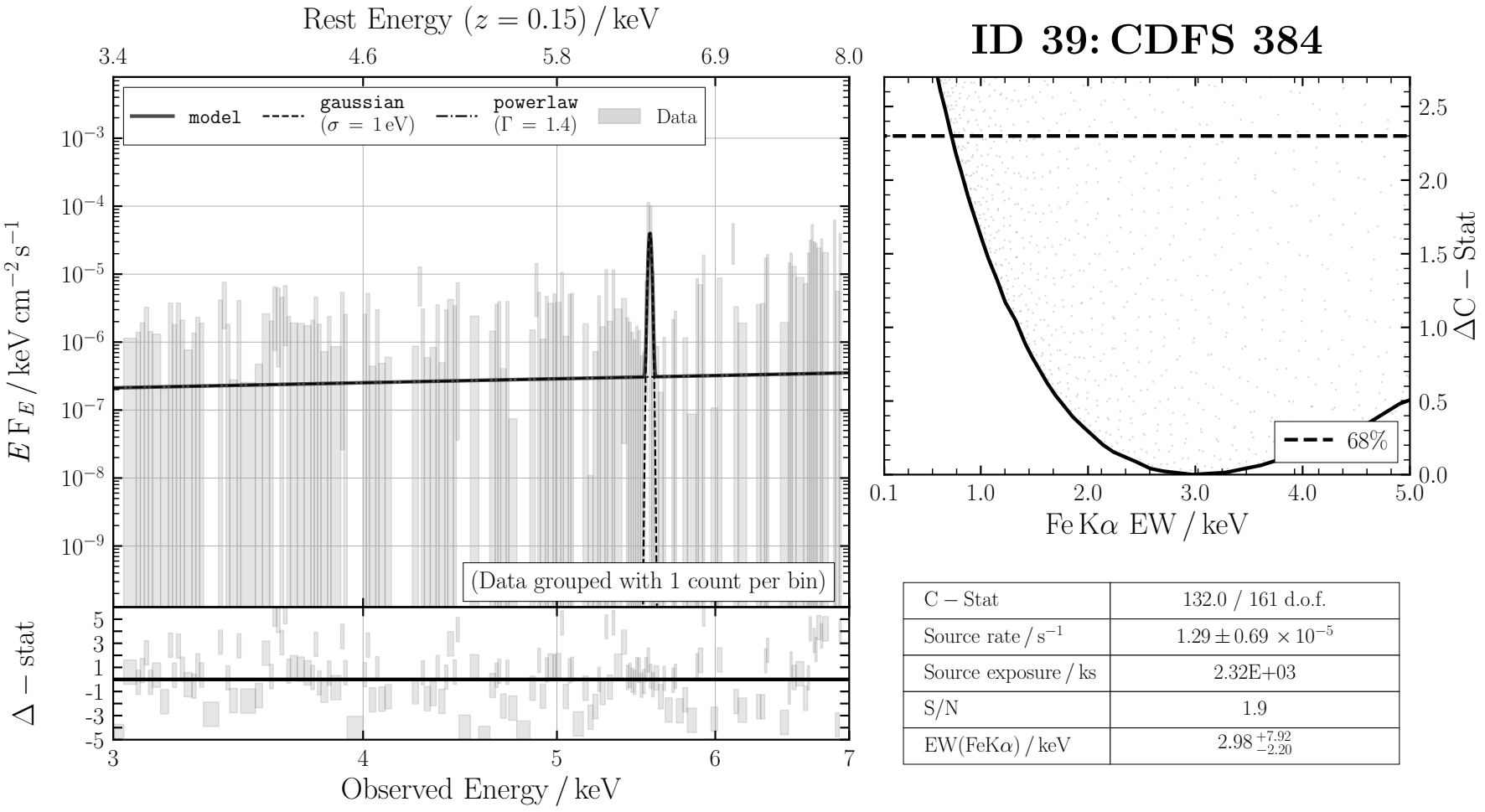

C − Stat	132.0 / 161 d.o.f.
Source rate / s^{-1}	$1.29 \pm 0.69 \times 10^{-5}$
Source exposure / ks	2.32E+03
S/N	1.9
EW(FeKα) / keV	$2.98\,^{+7.92}_{-2.20}$

FIGURE B.39: ID 39: CDFS 384

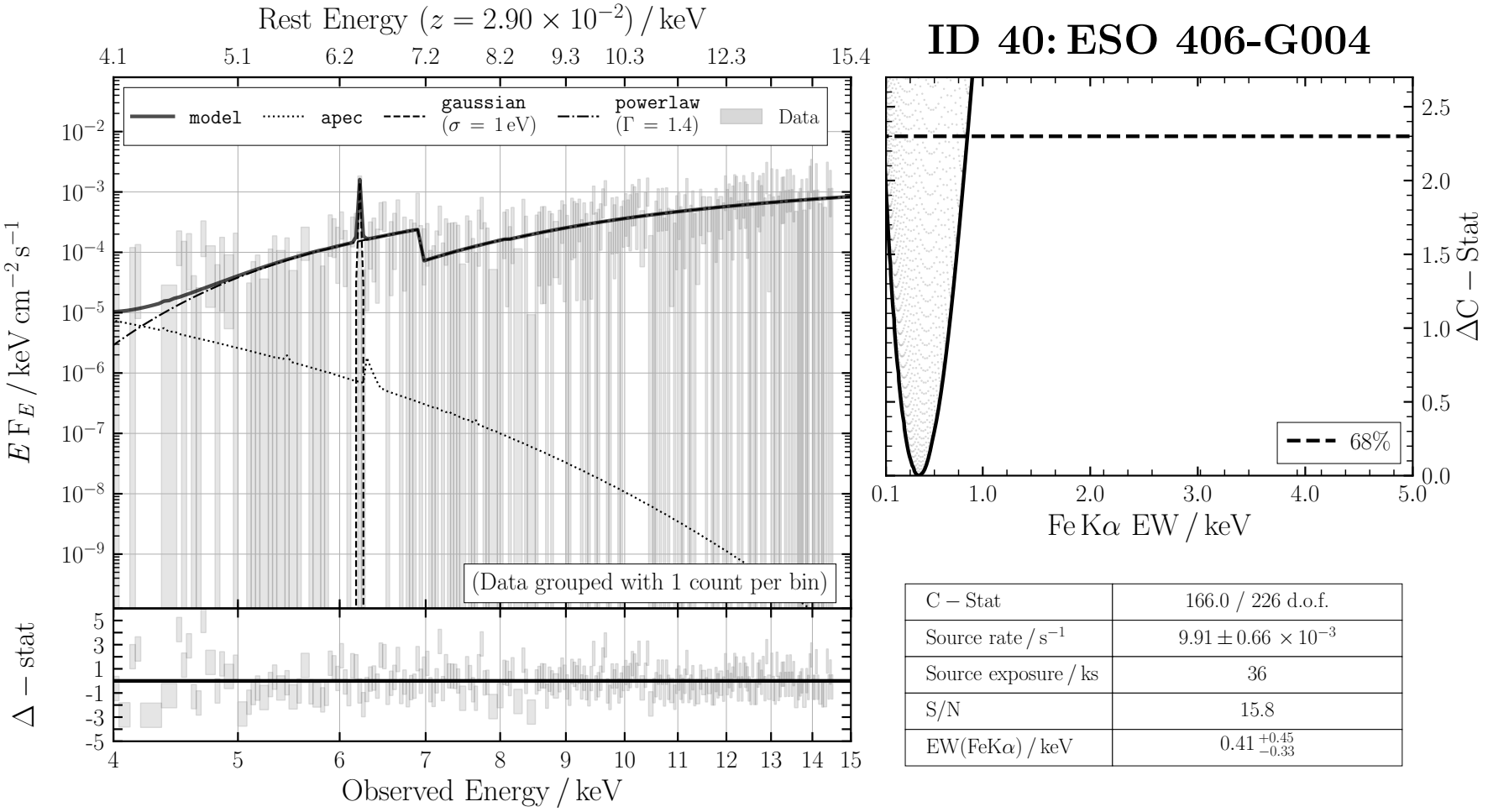

C − Stat	166.0 / 226 d.o.f.
Source rate / s^{-1}	$9.91 \pm 0.66 \times 10^{-3}$
Source exposure / ks	36
S/N	15.8
EW(FeKα) / keV	$0.41\,^{+0.45}_{-0.33}$

FIGURE B.40: ID 40: ESO 406-G004

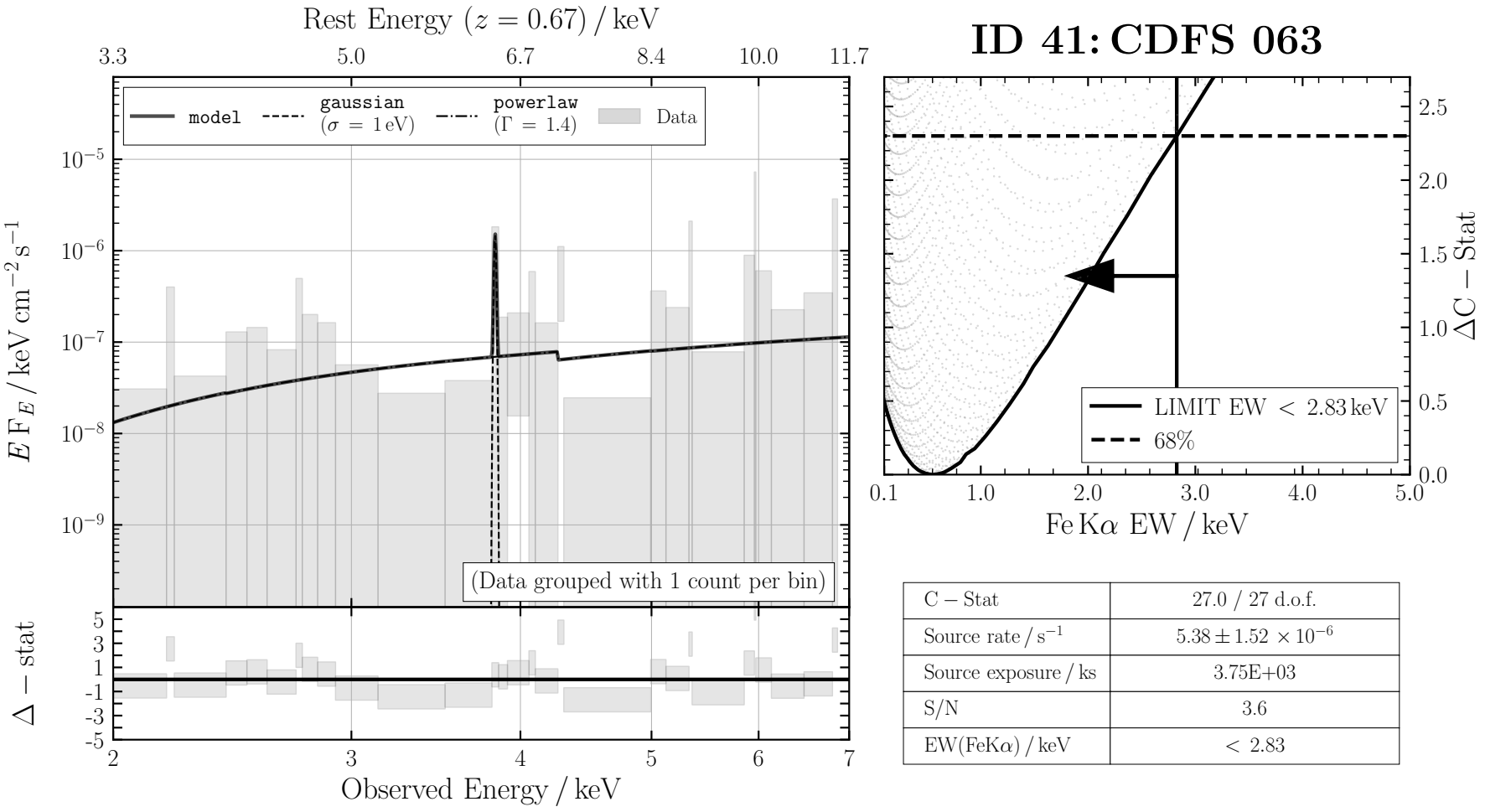

C − Stat	27.0 / 27 d.o.f.
Source rate / s^{-1}	$5.38 \pm 1.52 \times 10^{-6}$
Source exposure / ks	3.75E+03
S/N	3.6
EW(FeKα) / keV	< 2.83

FIGURE B.41: ID 41: CDFS 063

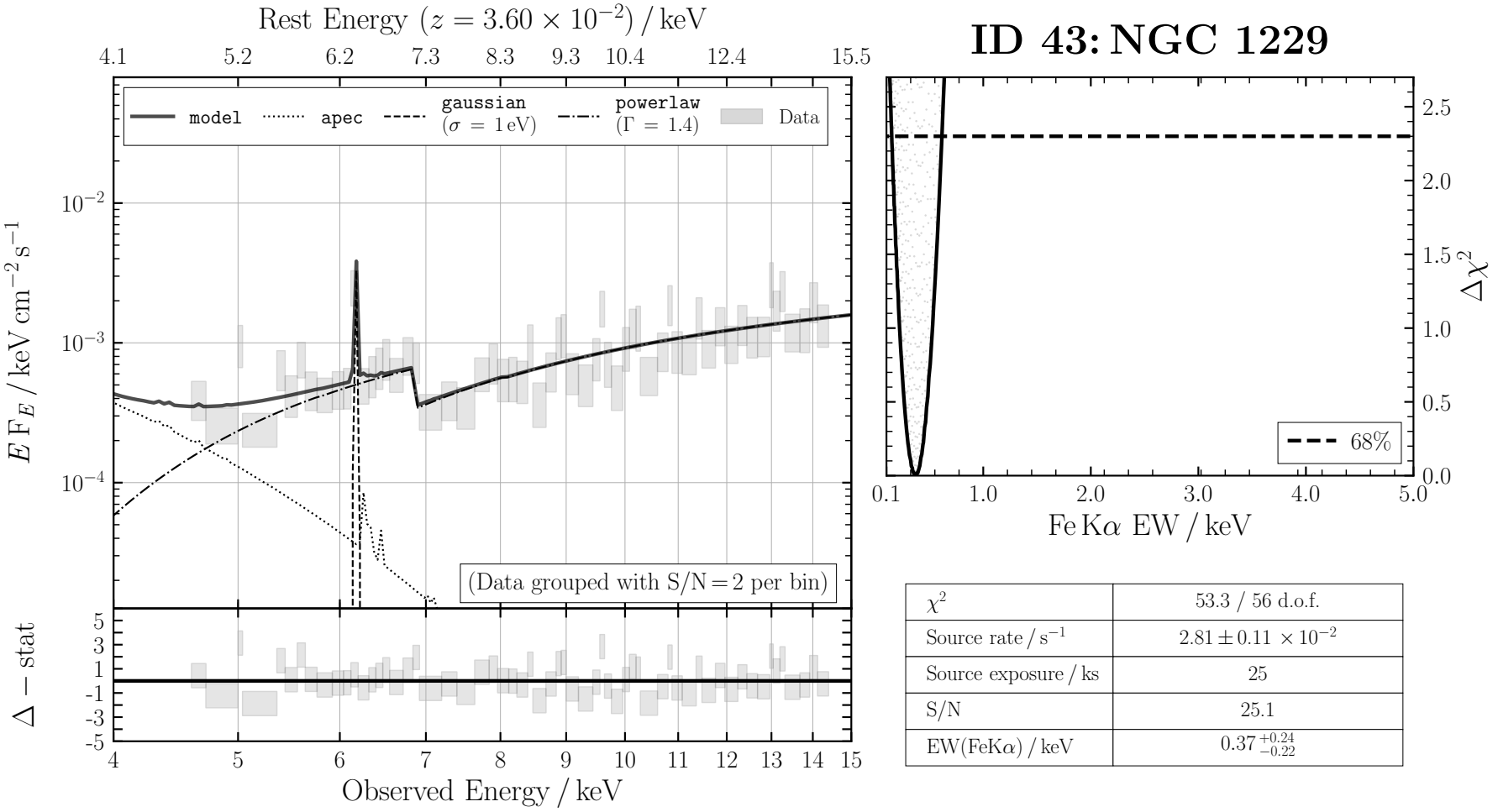

χ^2	53.3 / 56 d.o.f.
Source rate / s^{-1}	$2.81 \pm 0.11 \times 10^{-2}$
Source exposure / ks	25
S/N	25.1
EW(FeKα) / keV	$0.37^{+0.24}_{-0.22}$

FIGURE B.42: ID 43: NGC 1229

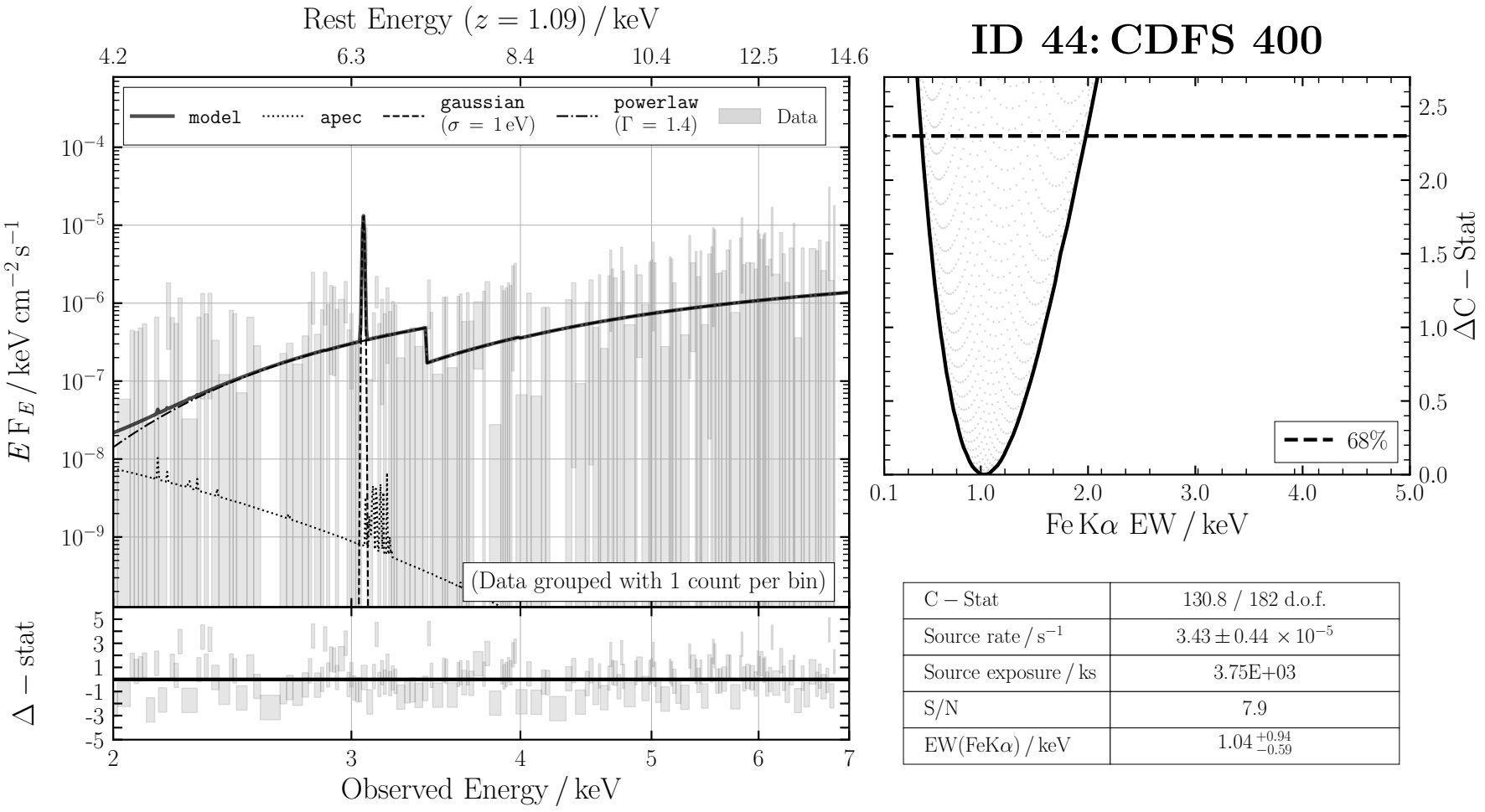

C − Stat	130.8 / 182 d.o.f.
Source rate / s^{-1}	$3.43 \pm 0.44 \times 10^{-5}$
Source exposure / ks	3.75E+03
S/N	7.9
EW(FeKα) / keV	$1.04\,^{+0.94}_{-0.59}$

FIGURE B.43: ID 44: CDFS 400

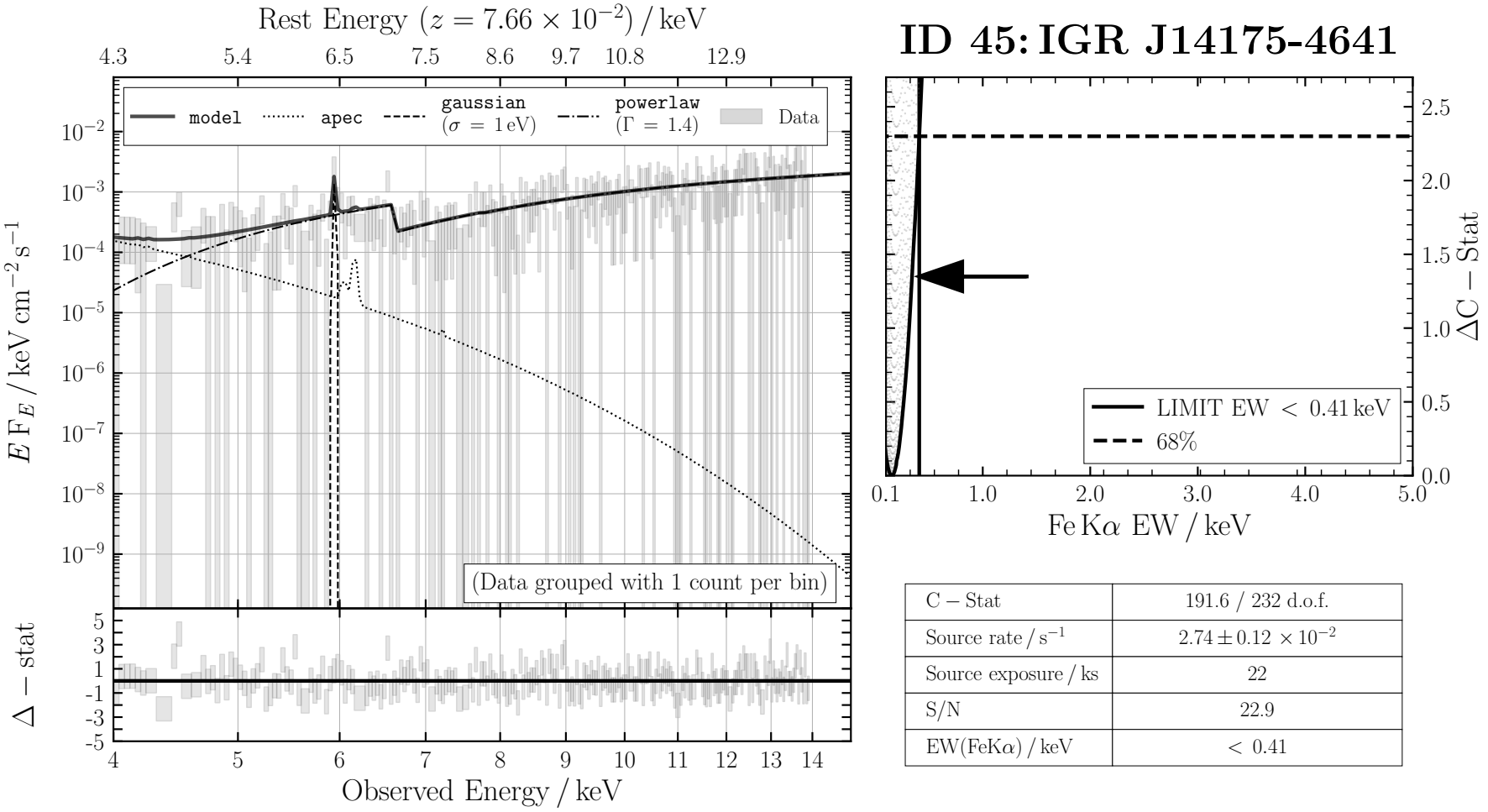

C − Stat	191.6 / 232 d.o.f.
Source rate / s^{-1}	$2.74 \pm 0.12 \times 10^{-2}$
Source exposure / ks	22
S/N	22.9
EW(FeKα) / keV	< 0.41

FIGURE B.44: ID 45: IGR J14175-4641

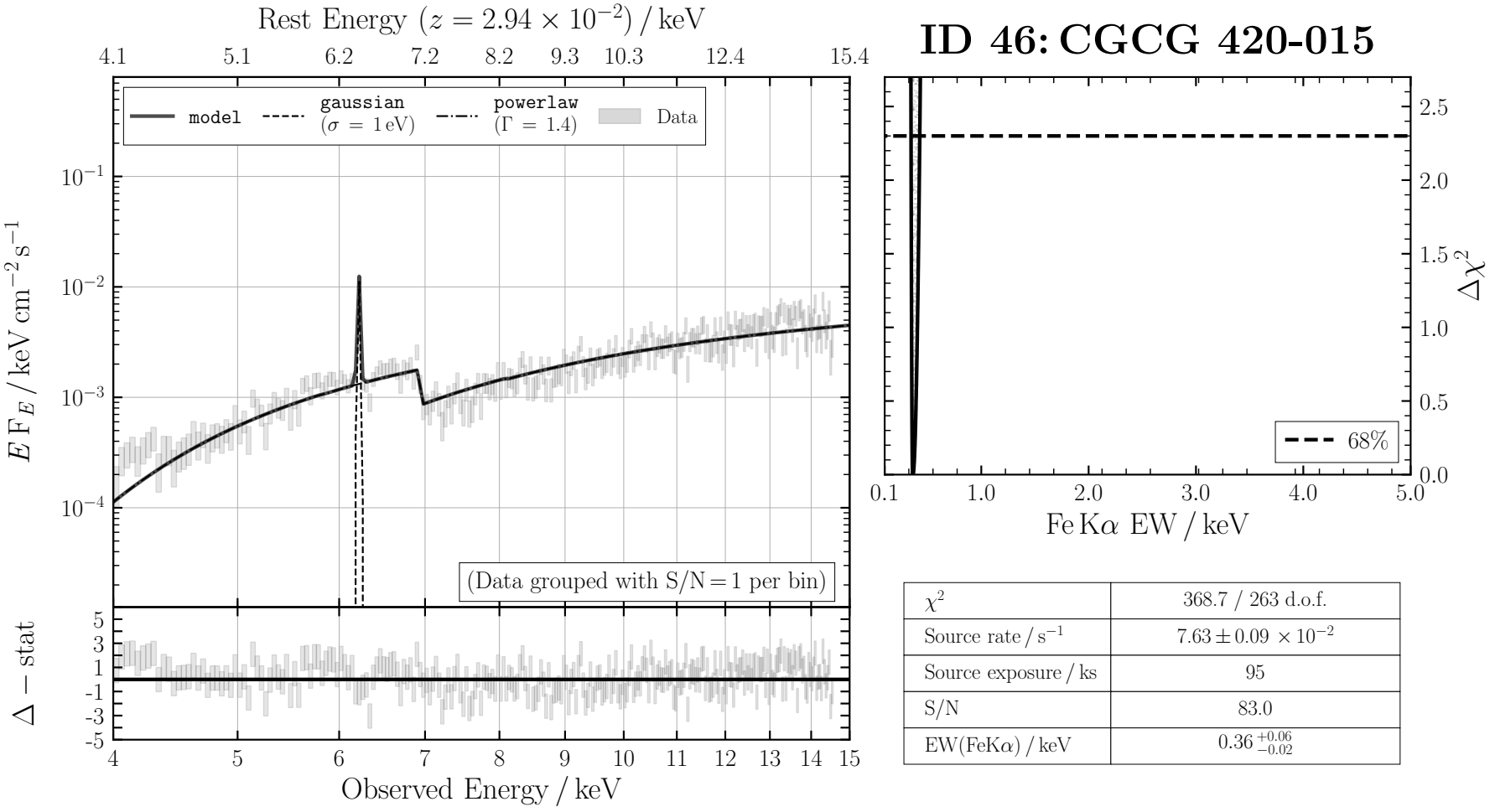

χ^2	368.7 / 263 d.o.f.
Source rate / s^{-1}	$7.63 \pm 0.09 \times 10^{-2}$
Source exposure / ks	95
S/N	83.0
EW(FeKα) / keV	$0.36^{+0.06}_{-0.02}$

FIGURE B.45: ID 46: CGCG 420-015

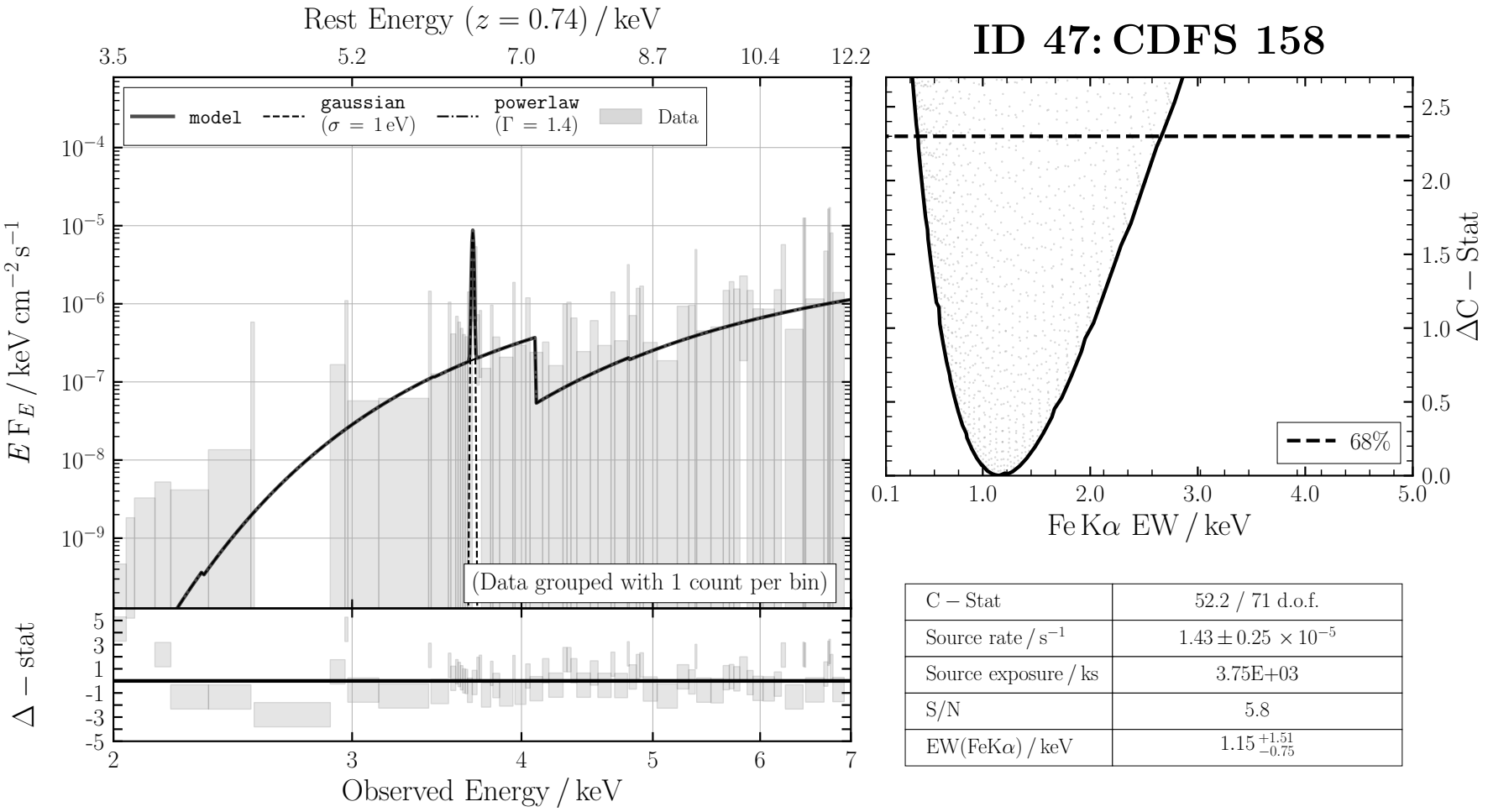

C − Stat	52.2 / 71 d.o.f.
Source rate / s^{-1}	$1.43 \pm 0.25 \times 10^{-5}$
Source exposure / ks	3.75E+03
S/N	5.8
EW(FeKα) / keV	$1.15\,^{+1.51}_{-0.75}$

FIGURE B.46: ID 47: CDFS 158

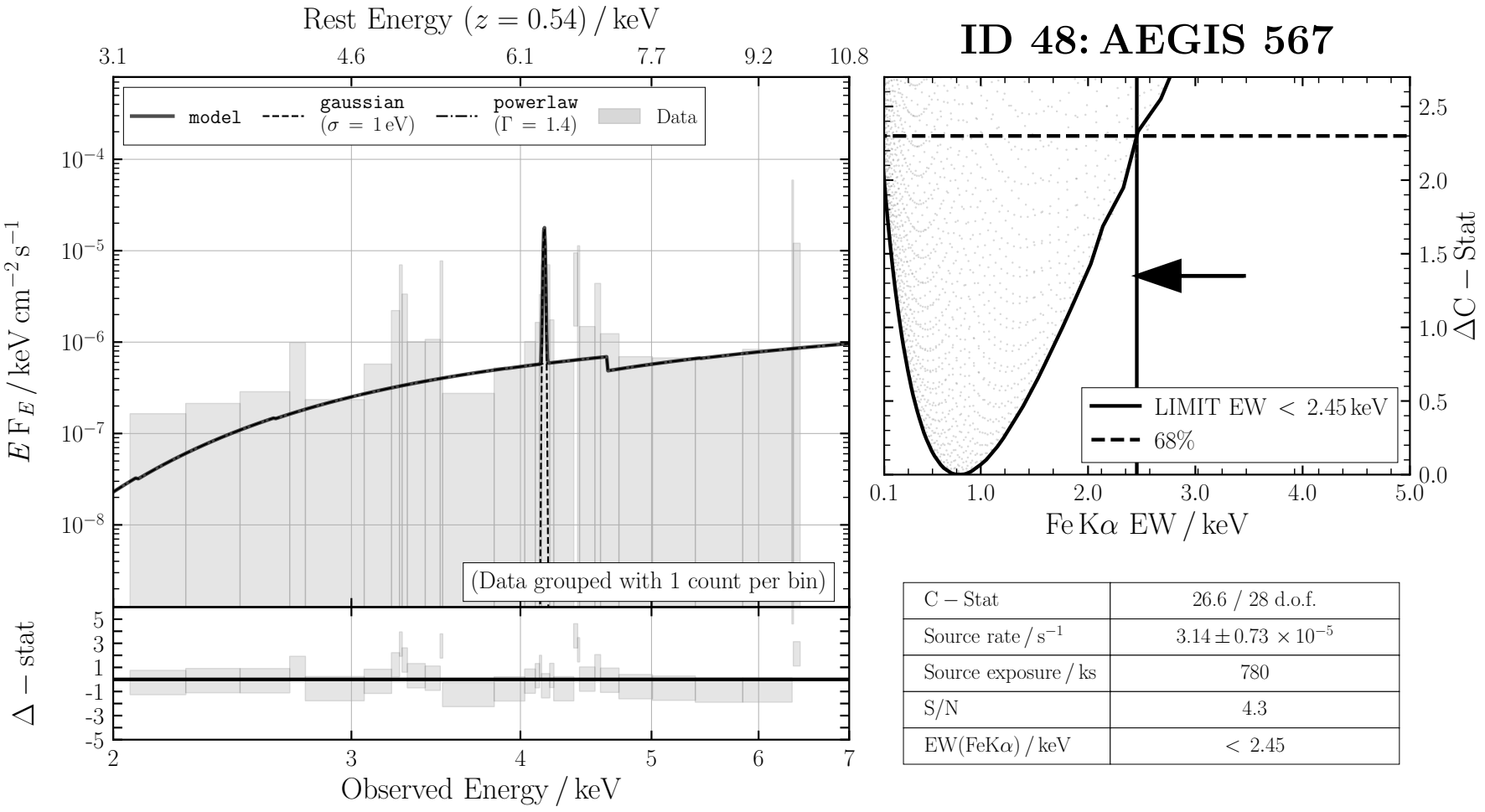

C − Stat	26.6 / 28 d.o.f.
Source rate / s^{-1}	$3.14 \pm 0.73 \times 10^{-5}$
Source exposure / ks	780
S/N	4.3
EW(FeKα) / keV	< 2.45

FIGURE B.47: ID 48: AEGIS 567

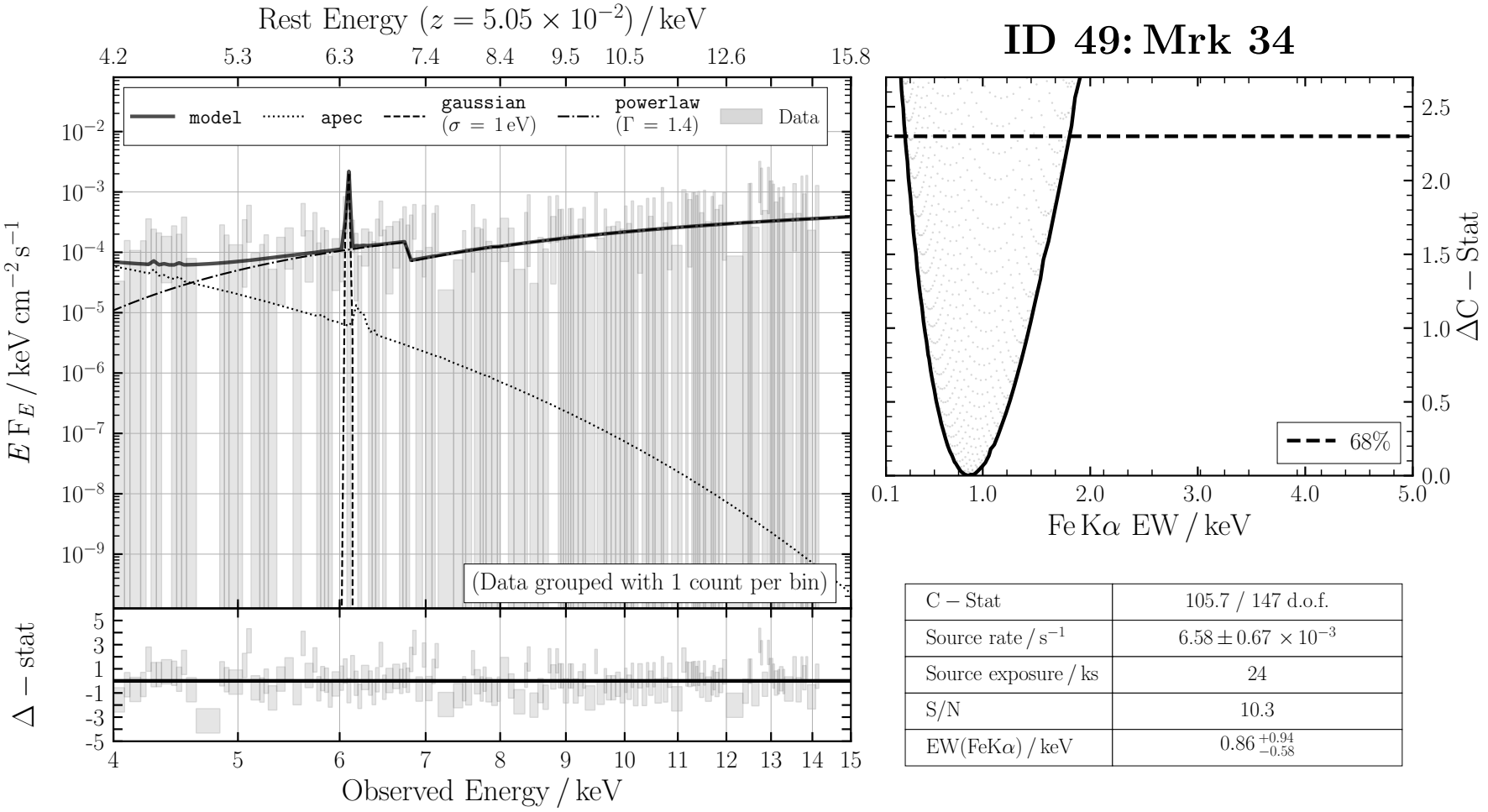

C − Stat	105.7 / 147 d.o.f.
Source rate / s^{-1}	$6.58 \pm 0.67 \times 10^{-3}$
Source exposure / ks	24
S/N	10.3
EW(FeKα) / keV	$0.86\,^{+0.94}_{-0.58}$

FIGURE B.48: ID 49: Mrk 34

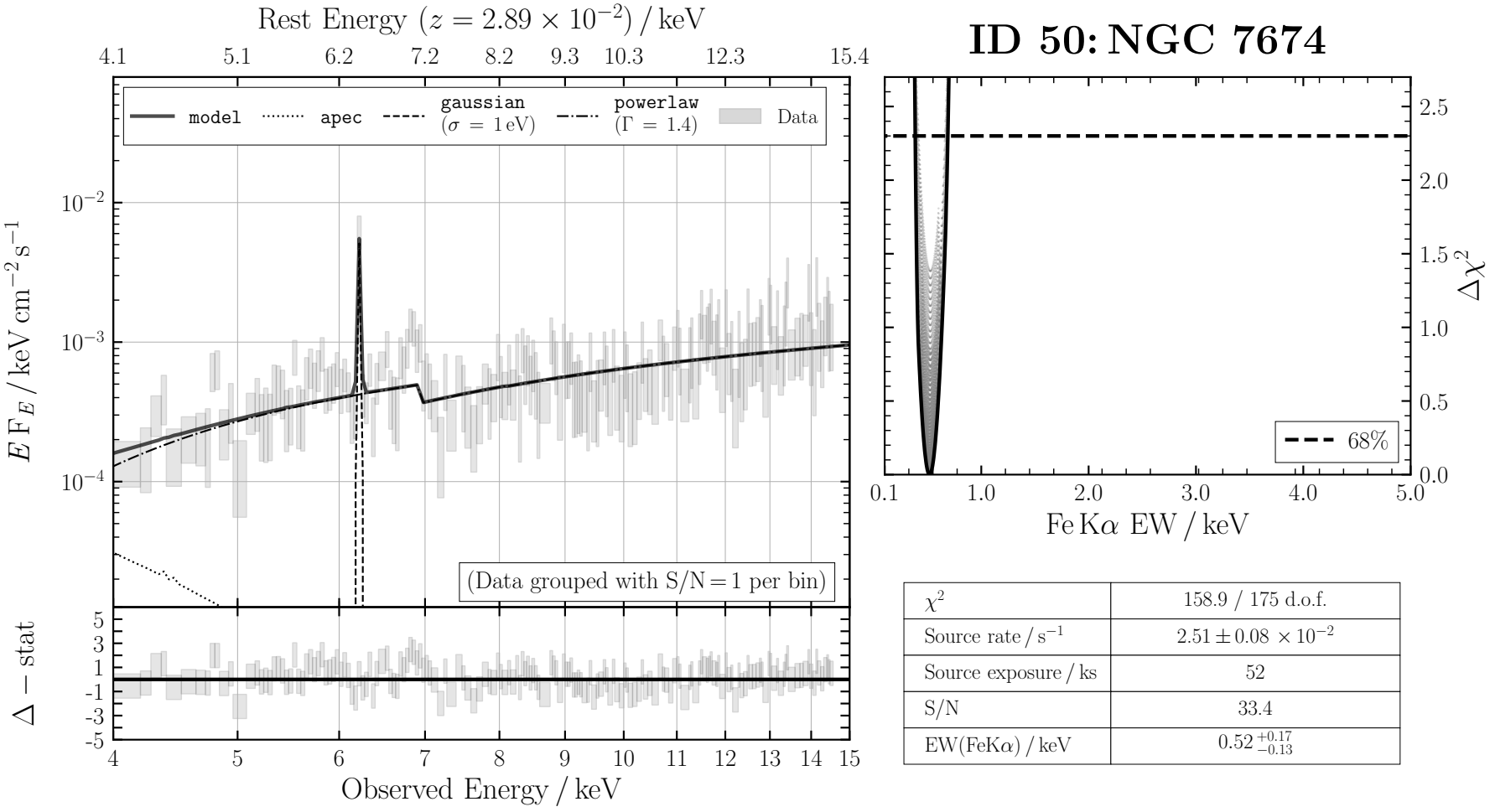

χ^2	158.9 / 175 d.o.f.
Source rate / s^{-1}	$2.51 \pm 0.08 \times 10^{-2}$
Source exposure / ks	52
S/N	33.4
EW(FeKα) / keV	$0.52^{+0.17}_{-0.13}$

FIGURE B.49: ID 50: NGC 7674

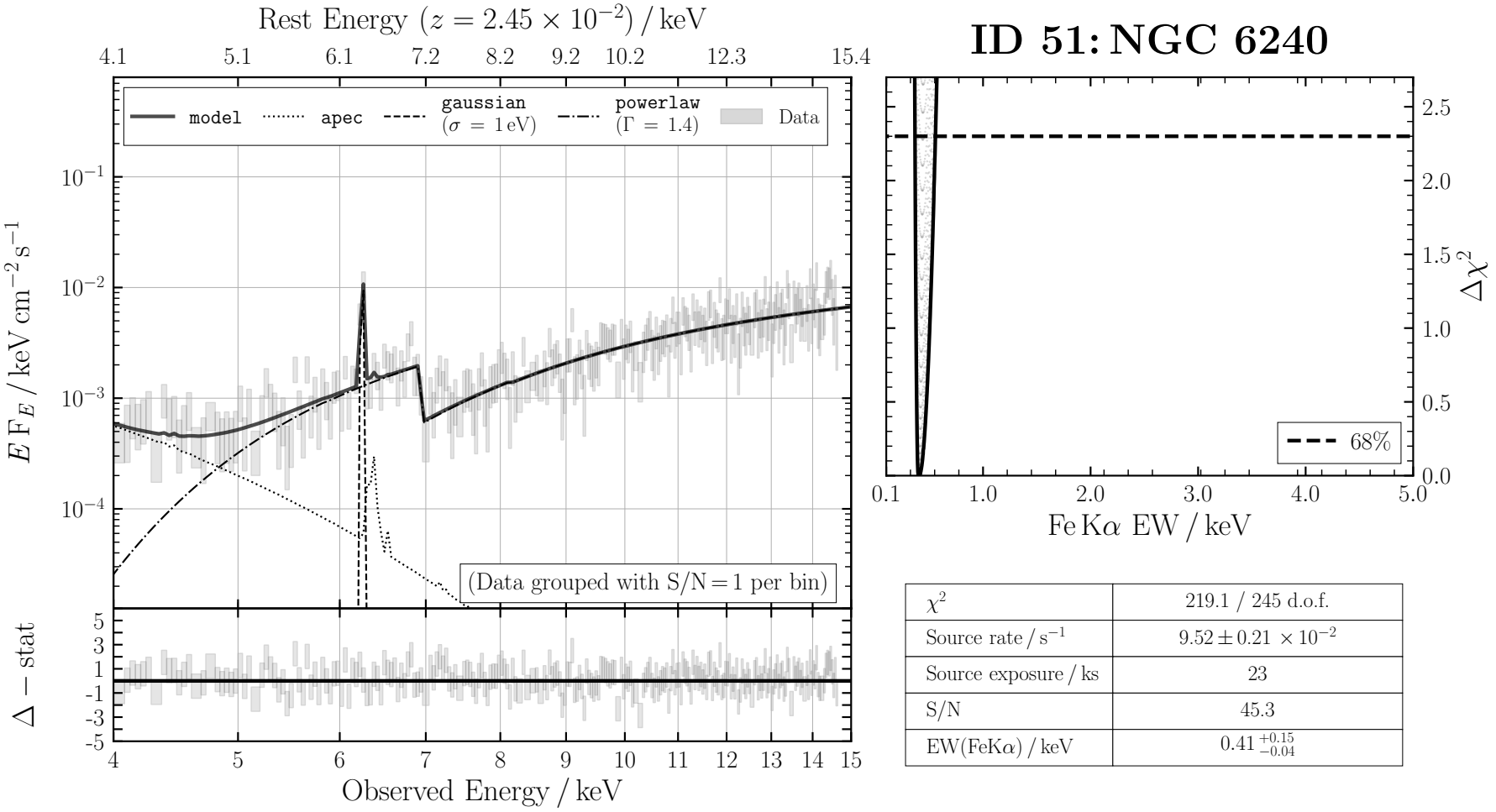

χ^2	219.1 / 245 d.o.f.
Source rate / s^{-1}	$9.52 \pm 0.21 \times 10^{-2}$
Source exposure / ks	23
S/N	45.3
EW(FeKα) / keV	$0.41\,^{+0.15}_{-0.04}$

FIGURE B.50: ID 51: NGC 6240

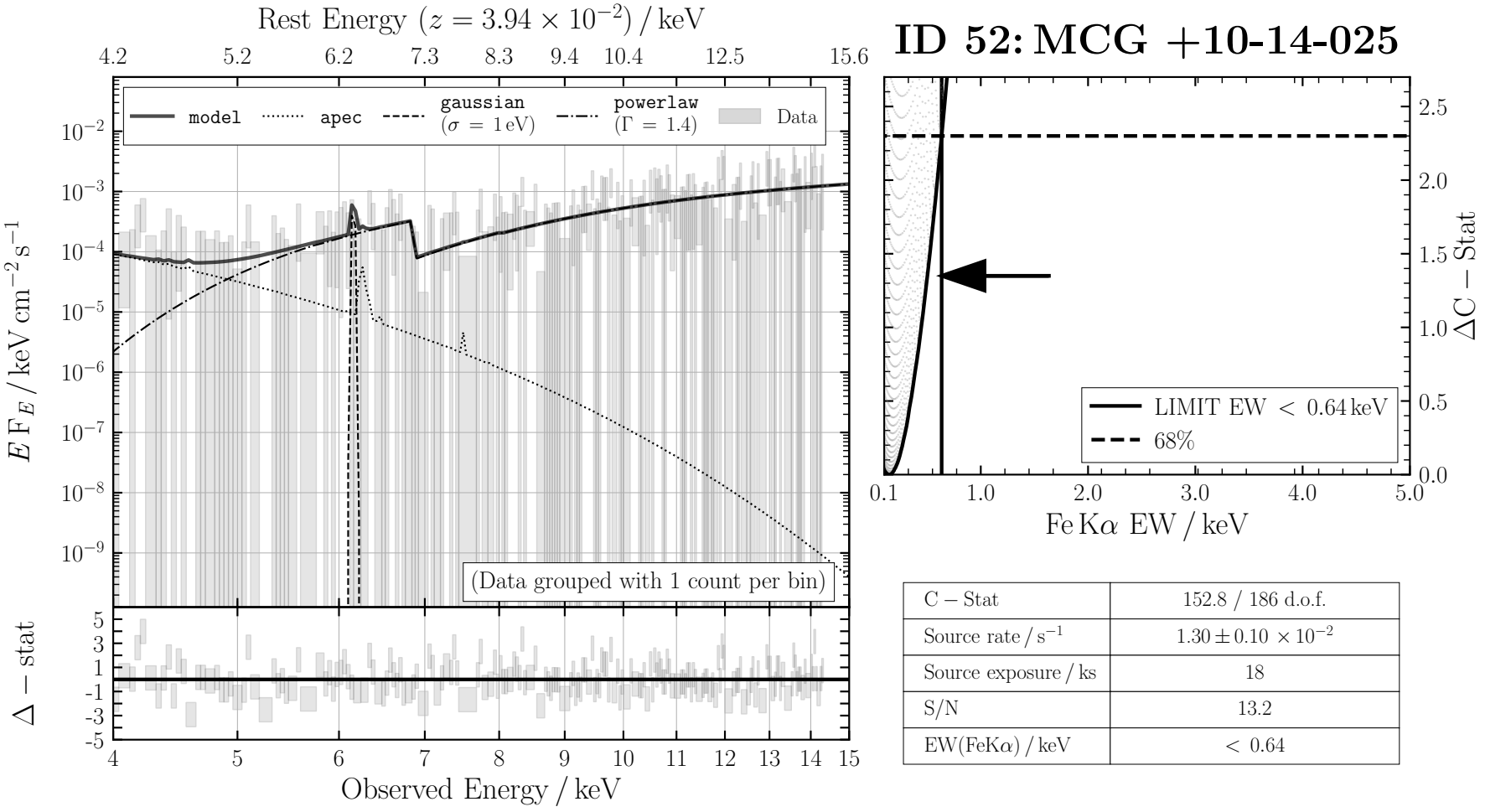

C − Stat	152.8 / 186 d.o.f.
Source rate / s^{-1}	$1.30 \pm 0.10 \times 10^{-2}$
Source exposure / ks	18
S/N	13.2
EW(FeKα) / keV	< 0.64

FIGURE B.51: ID 52: MCG +10-14-025

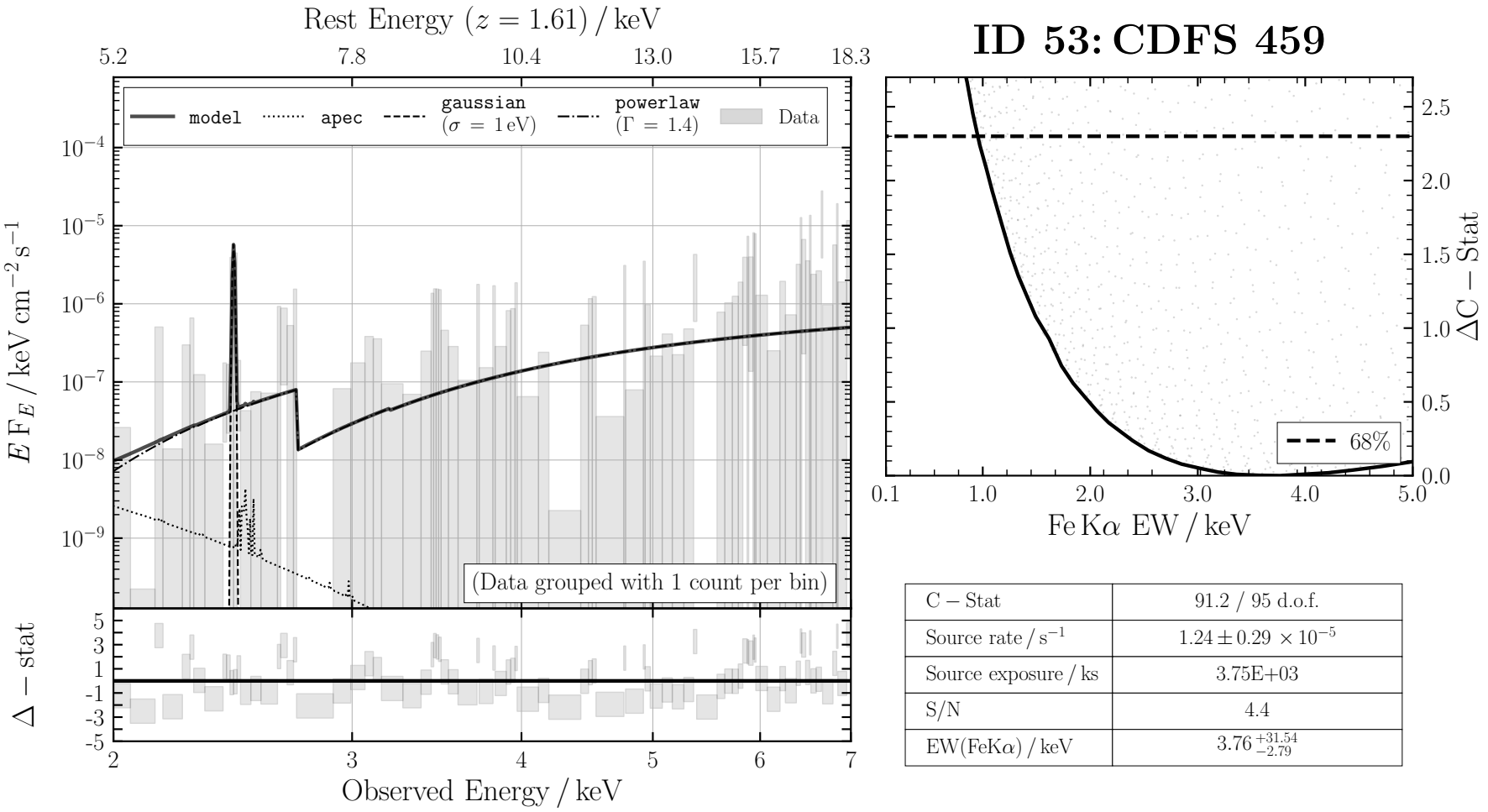

C − Stat	91.2 / 95 d.o.f.
Source rate / s^{-1}	$1.24 \pm 0.29 \times 10^{-5}$
Source exposure / ks	3.75E+03
S/N	4.4
EW(FeKα) / keV	$3.76\,^{+31.54}_{-2.79}$

FIGURE B.52: ID 53: CDFS 459

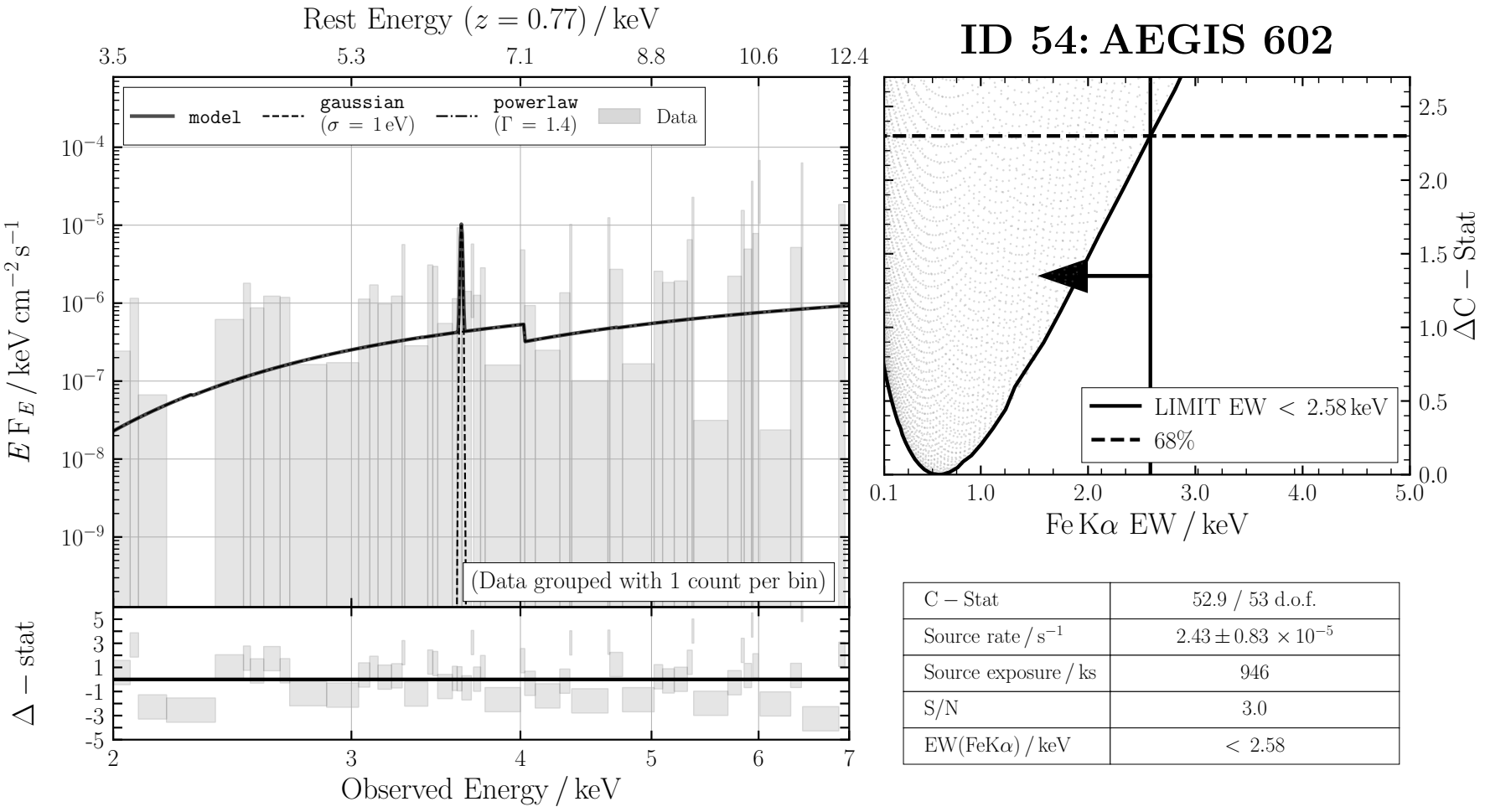

C − Stat	52.9 / 53 d.o.f.
Source rate / s^{-1}	$2.43 \pm 0.83 \times 10^{-5}$
Source exposure / ks	946
S/N	3.0
EW(FeKα) / keV	< 2.58

Figure B.53: ID 54: AEGIS 602

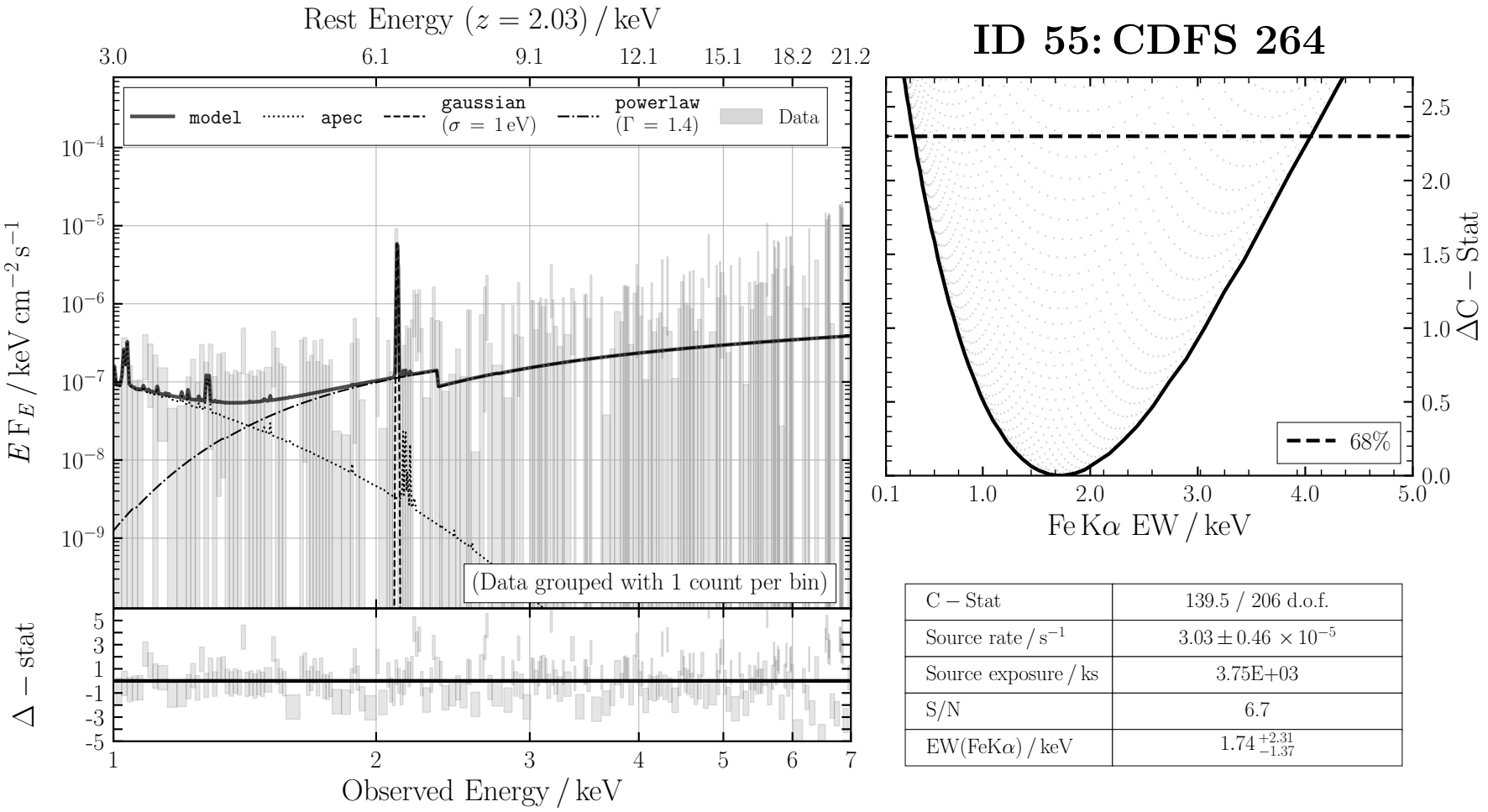

C − Stat	139.5 / 206 d.o.f.
Source rate / s^{-1}	$3.03 \pm 0.46 \times 10^{-5}$
Source exposure / ks	3.75E+03
S/N	6.7
EW(FeKα) / keV	$1.74^{+2.31}_{-1.37}$

FIGURE B.54: ID 55: CDFS 264

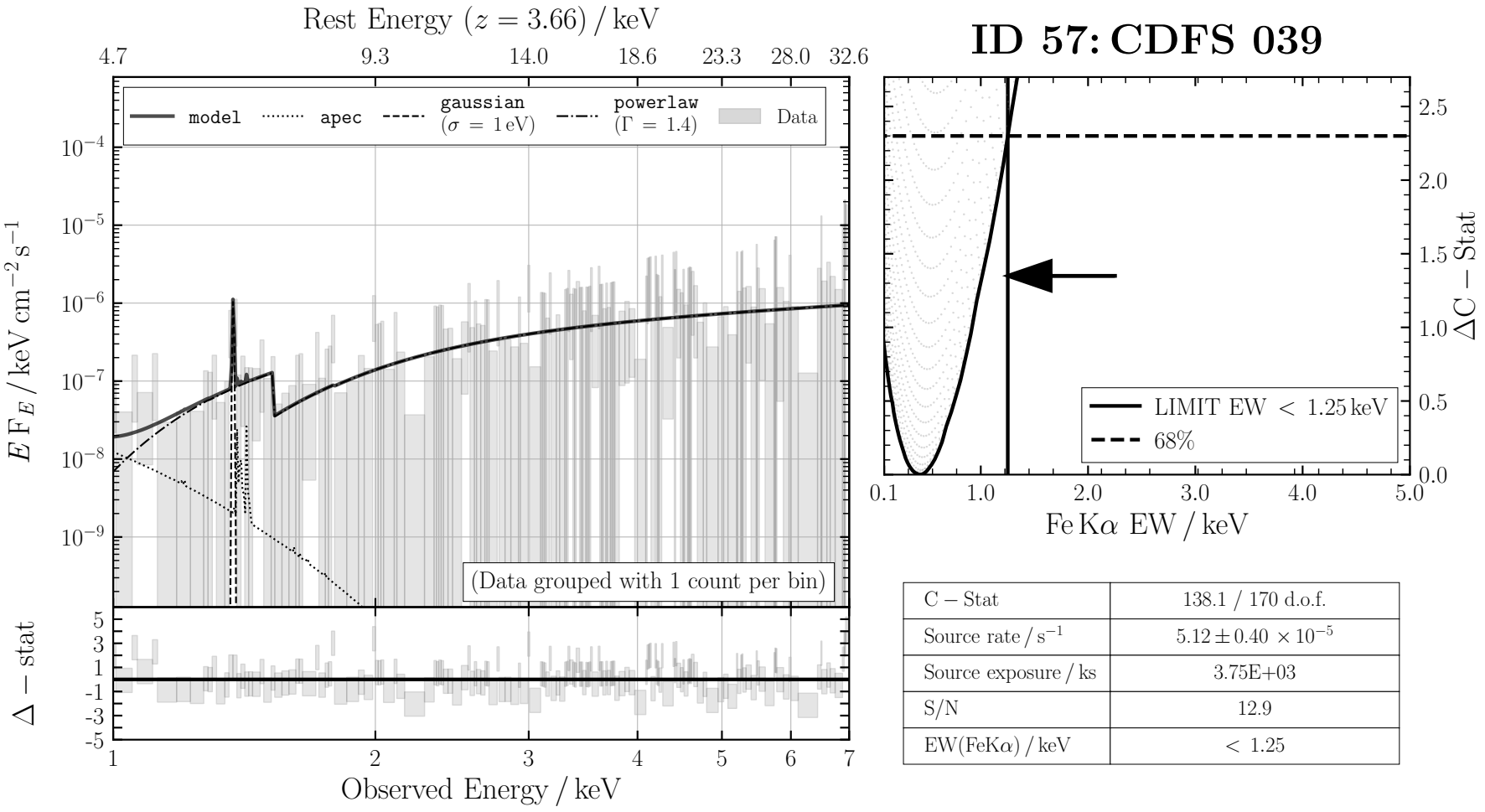

C − Stat	138.1 / 170 d.o.f.
Source rate / s^{-1}	$5.12 \pm 0.40 \times 10^{-5}$
Source exposure / ks	3.75E+03
S/N	12.9
EW(FeKα) / keV	< 1.25

FIGURE B.55: ID 57: CDFS 039

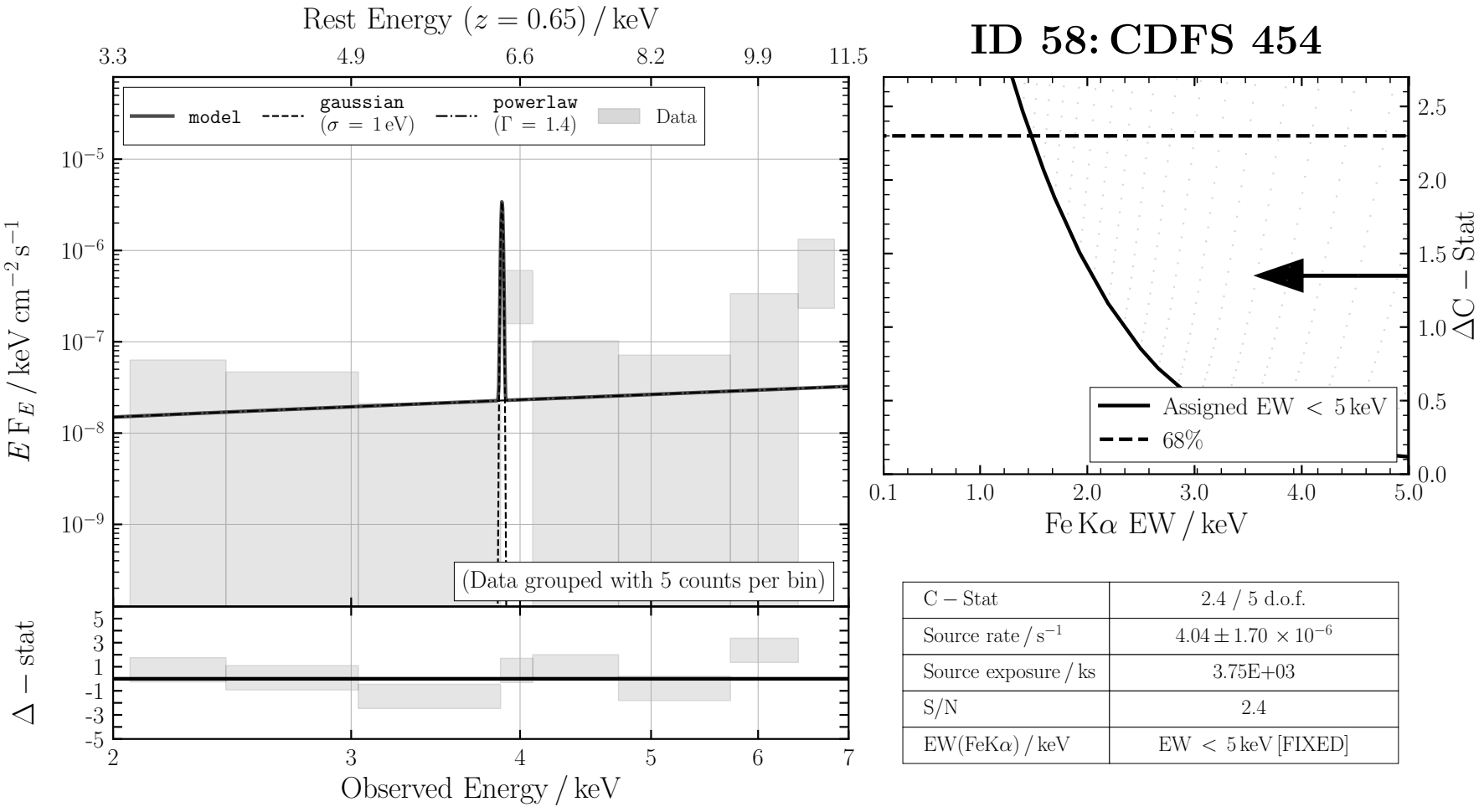

C − Stat	2.4 / 5 d.o.f.
Source rate / s^{-1}	$4.04 \pm 1.70 \times 10^{-6}$
Source exposure / ks	3.75E+03
S/N	2.4
EW(FeKα) / keV	EW < 5 keV [FIXED]

FIGURE B.56: ID 58: CDFS 454

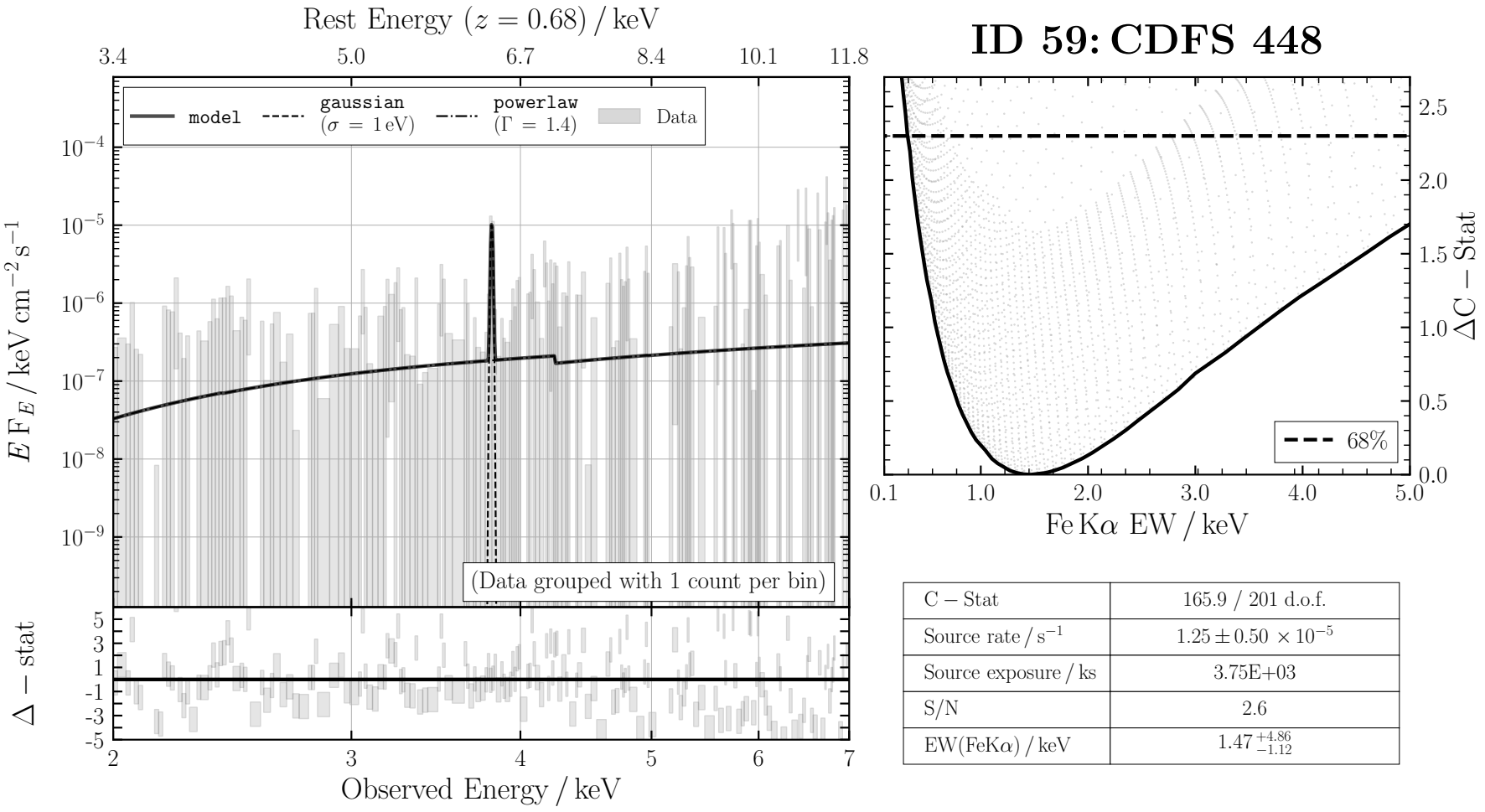

C − Stat	165.9 / 201 d.o.f.
Source rate / s^{-1}	$1.25 \pm 0.50 \times 10^{-5}$
Source exposure / ks	3.75E+03
S/N	2.6
EW(FeKα) / keV	$1.47^{+4.86}_{-1.12}$

FIGURE B.57: ID 59: CDFS 448

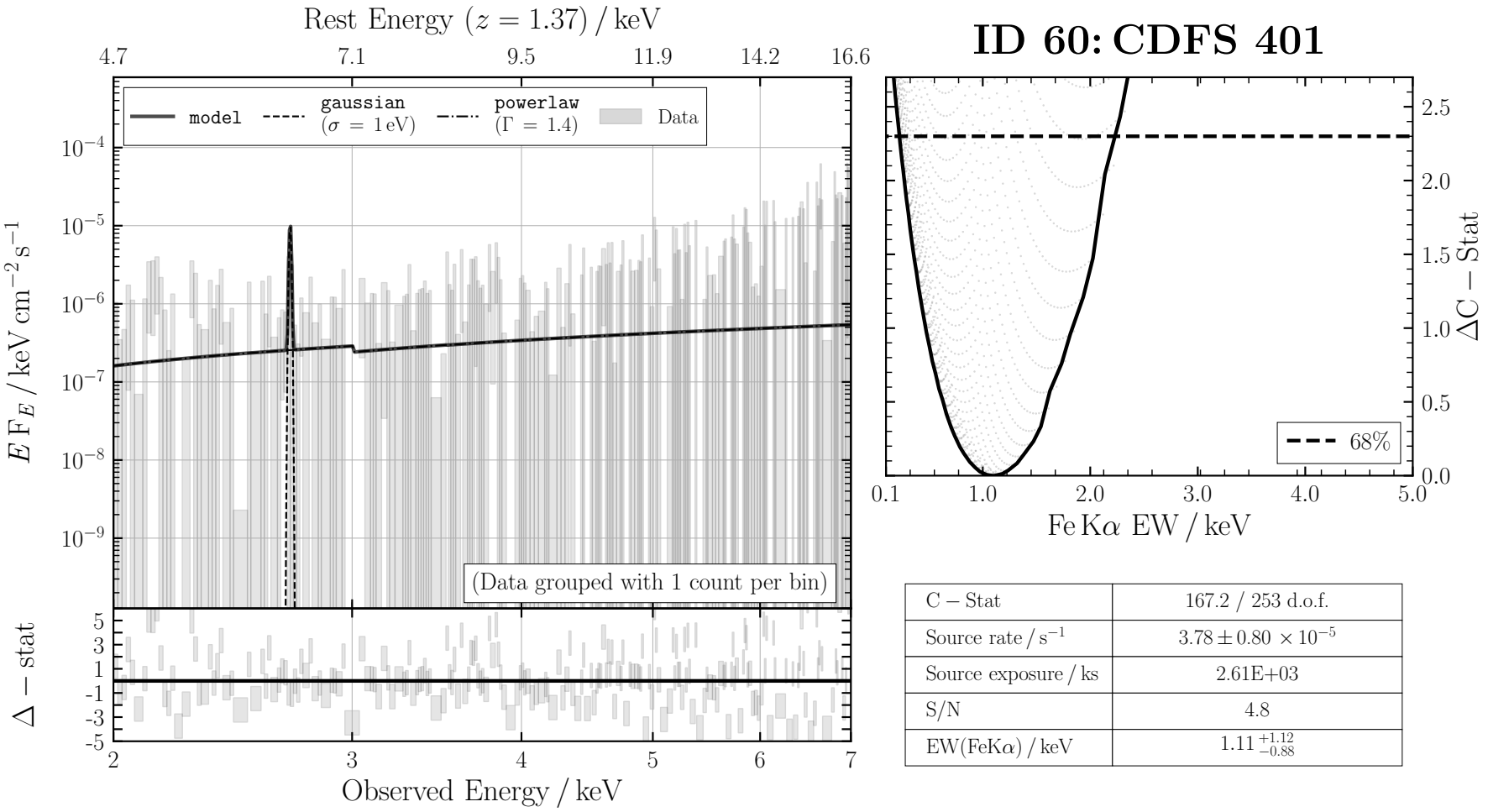

FIGURE B.58: ID 60: CDFS 401

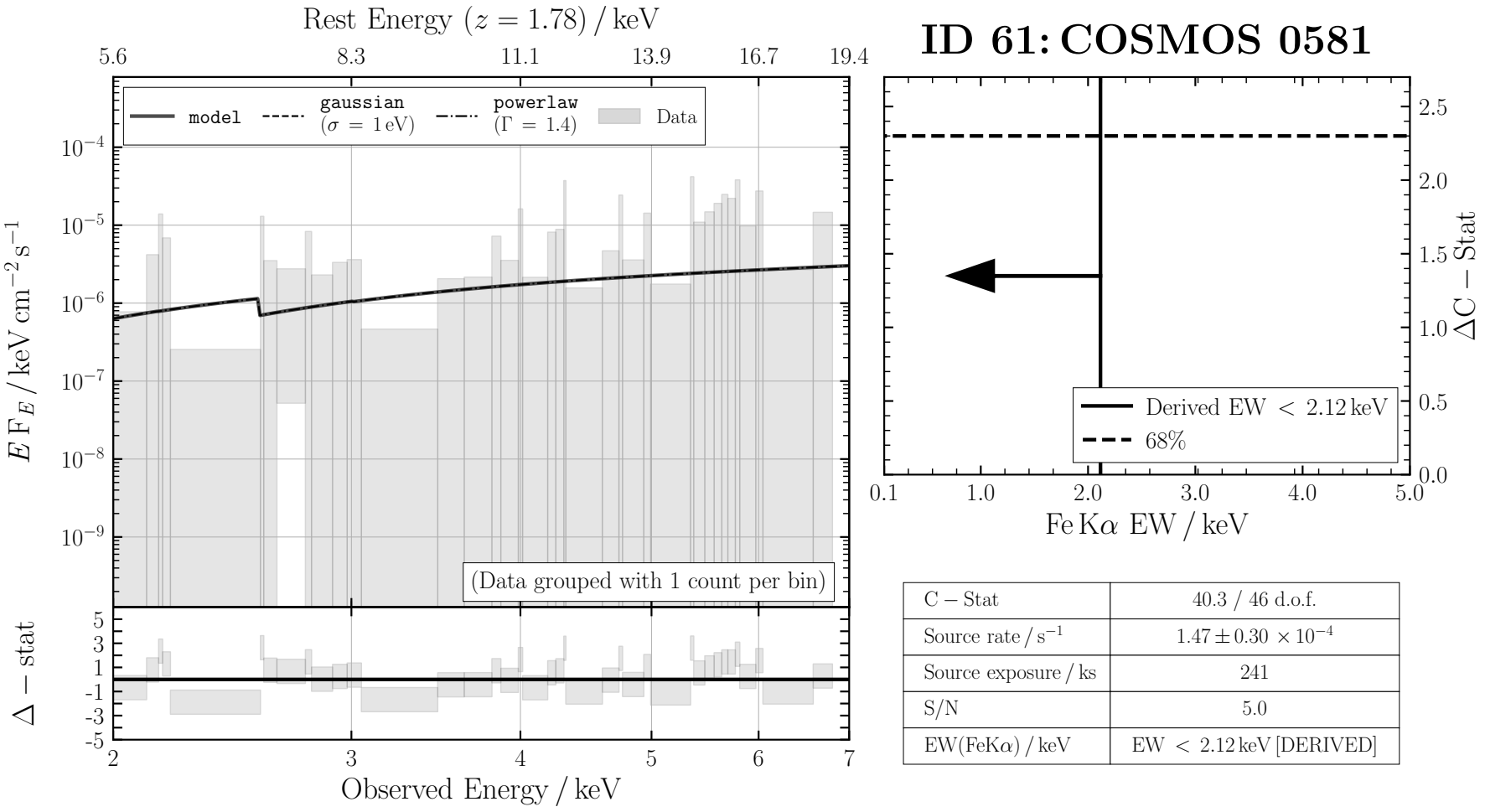

FIGURE B.59: ID 61: COSMOS 0581

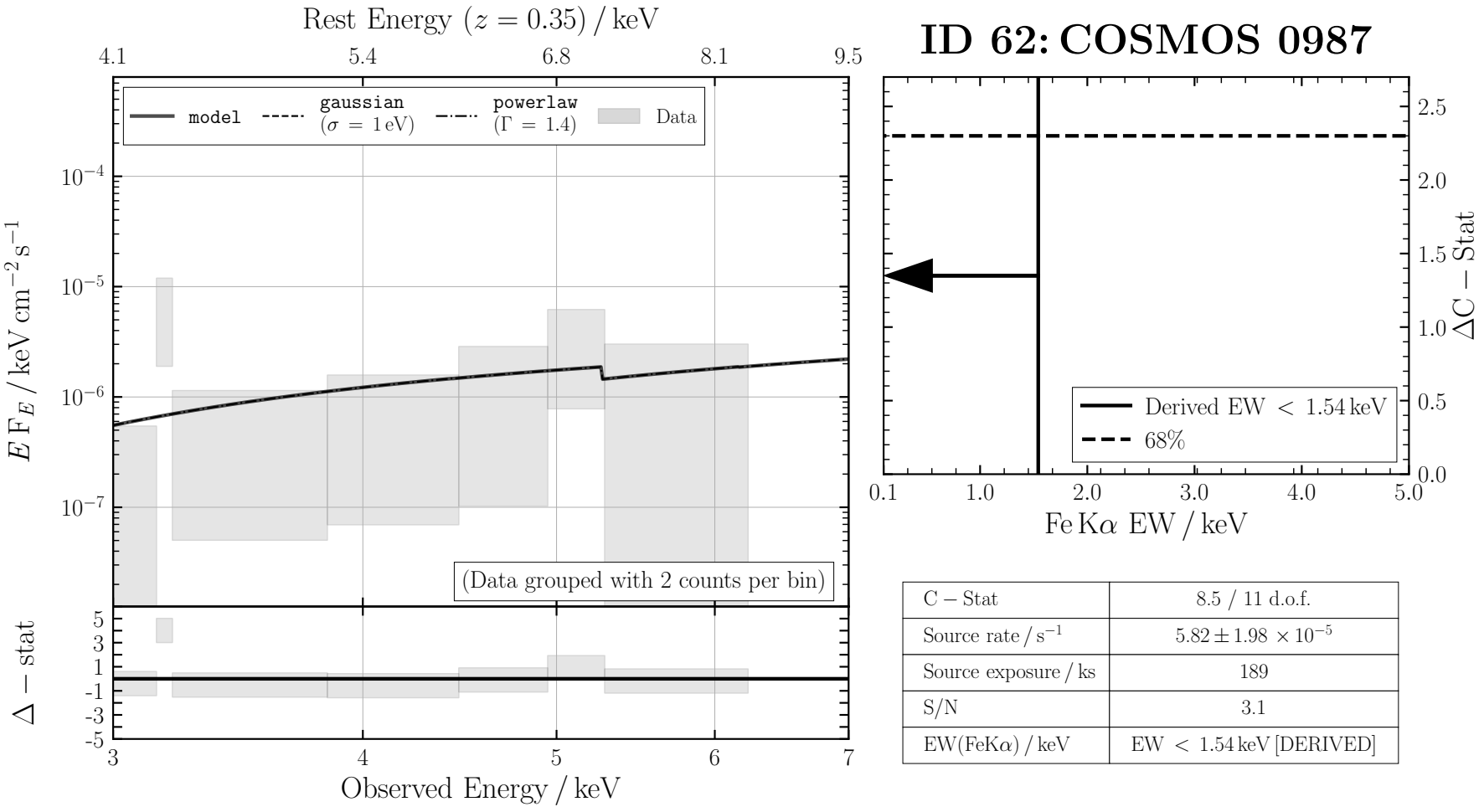

C − Stat	8.5 / 11 d.o.f.
Source rate / s^{-1}	$5.82 \pm 1.98 \times 10^{-5}$
Source exposure / ks	189
S/N	3.1
EW(FeKα) / keV	EW < 1.54 keV [DERIVED]

FIGURE B.60: ID 62: COSMOS 0987

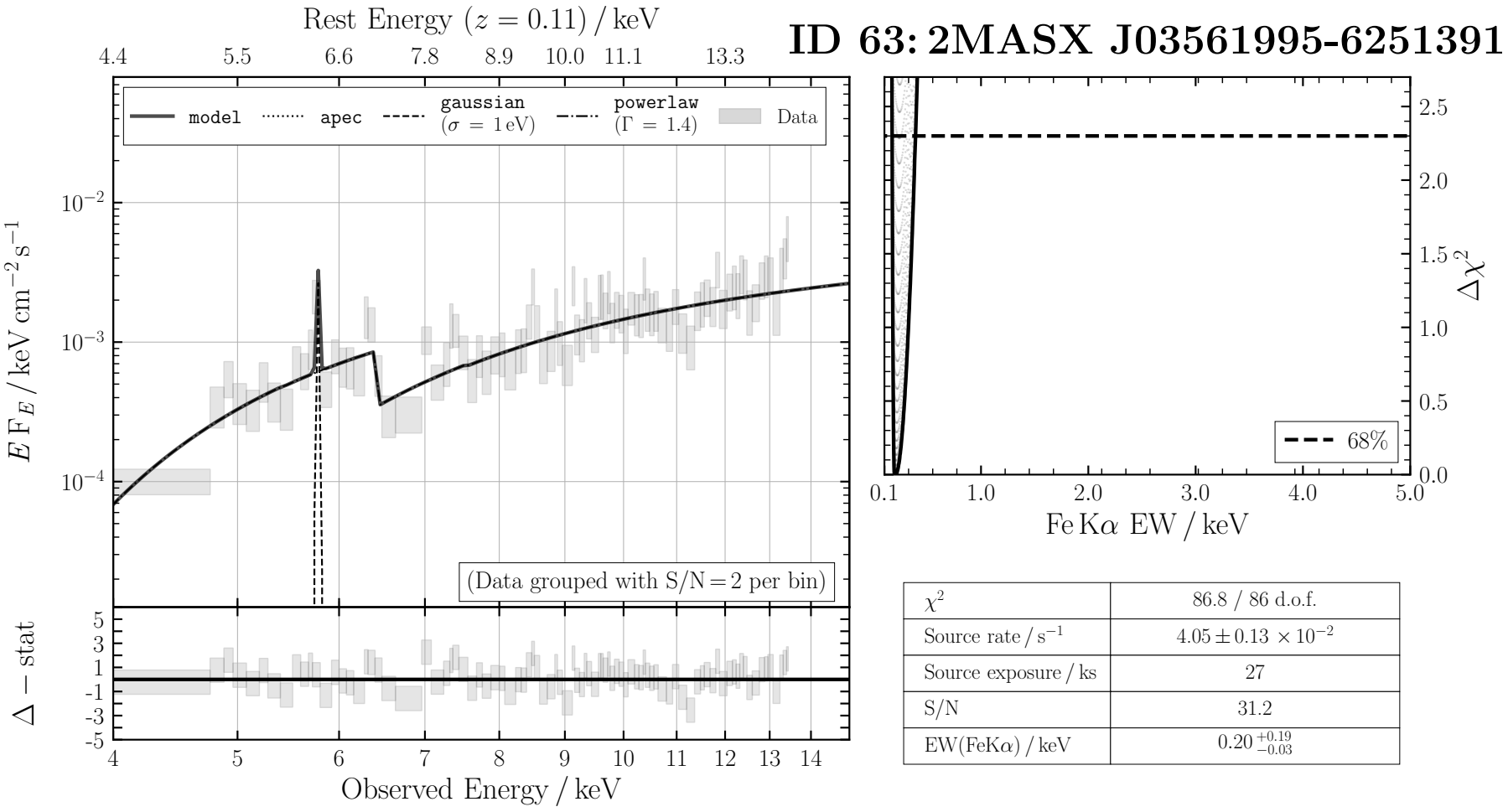

χ^2	86.8 / 86 d.o.f.
Source rate / s^{-1}	$4.05 \pm 0.13 \times 10^{-2}$
Source exposure / ks	27
S/N	31.2
EW(FeKα) / keV	$0.20^{+0.19}_{-0.03}$

FIGURE B.61: ID 63: 2MASX J03561995-6251391

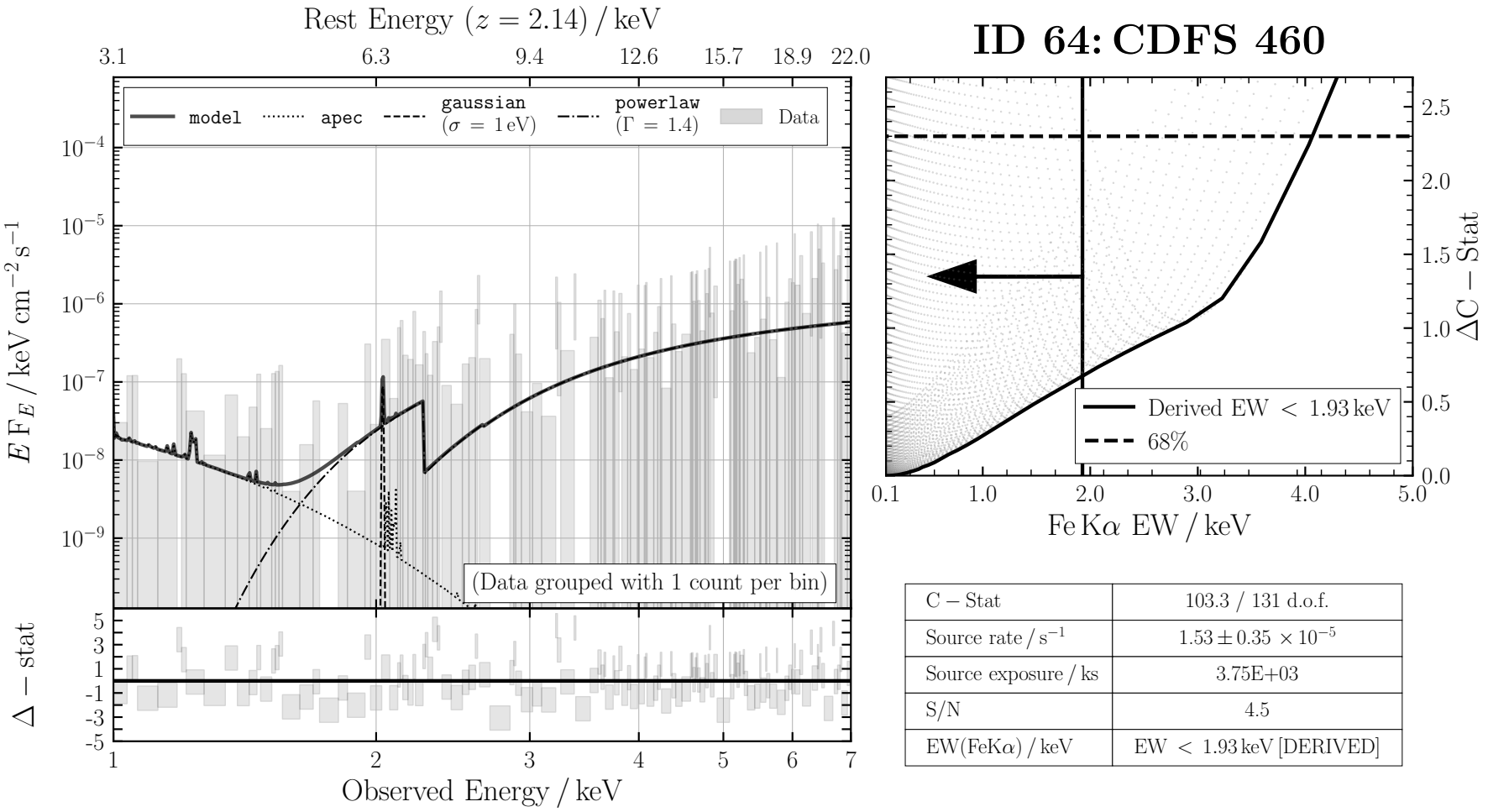

C − Stat	103.3 / 131 d.o.f.
Source rate / s^{-1}	$1.53 \pm 0.35 \times 10^{-5}$
Source exposure / ks	3.75E+03
S/N	4.5
EW(FeKα) / keV	EW < 1.93 keV [DERIVED]

FIGURE B.62: ID 64: CDFS 460

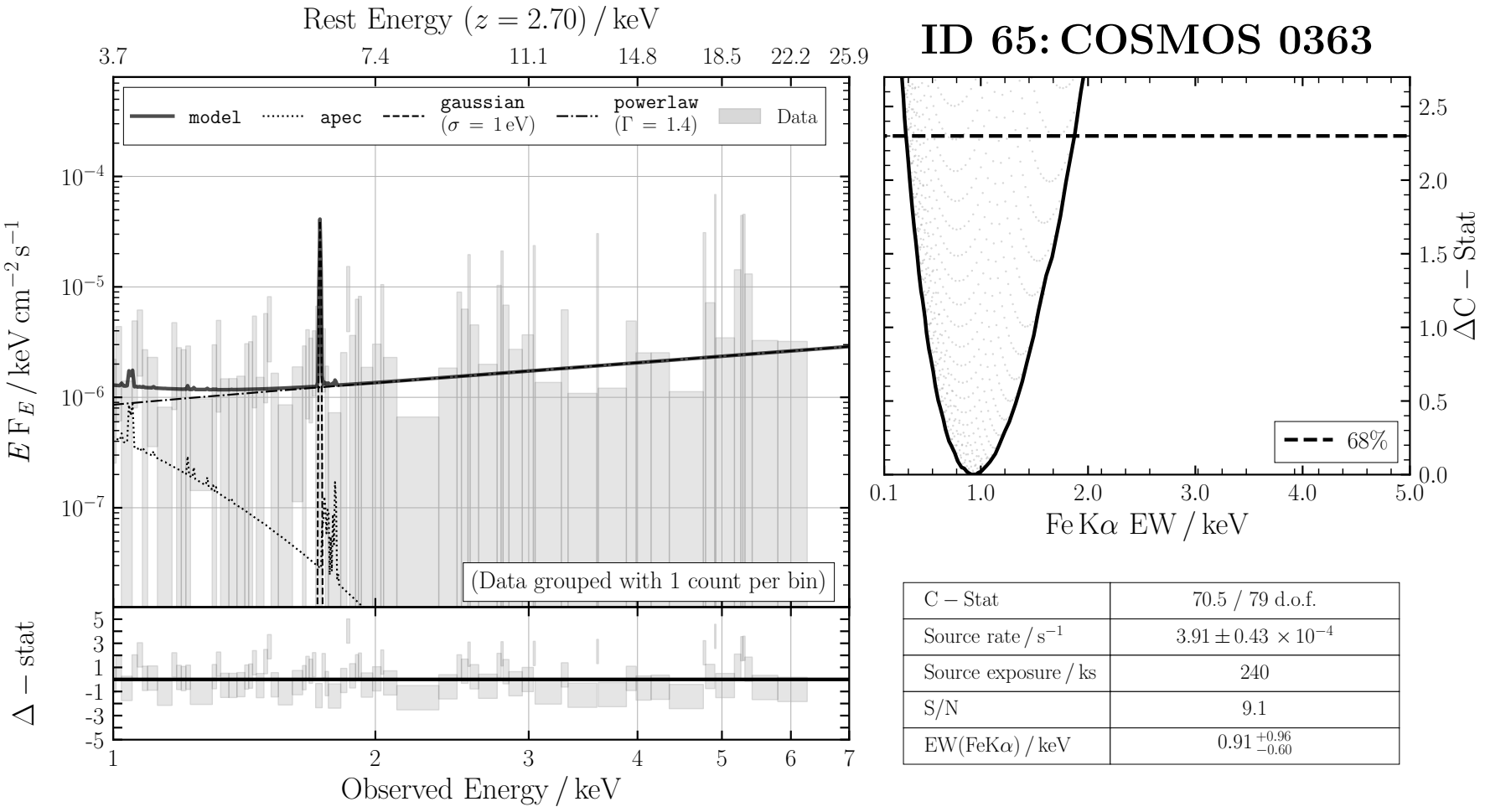

C − Stat	70.5 / 79 d.o.f.
Source rate / s^{-1}	$3.91 \pm 0.43 \times 10^{-4}$
Source exposure / ks	240
S/N	9.1
EW(FeKα) / keV	$0.91\,^{+0.96}_{-0.60}$

FIGURE B.63: ID 65: COSMOS 0363

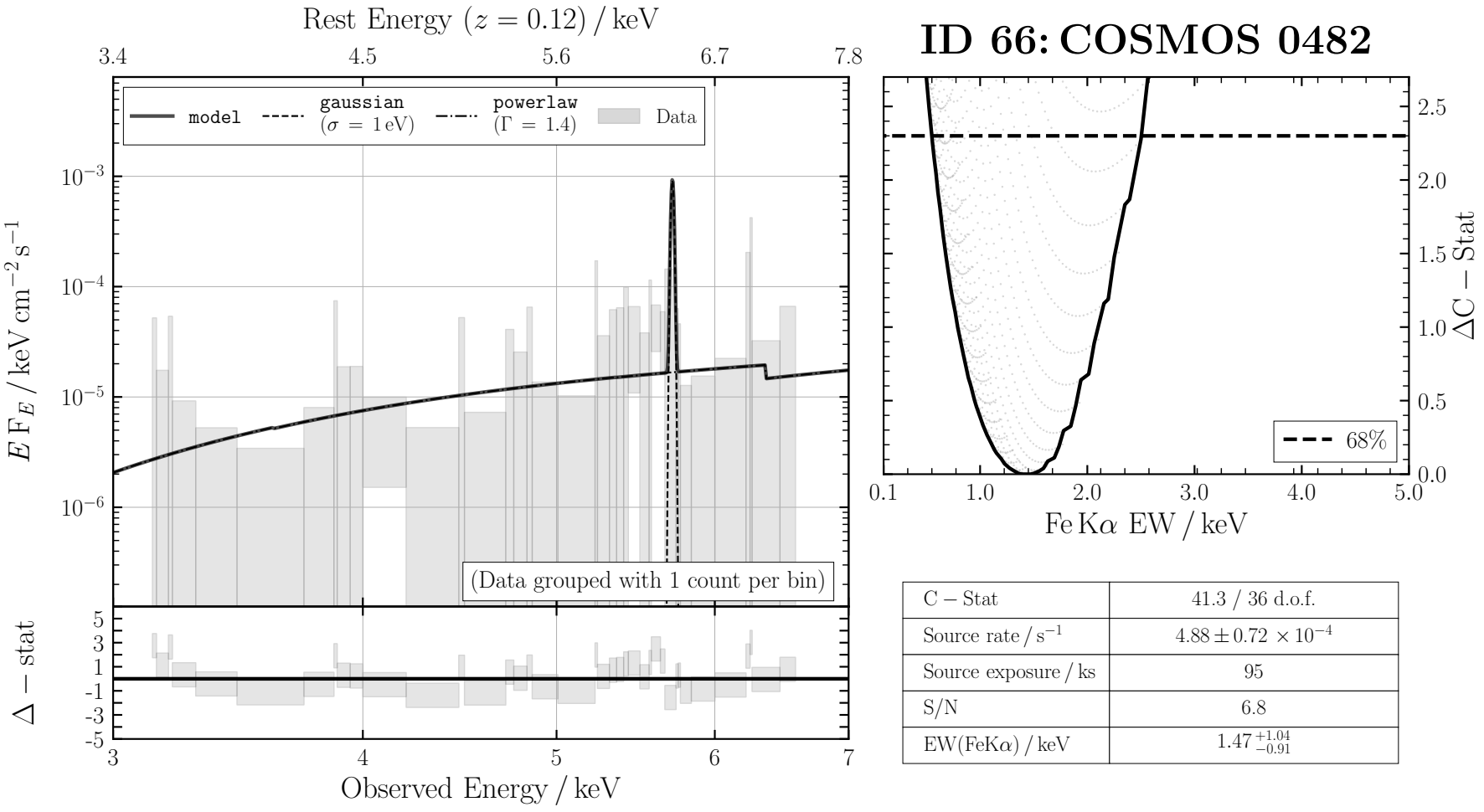

C − Stat	41.3 / 36 d.o.f.
Source rate / s^{-1}	$4.88 \pm 0.72 \times 10^{-4}$
Source exposure / ks	95
S/N	6.8
EW(FeKα) / keV	$1.47^{+1.04}_{-0.91}$

FIGURE B.64: ID 66: COSMOS 0482

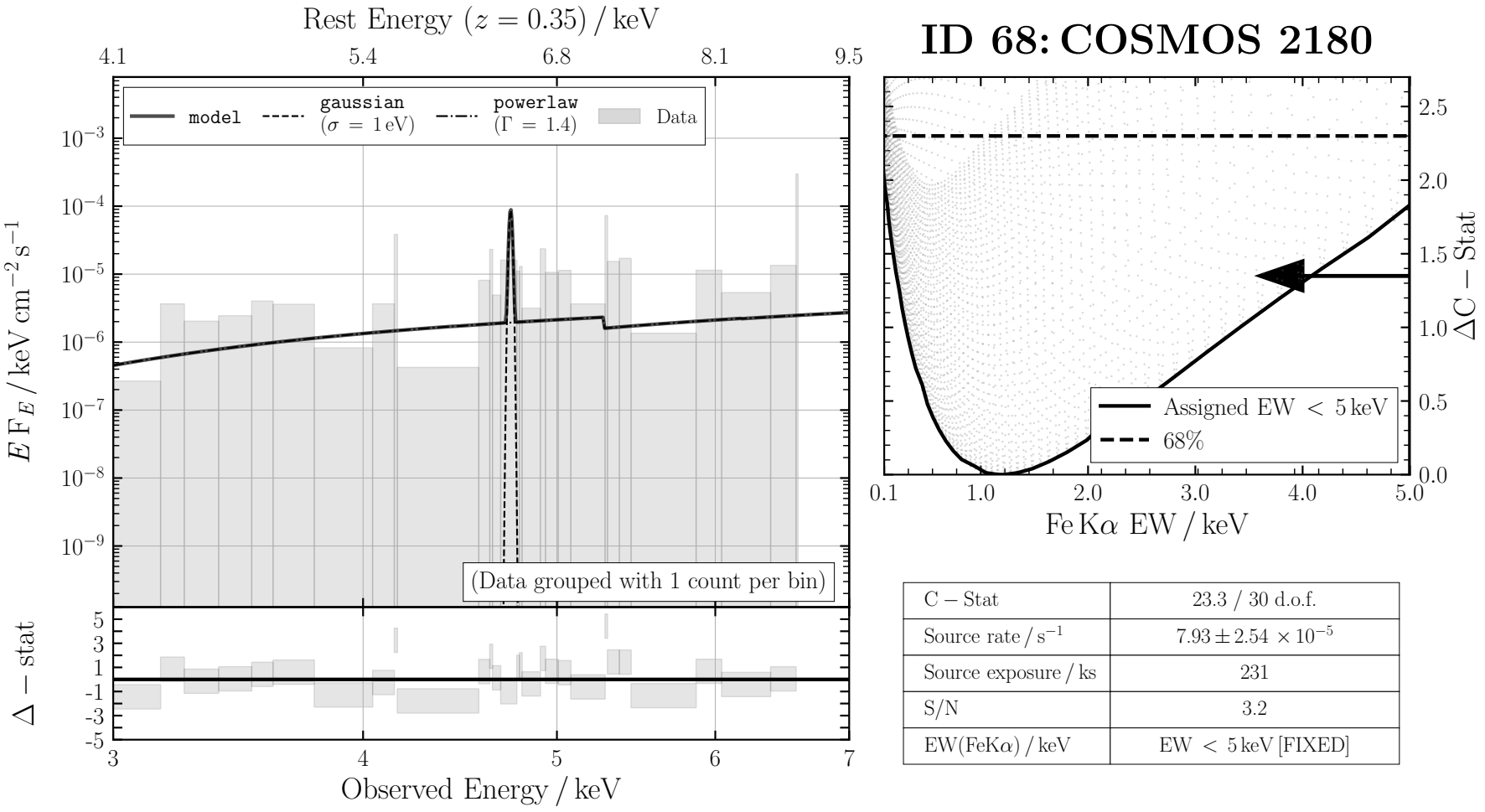

C − Stat	23.3 / 30 d.o.f.
Source rate / s^{-1}	$7.93 \pm 2.54 \times 10^{-5}$
Source exposure / ks	231
S/N	3.2
EW(FeKα) / keV	EW < 5 keV [FIXED]

FIGURE B.65: ID 68: COSMOS 2180

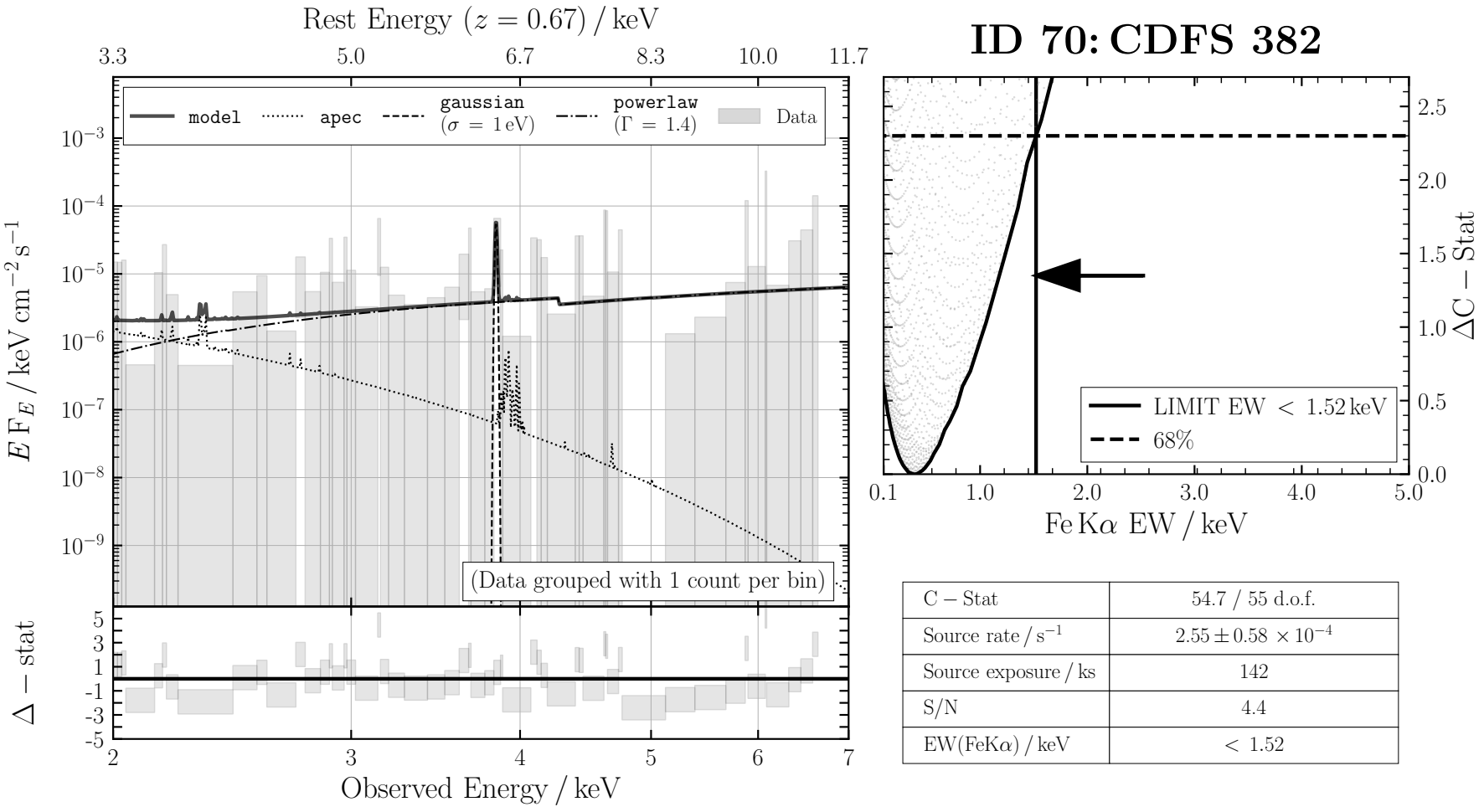

C − Stat	54.7 / 55 d.o.f.
Source rate / s^{-1}	$2.55 \pm 0.58 \times 10^{-4}$
Source exposure / ks	142
S/N	4.4
EW(FeKα) / keV	< 1.52

FIGURE B.66: ID 70: CDFS 382

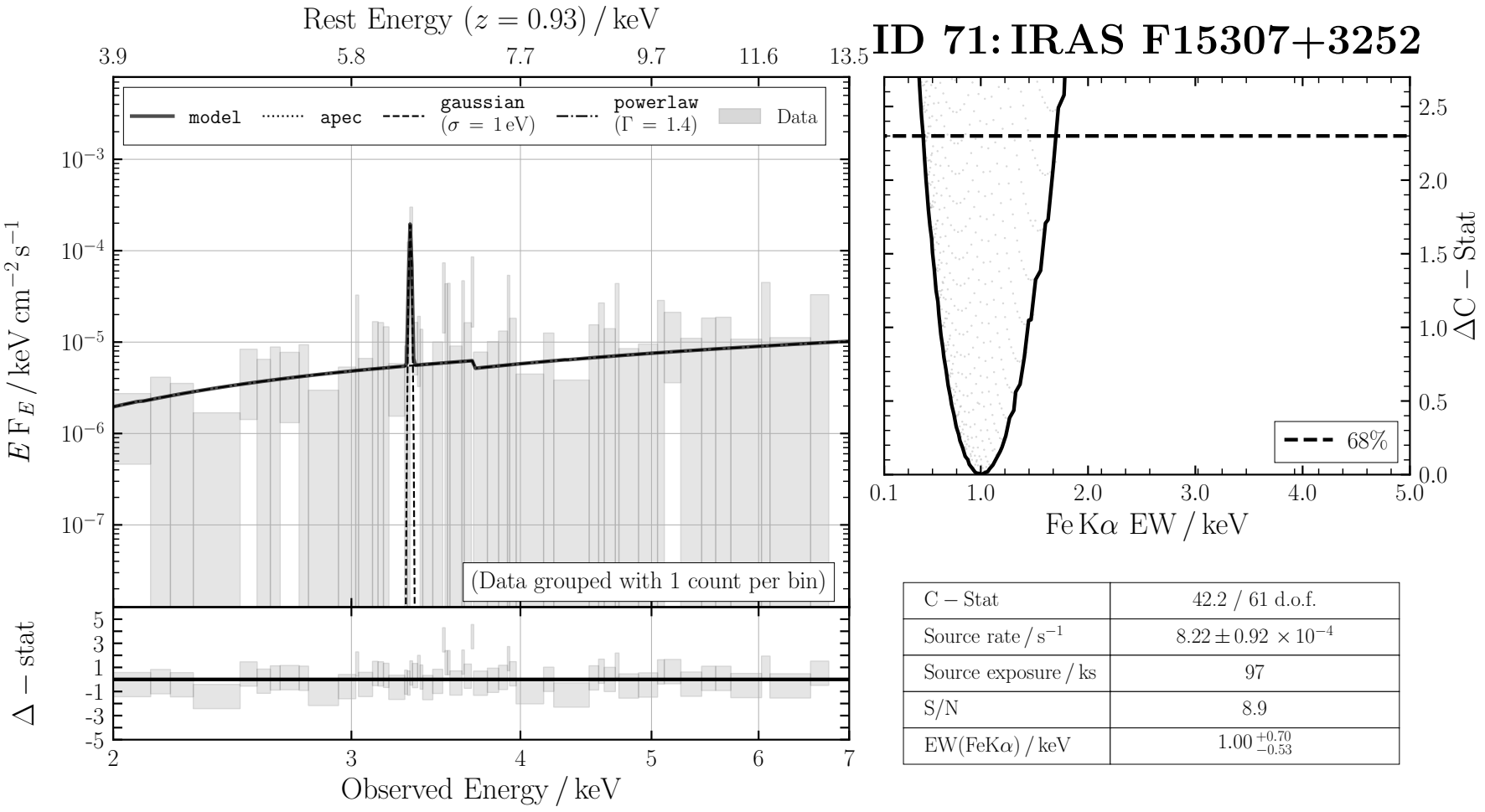

C − Stat	42.2 / 61 d.o.f.
Source rate / s^{-1}	$8.22 \pm 0.92 \times 10^{-4}$
Source exposure / ks	97
S/N	8.9
EW(FeKα) / keV	$1.00\,^{+0.70}_{-0.53}$

FIGURE B.67: ID 71: IRAS F15307+3252

Appendix C

The *NuSTAR* Local AGN $N_{\rm H}$ Distribution Survey: Prospects for Mitigating Obscuration Bias in Local AGN Selection

C.1 Observed *NuSTAR* Spectral Constraints for Legacy Targets

Here I present the spectral fits and Equivalent Width (EW) contours of each NuLANDS source observed as part of the extragalactic legacy survey. The left panel of each figure shows the observed *NuSTAR* spectrum (apart from three sources only observed by *XMM-Newton* so far). The right panel then displays the MCMC confidence constraint on the powerlaw photon index, as well as the EW of the Fe Kα line. The distribution of Fe Kα line EWs from the study carried out in Chapter 3 (for sources with $z < 0.1$) is overplotted with purple hatch to show the wide range of possible EWs for Compton-thick AGN.

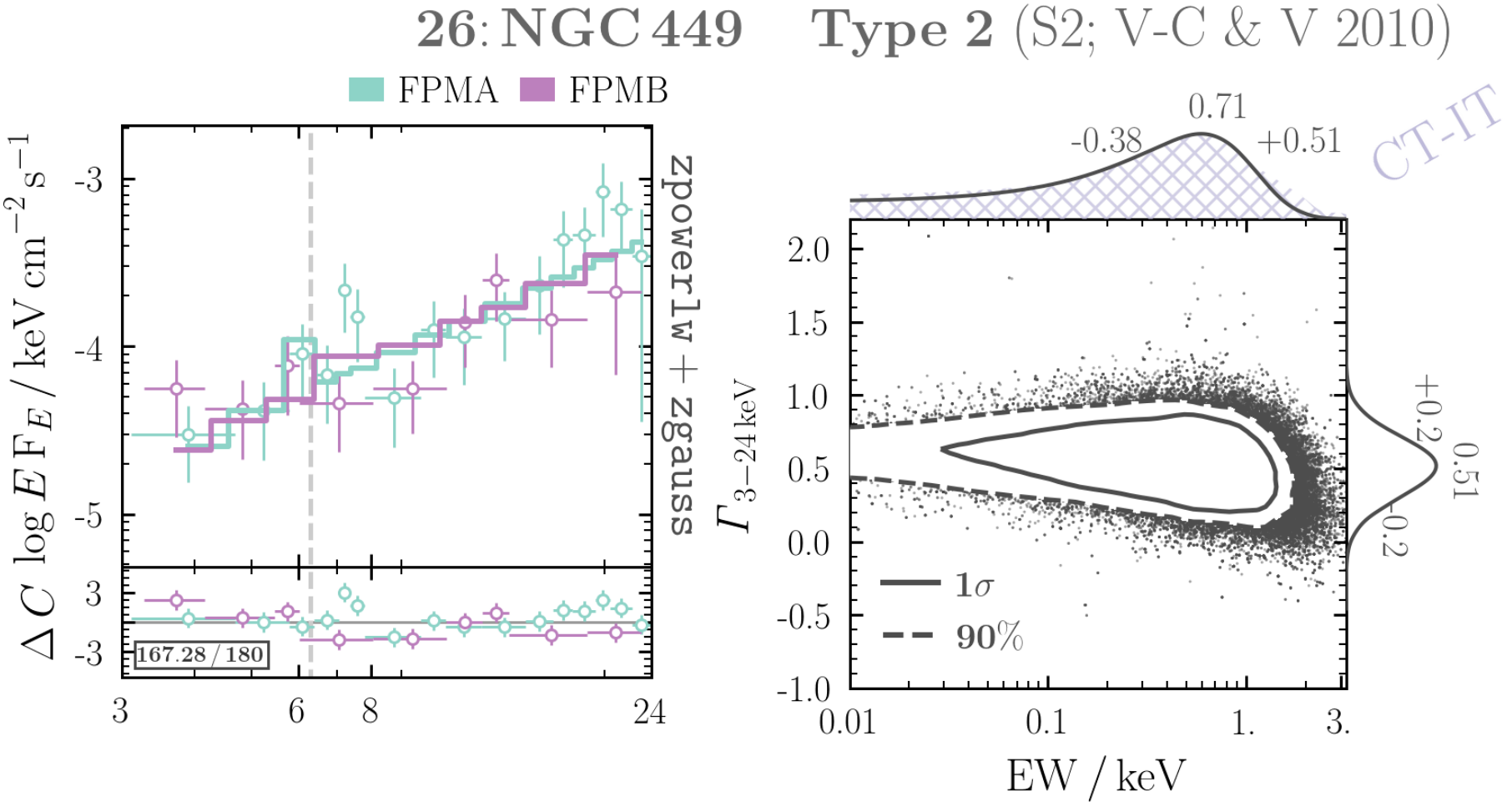

FIGURE C.1: Phenomenological Fit, ID 26: NGC 449

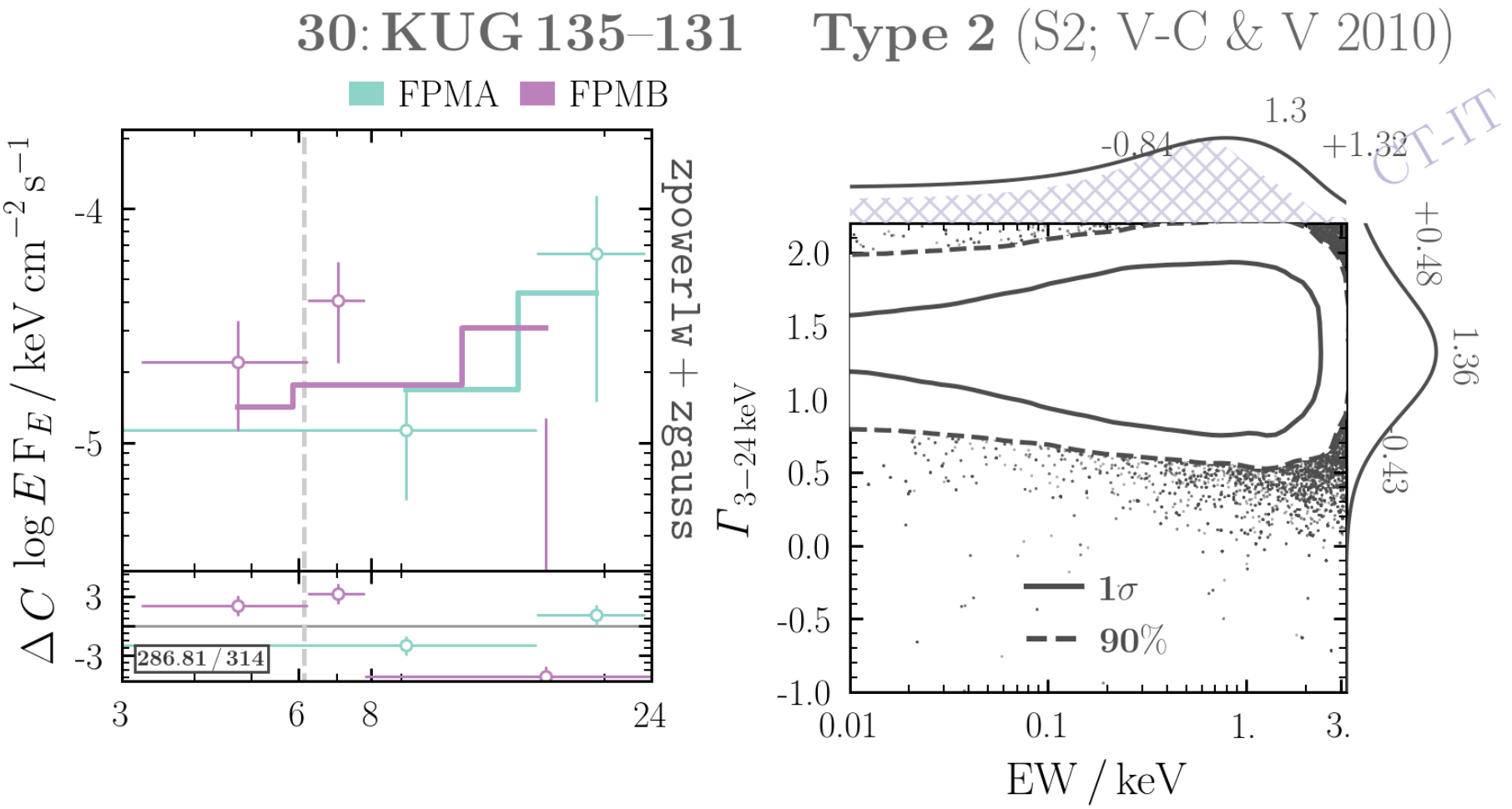

FIGURE C.2: Phenomenological Fit, ID 30: KUG 0135 –131

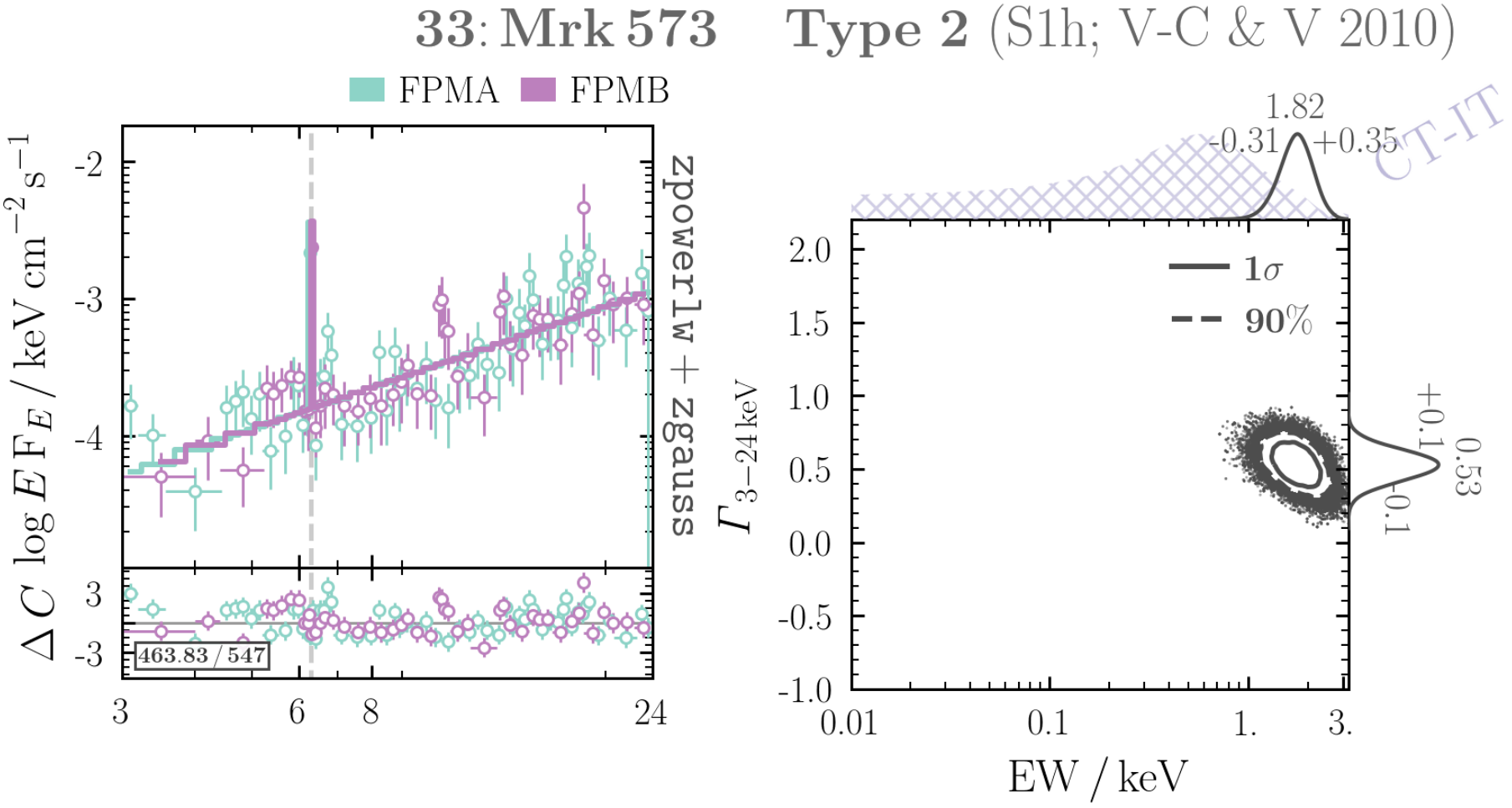

FIGURE C.3: Phenomenological Fit, ID 33: Mrk 573

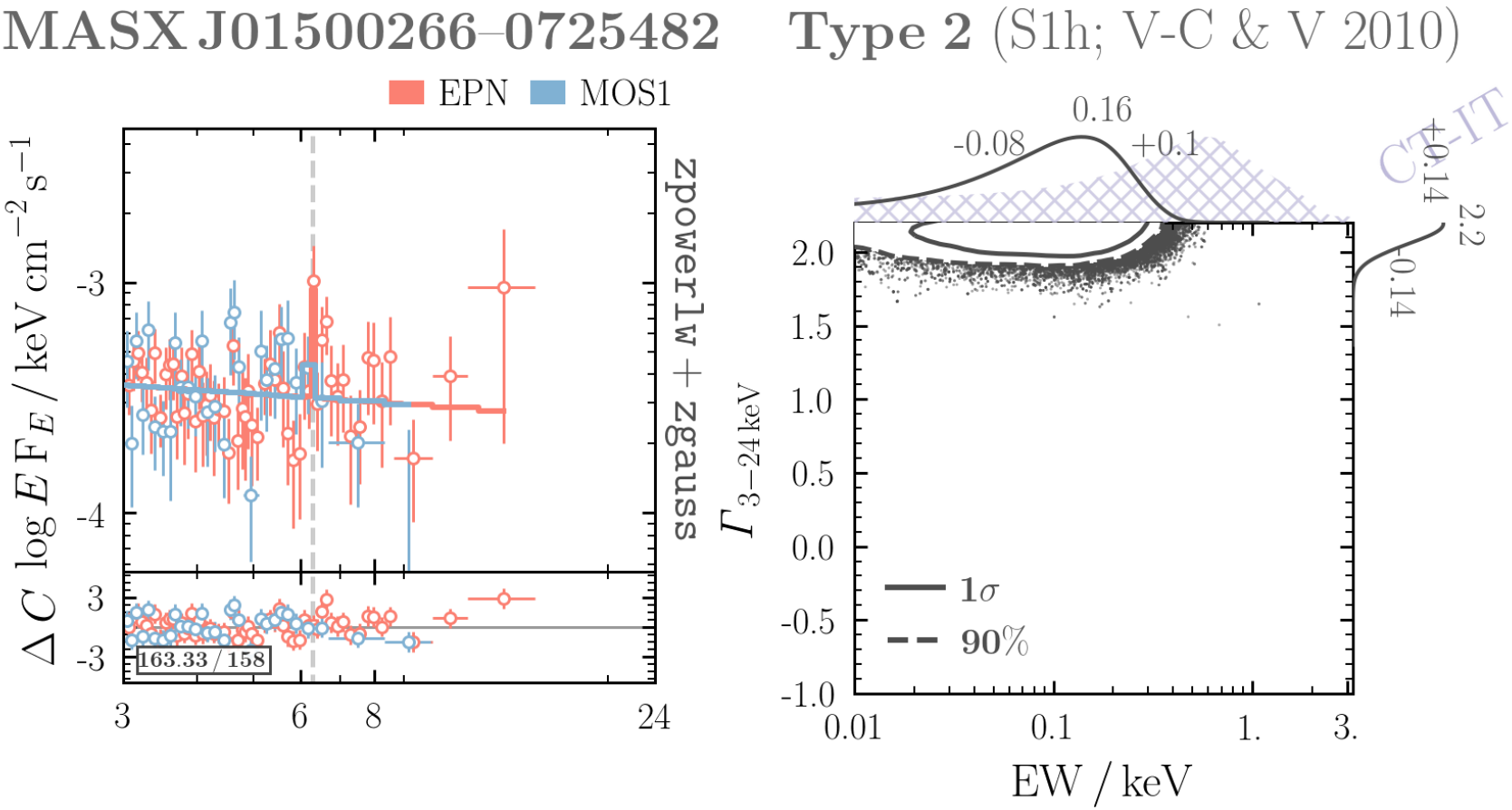

FIGURE C.4: Phenomenological Fit, ID 37: 2MASXJ 01500266 –0725482

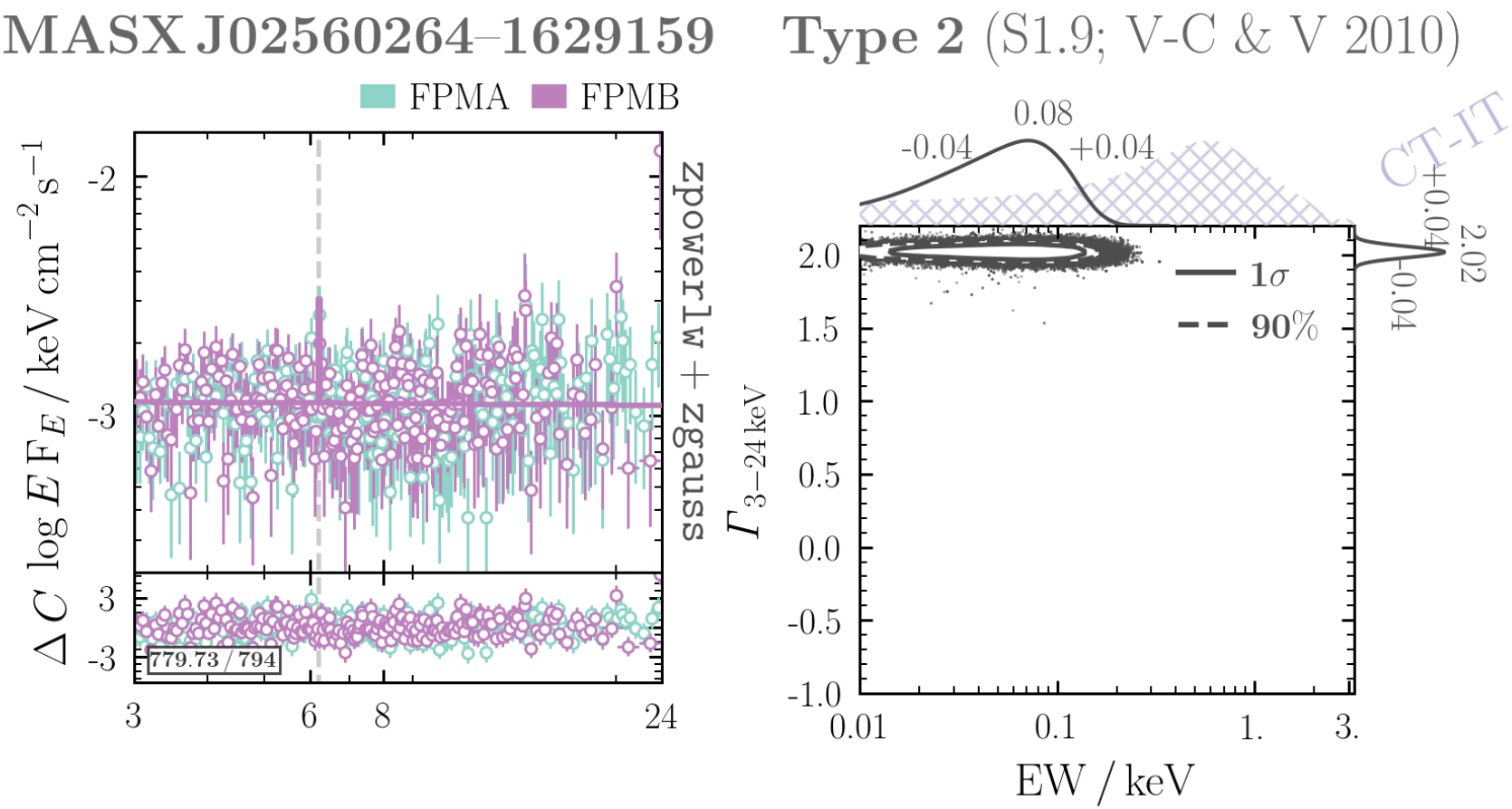

FIGURE C.5: Phenomenological Fit, ID 64: 2MASXJ 02560264 –1629159

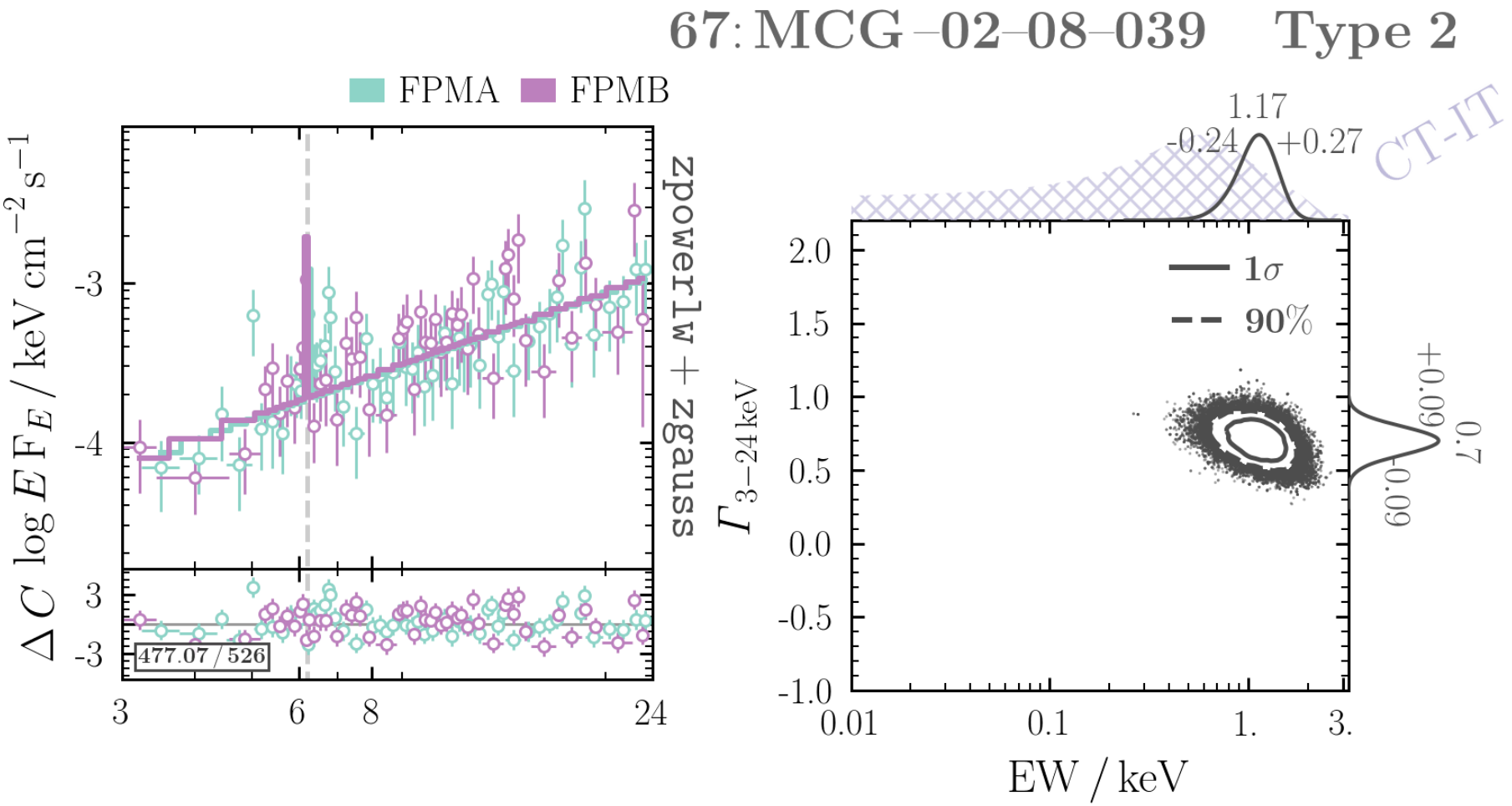

FIGURE C.6: Phenomenological Fit, ID 67: MCG –02–08–039

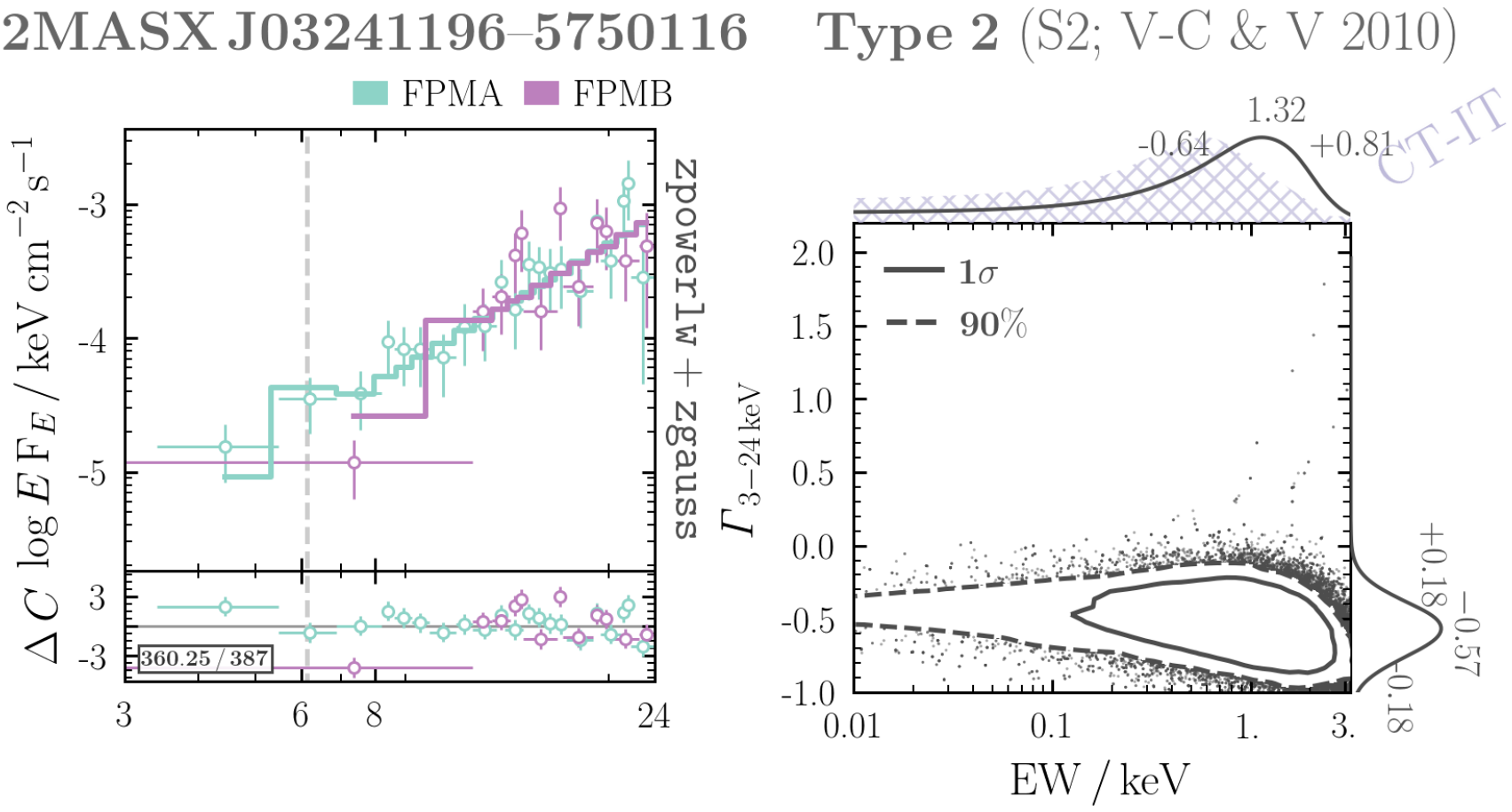

FIGURE C.7: Phenomenological Fit, ID 84: 2MASXJ 03241196 –5750116

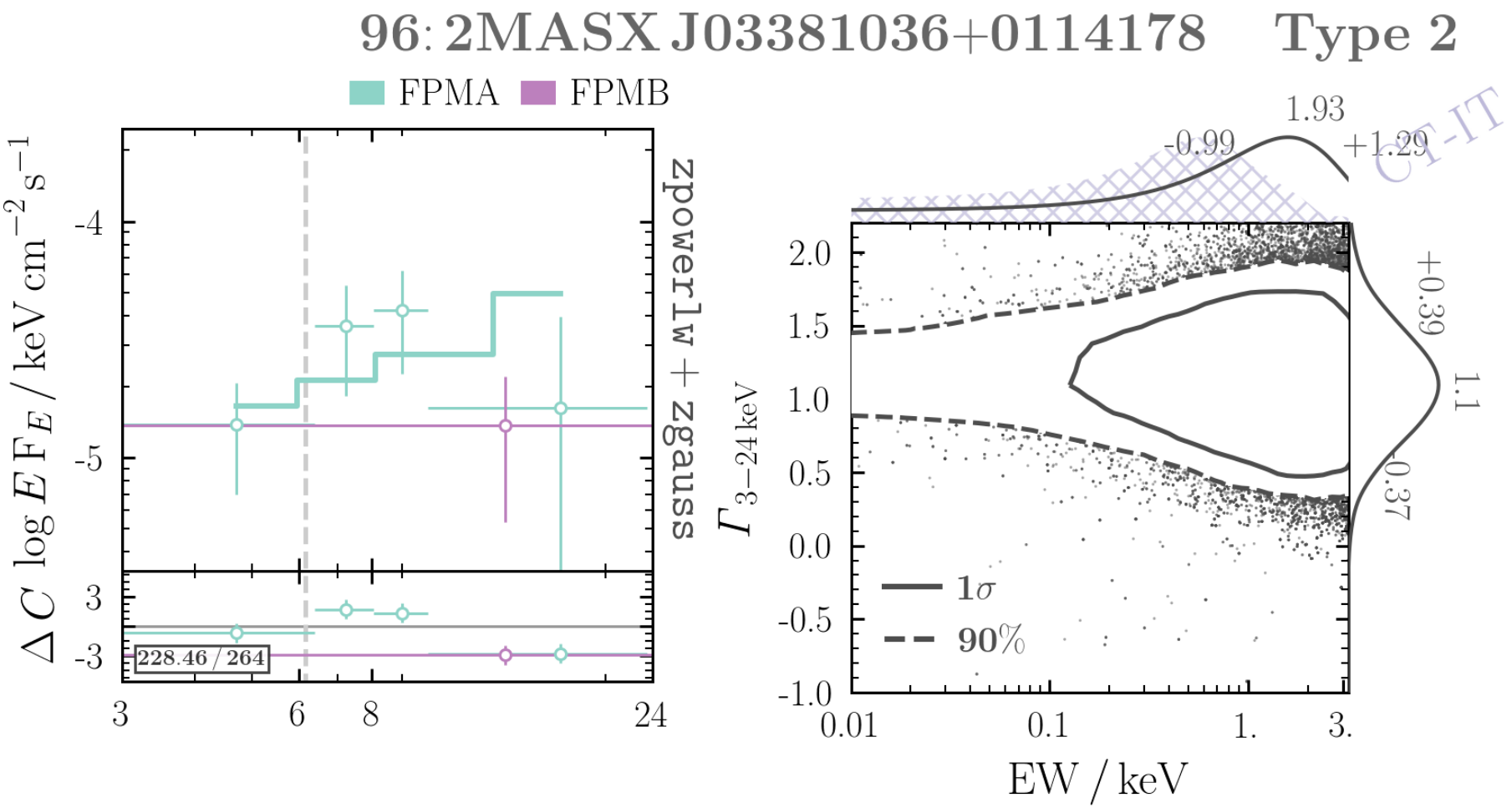

FIGURE C.8: Phenomenological Fit, ID 96: 2MASXJ 03381036 +0114178

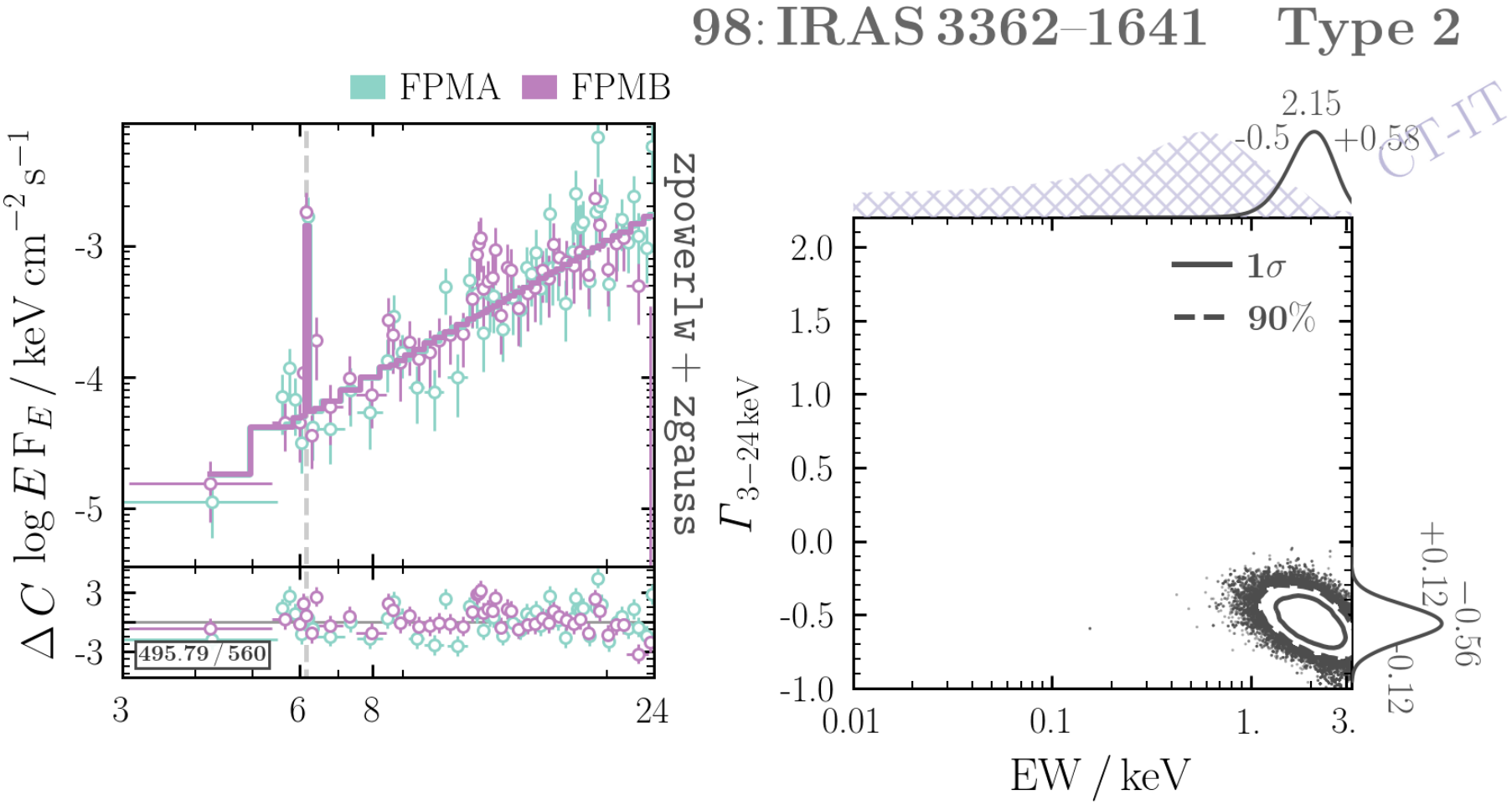

FIGURE C.9: Phenomenological Fit, ID 98: IRAS 3362 –1641

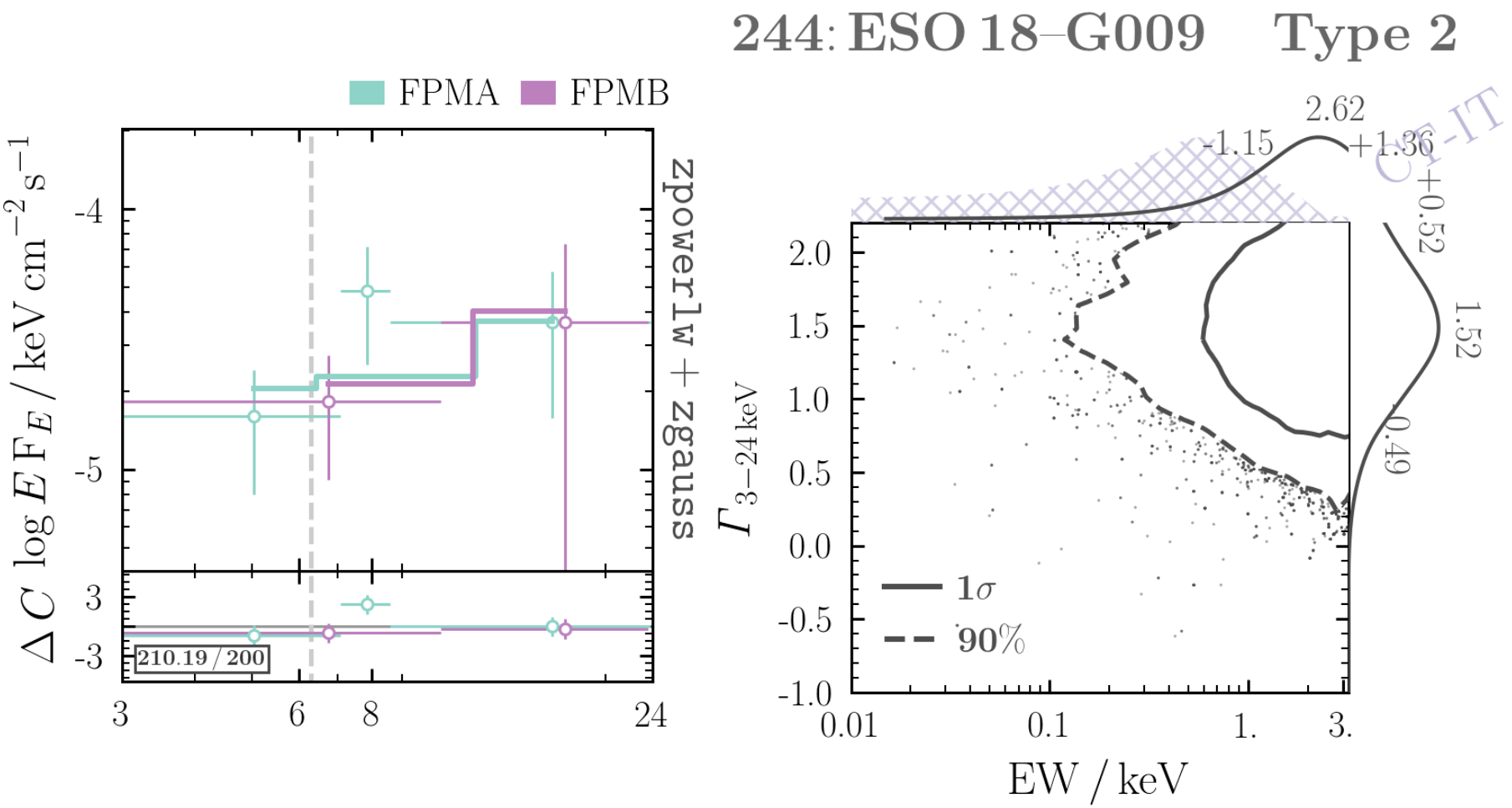

FIGURE C.10: Phenomenological Fit, ID 244: ESO 18–G009

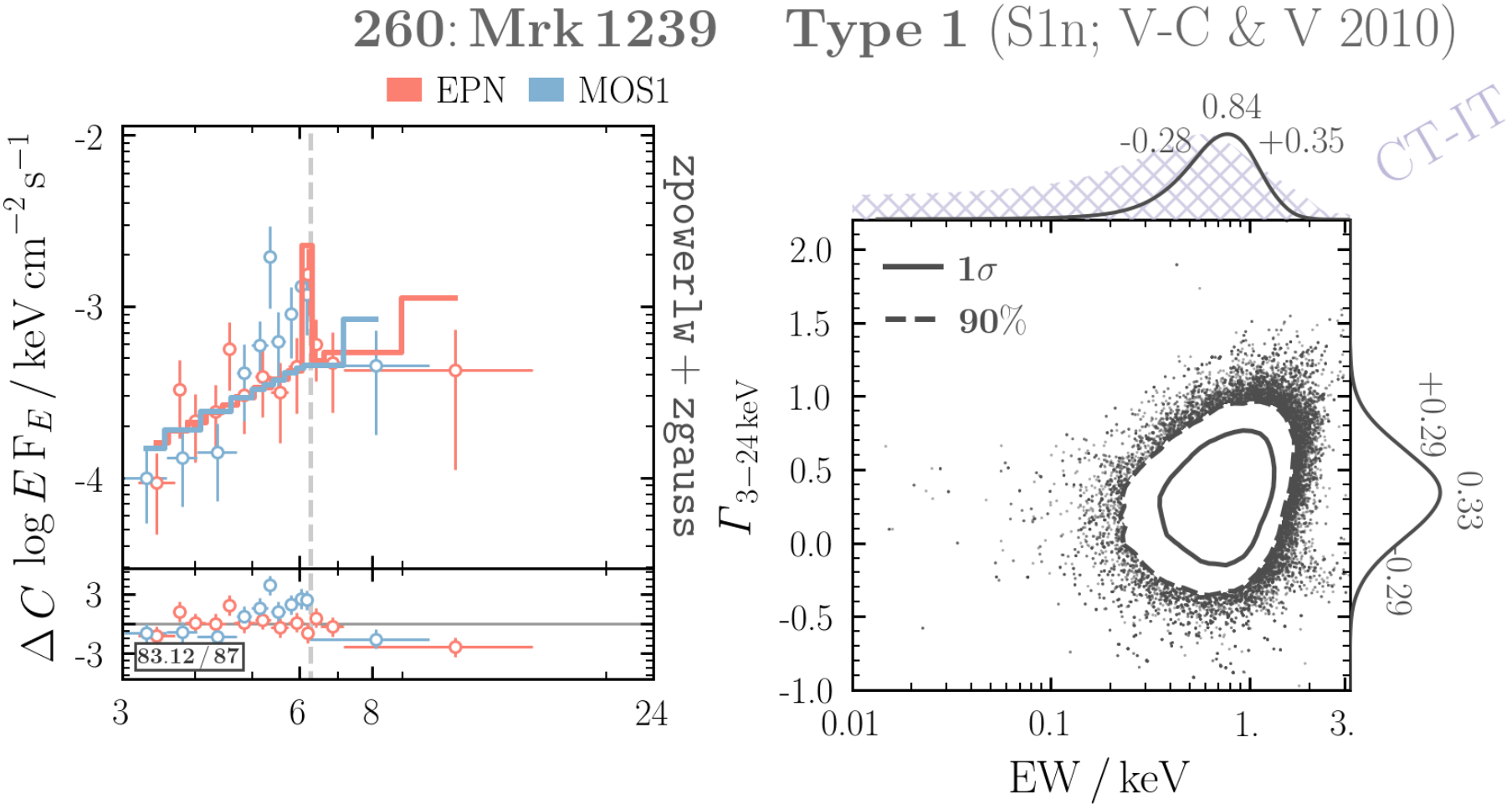

FIGURE C.11: Phenomenological Fit, ID 260: Mrk 1239

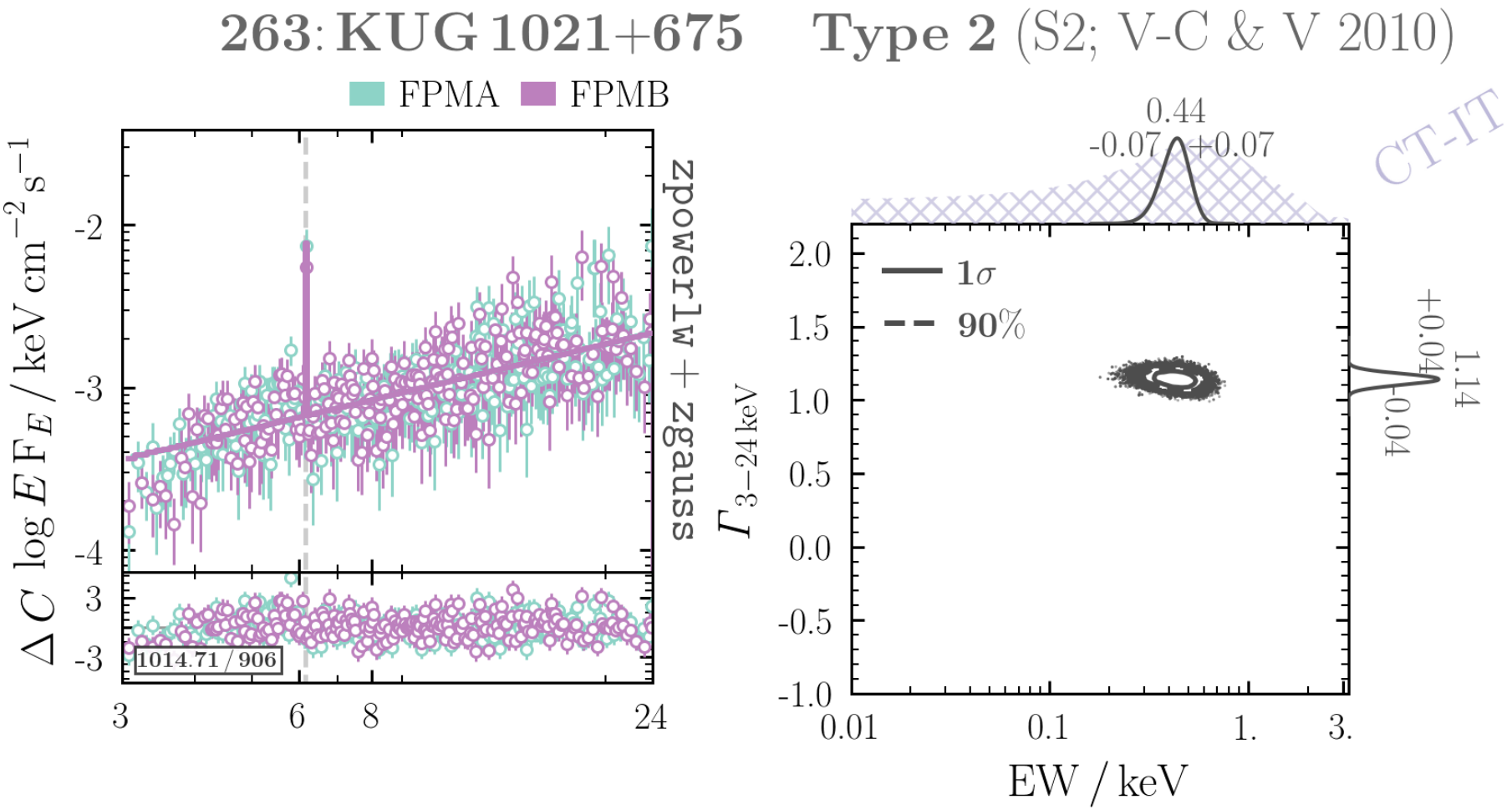

FIGURE C.12: Phenomenological Fit, ID 263: KUG 1021 +675

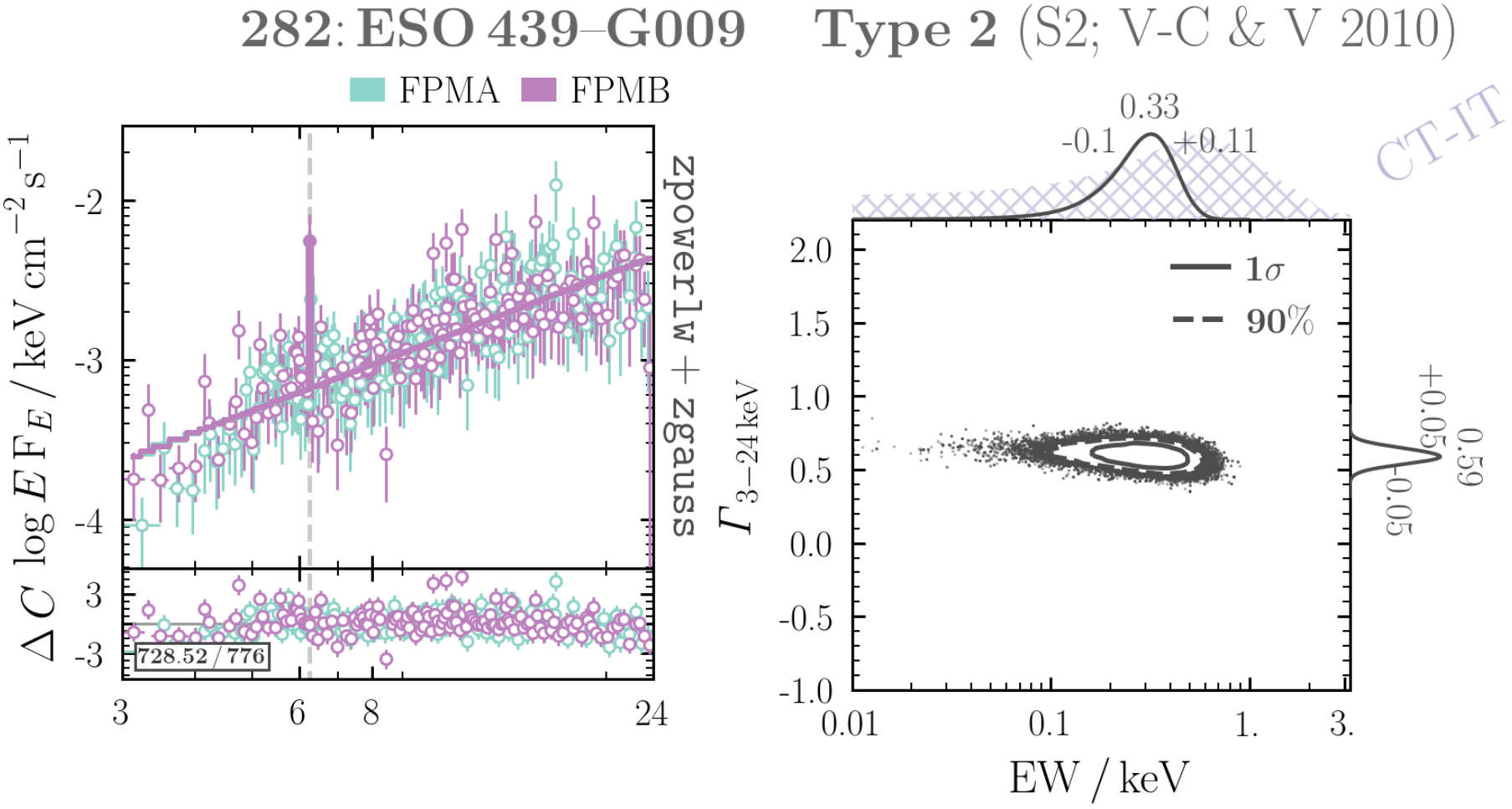

FIGURE C.13: Phenomenological Fit, ID 282: ESO 439–G009

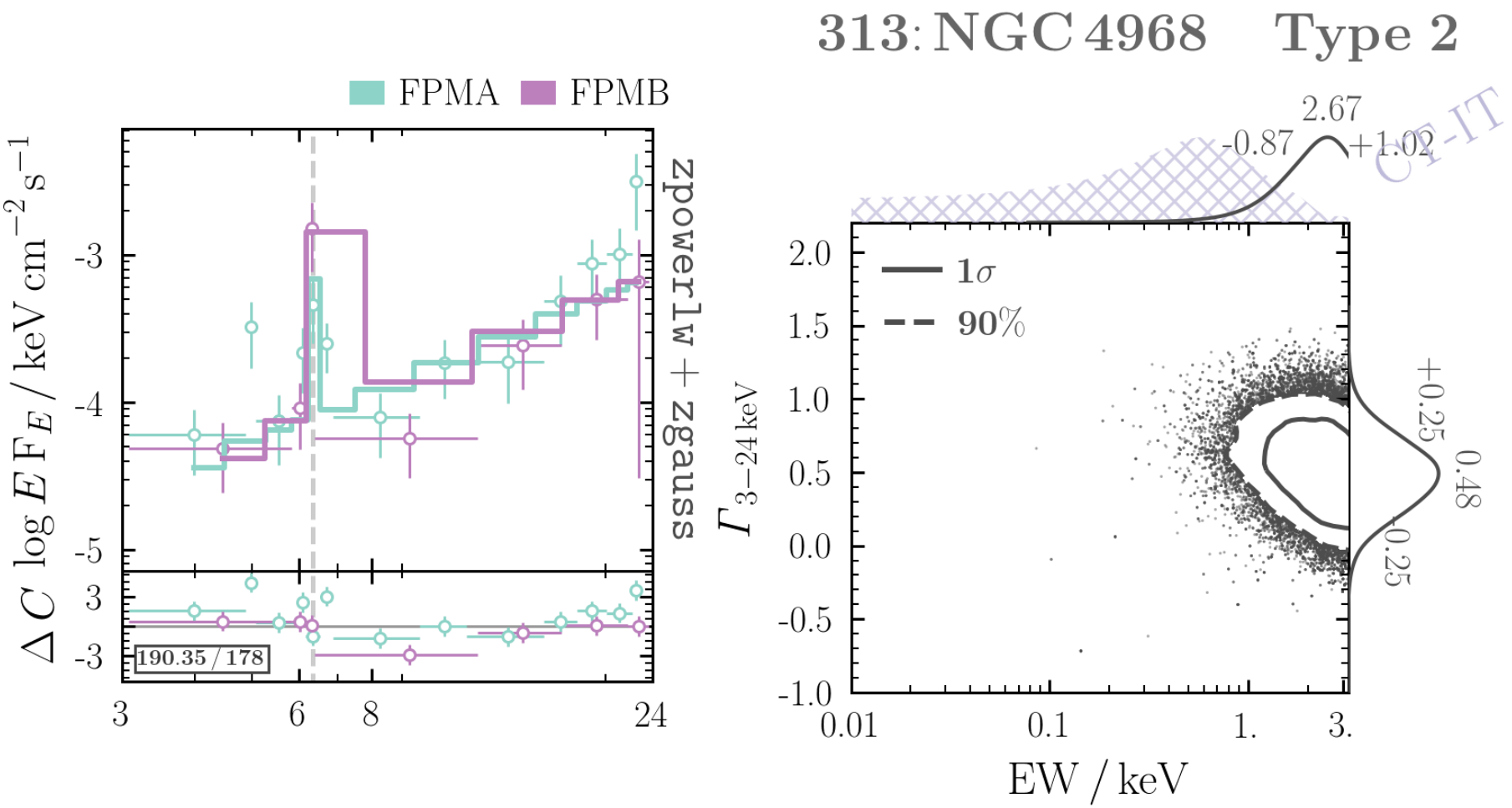

FIGURE C.14: Phenomenological Fit, ID 313: NGC 4968

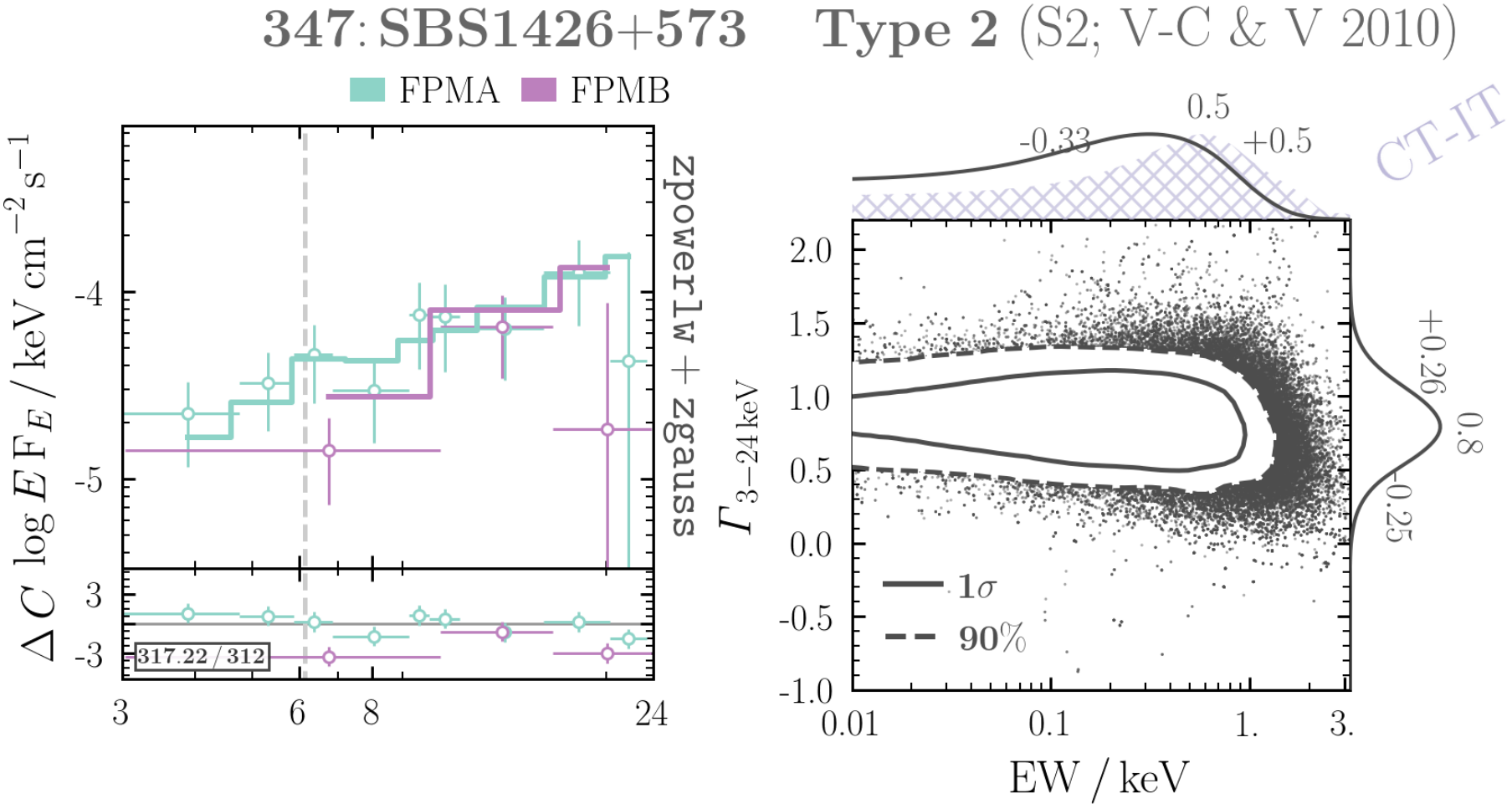

FIGURE C.15: Phenomenological Fit, ID 347: SBS 1426 +573

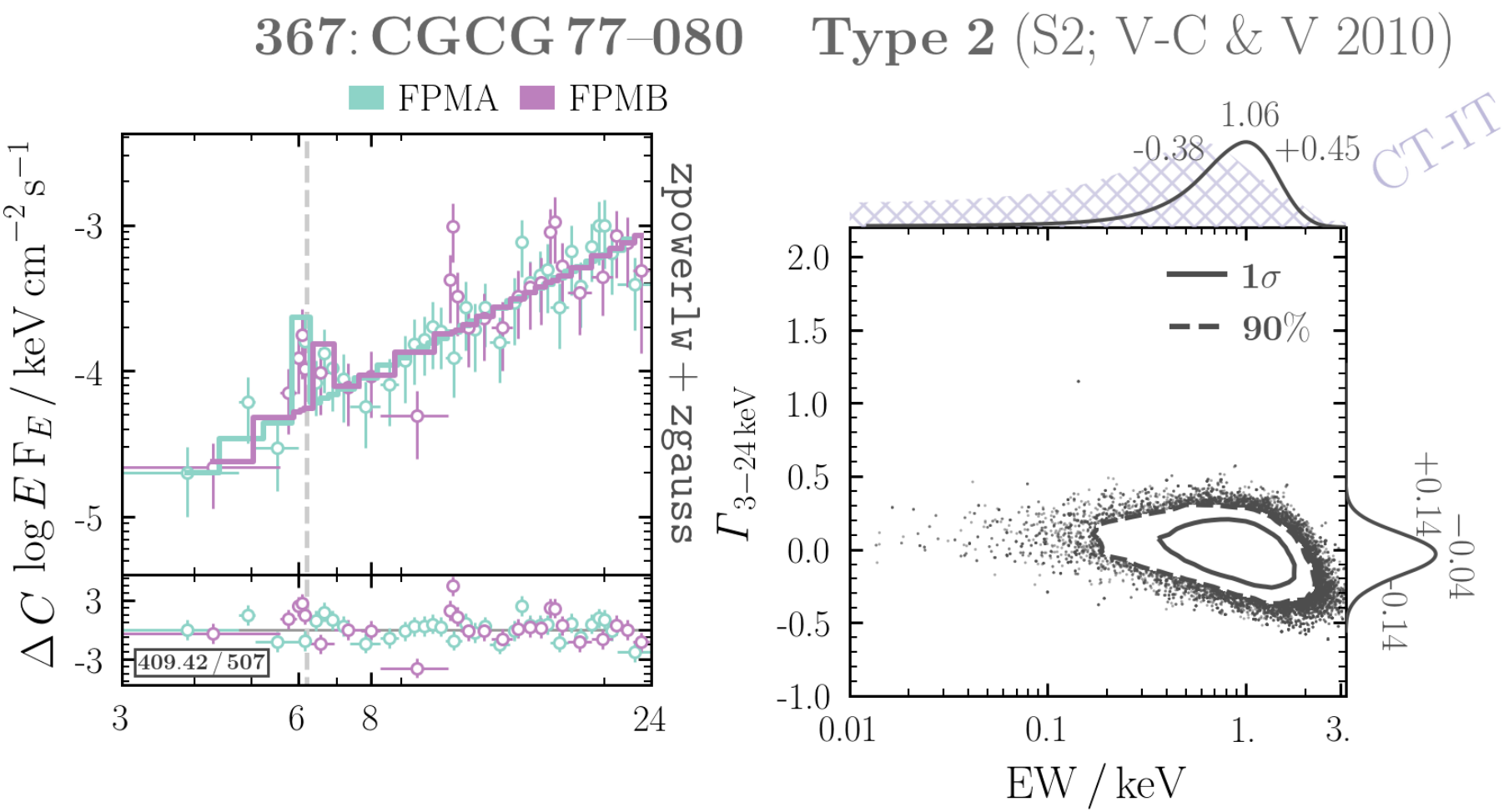

FIGURE C.16: Phenomenological Fit, ID 367: CGCG 77–080

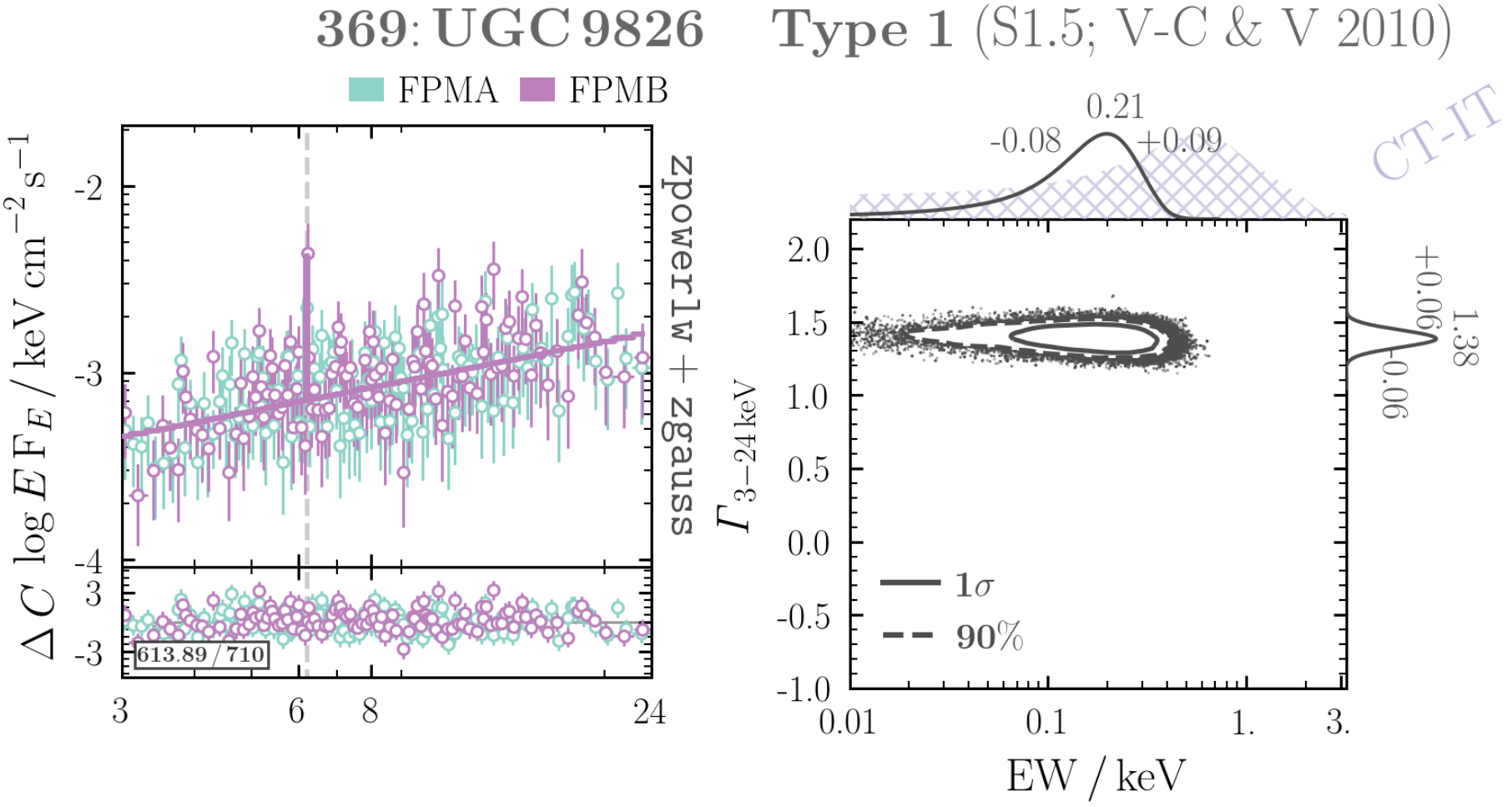

FIGURE C.17: Phenomenological Fit, ID 369: UGC 9826

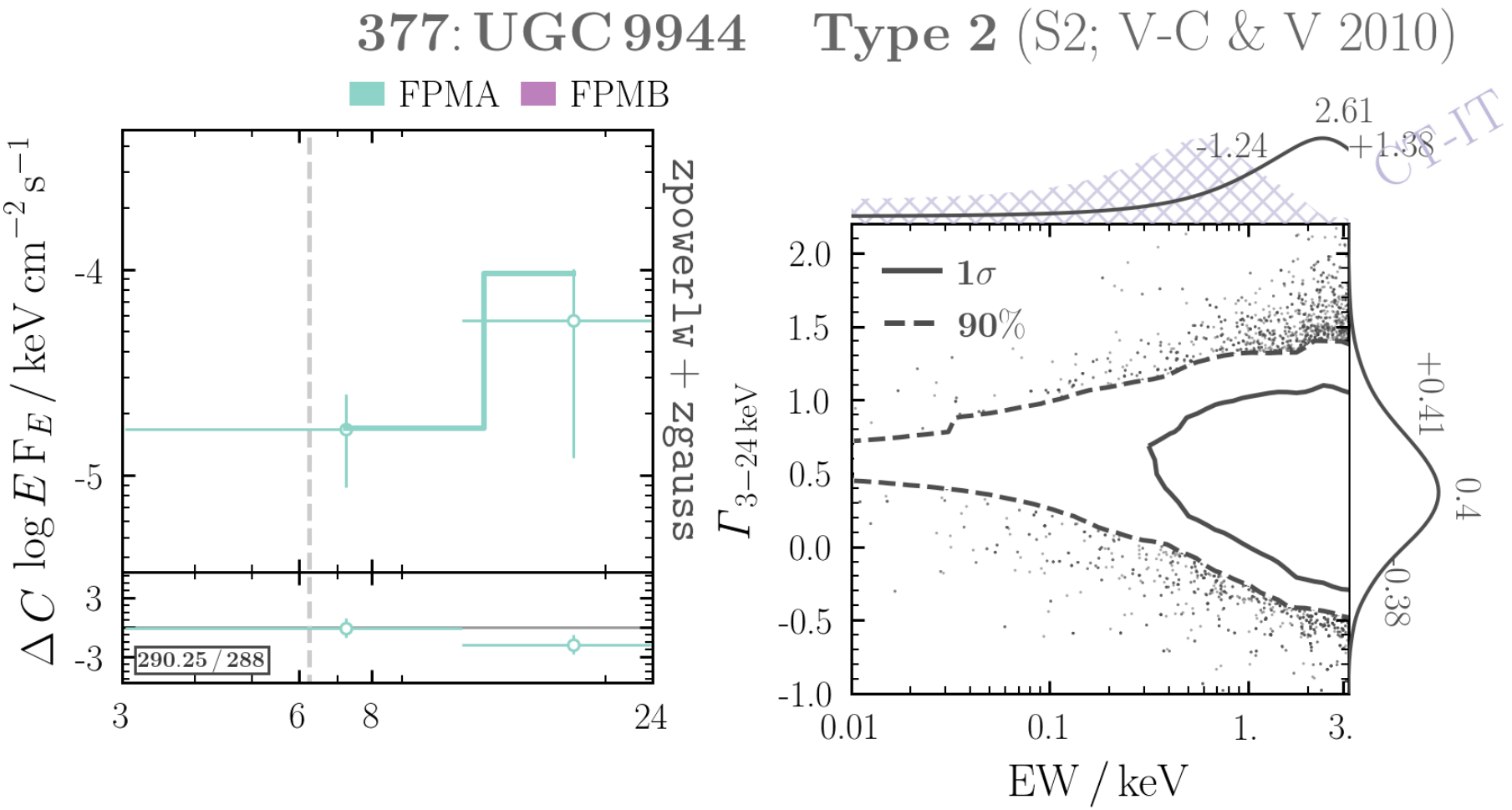

FIGURE C.18: Phenomenological Fit, ID 377: UGC 9944

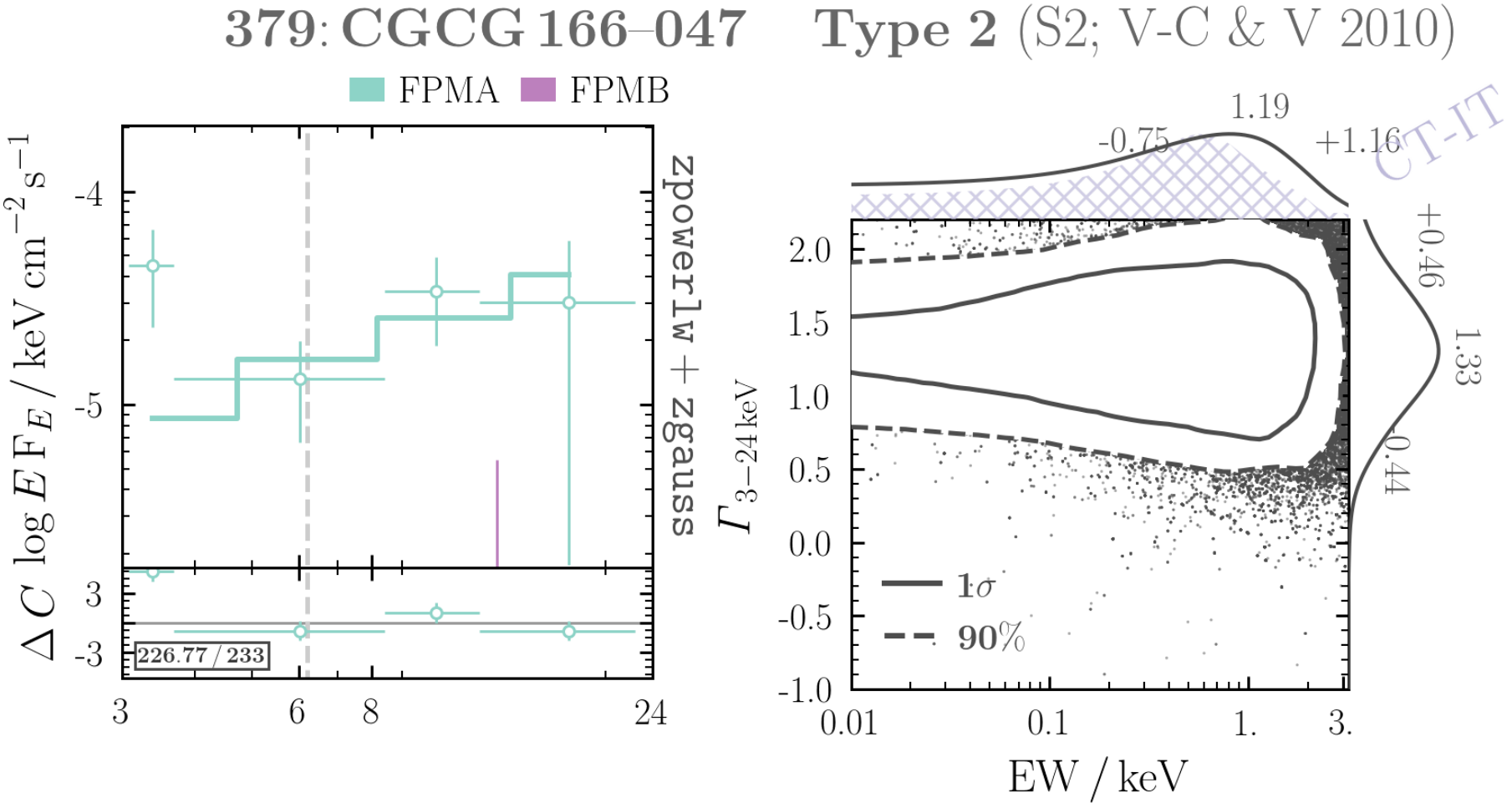

FIGURE C.19: Phenomenological Fit, ID 379: CGCG166–047

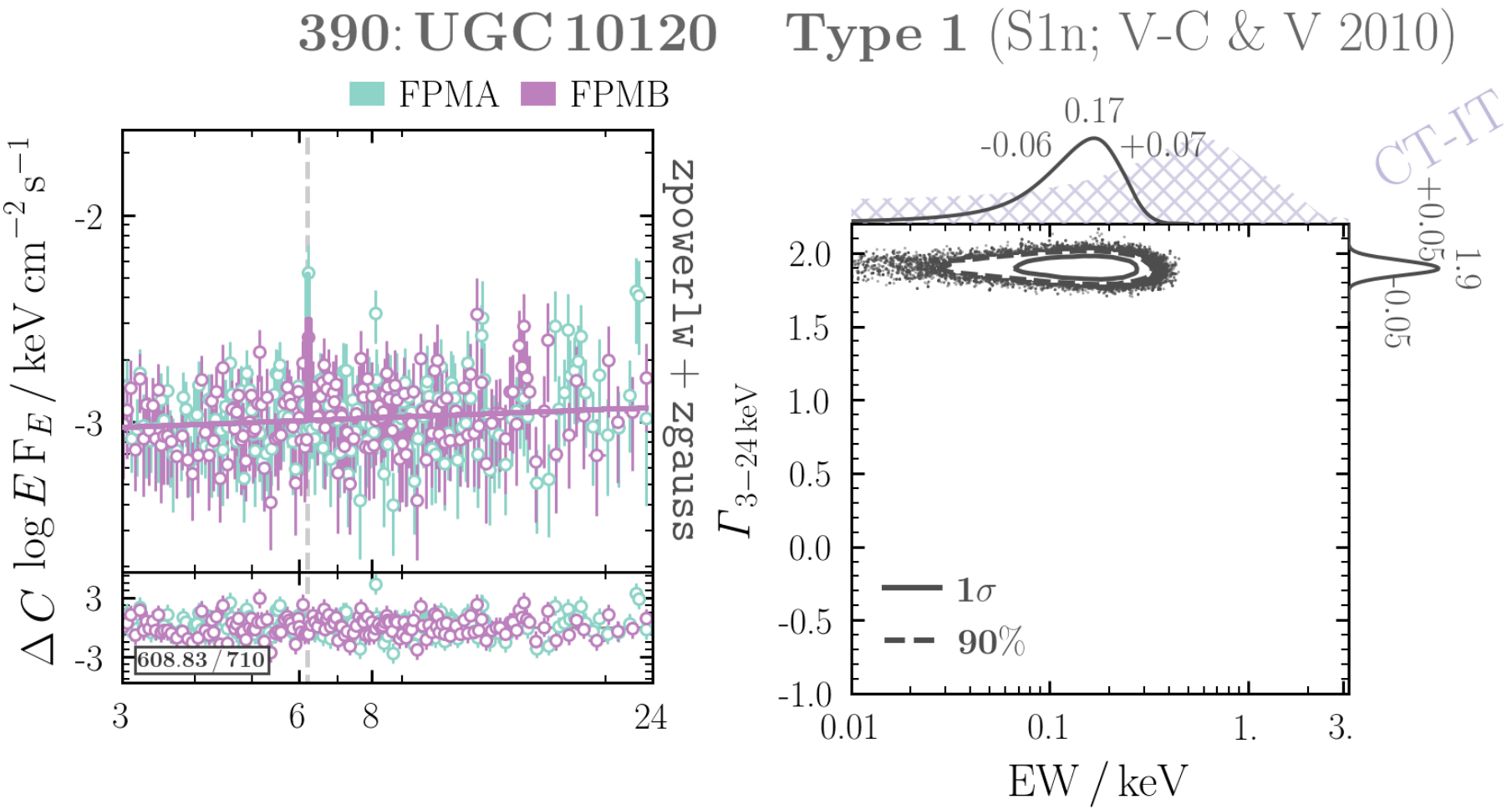

FIGURE C.20: Phenomenological Fit, ID 390: UGC 10120

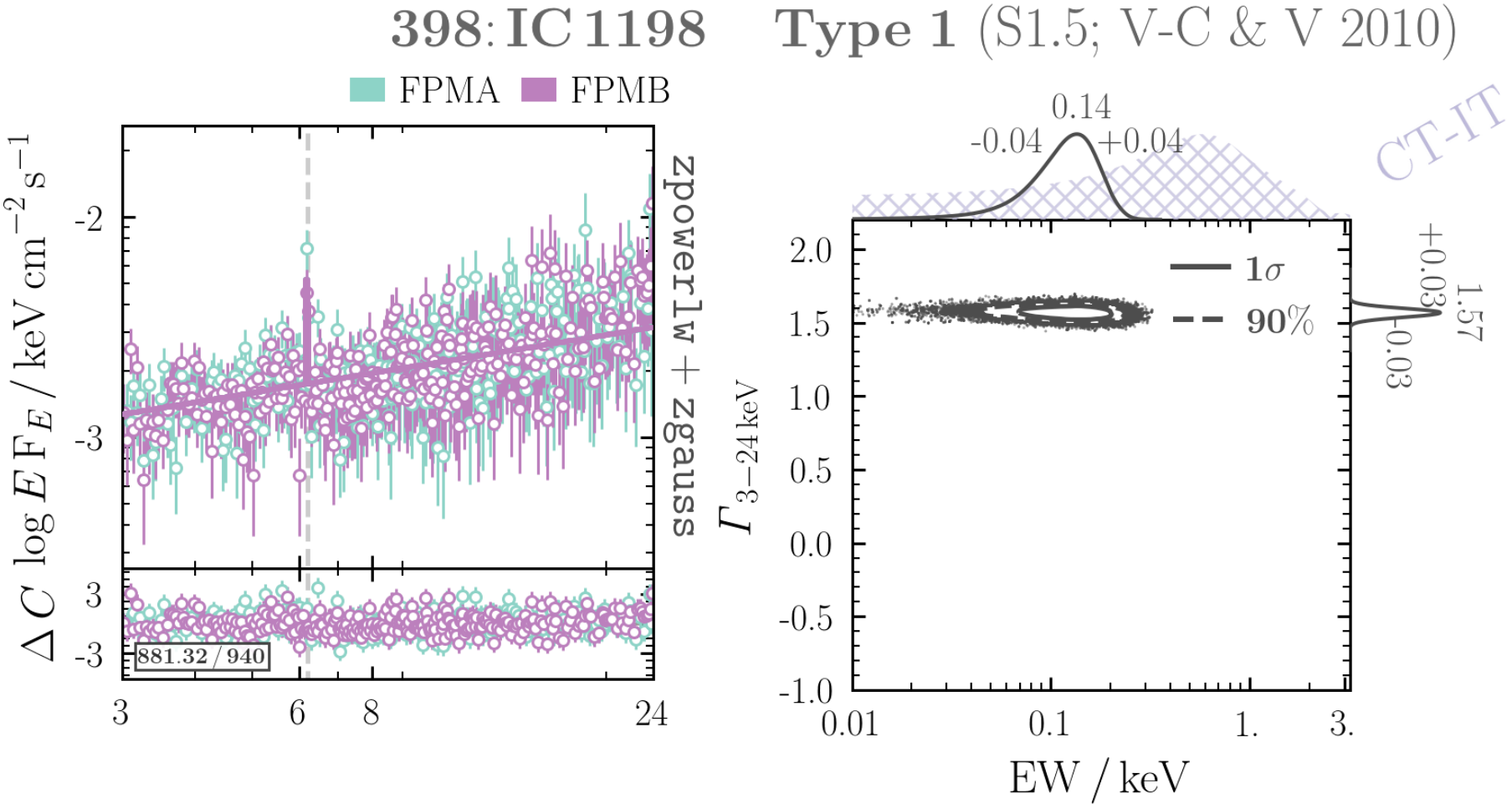

FIGURE C.21: Phenomenological Fit, ID 398: IC 1198

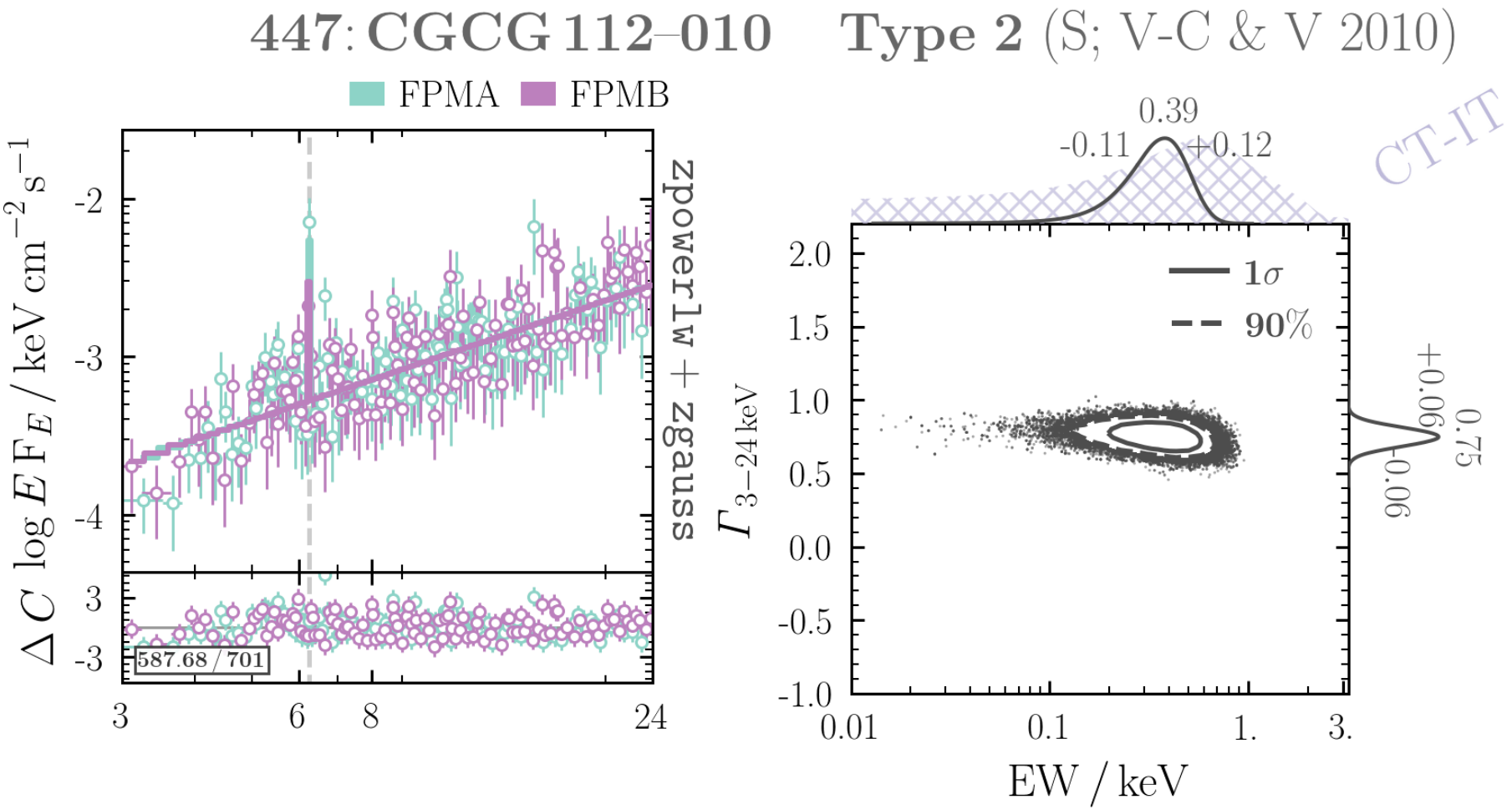

FIGURE C.22: Phenomenological Fit, ID 447: CGCG112–010

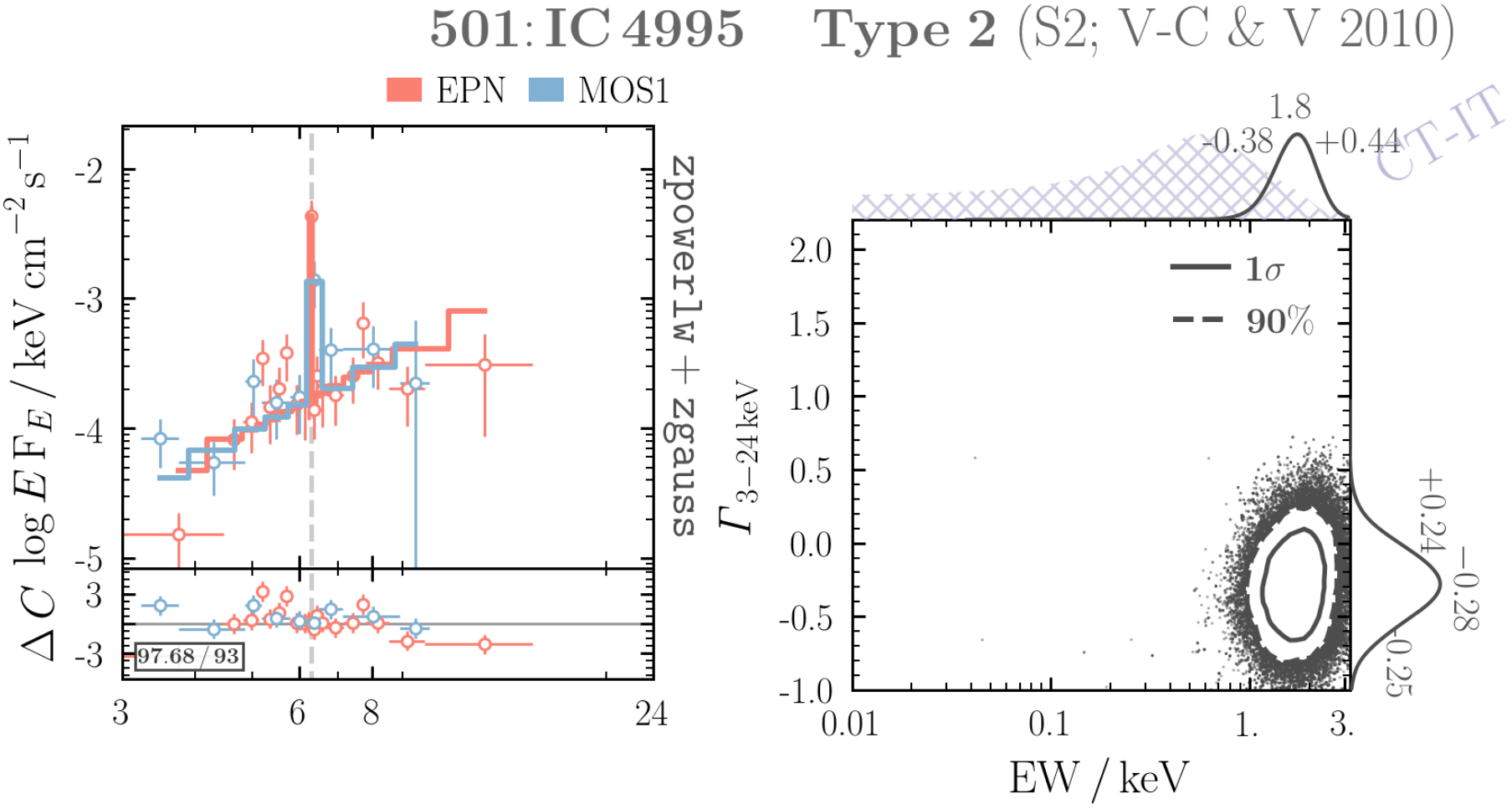

FIGURE C.23: Phenomenological Fit, ID 501: IC 4995

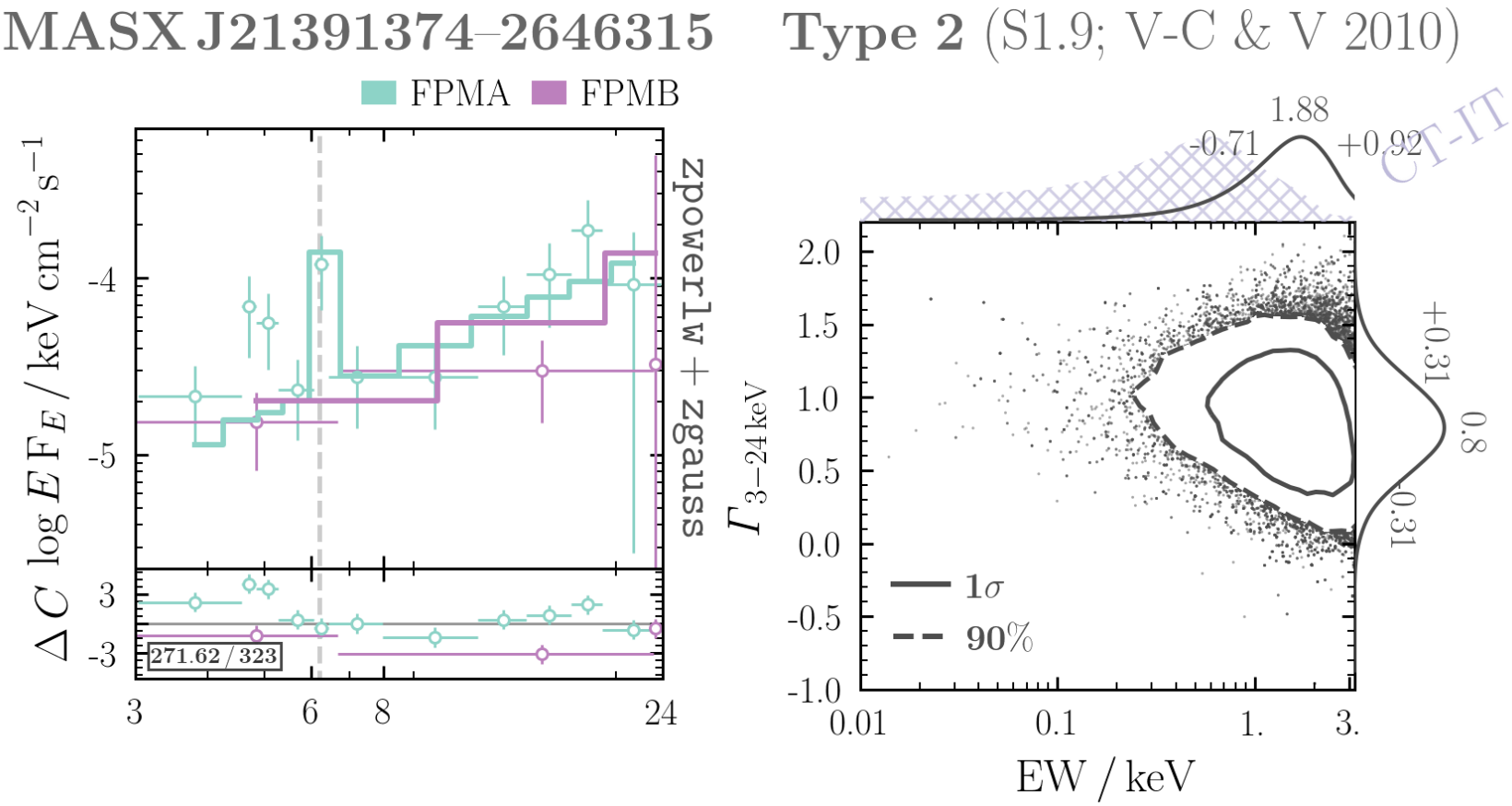

FIGURE C.24: Phenomenological Fit, ID 524: 2MASXJ 21391374 –2646315

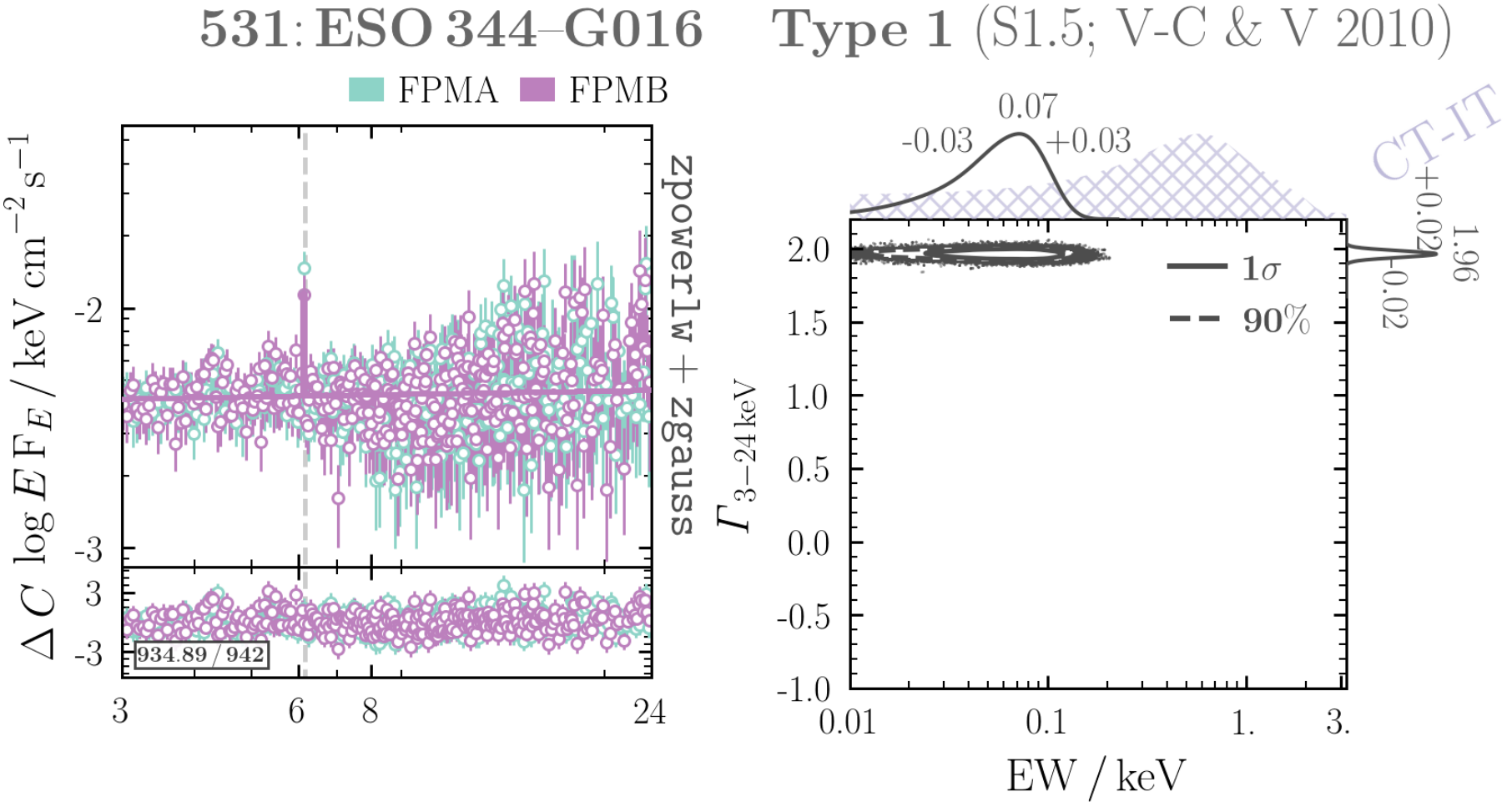

FIGURE C.25: Phenomenological Fit, ID 531: ESO 344–G016

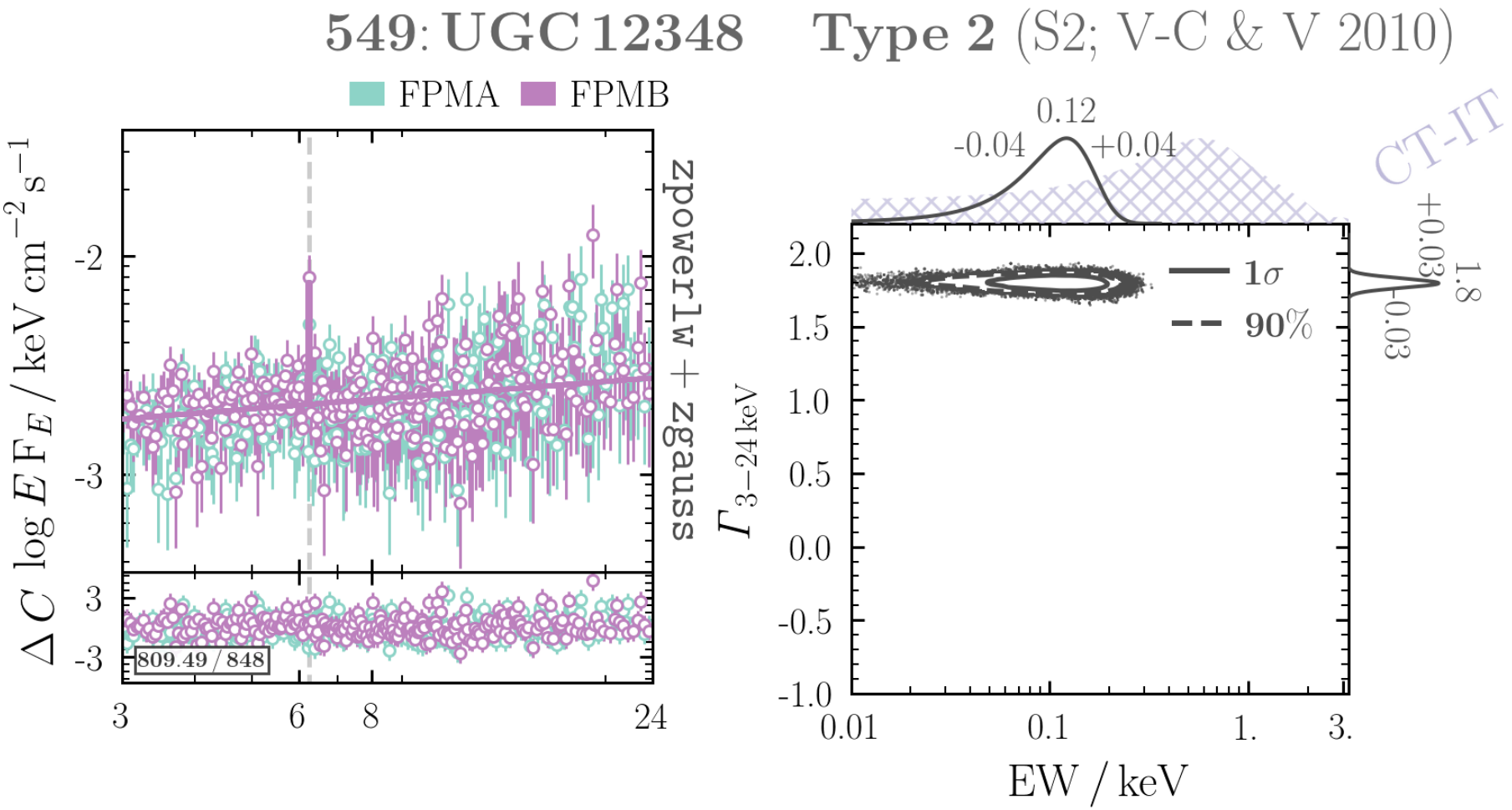

FIGURE C.26: Phenomenological Fit, ID 549: UGC 12348

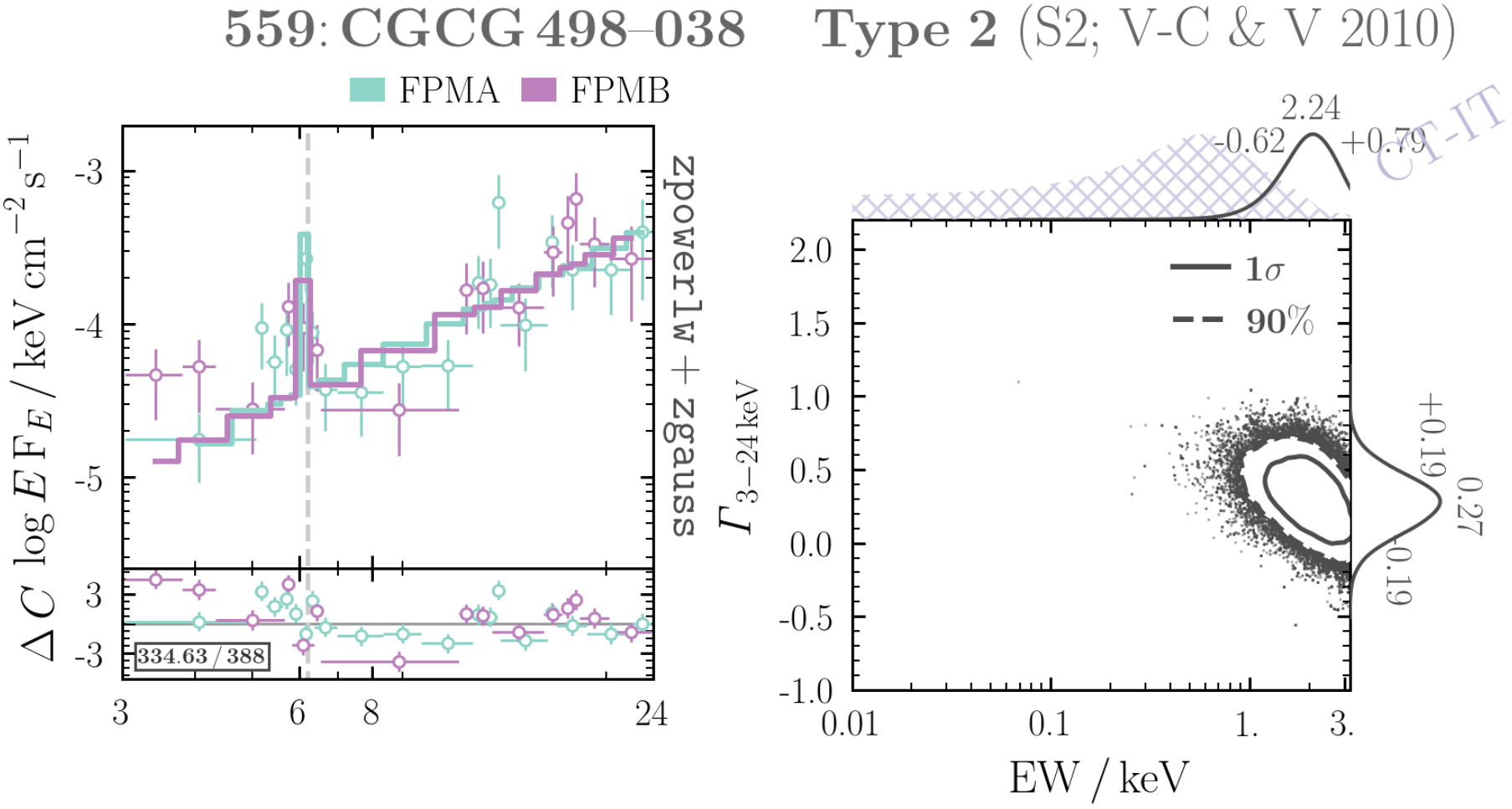

FIGURE C.27: Phenomenological Fit, ID 559: CGCG 498–038

C.2 X-ray Spectral Results Carried with Legacy *NuSTAR* Data

This section presents the key results for each source analysed in NuLANDS so far. Each figure comprises eight panels, with details from the top row downwards as follows:

- Row 1 left: Optical colour image, centered on the source with 1 arcmin^2 dimension.
- Row 1 right: Infrared images, with the top row showing the *IRAS* PSCv2.1 images for each of the photometric filters, and the lower row showing the *WISE* images.
- Row 2 left: Soft X-ray image, centered on the source. The dashed circle encompasses the source region used for extraction of counts.
- Row 2 right: Hard X-ray image from *NuSTAR*. The blue solid circle shows the source region used for extraction of counts.
- Row 3 left: Unfolded spectrum with the best-fitting model. The panels on the lower portion of the plot show the output from XSPEC's DEL command. Each DEL panel shown is labelled with the model used to generate it.
- Row 3 right: The MCMC contour for the confidence on line of sight column density vs. intrinsic 2 – 10 keV luminosity. The green upper distribution shows the constrain on $N_{\rm H}$ acquired when the intrinsic photon index and normalisation were fixed to give an intrinsic luminosity equal to the infrared one. The hatched green and orange distributions show the expected intrinsic X-ray luminosities derived from the optical [O III] and mid-infrared luminosity relations of Berney *et al.* (2015) and Asmus *et al.* (2015), respectively.
- Row 4 left: The *WISE* colours plotted with the full dG92 AGN sample shown in grey, and the source shown with a red square. The two AGN cuts are those from Mateos *et al.* (2012) and Assef *et al.* (2018, the Reliability 90% cut).
- Row 4 right: For Seyfert 2s, this panel displays the BPT diagnostic diagram for inferring AGN activity, used as evidence for an AGN present in the source. For Seyfert 1s, original AGN classifications from dG92 were made on line widths rather than flux ratios, such that I include an optical spectrum of the source to highlight the broad lines.

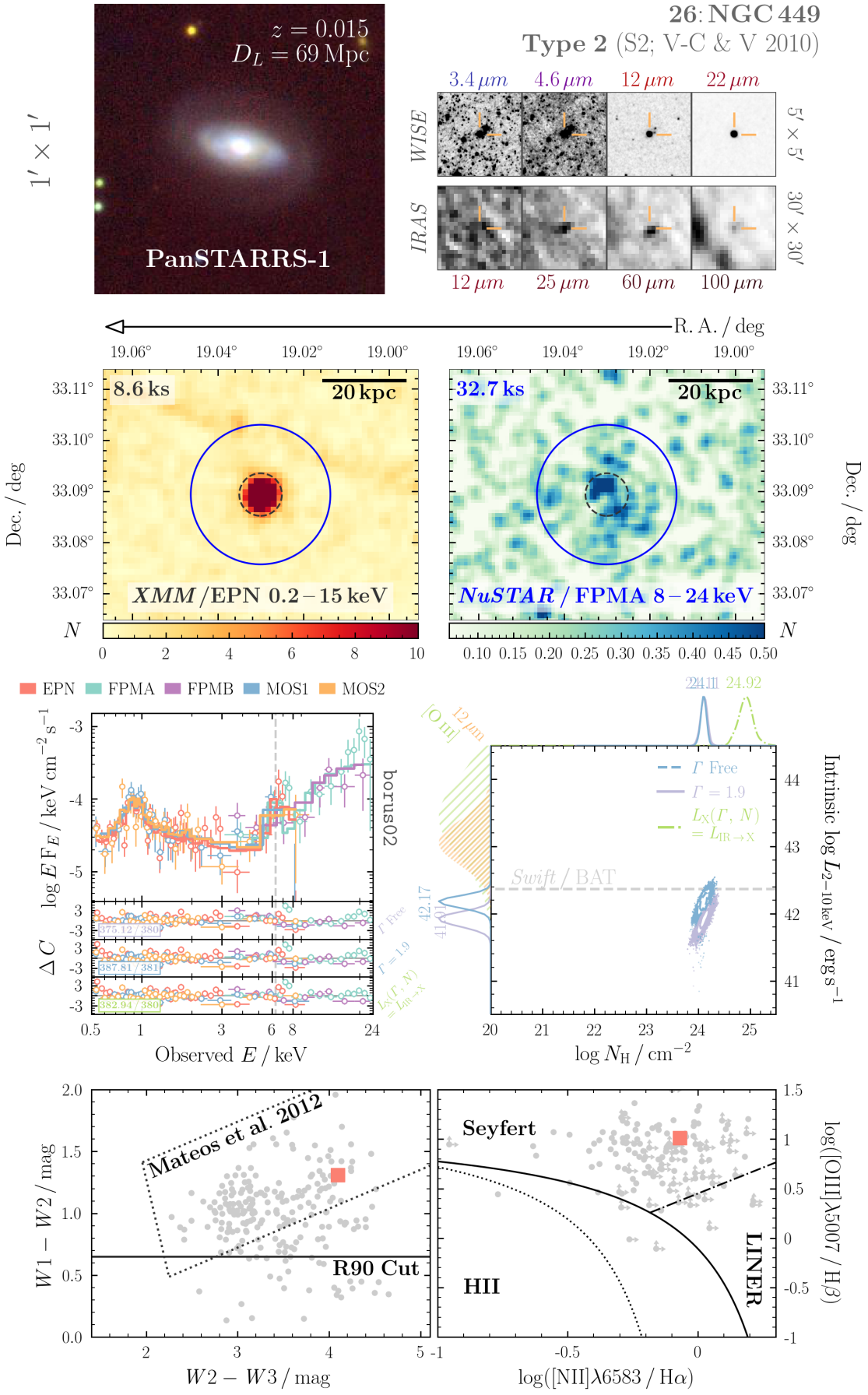

FIGURE C.28: $N_{\rm H}$ Determination, ID 26: NGC 449

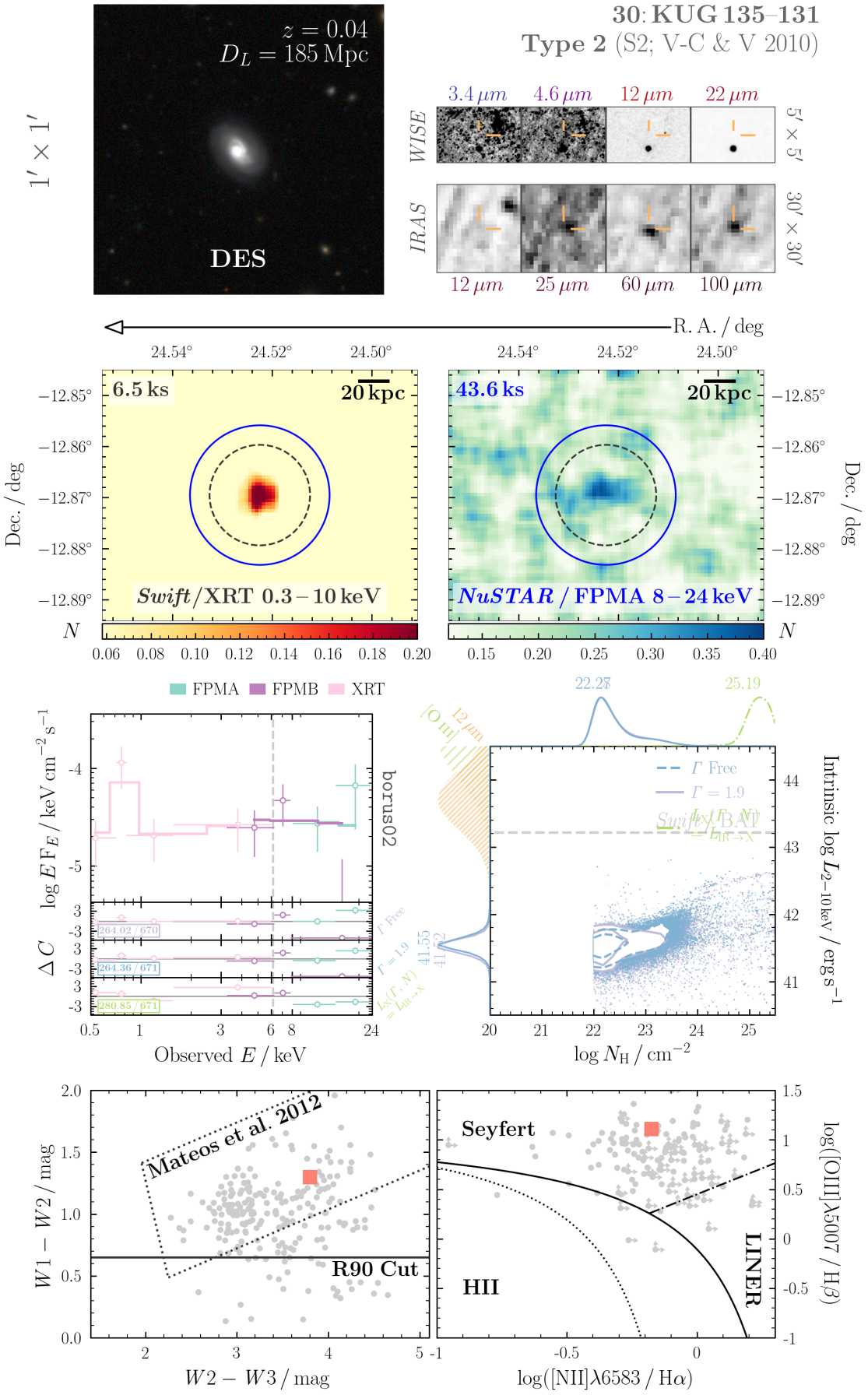

FIGURE C.29: $N_{\rm H}$ Determination, ID 30: KUG 135-131

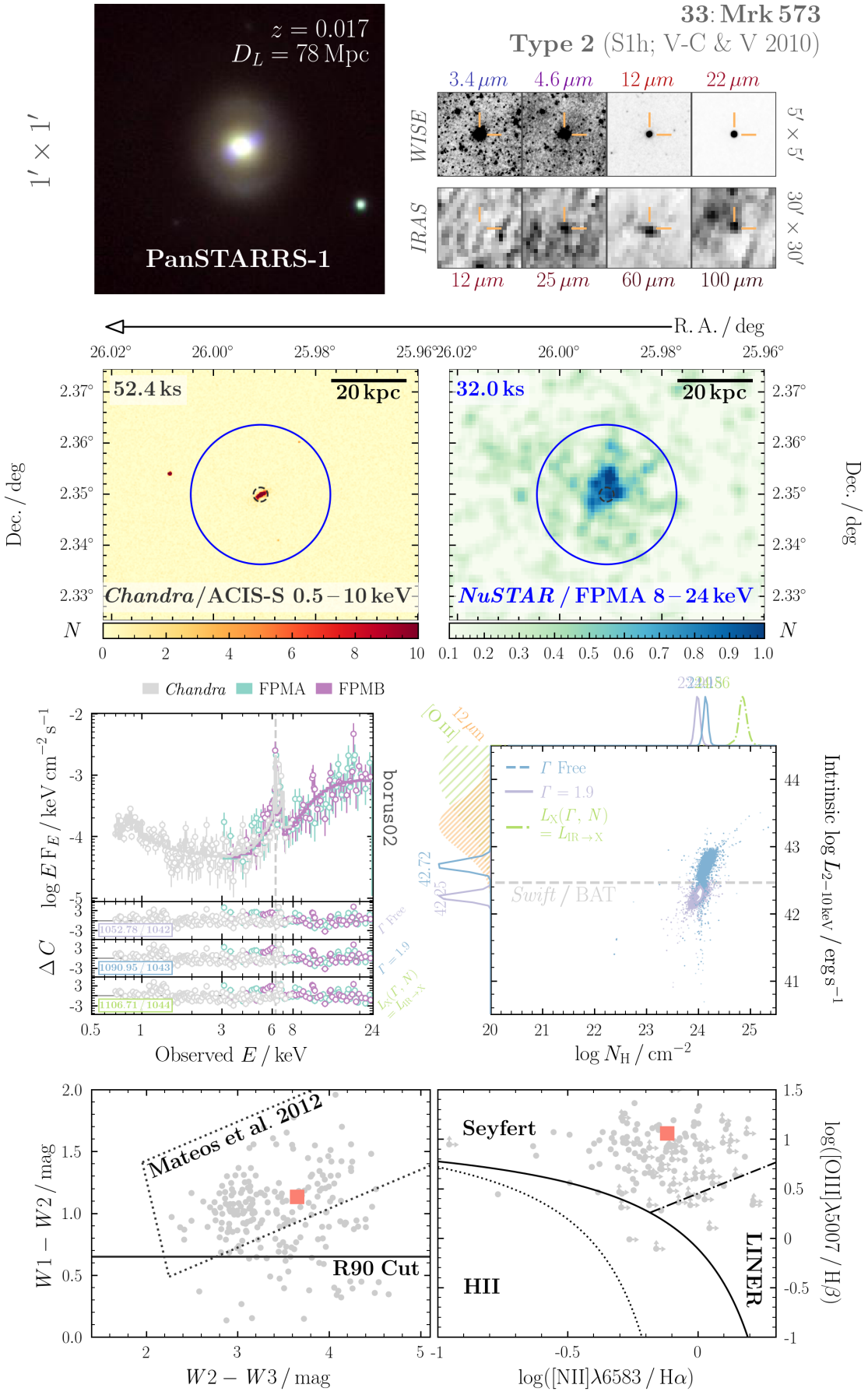

FIGURE C.30: $N_{\rm H}$ Determination, ID 33: Mrk 573

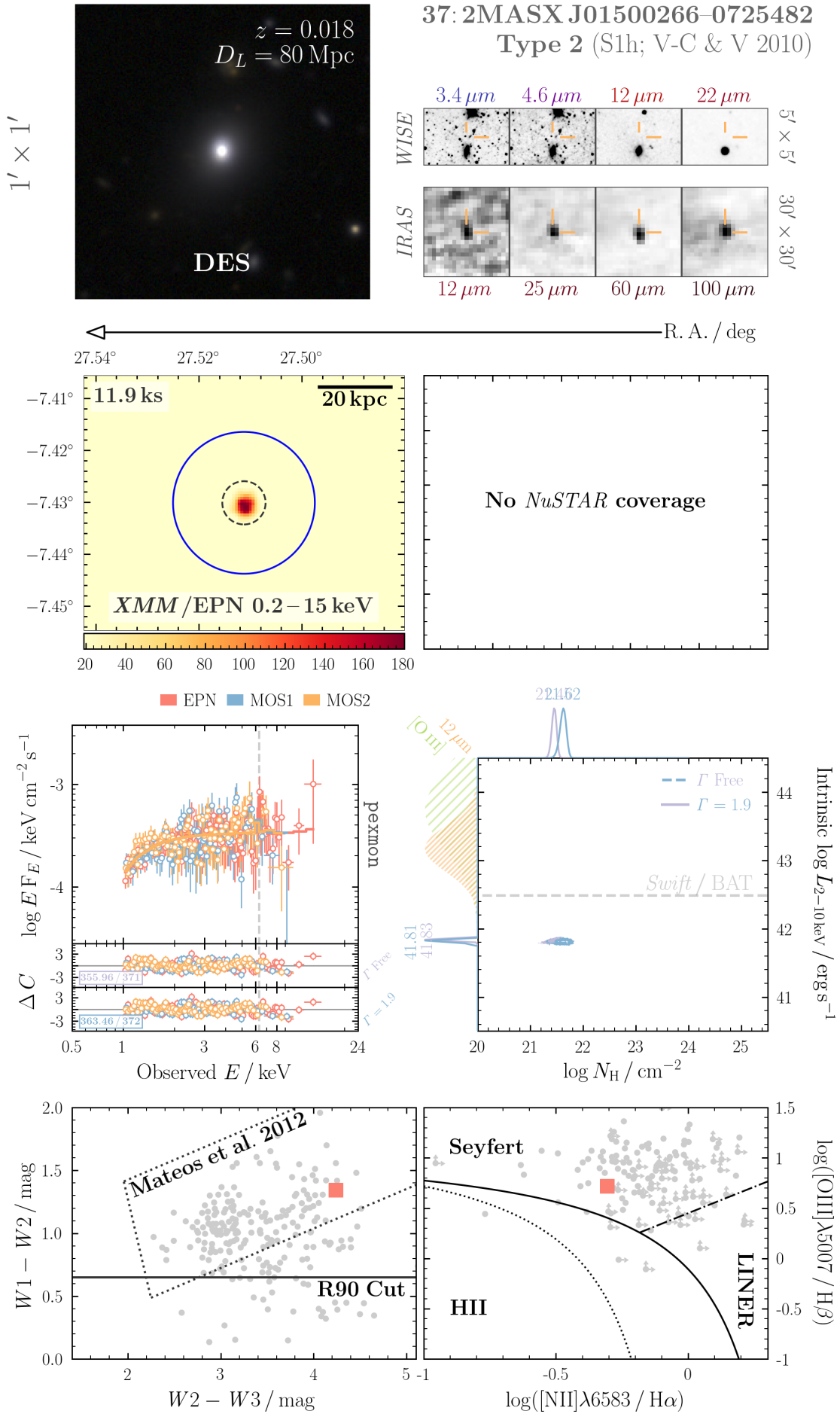

FIGURE C.31: $N_{\rm H}$ Determination, ID 37: 2MASX J01500266–0725482

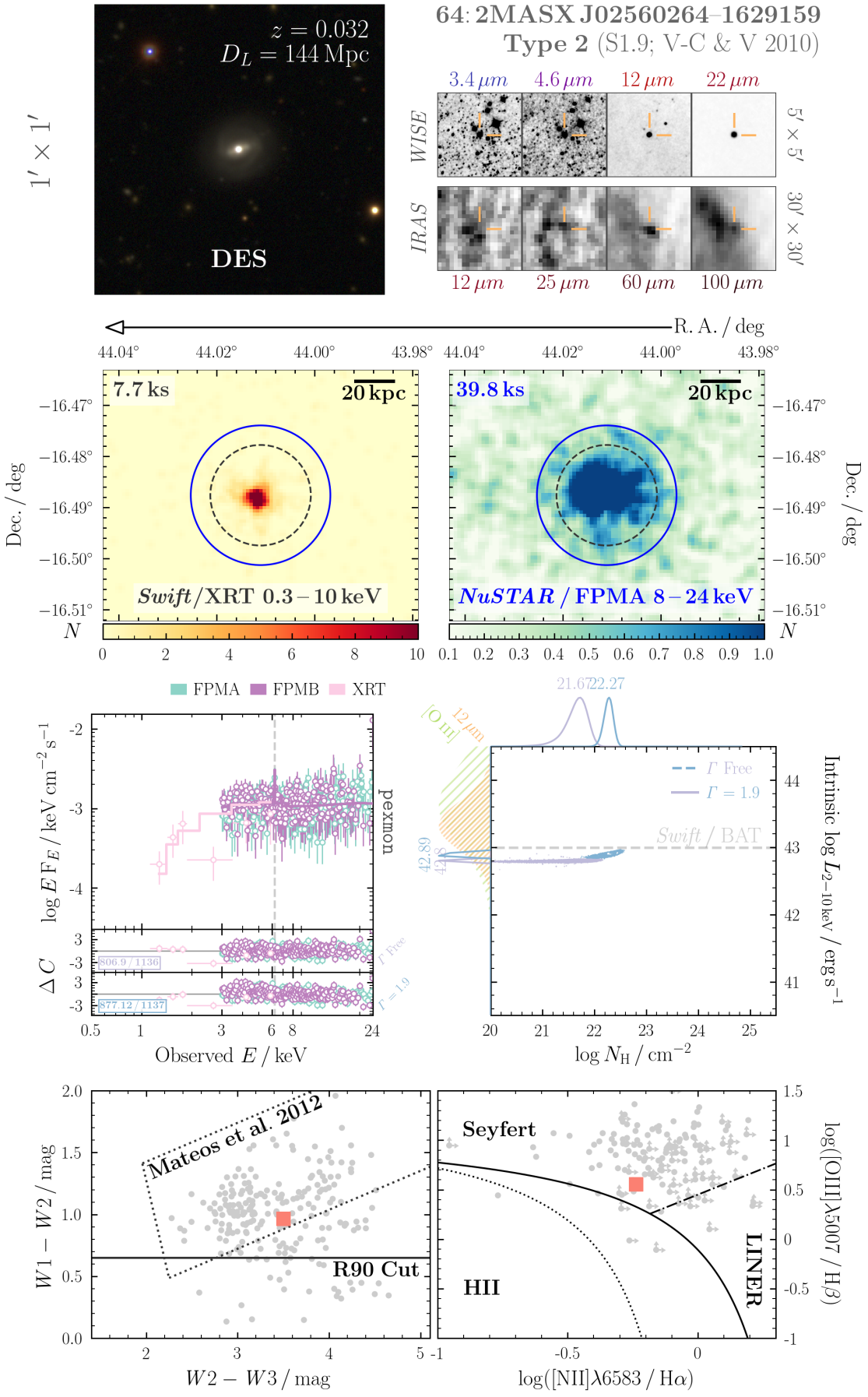

FIGURE C.32: $N_{\rm H}$ Determination, ID 64: 2MASX J02560264–1629159

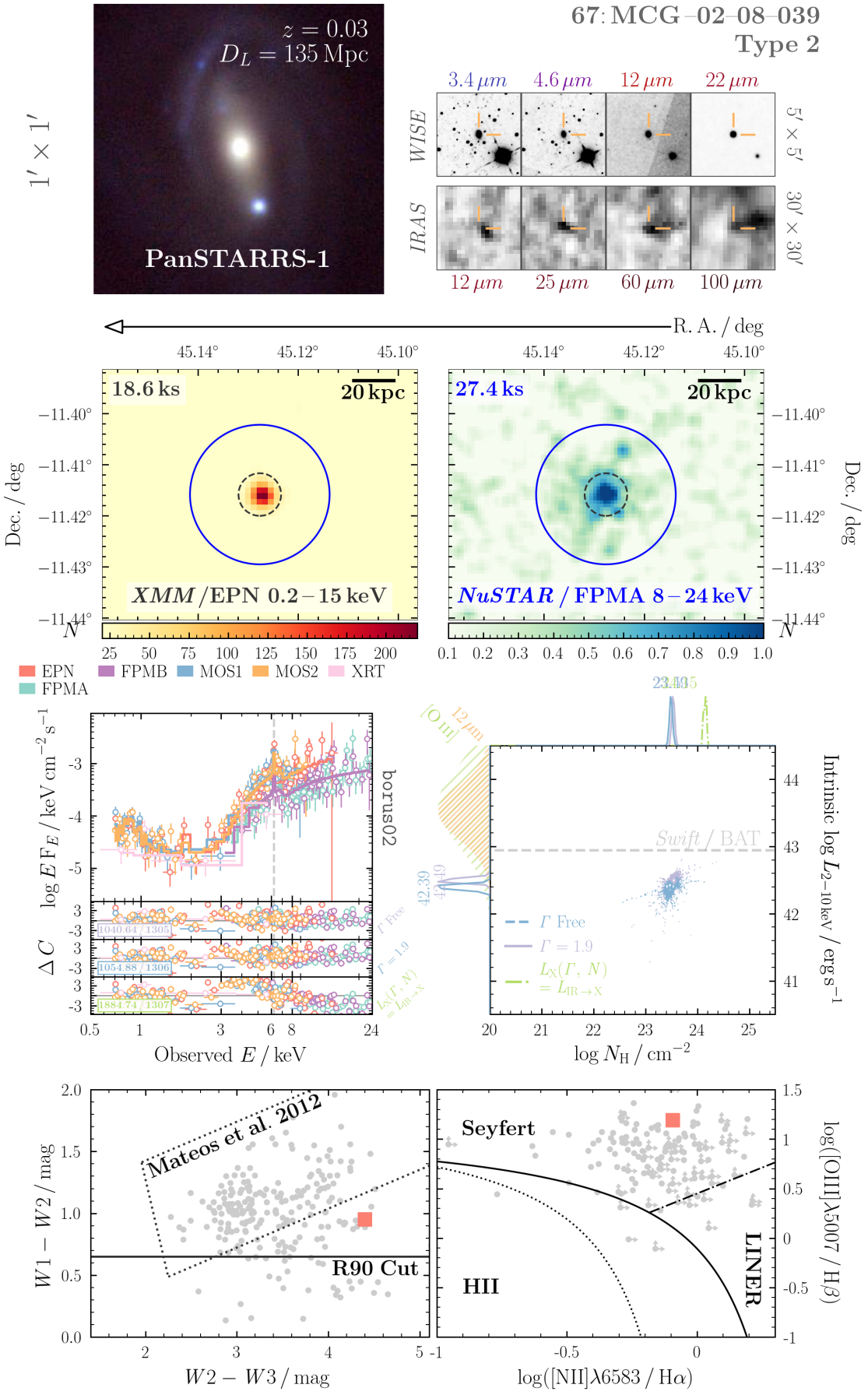

FIGURE C.33: $N_{\rm H}$ Determination, ID 67: MCG-02-08-039

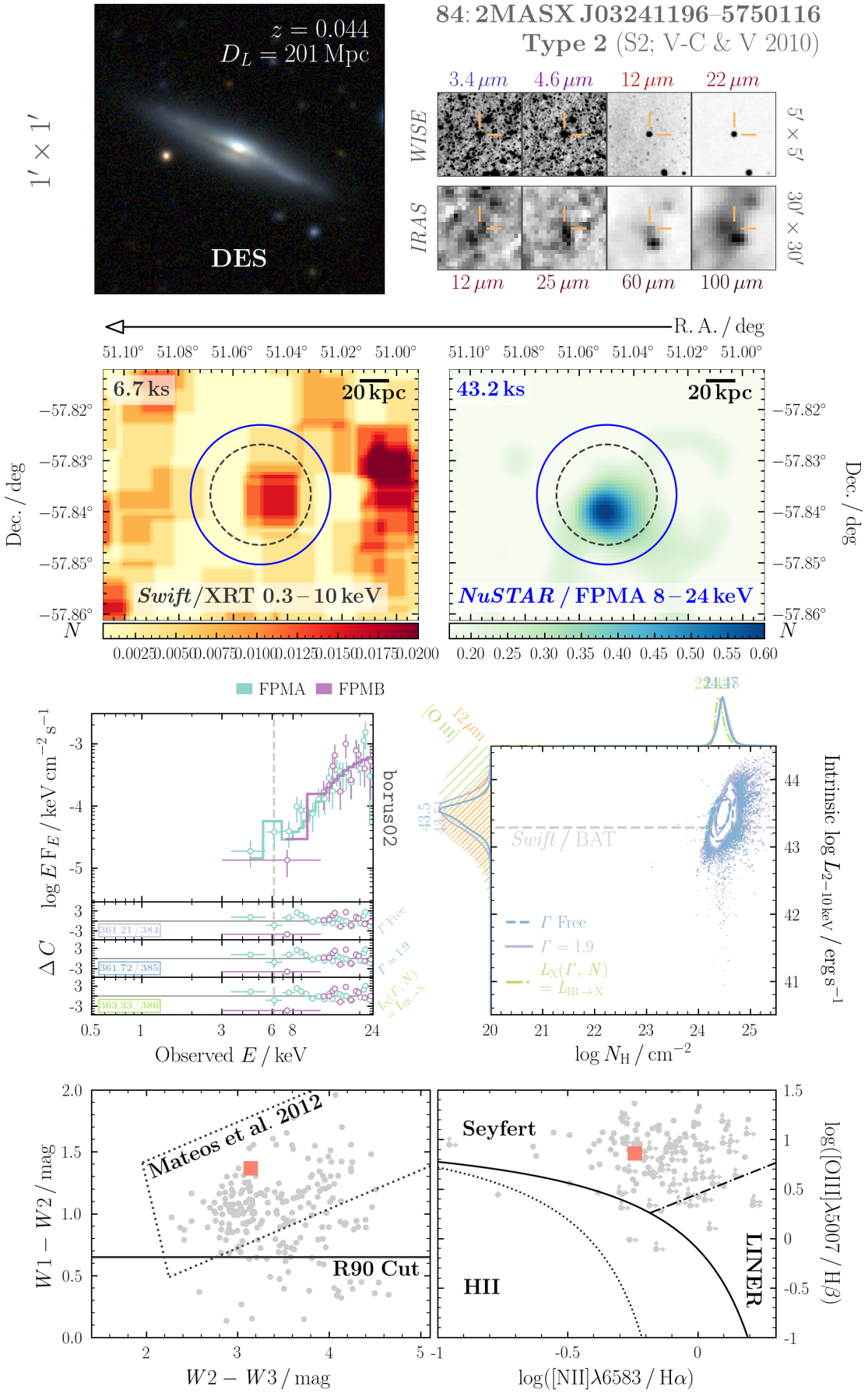

FIGURE C.34: $N_{\rm H}$ Determination, ID 84: 2MASX J03241196–5750116

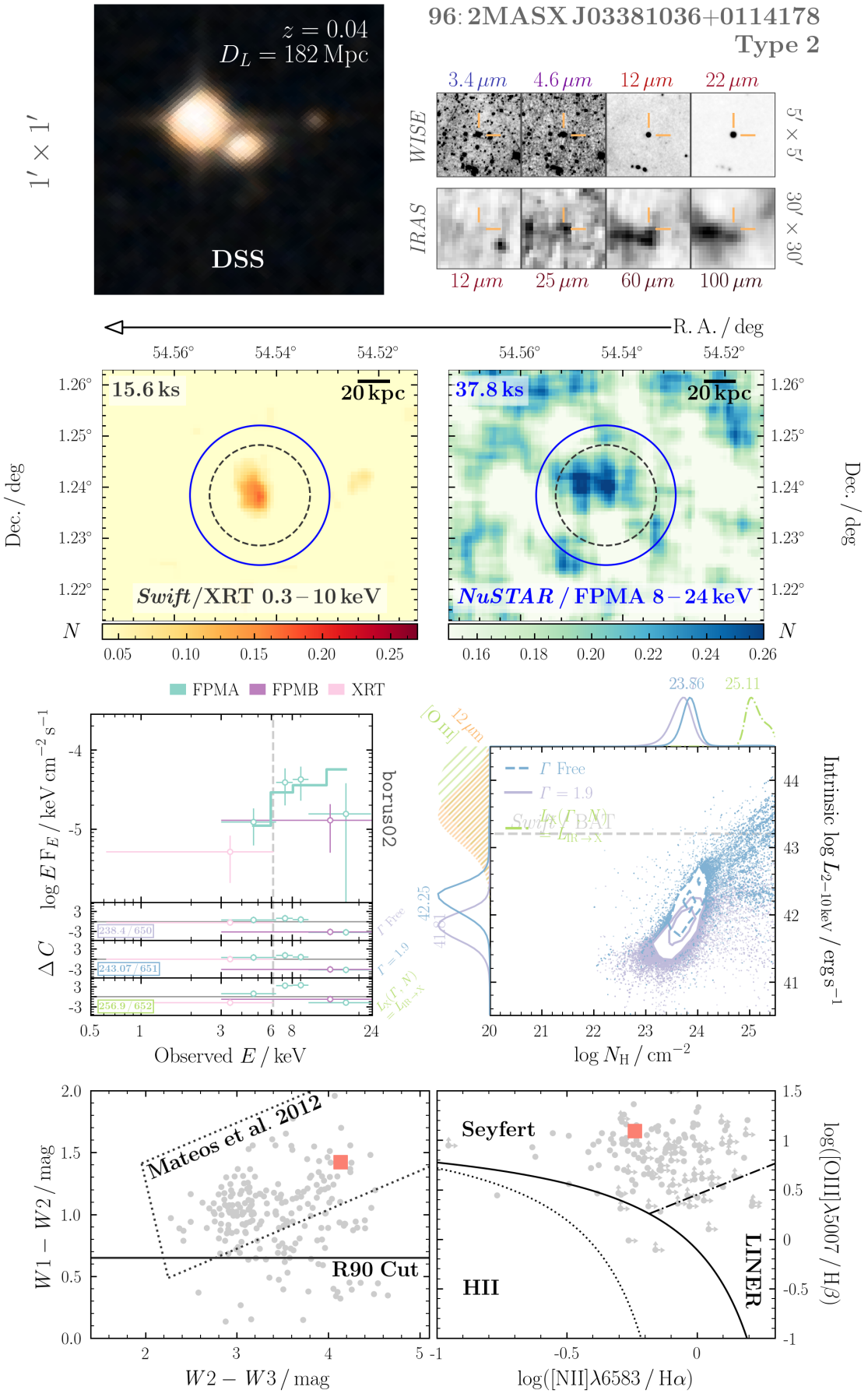

FIGURE C.35: $N_{\rm H}$ Determination, ID 96: 2MASX J03381036+0114178

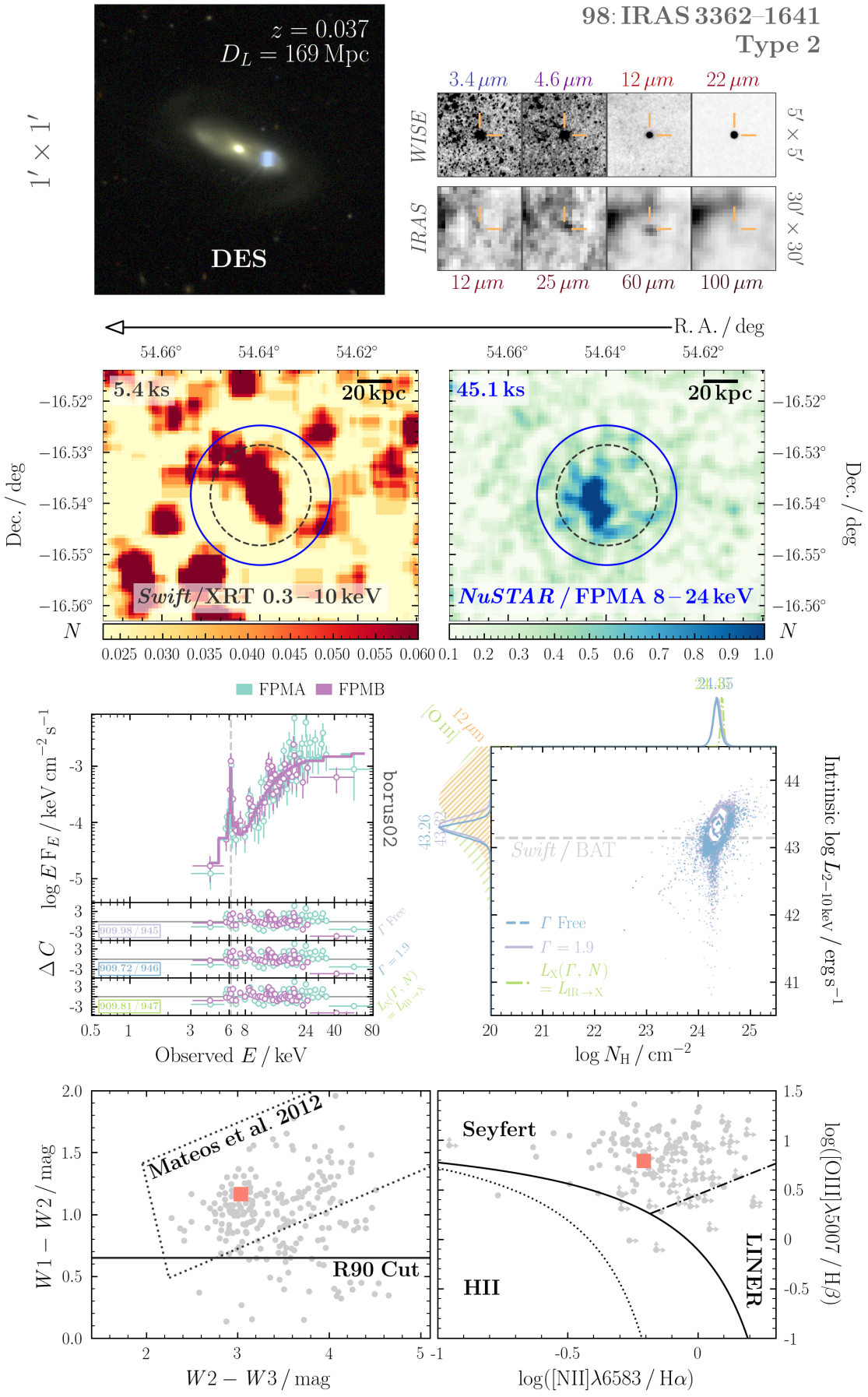

FIGURE C.36: $N_{\rm H}$ Determination, ID 98: IRAS 3362-1641

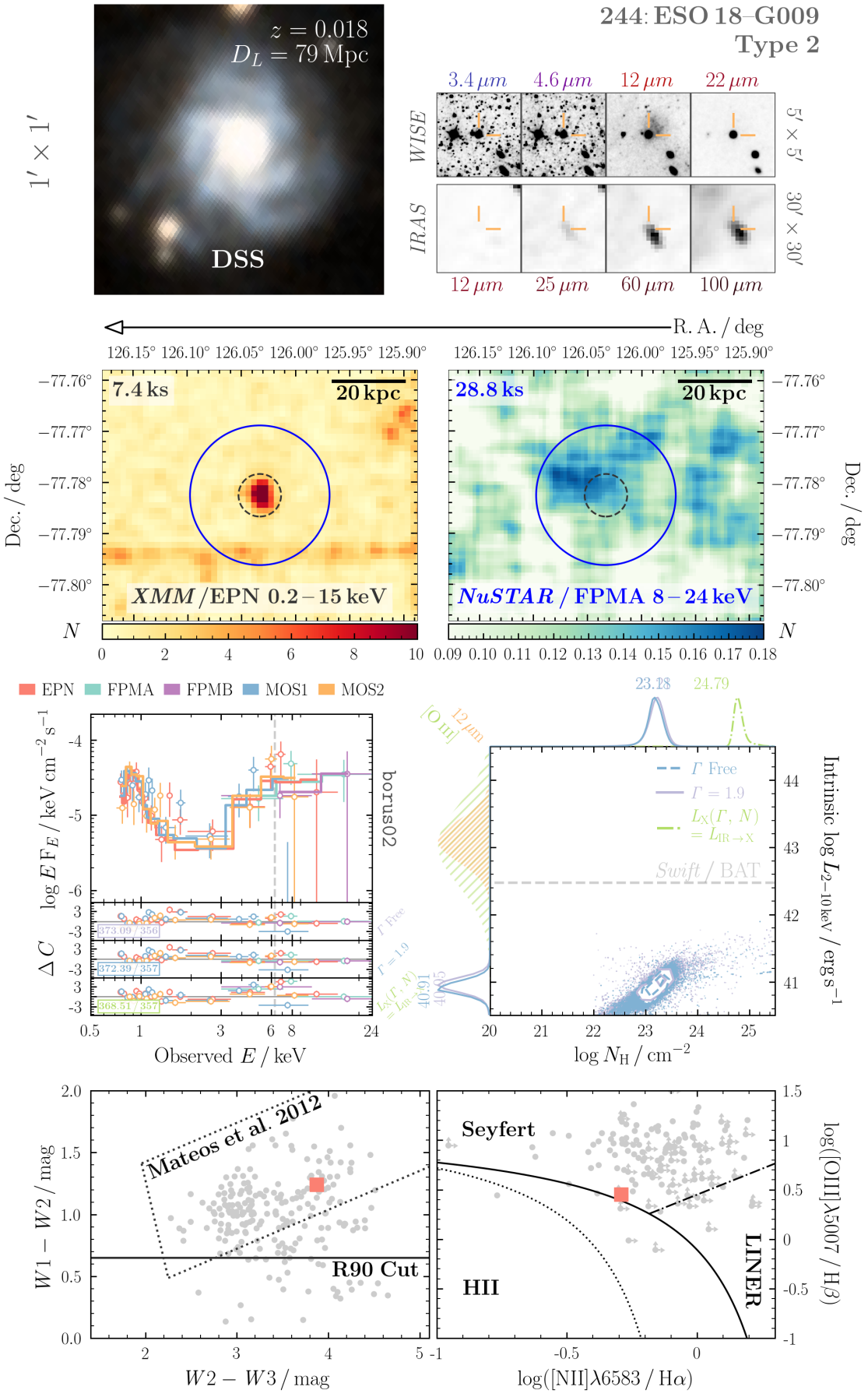

FIGURE C.37: $N_{\rm H}$ Determination, ID 244: ESO 18-G009

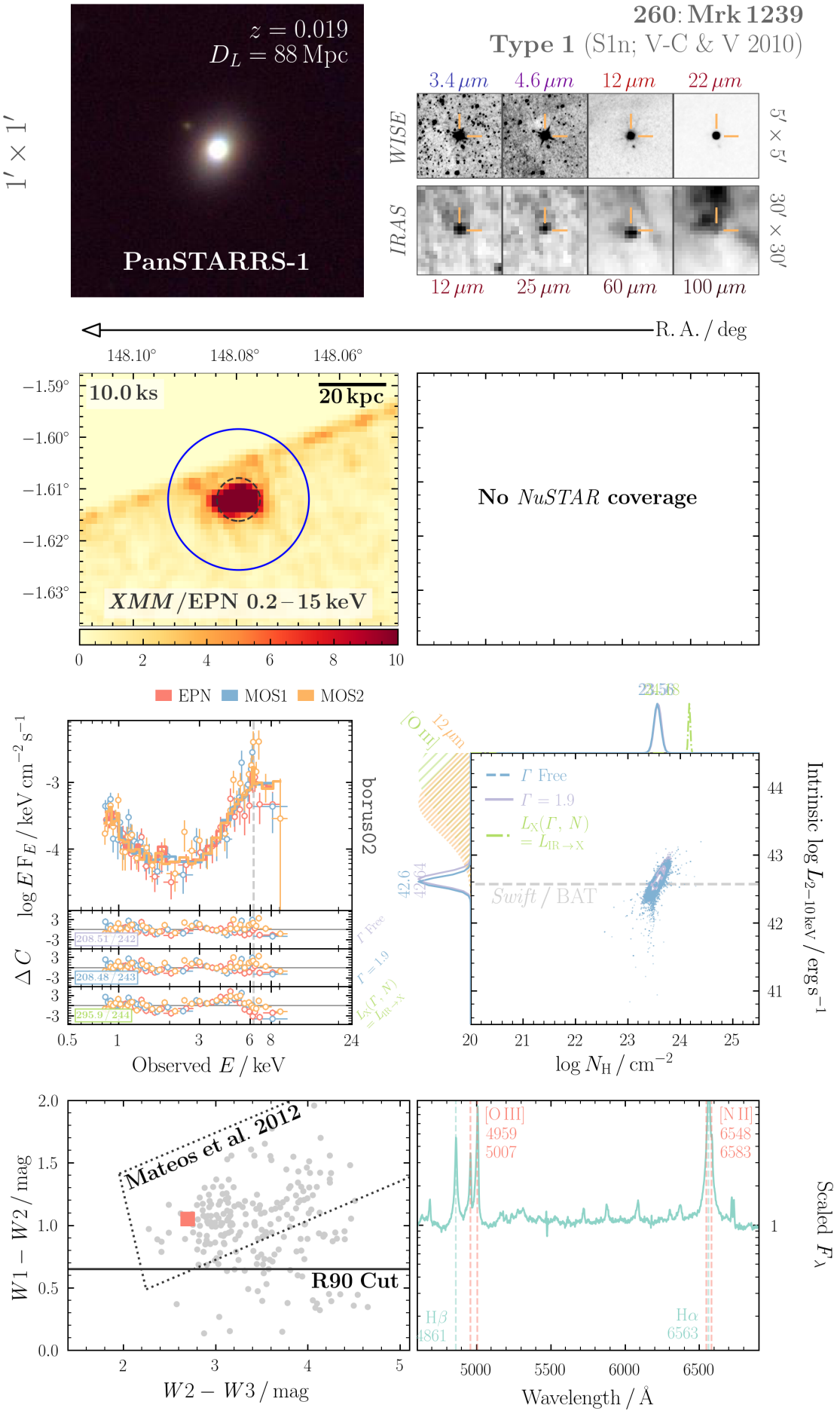

FIGURE C.38: $N_{\rm H}$ Determination, ID 260: Mrk 1239

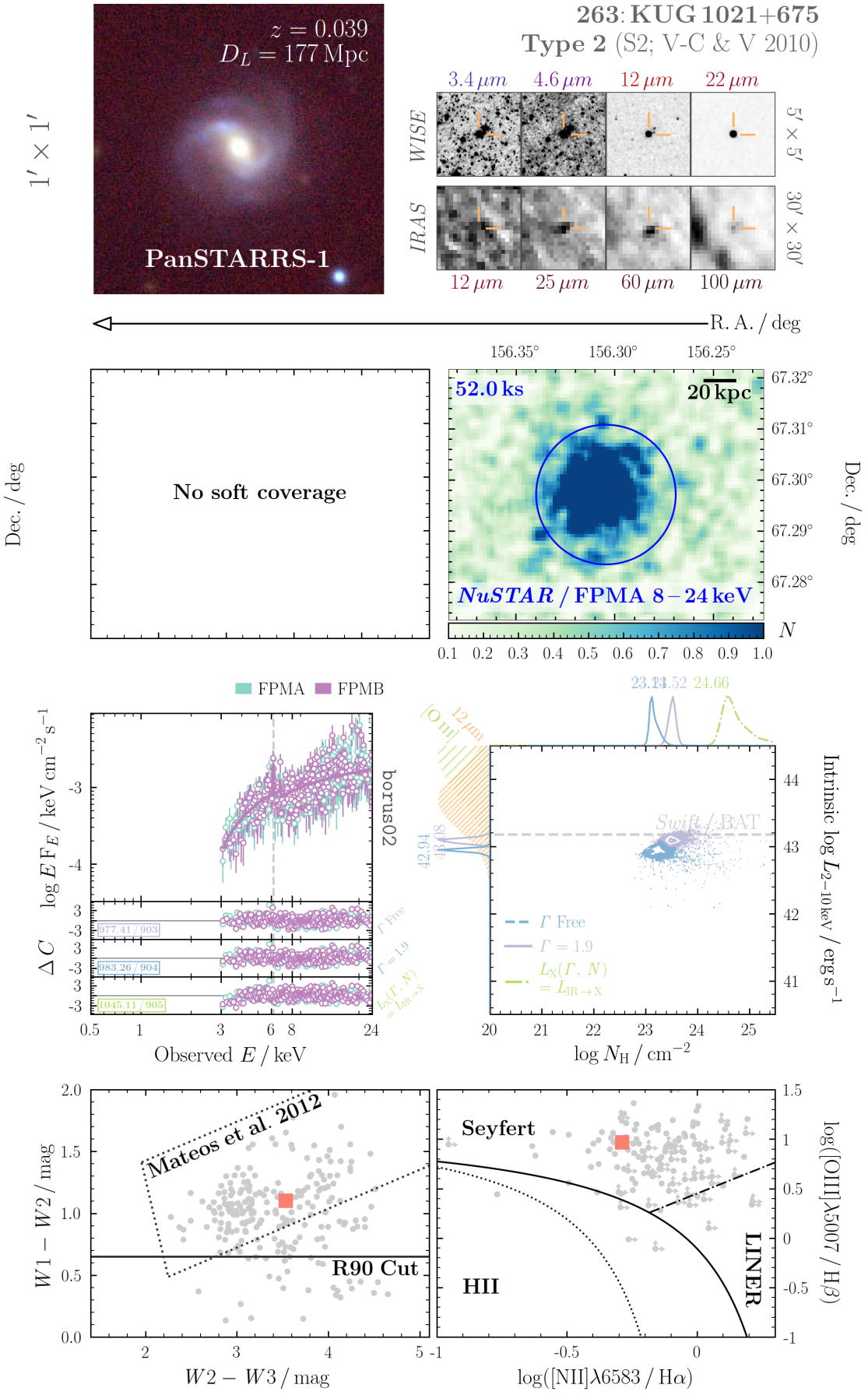

FIGURE C.39: $N_{\rm H}$ Determination, ID 263: KUG 1021+675

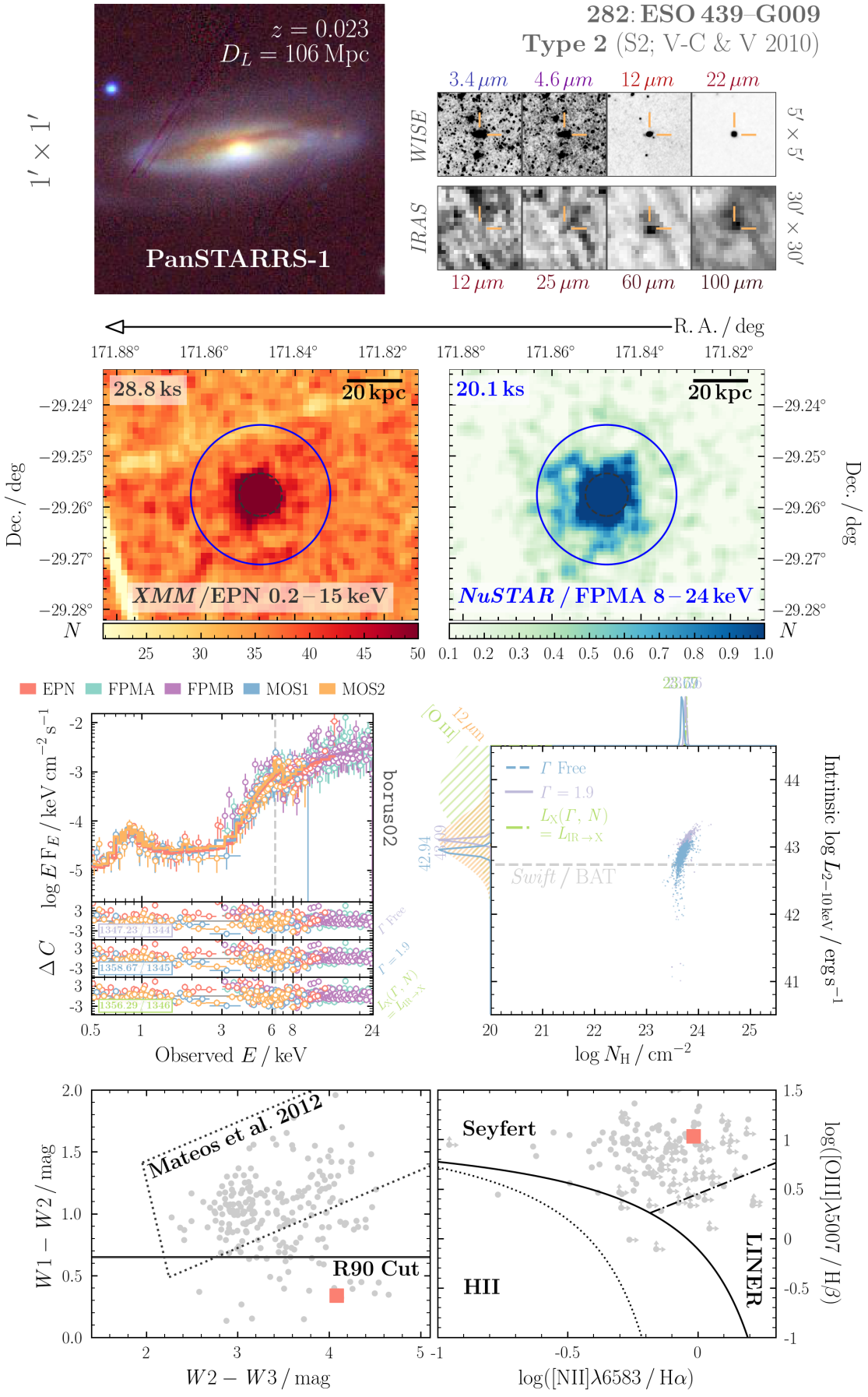

FIGURE C.40: $N_{\rm H}$ Determination, ID 282: ESO 439–G009

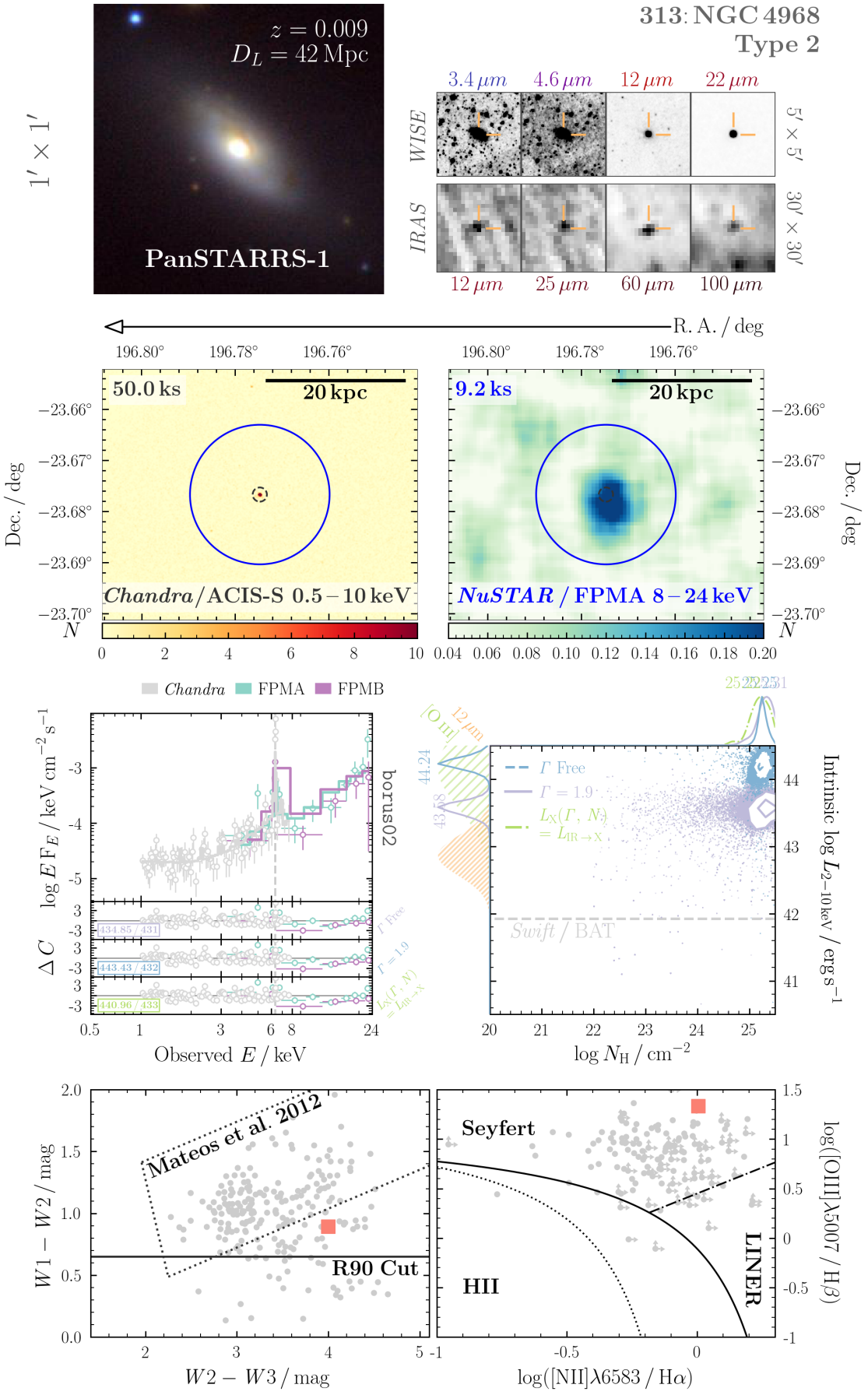

FIGURE C.41: $N_{\rm H}$ Determination, ID 313: NGC 4968

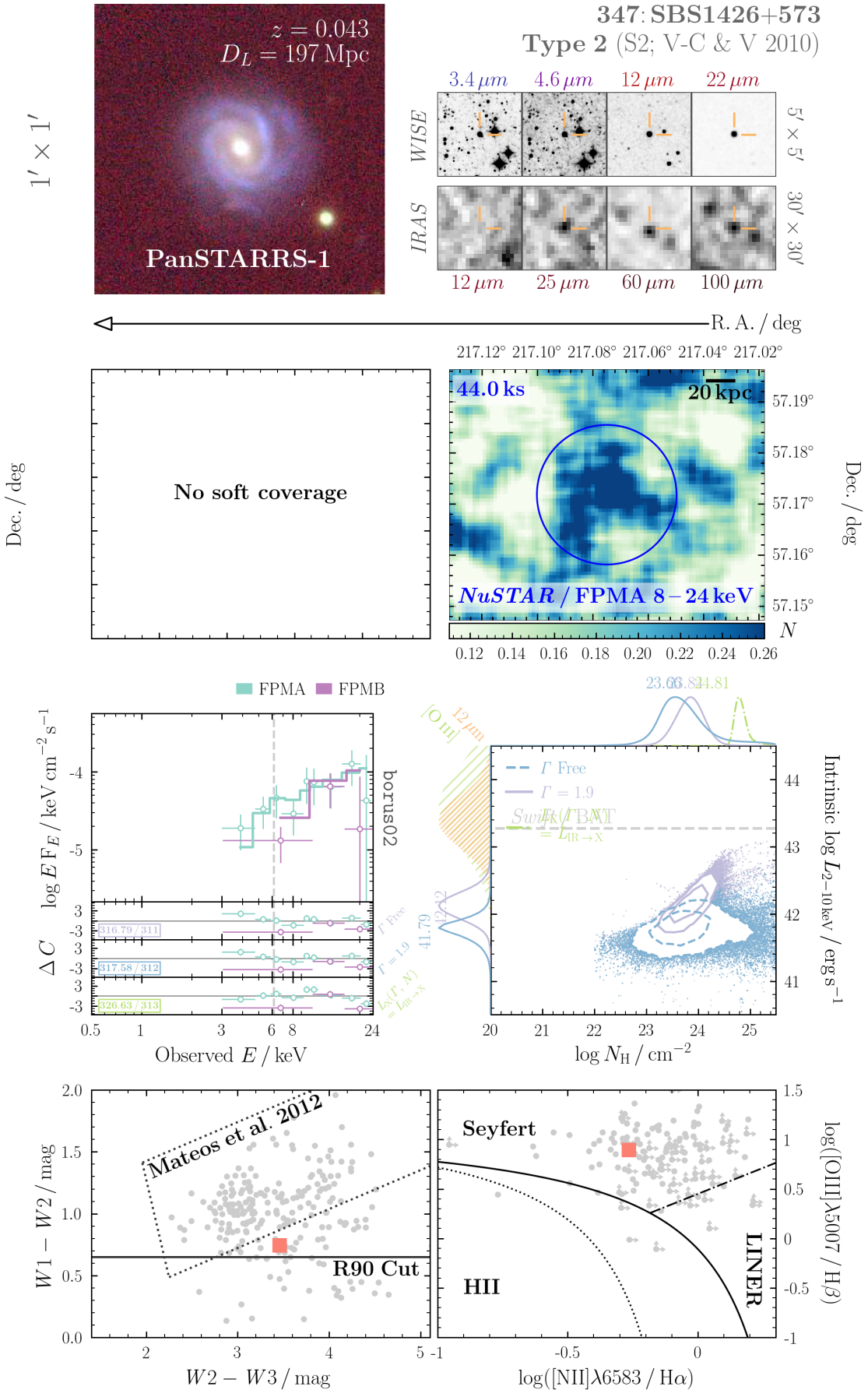

FIGURE C.42: $N_{\rm H}$ Determination, ID 347: SBS 1426+573

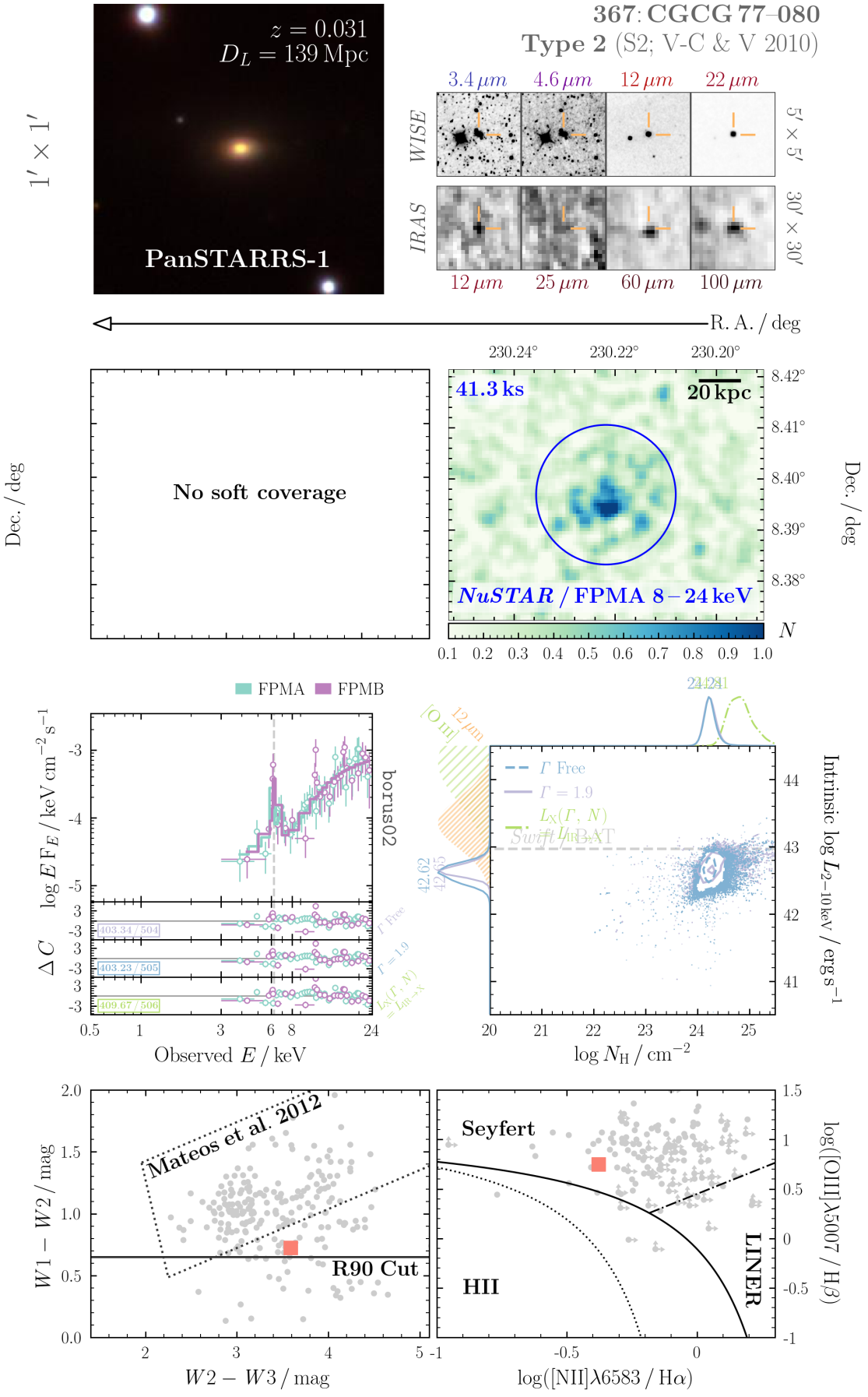

FIGURE C.43: $N_{\rm H}$ Determination, ID 367: CGCG 077-080

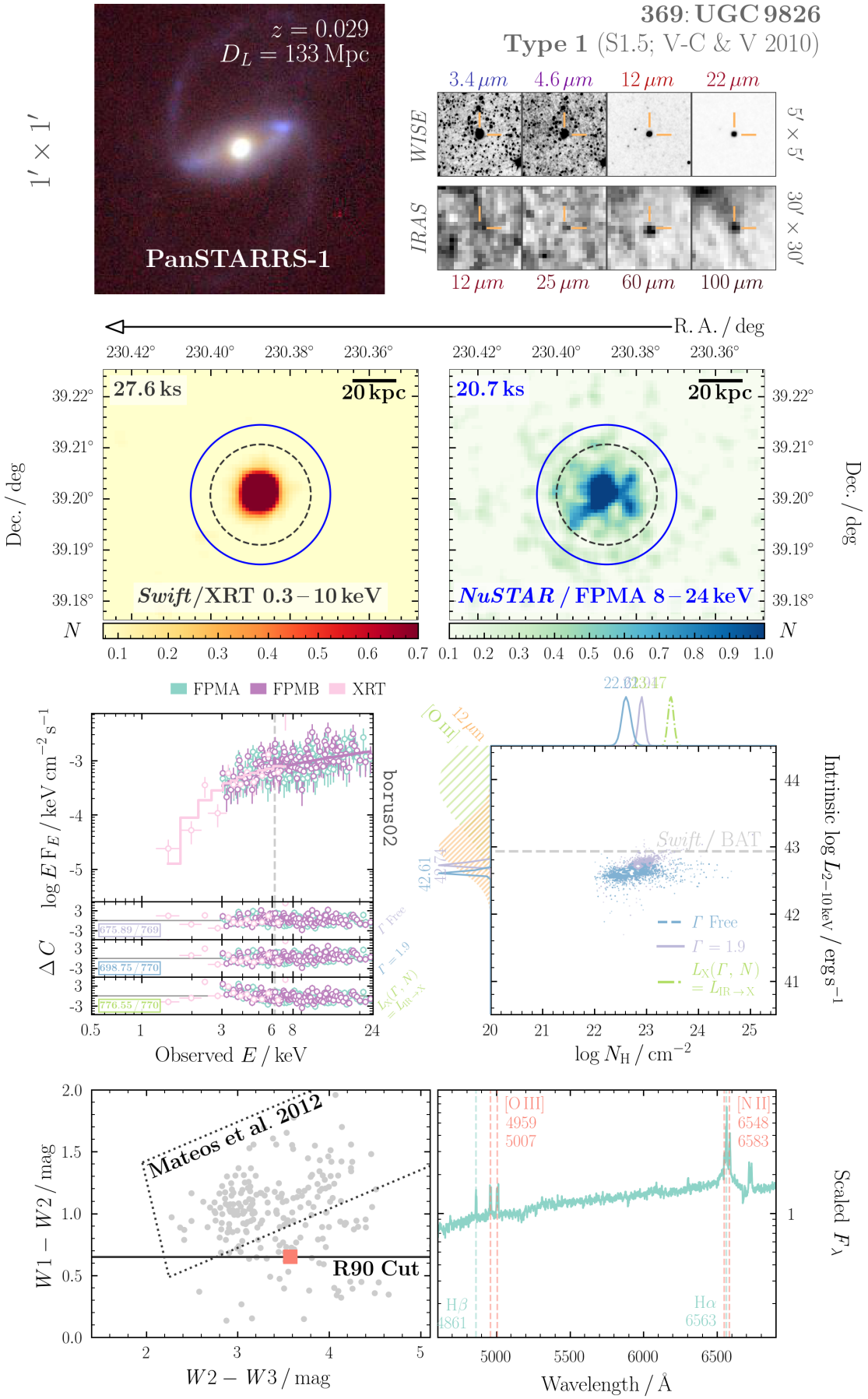

FIGURE C.44: $N_{\rm H}$ Determination, ID 369: UGC 9826

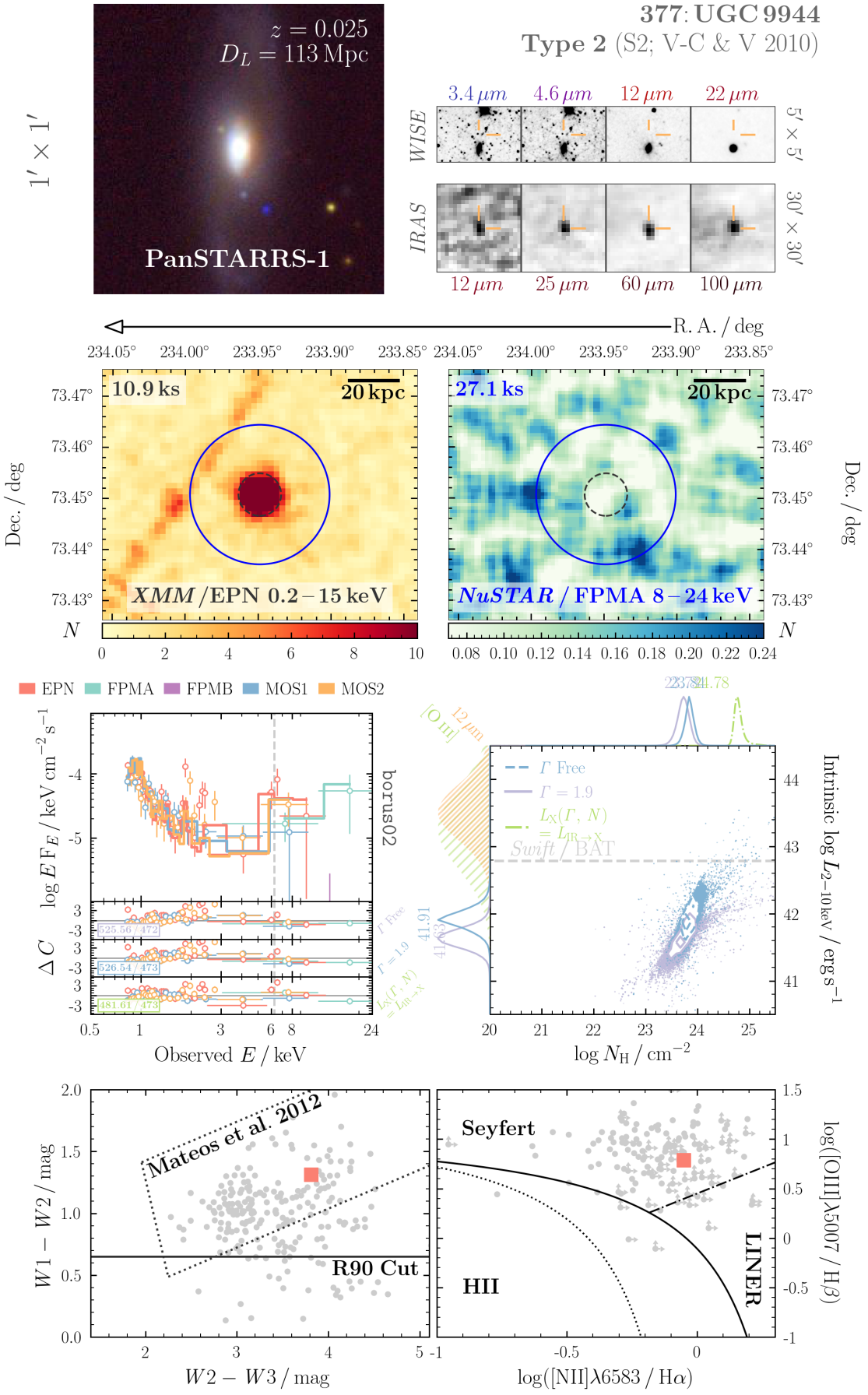

FIGURE C.45: $N_{\rm H}$ Determination, ID 377: UGC 9944

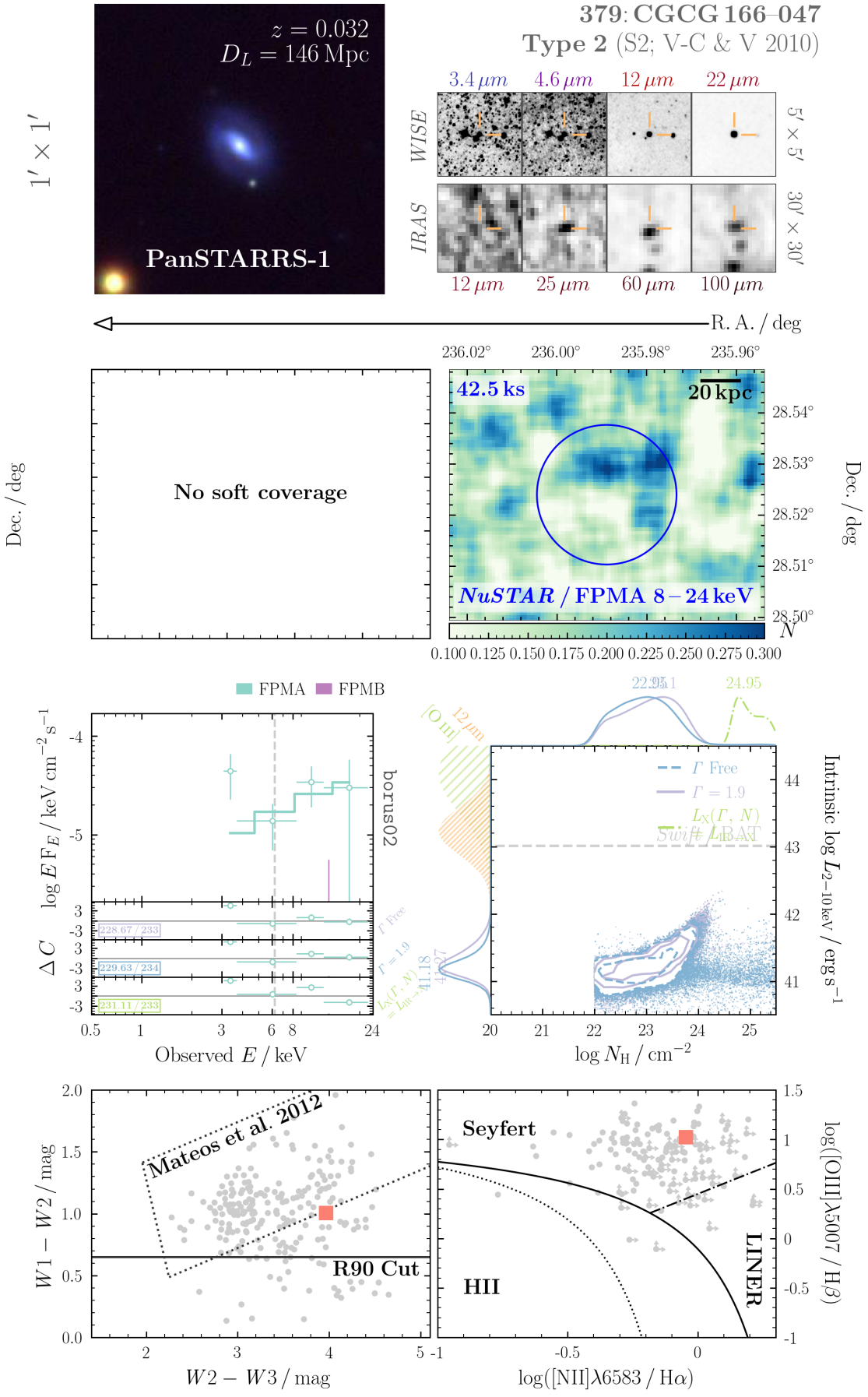

FIGURE C.46: $N_{\rm H}$ Determination, ID 379: CGCG 166-047

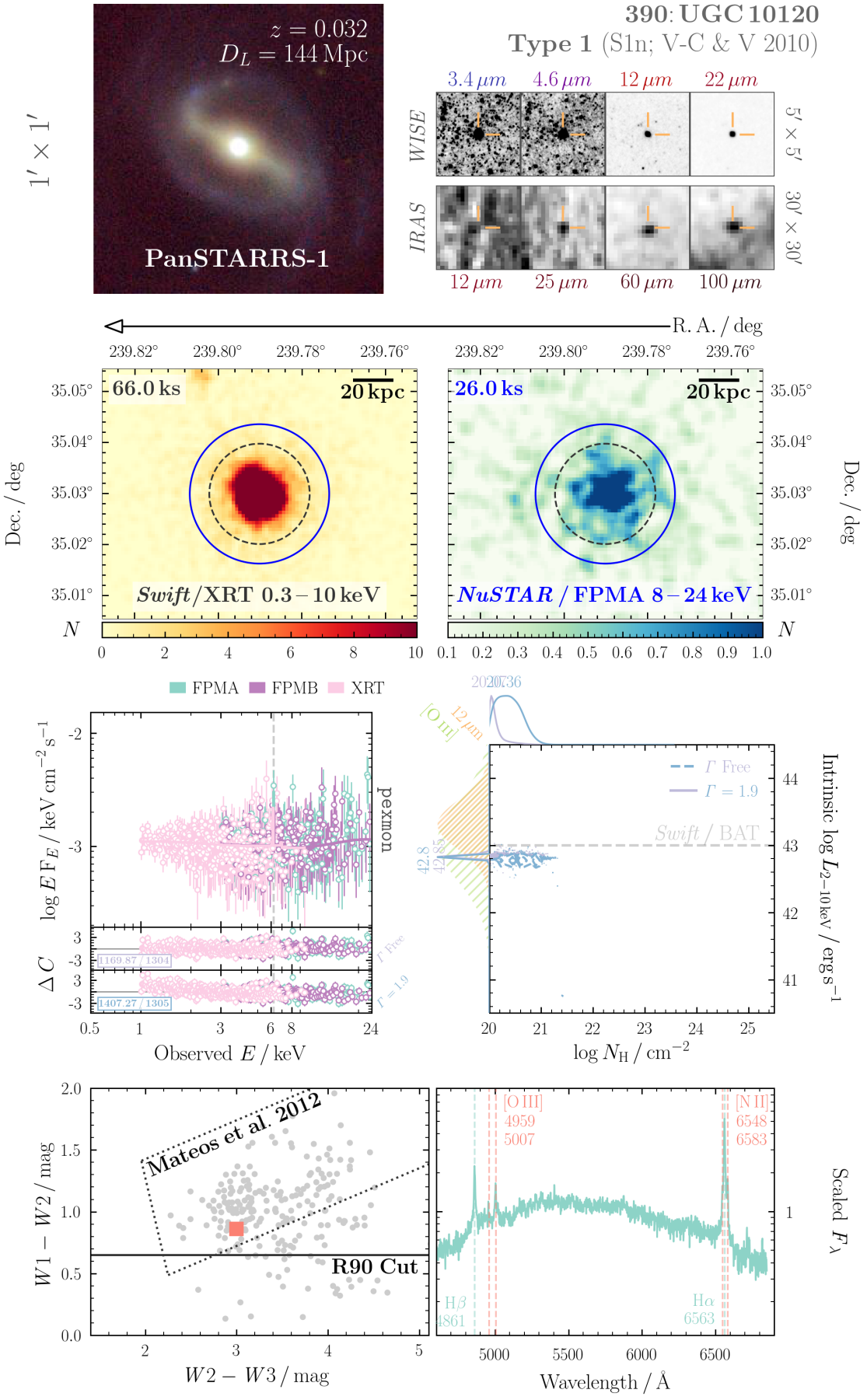

FIGURE C.47: $N_{\rm H}$ Determination, ID 390: UGC 10120

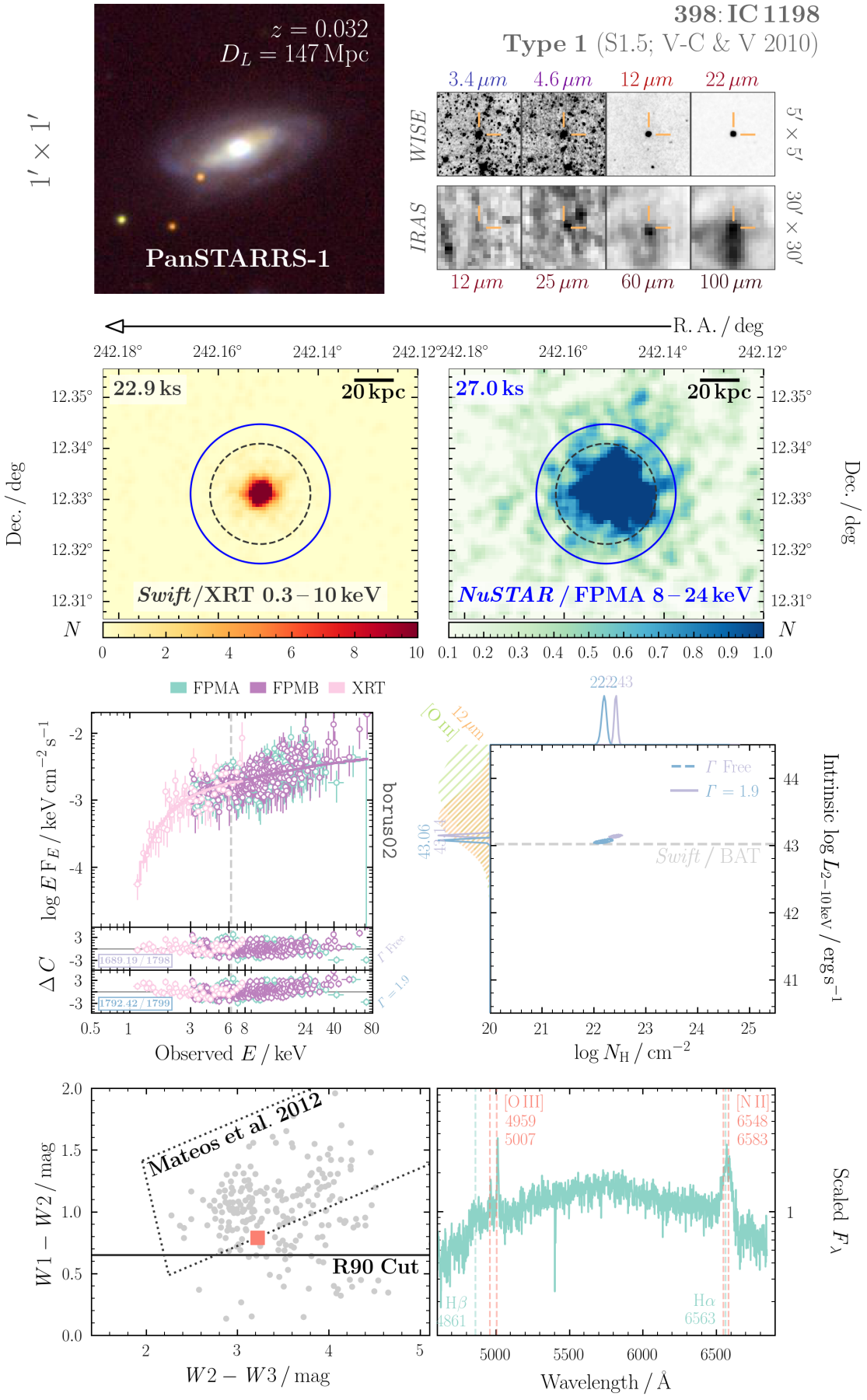

FIGURE C.48: $N_{\rm H}$ Determination, ID 398: IC 1198

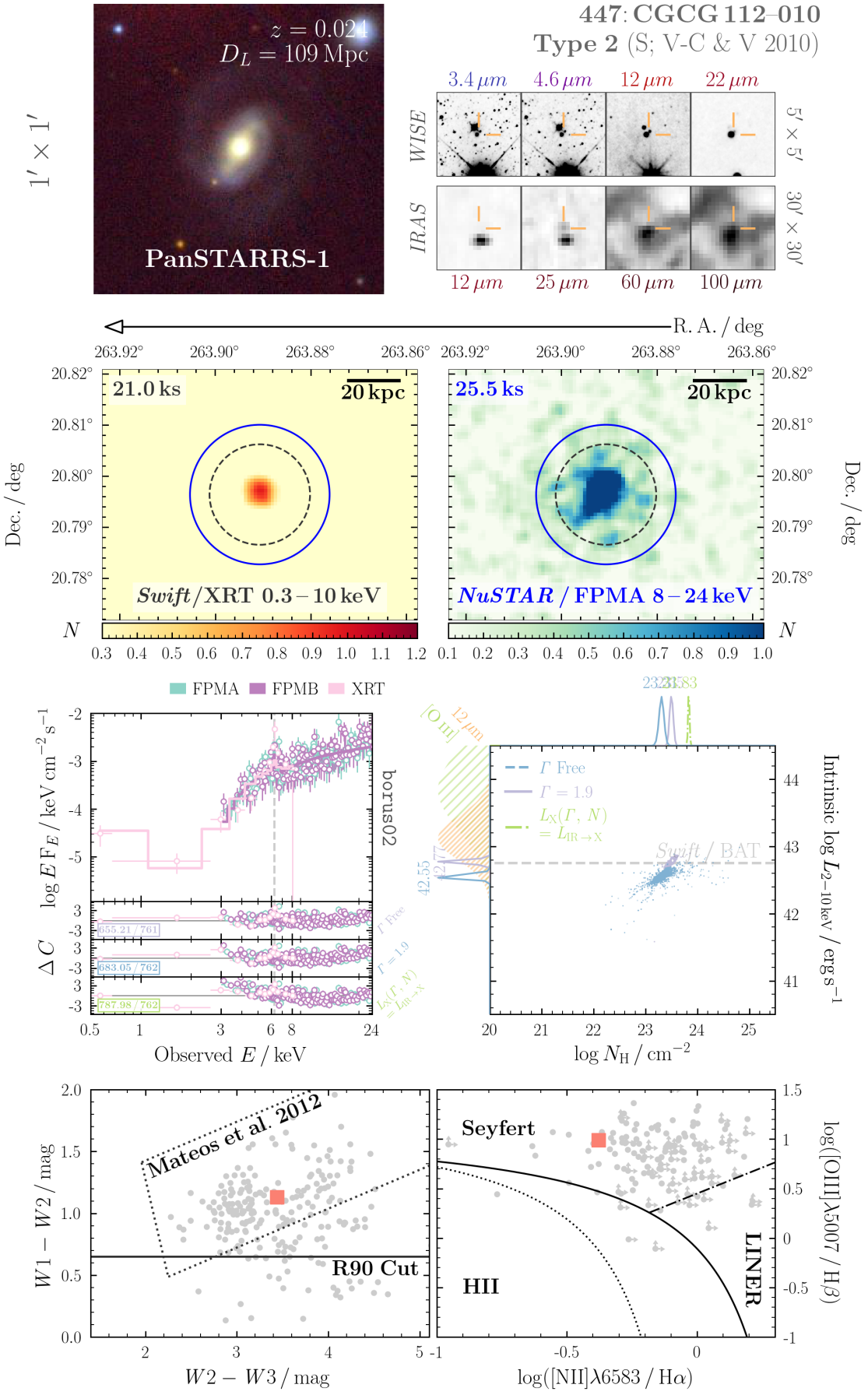

FIGURE C.49: $N_{\rm H}$ Determination, ID 447: CGCG 112-010

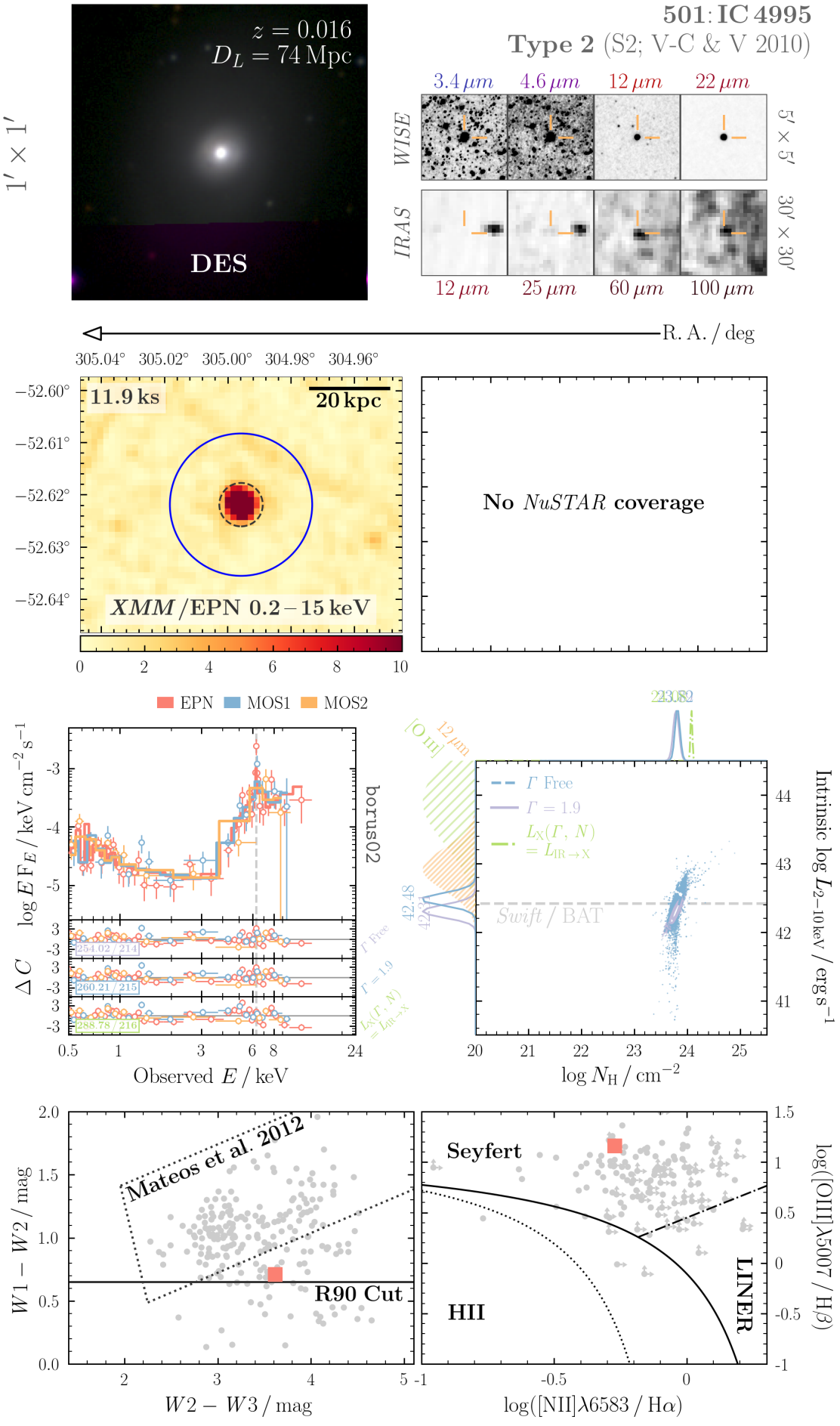

FIGURE C.50: $N_{\rm H}$ Determination, ID 501: IC 4995

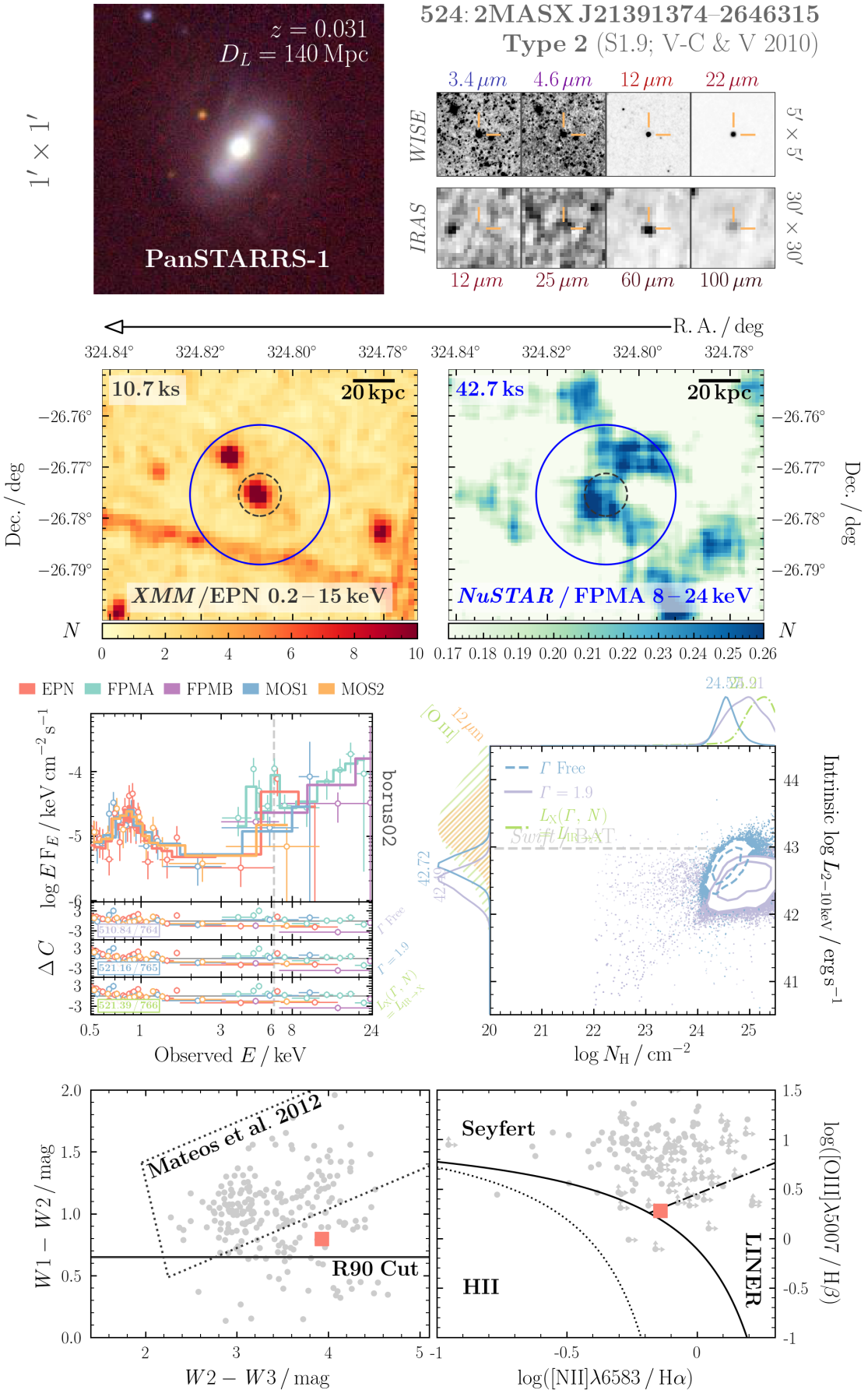

FIGURE C.51: $N_{\rm H}$ Determination, ID 524: 2MASX J21391374-2646315

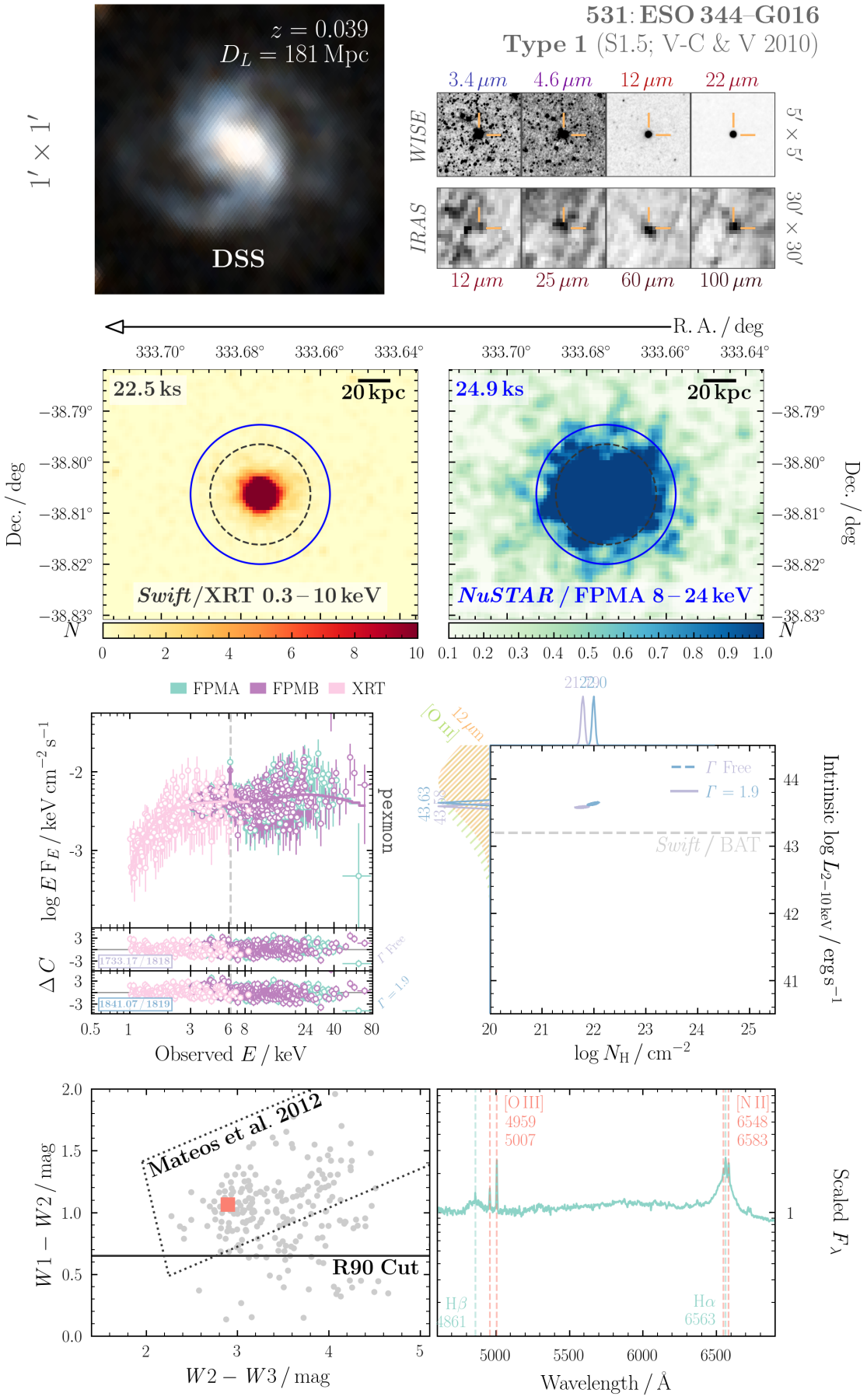

FIGURE C.52: $N_{\rm H}$ Determination, ID 531: ESO 344-G016

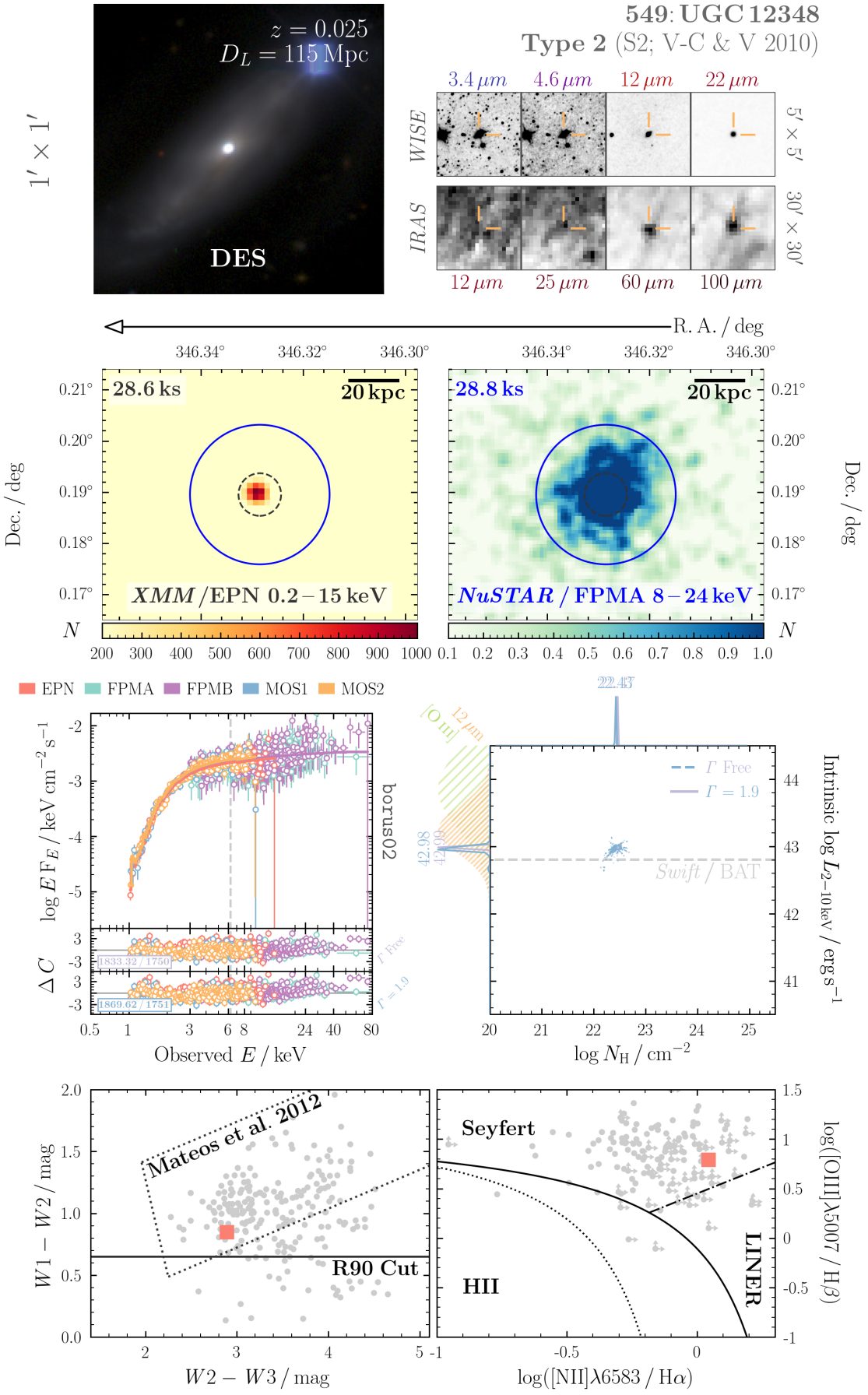

FIGURE C.53: $N_{\rm H}$ Determination, ID 549: UGC 12348

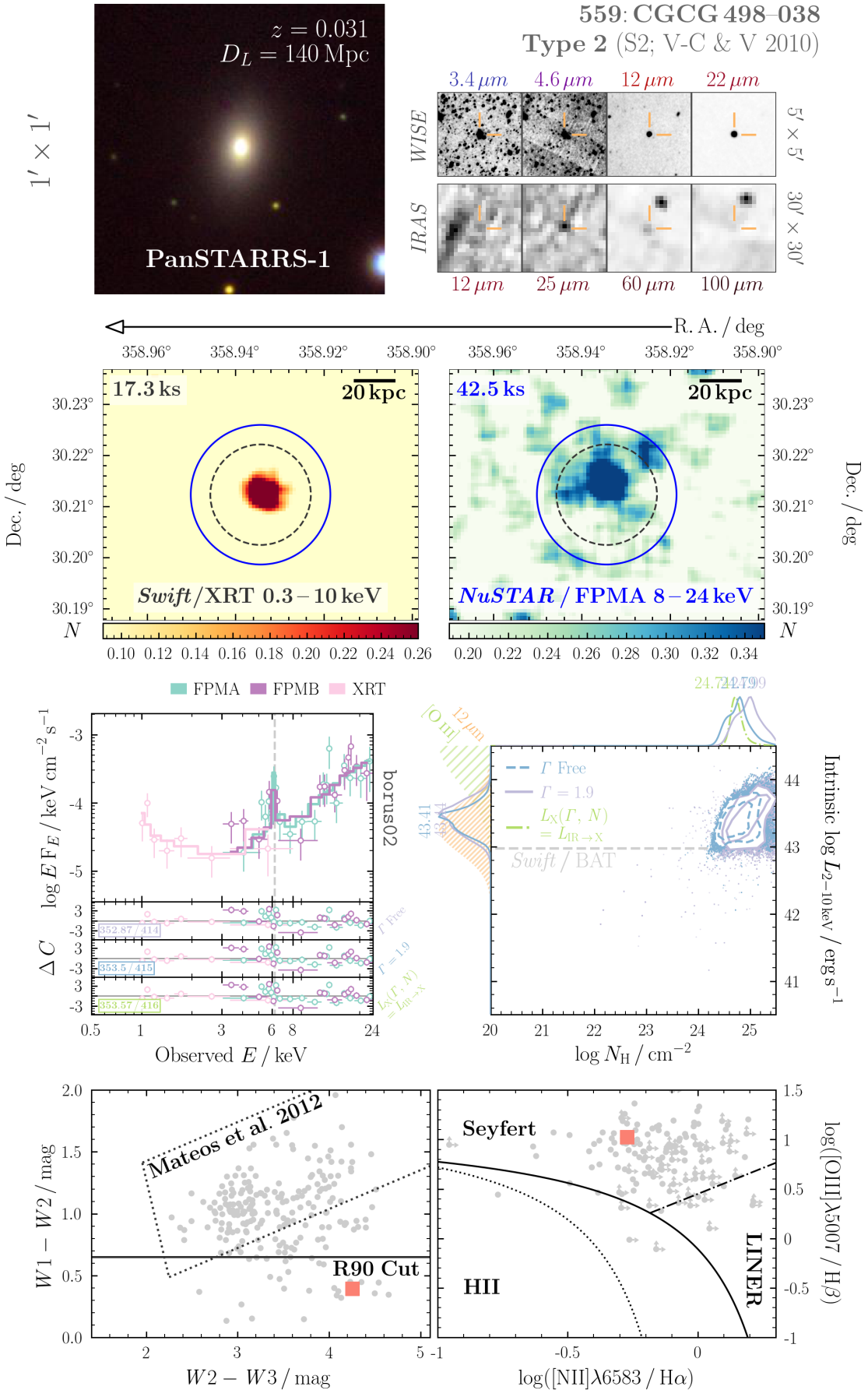

FIGURE C.54: $N_{\rm H}$ Determination, ID 559: CGCG 498-038

Bibliography

Agostino, C. J. and Salim, S. (2018). Crossing the Line: Active Galactic Nuclei in the Star-forming region of the BPT Diagram. *arXiv e-prints*.

Aird, J., Coil, A. L., Georgakakis, A., Nandra, K., Barro, G., and Pérez-González, P. G. (2015). The evolution of the X-ray luminosity functions of unabsorbed and absorbed AGNs out to z 5. *MNRAS*, 451:1892–1927.

Akylas, A., Georgakakis, A., Georgantopoulos, I., Brightman, M., and Nandra, K. (2012). Constraining the fraction of Compton-thick AGN in the Universe by modelling the diffuse X-ray background spectrum. *A&A*, 546:A98.

Akylas, A., Georgantopoulos, I., Ranalli, P., Gkiokas, E., Corral, A., and Lanzuisi, G. (2016). Compton-thick AGN in the 70-month Swift-BAT All-Sky Hard X-ray Survey: A Bayesian approach. *A&A*, 594:A73.

Alexander, D. M. and Hickox, R. C. (2012). What drives the growth of black holes? New A Rev., 56:93–121.

Ananna, T. T., Treister, E., Urry, C. M., Ricci, C., Kirkpatrick, A., LaMassa, S., Buchner, J., Civano, F., Tremmel, M., and Marchesi, S. (2019). The Accretion History of AGNs. I. Supermassive Black Hole Population Synthesis Model. *ApJ*, 871:240.

Annuar, A., Alexander, D. M., Gandhi, P., Lansbury, G. B., Asmus, D., Ballantyne, D. R., Bauer, F. E., Boggs, S. E., Boorman, P. G., Brandt, W. N., Brightman, M., Christensen, F. E., Craig, W. W., Farrah, D., Goulding, A. D., Hailey, C. J., Harrison, F. A., Koss, M. J., LaMassa, S. M., Murray, S. S., Ricci, C., Rosario, D. J., Stanley, F., Stern, D., and Zhang, W. (2017). A New Compton-thick AGN in our Cosmic Backyard: Unveiling the Buried Nucleus in NGC 1448 with NuSTAR. *ApJ*, 836:165.

Annuar, A., Gandhi, P., Alexander, D. M., Lansbury, G. B., Arévalo, P., Ballantyne, D. R., Baloković, M., Bauer, F. E., Boggs, S. E., Brandt, W. N., Brightman, M., Christensen, F. E., Craig, W. W., Del Moro, A., Hailey, C. J., Harrison, F. A., Hickox, R. C., Matt, G., Puccetti, S., Ricci, C., Rigby, J. R., Stern, D., Walton, D. J., Zappacosta, L., and Zhang, W. (2015). NuSTAR Observations of the Compton-thick Active

Galactic Nucleus and Ultraluminous X-Ray Source Candidate in NGC 5643. *ApJ*, 815:36.

Antonucci, R. (1993). Unified models for active galactic nuclei and quasars. *ARA&A*, 31:473–521.

Antonucci, R. R. J. (1984). Optical spectropolarimetry of radio galaxies. *ApJ*, 278:499–520.

Arévalo, P., Bauer, F. E., Puccetti, S., Walton, D. J., Koss, M., Boggs, S. E., Brandt, W. N., Brightman, M., Christensen, F. E., Comastri, A., Craig, W. W., Fuerst, F., Gandhi, P., Grefenstette, B. W., Hailey, C. J., Harrison, F. A., Luo, B., Madejski, G., Madsen, K. K., Marinucci, A., Matt, G., Saez, C., Stern, D., Stuhlinger, M., Treister, E., Urry, C. M., and Zhang, W. W. (2014). The 2-79 keV X-Ray Spectrum of the Circinus Galaxy with NuSTAR, XMM-Newton, and Chandra: A Fully Compton-thick Active Galactic Nucleus. *ApJ*, 791:81.

Arnaud, K. A. (1996). XSPEC: The First Ten Years. In Jacoby, G. H. and Barnes, J., editors, *Astronomical Data Analysis Software and Systems V*, volume 101 of *Astronomical Society of the Pacific Conference Series*, page 17.

Aschenbach, B. (1985). X-ray telescopes. *Reports on Progress in Physics*, 48:579–629.

Asmus, D., Gandhi, P., Hönig, S. F., Smette, A., and Duschl, W. J. (2015). The subarcsecond mid-infrared view of local active galactic nuclei - II. The mid-infrared-X-ray correlation. *MNRAS*, 454:766–803.

Asmus, D., Hönig, S. F., and Gandhi, P. (2016). The Subarcsecond Mid-infrared View of Local Active Galactic Nuclei. III. Polar Dust Emission. *ApJ*, 822:109.

Asmus, D., Hönig, S. F., Gandhi, P., Smette, A., and Duschl, W. J. (2014). The subarcsecond mid-infrared view of local active galactic nuclei - I. The N- and Q-band imaging atlas. *MNRAS*, 439:1648–1679.

Assef, R. J., Kochanek, C. S., Brodwin, M., Cool, R., Forman, W., Gonzalez, A. H., Hickox, R. C., Jones, C., Le Floc'h, E., Moustakas, J., Murray, S. S., and Stern, D. (2010). Low-Resolution Spectral Templates for Active Galactic Nuclei and Galaxies from 0.03 to 30 μm. *ApJ*, 713:970–985.

Assef, R. J., Stern, D., Noirot, G., Jun, H. D., Cutri, R. M., and Eisenhardt, P. R. M. (2018). The WISE AGN Catalog. *ApJS*, 234:23.

Balbus, S. A. and Hawley, J. F. (1991). A Powerful Local Shear Instability in Weakly Magnetized Disks. I. Linear Analysis. *ApJ*, 376:214.

Baldi, R. D., Williams, D. R. A., McHardy, I. M., Beswick, R. J., Argo, M. K., Dullo, B. T., Knapen, J. H., Brinks, E., Muxlow, T. W. B., Aalto, S., Alberdi, A., Bendo, G. J., Corbel, S., Evans, R., Fenech, D. M., Green, D. A., Klöckner, H.-R., Körding, E., Kharb, P., Maccarone, T. J., Martí-Vidal, I., Mundell, C. G., Panessa, F., Peck, A. B., Pérez-Torres, M. A., Saikia, D. J., Saikia, P., Shankar, F., Spencer, R. E., Stevens, I. R., Uttley, P., and Westcott, J. (2018). LeMMINGs - I. The eMERLIN legacy survey of nearby galaxies. 1.5-GHz parsec-scale radio structures and cores. *MNRAS*, 476:3478–3522.

Baldwin, J. A. (1977). Luminosity Indicators in the Spectra of Quasi-Stellar Objects. *ApJ*, 214:679–684.

Baldwin, J. A., Phillips, M. M., and Terlevich, R. (1981). Classification parameters for the emission-line spectra of extragalactic objects. *PASP*, 93:5–19.

Ballantyne, D. R. (2014). The average 0.5-200 keV spectrum of local active galactic nuclei and a new determination of the 2-10 keV luminosity function at z $\sim$ 0. *MNRAS*, 437:2845–2855.

Balmaverde, B. and Capetti, A. (2015). The naked nuclei of low ionization nuclear emission line regions. *A&A*, 581:A76.

Baloković, M., Brightman, M., Harrison, F. A., Comastri, A., Ricci, C., Buchner, J., Gandhi, P., Farrah, D., and Stern, D. (2018). New Spectral Model for Constraining Torus Covering Factors from Broadband X-Ray Spectra of Active Galactic Nuclei. *ApJ*, 854:42.

Baloković, M., Comastri, A., Harrison, F. A., Alexander, D. M., Ballantyne, D. R., Bauer, F. E., Boggs, S. E., Brandt, W. N., Brightman, M., Christensen, F. E., Craig, W. W., Del Moro, A., Gandhi, P., Hailey, C. J., Koss, M., Lansbury, G. B., Luo, B., Madejski, G. M., Marinucci, A., Matt, G., Markwardt, C. B., Puccetti, S., Reynolds, C. S., Risaliti, G., Rivers, E., Stern, D., Walton, D. J., and Zhang, W. W. (2014). The NuSTAR View of Nearby Compton-thick Active Galactic Nuclei: The Cases of NGC 424, NGC 1320, and IC 2560. *ApJ*, 794:111.

Baloković, M., Harrison, F. A., Stern, D., Boggs, S. E., Christensen, F. E., Craig, W. W., Grefenstette, B. W., Hailey, C. J., and Zhang, W. W. (in prep.). The nustar-swift/bat legacy survey: Sy ii sample definition and phenomenology. *ApJ*.

Barnes, D. G. and Webster, R. L. (2001). A study of neutral hydrogen in five small galaxy groups. *MNRAS*, 324:859–876.

Bauer, F. E., Arévalo, P., Walton, D. J., Koss, M. J., Puccetti, S., Gandhi, P., Stern, D., Alexander, D. M., Baloković, M., Boggs, S. E., Brandt, W. N., Brightman, M.,

Christensen, F. E., Comastri, A., Craig, W. W., Del Moro, A., Hailey, C. J., Harrison, F. A., Hickox, R., Luo, B., Markwardt, C. B., Marinucci, A., Matt, G., Rigby, J. R., Rivers, E., Saez, C., Treister, E., Urry, C. M., and Zhang, W. W. (2015). NuSTAR Spectroscopy of Multi-component X-Ray Reflection from NGC 1068. *ApJ*, 812:116.

Baumgartner, W. H., Tueller, J., Markwardt, C. B., Skinner, G. K., Barthelmy, S., Mushotzky, R. F., Evans, P. A., and Gehrels, N. (2013). The 70 Month Swift-BAT All-sky Hard X-Ray Survey. *ApJS*, 207:19.

Begelman, M. C., Blandford, R. D., and Rees, M. J. (1984). Theory of extragalactic radio sources. *Reviews of Modern Physics*, 56(2):255–351.

Beichman, C. A., Neugebauer, G., Habing, H. J., Clegg, P. E., and Chester, T. J., editors (1988). *Infrared astronomical satellite (IRAS) catalogs and atlases. Volume 1: Explanatory supplement*, volume 1.

Berney, S., Koss, M., Trakhtenbrot, B., Ricci, C., Lamperti, I., Schawinski, K., Baloković, M., Crenshaw, D. M., Fischer, T., Gehrels, N., Harrison, F., Hashimoto, Y., Ichikawa, K., Mushotzky, R., Oh, K., Stern, D., Treister, E., Ueda, Y., Veilleux, S., and Winter, L. (2015). BAT AGN spectroscopic survey-II. X-ray emission and high-ionization optical emission lines. *MNRAS*, 454:3622–3634.

Beswick, R., Argo, M. K., Evans, R., McHardy, I., Williams, D. R. A., and Westcott, J. (2014). LeMMINGs e-MERLIN survey of nearby galaxies. In *Proceedings of the 12th European VLBI Network Symposium and Users Meeting (EVN 2014). 7-10 October 2014. Cagliari*, page 10.

Bevington, P. R. (1969). *Data reduction and error analysis for the physical sciences.* New York: McGraw-Hill.

Bianchi, S., Chiaberge, M., Evans, D. A., Guainazzi, M., Baldi, R. D., Matt, G., and Piconcelli, E. (2010). High-resolution X-ray spectroscopy and imaging of Mrk 573. *MNRAS*, 405:553–563.

Bianchi, S., Guainazzi, M., Matt, G., and Fonseca Bonilla, N. (2007). On the Iwasawa-Taniguchi effect of radio-quiet AGN. *A&A*, 467:L19–L22.

Boella, G., Butler, R. C., Perola, G. C., Piro, L., Scarsi, L., and Bleeker, J. A. M. (1997). BeppoSAX, the wide band mission for X-ray astronomy. *A&AS*, 122:299–307.

Boorman, P. G., Gandhi, P., Alexander, D. M., Annuar, A., Ballantyne, D. R., Bauer, F., Boggs, S. E., Brandt, W. N., Brightman, M., Christensen, F. E., Craig, W. W., Farrah, D., Hailey, C. J., Harrison, F. A., Hönig, S. F., Koss, M., LaMassa, S. M.,

Masini, A., Ricci, C., Risaliti, G., Stern, D., and Zhang, W. W. (2016). IC 3639 – a New Bona Fide Compton-Thick AGN Unveiled by NuSTAR. *ApJ*, 833:245.

Brandl, B. R., Bernard-Salas, J., Spoon, H. W. W., Devost, D., Sloan, G. C., Guilles, S., Wu, Y., Houck, J. R., Weedman, D. W., Armus, L., Appleton, P. N., Soifer, B. T., Charmandaris, V., Hao, L., Higdon, J. A., Marshall, S. J., and Herter, T. L. (2006). The Mid-Infrared Properties of Starburst Galaxies from Spitzer-IRS Spectroscopy. *ApJ*, 653:1129–1144.

Brandt, W. N. and Alexander, D. M. (2015). Cosmic X-ray surveys of distant active galaxies. The demographics, physics, and ecology of growing supermassive black holes. *A&A Rev.*, 23:1.

Braun, R., Bourke, T., Green, J. A., Keane, E., and Wagg, J. (2015). Advancing Astrophysics with the Square Kilometre Array. In *Advancing Astrophysics with the Square Kilometre Array (AASKA14)*, page 174.

Brightman, M., Baloković, M., Stern, D., Arévalo, P., Ballantyne, D. R., Bauer, F. E., Boggs, S. E., Craig, W. W., Christensen, F. E., Comastri, A., Fuerst, F., Gandhi, P., Hailey, C. J., Harrison, F. A., Hickox, R. C., Koss, M., LaMassa, S., Puccetti, S., Rivers, E., Vasudevan, R., Walton, D. J., and Zhang, W. W. (2015). Determining the Covering Factor of Compton-thick Active Galactic Nuclei with NuSTAR. *ApJ*, 805:41.

Brightman, M., Masini, A., Ballantyne, D. R., Baloković, M., Brandt, W. N., Chen, C.-T., Comastri, A., Farrah, D., Gandhi, P., Harrison, F. A., Ricci, C., Stern, D., and Walton, D. J. (2016). A Growth-rate Indicator for Compton-thick Active Galactic Nuclei. *ApJ*, 826:93.

Brightman, M. and Nandra, K. (2011a). An XMM-Newton spectral survey of 12 μm selected galaxies - I. X-ray data. *MNRAS*, 413:1206–1235.

Brightman, M. and Nandra, K. (2011b). An XMM-Newton spectral survey of 12 μm selected galaxies - II. Implications for AGN selection and unification. *MNRAS*, 414:3084–3104.

Brightman, M., Nandra, K., Salvato, M., Hsu, L.-T., Aird, J., and Rangel, C. (2014). Compton thick active galactic nuclei in Chandra surveys. *MNRAS*, 443:1999–2017.

Brightman, M., Silverman, J. D., Mainieri, V., Ueda, Y., Schramm, M., Matsuoka, K., Nagao, T., Steinhardt, C., Kartaltepe, J., Sanders, D. B., Treister, E., Shemmer, O., Brandt, W. N., Brusa, M., Comastri, A., Ho, L. C., Lanzuisi, G., Lusso, E., Nandra, K., Salvato, M., Zamorani, G., Akiyama, M., Alexander, D. M., Bongiorno, A., Capak, P., Civano, F., Del Moro, A., Doi, A., Elvis, M., Hasinger, G., Laird, E. S., Masters,

D., Mignoli, M., Ohta, K., Schawinski, K., and Taniguchi, Y. (2013). A statistical relation between the X-ray spectral index and Eddington ratio of active galactic nuclei in deep surveys. *MNRAS*, 433:2485–2496.

Buchanan, C. L., Gallimore, J. F., O'Dea, C. P., Baum, S. A., Axon, D. J., Robinson, A., Elitzur, M., and Elvis, M. (2006). Spitzer IRS Spectra of a Large Sample of Seyfert Galaxies: A Variety of Infrared Spectral Energy Distributions in the Local Active Galactic Nucleus Population. *AJ*, 132:401–419.

Buchner, J., Georgakakis, A., Nandra, K., Brightman, M., Menzel, M.-L., Liu, Z., Hsu, L.-T., Salvato, M., Rangel, C., Aird, J., Merloni, A., and Ross, N. (2015). Obscuration-dependent Evolution of Active Galactic Nuclei. *ApJ*, 802:89.

Buchner, J., Schulze, S., and Bauer, F. E. (2017). Galaxy gas as obscurer - I. GRBs x-ray galaxies and find an $N_H{}^3 \propto$ M_{star} relation. *MNRAS*, 464:4545–4566.

Burlon, D., Ajello, M., Greiner, J., Comastri, A., Merloni, A., and Gehrels, N. (2011). Three-year Swift-BAT Survey of Active Galactic Nuclei: Reconciling Theory and Observations? *ApJ*, 728:58.

Burtscher, L., Meisenheimer, K., Tristram, K. R. W., Jaffe, W., Hönig, S. F., Davies, R. I., Kishimoto, M., Pott, J. U., Röttgering, H., Schartmann, M., Weigelt, G., and Wolf, S. (2013). A diversity of dusty AGN tori. Data release for the VLTI/MIDI AGN Large Program and first results for 23 galaxies. *A&A*, 558:A149.

Cameron, E. (2011). On the Estimation of Confidence Intervals for Binomial Population Proportions in Astronomy: The Simplicity and Superiority of the Bayesian Approach. *PASA*, 28:128–139.

Capetti, A., Axon, D. J., Macchetto, F., Sparks, W. B., and Boksenberg, A. (1996). Radio Outflows and the Origin of the Narrow-Line Region in Seyfert Galaxies. *ApJ*, 469:554.

Cash, W. (1979). Parameter estimation in astronomy through application of the likelihood ratio. *ApJ*, 228:939–947.

Chen, C.-T. J., Hickox, R. C., Goulding, A. D., Stern, D., Assef, R., Kochanek, C. S., Brown, M. J. I., Harrison, C. M., Hainline, K. N., Alberts, S., Alexander, D. M., Brodwin, M., Del Moro, A., Forman, W. R., Gorjian, V., Jones, C., Murray, S. S., Pope, A., and Rovilos, E. (2017). The X-Ray and Mid-infrared Luminosities in Luminous Type 1 Quasars. *ApJ*, 837:145.

Comastri, A., Gilli, R., Marconi, A., Risaliti, G., and Salvati, M. (2015). Mass without radiation: Heavily obscured AGNs, the X-ray background, and the black hole mass density. *A&A*, 574:L10.

Comastri, A., Setti, G., Zamorani, G., and Hasinger, G. (1995). The contribution of AGNs to the X-ray background. *A&A*, 296:1.

Corral, A., Georgantopoulos, I., Comastri, A., Ranalli, P., Akylas, A., Salvato, M., Lanzuisi, G., Vignali, C., and Koutoulidis, L. (2016). X-ray observations of dust obscured galaxies in the Chandra deep field south. *A&A*, 592:A109.

Dadina, M. (2007). BeppoSAX observations in the 2-100 keV band of the nearby Seyfert galaxies: an atlas of spectra. *A&A*, 461:1209–1252.

Dale, D. A., Helou, G., Contursi, A., Silbermann, N. A., and Kolhatkar, S. (2001). The Infrared Spectral Energy Distribution of Normal Star-forming Galaxies. *ApJ*, 549:215–227.

de Grijp, M. H. K., Keel, W. C., Miley, G. K., Goudfrooij, P., and Lub, J. (1992). Warm IRAS sources. II - Optical spectroscopy of objects from the point source catalog. *A&AS*, 96:389–428.

de Grijp, M. H. K., Lub, J., and Miley, G. K. (1987). Warm IRAS sources. I. A. Catalogue of AGN candidates from the point source catalog. *A&AS*, 70:95–114.

de Grijp, M. H. K., Miley, G. K., Lub, J., and de Jong, T. (1985). Infrared Seyferts - A new population of active galaxies? *Nature*, 314:240–242.

Dewangan, G. C. (2002). The Correlation between the X-Ray Spectral Slope and the Fe Kα Line Energy in Radio-quiet Active Galactic Nuclei. *ApJ*, 581:L71–L75.

Dey, A., Soifer, B. T., Desai, V., Brand, K., Le Floc'h, E., Brown, M. J. I., Jannuzi, B. T., Armus, L., Bussmann, S., Brodwin, M., Bian, C., Eisenhardt, P., Higdon, S. J., Weedman, D., and Willner, S. P. (2008). A Significant Population of Very Luminous Dust-Obscured Galaxies at Redshift z ˜ 2. *ApJ*, 677:943–956.

Diamond-Stanic, A. M., Rieke, G. H., and Rigby, J. R. (2009). Isotropic Luminosity Indicators in a Complete AGN Sample. *ApJ*, 698:623–631.

Dicken, D., Tadhunter, C., Morganti, R., Axon, D., Robinson, A., Magagnoli, M., Kharb, P., Ramos Almeida, C., Mingo, B., Hardcastle, M., Nesvadba, N. P. H., Singh, V., Kouwenhoven, M. B. N., Rose, M., Spoon, H., Inskip, K. J., and Holt, J. (2014). Spitzer Mid-IR Spectroscopy of Powerful 2Jy and 3CRR Radio Galaxies. II. AGN Power Indicators and Unification. *ApJ*, 788:98.

Dickey, J. M. and Lockman, F. J. (1990). H I in the Galaxy. *ARA&A*, 28:215–261.

Draine, B. T. (2003). Scattering by Interstellar Dust Grains. II. X-Rays. *ApJ*, 598:1026–1037.

Draper, A. R. and Ballantyne, D. R. (2010). The Evolution and Eddington Ratio Distribution of Compton Thick Active Galactic Nuclei. *ApJ*, 715:L99–L103.

Dwelly, T. and Page, M. J. (2006). The distribution of absorption in AGN detected in the XMM-Newton observations of the CDFS. *MNRAS*, 372(4):1755–1775.

Edge, D. O., Shakeshaft, J. R., McAdam, W. B., Baldwin, J. E., and Archer, S. (1959). A survey of radio sources at a frequency of 159 Mc/s. MmRAS, 68:37–60.

Elvis, M., Maccacaro, T., Wilson, A. S., Ward, M. J., Penston, M. V., Fosbury, R. A. E., and Perola, G. C. (1978). Seyfert galaxies as X-ray sources. *MNRAS*, 183:129–157.

Elvis, M., Wilkes, B. J., McDowell, J. C., Green, R. F., Bechtold, J., Willner, S. P., Oey, M. S., Polomski, E., and Cutri, R. (1994). Atlas of quasar energy distributions. *ApJS*, 95:1–68.

Emmanoulopoulos, D., Papadakis, I. E., Dovčiak, M., and McHardy, I. M. (2014). General relativistic modelling of the negative reverberation X-ray time delays in AGN. *MNRAS*, 439(4):3931–3950.

Event Horizon Telescope Collaboration, Akiyama, K., Alberdi, A., Alef, W., Asada, K., Azulay, R., Baczko, A.-K., Ball, D., Baloković, M., Barrett, J., and et al. (2019). First M87 Event Horizon Telescope Results. IV. Imaging the Central Supermassive Black Hole. *ApJ*, 875:L4.

Ezhikode, S. H., Gandhi, P., Done, C., Ward, M., Dewangan, G. C., Misra, R., and Philip, N. S. (2017). Determining the torus covering factors for a sample of type 1 AGN in the local Universe. *MNRAS*, 472(3):3492–3511.

Fabian, A. C. (2012). Observational Evidence of Active Galactic Nuclei Feedback. *ARA&A*, 50:455–489.

Fabian, A. C. and Iwasawa, K. (1999a). The mass density in black holes inferred from the X-ray background. *MNRAS*, 303:L34–L36.

Fabian, A. C. and Iwasawa, K. (1999b). The mass density in black holes inferred from the X-ray background. *MNRAS*, 303(2):L34–L36.

Fabian, A. C., Lohfink, A., Kara, E., Parker, M. L., Vasudevan, R., and Reynolds, C. S. (2015). Properties of AGN coronae in the NuSTAR era. *MNRAS*, 451(4):4375–4383.

Fabian, A. C., Vasudevan, R. V., and Gandhi, P. (2008). The effect of radiation pressure on dusty absorbing gas around active galactic nuclei. *MNRAS*, 385(1):L43–L47.

Fabian, A. C., Zoghbi, A., Ross, R. R., Uttley, P., Gallo, L. C., Brandt, W. N., Blustin, A. J., Boller, T., Caballero-Garcia, M. D., Larsson, J., Miller, J. M., Miniutti, G., Ponti, G., Reis, R. C., Reynolds, C. S., Tanaka, Y., and Young, A. J. (2009). Broad line emission from iron K- and L-shell transitions in the active galaxy 1H0707-495. *Nature*, 459(7246):540–542.

Farrah, D., Baloković, M., Stern, D., Harris, K., Kunimoto, M., Walton, D. J., Alexander, D. M., Arévalo, P., Ballantyne, D. R., Bauer, F. E., Boggs, S., Brandt, W. N., Brightman, M., Christensen, F., Clements, D. L., Craig, W., Fabian, A., Hailey, C., Harrison, F., Koss, M., Lansbury, G. B., Luo, B., Paine, J., Petty, S., Pitchford, K., Ricci, C., and Zhang, W. (2016). The Geometry of the Infrared and X-Ray Obscurer in a Dusty Hyperluminous Quasar. *ApJ*, 831:76.

Farrah, D., Bernard-Salas, J., Spoon, H. W. W., Soifer, B. T., Armus, L., Brandl, B., Charmandaris, V., Desai, V., Higdon, S., Devost, D., and Houck, J. (2007). High-Resolution Mid-Infrared Spectroscopy of Ultraluminous Infrared Galaxies. *ApJ*, 667:149–169.

Fath, E. A. (1909). The spectra of some spiral nebulae and globular star clusters. *Lick Observatory Bulletin*, 5:71–77.

Feruglio, C., Daddi, E., Fiore, F., Alexander, D. M., Piconcelli, E., and Malacaria, C. (2011). Discovery of Strong Iron Kα Emitting Compton Thick Quasars at z = 2.5 and 2.9. *ApJ*, 729:L4.

Filippenko, A. V. and Sargent, W. L. W. (1985). A search for "dwarf" Seyfert 1 nuclei. I. The initial data and results. *ApJS*, 57:503–522.

Fiore, F., Giommi, P., La Franca, F., Matt, G., Perola, G. C., Comastri, A., Molendi, S., Elvis, M., Gioia, I., Tamburelli, F., Ricci, D., and Pompilio, F. (1998). The BeppoSAX High Energy Large Area Survey (HELLAS). In *Science with XMM*.

Fischer, T. C., Crenshaw, D. M., Kraemer, S. B., and Schmitt, H. R. (2013). Determining Inclinations of Active Galactic Nuclei via their Narrow-line Region Kinematics. I. Observational Results. *ApJS*, 209:1.

Foreman-Mackey, D., Hogg, D. W., Lang, D., and Goodman, J. (2013). emcee: The MCMC Hammer. *PASP*, 125(925):306.

Gandhi, P., Annuar, A., Lansbury, G. B., Stern, D., Alexander, D. M., Bauer, F. E., Bianchi, S., Boggs, S. E., Boorman, P. G., Brandt, W. N., Brightman, M., Christensen, F. E., Comastri, A., Craig, W. W., Del Moro, A., Elvis, M., Guainazzi, M., Hailey, C. J., Harrison, F. A., Koss, M., Lamperti, I., Malaguti, G., Masini, A., Matt, G.,

Puccetti, S., Ricci, C., Rivers, E., Walton, D. J., and Zhang, W. W. (2017). The weak Fe fluorescence line and long-term X-ray evolution of the Compton-thick active galactic nucleus in NGC 7674. *MNRAS*, 467:4606–4621.

Gandhi, P. and Fabian, A. C. (2003). X-ray background synthesis: the infrared connection. *MNRAS*, 339:1095–1102.

Gandhi, P., Fabian, A. C., Suebsuwong, T., Malzac, J., Miniutti, G., and Wilman, R. J. (2007). Constraints on light bending and reflection from the hard X-ray background. *MNRAS*, 382:1005–1018.

Gandhi, P., Hönig, S. F., and Kishimoto, M. (2015a). The Dust Sublimation Radius as an Outer Envelope to the Bulk of the Narrow Fe Kalpha Line Emission in Type 1 AGNs. *ApJ*, 812:113.

Gandhi, P., Horst, H., Smette, A., Hönig, S., Comastri, A., Gilli, R., Vignali, C., and Duschl, W. (2009). Resolving the mid-infrared cores of local Seyferts. *A&A*, 502:457–472.

Gandhi, P., Lansbury, G. B., Alexander, D. M., Stern, D., Arévalo, P., Ballantyne, D. R., Baloković, M., Bauer, F. E., Boggs, S. E., Brandt, W. N., Brightman, M., Christensen, F. E., Comastri, A., Craig, W. W., Del Moro, A., Elvis, M., Fabian, A. C., Hailey, C. J., Harrison, F. A., Hickox, R. C., Koss, M., LaMassa, S. M., Luo, B., Madejski, G. M., Ptak, A. F., Puccetti, S., Teng, S. H., Urry, C. M., Walton, D. J., and Zhang, W. W. (2014). NuSTAR Unveils a Compton-thick Type 2 Quasar in Mrk 34. *ApJ*, 792:117.

Gandhi, P., Terashima, Y., Yamada, S., Mushotzky, R. F., Ueda, Y., Baumgartner, W. H., Alexander, D. M., Malzac, J., Vaghmare, K., Takahashi, T., and Done, C. (2013). Reflection-dominated Nuclear X-Ray Emission in the Early-type Galaxy ESO 565-G019. *ApJ*, 773:51.

Gandhi, P., Yamada, S., Ricci, C., Asmus, D., Mushotzky, R. F., Ueda, Y., Terashima, Y., and La Parola, V. (2015b). A Compton-thick AGN in the barred spiral galaxy NGC 4785. *MNRAS*, 449:1845–1855.

García, J., Dauser, T., Reynolds, C. S., Kallman, T. R., McClintock, J. E., Wilms, J., and Eikmann, W. (2013). X-Ray Reflected Spectra from Accretion Disk Models. III. A Complete Grid of Ionized Reflection Calculations. *ApJ*, 768:146.

García-Burillo, S., Combes, F., Ramos Almeida, C., Usero, A., Krips, M., Alonso-Herrero, A., Aalto, S., Casasola, V., Hunt, L. K., Martín, S., Viti, S., Colina, L., Costagliola, F., Eckart, A., Fuente, A., Henkel, C., Márquez, I., Neri, R., Schinnerer,

E., Tacconi, L. J., and van der Werf, P. P. (2016). ALMA Resolves the Torus of NGC 1068: Continuum and Molecular Line Emission. *ApJ*, 823(1):L12.

Gehrels, N. (1986). Confidence limits for small numbers of events in astrophysical data. *ApJ*, 303:336–346.

Georgakakis, A., Salvato, M., Liu, Z., Buchner, J., Brandt, W. N., Ananna, T. T., Schulze, A., Shen, Y., LaMassa, S., Nandra, K., Merloni, A., and McGreer, I. D. (2017). X-ray constraints on the fraction of obscured active galactic nuclei at high accretion luminosities. *MNRAS*, 469:3232–3251.

Georgantopoulos, I., Comastri, A., Vignali, C., Ranalli, P., Rovilos, E., Iwasawa, K., Gilli, R., Cappelluti, N., Carrera, F., Fritz, J., Brusa, M., Elbaz, D., Mullaney, R. J., Castello-Mor, N., Barcons, X., Tozzi, P., Balestra, I., and Falocco, S. (2013). The XMM deep survey in the CDF-S. IV. Compton-thick AGN candidates. *A&A*, 555:A43.

Giacconi, R., Gursky, H., Paolini, F. R., and Rossi, B. B. (1962). Evidence for x Rays From Sources Outside the Solar System. *Physical Review Letters*, 9:439–443.

Giacconi, R., Murray, S., Gursky, H., Kellogg, E., Schreier, E., Matilsky, T., Koch, D., and Tananbaum, H. (1974). The Third UHURU Catalog of X-Ray Sources. *ApJS*, 27:37.

Gilli, R., Comastri, A., and Hasinger, G. (2007). The synthesis of the cosmic X-ray background in the Chandra and XMM-Newton era. *A&A*, 463:79–96.

Gilli, R., Norman, C., Vignali, C., Vanzella, E., Calura, F., Pozzi, F., Massardi, M., Mignano, A., Casasola, V., Daddi, E., Elbaz, D., Dickinson, M., Iwasawa, K., Maiolino, R., Brusa, M., Vito, F., Fritz, J., Feltre, A., Cresci, G., Mignoli, M., Comastri, A., and Zamorani, G. (2014). ALMA reveals a warm and compact starburst around a heavily obscured supermassive black hole at z = 4.75. *A&A*, 562:A67.

Gilli, R., Su, J., Norman, C., Vignali, C., Comastri, A., Tozzi, P., Rosati, P., Stiavelli, M., Brandt, W. N., Xue, Y. Q., Luo, B., Castellano, M., Fontana, A., Fiore, F., Mainieri, V., and Ptak, A. (2011). A Compton-thick Active Galactic Nucleus at z ˜ 5 in the 4 Ms Chandra Deep Field South. *ApJ*, 730:L28.

Giuricin, G., Mardirossian, F., Mezzetti, M., and Bertotti, G. (1990). The radio properties of bright Seyfert galaxies. *ApJS*, 72:551–565.

Gohil, R. and Ballantyne, D. R. (2015). On the equivalent width of the Fe Kα line produced by a dusty absorber in active galactic nuclei. *MNRAS*, 449:1449–1453.

Goodman, J. and Weare, J. (2010). Ensemble samplers with affine invariance. *Communications in Applied Mathematics and Computational Science, Vol. 5, No. 1, p. 65-80, 2010*, 5:65–80.

Goulding, A. D. and Alexander, D. M. (2009). Towards a complete census of AGN in nearby Galaxies: a large population of optically unidentified AGN. *MNRAS*, 398:1165–1193.

Goulding, A. D., Alexander, D. M., Bauer, F. E., Forman, W. R., Hickox, R. C., Jones, C., Mullaney, J. R., and Trichas, M. (2012). Deep Silicate Absorption Features in Compton-thick Active Galactic Nuclei Predominantly Arise due to Dust in the Host Galaxy. *ApJ*, 755:5.

Guainazzi, M., Matt, G., and Perola, G. C. (2005). X-ray obscuration and obscured AGN in the local universe. *A&A*, 444:119–132.

Guainazzi, M., Risaliti, G., Nucita, A., Wang, J., Bianchi, S., Soria, R., and Zezas, A. (2009). AGN/starburst connection in action: the half million second RGS spectrum of NGC 1365. *A&A*, 505:589–600.

Guainazzi, M. and Tashiro, M. S. (2018). The Hot Universe with XRISM and Athena. *ArXiv e-prints*.

Gültekin, K., Richstone, D. O., Gebhardt, K., Lauer, T. R., Tremaine, S., Aller, M. C., Bender, R., Dressler, A., Faber, S. M., Filippenko, A. V., Green, R., Ho, L. C., Kormendy, J., Magorrian, J., Pinkney, J., and Siopis, C. (2009). The M-σ and M-L Relations in Galactic Bulges, and Determinations of Their Intrinsic Scatter. *ApJ*, 698:198–221.

Haardt, F. and Maraschi, L. (1991). A two-phase model for the X-ray emission from Seyfert galaxies. *ApJ*, 380:L51–L54.

Haardt, F. and Maraschi, L. (1993). X-ray spectra from two-phase accretion disks. *ApJ*, 413:507–517.

Hao, H., Elvis, M., Civano, F., Lanzuisi, G., Brusa, M., Lusso, E., Zamorani, G., Comastri, A., Bongiorno, A., Impey, C. D., Koekemoer, A. M., Le Floc'h, E., Salvato, M., Sanders, D., Trump, J. R., and Vignali, C. (2010). Hot-dust-poor Type 1 Active Galactic Nuclei in the COSMOS Survey. *ApJ*, 724:L59–L63.

Häring, N. and Rix, H.-W. (2004). On the Black Hole Mass-Bulge Mass Relation. *ApJ*, 604(2):L89–L92.

Harrison, F. A., Aird, J., Civano, F., Lansbury, G., Mullaney, J. R., Ballantyne, D. R., Alexander, D. M., Stern, D., Ajello, M., Barret, D., Bauer, F. E., Balokovic, M., Brandt, W. N., Brightman, M., Boggs, S. E., Christensen, F. E., Comastri, A., Craig, W. W., Del Moro, A., Forster, K., Gandhi, P., Giommi, P., Grefenstette, B. W., Hailey, C. J., Hickox, R. C., Hornstrup, A., Kitaguchi, T., Koglin, J., Luo, B., Madsen, K. K., Mao, P. H., Miyasaka, H., Mori, K., Perri, M., Pivovaroff, M., Puccetti, S., Rana, V., Treister, E., Walton, D., Westergaard, N. J., Wik, D., Zappacosta, L., Zhang, W. W., and Zoglauer, A. (2015). The NuSTAR Extragalactic Surveys: The Number Counts of Active Galactic Nuclei and the Resolved Fraction of the Cosmic X-ray Background. *ArXiv e-prints*.

Harrison, F. A., Craig, W. W., Christensen, F. E., Hailey, C. J., Zhang, W. W., Boggs, S. E., Stern, D., Cook, W. R., Forster, K., Giommi, P., Grefenstette, B. W., Kim, Y., Kitaguchi, T., Koglin, J. E., Madsen, K. K., Mao, P. H., Miyasaka, H., Mori, K., Perri, M., Pivovaroff, M. J., Puccetti, S., Rana, V. R., Westergaard, N. J., Willis, J., Zoglauer, A., An, H., Bachetti, M., Barrière, N. M., Bellm, E. C., Bhalerao, V., Brejnholt, N. F., Fuerst, F., Liebe, C. C., Markwardt, C. B., Nynka, M., Vogel, J. K., Walton, D. J., Wik, D. R., Alexander, D. M., Cominsky, L. R., Hornschemeier, A. E., Hornstrup, A., Kaspi, V. M., Madejski, G. M., Matt, G., Molendi, S., Smith, D. M., Tomsick, J. A., Ajello, M., Ballantyne, D. R., Baloković, M., Barret, D., Bauer, F. E., Blandford, R. D., Brandt, W. N., Brenneman, L. W., Chiang, J., Chakrabarty, D., Chenevez, J., Comastri, A., Dufour, F., Elvis, M., Fabian, A. C., Farrah, D., Fryer, C. L., Gotthelf, E. V., Grindlay, J. E., Helfand, D. J., Krivonos, R., Meier, D. L., Miller, J. M., Natalucci, L., Ogle, P., Ofek, E. O., Ptak, A., Reynolds, S. P., Rigby, J. R., Tagliaferri, G., Thorsett, S. E., Treister, E., and Urry, C. M. (2013). The Nuclear Spectroscopic Telescope Array (NuSTAR) High-energy X-Ray Mission. *ApJ*, 770:103.

Heckman, T. M. (1980). An optical and radio survey of the nuclei of bright galaxies - Activity in normal galactic nuclei. *A&A*, 87:152–164.

Hitomi Collaboration, Aharonian, F., Akamatsu, H., Akimoto, F., Allen, S. W., Angelini, L., Audard, M., Awaki, H., Axelsson, M., Bamba, A., Bautz, M. W., Blandford, R., Brenneman, L. W., Brown, G. V., Bulbul, E., Cackett, E. M., Chernyakova, M., Chiao, M. P., Coppi, P. S., Costantini, E., de Plaa, J., de Vries, C. P., den Herder, J.-W., Done, C., Dotani, T., Ebisawa, K., Eckart, M. E., Enoto, T., Ezoe, Y., Fabian, A. C., Ferrigno, C., Foster, A. R., Fujimoto, R., Fukazawa, Y., Furuzawa, A., Galeazzi, M., Gallo, L. C., Gandhi, P., Giustini, M., Goldwurm, A., Gu, L., Guainazzi, M., Haba, Y., Hagino, K., Hamaguchi, K., Harrus, I. M., Hatsukade, I., Hayashi, K., Hayashi, T., Hayashida, K., Hiraga, J. S., Hornschemeier, A., Hoshino, A., Hughes, J. P., Ichinohe, Y., Iizuka, R., Inoue, H., Inoue, Y., Ishida, M., Ishikawa, K., Ishisaki, Y., Iwai, M.,

Kaastra, J., Kallman, T., Kamae, T., Kataoka, J., Katsuda, S., Kawai, N., Kelley, R. L., Kilbourne, C. A., Kitaguchi, T., Kitamoto, S., Kitayama, T., Kohmura, T., Kokubun, M., Koyama, K., Koyama, S., Kretschmar, P., Krimm, H. A., Kubota, A., Kunieda, H., Laurent, P., Lee, S.-H., Leutenegger, M. A., Limousin, O. O., Loewenstein, M., Long, K. S., Lumb, D., Madejski, G., Maeda, Y., Maier, D., Makishima, K., Markevitch, M., Matsumoto, H., Matsushita, K., McCammon, D., McNamara, B. R., Mehdipour, M., Miller, E. D., Miller, J. M., Mineshige, S., Mitsuda, K., Mitsuishi, I., Miyazawa, T., Mizuno, T., Mori, H., Mori, K., Mukai, K., Murakami, H., Mushotzky, R. F., Nakagawa, T., Nakajima, H., Nakamori, T., Nakashima, S., Nakazawa, K., Nobukawa, K. K., Nobukawa, M., Noda, H., Odaka, H., Ohashi, T., Ohno, M., Okajima, T., Ota, N., Ozaki, M., Paerels, F., Paltani, S., Petre, R., Pinto, C., Porter, F. S., Pottschmidt, K., Reynolds, C. S., Safi-Harb, S., Saito, S., Sakai, K., Sasaki, T., Sato, G., Sato, K., Sato, R., Sawada, M., Schartel, N., Serlemitsos, P. J., Seta, H., Shidatsu, M., Simionescu, A., Smith, R. K., Soong, Y., Stawarz, Ł., Sugawara, Y., Sugita, S., Szymkowiak, A., Tajima, H., Takahashi, H., Takahashi, T., Takeda, S., Takei, Y., Tamagawa, T., Tamura, T., Tanaka, T., Tanaka, Y., Tanaka, Y. T., Tashiro, M. S., Tawara, Y., Terada, Y., Terashima, Y., Tombesi, F., Tomida, H., Tsuboi, Y., Tsujimoto, M., Tsunemi, H., Tsuru, T. G., Uchida, H., Uchiyama, H., Uchiyama, Y., Ueda, S., Ueda, Y., Uno, S., Urry, C. M., Ursino, E., Watanabe, S., Werner, N., Wilkins, D. R., Williams, B. J., Yamada, S., Yamaguchi, H., Yamaoka, K., Yamasaki, N. Y., Yamauchi, M., Yamauchi, S., Yaqoob, T., Yatsu, Y., Yonetoku, D., Zhuravleva, I., Zoghbi, A., and Kawamuro, T. (2017). Hitomi Observation of Radio Galaxy NGC 1275: The First X-ray Microcalorimeter Spectroscopy of Fe-K{\alpha} Line Emission from an Active Galactic Nucleus. *ArXiv e-prints*.

Hlavacek-Larrondo, J., Gandhi, P., Hogan, M. T., Gendron-Marsolais, M.-L., Edge, A. C., Fabian, A. C., Russell, H. R., Iwasawa, K., and Mezcua, M. (2017). Chandra X-ray observations of the hyper-luminous infrared galaxy IRAS F15307+3252. *MNRAS*, 464:2223–2233.

Hönig, S. F. and Kishimoto, M. (2017). Dusty Winds in Active Galactic Nuclei: Reconciling Observations with Models. *ApJ*, 838:L20.

Hönig, S. F., Kishimoto, M., Tristram, K. R. W., Prieto, M. A., Gandhi, P., Asmus, D., Antonucci, R., Burtscher, L., Duschl, W. J., and Weigelt, G. (2013). Dust in the Polar Region as a Major Contributor to the Infrared Emission of Active Galactic Nuclei. *ApJ*, 771:87.

Hönig, S. F., Leipski, C., Antonucci, R., and Haas, M. (2011). Quantifying the Anisotropy in the Infrared Emission of Powerful Active Galactic Nuclei. *ApJ*, 736:26.

Hopkins, P. F., Hernquist, L., Cox, T. J., and Kereš, D. (2008). A Cosmological Framework for the Co-Evolution of Quasars, Supermassive Black Holes, and Elliptical Galaxies. I. Galaxy Mergers and Quasar Activity. *ApJS*, 175:356–389.

Horst, H., Gandhi, P., Smette, A., and Duschl, W. J. (2008). The mid IR - hard X-ray correlation in AGN and its implications for dusty torus models. *A&A*, 479:389–396.

Hubble, E. P. (1926). Extragalactic nebulae. *ApJ*, 64.

Ikeda, S., Awaki, H., and Terashima, Y. (2009). Study on X-Ray Spectra of Obscured Active Galactic Nuclei Based on Monte Carlo Simulation – An Interpretation of Observed Wide-Band Spectra. *ApJ*, 692:608–617.

Iwasawa, K., Sanders, D. B., Evans, A. S., Mazzarella, J. M., Armus, L., and Surace, J. A. (2009). High-Ionization Fe K Emission From Luminous Infrared Galaxies. *ApJ*, 695:L103–L106.

Iwasawa, K. and Taniguchi, Y. (1993). The X-ray Baldwin effect. *ApJ*, 413:L15–L18.

Iwasawa, K., U, V., Mazzarella, J. M., Medling, A. M., Sanders, D. B., and Evans, A. S. (2017). Testing a double AGN hypothesis for Mrk 273. *ArXiv e-prints*.

Jarvis, M. J. (2007). Science with the Next Generation of Radio Surveys from LOFAR to the SKA. In Afonso, J., Ferguson, H. C., Mobasher, B., and Norris, R., editors, *Deepest Astronomical Surveys*, volume 380 of *Astronomical Society of the Pacific Conference Series*, page 251.

Jiang, P., Wang, J. X., and Wang, T. G. (2006). On the X-Ray Baldwin Effect for Narrow Fe Kα Emission Lines. *ApJ*, 644:725–732.

Kalberla, P. M. W., Burton, W. B., Hartmann, D., Arnal, E. M., Bajaja, E., Morras, R., and Pöppel, W. G. L. (2005). The Leiden/Argentine/Bonn (LAB) Survey of Galactic HI. Final data release of the combined LDS and IAR surveys with improved stray-radiation corrections. *A&A*, 440:775–782.

Kammoun, E. S., Miller, J. M., Zoghbi, A., Oh, K., Koss, M., Mushotzky, R. F., Brenneman, L. W., Brand t, W. N., Proga, D., Lohfink, A. M., Kaastra, J. S., Barret, D., Behar, E., and Stern, D. (2019). A hard look at NGC 5347: revealing a nearby Compton-thick AGN. *arXiv e-prints*, page arXiv:1904.11028.

Kamraj, N., Harrison, F. A., Baloković, M., Lohfink, A., and Brightman, M. (2018). Coronal Properties of Swift/BAT-selected Seyfert 1 AGNs Observed with NuSTAR. *ApJ*, 866:124.

Kaplan, E. L. and Meier, P. (1958). Nonparametric estimation from incomplete observations. *Journal of the American Statistical Association*, 53(282):457–481.

Kauffmann, G., Heckman, T. M., Tremonti, C., Brinchmann, J., Charlot, S., White, S. D. M., Ridgway, S. E., Brinkmann, J., Fukugita, M., Hall, P. B., Ivezić, Ž., Richards, G. T., and Schneider, D. P. (2003). The host galaxies of active galactic nuclei. *MNRAS*, 346:1055–1077.

Keel, W. C., de Grijp, M. H. K., Miley, G. K., and Zheng, W. (1994). Warm IRAS Sources from the Point Source Catalog - Part Three - Emission Line Properties Correlations and AGN / Active Galactic Nuclei / Unified Models. *A&A*, 283:791.

Kewley, L. J., Dopita, M. A., Sutherland, R. S., Heisler, C. A., and Trevena, J. (2001). Theoretical Modeling of Starburst Galaxies. *ApJ*, 556:121–140.

Khachikian, E. Y. and Weedman, D. W. (1974). An atlas of Seyfert galaxies. *ApJ*, 192:581–589.

Kharb, P., Lal, D. V., and Merritt, D. (2017). A candidate sub-parsec binary black hole in the Seyfert galaxy NGC 7674. *Nature Astronomy*, 1:727–733.

Kormendy, J. and Ho, L. C. (2013). Coevolution (Or Not) of Supermassive Black Holes and Host Galaxies. *ARA&A*, 51(1):511–653.

Koss, M., Trakhtenbrot, B., Ricci, C., Lamperti, I., Oh, K., Berney, S., Schawinski, K., Baloković, M., Baronchelli, L., Crenshaw, D. M., Fischer, T., Gehrels, N., Harrison, F., Hashimoto, Y., Hogg, D., Ichikawa, K., Masetti, N., Mushotzky, R., Sartori, L., Stern, D., Treister, E., Ueda, Y., Veilleux, S., and Winter, L. (2017). BAT AGN Spectroscopic Survey. I. Spectral Measurements, Derived Quantities, and AGN Demographics. *ApJ*, 850:74.

Koss, M. J., Glidden, A., Baloković, M., Stern, D., Lamperti, I., Assef, R., Bauer, F., Ballantyne, D., Boggs, S. E., Craig, W. W., Farrah, D., Fürst, F., Gandhi, P., Gehrels, N., Hailey, C. J., Harrison, F. A., Markwardt, C., Masini, A., Ricci, C., Treister, E., Walton, D. J., and Zhang, W. W. (2016a). NuSTAR Resolves the First Dual AGN above 10 keV in SWIFT J2028.5+2543. *ApJ*, 824:L4.

Koss, M. J., Glidden, A., Baloković, M., Stern, D., Lamperti, I., Assef, R., Bauer, F., Ballantyne, D., Boggs, S. E., Craig, W. W., Farrah, D., Fürst, F., Gandhi, P., Gehrels, N., Hailey, C. J., Harrison, F. A., Markwardt, C., Masini, A., Ricci, C., Treister, E., Walton, D. J., and Zhang, W. W. (2016b). NuSTAR Resolves the First Dual AGN above 10 keV in SWIFT J2028.5+2543. *ApJ*, 824:L4.

Koss, M. J., Romero-Cañizales, C., Baronchelli, L., Teng, S. H., Baloković, M., Puccetti, S., Bauer, F. E., Arévalo, P., Assef, R., Ballantyne, D. R., Brandt, W. N., Brightman, M., Comastri, A., Gandhi, P., Harrison, F. A., Luo, B., Schawinski, K., Stern, D., and Treister, E. (2015). Broadband Observations of the Compton-thick Nucleus of NGC 3393. *ApJ*, 807:149.

Krabbe, A., Böker, T., and Maiolino, R. (2001). N-Band Imaging of Seyfert Nuclei and the Mid-Infrared-X-Ray Correlation. *ApJ*, 557:626–636.

Krolik, J. H. and Begelman, M. C. (1988). Molecular tori in Seyfert galaxies - Feeding the monster and hiding it. *ApJ*, 329:702–711.

Krolik, J. H. and Kallman, T. R. (1987). Fe K features as probes of the nuclear reflection region in Seyfert galaxies. *ApJ*, 320:L5–L8.

Krolik, J. H., Madau, P., and Zycki, P. T. (1994). X-ray bumps, iron K-alpha lines, and X-ray suppression by obscuring tori in Seyfert galaxies. *ApJ*, 420:L57–L61.

La Franca, F., Fiore, F., Comastri, A., Perola, G. C., Sacchi, N., Brusa, M., Cocchia, F., Feruglio, C., Matt, G., Vignali, C., Carangelo, N., Ciliegi, P., Lamastra, A., Maiolino, R., Mignoli, M., Molendi, S., and Puccetti, S. (2005). The HELLAS2XMM Survey. VII. The Hard X-Ray Luminosity Function of AGNs up to z = 4: More Absorbed AGNs at Low Luminosities and High Redshifts. *ApJ*, 635:864–879.

Lacy, M., Petric, A. O., Sajina, A., Canalizo, G., Storrie-Lombardi, L. J., Armus, L., Fadda, D., and Marleau, F. R. (2007). Optical Spectroscopy and X-Ray Detections of a Sample of Quasars and Active Galactic Nuclei Selected in the Mid-Infrared from Two Spitzer Space Telescope Wide-Area Surveys. *AJ*, 133:186–205.

LaMassa, S. M., Georgakakis, A., Vivek, M., Salvato, M., Tasnim Ananna, T., Urry, C. M., MacLeod, C., and Ross, N. (2019). SDSS-IV eBOSS Spectroscopy of X-ray and WISE AGN in Stripe 82X: Overview of the Demographics of X-ray and Mid-Infrared Selected Active Galactic Nuclei. *arXiv e-prints*, page arXiv:1902.09408.

LaMassa, S. M., Heckman, T. M., Ptak, A., Martins, L., Wild, V., and Sonnentrucker, P. (2010). Indicators of Intrinsic Active Galactic Nucleus Luminosity: A Multi-wavelength Approach. *ApJ*, 720:786–810.

LaMassa, S. M., Yaqoob, T., Levenson, N. A., Boorman, P., Heckman, T. M., Gandhi, P., Rigby, J. R., Urry, C. M., and Ptak, A. F. (2017). Chandra Reveals Heavy Obscuration and Circumnuclear Star Formation in Seyfert 2 Galaxy NGC 4968. *ApJ*, 835:91.

Lansbury, G. B., Alexander, D. M., Aird, J., Gandhi, P., Stern, D., Koss, M., Lamperti, I., Ajello, M., Annuar, A., Assef, R. J., Ballantyne, D. R., Baloković, M., Bauer, F. E.,

Brandt, W. N., Brightman, M., Chen, C.-T. J., Civano, F., Comastri, A., Del Moro, A., Fuentes, C., Harrison, F. A., Marchesi, S., Masini, A., Mullaney, J. R., Ricci, C., Saez, C., Tomsick, J. A., Treister, E., Walton, D. J., and Zappacosta, L. (2017). The NuSTAR Serendipitous Survey: Hunting for the Most Extreme Obscured AGN at >10 keV. *ApJ*, 846:20.

Lanzuisi, G., Civano, F., Marchesi, S., Comastri, A., Brusa, M., Gilli, R., Vignali, C., Zamorani, G., Brightman, M., Griffiths, R. E., and Koekemoer, A. M. (2018). The Chandra COSMOS Legacy Survey: Compton Thick AGN at high redshift. *ArXiv e-prints*.

Lanzuisi, G., Piconcelli, E., Fiore, F., Feruglio, C., Vignali, C., Salvato, M., and Gruppioni, C. (2009). Revealing X-ray obscured quasars in SWIRE sources with extreme mid-IR/optical flux ratios. *A&A*, 498:67–81.

Lanzuisi, G., Ranalli, P., Georgantopoulos, I., Georgakakis, A., Delvecchio, I., Akylas, T., Berta, S., Bongiorno, A., Brusa, M., Cappelluti, N., Civano, F., Comastri, A., Gilli, R., Gruppioni, C., Hasinger, G., Iwasawa, K., Koekemoer, A., Lusso, E., Marchesi, S., Mainieri, V., Merloni, A., Mignoli, M., Piconcelli, E., Pozzi, F., Rosario, D. J., Salvato, M., Silverman, J., Trakhtenbrot, B., Vignali, C., and Zamorani, G. (2015). Compton thick AGN in the XMM-COSMOS survey. *A&A*, 573:A137.

Lawrence, A. (1991). The relative frequency of broad-lined and narrow-lined active galactic nuclei - Implications for unified schemes. *MNRAS*, 252:586–592.

Lawrence, A. and Elvis, M. (1982). Obscuration and the various kinds of Seyfert galaxies. *ApJ*, 256:410–426.

Lawrence, A. and Elvis, M. (2010). Misaligned Disks as Obscurers in Active Galaxies. *ApJ*, 714:561–570.

Lehmer, B. D., Xue, Y. Q., Brandt, W. N., Alexander, D. M., Bauer, F. E., Brusa, M., Comastri, A., Gilli, R., Hornschemeier, A. E., Luo, B., Paolillo, M., Ptak, A., Shemmer, O., Schneider, D. P., Tozzi, P., and Vignali, C. (2012). The 4 Ms Chandra Deep Field-South Number Counts Apportioned by Source Class: Pervasive Active Galactic Nuclei and the Ascent of Normal Galaxies. *ApJ*, 752:46.

Levenson, N. A., Krolik, J. H., Życki, P. T., Heckman, T. M., Weaver, K. A., Awaki, H., and Terashima, Y. (2002). Extreme X-Ray Iron Lines in Active Galactic Nuclei. *ApJ*, 573:L81–L84.

Levenson, N. A., Radomski, J. T., Packham, C., Mason, R. E., Schaefer, J. J., and Telesco, C. M. (2009). Isotropic Mid-Infrared Emission from the Central 100 pc of Active Galaxies. *ApJ*, 703:390–398.

Lightman, A. P. and White, T. R. (1988). Effects of cold matter in active galactic nuclei - A broad hump in the X-ray spectra. *ApJ*, 335:57–66.

Liu, Y. and Li, X. (2015). A direct comparison of X-ray spectral models for tori in active galactic nuclei. *MNRAS*, 448:L53–L57.

Lu, Y. and Yu, Q. (1999). Two Different Accretion Classes in Seyfert 1 Galaxies and QSOS. *ApJ*, 526:L5–L8.

Luo, B., Brandt, W. N., Xue, Y. Q., Lehmer, B., Alexander, D. M., Bauer, F. E., Vito, F., Yang, G., Basu-Zych, A. R., Comastri, A., Gilli, R., Gu, Q.-S., Hornschemeier, A. E., Koekemoer, A., Liu, T., Mainieri, V., Paolillo, M., Ranalli, P., Rosati, P., Schneider, D. P., Shemmer, O., Smail, I., Sun, M., Tozzi, P., Vignali, C., and Wang, J.-X. (2017). The Chandra Deep Field-South Survey: 7 Ms Source Catalogs. *ApJS*, 228:2.

Lusso, E., Hennawi, J. F., Comastri, A., Zamorani, G., Richards, G. T., Vignali, C., Treister, E., Schawinski, K., Salvato, M., and Gilli, R. (2013). The Obscured Fraction of Active Galactic Nuclei in the XMM-COSMOS Survey: A Spectral Energy Distribution Perspective. *ApJ*, 777:86.

Lutz, D., Maiolino, R., Spoon, H. W. W., and Moorwood, A. F. M. (2004). The relation between AGN hard X-ray emission and mid-infrared continuum from ISO spectra: Scatter and unification aspects. *A&A*, 418:465–473.

Maccacaro, T., della Ceca, R., Gioia, I. M., Morris, S. L., Stocke, J. T., and Wolter, A. (1991). The properties of X-ray-selected active galactic nuclei. I - Luminosity function, cosmological evolution, and contribution to the diffuse X-ray background. *ApJ*, 374:117–133.

Madsen, K. K., Christensen, F. E., Craig, W. W., Forster, K. W., Grefenstette, B. W., Harrison, F. A., Miyasaka, H., and Rana, V. (2017). Observational artifacts of Nuclear Spectroscopic Telescope Array: ghost rays and stray light. *Journal of Astronomical Telescopes, Instruments, and Systems*, 3:044003.

Madsen, K. K., Harrison, F. A., Markwardt, C. B., An, H., Grefenstette, B. W., Bachetti, M., Miyasaka, H., Kitaguchi, T., Bhalerao, V., Boggs, S., Christensen, F. E., Craig, W. W., Forster, K., Fuerst, F., Hailey, C. J., Perri, M., Puccetti, S., Rana, V., Stern, D., Walton, D. J., Jørgen Westergaard, N., and Zhang, W. W. (2015). Calibration of the NuSTAR High-energy Focusing X-ray Telescope. *ApJS*, 220:8.

Magdziarz, P. and Zdziarski, A. A. (1995). Angle-dependent Compton reflection of X-rays and gamma-rays. *MNRAS*, 273:837–848.

Magorrian, J., Tremaine, S., Richstone, D., Bender, R., Bower, G., Dressler, A., Faber, S. M., Gebhardt, K., Green, R., Grillmair, C., Kormendy, J., and Lauer, T. (1998). The Demography of Massive Dark Objects in Galaxy Centers. *AJ*, 115(6):2285–2305.

Maiolino, R., Shemmer, O., Imanishi, M., Netzer, H., Oliva, E., Lutz, D., and Sturm, E. (2007). Dust covering factor, silicate emission, and star formation in luminous QSOs. *A&A*, 468(3):979–992.

Malizia, A., Molina, M., Bassani, L., Stephen, J. B., Bazzano, A., Ubertini, P., and Bird, A. J. (2014). The INTEGRAL High-energy Cut-off Distribution of Type 1 Active Galactic Nuclei. *ApJ*, 782:L25.

Malizia, A., Stephen, J. B., Bassani, L., Bird, A. J., Panessa, F., and Ubertini, P. (2009). The fraction of Compton-thick sources in an INTEGRAL complete AGN sample. *MNRAS*, 399:944–951.

Marchese, E., Della Ceca, R., Caccianiga, A., Severgnini, P., Corral, A., and Fanali, R. (2012). The optical-UV spectral energy distribution of the unabsorbed AGN population in the XMM-Newton Bright Serendipitous Survey. *A&A*, 539:A48.

Marchesi, S., Ajello, M., Comastri, A., Cusumano, G., La Parola, V., and Segreto, A. (2017). X-Ray Spectral Properties of Seven Heavily Obscured Seyfert 2 Galaxies. *ApJ*, 836:116.

Marchesi, S., Ajello, M., Marcotulli, L., Comastri, A., Lanzuisi, G., and Vignali, C. (2018). Compton-thick AGNs in the NuSTAR Era. *ApJ*, 854:49.

Marinucci, A., Bianchi, S., Matt, G., Alexander, D. M., Baloković, M., Bauer, F. E., Brandt, W. N., Gandhi, P., Guainazzi, M., Harrison, F. A., Iwasawa, K., Koss, M., Madsen, K. K., Nicastro, F., Puccetti, S., Ricci, C., Stern, D., and Walton, D. J. (2016). NuSTAR catches the unveiling nucleus of NGC 1068. *MNRAS*, 456:L94–L98.

Marinucci, A., Bianchi, S., Nicastro, F., Matt, G., and Goulding, A. D. (2012). The Link between the Hidden Broad Line Region and the Accretion Rate in Seyfert 2 Galaxies. *ApJ*, 748:130.

Markowitz, A., Takahashi, T., Watanabe, S., Nakazawa, K., Fukazawa, Y., Kokubun, M., Makishima, K., Awaki, H., Bamba, A., Isobe, N., Kataoka, J., Madejski, G., Mushotzky, R., Okajima, T., Ptak, A., Reeves, J. N., Ueda, Y., Yamasaki, T., and Yaqoob, T. (2007). The Suzaku Observation of the Nucleus of the Radio-loud Active Galaxy Centaurus A: Constraints on Abundances of the Accreting Material. *ApJ*, 665:209–224.

Martín-Navarro, I. and Mezcua, M. (2018). Exploring the Limits of AGN Feedback: Black Holes and the Star Formation Histories of Low-mass Galaxies. *ApJ*, 855(2):L20.

Masini, A., Civano, F., Comastri, A., Fornasini, F., Ballantyne, D. R., Lansbury, G. B., Treister, E., Alexander, D. M., Boorman, P. G., Brandt, W. N., Farrah, D., Gandhi, P., Harrison, F. A., Hickox, R. C., Kocevski, D. D., Lanz, L., Marchesi, S., Puccetti, S., Ricci, C., Saez, C., Stern, D., and Zappacosta, L. (2018). The NuSTAR Extragalactic Surveys: Source Catalog and the Compton-thick Fraction in the UDS Field. *ApJS*, 235:17.

Masini, A., Comastri, A., Baloković, M., Zaw, I., Puccetti, S., Ballantyne, D. R., Bauer, F. E., Boggs, S. E., Brandt, W. N., Brightman, M., Christensen, F. E., Craig, W. W., Gandhi, P., Hailey, C. J., Harrison, F. A., Koss, M. J., Madejski, G., Ricci, C., Rivers, E., Stern, D., and Zhang, W. W. (2016). NuSTAR observations of water megamaser AGN. *A&A*, 589:A59.

Masini, A., Comastri, A., Puccetti, S., Baloković, M., Gandhi, P., Guainazzi, M., Bauer, F. E., Boggs, S. E., Boorman, P. G., Brightman, M., Christensen, F. E., Craig, W. W., Farrah, D., Hailey, C. J., Harrison, F. A., Koss, M. J., LaMassa, S. M., Ricci, C., Stern, D., Walton, D. J., and Zhang, W. W. (2017). The Phoenix galaxy as seen by NuSTAR. *A&A*, 597:A100.

Mateos, S., Alonso-Herrero, A., Carrera, F. J., Blain, A., Watson, M. G., Barcons, X., Braito, V., Severgnini, P., Donley, J. L., and Stern, D. (2012). Using the Bright Ultrahard XMM-Newton survey to define an IR selection of luminous AGN based on WISE colours. *MNRAS*, 426:3271–3281.

Mateos, S., Barcons, X., Carrera, F. J., Ceballos, M. T., Caccianiga, A., Lamer, G., Maccacaro, T., Page, M. J., Schwope, A., and Watson, M. G. (2005). X-ray spectra of XMM-Newton serendipitous medium flux sources. *A&A*, 433:855–873.

Mateos, S., Carrera, F. J., Alonso-Herrero, A., Rovilos, E., Hernán-Caballero, A., Barcons, X., Blain, A., Caccianiga, A., Della Ceca, R., and Severgnini, P. (2015). Revisiting the relationship between 6 μm and 2-10 keV continuum luminosities of AGN. *MNRAS*, 449:1422–1440.

Mateos, S., Carrera, F. J., Barcons, X., Alonso-Herrero, A., Hernán-Caballero, A., Page, M., Ramos Almeida, C., Caccianiga, A., Miyaji, T., and Blain, A. (2017). Survival of the Obscuring Torus in the Most Powerful Active Galactic Nuclei. *ApJ*, 841:L18.

Mather, J. C., Cheng, E. S., Cottingham, D. A., Eplee, Jr., R. E., Fixsen, D. J., Hewagama, T., Isaacman, R. B., Jensen, K. A., Meyer, S. S., Noerdlinger, P. D., Read, S. M., Rosen, L. P., Shafer, R. A., Wright, E. L., Bennett, C. L., Boggess,

N. W., Hauser, M. G., Kelsall, T., Moseley, Jr., S. H., Silverberg, R. F., Smoot, G. F., Weiss, R., and Wilkinson, D. T. (1994). Measurement of the cosmic microwave background spectrum by the COBE FIRAS instrument. *ApJ*, 420:439–444.

Matt, G., Fabian, A. C., Guainazzi, M., Iwasawa, K., Bassani, L., and Malaguti, G. (2000). The X-ray spectra of Compton-thick Seyfert 2 galaxies as seen by BeppoSAX. *MNRAS*, 318:173–179.

Matt, G. and Iwasawa, K. (2019). A receding torus model for the Iwasawa-Taniguchi effect for Compton-thick AGN. *MNRAS*, 482:151–153.

McHardy, I. M., Lawrence, A., Pye, J. P., and Pounds, K. A. (1981). The Ariel V /3 A/ catalogue of X-ray sources. II - Sources at high galactic latitude /absolute value of B greater than 10 deg/. *MNRAS*, 197:893–919.

Meléndez, M., Kraemer, S. B., Armentrout, B. K., Deo, R. P., Crenshaw, D. M., Schmitt, H. R., Mushotzky, R. F., Tueller, J., Markwardt, C. B., and Winter, L. (2008). New Indicators for AGN Power: The Correlation between [O IV] 25.89 μm and Hard X-Ray Luminosity for Nearby Seyfert Galaxies. *ApJ*, 682:94–103.

Merloni, A., Bongiorno, A., Bolzonella, M., Brusa, M., Civano, F., Comastri, A., Elvis, M., Fiore, F., Gilli, R., Hao, H., Jahnke, K., Koekemoer, A. M., Lusso, E., Mainieri, V., Mignoli, M., Miyaji, T., Renzini, A., Salvato, M., Silverman, J., Trump, J., Vignali, C., Zamorani, G., Capak, P., Lilly, S. J., Sanders, D., Taniguchi, Y., Bardelli, S., Carollo, C. M., Caputi, K., Contini, T., Coppa, G., Cucciati, O., de la Torre, S., de Ravel, L., Franzetti, P., Garilli, B., Hasinger, G., Impey, C., Iovino, A., Iwasawa, K., Kampczyk, P., Kneib, J. P., Knobel, C., Kovač, K., Lamareille, F., Le Borgne, J. F., Le Brun, V., Le Fèvre, O., Maier, C., Pello, R., Peng, Y., Perez Montero, E., Ricciardelli, E., Scodeggio, M., Tanaka, M., Tasca, L. A. M., Tresse, L., Vergani, D., and Zucca, E. (2010). On the Cosmic Evolution of the Scaling Relations Between Black Holes and Their Host Galaxies: Broad-Line Active Galactic Nuclei in the zCOSMOS Survey. *ApJ*, 708(1):137–157.

Merloni, A., Bongiorno, A., Brusa, M., Iwasawa, K., Mainieri, V., Magnelli, B., Salvato, M., Berta, S., Cappelluti, N., Comastri, A., Fiore, F., Gilli, R., Koekemoer, A., Le Floc'h, E., Lusso, E., Lutz, D., Miyaji, T., Pozzi, F., Riguccini, L., Rosario, D. J., Silverman, J., Symeonidis, M., Treister, E., Vignali, C., and Zamorani, G. (2014). The incidence of obscuration in active galactic nuclei. *MNRAS*, 437:3550–3567.

Merloni, A. and Heinz, S. (2008). A synthesis model for AGN evolution: supermassive black holes growth and feedback modes. *MNRAS*, 388(3):1011–1030.

Merloni, A., Predehl, P., Becker, W., Böhringer, H., Boller, T., Brunner, H., Brusa, M., Dennerl, K., Freyberg, M., Friedrich, P., Georgakakis, A., Haberl, F., Hasinger, G., Meidinger, N., Mohr, J., Nandra, K., Rau, A., Reiprich, T. H., Robrade, J., Salvato, M., Santangelo, A., Sasaki, M., Schwope, A., Wilms, J., and German eROSITA Consortium, t. (2012). eROSITA Science Book: Mapping the Structure of the Energetic Universe. *arXiv e-prints*, page arXiv:1209.3114.

Mineo, S., Gilfanov, M., and Sunyaev, R. (2012). X-ray emission from star-forming galaxies - II. Hot interstellarmedium. *MNRAS*, 426:1870–1883.

Miyazawa, T., Haba, Y., and Kunieda, H. (2009). Broad-Band Temporal and Spectral Variation of 36 Active Galactic Nuclei Observed with Suzaku. *PASJ*, 61:1331–1354.

Moran, E. C., Filippenko, A. V., and Chornock, R. (2002). "Hidden" Seyfert 2 Galaxies and the X-Ray Background. *ApJ*, 579:L71–L74.

Mullaney, J. R., Alexander, D. M., Goulding, A. D., and Hickox, R. C. (2011). Defining the intrinsic AGN infrared spectral energy distribution and measuring its contribution to the infrared output of composite galaxies. *MNRAS*, 414:1082–1110.

Murphy, E. J., Chary, R.-R., Dickinson, M., Pope, A., Frayer, D. T., and Lin, L. (2011). An Accounting of the Dust-obscured Star Formation and Accretion Histories Over the Last ˜11 Billion Years. *ApJ*, 732:126.

Murphy, K. D. and Yaqoob, T. (2009). An X-ray spectral model for Compton-thick toroidal reprocessors. *MNRAS*, 397:1549–1562.

Mushotzky, R. F., Cowie, L. L., Barger, A. J., and Arnaud, K. A. (2000). Resolving the extragalactic hard X-ray background. *Nature*, 404:459–464.

Nandra, K., Barret, D., Barcons, X., Fabian, A., den Herder, J.-W., Piro, L., Watson, M., Adami, C., Aird, J., Afonso, J. M., and et al. (2013). The Hot and Energetic Universe: A White Paper presenting the science theme motivating the Athena+ mission. *ArXiv e-prints*.

Nandra, K., O'Neill, P. M., George, I. M., and Reeves, J. N. (2007). An XMM-Newton survey of broad iron lines in Seyfert galaxies. *MNRAS*, 382:194–228.

Nenkova, M., Sirocky, M. M., Nikutta, R., Ivezić, Ž., and Elitzur, M. (2008). AGN Dusty Tori. II. Observational Implications of Clumpiness. *ApJ*, 685:160–180.

Netzer, H. (2015). Revisiting the Unified Model of Active Galactic Nuclei. *ARA&A*, 53:365–408.

Neugebauer, G., Habing, H. J., van Duinen, R., Aumann, H. H., Baud, B., Beichman, C. A., Beintema, D. A., Boggess, N., Clegg, P. E., de Jong, T., Emerson, J. P., Gautier, T. N., Gillett, F. C., Harris, S., Hauser, M. G., Houck, J. R., Jennings, R. E., Low, F. J., Marsden, P. L., Miley, G., Olnon, F. M., Pottasch, S. R., Raimond, E., Rowan-Robinson, M., Soifer, B. T., Walker, R. G., Wesselius, P. R., and Young, E. (1984). The Infrared Astronomical Satellite (IRAS) mission. *ApJ*, 278:L1–L6.

Norris, R. P., Hopkins, A. M., Afonso, J., Brown, S., Condon, J. J., Dunne, L., Feain, I., Hollow, R., Jarvis, M., Johnston-Hollitt, M., Lenc, E., Middelberg, E., Padovani, P., Prandoni, I., Rudnick, L., Seymour, N., Umana, G., Andernach, H., Alexander, D. M., Appleton, P. N., Bacon, D., Banfield, J., Becker, W., Brown, M. J. I., Ciliegi, P., Jackson, C., Eales, S., Edge, A. C., Gaensler, B. M., Giovannini, G., Hales, C. A., Hancock, P., Huynh, M. T., Ibar, E., Ivison, R. J., Kennicutt, R., Kimball, A. E., Koekemoer, A. M., Koribalski, B. S., López-Sánchez, Á. R., Mao, M. Y., Murphy, T., Messias, H., Pimbblet, K. A., Raccanelli, A., Randall, K. E., Reiprich, T. H., Roseboom, I. G., Röttgering, H., Saikia, D. J., Sharp, R. G., Slee, O. B., Smail, I., Thompson, M. A., Urquhart, J. S., Wall, J. V., and Zhao, G. B. (2011). EMU: Evolutionary Map of the Universe. *PASA*, 28(3):215–248.

Odaka, H., Yoneda, H., Takahashi, T., and Fabian, A. (2016). Sensitivity of the Fe Kα Compton shoulder to the geometry and variability of the X-ray illumination of cosmic objects. *MNRAS*, 462(3):2366–2381.

Oh, K., Koss, M., Markwardt, C. B., Schawinski, K., Baumgartner, W. H., Barthelmy, S. D., Cenko, S. B., Gehrels, N., Mushotzky, R., Petulante, A., Ricci, C., Lien, A., and Trakhtenbrot, B. (2018). The 105-Month Swift-BAT All-sky Hard X-Ray Survey. *ApJS*, 235:4.

Orr, M. J. L. and Browne, I. W. A. (1982). Relativistic beaming and quasar statistics. *MNRAS*, 200:1067–1080.

Osterbrock, D. E. (1981). Seyfert galaxies with weak broad H alpha emission lines. *ApJ*, 249:462–470.

Osterbrock, D. E. and Pogge, R. W. (1985). The spectra of narrow-line Seyfert 1 galaxies. *ApJ*, 297:166–176.

Packham, C., Radomski, J. T., Roche, P. F., Aitken, D. K., Perlman, E., Alonso-Herrero, A., Colina, L., and Telesco, C. M. (2005). The Extended Mid-Infrared Structure of the Circinus Galaxy. *ApJ*, 618(1):L17–L20.

Padovani, P., Alexander, D. M., Assef, R. J., De Marco, B., Giommi, P., Hickox, R. C., Richards, G. T., Smolčić, V., Hatziminaoglou, E., Mainieri, V., and Salvato, M. (2017). Active galactic nuclei: what's in a name? *A&A Rev.*, 25(1):2.

Page, K. L., O'Brien, P. T., Reeves, J. N., and Turner, M. J. L. (2004). An X-ray Baldwin effect for the narrow Fe Kα lines observed in active galactic nuclei. *MNRAS*, 347:316–322.

Panessa, F., Baldi, R. D., Laor, A., Padovani, P., Behar, E., and McHardy, I. (2019). The Origin of Radio Emission from Radio-Quiet AGN. *arXiv e-prints*, page arXiv:1902.05917.

Panessa, F., Bassani, L., Cappi, M., Dadina, M., Barcons, X., Carrera, F. J., Ho, L. C., and Iwasawa, K. (2006). On the X-ray, optical emission line and black hole mass properties of local Seyfert galaxies. *A&A*, 455:173–185.

Panessa, F., Bassani, L., Landi, R., Bazzano, A., Dallacasa, D., La Franca, F., Malizia, A., Venturi, T., and Ubertini, P. (2016). The column density distribution of hard X-ray radio galaxies. *MNRAS*, 461:3153–3164.

Parker, M. L., Pinto, C., Fabian, A. C., Lohfink, A., Buisson, D. J. K., Alston, W. N., Kara, E., Cackett, E. M., Chiang, C.-Y., Dauser, T., De Marco, B., Gallo, L. C., Garcia, J., Harrison, F. A., King, A. L., Middleton, M. J., Miller, J. M., Miniutti, G., Reynolds, C. S., Uttley, P., Vasudevan, R., Walton, D. J., Wilkins, D. R., and Zoghbi, A. (2017). The response of relativistic outflowing gas to the inner accretion disk of a black hole. *Nature*, 543:83–86.

Penzias, A. A. and Wilson, R. W. (1965). A Measurement of Excess Antenna Temperature at 4080 Mc/s. *ApJ*, 142:419–421.

Peterson, B. M. (1997). *An Introduction to Active Galactic Nuclei*. University of Cambridge.

Petre, R. and Serlemitsos, P. J. (1985). The Broad Band X-ray telescope. Space Sci. Rev., 40:707–713.

Piconcelli, E., Jimenez-Bailón, E., Guainazzi, M., Schartel, N., Rodríguez-Pascual, P. M., and Santos-Lleó, M. (2005). The XMM-Newton view of PG quasars. I. X-ray continuum and absorption. *A&A*, 432:15–30.

Planck Collaboration (2014). Planck 2013 results. XVI. Cosmological parameters. *A&A*, 571:A16.

Polletta, M., Tajer, M., Maraschi, L., Trinchieri, G., Lonsdale, C. J., Chiappetti, L., Andreon, S., Pierre, M., Le Fèvre, O., Zamorani, G., Maccagni, D., Garcet, O., Surdej, J., Franceschini, A., Alloin, D., Shupe, D. L., Surace, J. A., Fang, F., Rowan-Robinson, M., Smith, H. E., and Tresse, L. (2007). Spectral Energy Distributions of Hard X-Ray Selected Active Galactic Nuclei in the XMM-Newton Medium Deep Survey. *ApJ*, 663:81–102.

Ptak, A., Hornschemeier, A., Zezas, A., Lehmer, B., Yukita, M., Wik, D., Antoniou, V., Argo, M. K., Ballo, L., Bechtol, K., Boggs, S., Della Ceca, R., Christensen, F. E., Craig, W. W., Hailey, C. J., Harrison, F. A., Krivonos, R., Maccarone, T. J., Stern, D., Tatum, M., Venters, T., and Zhang, W. W. (2015). A Focused, Hard X-Ray Look at Arp 299 with NuSTAR. *ApJ*, 800:104.

Puccetti, S., Comastri, A., Bauer, F. E., Brandt, W. N., Fiore, F., Harrison, F. A., Luo, B., Stern, D., Urry, C. M., Alexander, D. M., Annuar, A., Arévalo, P., Baloković, M., Boggs, S. E., Brightman, M., Christensen, F. E., Craig, W. W., Gandhi, P., Hailey, C. J., Koss, M. J., La Massa, S., Marinucci, A., Ricci, C., Walton, D. J., Zappacosta, L., and Zhang, W. (2016). Hard X-ray emission of the luminous infrared galaxy NGC 6240 as observed by NuSTAR. *A&A*, 585:A157.

Puccetti, S., Comastri, A., Fiore, F., Arévalo, P., Risaliti, G., Bauer, F. E., Brandt, W. N., Stern, D., Harrison, F. A., Alexander, D. M., Boggs, S. E., Christensen, F. E., Craig, W. W., Gandhi, P., Hailey, C. J., Koss, M. J., Lansbury, G. B., Luo, B., Madejski, G. M., Matt, G., Walton, D. J., and Zhang, W. (2014). The Variable Hard X-Ray Emission of NGC 4945 as Observed by NuSTAR. *ApJ*, 793:26.

Ramos Almeida, C. and Ricci, C. (2017). Nuclear obscuration in active galactic nuclei. *Nature Astronomy*, 1:679–689.

Reynolds, C., Ueda, Y., Awaki, H., Gallo, L., Gandhi, P., Haba, Y., Kawamuro, T., LaMassa, S., Lohfink, A., Ricci, C., Tazaki, F., Zoghbi, A., and on behalf of the ASTRO-H Science Working Group (2014). ASTRO-H White Paper - AGN Reflection. *ArXiv e-prints*.

Reynolds, C. S. (1999). Compton Reflection and Iron Fluorescence in Active Galactic Nuclei and Galactic Black Hole Candidates. In Poutanen, J. and Svensson, R., editors, *High Energy Processes in Accreting Black Holes*, volume 161 of *Astronomical Society of the Pacific Conference Series*, page 178.

Ricci, C., Assef, R. J., Stern, D., Nikutta, R., Alexander, D. M., Asmus, D., Ballantyne, D. R., Bauer, F. E., Blain, A. W., Boggs, S., Boorman, P. G., Brandt, W. N., Brightman, M., Chang, C. S., Chen, C.-T. J., Christensen, F. E., Comastri, A., Craig,

W. W., Díaz-Santos, T., Eisenhardt, P. R., Farrah, D., Gandhi, P., Hailey, C. J., Harrison, F. A., Jun, H. D., Koss, M. J., LaMassa, S., Lansbury, G. B., Markwardt, C. B., Stalevski, M., Stanley, F., Treister, E., Tsai, C.-W., Walton, D. J., Wu, J. W., Zappacosta, L., and Zhang, W. W. (2017a). NuSTAR Observations of WISE J1036+0449, a Galaxy at z˜1 Obscured by Hot Dust. *ApJ*, 835:105.

Ricci, C., Bauer, F. E., Arevalo, P., Boggs, S., Brandt, W. N., Christensen, F. E., Craig, W. W., Gandhi, P., Hailey, C. J., Harrison, F. A., Koss, M., Markwardt, C. B., Stern, D., Treister, E., and Zhang, W. W. (2016). IC 751: A New Changing Look AGN Discovered by NuSTAR. *ApJ*, 820:5.

Ricci, C., Bauer, F. E., Treister, E., Schawinski, K., Privon, G. C., Blecha, L., Arevalo, P., Armus, L., Harrison, F., Ho, L. C., Iwasawa, K., Sanders, D. B., and Stern, D. (2017b). Growing supermassive black holes in the late stages of galaxy mergers are heavily obscured. *MNRAS*, 468:1273–1299.

Ricci, C., Ho, L. C., Fabian, A. C., Trakhtenbrot, B., Koss, M. J., Ueda, Y., Lohfink, A., Shimizu, T., Bauer, F. E., Mushotzky, R., Schawinski, K., Paltani, S., Lamperti, I., Treister, E., and Oh, K. (2018). BAT AGN Spectroscopic Survey - XII. The relation between coronal properties of active galactic nuclei and the Eddington ratio. *MNRAS*, 480(2):1819–1830.

Ricci, C., Paltani, S., Awaki, H., Petrucci, P.-O., Ueda, Y., and Brightman, M. (2013a). Luminosity-dependent unification of active galactic nuclei and the X-ray Baldwin effect. *A&A*, 553:A29.

Ricci, C., Paltani, S., Ueda, Y., and Awaki, H. (2013b). On the role of the Γ - λ_{Edd} relation on the X-ray Baldwin effect in active galactic nuclei. *MNRAS*, 435:1840–1851.

Ricci, C., Trakhtenbrot, B., Koss, M. J., Ueda, Y., Del Vecchio, I., Treister, E., Schawinski, K., Paltani, S., Oh, K., Lamperti, I., Berney, S., Gandhi, P., Ichikawa, K., Bauer, F. E., Ho, L. C., Asmus, D., Beckmann, V., Soldi, S., Baloković, M., Gehrels, N., and Markwardt, C. B. (2017c). BAT AGN Spectroscopic Survey. V. X-Ray Properties of the Swift/BAT 70-month AGN Catalog. *ApJS*, 233:17.

Ricci, C., Trakhtenbrot, B., Koss, M. J., Ueda, Y., Schawinski, K., Oh, K., Lamperti, I., Mushotzky, R., Treister, E., Ho, L. C., Weigel, A., Bauer, F. E., Paltani, S., Fabian, A. C., Xie, Y., and Gehrels, N. (2017d). The close environments of accreting massive black holes are shaped by radiative feedback. *Nature*, 549(7673):488–491.

Ricci, C., Ueda, Y., Koss, M. J., Trakhtenbrot, B., Bauer, F. E., and Gandhi, P. (2015). Compton-thick Accretion in the Local Universe. *ApJ*, 815:L13.

Ricci, C., Ueda, Y., Paltani, S., Ichikawa, K., Gandhi, P., and Awaki, H. (2014). Iron Kα emission in type-I and type-II active galactic nuclei. *MNRAS*, 441:3622–3633.

Rigby, J. R., Diamond-Stanic, A. M., and Aniano, G. (2009). Calibration Of [O IV] 26 μm as a Measure of Intrinsic Active Galactic Nucleus Luminosity. *ApJ*, 700:1878–1883.

Risaliti, G., Bassani, L., Comastri, A., Dadina, M., Della Ceca, R., Gilli, R., Maiolino, R., Matt, G., Salvati, M., and Zamorani, G. (1999a). X-ray observations of Seyfert 2 galaxies: N_H distribution and the X ray background. Mem. Soc. Astron. Italiana, 70:73–76.

Risaliti, G., Elvis, M., Fabbiano, G., Baldi, A., Zezas, A., and Salvati, M. (2007). Occultation Measurement of the Size of the X-Ray-emitting Region in the Active Galactic Nucleus of NGC 1365. *ApJ*, 659:L111–L114.

Risaliti, G., Harrison, F. A., Madsen, K. K., Walton, D. J., Boggs, S. E., Christensen, F. E., Craig, W. W., Grefenstette, B. W., Hailey, C. J., Nardini, E., Stern, D., and Zhang, W. W. (2013). A rapidly spinning supermassive black hole at the centre of NGC 1365. *Nature*, 494:449–451.

Risaliti, G., Maiolino, R., and Salvati, M. (1999b). The Distribution of Absorbing Column Densities among Seyfert 2 Galaxies. *ApJ*, 522:157–164.

Risaliti, G., Young, M., and Elvis, M. (2009). The Sloan Digital Sky Survey/XMM-Newton Quasar Survey: Correlation Between X-Ray Spectral Slope and Eddington Ratio. *ApJ*, 700:L6–L10.

Rivers, E., Baloković, M., Arévalo, P., Bauer, F. E., Boggs, S. E., Brandt, W. N., Brightman, M., Christensen, F. E., Craig, W. W., Gandhi, P., Hailey, C. J., Harrison, F., Koss, M., Ricci, C., Stern, D., Walton, D. J., and Zhang, W. W. (2015). The NuSTAR View of Reflection and Absorption in NGC 7582. *ApJ*, 815:55.

Rush, B., Malkan, M. A., and Spinoglio, L. (1993). The Extended 12 Micron Galaxy Sample. *ApJS*, 89:1.

Schawinski, K., Thomas, D., Sarzi, M., Maraston, C., Kaviraj, S., Joo, S.-J., Yi, S. K., and Silk, J. (2007). Observational evidence for AGN feedback in early-type galaxies. *MNRAS*, 382:1415–1431.

Schmidt, M. (1963). 3C 273 : A Star-Like Object with Large Red-Shift. *Nature*, 197(4872):1040.

Setti, G. and Woltjer, L. (1989). Active Galactic Nuclei and the spectrum of the X-ray background. *A&A*, 224:L21–L23.

Seyfert, C. K. (1943). Nuclear Emission in Spiral Nebulae. *ApJ*, 97:28.

Shakura, N. I. and Sunyaev, R. A. (1973). Black holes in binary systems. Observational appearance. *A&A*, 24:337–355.

Shemmer, O., Brandt, W. N., Netzer, H., Maiolino, R., and Kaspi, S. (2006). The Hard X-Ray Spectral Slope as an Accretion Rate Indicator in Radio-quiet Active Galactic Nuclei. *ApJ*, 646:L29–L32.

Shu, X. W., Wang, J. X., Yaqoob, T., Jiang, P., and Zhou, Y. Y. (2012). On the X-Ray Baldwin Effect in Active Galactic Nuclei Observed by the Chandra High-energy Grating. *ApJ*, 744:L21.

Shu, X. W., Yaqoob, T., and Wang, J. X. (2011). Chandra High-energy Grating Observations of the Fe Kα Line Core in Type II Seyfert Galaxies: A Comparison with Type I Nuclei. *ApJ*, 738:147.

Simpson, C. (2005). The luminosity dependence of the type 1 active galactic nucleus fraction. *MNRAS*, 360(2):565–572.

Singh, V., Shastri, P., Ishwara-Chandra, C. H., and Athreya, R. (2013). Low-frequency radio observations of Seyfert galaxies: A test of the unification scheme. *A&A*, 554:A85.

Slipher, V. M. (1917). The spectrum and velocity of the nebula N.G.C. 1068 (M 77). *Lowell Observatory Bulletin*, 3:59–62.

Smith, R. K., Brickhouse, N. S., Liedahl, D. A., and Raymond, J. C. (2001). Collisional Plasma Models with APEC/APED: Emission-Line Diagnostics of Hydrogen-like and Helium-like Ions. *ApJ*, 556:L91–L95.

Sołtan, A. (1982). Masses of quasars. *MNRAS*, 200:115–122.

Stalevski, M., Asmus, D., and Tristram, K. R. W. (2017). Dissecting the active galactic nucleus in Circinus - I. Peculiar mid-IR morphology explained by a dusty hollow cone. *MNRAS*, 472:3854–3870.

Stern, D. (2015). The X-Ray to Mid-infrared Relation of AGNs at High Luminosity. *ApJ*, 807:129.

Stern, D., Assef, R. J., Benford, D. J., Blain, A., Cutri, R., Dey, A., Eisenhardt, P., Griffith, R. L., Jarrett, T. H., Lake, S., Masci, F., Petty, S., Stanford, S. A., Tsai, C.-W., Wright, E. L., Yan, L., Harrison, F., and Madsen, K. (2012). Mid-infrared Selection of Active Galactic Nuclei with the Wide-Field Infrared Survey Explorer. I. Characterizing WISE-selected Active Galactic Nuclei in COSMOS. *ApJ*, 753:30.

Tasnim Ananna, T., Treister, E., Urry, C. M., Ricci, C., Kirkpatrick, A., LaMassa, S., Buchner, J., and Tremmel, M. (2018). The Accretion History of AGN I: Supermassive Black Hole Population Synthesis Model. *ArXiv e-prints*.

Teng, S. H., Brandt, W. N., Harrison, F. A., Luo, B., Alexander, D. M., Bauer, F. E., Boggs, S. E., Christensen, F. E., Comastri, A., Craig, W. W., Fabian, A. C., Farrah, D., Fiore, F., Gandhi, P., Grefenstette, B. W., Hailey, C. J., Hickox, R. C., Madsen, K. K., Ptak, A. F., Rigby, J. R., Risaliti, G., Saez, C., Stern, D., Veilleux, S., Walton, D. J., Wik, D. R., and Zhang, W. W. (2014). NuSTAR Reveals an Intrinsically X-Ray Weak Broad Absorption Line Quasar in the Ultraluminous Infrared Galaxy Markarian 231. *ApJ*, 785:19.

Trakhtenbrot, B., Ricci, C., Koss, M. J., Schawinski, K., Mushotzky, R., Ueda, Y., Veilleux, S., Lamperti, I., Oh, K., Treister, E., Stern, D., Harrison, F., Baloković, M., and Gehrels, N. (2017). BAT AGN Spectroscopic Survey (BASS) - VI. The Γ_X-L/L_{Edd} relation. *MNRAS*, 470:800–814.

Treister, E., Krolik, J. H., and Dullemond, C. (2008). Measuring the Fraction of Obscured Quasars by the Infrared Luminosity of Unobscured Quasars. *ApJ*, 679(1):140–148.

Treister, E., Urry, C. M., and Virani, S. (2009). The Space Density of Compton-Thick Active Galactic Nucleus and the X-Ray Background. *ApJ*, 696:110–120.

Ueda, Y., Akiyama, M., Hasinger, G., Miyaji, T., and Watson, M. G. (2014). Toward the Standard Population Synthesis Model of the X-Ray Background: Evolution of X-Ray Luminosity and Absorption Functions of Active Galactic Nuclei Including Compton-thick Populations. *ApJ*, 786:104.

Ueda, Y., Akiyama, M., Ohta, K., and Miyaji, T. (2003). Cosmological Evolution of the Hard X-Ray Active Galactic Nucleus Luminosity Function and the Origin of the Hard X-Ray Background. *ApJ*, 598:886–908.

Ueda, Y., Hashimoto, Y., Ichikawa, K., Ishino, Y., Kniazev, A. Y., Väisänen, P., Ricci, C., Berney, S., Gandhi, P., Koss, M., Mushotzky, R., Terashima, Y., Trakhtenbrot, B., and Crenshaw, M. (2015). [O iii] λ5007 and X-Ray Properties of a Complete Sample of Hard X-Ray Selected AGNs in the Local Universe. *ApJ*, 815:1.

Ueda, Y., Hiroi, K., Isobe, N., Hayashida, M., Eguchi, S., Sugizaki, M., Kawai, N., Tsunemi, H., Mihara, T., Matsuoka, M., Ishikawa, M., Kimura, M., Kitayama, H., Kohama, M., Matsumura, T., Morii, M., Nakagawa, Y. E., Nakahira, S., Nakajima, M., Negoro, H., Serino, M., Shidatsu, M., Sootome, T., Sugimori, K., Suwa, F., Toizumi,

T., Tomida, H., Tsuboi, Y., Ueno, S., Usui, R., Yamamoto, T., Yamaoka, K., Yamazaki, K., and Yoshida, A. (2011). Revisit of Local X-Ray Luminosity Function of Active Galactic Nuclei with the MAXI Extragalactic Survey. *PASJ*, 63:S937–S945.

Urry, C. M. and Padovani, P. (1995). Unified Schemes for Radio-Loud Active Galactic Nuclei. *PASP*, 107:803.

van Haarlem, M. P., Wise, M. W., Gunst, A. W., Heald, G., McKean, J. P., Hessels, J. W. T., de Bruyn, A. G., Nijboer, R., Swinbank, J., Fallows, R., Brentjens, M., Nelles, A., Beck, R., Falcke, H., Fender, R., Hörandel, J., Koopmans, L. V. E., Mann, G., Miley, G., Röttgering, H., Stappers, B. W., Wijers, R. A. M. J., Zaroubi, S., van den Akker, M., Alexov, A., Anderson, J., Anderson, K., van Ardenne, A., Arts, M., Asgekar, A., Avruch, I. M., Batejat, F., Bähren, L., Bell, M. E., Bell, M. R., van Bemmel, I., Bennema, P., Bentum, M. J., Bernardi, G., Best, P., Bîrzan, L., Bonafede, A., Boonstra, A. J., Braun, R., Bregman, J., Breitling, F., van de Brink, R. H., Broderick, J., Broekema, P. C., Brouw, W. N., Brüggen, M., Butcher, H. R., van Cappellen, W., Ciardi, B., Coenen, T., Conway, J., Coolen, A., Corstanje, A., Damstra, S., Davies, O., Deller, A. T., Dettmar, R. J., van Diepen, G., Dijkstra, K., Donker, P., Doorduin, A., Dromer, J., Drost, M., van Duin, A., Eislöffel, J., van Enst, J., Ferrari, C., Frieswijk, W., Gankema, H., Garrett, M. A., de Gasperin, F., Gerbers, M., de Geus, E., Grießmeier, J. M., Grit, T., Gruppen, P., Hamaker, J. P., Hassall, T., Hoeft, M., Holties, H. A., Horneffer, A., van der Horst, A., van Houwelingen, A., Huijgen, A., Iacobelli, M., Intema, H., Jackson, N., Jelic, V., de Jong, A., Juette, E., Kant, D., Karastergiou, A., Koers, A., Kollen, H., Kondratiev, V. I., Kooistra, E., Koopman, Y., Koster, A., Kuniyoshi, M., Kramer, M., Kuper, G., Lambropoulos, P., Law, C., van Leeuwen, J., Lemaitre, J., Loose, M., Maat, P., Macario, G., Markoff, S., Masters, J., McFadden, R. A., McKay-Bukowski, D., Meijering, H., Meulman, H., Mevius, M., Middelberg, E., Millenaar, R., Miller-Jones, J. C. A., Mohan, R. N., Mol, J. D., Morawietz, J., Morganti, R., Mulcahy, D. D., Mulder, E., Munk, H., Nieuwenhuis, L., van Nieuwpoort, R., Noordam, J. E., Norden, M., Noutsos, A., Offringa, A. R., Olofsson, H., Omar, A., Orrú, E., Overeem, R., Paas, H., Pand ey-Pommier, M., Pandey, V. N., Pizzo, R., Polatidis, A., Rafferty, D., Rawlings, S., Reich, W., de Reijer, J. P., Reitsma, J., Renting, G. A., Riemers, P., Rol, E., Romein, J. W., Roosjen, J., Ruiter, M., Scaife, A., van der Schaaf, K., Scheers, B., Schellart, P., Schoenmakers, A., Schoonderbeek, G., Serylak, M., Shulevski, A., Sluman, J., Smirnov, O., Sobey, C., Spreeuw, H., Steinmetz, M., Sterks, C. G. M., Stiepel, H. J., Stuurwold, K., Tagger, M., Tang, Y., Tasse, C., Thomas, I., Thoudam, S., Toribio, M. C., van der Tol, B., Usov, O., van Veelen, M., van der Veen, A. J., ter Veen, S., Verbiest, J. P. W., Vermeulen, R., Vermaas, N., Vocks, C., Vogt, C., de Vos, M., van der Wal, E., van Weeren, R., Weggemans, H., Weltevrede, P., White, S.,

Wijnholds, S. J., Wilhelmsson, T., Wucknitz, O., Yatawatta, S., Zarka, P., Zensus, A., and van Zwieten, J. (2013). LOFAR: The LOw-Frequency ARray. *A&A*, 556:A2.

Vasudevan, R. V., Fabian, A. C., Gandhi, P., Winter, L. M., and Mushotzky, R. F. (2010). The power output of local obscured and unobscured AGN: crossing the absorption barrier with Swift/BAT and IRAS. *MNRAS*, 402:1081–1098.

Vasudevan, R. V., Fabian, A. C., Reynolds, C. S., Aird, J., Dauser, T., and Gallo, L. C. (2016). A selection effect boosting the contribution from rapidly spinning black holes to the cosmic X-ray background. *MNRAS*, 458:2012–2023.

Veilleux, S. and Osterbrock, D. E. (1987). Spectral classification of emission-line galaxies. *ApJS*, 63:295–310.

Véron-Cetty, M.-P. and Véron, P. (2010). A catalogue of quasars and active nuclei: 13th edition. *A&A*, 518:A10.

Villarroel, B., Nyholm, A., Karlsson, T., Comerón, S., Korn, A. J., Sollerman, J., and Zackrisson, E. (2017). AGN Luminosity and Stellar Age: Two Missing Ingredients for AGN Unification as Seen with iPTF Supernovae. *ApJ*, 837:110.

Vito, F., Brandt, W. N., Stern, D., Assef, R. J., Chen, C.-T. J., Brightman, M., Comastri, A., Eisenhardt, P., Garmire, G. P., Hickox, R., Lansbury, G., Tsai, C.-W., Walton, D. J., and Wu, J. W. (2018). Heavy X-ray obscuration in the most luminous galaxies discovered by WISE. *MNRAS*, 474:4528–4540.

Vito, F., Gilli, R., Vignali, C., Comastri, A., Brusa, M., Cappelluti, N., and Iwasawa, K. (2014). The hard X-ray luminosity function of high-redshift ($3 < z \lesssim 5$) active galactic nuclei. *MNRAS*, 445:3557–3574.

Wachter, K., Leach, R., and Kellogg, E. (1979). Parameter estimation in X-ray astronomy using maximum likelihood. *ApJ*, 230:274–287.

Walton, D. J., Risaliti, G., Harrison, F. A., Fabian, A. C., Miller, J. M., Arevalo, P., Ballantyne, D. R., Boggs, S. E., Brenneman, L. W., Christensen, F. E., Craig, W. W., Elvis, M., Fuerst, F., Gandhi, P., Grefenstette, B. W., Hailey, C. J., Kara, E., Luo, B., Madsen, K. K., Marinucci, A., Matt, G., Parker, M. L., Reynolds, C. S., Rivers, E., Ross, R. R., Stern, D., and Zhang, W. W. (2014). NuSTAR and XMM-NEWTON Observations of NGC 1365: Extreme Absorption Variability and a Constant Inner Accretion Disk. *ApJ*, 788:76.

Wilkes, B. J., Kuraszkiewicz, J., Haas, M., Barthel, P., Leipski, C., Willner, S. P., Worrall, D. M., Birkinshaw, M., Antonucci, R., Ashby, M. L. N., Chini, R., Fazio, G. G., Lawrence, C., Ogle, P., and Schulz, B. (2013). Revealing the Heavily Obscured

Active Galactic Nucleus Population of High-redshift 3CRR Sources with Chandra X-Ray Observations. *ApJ*, 773(1):15.

Wright, E. L., Eisenhardt, P. R. M., Mainzer, A. K., Ressler, M. E., Cutri, R. M., Jarrett, T., Kirkpatrick, J. D., Padgett, D., McMillan, R. S., Skrutskie, M., Stanford, S. A., Cohen, M., Walker, R. G., Mather, J. C., Leisawitz, D., Gautier, III, T. N., McLean, I., Benford, D., Lonsdale, C. J., Blain, A., Mendez, B., Irace, W. R., Duval, V., Liu, F., Royer, D., Heinrichsen, I., Howard, J., Shannon, M., Kendall, M., Walsh, A. L., Larsen, M., Cardon, J. G., Schick, S., Schwalm, M., Abid, M., Fabinsky, B., Naes, L., and Tsai, C.-W. (2010). The Wide-field Infrared Survey Explorer (WISE): Mission Description and Initial On-orbit Performance. *AJ*, 140:1868–1881.

Wu, J., Tsai, C.-W., Sayers, J., Benford, D., Bridge, C., Blain, A., Eisenhardt, P. R. M., Stern, D., Petty, S., Assef, R., Bussmann, S., Comerford, J. M., Cutri, R., Evans, II, N. J., Griffith, R., Jarrett, T., Lake, S., Lonsdale, C., Rho, J., Stanford, S. A., Weiner, B., Wright, E. L., and Yan, L. (2012). Submillimeter Follow-up of WISE-selected Hyperluminous Galaxies. *ApJ*, 756:96.

Wu, Y., Charmandaris, V., Huang, J., Spinoglio, L., and Tommasin, S. (2009). Spitzer/IRS 5-35 μm Low-resolution Spectroscopy of the 12 μm Seyfert Sample. *ApJ*, 701:658–676.

Yang, H., Wang, J., and Liu, T. (2015). On the Anisotropy of Nuclei Mid-Infrared Radiation in Nearby Active Galactic Nuclei. *ApJ*, 799:91.

Yaqoob, T. (2012). The nature of the Compton-thick X-ray reprocessor in NGC 4945. *MNRAS*, 423:3360–3396.

Yaqoob, T., Murphy, K. D., Miller, L., and Turner, T. J. (2010). On the efficiency of production of the Fe Kα emission line in neutral matter. *MNRAS*, 401:411–417.

Zoghbi, A., Fabian, A. C., Reynolds, C. S., and Cackett, E. M. (2012). Relativistic iron K X-ray reverberation in NGC 4151. *MNRAS*, 422(1):129–134.

Zou, F., Yang, G., Brandt, W. N., and Xue, Y. (2019). The Host-Galaxy Properties of Type 1 Versus Type 2 Active Galactic Nuclei. *arXiv e-prints*, page arXiv:1904.13286.